Systems Biology of Bacterial Immune Systems: Regulation of Restriction-Modification and CRISPR-Cas Systems

Check for updates

Andjela Rodic, Bojana Blagojevic, and Marko Djordjevic

Contents

Abstract Restriction-modification (R-M) and CRISPR-Cas are bacterial immune systems which defend their prokaryotic hosts from invasive DNA. Understanding how these systems are regulated is necessary for both biotechnology applications, and for understanding how they modulate horizontal gene transfer (including acquisition of virulence factors). We here review results on modeling these systems which point to common general principles underlying their architecture and dynamical response, with particular emphasis on modeling methods. We show that the modeling predictions are in a good agreement with both in vitro measurements

A. Rodic
Institute of Physiology and Biochemistry, Faculty of Biology, University of Belgrade, Belgrade, Serbia

Multidisciplinary PhD program in Biophysics, University of Belgrade, Belgrade, Serbia

M. Djordjevic (✉)
Institute of Physiology and Biochemistry, Faculty of Biology, University of Belgrade, Belgrade, Serbia
e-mail: dmarko@bio.bg.ac.rs

B. Blagojevic
Institute of Physics, University of Belgrade, Belgrade, Serbia

of promoter transcription activity and the first in vivo measurements of gene expression dynamics in R-M systems. Modeling induction of CRISPR-Cas systems is challenging, as signaling which leads to their activation is currently unknown. However, based on similarities between transcription regulation in CRISPR-Cas and some R-M systems, we argue that transcription regulation of much simpler (and better studied) R-M systems can be used as a proxy for CRISPR-Cas transcription regulation, allowing to in silico assess CRISPR-Cas dynamical properties. Based on the obtained results, we propose that mechanistically otherwise different bacterial immune systems, presumably due to a common function, share the same unifying principles governing their expression dynamics.

Keywords Thermodynamic modeling · Restriction-modification systems · CRISPR-Cas · Gene expression regulation · Regulatory dynamics

1 Introduction

Two types of prokaryotic "immune systems," known as restriction-modification (R-M) and CRISPR-Cas (*C*lustered, *r*egularly *i*nterspaced *s*hort *p*alindromic *r*epeats-*C*RISPR-*a*ssociated *p*roteins) systems, resemble the mammalian immune system in their ability to actively and with high selectivity combat infectious elements (foreign DNA) (Goldberg and Marraffini 2015). Apart from their immune function, these systems significantly influence evolution and ecology of prokaryotes in a number of ways and have a range of applications in biotechnology (Ershova et al. 2015; Hille and Charpentier 2016).

In type II R-M systems, which are often found on plasmids, separate genes code for two main system components: a restriction enzyme, which cuts specific DNA sequences, and a methyltransferase, which methylates the same sequences and thereby protects them from cutting (Nagornykh et al. 2008). It is widely considered that the main condition for safely and efficiently establishing an R-M system in a naïve host cell, is a delayed beginning of expression of restriction enzyme with respect to methyltransferase. This delay provides enough time for a methyltransferase to protect a host genome, so that restriction enzyme later targets only invasive DNA. Apart from this constraint on their dynamics imposed by their function, we propose other potentially common R-M system dynamical properties, and ask if these can be achieved by a wide variety of R-M systems architectures and regulatory features (Rodic et al. 2017b). These hypotheses are tested by analyzing dynamical properties of different R-M systems, predicted by biophysical models including thermodynamically modeled transcription regulation and dynamically modeled transcript and protein expression.

Unlike R-M systems, which are considered rudimentary for their lack of ability to memorize past infections, CRISPR-Cas are advanced, adaptive prokaryotic immune systems, which store partial DNA sequences of former infectors as spacers flanked by direct repeats in a so-called CRISPR array (Hille and Charpentier 2016). Another constitutive part of a CRISPR-Cas system are genes coding for Cas proteins. In Type

I-E CRISPR-Cas system in *E. coli*, which is a model system for studying CRISPR-Cas regulation, CRISPR array is transcribed as a long pre-crRNA molecule which is further cut by Cas6e protein into small crRNAs, containing separate spacers. These crRNAs guide Cascade complexes constituted of Cas proteins to complementary foreign DNA, which is consequently destroyed. Somewhat surprisingly, while CRISPR-Cas is extensively used for designing various biotechnological tools, its native function and regulation in bacterial cells are not well understood. In particular, CRISPR-Cas is silenced in *E. coli* cells under standard conditions, which hinders observing its expression dynamics (Pul et al. 2010). However, transcription regulation of this system involves general features similar to those found in certain R-M systems, which can be used to predict the main features of CRISPR-Cas expression dynamics (Rodic et al. 2017a).

In this chapter, we aim to explain how a thermodynamic model of a given promoter regulation is formulated, by briefly describing a theoretical basis of thermodynamic modeling and showing how this approach is applied on examples of R-M systems, AhdI and EcoRV. Further, thermodynamic modeling of transcription is used as an input for dynamic modeling, predicting appropriate protein expression in a cell in time, which is discussed on the example of Esp1396I R-M system, for which protein expression dynamics were experimentally measured. We also show how measures for dynamical properties of interest were defined to compare expression dynamics of different R-M systems and to propose unifying principles that characterize their regulatory dynamics. To in silico predict the main qualitative properties of CRISPR-Cas dynamics, and to understand the significance of few characteristic regulatory features found in CRISPR-Cas, we introduce the idea of using a synthetic setup where R-M system transcription regulation with similar features is used as a proxy for not–well understood CRISPR-Cas transcription regulation. Based on the obtained results, we propose that regulatory dynamics of CRISPR-Cas and R-M systems may be governed by similar design principles imposed by their immune function.

2 Thermodynamic Modeling of Transcription Regulation

Thermodynamic modeling approach of gene transcription control is based on principles of statistical mechanics. As an input it takes levels of transcription factors, and patterns and affinities of their binding sites, while as an output it provides predictions of promoter transcription activity (Dresch et al. 2013).

As regulation of transcription initiation, which is a rate-limiting step in gene transcription, involves binding of protein molecules (RNA polymerase, transcription factors) to DNA (promoter region), let us start with a simple scenario in which one molecule of protein, present in some copy number in a cell, binds to one binding site on DNA. From a thermodynamics point of view, the cell interior can be approximated by a system exchanging energy with a much larger heat reservoir (its surroundings) (Phillips et al. 2012). Protein molecules in this system, among

which energy is distributed, are approximated by noninteracting particles randomly moving in space confined to the cell volume. These particles can be arranged in a number of different ways, and every unique arrangement of particles corresponds to a particular *microstate* of the system. The probability of finding different microstates is given by the Boltzmann distribution, which we derive below.

2.1 Derivation of the Boltzmann Distribution

Consider a system (s) in contact with a thermal reservoir (r), which together constitute an isolated system with fixed total energy $E = E^{(s)} + E^{(r)}$. According to the second law of thermodynamics, such an isolated system evolves toward such partition of energy between the system and the reservoir, which corresponds to the largest number of microstates of the whole system (Phillips et al. 2012). Therefore, the probability that the system has energy $E_i^{(s)}$ is proportional to the number of the corresponding microstates of the overall system, $\Omega(E, E_i^{(s)}) = \Omega^{(s)}(E_i^{(s)}) \times \Omega^{(r)}(E - E_i^{(s)})$. System degeneracy is directly related to its entropy $S = k_B \ln(\Omega)$, where k_B is the Boltzmann constant, so the probability that the system has energy $E_i^{(s)}$ reads:

$$
\begin{aligned}
P\left(E_i^{(s)}\right) &\propto \exp\left(S^{(s)}\left(E_i^{(s)}\right)/k_B\right) \cdot \exp\left(S^{(r)}\left(E - E_i^{(s)}\right)/k_B\right) \\
&\approx \exp\left(S^{(s)}\left(E_i^{(s)}\right)/k_B\right) \cdot \exp\left(\left(S^{(r)}(E) - \frac{dS^{(r)}}{dE} \cdot E_i^{(s)}\right)/k_B\right) \\
&\propto \exp\left(S^{(s)}\left(E_i^{(s)}\right)/k_B\right) \cdot \exp\left(-E_i^{(s)}/(k_B \cdot T)\right),
\end{aligned}
\tag{1}
$$

where in the second step, the reservoir entropy is expended about $S^{(r)}(E)$ (note that this approximation is valid when a reservoir is much bigger than a system, so $E_i^{(s)} << E$), while in the third step the thermodynamic definition of temperature $(\partial S/\partial E)_{V,N} = 1/T$ is used. The first term in Eq. (1) gives the number of microstates of a system with energy $E_i^{(s)}$ (i.e., $\Omega^{(s)}(E_i^{(s)})$), while the second term is called the Boltzmann factor, and represents the unnormalized probability of selecting one particular system microstate at energy $E_i^{(s)}$, i.e. it represents a statistical weight of that microstate (Sneppen and Zocchi 2005).

2.2 Statistical Weights from Statistical Mechanics

In the problem of binding of a protein to its binding site considered above, all of the microstates can be grouped in one of the two system *macrostates*: the one in which the DNA binding site is occupied by the protein, or the one in which it is empty, where binding sites in these two states are characterized by the energies $\varepsilon_i^{(bs)}$ (so that i corresponds to *bound* or *unbound*). Thereby, the energy of the system $(E_i^{(s)})$ is a sum of the binding site energy and the kinetic energies of all unbound

protein molecules. Since the probability of finding different microstates is given by the Boltzmann distribution, the weight associated with the macrostate with energy $E_i^{(s)}$ is proportional to the corresponding number of the system microstates ($\Omega^{(s)}$), multiplied by the Boltzmann factor (the numerator in the equation below):

$$P\left(E_i^{(s)}\right) = \frac{\Omega^{(s)}\left(E_i^{(s)}\right) \cdot e^{-E_i^{(s)}/(k_B \cdot T)}}{\sum_i \left(\Omega^{(s)}\left(E_i^{(s)}\right) \cdot e^{-E_i^{(s)}/(k_B \cdot T)}\right)}. \tag{2}$$

In the denominator of Eq. (2) is the so-called *partition function,* which represents a sum of statistical weights of all possible system microstates.

To determine $\Omega^{(s)}$ from Eq. (2), i.e. to count in how many ways protein molecules can be arranged, one needs to know how many states are available to one freely moving protein molecule with kinetic energy $\varepsilon_k = p^2/(2m)$ in a cell. According to the uncertainty principle from quantum mechanics, this question amounts to counting discrete cells of the size h (Planck's constant) in the phase-space containing three dimensions of particle position (r) and three dimensions of its momentum (p) (Stowe 2007; Sneppen and Zocchi 2005).

Therefore, the statistical weight of the system macrostate with binding site energy $\varepsilon_{bound}^{(bs)}$, where the protein binding site is occupied, is obtained by summing through all possible arrangements (permutations) of $N-1$ indistinguishable protein molecules (because 1 is bound) in a cell phase-space, with that sum weighted by a corresponding Boltzmann factor (Phillips et al. 2012; Sneppen and Zocchi 2005):

$$Z_{ON} = \frac{1}{(N-1)!}\left(\int_V \int \frac{d^3r \cdot d^3p}{h^3} e^{-p^2/(2mk_BT)}\right)^{N-1} e^{-\varepsilon_{bound}^{(bs)}/(k_BT)}$$
$$\propto k^{N-1}\rho^{-(N-1)}e^{-\varepsilon_{bound}^{(bs)}/(k_BT)}, \tag{3}$$

where $k = (2mk_BT\pi/h^2)^{3/2}$ and $\rho = N/V$ (V is cell volume). Equivalently, a statistical weight of a system macrostate in which all protein molecules are free in a cell (with binding site energy $\varepsilon_{unbound}^{(bs)}$) reads:

$$Z_{OFF} = \frac{1}{N!}\left(\int_V \int \frac{d^3r \cdot d^3p}{h^3} e^{-p^2/(2mk_BT)}\right)^{N} e^{-\varepsilon_{unbound}^{(bs)}/(k_BT)}$$
$$\propto k^{N}\rho^{-N}e^{-\varepsilon_{unbound}^{(bs)}/(k_BT)}. \tag{4}$$

Taking into account that the total statistical weight (partition function) of this system is $Z = Z_{ON} + Z_{OFF}$, one can express the ratio of probabilities of finding a binding site in occupied and unoccupied state:

$$\frac{P_{ON}}{P_{OFF}} = \frac{Z_{ON}}{Z} \cdot \left(\frac{Z_{OFF}}{Z}\right)^{-1} = \frac{\rho}{k}e^{-\Delta\varepsilon/(k_BT)}, \tag{5}$$

where $\Delta\varepsilon = \varepsilon_{bound}^{(bs)} - \varepsilon_{unbound}^{(bs)}$ is the binding energy. Conveniently, statistical weights are expressed in terms of $\Delta\varepsilon$ (i.e., normalized with Z_{OFF}). One should have in mind that binding of a protein to DNA induces significant conformational changes in both molecules, so $\Delta\varepsilon$ in the above equations corresponds to the (Gibbs) free energy of binding (often written as ΔG, which we will adopt below).

2.3 Statistical Weights from Equilibrium Biochemical Reactions

Binding of a protein present in a cell in concentration [P], to a binding site of concentration [BS] is, alternatively, described by the following chemical reaction:

$$[P] + [BS] \xrightleftharpoons[K_d]{} [P \sim BS], \tag{6}$$
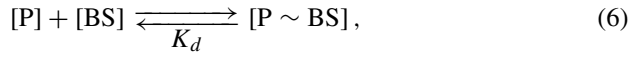
characterized by the equilibrium dissociation constant $K_d = [P]\cdot[BS]/[P \sim BS]$. The ratio of probabilities of finding a binding site occupied and unoccupied is then

$$\frac{P_{ON}}{P_{OFF}} = \frac{[P \sim BS]}{[BS]_{\text{tot}}} \cdot \left(\frac{[BS]}{[BS]_{\text{tot}}}\right)^{-1} = \frac{[P]}{K_d}, \tag{7}$$

where $[BS]_{\text{tot}} = [BS] + [P \sim BS]$ is a total binding site concentration. Equation (7) is equivalent to Eq. (5) obtained using statistical mechanics, where $[P] = \rho$ and $K_d = k\cdot\exp(\Delta\varepsilon/(k_B T))$ (Sneppen and Zocchi 2005).

If a protein from the analyzed example is RNA polymerase (RNAP) binding to a promoter site, the promoter transcription activity can be approximated through a classical assumption that the transcription activity is proportional to equilibrium binding probability of RNAP to the promoter (Shea and Ackers 1985). Transcription from promoters with more complex regulation, including combinatorial binding of multiple transcription factors which results in more than two promoter configurations, can also be modeled in this way, as in the following example.

2.4 Modeling Transcription Regulation of AhdI R-M System

Thermodynamic modeling approach introduced above was applied in modeling transcription regulation of the R-M system AhdI, which belongs to a large group of R-M systems coding for an additional, control protein (C) which regulates transcription of system genes (Bogdanova et al. 2008). In this system, an operon containing control protein and restriction endonuclease genes (*c* and *res*), and a gene coding for methyltransferase (*met*) are oriented convergently and transcribed from
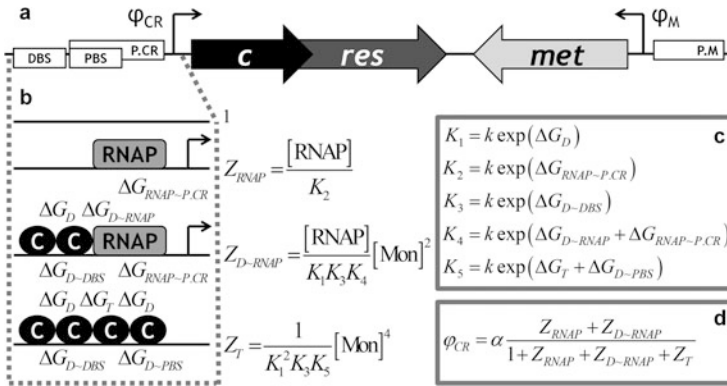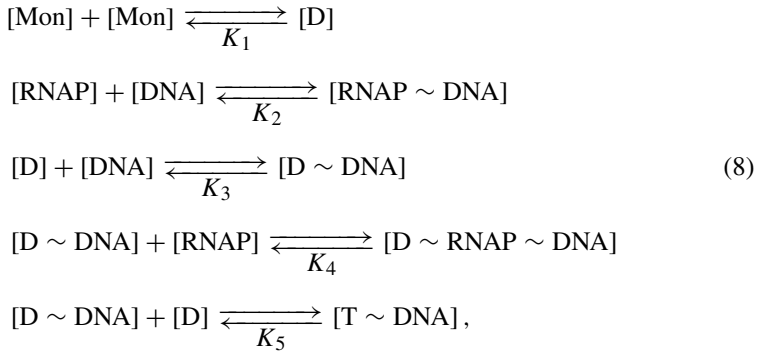
Fig. 1 Thermodynamic modeling of P.CR transcription regulation in AhdI R-M system. (**a**) Gene organization in AhdI system. P.CR, DBS, PBS, and P.M mark relative positions of the P.CR promoter, the distal and the proximal C protein binding site, and the P.M promoter, respectively. (**b**) Allowed P.CR configurations with their statistical weights denoted on the right, expressed in terms of the equilibrium dissociation constants (K) of reactions (8). Protein–DNA (below each configuration) and protein–protein (above interacting proteins) binding free energies (ΔG, in units of $k_B T$) are related to the appropriate equilibrium dissociation constants following the equations in (**c**). (**d**) P.CR transcription activity (φ_{CR}) is proportional to the fraction of statistical weights corresponding to transcriptionally active configurations (those containing an arrow in **b**)

the promoters denoted as P.CR and P.M, respectively (Fig. 1a). Methyltransferase methylates the P.M promoter, thereby repressing transcription of its own gene. On the other hand, transcription of the operon genes is regulated by binding of C protein dimers to the distal (DBS) and the proximal binding sites (PBS) in the P.CR promoter region.

Prior experiments of in vitro transcription from a wild type P.CR showed that transcription from this promoter is virtually inactive in the absence of C protein, and that it becomes first activated and then repressed with increasing C protein concentration (Bogdanova et al. 2008). This suggests that RNAP is presumably recruited to the promoter through a protein-protein contact with a bound C protein which, therefore, acts as a transcription activator. However, in the electrophoretic mobility shift assay experiments, only free DNA and complexes comprised of C protein tetramers bound to DNA were revealed in the whole range of varying C protein concentrations (Bogdanova et al. 2008; McGeehan et al. 2006). Furthermore, it was shown that DBS has a few orders of magnitude larger binding affinity than PBS, indicating that binding of C dimers to DNA is highly cooperative, i.e., a C dimer bound to DBS immediately recruits a second C dimer to PBS. As a bound C tetramer prevents RNAP from binding to the P.CR and thereby represses transcription of *c* and *res* genes, this raises a question of how transcription from the P.CR is activated. Therefore, quantitative modeling was used to test the proposed mechanism: that RNAP can passively outcompete a second C dimer from binding to PBS, which results in activation of transcription from the P.CR (Bogdanova et al. 2008).

The proposed thermodynamic model of the P.CR transcription regulation takes into account the following chemical reactions, characterized by the appropriate equilibrium dissociation constants (K):

$$[Mon] + [Mon] \underset{K_1}{\rightleftharpoons} [D]$$

$$[RNAP] + [DNA] \underset{K_2}{\rightleftharpoons} [RNAP \sim DNA]$$

$$[D] + [DNA] \underset{K_3}{\rightleftharpoons} [D \sim DNA] \qquad (8)$$

$$[D \sim DNA] + [RNAP] \underset{K_4}{\rightleftharpoons} [D \sim RNAP \sim DNA]$$

$$[D \sim DNA] + [D] \underset{K_5}{\rightleftharpoons} [T \sim DNA],$$

where [RNAP], [Mon], [D] and [DNA] stand for concentrations of RNA polymerase, C protein monomers and dimers, and DNA containing the P.CR promoter region, while [RNAP $\sim$ DNA], [D $\sim$ DNA], [D $\sim$ RNAP $\sim$ DNA] and [T $\sim$ DNA] denote concentrations of established complexes of, respectively, RNAP bound to the P.CR, a C dimer bound to DBS, RNAP recruited to the promoter by a bound C dimer, and a bound C tetramer. This system of reactions describes establishing of the allowed P.CR equilibrium configurations characterized by the following statistical weights (Fig. 1b):

- 1—empty promoter;
- $Z_{RNAP} = [RNAP \sim DNA]/[DNA]$—only RNAP bound to the promoter, which corresponds to basal transcription of the operon genes;
- $Z_{D\text{-}RNAP} = [D \sim RNAP \sim DNA]/[DNA]$—RNAP recruited to the promoter by a C dimer bound to DBS, resulting in transcription activation;
- $Z_T = [T \sim DNA]/[DNA]$—a second C dimer recruited to PBS by a C dimer bound to DBS, with obtained C tetramer repressing transcription.

Note that the configuration representing only a C dimer bound to PBS was not taken into account, as such a configuration was not observed in the experiments and has a very low probability due to a large cooperativity in C dimers binding. One should also note that this modeling approach involves the rapid equilibrium assumption applied to the binding reactions, which is justified by the fact that association and dissociation processes between a protein and a DNA molecule, or two protein molecules, are much faster compared to transcription, translation and protein/RNA degradation processes (Phillips et al. 2012). Consequently, the model considers only the frequency of different promoter configurations in equilibrium and cannot distinguish between different sequences of binding events leading to a given configuration—e.g., whether protein A binds to DNA first and prevents binding of protein B, or it displaces protein B when it is already bound to DNA.

The measured value of C protein dimerization constant (K_1) is by an order of magnitude larger than the range of C protein concentrations used in experiments, indicating that C protein is present in a cell in the form of monomers. Therefore, statistical weights of the corresponding configurations are expressed in terms of C monomer and RNAP concentrations and, either appropriate equilibrium dissociation constants (Fig. 1b), or binding free energies (Fig. 1c). According to the assumption introduced above, transcription activity of the P.CR is proportional to the fraction of statistical weights that correspond to bound RNAP (Fig. 1d). Absorbing all constants into few parameters (x, y, and z), P.CR transcription activity is obtained as a function of C protein monomer concentration:

$$\varphi_{CR}(\text{Mon}) = \alpha \frac{x + y[\text{Mon}]^2}{1 + x + y[\text{Mon}]^2 + z[\text{Mon}]^4}, \qquad (9)$$

where α is a proportionality constant with units transcript amount over time. Equation (9) was fitted to the experimentally measured data, obtained for a wild type system (Fig. 2a), but also for systems in which mutations were introduced in the DNA sequences of DBS or/and PBS (Fig. 2b–d), which corresponds to changing $\Delta G_{D\text{-}DBS}$ or/and $\Delta G_{D\text{-}PBS}$ (see Fig. 1b) (Bogdanova et al. 2008). Fig. 2 shows that the proposed model, with only three free parameters (x, y, and z; α was given the value 1), is in very good agreement with the data for both the wild type and the mutated systems. Furthermore, when fitted to the mutants data, parameter values change as expected with respect to the wild-type case—e.g., decreasing the affinity of DBS strongly negatively affects parameters y and z, while it has no effect on parameter x (compare the Eq. (9) with statistical weights in Fig. 1b and c). All of the above indicates that the modeling can realistically explain in vitro measured transcription activities and, accordingly, that the proposed model appropriately describes the P.CR transcription regulation in AhdI system.
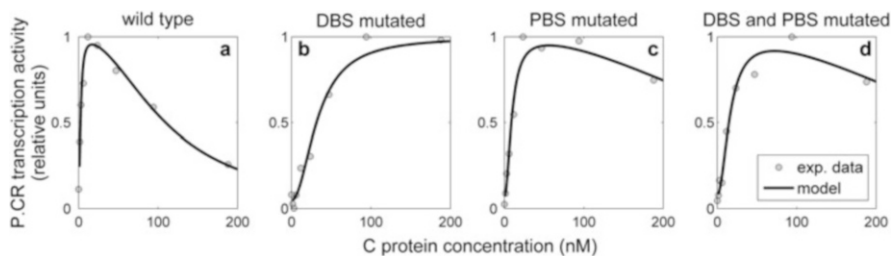

Fig. 2 Fitting experimentally measured dependence of P.CR transcription activity on C protein concentration in wild type and experimentally mutated systems, with a thermodynamic model of this promoter transcription regulation. Transcription activity was measured in arbitrary units and the values (grey circles) were normalized. Solid curves represent the fitted model Eq. (9). (**a**) Wild type system, (**b**) DBS affinity decreased, (**c**) PBS affinity decreased, (**d**) Decreased affinity of both DBS and PBS (Bogdanova et al. 2008)

3 Dynamic Modeling of Protein Expression

Dynamic modeling is the most common approach to model molecular networks and can be used to predict how protein amounts of interest—e.g. those of restriction enzyme and methyltransferase—change with time. State variables of the model represent concentrations (or numbers of molecules) of all mRNA and protein species in the system. These quantities dynamically depend on the combination of all processes that increase or decrease the corresponding amounts, characterized by appropriately defined rates (Le Novère 2015).

Experimentally observing dynamics of protein expression in a cell is, however, challenging due to a prerequisite for a synchronized cell population. Consequently, such measurements have been conducted on R-M systems in only two cases: for PvuII system, by introducing the system in a cell on a phage vector (Mruk and Blumenthal 2008), and for Esp1396I system, by monitoring fluorescently labeled R-M system proteins at the level of single cells (Morozova et al. 2016). In the latter case, experimental measurements were compared with predictions of a biophysical model of Esp1396I R-M system expression during its establishment in a newly transformed host (Morozova et al. 2016).

Similarly to AhdI system, Esp1396I system contains *c* and *res* genes in an operon, expressed from a promoter controlled by cooperative binding of two C dimers (see Fig. 1a and b). In contrast to an autoregulated *m* gene in AhdI system, in Esp1396I system, P.M is under control of C protein, where binding of one C dimer to its single binding site in this promoter region represses transcription of *m* gene (Bogdanova et al. 2009). P.CR and P.M regulation was thermodynamically modeled as explained above, to obtain relations for their transcription activities (φ_i) as functions of C protein concentration, which were further used as an input for a dynamic model describing how appropriate transcript (m_i) and protein (p_i) amounts change with time, for all three system components ($i = C, Res, Met$ denoting C protein, restriction enzyme, and methyltransferase, respectively):

$$\frac{dm_i(t)}{dt} = \varphi_i - \lambda_i^m \cdot m_i, \qquad \frac{dp_i(t)}{dt} = \kappa_i \cdot m_i - \lambda_i^p \cdot p_i \qquad (10)$$

Equation (10) takes into account that transcript and protein amounts are increased by transcription of the corresponding genes and translation of their transcripts (with translation constants κ_i), respectively, while these amounts are decreased with decay constants λ_i^m and λ_i^p, which account for both degradation and dilution of molecules due to cell division.

The proposed model of Esp1396I expression is minimal, in a sense that it takes into account only the experimentally established regulatory mechanisms, and that all model parameters are considered time-independent. Estimating the parameters by fitting this model to the data (Fig. 3a and b), is a difficult task due to the relatively large parameter space. This task is simplified by the fact that the parameters related to restriction enzyme expression can be estimated separately from those
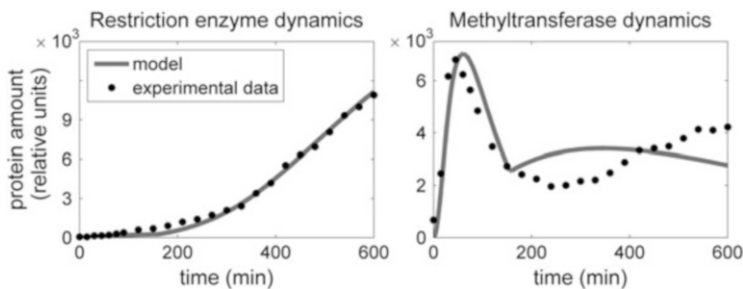
Fig. 3 Fitting experimentally measured data of single cell Esp1396I R-M system expression dynamics with a biophysical model. The zero time point corresponds to the plasmid entry in a naïve cell. (**a**) Restriction enzyme expression dynamics, (**b**) Methyltransferase expression dynamics (Morozova et al. 2016)

describing methytransferase expression, as methyltransferase does not control *c* and *res* expression. The observed good agreement of the model with the data is also supported by a subsequent experimental confirmation of very large restriction enzyme stability, which is consistent with inferred parameter values. Moreover, this minimal model can explain the main qualitative features of expression dynamics observed for Esp1396I system and proposed for R-M systems in general (Fig. 3a and b): a delayed beginning of restriction enzyme synthesis and high expression of methyltransferase early upon transforming a naïve cell. Improved quantitative agreement of the model with the data can likely be achieved by involving the dependence of at least some parameter values with time, imposed by changing conditions in a cell population or a desynchronization of cell and plasmid division. Specifically, during the first ∼160 min cells in the culture divided with different (faster) rate compared to the rest of the experiment (Morozova et al. 2016), which is taken into account through decay parameters in the model, as previously explained. Therefore, it is plausible to assume that population dynamics also has significant effect on some other parameters of the model, which may be a subject of future modeling.

4 Modeling Expression of EcoRV R-M System

In contrast to AhdI and Esp1396I systems presented above, in EcoRV R-M system P.CR and P.M are oriented divergently and partially overlap causing mutually exclusive binding of RNAP to these promoters (Fig. 4a), which represents the most distinctive regulatory feature of EcoRV system (Semenova et al. 2005). Consequently, P.CR and P.M control is strongly coupled, making transcription regulation of this system more complex compared to AhdI system. Furthermore,
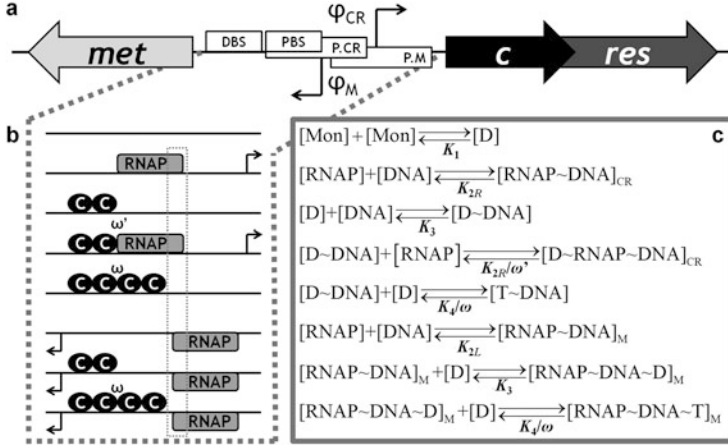
Fig. 4 Thermodynamic modeling of EcoRV R-M system transcription regulation. (**a**) Scheme of gene organization in EcoRV. Relative positions of operon and *met* promoters (P.CR and P.M) and distal and proximal C dimer binding sites (DBS and PBS) are denoted. (**b**) Allowed configurations of a DNA fragment separating *met* and *c* genes, with those transcriptionally active denoted with an arrow. Overlapping of P.CR and P.M is emphasized by framing their common fragment. (**c**) Chemical reactions in the model, with their equilibrium dissociation constants (K). Unlike in modeling AhdI transcription regulation (Fig. 1), cooperativities in binding of a second C dimer to PBS ($\omega \equiv \exp\left(-\Delta G_T\right)$) and of RNAP to P.CR ($\omega' \equiv \exp\left(-\Delta G_{D\sim RNAP}^{CR}\right)$) are here introduced as separate parameters, to enable perturbation of ω alone (see below in the text)

all characteristic AhdI regulatory features are absent from EcoRV. Namely: (1) no cooperativity in C dimers binding to DBS and PBS was experimentally found for EcoRV system, (2) *c* transcript is not leaderless in EcoRV, contrary to AhdI system whose leaderless *c* transcript is translated less efficiently than *res* and *met* transcripts, and (3) the equilibrium dissociation constant for a reaction of C protein dimerization is significantly lower than in AhdI system, leading to mostly C dimers in solution (Semenova et al. 2005).

To thermodynamically model EcoRV transcription regulation, one first needs to determine the allowed configurations of a DNA region separating the two divergent genes (Fig. 4b). Transcription regulation of the P.CR by C protein is similar to that found in AhdI system, except that now an additional configuration, consisting of only one C dimer bound to DBS, has to be included due to the absence of cooperativity. Regarding the P.M regulation, contrary to AhdI where it was C-independent, in EcoRV it is indirectly influenced by C protein, as it dictates when RNAP can bind to P.M due to overlapping promoters. From the equilibrium chemical reactions (Fig. 4c), which describe establishing of the allowed configurations, statistical weights can be determined and further used to obtain the

equations for P.CR and P.M transcription activities:

$$\varphi_{CR}(\text{Mon}) = \alpha \frac{\left(1 + \omega' \frac{[\text{Mon}]^2}{K_1 K_3}\right)}{u\left(1 + \frac{[\text{Mon}]^2}{K_1 K_3} + \omega \frac{[\text{Mon}]^4}{5K_1^2 K_3^2}\right) + \left(1 + \omega' \frac{[\text{Mon}]^2}{K_1 K_3}\right)}, \qquad (11)$$

$$\varphi_{M}(\text{Mon}) = \alpha \frac{u\left(1 + \frac{[\text{Mon}]^2}{K_1 K_3} + \omega \frac{[\text{Mon}]^4}{5K_1^2 K_3^2}\right)}{u\left(1 + \frac{[\text{Mon}]^2}{K_1 K_3} + \omega \frac{[\text{Mon}]^4}{5K_1^2 K_3^2}\right) + \left(1 + \omega' \frac{[\text{Mon}]^2}{K_1 K_3}\right)}, \qquad (12)$$

relying, again, on the assumption that promoter transcription activity is proportional to its equilibrium occupancy by RNAP. In deriving the above Eqs. (11) and (12), the following information from the experiments was used: a C dimer binds to DBS with approximately five times higher affinity compared to PBS, setting $K_4/K_3 = 5$, and the P.CR is considerably weaker than the P.M ($K_{2R} >> K_{2L}$, $u = K_{2R}/K_{2L}$) (Semenova et al. 2005). The thermodynamic model of EcoRV transcription regulation (Eqs. (11) and (12)) is incorporated in an appropriate dynamic model of transcript and protein expression, of the form given by Eq. (10). Furthermore, to estimate the model parameters, and since EcoRV expression dynamics has not been experimentally measured, it is useful to reduce their number by rescaling the appropriate variables. A detailed explanation of parameter estimation in the case of EcoRV is available in (Rodic et al. 2017b). Overall, this presents to our knowledge the first model of a divergent R-M system, which provides an opportunity to assess the effect of regulatory features found in such a system on its expression dynamics, by in silico introducing AhdI features in EcoRV system (see below).

5 Inferring Effects of R-M Systems Regulatory Features on Their Dynamical Properties

As all R-M systems share the same function, namely, efficiently destroying foreign DNA without harming the host cell, it is reasonable to hypothesize that their expression dynamics, constrained by their function, should exhibit some universal properties, regardless of the underlying regulation. Specifically, the following common dynamical properties of R-M system establishment in a naïve host cell have been proposed (Rodic et al. 2017b): (1) a time delay in expression of restriction enzyme with respect to methyltransferase, which provides time for genome protection, (2) a fast transition of restriction enzyme expression from the OFF to the ON state, to ensure rapid cell protection from incoming foreign DNA, and (3) a stable steady-state of the toxic molecule (restriction enzyme), as
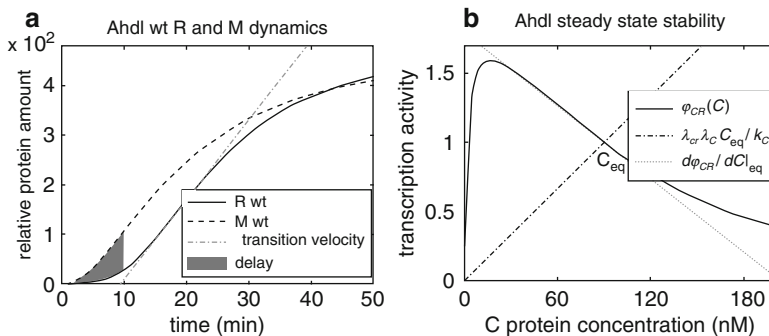
Fig. 5 Dynamical property observables. (**a**) Predicted restriction enzyme (R) and methyltransferase (M) expression dynamics upon system entry in a naïve bacterial host. Measures of R expression time delay and transition velocity are graphically represented, (**b**) Dependence of AhdI P.CR transcription activity on C protein concentration is provided by the full line, whose intersection with the dash-dotted line determines the equilibrium C protein concentration. Slope of the transcription activity curve at this equilibrium concentration (the dotted line) is related with the steady state stability (Rodic et al. 2017b)

fluctuations in restriction enzyme amount not matched by appropriate fluctuations in methyltransferase amount could lead to host cell death.

To quantify these properties, corresponding *dynamical property observables* were defined, which are graphically represented on the example of predicted AhdI wild type dynamics in Fig. 5 (Bogdanova et al. 2008; Rodic et al. 2017b). As a measure of the time delay, the ratio of the shaded areas in a perturbed and in a wild type system, spanning the first 10 min postinduction was introduced (Fig. 5a). A maximal slope of the sigmoidal restriction enzyme expression curve (the dash-dotted line in Fig. 5a) measures the transition velocity from the OFF (low restriction enzyme amount) to the ON (high restriction enzyme amount) state. Finally, the third dynamical property observable (Ω^2) related with the slopes of the dash-dotted and dotted curves shown in Fig. 5b quantifies stability of the restriction enzyme steady-state (Rodic et al. 2017b).

From Fig. 5 it can be readily inferred that AhdI exhibits all the listed dynamical properties. Moreover, perturbing characteristic AhdI regulatory features—i.e., large cooperativity in C dimers binding, high dissociation constant for C dimerization and low translation rate for the leaderless *c* transcript—abolishes these properties, leading to, presumably, less optimal AhdI expression dynamics (Rodic et al. 2017b). Thus, the requirement for the proposed dynamical properties might explain the existence of these characteristic AhdI regulatory features.

Despite missing all regulatory features inherent to AhdI system, and having a unique feature not present in AhdI (overlapping of P.CR and P.M), wild type EcoRV system also meets the same three dynamical properties (see the darkest R and M curves in Fig. 6a), arguing in favor of universality of these properties in different R-M systems. Therefore, the question emerges: why are AhdI regulatory features,
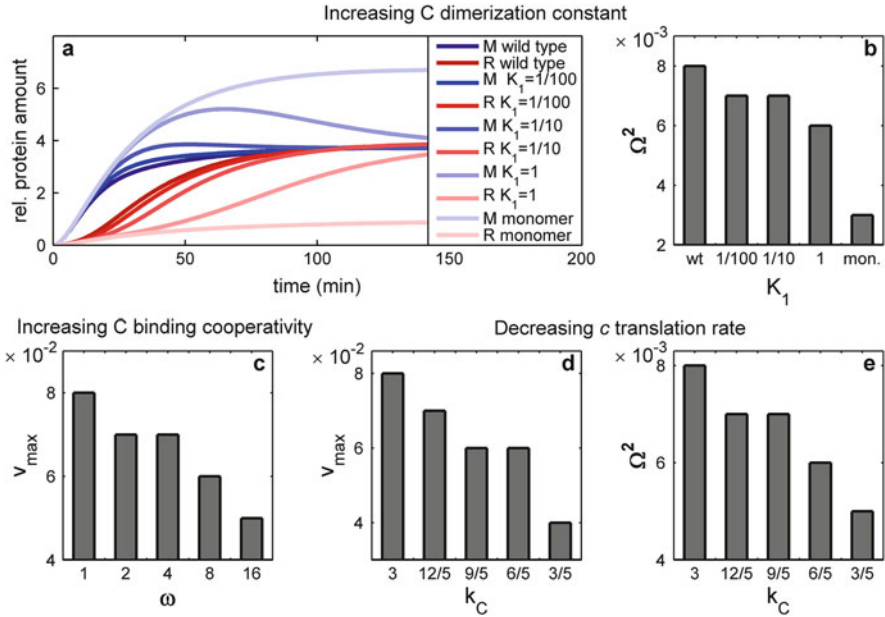
Fig. 6 In silico introducing AhdI-characteristic regulatory features in EcoRV system. Effect of increasing C dimerization constant K_1 on (**a**) dynamics of restriction enzyme (R) and methyltransferase (M) and (**b**) the steady-state stability. Effect of increasing cooperativity ω in C binding on (**c**) R OFF-ON transition velocity. Effect of decreasing the c translation constant k_C on (**d**) transition velocity and (**e**) steady-state stability (Rodic et al. 2017b)

apparently successful in optimizing this R-M system immune function, absent from EcoRV? This question can be addressed by in silico introducing characteristic AhdI regulatory features in EcoRV and observing their effect on the system dynamics (Rodic et al. 2017b).

To that end, the equilibrium dissociation constant of C dimerization (K_1 in Fig. 4c) was gradually increased toward an AhdI-characteristic value, which corresponds to a transition from the case where the solution contains mostly C dimers to the case where it contains mostly C monomers (Fig. 6a and b). This perturbation clearly has an adverse effect on two dynamical properties: on the OFF-ON transition velocity (note in Fig. 6a that the slope of R curves decreases as the dimerization constant is increased) and on the steady-state stability (Fig. 6b). Transition velocity of restriction enzyme expression is also decreased by introducing higher C binding cooperativity (increasing ω), as can be seen from Fig. 6c, and by decreasing c translation constant k_C (Fig. 6d). Less efficient c translation additionally leads to a less stable steady-state (Fig. 6e). Apparently, none of these three perturbations affect an extent of the time delay in restriction enzyme expression.

Overall, the observation that perturbing of the characteristic regulatory features abolishes one or more of the proposed dynamical properties for both AhdI and

EcoRV R-M systems (that are characterized by two different architectures, convergent and divergent), provides a possible unifying principle behind seemingly different designs of these systems. Particularly, specific combinations of different regulatory features found in these two systems appear to be optimized to meet the same dynamical properties, related with their successful establishment in a new host cell. Moreover, it seems that some regulatory features are specifically found together in the same system because of their complementary effects on system expression dynamics. Namely, high binding cooperativity in AhdI system is accompanied by a large C dimer dissociation constant, which may be a consequence of the opposite effects these features have on the steady-state level of restriction enzyme, thereby balancing the amount of this toxic molecule, while at the same time providing more optimal dynamical properties of system expression (Rodic et al. 2017b). In line with this proposal is the absence of both features in EcoRV system, where their separate introduction leads to abolishing of some of the dynamical properties and disrupting the steady-state ratio of the amounts of methyltransferase and restriction enzyme (see for example Fig. 6a). Furthermore, Esp1396I system with convergent gene organization and C regulated transcription similar as in AhdI system, exhibits both lower cooperativity in C binding and lower dissociation constant of dimerization compared to AhdI (Bogdanova et al. 2009). It would be interesting to see if other R-M systems, with different regulatory features, such as control by antisense RNAs or by translational coupling (Nagornykh et al. 2008), are similarly constrained by the proposed dynamical principles, and what are the roles of their regulatory features in achieving these principles.

6 Assessing the Significance of CRISPR-Cas Regulatory Features

Protection of a host bacterium by a CRISPR-Cas system requires its activation upon infection by foreign DNA, or upon setting the right environmental conditions (Ratner et al. 2015). However, expression dynamics of a native CRISPR-Cas have not been observed experimentally because this system (Type I-E) is silent in cells under standard conditions, even in the presence of an infecting phage, and signaling resulting in system activation is unknown (Pul et al. 2010). To date, experimental research on CRISPR-Cas transcription control in *E. coli* and *S. enterica* revealed some elements and regulatory features involved in system activation (Pul et al. 2010; Westra et al. 2010; Medina-Aparicio et al. 2011), specifically: (1) it is known that both CRISPR array and (Cascade) *cas* genes promoters are repressed by highly cooperative binding of global regulators, such as H-NS and LRP, (2) repressors can be outcompeted in binding by some global activators (e.g., LeuO), when present at elevated amounts. Therefore, highly cooperative repression, which is abolished by transcription activators, can be considered as one of the major Type I-E CRISPR-Cas regulatory features (Rodic et al. 2017a).

Fig. 7 Scheme of the proposed setup for CRISPR-Cas activation. (**a**) Pre-crRNA processing model scheme. Notation: φ—CRISPR array transcription rate (assumed constant in modeling), λ_{pre}, k and λ_{crRNA}—rates of the processes specified in the ovals (Djordjevic et al. 2012); (**b**) Equations which correspond to the scheme under **a** and which describe time dependence of pre-crRNA and crRNA amounts; (**c**) A schematic diagram of plasmid encoded c and cas genes under control of the Cas promoter (P.Cas), with a transcription rate φ_{Cas}. AhdI-like regulation of P.Cas by C protein, as denoted by a dashed arrow, is included in the cooperative model; (**d**) Dependence of a processing rate k on Cas6e amount is considered linear, in line with an experimentally determined very low amount of its substrate (pre-crRNA; k^*—processing constant) (Rodic et al. 2017a)

Furthermore, another key regulatory feature of CRISPR-Cas expression is the fast nonspecific pre-crRNA degradation by an unidentified endonuclease (Djordjevic et al. 2012). Particularly, it was shown by modeling CRISPR transcript processing upon artificial overexpression of Cas proteins (for a scheme of a model and corresponding dynamic equations see Fig. 7a and b), that the main mechanism responsible for a large increase in crRNA amount from a small decrease in substrate (pre-crRNA) amount is the fast substrate degradation. Processing of pre-crRNA by an elevated amount of Cas proteins diverts the whole molecule from the path of nonspecific degradation, thereby amplifying the equilibrium crRNA amount for a few orders of magnitude (Djordjevic et al. 2012).

However, to more realistically predict CRISPR-Cas expression dynamics and to understand the significance of the established main regulatory features of this system, an appropriate mathematical description of gradual expression of a processing Cas6e protein upon system induction is also needed, as the pre-crRNA processing rate (k) directly depends on the level of Cas6e (Fig. 7d). As a detailed mechanism of Cas promoter (P.Cas) control is unknown, one possible approach involves replacing transcription control (while keeping the CRISPR-Cas pre-crRNA processing regulation) of a native P.Cas with that of a qualitatively and mechanistically similar, but better explored system, and in silico analyzing expression dynamics of the obtained construct (Rodic et al. 2017a). Such an approach would allow assessing the significance of CRISPR-Cas regulatory features, with a minimum of guessing (if a system used as a proxy was already well-studied so that all its major parameters are fixed). At the same time, in silico analysis would provide

a much simpler and faster way of fulfilling the task of interest, in comparison to a complementary experimental approach, which would require creating an artificial gene circuit, extensive mutations of the system regulatory features and measuring in vivo expression dynamics of pre-crRNA and crRNA.

Similarities in transcription regulation can be noted between a well-studied AhdI R-M system, for which a biophysical model was already constructed and evaluated (see Fig. 1) (Bogdanova et al. 2008), and Type I-E CRISPR-Cas. Strong cooperative interactions are involved in both systems, in particular, in binding of C dimers to the P.CR region and in binding of H-NS molecules to the P.Cas region, thereby repressing transcription (Pul et al. 2010). This repression by H-NS can be abolished by transcriptional activator LeuO (Westra et al. 2010; Medina-Aparicio et al. 2011). Consequently, autoregulation (both positive and negative), similar to that exhibited by C protein in AhdI system, is likely found in CRISPR-Cas regulation, as LeuO activates, and also indirectly represses its own promoter (Chen et al. 2001; Stratmann et al. 2012). Thus, the main features of CRISPR-Cas transcription regulation, namely, gradual synthesis of Cas proteins, cooperativity in transcription regulation, and putative autoregulation, can be qualitatively mimicked by putting *cas* genes under transcription control found in AhdI. More precisely, the proposed setup for CRISPR-Cas activation analyzed in silico includes *cas* genes put under control of the P.CR promoter from AhdI (see Fig. 1b), which are introduced in a cell on a plasmid, marking the start of CRISPR-Cas activation (Fig. 7c); dynamics of crRNA generation due to the Cas6e processing activity is monitored.

To understand the effect of cooperative transcription regulation of *cas* genes, three (sub)models of *cas* genes regulation in the proposed setup are analyzed: (1) a baseline model, in which P.Cas transcription activity acquires its equilibrium value infinitely fast, (2) a constitutive model, with constant P.Cas transcription activity, and (3) a cooperative model, where P.Cas is cooperatively regulated by C protein in the same manner as the AhdI P.CR promoter. Figure 8 shows how the amount of crRNA, determined 20 min after the start of system activation, depends on the level of the processing rate k reached in equilibrium, in all three models. The crRNA
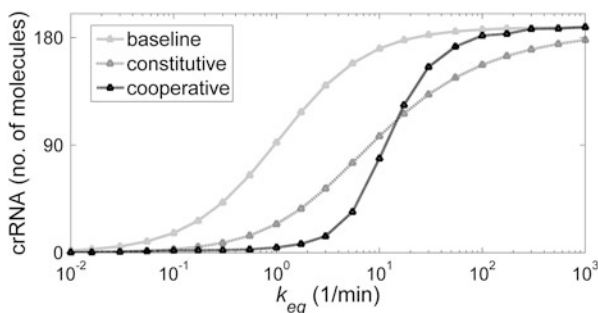

Fig. 8 Dependence of crRNA amount 20 min postinduction on the equilibrium value of a pre-crRNA processing rate k_{eq} in the three models of CRISPR-Cas activation (Rodic et al. 2017a)

amount at 20 min postinduction was specifically chosen, as this period is most relevant for a successful cell defense against an incoming virus.

The most prominent characteristic of the cooperative model is its switch-like behavior (Fig. 8), in contrast to much more gradual responses of the constitutive and the baseline models. This feature enables keeping the system in the OFF state in the case of possible leaks in P.Cas activity (corresponding to low k_{eq} values) and, on the other side, rapidly generating a sufficient amount of crRNAs once the induction signal is received, to efficiently combat viral infection. Furthermore, taking into account that the amount of crRNAs sufficient to negatively affect phage development was determined to be ∼10 molecules (Pougach et al. 2010), the models predict that enough crRNAs is generated even at low (somewhat larger than 1 1/min) k_{eq} values, corresponding to the activated system regime. Therefore, CRISPR-Cas system expression regulation is probably mainly constrained by a requirement of rapidly producing a large amount of crRNAs (Rodic et al. 2017a).

In line with its switch-like behavior, at low k_{eq} values the cooperative model produces less crRNAs than the constitutive one. However, at high k_{eq} values an interesting cross-over behavior is observed, where the cooperative model approaches the limit of infinitely fast crRNA production (given by the baseline model). Even more crRNAs can be generated by jointly activating transcription of both *cas* genes and a CRISPR array, which relieves the saturation obtained when increasing only *cas* expression (Djordjevic et al. 2012; Rodic et al. 2017a). As k values around 100 1/min were encountered in experiments with artificial overexpression of *cas* genes (Pougach et al. 2010; Djordjevic et al. 2012), it is tempting to speculate that such high rates of pre-crRNA processing may also be reached in the native system, providing highly efficient protection to a bacterium.

Effect of abolishing the second major CRISPR-Cas regulatory feature, i.e., of decreasing the pre-crRNA nonspecific degradation rate (λ_{pre}) in the cooperative model, can be deduced from Fig. 9. Namely, the crRNA dynamics curve is gradually deformed with respect to the standard Hill (sigmoidal) shape, indicating that fast
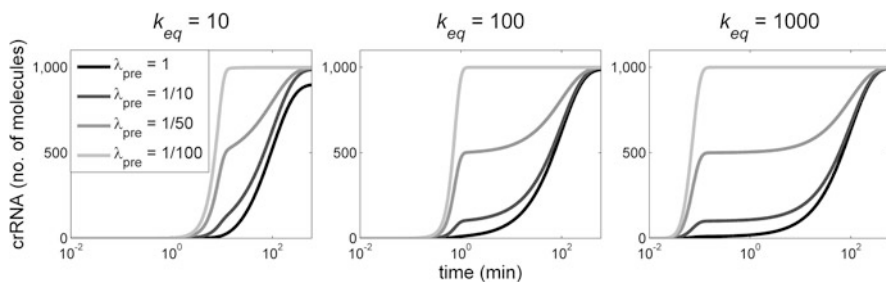

Fig. 9 Perturbing the fast nonspecific degradation of pre-crRNA. Effect of decreasing the pre-crRNA degradation rate λ_{pre} on crRNA expression dynamics at three different k_{eq} values can be seen in the figures under (**a**, **b**, and **c**). Native CRISPR-Cas is characterized by $\lambda_{pre} = 1$ 1/min. Zero time point corresponds to the start of system activation, i.e., to the moment of entrance of a plasmid carrying *cas* genes in a cell (Rodic et al. 2017a)

nonspecific pre-crRNA degradation is, together with cooperative transcription regulation, responsible for the system switch-like behavior. Another effect of decreasing λ_{pre}, which comes as a model prediction, is a decrease in the time delay of the onset of crRNA generation, most pronounced at high k_{eq} values. It has been shown previously that slow or delayed CRISPR interference (targeting of foreign DNA by Cascade-crRNA complexes) facilitates the *primed adaptation* (Künne et al. 2016; Musharova et al. 2017), i.e., the acquisition of invasive DNA fragments similar to already possessed spacers, to be incorporated as new spacers in the CRISPR array. This mechanism serves to minimize infection by phages with mutated genome sequences, which would otherwise evade the interference (Sternberg et al. 2016). The required delay could be achieved by a delay in crRNA generation, resulting from fast pre-crRNA degradation, as predicted by the model (Rodic et al. 2017a). Consequently, both main dynamical features, i.e., rapid transition of the system from OFF to ON state and the delay in the expression of the effector molecules (restriction enzyme and crRNAs), are observed in both R-M systems and mechanistically more complicated CRISPR-Cas systems.

7   Summary and Conclusion

Seemingly very different architectures and regulatory properties of AhdI and EcoRV systems can be explained by few common design principles, ensuring that expression dynamics of every R-M system is optimized to serve its purpose—namely, safe and efficient host cell protection from foreign DNA. Other R-M systems, representative of different regulatory mechanisms, should be investigated to test if unifying design principles can be defined at the level of the whole group of these prokaryotic immune systems. Moreover, having the same immune function, CRISPR-Cas systems may also obey similar design principles, as it was theoretically predicted by using a synthetic system to bypass the unknown CRISPR-Cas transcription control, while keeping the same transcript processing mechanism as in native CRISPR-Cas. Thereby, thermodynamic modeling proved to be an appropriate approach in describing R-M system transcription regulation, while in combination with a dynamic model of protein expression, it can be used to describe the main qualitative properties of R-M system dynamics of establishment in a single, naïve host cell. Further experimental and theoretical studies of CRISPR-Cas regulation may allow to more accurately understand its dynamics, in line with what is already done for R-M systems. Overall, the studies on bacterial immune systems summarized here underline a major goal of systems biology which is to discover common design principles in mechanistically otherwise different biological systems.

References

Bogdanova E, Djordjevic M, Papapanagiotou I et al (2008) Transcription regulation of the type II restriction-modification system AhdI. Nucleic Acids Res 36:1429–1442

Bogdanova E, Zakharova M, Streeter S et al (2009) Transcription regulation of restriction-modification system Esp1396I. Nucleic Acids Res 37:3354–3366

Chen C-C, Fang M, Majumder A et al (2001) A 72-base pair AT-rich DNA sequence element functions as a bacterial gene silencer. J Biol Chem 276:9478–9485

Djordjevic M, Djordjevic M, Severinov K (2012) CRISPR transcript processing: a mechanism for generating a large number of small interfering RNAs. Biol Direct 7:24–34

Dresch JM, Richards M, Ay A (2013) A primer on thermodynamic-based models for deciphering transcriptional regulatory logic. BBA-Gene Regul Mech 1829:946–953

Ershova A, Rusinov I, Spirin S et al (2015) Role of restriction-modification systems in prokaryotic evolution and ecology. Biochemistry-Moscow 80:1373–1386

Goldberg GW, Marraffini LA (2015) Resistance and tolerance to foreign elements by prokaryotic immune systems – curating the genome. Nat Rev Immunol 15:717–724

Hille F, Charpentier E (2016) CRISPR-Cas: biology, mechanisms and relevance. Philos T Roy Soc B 371:20150496

Künne T, Kieper SN, Bannenberg JW et al (2016) Cas3-derived target DNA degradation fragments fuel primed CRISPR adaptation. Mol Cell 63:852–864

Le Novère N (2015) Quantitative and logic modelling of molecular and gene networks. Nat Rev Genet 16:146–158

McGeehan J, Papapanagiotou I, Streeter S et al (2006) Cooperative binding of the C.AhdI controller protein to the C/R promoter and its role in endonuclease gene expression. J Mol Biol 358:523–531

Medina-Aparicio L, Rebollar-Flores J, Gallego-Hernández A et al (2011) The CRISPR/Cas immune system is an operon regulated by LeuO, H-NS, and leucine-responsive regulatory protein in Salmonella enterica serovar Typhi. J Bacteriol 193:2396–2407

Morozova N, Sabantsev A, Bogdanova E et al (2016) Temporal dynamics of methyltransferase and restriction endonuclease accumulation in individual cells after introducing a restriction-modification system. Nucleic Acids Res 44:790–800

Mruk I, Blumenthal RM (2008) Real-time kinetics of restriction–modification gene expression after entry into a new host cell. Nucleic Acids Res 36:2581–2593

Musharova O, Klimuk E, Datsenko KA et al (2017) Spacer-length DNA intermediates are associated with Cas1 in cells undergoing primed CRISPR adaptation. Nucleic Acids Res 45:3297–3307

Nagornykh M, Bogdanova E, Protsenko A et al (2008) Regulation of gene expression in a type II restriction-modification system. Russ J Genet 44:523–532

Phillips R, Kondev J, Theriot J et al (2012) Physical biology of the cell. Garland Science, New York

Pougach K, Semenova E, Bogdanova E et al (2010) Transcription, processing and function of CRISPR cassettes in Escherichia coli. Mol Microbiol 77:1367–1379

Pul Ü, Wurm R, Arslan Z et al (2010) Identification and characterization of E. coli CRISPR-cas promoters and their silencing by H-NS. Mol Microbiol 75:1495–1512

Ratner HK, Sampson TR, Weiss DS (2015) I can see CRISPR now, even when phage are gone: a view on alternative CRISPR-Cas functions from the prokaryotic envelope. Curr Opin Infect Dis 28:267–274

Rodic A, Blagojevic B, Djordjevic M et al (2017a) Features of CRISPR-Cas regulation key to highly efficient and temporally-specific crRNA production. Front Microbiol 8:2139

Rodic A, Blagojevic B, Zdobnov E et al (2017b) Understanding key features of bacterial restriction-modification systems through quantitative modeling. BMC Syst Biol 11:377–391

Semenova E, Minakhin L, Bogdanova E et al (2005) Transcription regulation of the EcoRV restriction–modification system. Nucleic Acids Res 33:6942–6951

Shea MA, Ackers GK (1985) The OR control system of bacteriophage lambda: a physical-chemical model for gene regulation. J Mol Biol 181:211–230

Sneppen K, Zocchi G (2005) Physics in molecular biology. Cambridge University Press, Cambridge

Sternberg SH, Richter H, Charpentier E et al (2016) Adaptation in CRISPR-Cas systems. Mol Cell 61:797–808

Stowe K (2007) An introduction to thermodynamics and statistical mechanics. Cambridge University Press, New York

Stratmann T, Pul Ü, Wurm R et al (2012) RcsB-BglJ activates the Escherichia coli leuO gene, encoding an H-NS antagonist and pleiotropic regulator of virulence determinants. Mol Microbiol 83:1109–1123

Westra ER, Pul Ü, Heidrich N et al (2010) H-NS-mediated repression of CRISPR-based immunity in Escherichia coli K12 can be relieved by the transcription activator LeuO. Mol Microbiol 77:1380–1393

Antibiotic-induced degradation of antitoxin enhances the transcription of acetyltransferase-type toxin-antitoxin operon

Peifei Li[1], Ying-Xian Goh [ID] [1], Bojana Ilic[2], Cui Tai[1], Zixin Deng[1], Zhaoyan Chen[3], Marko Djordjevic[4] and Hong-Yu Ou [ID] [1]*

[1]State Key Laboratory of Microbial Metabolism, Joint International Laboratory on Metabolic & Developmental Sciences, School of Life Sciences & Biotechnology, Shanghai Jiao Tong University, Shanghai 200240, China; [2]Institute of Physics Belgrade, University of Belgrade, Belgrade 11000, Serbia; [3]Intensive Care Unit, First Affiliated Hospital of Guangxi Medical University, Nanning, Guangxi Province, 530021, China; [4]Quantitative Biology Group, Institute of Physiology and Biochemistry, Faculty of Biology, University of Belgrade, Belgrade 11000, Serbia

*Corresponding author. E-mail: hyou@sjtu.edu.cn

Background: Bacterial toxin-antitoxin (TA) modules respond to various stressful conditions. The Gcn5-related *N*-acetyltransferase-type toxin (GNAT) protein encoded by the GNAT-RHH TA locus is involved in the antibiotic tolerance of *Klebsiella pneumoniae*.

Objectives: To investigate the transcriptional mechanism of the GNAT-RHH operon *kacAT* under antibiotic stress.

Methods: The transcriptional level of the *kacAT* operon of *K. pneumoniae* was measured by quantitative real-time (qRT) PCR assay. The degradation of antitoxin KacA was examined by western blot and fluorescent protein. The ratio of [KacA]:[KacT] was calculated by the fluorescence intensity of KacA-eGFP and mCherry-KacT. Mathematical modelling predicted protein and transcript synthesis dynamics.

Results: A meropenem-induced increase in transcript levels of *kacA* and *kacT* resulted from the relief from transcriptional autoregulation of the *kacAT* operon. Meropenem induces the degradation of KacA through Lon protease, resulting in a reduction in the ratio of [KacA]:[KacT]. The decreased ratio causes the dissociation of the KacAT complex from its promoter region, which eliminates the repression of *kacAT* transcription. In addition, our dynamic model of *kacAT* expression regulation quantitatively reproduced the experimentally observed reduction of the [KacA]:[KacT] ratio and a large increase in *kacAT* transcript levels under the condition of strong promoter autorepression by the KacAT complex.

Conclusions: Meropenem promotes the degradation of antitoxin by enhancing the expression of Lon protease. Degradation of antitoxin reduces the ratio of intracellular [antitoxin]:[toxin], leading to detachment of the TA complex from its promoter, and releasing repression of TA operon transcription. These results may provide an important insight into the transcriptional mechanism of GNAT-RHH TA modules under antibiotic stress.

Introduction

After the discovery of the toxin-antitoxin (TA) modules on bacterial plasmids,[1] these TA modules were also found on prokaryotic chromosomes.[2,3] Depending on the nature of the antitoxin and its interaction with the toxin, TA modules have been recently divided into eight types (types I–VIII).[4] A typical type II TA module consists of a stable toxin protein and a metabolically unstable antitoxin protein, forming a non-toxic TA complex.[5,6] Some toxins contain a Gcn5-related *N*-acetyltransferase (GNAT) domain that can inhibit protein translation by acetylating aminoacyl tRNAs, such as AtaT,[7] AtaT2[8] and ItaT[9] from *Escherichia coli*, TacT,

TacT2 and TacT3 from *Salmonella enterica*[10–12] and GmvT from *Shigella flexneri*.[13] Their cognate antitoxin proteins possess a ribbon-helix-helix (RHH) domain. Our previous study showed that KacAT is a typical GNAT-RHH TA module present in the *K. pneumoniae* clinical isolate HS11286, where KacT can halt *K. pneumoniae* growth and induce antibiotic tolerance.[14,15]

Because TA modules are usually transcriptionally up-regulated under stressful conditions, many studies have proposed them as stress-response elements.[16–18] The transcription of type II TA operons is usually autoregulated by the toxin-antitoxin complex.[4] In such TA modules, toxin-antitoxin complexes with different affinities for the operon region are formed due to different ratios of

antitoxin to the toxin, with antitoxin-saturated complexes showing a high affinity for their promoter.[19–21] When the ratio of antitoxin to the toxin becomes smaller, the repression of TA complexes on their promoter is alleviated, the autoregulation of TA operons is relieved and the translation of TA modules is increased.[16,19–21] We have previously confirmed that antibiotics can increase the transcription of *kacT*, and the transcriptional level of *kacAT* was automatically regulated by the KacA:KacT ratio.[15,21] However, the transcriptional mechanism and autoregulation of the *kacAT* operon under antibiotic conditions are still unclear.

The C-terminal domain or the entire antitoxin protein is often irregular and highly sensitive to cellular protease. ATP-dependent proteases have been identified as the most important intracellular proteolytic enzymes, including the Lon (La) and ClpP protease families.[17,22] Although proteases can degrade antitoxins, evidence also shows that once the antitoxin forms a stable complex with its cognate toxin, it will either not be degraded or degraded very slowly.[23,24] Recently, a study reported that the presence of toxin protein YoeB and MpsR enhances the stability of antitoxin YefM and MqsA under a heat-shock condition.[16] However, no study has yet explored whether KacA in the GNAT-RHH family can be degraded under the antibiotic condition, and whether the degradation of KacA is related to *kacAT* transcription.

In this study, we found that the increase in *kacAT* transcription induced by the carbapenem antibiotic meropenem resulted from the deregulation of *kacAT* operon autoregulation. Degradation of KacA under the meropenem condition by Lon protease reduced the ratio of KacA to KacT, which caused the dissociation of the KacAT complex from its promoter region. Eventually, the repression of *kacAT* transcription by the KacAT complex was relieved.

Materials and methods

Strains and plasmids

Details of all the strains and plasmids used in this study are provided in Table S1 (available as Supplementary data at *JAC* Online), and all the oligonucleotides used in this study are listed in Table S2.

Tolerance assay

The tolerance to meropenem was tested by the cfu/mL count after exposure to meropenem. Overnight cultures of *K. pneumoniae* strains containing different pBAD33 derivatives were diluted in fresh LB medium at a ratio of 1:100. Cells were incubated at 37°C for 1 h, and 0.2% arabinose was added to the cultures to induce the expression of the *araBAD* promoter. After 90 min of incubation, meropenem was added to the cultures at 5 µg/mL. The cultures were incubated for another 4 h at the 37°C shaker. To determine cfu/mL, aliquots of 100 µL culture were serially diluted and spotted on the LB solid plates to calculate the surviving cells. The survival rate was calculated by dividing the cfu/mL in the culture after 4 h of incubation with the meropenem by the cfu/mL before adding the meropenem.[15,25,26]

Western blot

The cells treated with meropenem or serine hydroxamic acid (SHX) were collected and lysed by sonication in lysis buffer (25 mM Tris, 500 mM NaCl, 500 µM phenylmethylsulfonyl fluoride, pH 8.0). After centrifugation, the cleared supernatant was boiled with a loading buffer for 10 min. As for SDS-PAGE and immunoblotting, 60 µg protein was loaded per lane and separated by SDS-PAGE using 10% polyacrylamide gels. After transferring the separated protein to the polyvinylidene fluoride membranes (PVDF; Merck Millipore, Germany), the PVDF membrane was blocked with 2.5% BSA in TBST (Tris-buffered saline with Tween-20: 30 mM Tris-base, 0.8% NaCl w/v, 0.1% Tween-20, pH 7.5) for 1 h at room temperature. Then, the PVDF membrane was washed three times with TBST and incubated with 6×His primary antibody at 4°C for a whole night. Following incubation, the PVDF membrane was washed three times using TBST and incubated with the corresponding second antibody at room temperature for 1 h. Finally, the PVDF membrane was washed with TBST and visualized by an automatic chemiluminescence image analysis system (Tanon 4600SF; Tanon, Shanghai, China).

LacZ activity assay

To construct the *lacZ* reporter plasmid, the *kacAT* promoter sequence was inserted upstream of the *lacZ* gene of a promoterless plasmid, pLACZ, forming the fusion plasmid pLACZ-P$_{kacAT}$. Different combinations of pLACZ-P$_{kacAT}$ and pBAD33 plasmid were co-transformed into RR2Δ(*kacAT lacZ*) and RR2Δ(*lon kacAT lacZ*) cells. The transformants were grown in an LB broth medium supplemented with 0.2% of arabinose for 3 h, then meropenem (5 µg/mL) and glucose (0.2%) were added. Samples for enzymatic activities were collected at the indicated time points (0, 15, 30 and 60 min). The β-galactosidase activity was measured according to the standard Miller method using chloroform and SDS to permeabilize the cells.[27]

Quantitative real-time (q-RT)-PCR experiments

The total RNA of cells was extracted according to the manufacturer's instructions using the RNeasy Kit (Qiagen, Germany). After the digestion of genomic DNA using DNase I, 1000 ng RNA was converted to cDNA using PrimeScript™ RT Reagent Kit (Takara, Japan). qPCR reaction mix (BeyoFast™ SYBR Green qPCR Mix, Category No.: D7260-1 mL) was purchased from Beyotime Biotechnology (Shanghai, China), and the reactions were performed on an ABI 7500 instrument (Applied Biosystems). Each reaction was performed in triplicate simultaneously, and the fold change of gene expression was calculated using the $2^{-\Delta\Delta CT}$ method.[28] The housekeeping gene (glyceraldehyde-3-phosphate dehydrogenase, *KPHS_20800*) was used to normalize the expression levels of the different samples.

Results and discussion

Meropenem induces the transcription of *kacA* and *kacT*

We first explored the growth state of different *K. pneumoniae* strains under the meropenem condition. Figure S1a shows that, except for the wild-type *K. pneumoniae* HS11286 containing the carbapenemase gene (*bla*$_{KPC-2}$), the OD$_{600}$ of *bla*$_{KPC-2}$ gene deletion strain HS11286-RR2 and its derived strains was decreased gradually after 1 h of treatment, meaning that cells began to die and lyse. Thus, we treated the strains with meropenem for 0, 15, 30 and 60 min.

To see the effect of meropenem on *kacAT*'s transcription level, we examined the transcription of *kacA* and *kacT* in *K. pneumoniae* HS11286-RR2 (referred to as RR2 hereafter) under the exposure of meropenem (5 µg/mL). At the same time, as a chemical that can stimulate a stringent response in bacteria,[29] SHX (100 µg/mL) was used to represent stress other than antibiotic stress and was used as a comparison with meropenem. As shown in Figure 1, meropenem caused a significant increase in *kacT*'s transcriptional level, which is consistent with our previous study.[15] Meropenem also increased the transcriptional level of *kacA*
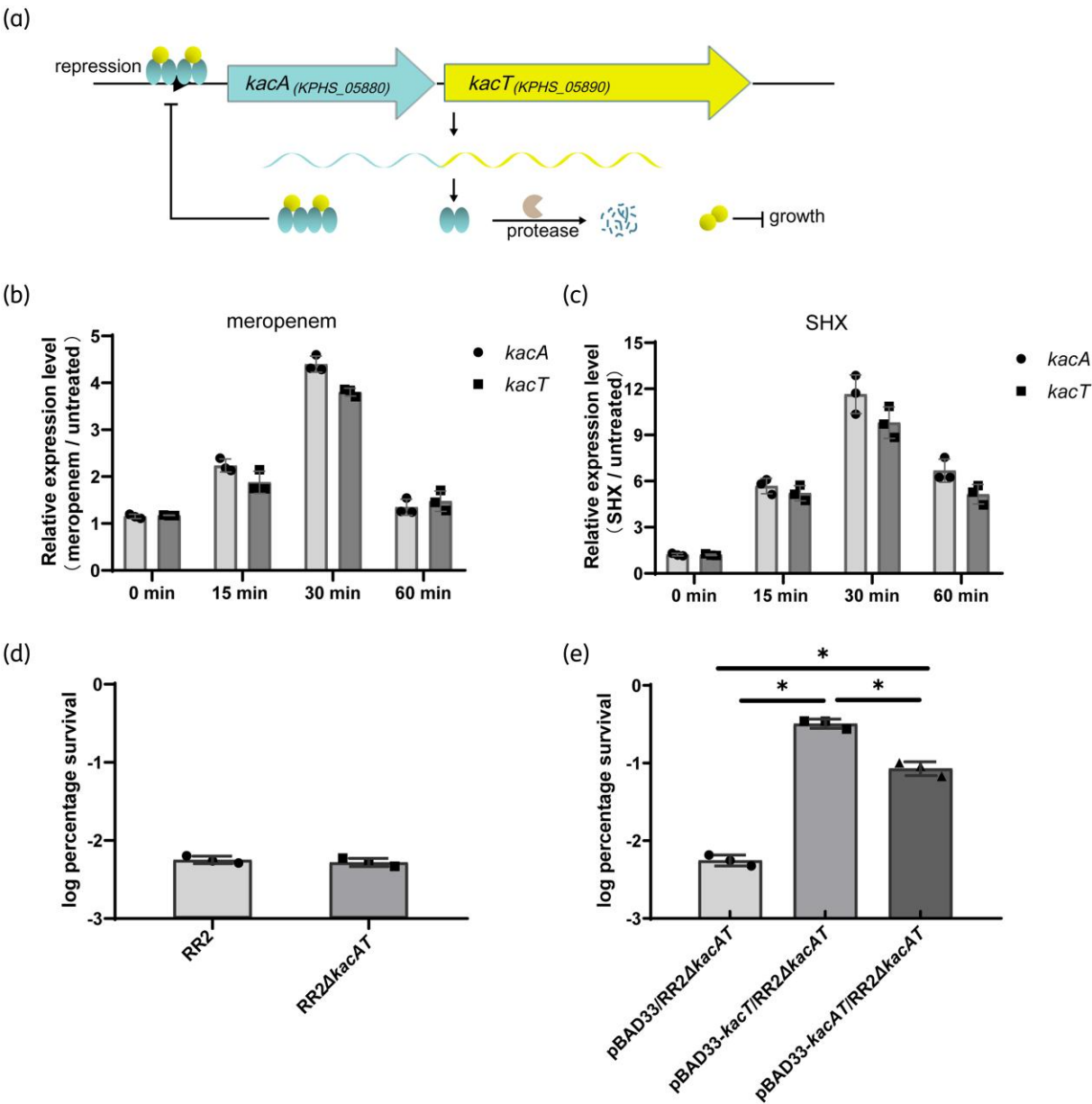
Figure 1. *kacAT* is involved in the response of *K. pneumoniae* to meropenem. (a) Schematic of acetyltransferase-type toxin-antitoxin pair, *kacAT*. *kacA* and *kacT* are co-transcribed. Two KacT molecules bind with four KacA molecules, forming a KacAT heterohexamer complex. The KacAT complex later binds and represses the *kacAT* promoter. KacT independently halts the growth of *K. pneumoniae*, whereas KacA can neutralize the toxicity of KacT. Proteases such as Lon can degrade KacA. Changes in *kacA* and *kacT* transcriptional levels responding to meropenem (b) or SHX (c) are depicted as measured by qRT-PCR. (d) The survival percentage of wild-type RR2 or *kacAT* knockout strain RR2ΔkacAT, treated by meropenem (5 μg/mL) for 4 h. (e) The survival percentage of RR2ΔkacAT strains harbouring empty vector pBAD33, KacT-expressing vector (pBAD33-*kacT*) or KacAT-expressing vector (pBAD33-*kacAT*) after exposure to 5 μg/mL meropenem for 4 h. The transcriptional levels of *kacA* and *kacT* genes were normalized using the housekeeping gene, *gapA*. The survival percentage was calculated by dividing the cfu/mL of the meropenem-treated culture by the cfu/mL of the culture before adding meropenem. SHX was used to compare with meropenem. The bar represents the mean of three independent experiments, and the error bar indicates the SD (*P value <0.05). This figure appears in colour in the online version of *JAC* and in black and white in the print version of *JAC*.

(Figure 1b). On the other hand, the transcriptional levels of *kacA* and *kacT* were also obviously enhanced by SHX (Figure 1c). These results indicated that, similar to other families of TA modules, the GNAT-RHH type TA module, KacAT, also responded to different stress conditions.

Overexpression of kacAT operon enhances the tolerance of K. pneumoniae to meropenem

The expression of the toxin gene *kacT* significantly inhibited the growth of *K. pneumoniae*, whereas the expression of *kacAT* or
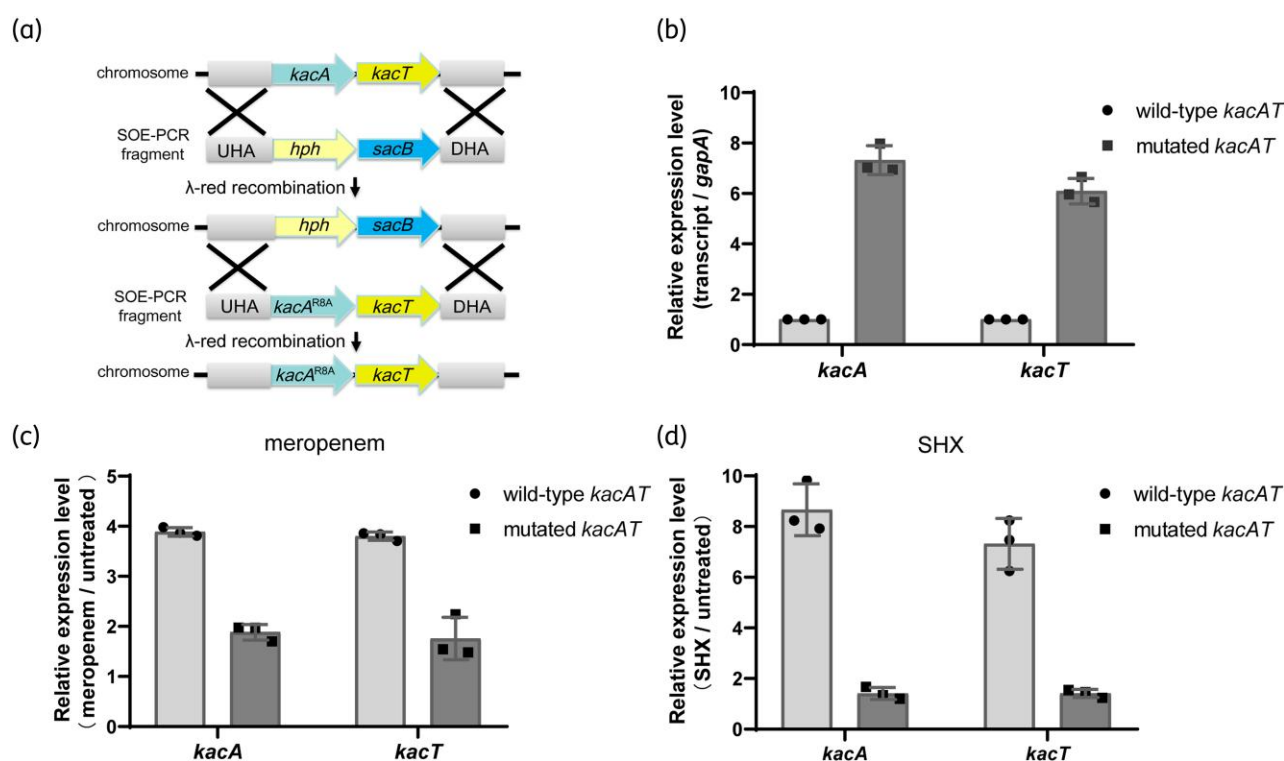
Figure 2. The increased transcription of *kacA* and *kacT* results from autoregulation relief under meropenem exposure. (a) Illustration of the method for constructing chromosomal point mutation strains. (b) Baseline transcriptional levels of *kacA* and *kacT* in wild-type RR2 and mutated KacA[R8A] strains under the normal condition. (c, d) Transcription levels of *kacA* and *kacT* in wild-type RR2 and mutated KacA[R8A] strains under stress conditions. SHX was used to compare with meropenem. Data are presented as mean ± SD (error bars); $n = 3$. DHA, downstream homologous arm; *hph*, hygromycin resistance gene; SOE, gene splicing by overlap extension; UHA, upstream homologous arm; λ-red, phage λ Red recombinase (gam, bet, exo). This figure appears in colour in the online version of *JAC* and in black and white in the print version of *JAC*.

empty pBAD33 plasmid did not (Figure S1b and c). Additionally, we previously found that KacT overexpression induced meropenem tolerance in *K. pneumoniae*.[15] However, the effect of the *kacAT* operon on meropenem tolerance remains to be elucidated. We examined whether the *kacAT* operon affects meropenem tolerance in RR2. As Figure 1d shows, the survivability of RR2 under meropenem exposure was not affected, disregarding the presence of the *kacAT* operon. It is worth noting that, except for KacT, overexpression of KacAT also induced meropenem tolerance in RR2Δ*kacAT* regardless of meropenem concentration (Figure 1e and Figure S1d). The enzymatic activity (detected by the WST-1 cell proliferation and cytotoxicity assay kit) of meropenem-treated *K. pneumoniae* HS11286-RR2Δ*kacAT* was significantly decreased, but the enzymatic activity of strains expressing KacT or KacAT was higher than that of the strain expressing the empty plasmid (Figure S1e). Additionally, we found that the overexpression of KacT and KacAT also increased the tolerance of RR2Δ*kacAT* to imipenem (Figure S1f).

Meropenem-induced *kacAT* transcription results from relief from autoregulation

Type II TA modules strictly obey transcriptional autoregulation performed through conditional cooperativity.[5] We have previously reported that the transcriptional level of *kacAT* is autoregulated

by the [KacA]:[KacT] ratio.[21] Hence, we constructed a chromosomal point mutation in a KacA residue (KacA[R8A]). The residue is required for DNA binding, and the mutated KacA loses the ability to bind its promoter.[21] Then, we measured the transcriptional level of *kacA* and *kacT* under normal or stress conditions using the wild-type RR2 strain, and the KacA-mutated strain (KacA[R8A]). The baseline expression levels of *kacA* and *kacT* in mutated strains were elevated compared with that in the wild-type RR2 strain (Figure 2b). However, the mutated strain's *kacA* and *kacT* transcriptional levels no longer significantly increased, as with the wild-type strain (Figure 2c and d). These results indicated that, under the meropenem condition, relief of *kacAT* autoregulation can increase *kacA* and *kacT* transcription levels in the wild-type RR2 strain.

Lon protease affects transcription of the *kacAT* operon under the meropenem condition

It is proposed that proteases such as Lon or ClpP can degrade antitoxins, freeing toxins to regulate bacterial growth.[17] To test whether the protease genes (*lon* and *clpP*) in RR2 were up-regulated after meropenem treatment, the transcript levels of *lon* and *clpP* were quantified. As shown in Figure 3, the transcription of *lon* increased gradually after meropenem or SHX treatment whereas the transcription level of *clpP* remained constant
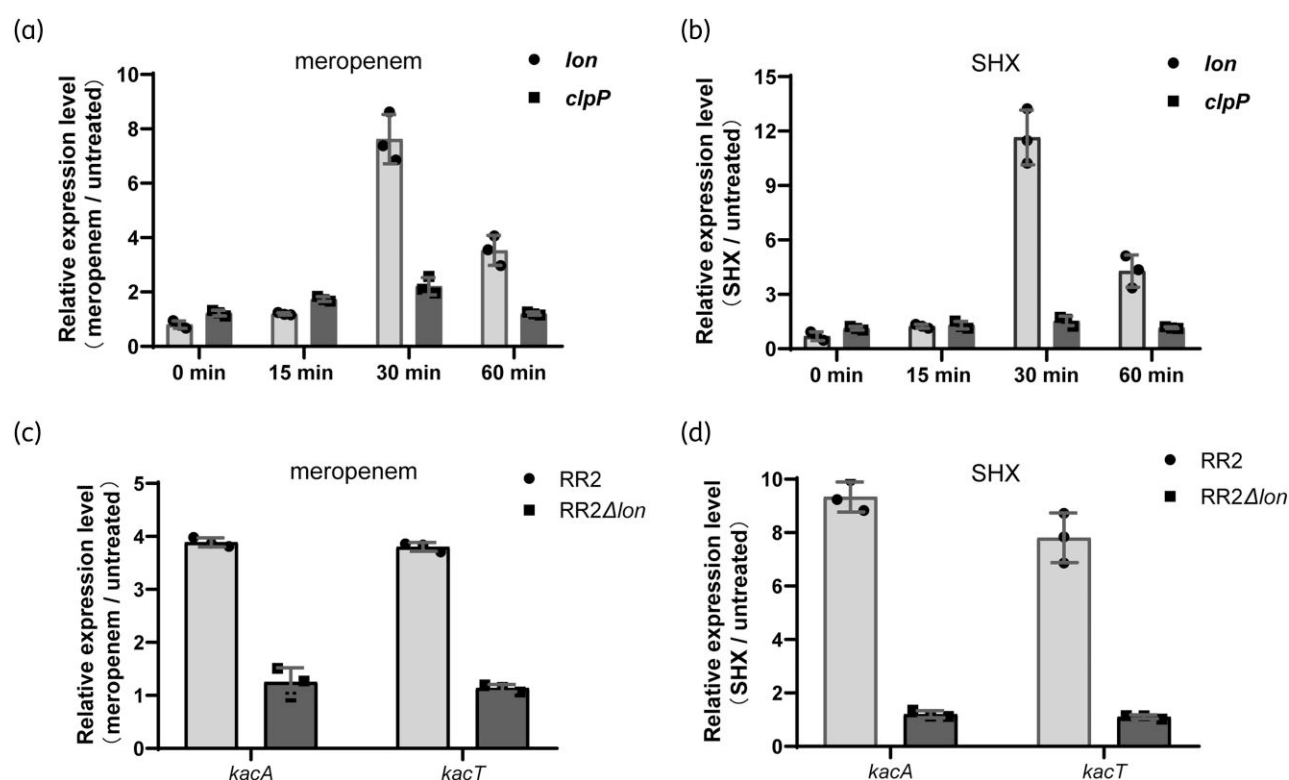
Figure 3. Meropenem induces *lon* transcription that eventually affects *kacAT* transcription. Changes in the *clpP* and *lon* transcription levels in response to meropenem (a) or SHX (b) were measured using qRT-PCR. The transcriptional levels of *kacA* and *kacT* in wild-type RR2 and *lon*-deleted RR2Δ*lon* strain under exposure to meropenem (c) or SHX (d) are depicted. Transcriptional levels of *lon*, *clpP*, *kacA* and *kacT* were normalized using the housekeeping gene *gapA*. SHX was used to compare with meropenem. Data are presented as mean ± SD (error bars); $n = 3$.

(Figure 3a and b). Using the wild-type RR2 and RR2Δ*lon* strains, we further examined the effect of *lon* on *kacAT's* transcription after meropenem exposure. Our results showed that the transcription levels of *kacA* and *kacT* in the RR2Δ*lon* strain were remarkably lower than in the wild-type RR2 strain after meropenem or SHX exposure (Figure 3c and d). These results suggest that *lon* is transcribed at a higher rate under meropenem exposure, possibly translating more Lon protease that could affect *kacA* and *kacT* transcription.

Meropenem leads to KacA degradation through Lon protease

The *in vivo* degradation rate of KacA was examined. We first used western blotting to explore the stability of KacA under meropenem conditions. In the wild-type RR2 cells, compared with the untreated control group, the 6×His-KacA was significantly degraded after meropenem or SHX treatment (Figure 4a). In contrast, for the RR2Δ*lon* cells, the 6×His-KacA did not degrade as much as in RR2 cells (Figure 4b).

Furthermore, it was reported that the existence of toxins YoeB and MqsR can improve the stability of their cognate antitoxins YefM and MqsA, respectively, under heat-shock conditions.[16] However, in another independent study, the authors demonstrated that the antitoxin HipB2 in *Caulobacter* was degraded, although the cognate toxin HipA2 was also present.[30] We thus

explored whether the existence of KacT can slow the degradation rate of KacA. We showed that, in the presence of KacT, KacA did not show visible degradation under SHX pressure, which is consistent with a previous report.[16] Nevertheless, significant degradation of KacA still occurred under the meropenem condition, although the degradation rate was slower than in the absence of KacT (Figure 4c). Apart from that, the 6×His-KacA in RR2Δ*lon* cells did not obviously degrade when KacT was present (Figure 4d). These results suggest that, under the meropenem condition, Lon protease can degrade KacA regardless of the presence of KacT.

We also used fluorescent protein to detect the stability of KacA. We first explored the influence of fluorescent protein on the normal function of KacA and KacT. From Figure S2a, we see that only KacT fused to mCherry at the N-terminal (mCherry-KacT) could inhibit the growth of *K. pneumoniae* similarly to wild-type KacT. KacA fused to eGFP at either N-terminal or C-terminal (eGFP-KacA and KacA-eGFP) could relieve the inhibition of *K. pneumoniae* growth by KacT (Figure S2b). We also found that both eGFP-KacA and KacA-eGFP could neutralize mCherry-KacT's toxicity (Figure S2c). Additionally, the complex formed by KacA-eGFP and mCherry-KacT could bind to P_{kacAT} and inhibit the translation of LacZ (Figure S2d). We also observed the *in vivo* expression of KacA-eGFP and mCherry-KacT (Figure S3a). Furthermore, the stability of KacA-eGFP was measured by using a microplate reader. After treatment with
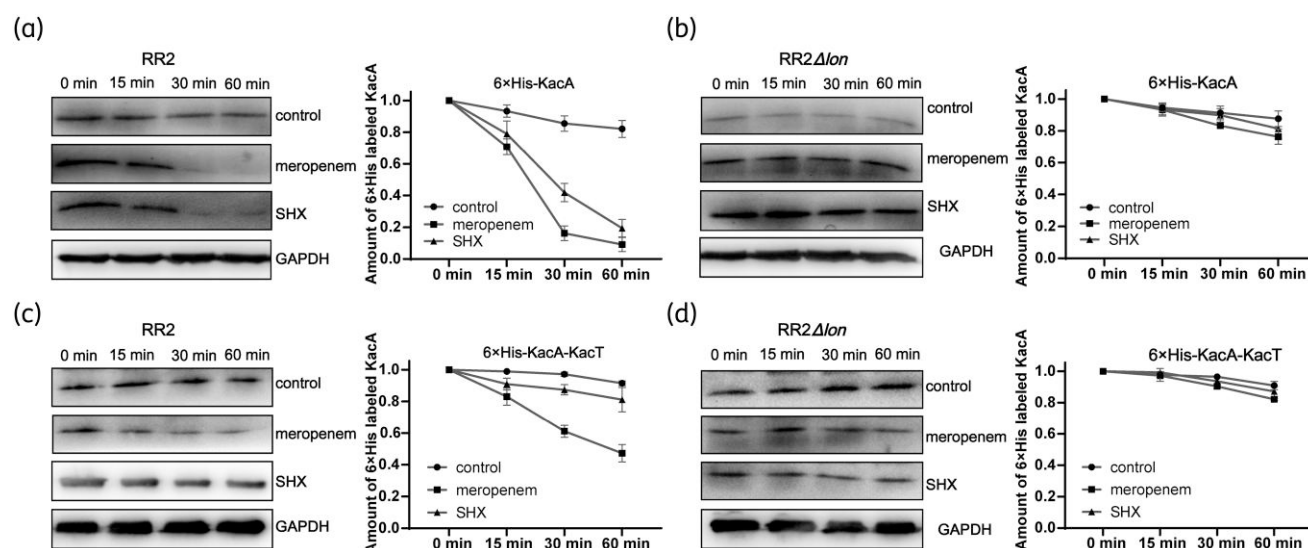
Figure 4. Meropenem induces KacA degradation through Lon protease. Wild-type RR2 and *lon*-deletion (RR2*Δlon*) strains harbouring the pBAD33 vector that expresses (a, b) only 6×His-KacA and (c, d) with KacT. The strains were grown in LB medium at 37°C, $OD_{600} = 0.3$, with 0.2% (w/v) of arabinose. After 90 min of induction, 0.2% (w/v) of glucose was added to inhibit KacA expression together with meropenem. Samples for western blot were collected at the indicated time points (0, 15, 30 and 60 min). (a) and (b) show that the free KacA is degraded by Lon protease after meropenem exposure. (c) and (d) show that KacT could not stabilize KacA under meropenem exposure. SHX was used to compare with meropenem. Data are presented as mean ± SD (error bars); $n = 3$. GAPDH, Glyceraldehyde-3-phosphate dehydrogenase.
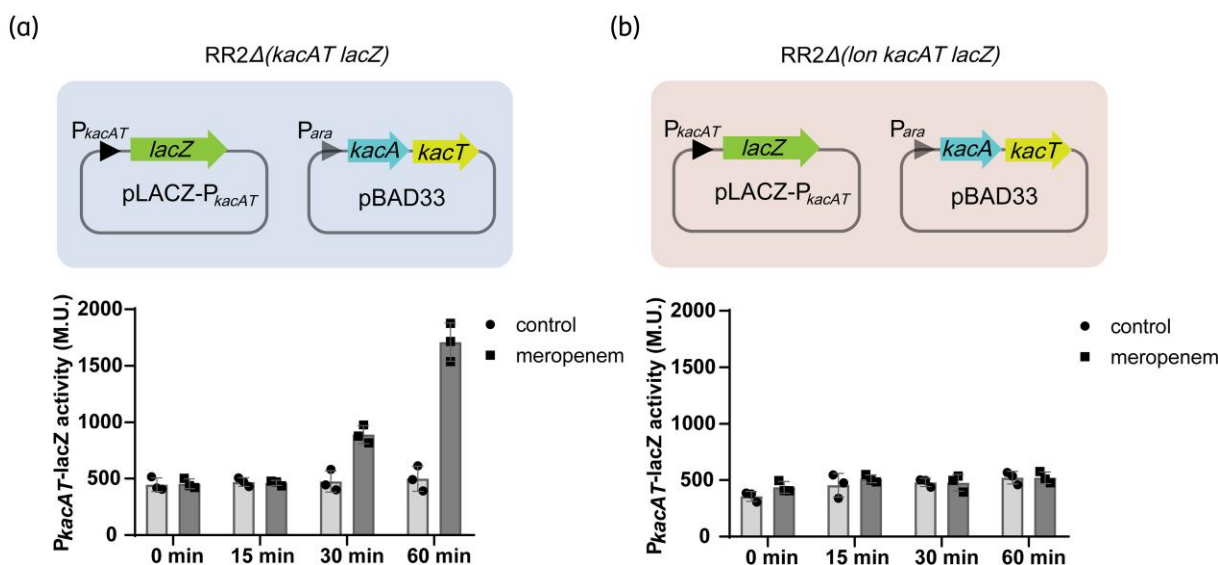

Figure 5. Meropenem promotes the dissociation of the KacAT complex from its promoter. *kacAT* promoter (P_{kacAT}) and the downstream *lacZ* were cloned on the pLACZ-P_{kacAT} plasmid, whereas *kacA* and *kacT* were on the pBAD33 plasmid. pLACZ-P_{kacAT} and pBAD33 in combination expressing KacA and KacT were co-transformed into RR2*Δ*(*kacAT lacZ*) (a) and RR2*Δ*(*lon kacAT lacZ*) (b) cells. Meropenem and 0.2% glucose were added after 3 h of induction of KacA and KacT by arabinose (0.2%). Samples for enzymatic activities were collected at the indicated timepoints (0, 15, 30 and 60 min). MU, miller unit. This figure appears in colour in the online version of *JAC* and in black and white in the print version of *JAC*.

meropenem or SHX, the fluorescence intensity of KacA-eGFP was significantly decreased in the wild-type RR2 compared with RR2*Δlon* cells (Figure S3b and c). Despite the presence of KacT, the fluorescence intensity of KacA-eGFP in wild-type RR2 was still significantly reduced after meropenem treatment compared with the RR2*Δlon* strain (Figure S3d and e), which is consistent with the results of western blot. Besides, we also found that imipenem caused reduced fluorescence intensity of KacA-eGFP in wild-type RR2 compared with RR2*Δlon* cells, which implies that imipenem can also induce the degradation of KacA (Figure S4).
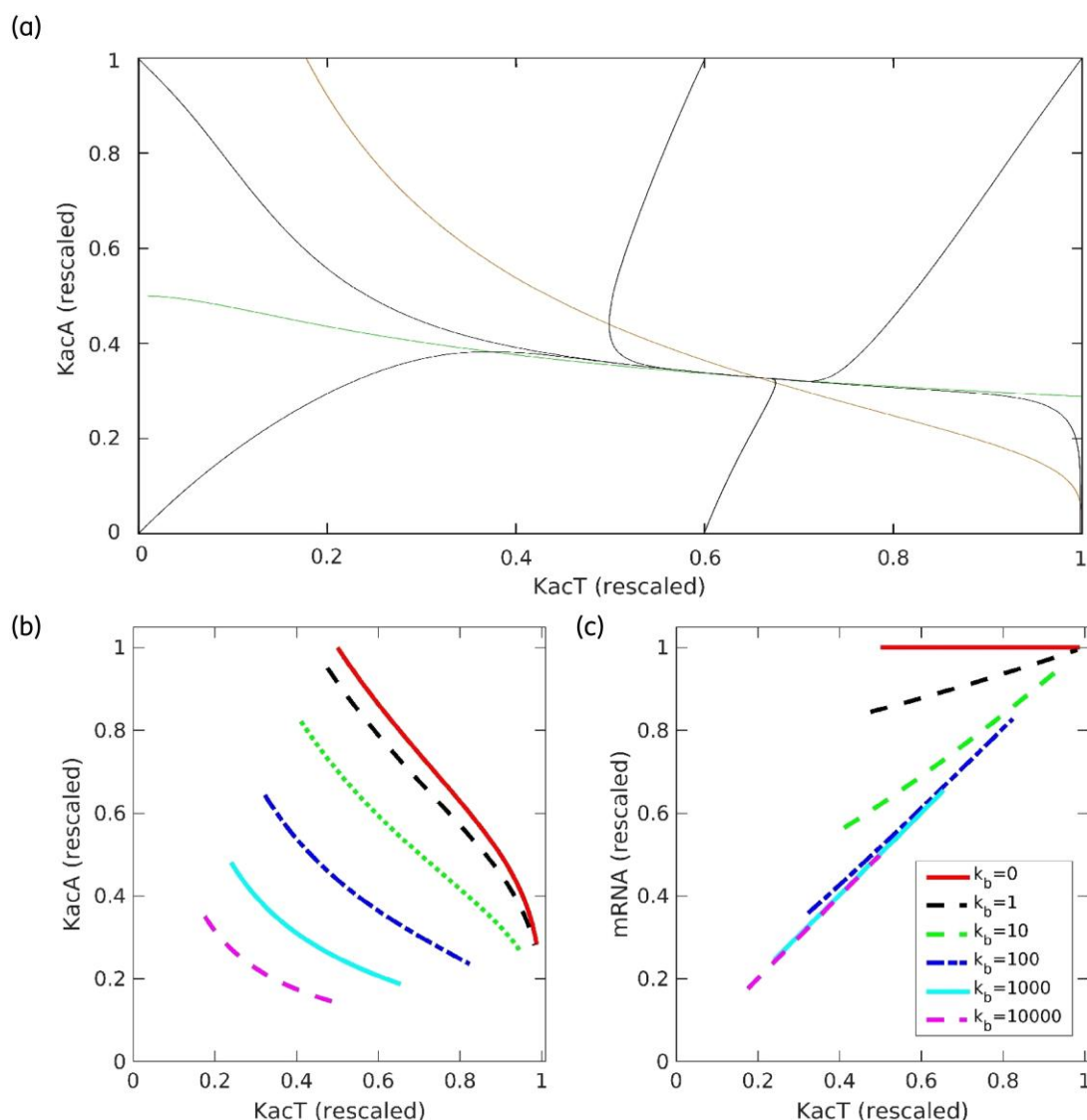
(a)

(b)

(c)

Figure 6. Result of modeling *kacAT* expression dynamics. Phase plane analysis of the system dynamics for the rescaled parameter values $\tilde{\varphi} = 1$, $\tilde{K}_T = 1$, $\tilde{K}_B = 100$, $\Delta\tilde{\lambda} = 3$ (see Materials and methods). The orange and green curves correspond to KacA and KacT nullclines, respectively, with their intersection determining the system's steady state. Solid black curves present trajectories for different system initial conditions (a). Equilibrium values of KacA versus KacT (b) and *kacAT* mRNA versus KacT (c). Different curves correspond to different $\tilde{K}_B$ values indicated in the legend. Points on each curve correspond to changing $\Delta\tilde{\lambda}$ from 0 (left edge) to 6 (right edge), and the values on the axes are rescaled. This figure appears in colour in the online version of *JAC* and in black and white in the print version of *JAC*.

Additionally, we studied whether meropenem could induce KacT's degradation. Under meropenem treatment, the non-toxic KacT^{Y145F} in RR2 or RR2*Δlon* did not degrade much (Figure S5a and b). Likewise, the fluorescence intensity of mCherry-KacT^{Y145F} in wild-type RR2 did not change after meropenem treatment (Figure S5c and d).

Meropenem promotes dissociation of the KacAT complex from its promoter

Because meropenem can promote the degradation of KacA but not KacT, meropenem likely alters the intracellular ratio of [KacA]:[KacT]. To our knowledge, the change in antitoxin to toxin ratio has not been successfully investigated *in vivo* although some approaches have been tried such as the pulse-chase assay.[16] We initially used western blotting to explore changes in the [KacA]:[KacT] ratio but also failed (data not shown). Hence, we fused KacA and KacT with eGFP and mCherry, respectively. The fluorescence intensity of KacA-eGFP and mCherry-KacT, under meropenem stress, was measured by a microplate reader. Our results showed that the ratio of remaining KacA-eGFP to mCherry-KacT was significantly reduced in the wild-type RR2 under the meropenem condition (Figure S6a). Meanwhile, the ratio of [KacA]:[KacT] in the *lon* deletion strain remained unchanged (Figure S6b).
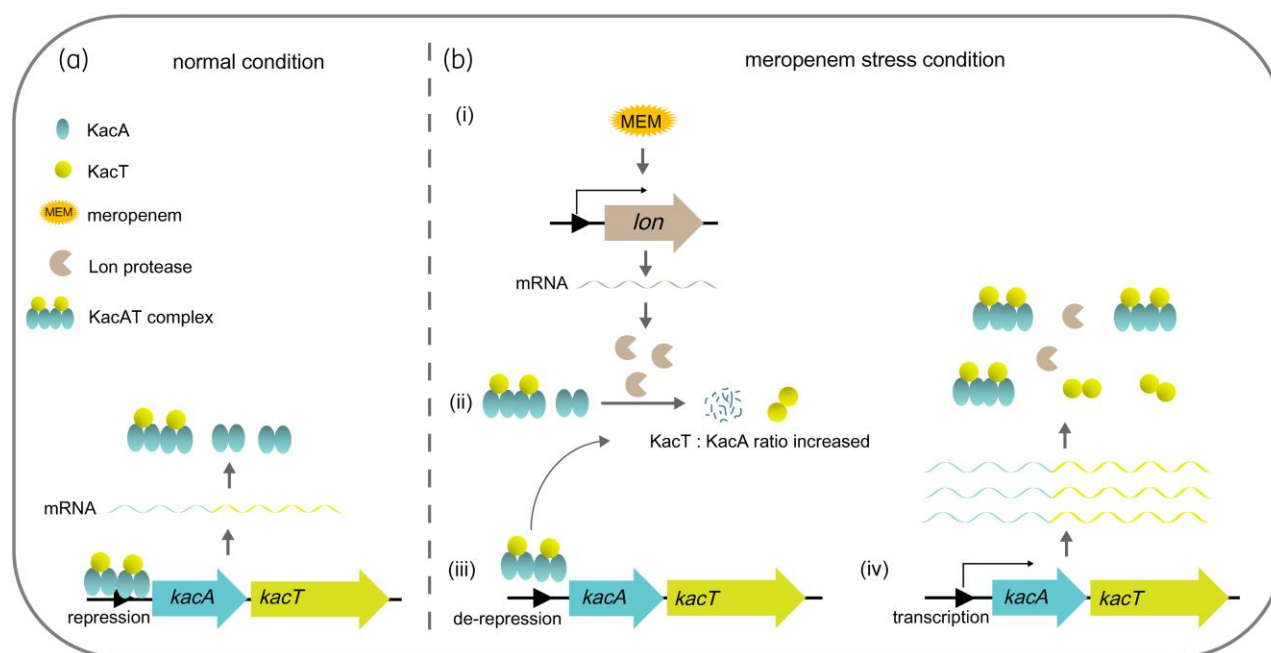
Figure 7. Transcription of the *kacAT* operon under the normal condition (a) and the meropenem stress (b). Meropenem (MEM) induces the enhanced expression of Lon protease, which degrades KacA, resulting in a reduction in the ratio of KacA:KacT. Then, the KacAT complex dissociates from its promoter region, and the transcription of *kacA* and *kacT* is elevated. This figure appears in colour in the online version of *JAC* and in black and white in the print version of *JAC*.

Due to the reduced ratio of [KacA]:[KacT] caused by meropenem, we suggest that meropenem can promote the dissociation of the KacAT complex from its promoter region. We performed a LacZ activity experiment in the *kacAT* promoter (P$_{kacAT}$). Our results showed that, with the prolongation of meropenem treatment time, LacZ activity in RR2Δ(*kacAT lacZ*) harbouring KacA and KacT increased, whereas the RR2Δ(*lon kacAT lacZ*) did not (Figure 5). Additionally, in RR2Δ(*kacAT lacZ*) and RR2Δ(*lon kacAT lacZ*) containing the empty pBAD33 plasmid, LacZ activity was also unchanged under the meropenem conditions (Figure S7). A plausible explanation is that, under meropenem conditions, the KacAT complex dissociates from its promoter P$_{kacAT}$, leading to the transcription of LacZ.

A quantitative model of kacAT expression dynamics explains experimental observations

Based on the experimental results presented above, we developed a quantitative model that can predict protein and transcript synthesis dynamics (see Supplemental methods). We aimed to achieve the following through the model: (1) Check if and under what conditions (parameter range) the model can explain the experimentally observed system response to antibiotic stress, in particular, the significant increase in *kacAT* transcript amounts and the decrease in [KacA]:[KacT] ratio. (2) Predict the dynamics of KacT under antibiotic stress, i.e. upon an increase in KacA degradation. In particular, we aimed to understand the somewhat perplexing observation that KacAT overexpression induces antibiotic stress tolerance, whereas *kacAT* deletion does not affect this tolerance. (3) Infer general properties of *kacAT* expression

dynamics, such as the steady state's number and stability, and how the steady states change with changing parameter values (which is also related to the two previous points).

We start with (3) above, with Figure 6a presenting the phase space analysis of the system dynamics. The system has one steady state corresponding to the intersection of the two nullclines (the orange and the green curves). Linear stability analysis leads to two negative real eigenvalues for this steady state, corresponding to a stable node. Figure 6a shows that trajectories with different initial conditions converge to this stable node. As the system parameters are changed, the phase space topology does not change, but the position of the steady state changes its location in the phase space (not shown in Figure 6a).

We next analyse how the steady state changes as $\Delta\tilde{\lambda}$ (scaled degradation rate of KacA) and $\tilde{K}_B$ (scaled binding affinity of KacAT complex to the promoter) are changed. $\Delta\tilde{\lambda}$ is variable as the experimental analysis found that, via this parameter, the antibiotic stress influences the system dynamics, where $\Delta\tilde{\lambda}$ is changed from 0 (the absence of antibiotic stress) to the relatively high value of $\Delta\tilde{\lambda} = 6$. It is also clear that $\tilde{K}_B$ is a crucial parameter controlling system behaviour, given the reported derepression of the promoter upon antibiotic stress. $\tilde{K}_B = 0$ corresponds to a constitutive (unregulated) promoter, allowing investigation of the system's behaviour during overexpression experiments. Similarly, high values of $\tilde{K}_B$ correspond to strong KacAT complex binding to the promoter, and we change $\tilde{K}_B$ on an exponential scale from 0 to 10^4 (see legend for Figure 6c).

Figure 6b and c show how (rescaled) equilibrium values of KacA, KacT and *kacAT* mRNA change with variations of $\Delta\tilde{\lambda}$ and $\tilde{K}_B$. For each curve, the left edge corresponds to $\Delta\tilde{\lambda} = 0$, and the

right edge to $\Delta\tilde{\lambda} = 6$, and different curves correspond to different $\tilde{K}_B$ values (see the legend). In Figure 6b, we see that irrespective of $\tilde{K}_B$, the ratio [KacA]:[KacT] decreases as $\Delta\tilde{\lambda}$ increases, consistent with experimental observations. Moreover, we obtain a robust (independent of parameter values) prediction that antibiotic stress leads to decreased KacA and increased KacT. This prediction is non-trivial because the decrease of the [KacA]:[KacT] ratio can also be realized through other scenarios, e.g. if KacT remains constant or even decreases, accompanied by a faster decline of KacA.

Figure 6c shows *kacAT* mRNA versus KacT steady-state values. Different lines correspond to different $\tilde{K}_B$ values, and points on each line correspond to increasing (from left to right along the lines) $\Delta\tilde{\lambda}$ values. The horizontal (topmost) line corresponds to the constitutive promoter ($\tilde{K}_B=0$), i.e. to the conditions of the overexpression experiment. The figure shows that smaller $\tilde{K}_B$ values do not lead to a significant increase in the transcript amounts, contrary to what was experimentally observed. Consequently, the strong binding of the complex to the promoter (high $\tilde{K}_B$ values) is consistent with the experimental results. Interestingly, for high $\tilde{K}_B$ values (see the bottommost line corresponding to $\tilde{K}_B = 10^4$), the highest value of KacT (the right edge of the line, obtained for the highest value of $\Delta\tilde{\lambda}$) is still smaller than the lowest KacT value (the left line edge corresponding to $\Delta\tilde{\lambda} = 0$) in the constitutive case. This prediction might explain the naively surprising result that the overexpression experiment led to antibiotic stress tolerance, which is not the case for the native (autoregulated) system. That is, due to the strong binding affinity of the repression complex to promoter DNA, even a significant increase in KacA degradation rate might not be enough to achieve large enough KacT levels necessary to observe antibiotic tolerance.

Transcriptional mechanism of the *kacAT* operon under meropenem stress

Based on the above, we propose a putative model that explains the transcriptional mechanism of the *kacAT* operon under the meropenem condition (Figure 7). In normal circumstances, the relatively lower translation efficiency of KacT ensures the amount of KacA molecules is more than that of KacT. KacA molecules counteract all KacT molecules to form the KacAT complex without releasing the toxicity of KacT. The KacAT complex can bind to its promoter DNA region and block the transcription of *kacAT*. Once the living conditions are changed, such as in meropenem stress, the transcriptional level of the Lon protease gene is increased, resulting in the degradation of unstable KacA. Due to the degradation of KacA, the ratio of [KacA]:[KacT] becomes <1, and the KacAT complex subsequently dissociates from the promotor region of the *kacAT* operon, thereby relieving repression of *kacAT* transcription.

Transparency declarations

All authors: none to declare.

Supplementary data

Figures S1 to S7, Tables S1 and S2, and Supplemental methods are available as Supplementary data at *JAC* Online.

References

1 Gerdes K, Rasmussen PB, Molin S. Unique type of plasmid maintenance function: postsegregational killing of plasmid-free cells. *Proc Natl Acad Sci U S A* 1986; **83**: 3116–20. https://doi.org/10.1073/pnas.83.10.3116

2 Xie Y, Wei Y, Shen Y *et al*. TADB 2.0: an updated database of bacterial type II toxin-antitoxin loci. *Nucleic Acids Res* 2018; **46**: D749–D53. https://doi.org/10.1093/nar/gkx1033

3 Shao Y, Harrison EM, Bi D *et al*. TADB: a web-based resource for type 2 toxin-antitoxin loci in bacteria and archaea. *Nucleic Acids Res* 2011; **39**: D606–D11. https://doi.org/10.1093/nar/gkq908

4 Jurenas D, Fraikin N, Goormaghtigh F *et al*. Biology and evolution of bacterial toxin-antitoxin systems. *Nat Rev Microbiol* 2022; **20**: 335–50. https://doi.org/10.1038/s41579-021-00661-1

5 Harms A, Brodersen DE, Mitarai N *et al*. Toxins, targets, and triggers: an overview of toxin-antitoxin biology. *Mol Cell* 2018; **70**: 768–84. https://doi.org/10.1016/j.molcel.2018.01.003

6 Page R, Peti W. Toxin-antitoxin systems in bacterial growth arrest and persistence. *Nat Chem Biol* 2016; **12**: 208–14. https://doi.org/10.1038/nchembio.2044

7 Jurenas D, Chatterjee S, Konijnenberg A *et al*. Atat blocks translation initiation by N-acetylation of the initiator tRNA^fMet. *Nat Chem Biol* 2017; **13**: 640–6. https://doi.org/10.1038/nchembio.2346

8 Ovchinnikov SV, Bikmetov D, Livenskyi A *et al*. Mechanism of translation inhibition by type II GNAT toxin AtaT2. *Nucleic Acids Res* 2020; **48**: 8617–25. https://doi.org/10.1093/nar/gkaa551

9 Wilcox B, Osterman I, Serebryakova M *et al*. *Escherichia coli* ItaT is a type II toxin that inhibits translation by acetylating isoleucyl-tRNA^Ile. *Nucleic Acids Res* 2018; **46**: 7873–85. https://doi.org/10.1093/nar/gky560

10 Cheverton AM, Gollan B, Przydacz M *et al*. A *Salmonella* toxin promotes persister formation through acetylation of tRNA. *Mol Cell* 2016; **63**: 86–96. https://doi.org/10.1016/j.molcel.2016.05.002

11 CoRycroft JA, Gollan B, Grabe GJ *et al*. Activity of acetyltransferase toxins involved in *Salmonella* persister formation during macrophage infection. *Nat Commun* 2018; **9**: 1993. https://doi.org/10.1038/s41467-018-04472-6

12 Grabe GJ, Giorgio RT, Hall AMJ *et al*. Auxiliary interfaces support the evolution of specific toxin-antitoxin pairing. *Nat Chem Biol* 2021; **17**: 1296–304. https://doi.org/10.1038/s41589-021-00862-y

13 McVicker G, Tang CM. Deletion of toxin-antitoxin systems in the evolution of *Shigella sonnei* as a host-adapted pathogen. *Nat Microbiol* 2017; **2**: 16204. https://doi.org/10.1038/nmicrobiol.2016.204

14 Liu P, Li P, Jiang X *et al*. Complete genome sequence of *Klebsiella pneumoniae* subsp pneumoniae HS11286, a multidrug-resistant strain isolated from human sputum. *J Bacteriol* 2012; **194**: 1841–2. https://doi.org/10.1128/JB.00043-12

15 Qian H, Yao Q, Tai C *et al*. Identification and characterization of acetyltransferase-type toxin-antitoxin locus in *Klebsiella pneumoniae*. *Mol Microbiol* 2018; **108**: 336–49. https://doi.org/10.1111/mmi.13934

16 LeRoux M, Culviner PH, Liu YJ *et al*. Stress can induce transcription of toxin-antitoxin systems without activating toxin. *Mol Cell* 2020; **79**: 280–92. https://doi.org/10.1016/j.molcel.2020.05.028

17 Muthuramalingam M, White JC, Bourne CR. Toxin-antitoxin modules are pliable switches activated by multiple protease pathways. *Toxins (Basel)* 2016; **8**: 214. https://doi.org/10.3390/toxins8070214

18 Ronneau S, Helaine S. Clarifying the link between toxin-antitoxin modules and bacterial persistence. *J Mol Biol* 2019; **431**: 3462–71. https://doi.org/10.1016/j.jmb.2019.03.019

19 Overgaard M, Borch J, Jorgensen MG *et al*. Messenger RNA interferase RelE controls *relBE* transcription by conditional cooperativity. *Mol Microbiol* 2008; **69**: 841–57. https://doi.org/10.1111/j.1365-2958.2008.06313.x

20 Garcia-Pino A, Balasubramanian S, Wyns L *et al*. Allostery and intrinsic disorder mediate transcription regulation by conditional cooperativity. *Cell* 2010; **142**: 101–11. https://doi.org/10.1016/j.cell.2010.05.039

21 Qian H, Yu H, Li P *et al*. Toxin-antitoxin operon *kacAT* of *Klebsiella pneumoniae* is regulated by conditional cooperativity via a W-shaped KacA-KacT complex. *Nucleic Acids Res* 2019; **47**: 7690–702. https://doi.org/10.1093/nar/gkz563

22 Bordes P, Genevaux P. Control of toxin-antitoxin systems by proteases in *Mycobacterium tuberculosis*. *Front Mol Biosci* 2021; **8**: 691399. https://doi.org/10.3389/fmolb.2021.691399

23 Dubiel A, Wegrzyn K, Kupinski AP *et al*. ClpAP protease is a universal factor that activates the *parDE* toxin-antitoxin system from a broad host range RK2 plasmid. *Sci Rep* 2018; **8**: 15287. https://doi.org/10.1038/s41598-018-33726-y

24 Lunge A, Gupta R, Choudhary E *et al*. The unfoldase ClpC1 of *Mycobacterium tuberculosis* regulates the expression of a distinct subset of proteins having intrinsically disordered termini. *J Biol Chem* 2020; **295**: 9455–73. https://doi.org/10.1074/jbc.RA120.013456

25 Maisonneuve E, Shakespeare LJ, Jorgensen MG *et al*. Bacterial persistence by RNA endonucleases. *Proc Natl Acad Sci U S A* 2011; **108**: 13206–11. https://doi.org/10.1073/pnas.1100186108

26 Pu Y, Zhao Z, Li Y *et al*. Enhanced efflux activity facilitates drug tolerance in dormant bacterial cells. *Mol Cell* 2016; **62**: 284–94. https://doi.org/10.1016/j.molcel.2016.03.035

27 Griffith KL, Wolf RE. Measuring beta-galactosidase activity in bacteria: cell growth, permeabilization, and enzyme assays in 96-well arrays. *Biochem Bioph Res Co* 2002; **290**: 397–402. https://doi.org/10.1006/bbrc.2001.6152

28 Livak KJ, Schmittgen TD. Analysis of relative gene expression data using real-time quantitative PCR and the $2^{-\Delta\Delta C_T}$ method. *Methods* 2001; **25**: 402–8. https://doi.org/10.1006/meth.2001.1262

29 Haddadin FT, Kurtz H, Harcum SW. Serine hydroxamate and the transcriptome of high cell density recombinant *Escherichia coli* MG1655. *Appl Biochem Biotechnol* 2009; **157**: 124–39. https://doi.org/10.1007/s12010-008-8241-0

30 Zhou X, Eckart MR, Shapiro L. A bacterial toxin perturbs intracellular amino acid balance to induce persistence. *mBio* 2021; **12**: e03020-20. https://doi.org/10.1128/mBio.03020-20

An analytical framework for understanding infection progression under social mitigation measures

Bojana Ilic · Igor Salom · Marko Djordjevic · Magdalena Djordjevic

Abstract While there has been much computational work on the effect of intervention measures, such as vaccination or quarantine, the influence of social distancing on the epidemics' outbursts is not well understood. We present a realistic, analytically solvable, framework for COVID-19 dynamics in the presence of social distancing measures. The model is a generalization of the compartmental SEIR model that accounts for the effects of these measures. We derive a closed-form mathematical expressions for the time dependence of epidemiological observables, in particular, the detected cases and fatalities. These analytical solutions indicate simple quantitative relations between the model variables and epidemiological observables, which give insights into cause-effect connections that underlie the outburst dynamics but are obscured in more standard (numerical) approaches. While the obtained results and conclusions are based on the study of the COVID-19 pandemic, the presented analysis has general applicability to infection outbursts. Our findings are particularly important in the emergence of new pandemics when effective pharmaceutical treatments are unavailable, and one must rely on well-timed and appropriately chosen social mitigation measures.

1 Introduction

Numerical computation methods and/or simulations are routinely used to study epidemiological dynamics. These tools can easily produce predictions of even very complex epidemiological models. Yet, in a certain sense, the numerical computation/simulation is comparable to a black-box system that converts given model parameters to the prediction outcomes, hardly facilitating any direct and deeper understanding of the influences of individual parameters on model observables. Additionally, inferring the parameter values from the observed data, analogous to reverse-engineering of the black-box functioning, often becomes a difficult task.

These problems have become additionally pronounced in the context of the current COVID-19 pandemic, which, since being unprecedented in many aspects, underlines the necessity to expand the commonly used epidemiological models. Progress has been made in various directions, e.g. by taking into account the effects of quarantine [1,2], temporary immunity [3], recurrent outbreaks [4], vaccination [5–8], different levels of population susceptibility [9], comorbidi-

B. Ilic · I. Salom · M. Djordjevic (✉)
Institute of Physics Belgrade, National Institute of the Republic of Serbia, University of Belgrade, Pregrevica 118, Belgrade 11080, Serbia
e-mail: magda@ipb.ac.rs

M. Djordjevic
Quantitative Biology Group, Faculty of Biology, University of Belgrade, Studentski trg 3, Belgrade 11000, Serbia

ties [8,10], stratification by age [11–13], competitive virus strains of different severity and/or transmissibility [14,15], spatial diffusion [16], human mobility between different regions [17–19], availability of testing kits [20], hospital infrastructure [21] and media coverage [22,23] to name a few. In particular, the attempts to combat the disease led to the introduction of social distancing measures on the scales hardly imaginable before [24].

While it is evident that social distancing measures seriously impact the epidemiological dynamic, their effects are not yet well understood [25–27], despite a lot of undergoing effort to incorporate the influence of these measures into the existing epidemiological models [4,8,22,28–39]. These studies often use an analytical approach to analyze and reveal some of the system's characteristics—e.g., system equilibria, positivity and boundness of variables, stability, sensitivity and bifurcation analysis [8,35–39]. Thus, they allowed insights into some important aspects of the system's behavior, and the role played by the social measures. For example, analytical calculations provided a better understanding of the interventions required to control the disease, such as the interplay between governmental actions and the public response [39], and quarantine [35]. However, to our knowledge, no attempts were made to analytically solve complex systems of nonlinear differential equations stemming from these extended epidemiological models (neither from the models aimed to include the effects of mitigation measures nor from those trying to incorporate other relevant factors). Instead, computer simulations and/or numerical solving of differential equations are commonly used to compute and analyze the time evolution of the epidemic (e.g., to make comparisons with the actual epidemiological data). Consequently, despite the ability to include intricate details of the models, these studies lacked the full analytical approach to establish direct functional relations between variables and outcomes, thus missing the advantages of having analytical formulas describing the entire time evolution of the system variables.

While the advantages of the analytical approach are clear, all of the studied models in epidemiology, including the very basic ones such as SIR (Susceptible-Infected-Removed [40]), are nonlinear and the corresponding differential equations cannot be solved in a straightforward manner [41]. Nevertheless, in the last two decades, there was significant progress in

the field. To our knowledge, the earliest advances in this direction appeared with the turn of the century and were related to the SIR model, on networks [42] and its stochastic variant [43], followed by solutions given in the forms of convergent series, for SIR [44] and then also for SIR and SIS (Susceptible-Infected-Susceptible) models [45]. Further progress was made by Harko et al. in 2014 [46], by providing the SIR model analytical solutions, albeit in parametric form and up to an integral inexpressible by elementary functions. COVID-19 pandemic has intensified the efforts in this direction, resulting in new forms of solutions for SIR model: as infinite series (using Asymptotic Approximants method) [47], as an inverse solution with an approximated integral [48], using integrals inexpressible in terms of elementary functions [49], and a direct approximated solution [50,51]. Some of these approaches preserve (approximative) integrability even when constant model parameters (such as infection rate) are replaced by time-varying functions (though with certain constraints). Recently, there has been also some progress even with compartmental models more complex than the basic SIR variant. More precisely, papers [52] and [53] analytically treat SEIR (Susceptible-Exposed-Infected-Removed) model and find, respectively, a solution in the form of a well converging infinite series and as an exact solution to an approximative reduced model.

Along with the attempts to analytically solve the equations governing the epidemic dynamics, there was an ongoing effort to find useful analytical relations between the relevant epidemiological variables. One such simple but transcendental equation, relating the basic reproductive number with the final size of the susceptible compartment, was an immediate consequence of the SIR model [40], and a similar result was obtained for the SEIR model [53] (the robustness of such relations is discussed in [54]). Moreover, it often turns out to be possible to derive useful simple analytical expressions for the time of the infection peak and/or the fraction of immunized required to stop the epidemic [48,50,51,53,55,56]. These formulas, obtained at a low cost of applying practically negligible approximations to the starting equations or intermediary expressions, turn out to be very accurate (when compared to precise numerical computations).

All these analytical results were obtained only in the context of SIR and SEIR models, and the presence of intervention measures likely renders them unus-

able. Therefore, this study aims, for the first time, to establish a realistic—analytically solvable— model of COVID-19 dynamics in the presence of social distancing measures and to demonstrate the benefits of such an approach. The model is a generalization of the compartmental SEIR model— so-called SPEIRD [57,58]— that accounts for the influence of social measures by mathematically representing them as an effect that removes susceptibles from the transmission process (and places them in a newly introduced Protected compartment). A similar approach to introduce the effects of distancing in compartmental models can be found in [32,34–37] and is in certain aspects advantageous over simply varying transmission coefficients in time, implemented in many models [4,8,22,33,38,39]. SPEIRD also introduces additional compartments that directly correspond to epidemiological observables: the number of detected cases and fatalities. The model was introduced in [57], but due to the complex system of nonlinear differential equations, no attempts were made to solve them analytically. However, it turned out that, despite complicated equations, it was possible to analytically compute the closed-form expression for the number of infected cases as a function of time. This partial result was published in [58] and presents a starting point in this study. However, due to its complexity, we were unable to make further progress toward computing other system variables. We only recently managed to analytically compute the time evolution of all relevant variables (i.e., the closed-form expressions for the full-time evolution of the number of confirmed (detected) cases and fatalities). These two variables have been used as crucial measures for tracking epidemic progression and its severity, and this manuscript presents the full analytical treatment of the equations by deriving their closed-form mathematical expressions.

The time evolutions derived here allow us to analytically investigate the effect of different model parameters on the infection outcome and to recognize particular interplays. Knowing explicitly the relations between input and output variables not only vastly simplifies our ability to extract model parameters from experimental data (e.g., by distinguishing special regimes in which equations have characteristic behavior [58]) but, more importantly, to straightforwardly draw conclusions that may simplify public policy decision making. In particular, the asymptotic expressions obtained here for the cumulative numbers of COVID-19 detected cases and fatalities, quantitatively reveal a simple interplay

between the basic reproduction number R_0, the strength of introduced social measures, and the timing of their introduction. Namely, it turns out, as we show in Sect. 4 and further elaborate in Sect. 5, that more flexible, i.e., relaxed measured can be easily afforded if they are timely introduced (to the same overall effect as with far more stringent measures introduced just a week or two later). Moreover, we provide simple analytical expressions for estimating the timing of the peak, the tipping points of the epidemic wave, as well as the maximum of detected cases per day. Providing an analytical framework to understand such epidemiological behavior may have a significant impact both on the economy and the quality of human lives.

While the obtained results and conclusions were based on the study of the COVID-19 pandemic (and tested on corresponding epidemiological data), the analysis presented here is of general validity and therefore directly applicable to any possible infection outbreak in the future. While at this stage of the COVID-19 pandemic, we already have additional tools to combat the disease (e.g., vaccines and mounting clinical experience), general conclusions drawn from the models like this one can be a particularly valuable aid in the initial stages of any new epidemic.

2 Methodology

To assess the dynamics of COVID-19 infection, we employ a mechanistic model SPEIRD, which we developed in Refs. [57,58]. More precisely, concerning the standard compartmental models in epidemiology [25–27], which comprise susceptible (S), exposed (E), infectious (I), and undiagnosed recovered (R) pools, we added a few additional compartments. These are introduced to take into account the available data (direct observable quantities), such as the total number of detected (confirmed and thereupon quarantined) cases (D), active cases (A), and fatalities (F). It also accounts for the effects of the social protection measures by adding a compartment (P) of protected individuals (denoting those effectively removed from susceptible category due to social distancing). The corresponding equations, describing the model dynamics, read:

$$\frac{\mathrm{d}S}{\mathrm{d}t} = -\frac{\beta SI}{N} - \frac{\mathrm{d}P}{\mathrm{d}t}, \tag{1}$$

$$\frac{\mathrm{d}P}{\mathrm{d}t} = \frac{\alpha S}{1 + (t_0/t)^n}, \tag{2}$$

$$\frac{\mathrm{d}E}{\mathrm{d}t} = \frac{\beta SI}{N} - \sigma E, \tag{3}$$

$$\frac{\mathrm{d}I}{\mathrm{d}t} = \sigma E - \gamma I - \epsilon \delta I, \tag{4}$$

$$\frac{\mathrm{d}R}{\mathrm{d}t} = \gamma I, \tag{5}$$

$$\frac{\mathrm{d}D}{\mathrm{d}t} = \epsilon \delta I, \tag{6}$$

$$\frac{\mathrm{d}A}{\mathrm{d}t} = \epsilon \delta I - hA - mA, \tag{7}$$

$$\frac{\mathrm{d}F}{\mathrm{d}t} = mA. \tag{8}$$

In the above equations, N stands for the total population number, while parameters have the following meaning: β— the transmission rate; α— strength of the social measures; σ— the inverse of the latency period; γ— the inverse of the infectious period; δ— the inverse of the infected detection period; ϵ— the detection efficiency; h and m— the recovery and the mortality rate, respectively. According to [59–61], we assume $\sigma = 1/3 \, \mathrm{day}^{-1}$ and $\gamma = 1/4 \, \mathrm{day}^{-1}$. The gradual effect of social measures is introduced through Eq. (2) where t_0 denotes the time when the measures are enforced. In [58], it was shown that Hill function [62] can be reliably replaced by the step function of the form $\alpha \theta(t - t_0)$, which we further apply. We also assume that, after t_0, the 2nd term in Eq. (1) dominates over the 1st term, i.e., $S(t) \sim \mathrm{e}^{-\alpha t}$, which we previously numerically showed to hold well for a wide range of countries in the first COVID-19 wave [58].

In Fig. 1, we provide a schematic representation of the SPEIRD model (Eqs. (1)-(8)). Thus, Eq. (1) determines the rate of depletion of the susceptible population due to both the infection process and the social distancing measures. These measures result in a transition of the susceptible to the protected compartment, described by Eq. (2). In Eq. (3), the exposed pool increases due to the infection events. Simultaneously, it decreases due to a transition to the infectious compartment with the rate σ. Equation (4) describes how the number of infectious individuals grows due to the transition from exposed to the infectious category, while it decreases with the rate γ (recovery of undiagnosed infected to R compartment) or with rate $\epsilon \delta$ (corresponding to their detection and subsequent quarantine, resulting in a transition to the detected compartment D). Equation (7) fixes

the rate at which the active compartment is depleted through two channels − by being healed (rate h) or by dying from the virus (rate m). Equation (8) describes the growth of the fatalities.

The model corresponds to the infection phase, where social distancing measures are first introduced (in our case, the first COVID-19 wave), corresponding to the effective transition from S to P compartment. As the measures later got eased, there can also be a transition from P back to S. This is, for simplicity, not implemented in SPEIRD (and usually neither in similar models, see e.g. Refs. [32,34–37]), i.e., only the first phase of epidemics (and the social measure introduction) is considered. We implement our model deterministically, as publicly available COVID-19 counts [63] are very high in most countries, making the relative importance of fluctuations low, and the deterministic description appropriate [62]. The advantage of such an approach is the analytical tractability and more intuitive understanding of the obtained results.

Despite the complexity of the system of equations (1)-(8), we show that the model can be analytically treated. As a starting point in our calculation, we use the explicit expression for the number of infectious individuals as a function of time, obtained in [58]:

$$I(t) = \theta(t_0-t)I_0\mathrm{e}^{\lambda_+ t} + \theta(t-t_0)I_0\mathrm{e}^{\lambda_+ t_0}\mathrm{e}^{-\frac{\gamma+\epsilon\delta+\sigma}{2}(t-t_0)}$$
$$\times \frac{\mathrm{K}\left(\frac{\gamma+\epsilon\delta-\sigma}{\alpha}, \frac{2\sqrt{\mathrm{e}^{-\alpha(t-t_0)}\beta\sigma}}{\alpha}\right)}{\mathrm{K}\left(\frac{\gamma+\epsilon\delta-\sigma}{\alpha}, \frac{2\sqrt{\beta\sigma}}{\alpha}\right)}, \tag{9}$$

where $\mathrm{K}(n, x)$ stands for the modified Bessel function of the second kind [64], $\lambda_+ = \frac{\sqrt{(\gamma+\epsilon\delta-\sigma)^2+4\beta\sigma}-(\gamma+\epsilon\delta+\sigma)}{2}$, $\theta(t)$ denotes Heaviside step function and I_0 is the initial number of infectious individuals in population.

The main result of this paper is the derivation of the time-dependent expressions for the numbers of fatalities $F(t)$ and detected cases $D(t)$, which are continuously tracked and publicly available quantities for a vast number of countries and regions [63]. The analytical derivations of these expressions are presented in Appendix A. Essentially, Eqs. (6)-(8) lead to two disentangled differential equations determining $F(t)$ and $D(t)$:

$$\frac{\mathrm{d}^2 F(t)}{\mathrm{d}t^2} + (h+m)\frac{\mathrm{d}F(t)}{\mathrm{d}t} - m\epsilon\delta I(t) = 0, \tag{10}$$
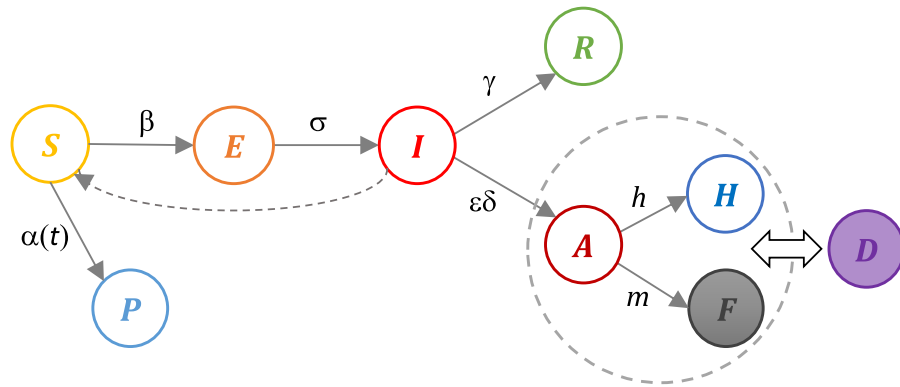
Fig. 1 Scheme of the SPEIRD model. The compartments are represented with circles and named as indicated in the text. The transitions between different compartments are denoted by arrows, with labels corresponding to the appropriate transition rates, as explained in the text. The two main categories for our study (also corresponding to widely tracked observable quantities) — fatalities (F) and detected cases (D) are denoted by the full gray and purple circles, respectively. The dashed circle indicates that A, H, and F compartments from the original model compose the detected cases D

$$D(t) = \epsilon\delta \int I(t)\, \mathrm{d}t + C. \tag{11}$$

Here, $I(t)$ is given by Eq. (9) and C stands for the constant of integration. All constants of integration are determined from the requirement of continuity of functions, their first derivatives, and/or the initial conditions: $F(0) = 0$ and $D(0) = D_0$, where D_0 is the initial number of detected cases at onset of infection progression in a population.

Solving these equations is highly nontrivial due to the complex form (see Eq. (9)) of the function $I(t)$. To accomplish this task, aside from commonly used methods for solving differential equations (i.e., known methods for second-order inhomogeneous Cauchy–Euler equation), we used a number of special properties of modified Bessel functions of the first and second kind, of upper incomplete gamma functions, and of regularized generalized hypergeometric functions, as detailed in Appendix A.

3 Analytical results

Using the methodology outlined in the previous section, in Appendix A, we derived closed-form expressions for the number of fatalities and the cumulative number of detected cases, as functions of time. The number of fatalities $F(t)$ has the following form:

$$
\begin{aligned}
F(t) = {} & \theta(t_0 - t)\frac{I_0\epsilon\delta}{\lambda_+}\frac{m}{m+h} \\
& \left\{ -1 + \frac{\lambda_+}{h+m+\lambda_+}e^{-(h+m)t} \right. \\
& \left. + \frac{h+m}{h+m+\lambda_+}e^{\lambda_+ t} \right\} \\
& + \theta(t - t_0)\left\{ C_1 + C_2 e^{-(h+m)t} \right. \\
& \left. + C_1(t) + C_2(t)\left(\frac{2\sqrt{\beta\sigma}}{\alpha}\right)^{\frac{2(h+m)}{\alpha}} e^{-(h+m)t} \right\},
\end{aligned}
\tag{12}
$$

where:

$$
\begin{aligned}
C_1(t) = {} & C_0 \left[\left(\frac{\sqrt{\beta\sigma}}{\alpha}\right)^{\frac{\gamma+\epsilon\delta-\sigma}{\alpha}} e^{-(\gamma+\epsilon\delta)t}\Gamma\left(\frac{\gamma+\epsilon\delta}{\alpha}\right) \right. \\
& \times {}_1\tilde{F}_2\left(\frac{\gamma+\epsilon\delta}{\alpha}; 1+\frac{\gamma+\epsilon\delta}{\alpha}, 1 \right. \\
& \left. +\frac{\gamma+\epsilon\delta-\sigma}{\alpha}; \frac{e^{-\alpha t}\beta\sigma}{\alpha^2}\right) \\
& - \left(\frac{\sqrt{\beta\sigma}}{\alpha}\right)^{-\frac{\gamma+\epsilon\delta-\sigma}{\alpha}} e^{-\sigma t}\Gamma\left(\frac{\sigma}{\alpha}\right) \\
& \left. \times {}_1\tilde{F}_2\left(\frac{\sigma}{\alpha}; 1+\frac{\sigma}{\alpha}, 1+\frac{\sigma-\gamma-\epsilon\delta}{\alpha}; \frac{e^{-\alpha t}\beta\sigma}{\alpha^2}\right) \right]
\end{aligned}
$$

$$\frac{\pi}{2}\csc\left[\frac{\pi(\gamma+\epsilon\delta-\sigma)}{\alpha}\right]$$

$$
\begin{aligned}
C_2(t) = -C_0\Bigg[&\left(\frac{\sqrt{\beta\sigma}}{\alpha}\right)^{\frac{\gamma+\epsilon\delta-\sigma}{\alpha}} \\
&\mathrm{e}^{-(\gamma+\epsilon\delta)t}\Gamma\left(\frac{\gamma+\epsilon\delta-h-m}{\alpha}\right) \\
&\times {}_1\tilde{\mathrm{F}}_2\left(\frac{\gamma+\epsilon\delta-h-m}{\alpha};1\right.\\
&\qquad +\frac{\gamma+\epsilon\delta-h-m}{\alpha},1 \\
&\qquad \left.+\frac{\gamma+\epsilon\delta-\sigma}{\alpha};\frac{\mathrm{e}^{-\alpha t}\beta\sigma}{\alpha^2}\right) \\
&-\left(\frac{\sqrt{\beta\sigma}}{\alpha}\right)^{-\frac{\gamma+\epsilon\delta-\sigma}{\alpha}}\mathrm{e}^{-\sigma t}\Gamma\left(\frac{\sigma-h-m}{\alpha}\right) \\
&\times {}_1\tilde{\mathrm{F}}_2\left(\frac{\sigma-h-m}{\alpha};1+\frac{\sigma-h-m}{\alpha},1\right.\\
&\qquad \left.+\frac{\sigma-\gamma-\epsilon\delta}{\alpha};\frac{\mathrm{e}^{-\alpha t}\beta\sigma}{\alpha^2}\right)\Bigg] \\
&\frac{\pi}{2}\csc\left[\frac{\pi(\gamma+\epsilon\delta-\sigma)}{\alpha}\right],
\end{aligned}
$$
(13)

$$
\begin{aligned}
C_1 = I_0\epsilon\delta\frac{m}{(h+m)}\frac{\mathrm{e}^{\lambda_++t_0}-1}{\lambda_+}-C_0 \\
\left[\left(\frac{\sqrt{\beta\sigma}}{\alpha}\right)^{\frac{\gamma+\epsilon\delta-\sigma}{\alpha}}\Gamma\left(\frac{\gamma+\epsilon\delta}{\alpha}\right)\right.\\
\times {}_1\tilde{\mathrm{F}}_2\left(\frac{\gamma+\epsilon\delta}{\alpha};1+\frac{\gamma+\epsilon\delta}{\alpha},1\right.\\
\left.+\frac{\gamma+\epsilon\delta-\sigma}{\alpha};\frac{\beta\sigma}{\alpha^2}\right)\\
-\left(\frac{\sqrt{\beta\sigma}}{\alpha}\right)^{-\frac{\gamma+\epsilon\delta-\sigma}{\alpha}}\Gamma\left(\frac{\sigma}{\alpha}\right)\\
\left.\times {}_1\tilde{\mathrm{F}}_2\left(\frac{\sigma}{\alpha};1+\frac{\sigma}{\alpha},1+\frac{\sigma-\gamma-\epsilon\delta}{\alpha};\frac{\beta\sigma}{\alpha^2}\right)\right]\\
\times \frac{\pi}{2}\csc\left[\frac{\pi(\gamma+\epsilon\delta-\sigma)}{\alpha}\right]
\end{aligned}
$$
(14)

$$
\begin{aligned}
C_2 = I_0\epsilon\delta\frac{m}{(h+m)}\frac{\mathrm{e}^{-(h+m)t_0}-\mathrm{e}^{\lambda_+t_0}}{h+m+\lambda_+} \\
+C_0\Bigg[\left(\frac{\sqrt{\beta\sigma}}{\alpha}\right)^{\frac{\gamma+\epsilon\delta-\sigma}{\alpha}}\Gamma\left(\frac{\gamma+\epsilon\delta-h-m}{\alpha}\right)\\
\times {}_1\tilde{\mathrm{F}}_2\left(\frac{\gamma+\epsilon\delta-h-m}{\alpha};1+\frac{\gamma+\epsilon\delta-h-m}{\alpha},1\right.
\end{aligned}
$$

$$
\begin{aligned}
&\qquad \left.+\frac{\gamma+\epsilon\delta-\sigma}{\alpha};\frac{\beta\sigma}{\alpha^2}\right)\\
&-\left(\frac{\sqrt{\beta\sigma}}{\alpha}\right)^{-\frac{\gamma+\epsilon\delta-\sigma}{\alpha}}\Gamma\left(\frac{\sigma-h-m}{\alpha}\right)\\
&\times {}_1\tilde{\mathrm{F}}_2\left(\frac{\sigma-h-m}{\alpha};1+\frac{\sigma-h-m}{\alpha},1\right.\\
&\qquad \left.+\frac{\sigma-\gamma-\epsilon\delta}{\alpha};\frac{\beta\sigma}{\alpha^2}\right)\Bigg].\\
&\frac{\pi}{2}\csc\left[\frac{\pi(\gamma+\epsilon\delta-\sigma)}{\alpha}\right]
\end{aligned}
$$
(15)

In these formulas $C_0 = \frac{I_0\epsilon\delta}{\alpha}\frac{m}{h+m}\mathrm{e}^{\lambda_++t_0}/\mathrm{K}\left(\frac{\gamma+\epsilon\delta-\sigma}{\alpha},\frac{2\sqrt{\beta\sigma}}{\alpha}\right)$, while $_p\tilde{\mathrm{F}}_q(a_1,a_2,...a_p;b_1,b_2,...b_q;z)$ denotes regularized generalized hypergeometric function [65].

While these expressions jointly constitute the exact solution to the differential equations governing the dynamics of $F(t)$, their form is too complex to convey a useful conclusion about the epidemic dynamics. However, by applying a combination of appropriate mathematical transformations and by using Hankel's asymptotic expression for Bessel functions (see Appendix A.1 for details), we arrive at the following approximate expression for $F(t)$:

$$
\begin{aligned}
F(t) = I_0\epsilon\delta\frac{m}{h+m} \\
\Bigg[\theta(t_0-t)\left(\frac{\mathrm{e}^{\lambda_+t}-1}{\lambda_+}+\frac{\mathrm{e}^{-(h+m)t}-\mathrm{e}^{\lambda_+t}}{h+m+\lambda_+}\right)\\
+\theta(t-t_0)\\
\left(\frac{\mathrm{e}^{\lambda_+t_0}-1}{\lambda_+}-\mathrm{e}^{-(h+m)t}\frac{\mathrm{e}^{(h+m+\lambda_+)t_0}-1}{h+m+\lambda_+}\right.\\
+\frac{2}{\alpha}\left(\frac{2\sqrt{\beta\sigma}}{\alpha}\right)^{-\frac{\gamma+\epsilon\delta+\sigma}{\alpha}+\frac{1}{2}}\mathrm{e}^{\lambda_+t_0+\frac{2\sqrt{\beta\sigma}}{\alpha}}\\
\times\left\{\Gamma\left(\frac{\gamma+\epsilon\delta+\sigma}{\alpha}-\frac{1}{2},\frac{2\sqrt{\mathrm{e}^{-\alpha(t-t_0)}\beta\sigma}}{\alpha}\right)\right.\\
-\Gamma\left(\frac{\gamma+\epsilon\delta+\sigma}{\alpha}-\frac{1}{2},\frac{2\sqrt{\beta\sigma}}{\alpha}\right)\\
+\left(\frac{2\sqrt{\mathrm{e}^{-\alpha(t-t_0)}\beta\sigma}}{\alpha}\right)^{\frac{2(h+m)}{\alpha}}\\
\times\left[\Gamma\left(\frac{\gamma+\epsilon\delta+\sigma-2(h+m)}{\alpha}-\frac{1}{2},\frac{2\sqrt{\beta\sigma}}{\alpha}\right)\right.\\
-\Gamma\left(\frac{\gamma+\epsilon\delta+\sigma-2(h+m)}{\alpha}\right.\\
\left.\left.\left.\left.-\frac{1}{2},\frac{2\sqrt{\mathrm{e}^{-\alpha(t-t_0)}\beta\sigma}}{\alpha}\right)\right]\right\}\right)\Bigg].
\end{aligned}
$$
(16)

This expression replaces expressions (12)-(15) while not significantly deviating from the full solution (the deviations are essentially negligible, having in mind the limited precision with which we know most of the COVID-19 epidemiological parameters).

As expected, the $F(t)$ saturates at some maximal, asymptotic value as $t \to \infty$ (for details see Appendices A.3 and A.4). This value corresponds to the total (final) number of COVID-19 fatalities F_{fin} in the observed epidemic outburst:

$$F_{fin} \approx \frac{2I_0\epsilon\delta}{\alpha}\frac{m}{h+m}\left(\frac{2\sqrt{\beta\sigma}}{\alpha}\right)^{-\frac{\gamma+\epsilon\delta+\sigma}{\alpha}+\frac{1}{2}} e^{\lambda_+ t_0 + \frac{2\sqrt{\beta\sigma}}{\alpha}}$$
$$\times \Gamma\left(\frac{\gamma+\epsilon\delta+\sigma}{\alpha}-\frac{1}{2}\right). \quad (17)$$

Furthermore, due to the fact that for realistic values of epidemiological parameters [58] $(\gamma+\epsilon\delta+\sigma)/\alpha-1/2$ is high enough, we utilize Stirling's formula [66] (for large n): $\Gamma(n+1) \approx \sqrt{2\pi n}\left(\frac{n}{e}\right)^n$. After making use of $4\beta\sigma \gg (\gamma+\delta\epsilon-\sigma)^2$ (for multiple times) Eq. (17) reduces to:

$$F_{fin}^{approx} \approx 2D_0\frac{m}{h+m}e^{\frac{3}{2}}\sqrt{\frac{2\pi/\alpha}{\gamma+\epsilon\delta+\sigma-\frac{3}{2}\alpha}}\lambda_+$$
$$\times \left(\frac{2\lambda_++\gamma+\epsilon\delta+\sigma}{\gamma+\epsilon\delta+\sigma-\frac{3}{2}\alpha}\right)^{\frac{1}{2}-\frac{\gamma+\epsilon\delta+\sigma}{\alpha}}e^{\left(t_0+\frac{2}{\alpha}\right)\lambda_+}, \quad (18)$$

where $D(0) = D_0 = I_0\epsilon\delta/\lambda_+$.

By applying a similar procedure, we straightforwardly obtain the equivalent expressions for the time evolution of the number of detected cases (see Appendix A.2). For brevity, we here provide only the final results:

$$D(t) = \frac{I_0\epsilon\delta}{\lambda_+}\left(\theta(t_0-t)e^{\lambda_+ t} + \theta(t-t_0)e^{\lambda_+ t_0}\right.$$
$$\times \left\{1 + \frac{2\lambda_+}{\alpha}\left(\frac{2\sqrt{\beta\sigma}}{\alpha}\right)^{-\frac{\gamma+\epsilon\delta+\sigma}{\alpha}+\frac{1}{2}}e^{\frac{2\sqrt{\beta\sigma}}{\alpha}}\right.$$
$$\times \left[\Gamma\left(\frac{\gamma+\epsilon\delta+\sigma}{\alpha}-\frac{1}{2}, \frac{2\sqrt{e^{-\alpha(t-t_0)}\beta\sigma}}{\alpha}\right)\right.$$
$$\left.\left.\left.-\Gamma\left(\frac{\gamma+\epsilon\delta+\sigma}{\alpha}-\frac{1}{2}, \frac{2\sqrt{\beta\sigma}}{\alpha}\right)\right]\right\}\right) \quad (19)$$

and for the total number of detected cases at the end of the epidemic wave:

$$D_{fin} \approx \frac{2I_0\epsilon\delta}{\alpha}\left(\frac{2\sqrt{\beta\sigma}}{\alpha}\right)^{-\frac{\gamma+\epsilon\delta+\sigma}{\alpha}+\frac{1}{2}}e^{\lambda_+ t_0 + \frac{2\sqrt{\beta\sigma}}{\alpha}}$$
$$\times \Gamma\left(\frac{\gamma+\epsilon\delta+\sigma}{\alpha}-\frac{1}{2}\right), \quad (20)$$

that can be again approximated to the form:

$$D_{fin}^{approx} \approx 2D_0 e^{\frac{3}{2}}\sqrt{\frac{2\pi/\alpha}{\gamma+\epsilon\delta+\sigma-\frac{3}{2}\alpha}}\lambda_+$$
$$\times \left(\frac{2\lambda_++\gamma+\epsilon\delta+\sigma}{\gamma+\epsilon\delta+\sigma-\frac{3}{2}\alpha}\right)^{\frac{1}{2}-\frac{\gamma+\epsilon\delta+\sigma}{\alpha}}e^{\left(t_0+\frac{2}{\alpha}\right)\lambda_+}. \quad (21)$$

Consequently, the estimate for Case Fatality Rate (CFR), which is defined as the final number of fatalities per detected cases ($CFR = F_{fin}/D_{fin}$), acquires a simple form [67], involving a ratio of mortality (m) and healing (h) rates:

$$CFR = \frac{m}{h+m}, \quad (22)$$

further supporting that our analytical derivation is plausible.

The explicit formulas (18) and (21) provide analogs—though now in the entirely different context with social distancing—of the final size (i.e. asymptotic value) relations for SIR [40,54] and SEIR models [53]. Based on our analytical solution, we can also provide a fairly simple relation for the timing of the epidemic peak (see Appendix A.5 for details), which is another quantity that has been previously analytically derived in simpler scenarios of SIR [48,50,51,55,56] and SEIR [53] models:

$$t_{max} = t_0 + \frac{1}{\alpha}\ln\left[\frac{16\beta\sigma}{(2(\gamma+\epsilon\delta+\sigma)-\alpha)^2}\right]. \quad (23)$$

From Eq. (23), we can also obtain the maximal number of detected cases per day during the outburst:

$$\left(\frac{dD}{dt}\right)_{max} = D_0\lambda_+ e^{\lambda_+\left(t_0+\frac{2}{\alpha}\right)+\frac{1}{2}}$$
$$\left(\frac{4\sqrt{\beta\sigma}}{2(\gamma+\epsilon\delta+\sigma)-\alpha}\right)^{\frac{1}{2}-\frac{\gamma+\epsilon\delta+\sigma}{\alpha}} \quad (24)$$

which we will further analyze in the next section.

The infection tipping points (see Appendix A.5) correspond to the inflection points of the bell-shaped infected curve. We can explicitly express the two tipping points, from which we can obtain the duration of the epidemic peak (cf. Figure 1D in [58]), corresponding to the time interval between these two points:

$$\Delta t_{peak} = \frac{4}{\alpha} \ln \left(\frac{\gamma + \epsilon\delta + \sigma + \sqrt{\alpha(\gamma + \epsilon\delta + \sigma - \frac{\alpha}{4})}}{\gamma + \epsilon\delta + \sigma - \alpha/2} \right). \tag{25}$$

When $\alpha << (\gamma + \sigma)$ this formula effectively simplifies to:

$$\Delta t_{peak} \approx \frac{4}{\sqrt{\alpha(\gamma + \epsilon\delta + \sigma)}}, \tag{26}$$

where we used [68] $\ln(1 + x) \approx x$ for $x \ll 1$. Note that Δt_{peak} is independent of the transmission rate β, which is a nontrivial result. Δt_{peak} provides an estimate of the time interval during which the infected are at a high level, and the chance of contracting the infection is the highest.

4 Numerical analysis

To test the model reliability, we first compare our full-fledged predictions for case counts (detected cases and fatalities) with the observed data counts for three representative countries: Austria, Switzerland, and Israel. Figure 2 shows that we obtain an overall good agreement between our predictions and the data for all three countries. In particular, we see that the time delay, much discussed in interpreting COVID-19 case counts data [12,61], is also well reproduced. This agreement provides confidence that the analytical expressions, which we derived from our model, indeed reasonably represent the observed case counts data.

The obtained results allow us to analyze the effect of each model parameter on $D(t)$ and $F(t)$ curves. For succinctly presenting the results in Figs. 3, 4, 5 and 6, we will further use the parameter values that were extracted for Israel in Fig. 2. We note that the obtained results are independent of the analyzed country, as long as the data are continuously tracked with moderate testing capacities and fairly transparent reporting policies. First, we will consider the influence of the ϵ parameter—the fraction of the infections that are

detected and consequently quarantined. We here, and in the subsequent analysis, fix the initial (observed) number of detected cases $D_0 = D(t = 0)$. The trivial (direct) proportionality dependence of $D(t)$ on ϵ in Eq. (6) then gets absorbed in D_0, so that we investigate the nontrivial effect of the quarantine (ϵ) on the case count dynamics from Eq. (4). For this, we opt for two limiting cases $\epsilon = 0.1$ and $\epsilon = 0.5$, which respectively correspond to the low and high detection rates inferred from the observed data [58]. From Fig. 3, which represents the time evolution of detected cases and fatalities, we observe that a substantial change of this parameter leads to at most $\sim 20\%$ change in saturation value of D and F. In comparison to changes due to variations of other parameters, see below, we will see that this is a minor effect. Expectedly, better detection efficacy (i.e., the higher ϵ value) leads to lower overall numbers of case counts, simply because the larger part of infected individuals is timely quarantined. The value of ϵ has practically no impact on the steepness of these time-evolution curves. Consequently, detected cases and fatalities are nearly independent of ϵ, and, for simplicity, we will further set this value to be 0.1. (Note that, if not indicated otherwise, full-fledged expressions are used for generating predictions through the entire section.)

Next, we assess how sensitive case counts are on the initial slope (on a log scale) of the exponential growth of the infectious curve, quantified by λ_+. Indirectly, in this way, we also test the dependence of the curves on the closely related basic reproduction number R_0 (quantifying inherent virus transmissibility in population [69]), which relates to λ_+ by $R_0 = \beta/\gamma = \frac{\lambda_+^2 + \lambda_+(\gamma + \epsilon\delta + \sigma) + (\gamma + \epsilon\delta)\sigma}{\sigma\gamma}$ [57,70]. To this end, we vary λ_+ in the range between 0.1/day and 0.4/day, based on our previously inferred λ_+ values for a large number of analyzed countries [70,71]. From the left plot in Fig. 4, we observe that $D(t)$ is highly sensitive to this parameter, to the extent that the linear–linear plot is unable to adequately illustrate this dependency. The log-linear plot in the inset is much better suited for this: it clearly demonstrates that the greater the λ_+ is, the $D(t)$ curve is steeper, and the final saturation value becomes exponentially larger. The same tendency is preserved in the case of $F(t)$ dependence on λ_+ (see middle plot in Fig. 4), where we *ab initio* opt for log-linear display.

To gain some further insight on the influence of λ_+ on case counts saturation values, we note that the dom-
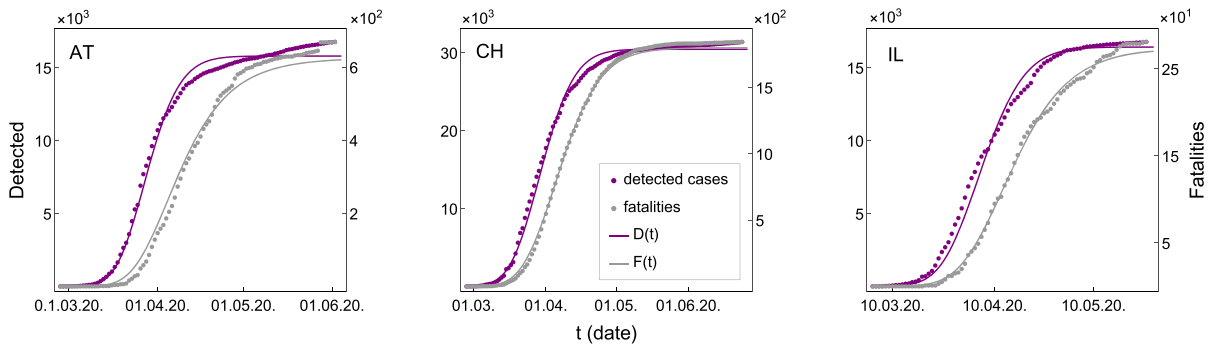
Fig. 2 Comparison between model prediction and data for Austria (the left plot), Switzerland (the central plot), and Israel (the right plot), as indicated by abbreviations in the upper left corners. The predictions are generated for the evolution of detected cases (the purple curves) and fatalities (the gray curves). The observed detected counts are denoted as purple dots, while the fatality counts are represented by gray dots. The left and the right y-axis of each plot corresponds to detected cases and fatalities, respectively, while the ticks on the x-axis denote the dates given in DD/MM/YY format. The data for detected cases and fatalities are taken from [63]

Fig. 3 The dependence on the infection detection efficiency ϵ of detected cases (the left plot) and fatalities (the right plot). The blue and the orange curves correspond to $\epsilon = 0.1$ and $\epsilon = 0.5$, respectively
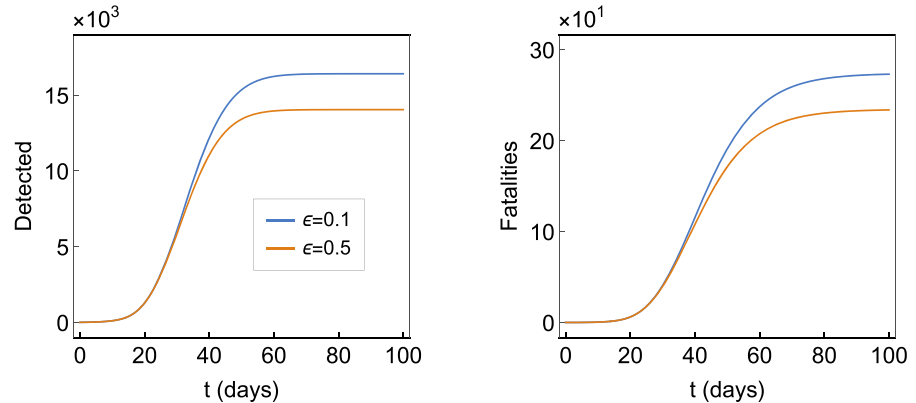
inant λ_+ dependence in Eqs. (18) and (21) is exponential, of the form $e^{(t_0 + \frac{2}{\alpha})\lambda_+}$. However, it can be shown that λ_+ terms outside of the exponent in Eqs. (18) and (21) still contribute by effectively lowering the exponent from $e^{(t_0 + \frac{2}{\alpha})\lambda_+}$ to $t_\alpha = t_0 + 1/\alpha$. In Ref. [57], we introduced t_α as the, so-called, protection time (the time at which $\sim \frac{1}{2}$ of the population moves to the protected category), so that there is a simple, overall, dependence of the case counts on λ_+ as $\sim e^{t_\alpha \lambda_+}$.

The λ_+ dependence of three curves: D_{fin}, D_{fin}^{approx} and our estimate $\sim e^{(t_0 + \frac{1}{\alpha})\lambda_+}$, is presented in the rightmost plot of Fig. 4. The practically overlapping D_{fin} and D_{fin}^{approx} curves confirm the adequacy of the approximation applied in Eqs. (18) and (21). Moreover, the fact that the simple exponential dependence $e^{t_\alpha \lambda_+}$ very well qualitatively and quantitatively reproduces

$D(\lambda_+)$, highlights usefulness of the protection time in assessing infection risks.

Finally, we concentrate on the effect of the social distancing strength α on the case counts. We assume that α lies in the range between 0.03 and 0.3, as inferred from the observed data by our previous numerical analysis [58]. All plots on Fig. 5 are again presented in log-linear scale. From the left and central plot in Fig. 5, we see that both $D(t)$ and $F(t)$ are strongly affected by the change of α. As the epidemic progresses, the stronger social measures result in a significantly lower plateau of case counts. The effect of α on these two observables is the opposite of the one of λ_+, as expected.

To further clarify the dependence of D and F on α, we again use Eq. (21). After taking a logarithm, we obtain:
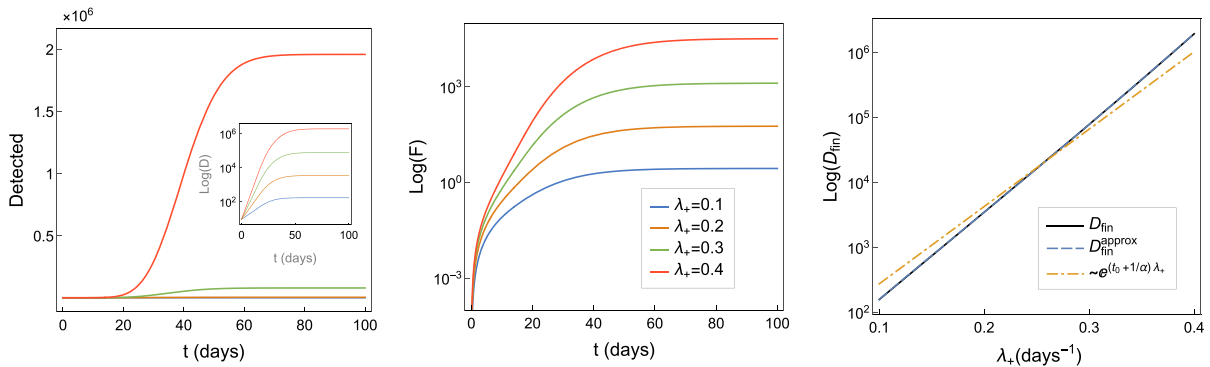
Fig. 4 The effect of initial slope of infectious curve λ_+ on the main observables. The time evolution of detected cases is presented in the left plot, with inset on a more pronounced log-linear plot. The central plot shows fatalities versus time on a log-linear scale. λ_+ values are indicated in the legend. In the right plot, λ_+ dependence of detected cases at saturation is displayed on a log-linear scale. D_{fin}, D_{fin}^{approx} and $e^{t_\alpha \lambda_+}$ are denoted by the solid black, the dashed blue and dot-dashed orange curves, respectively

$$\ln\left(D_{fin}^{approx}\right) \approx \kappa_1 + \frac{2\lambda_+}{\alpha} + \left(\frac{\kappa_2}{\alpha} - 1\right)$$
$$\ln\left(\kappa_2 - \frac{3}{2}\alpha\right) - \frac{\ln(\alpha)}{2}, \qquad (27)$$

where $\kappa_1 = \ln\left(2D_0\lambda_+\sqrt{2\pi}\right) + \lambda_+ t_0 + \frac{3}{2} + \left(\frac{1}{2} - \frac{\gamma+\epsilon\delta+\sigma}{\alpha}\right) \times \ln\left(\gamma + \epsilon\delta + \sigma + 2\lambda_+\right)$ and $\kappa_2 = \gamma + \epsilon\delta + \sigma$. The dominant term on the right-hand side of Eq. (27) is proportional to $1/\alpha$, i.e., the logarithmic terms could be neglected. To test this obtained simple dependance, in the rightmost plot of Fig. 5 we compare D_{fin}, D_{fin}^{approx} and our estimate $\sim e^{0.8\lambda_+/\alpha}$, as functions of α, on log-linear scale. The very good agreement between D_{fin} and D_{fin}^{approx} again confirms the validity of our approximations. Moreover, we demonstrate that the influence of the strength of social distancing on detected cases (and fatalities) can be reduced (at saturation) to a simple dependence of the form $\sim e^{0.8\lambda_+/\alpha}$.

From Figs. 4 and 5, we also see that λ^+ has no significant effect on infection extinguishing time, i.e., the time for case counts to enter saturation. That is, its most prominent effect is on the total case counts. On the other hand, the strength of social distancing measures affects (i.e., diminish) both the total case counts and the time needed for extinguishing the infection.

Finally, in Fig. 6, we show how the maximal value of detected cases per day depend on λ_+ and α. For λ_+, we see that, similarly to D_{fin} and F_{fin}, simple exponential dependence $e^{t_\alpha \lambda_+}$ well reproduces $(\frac{dD}{dt})_{max}$, further highlighting the importance of the lower protection

time for reducing the infection risks. For social distancing strength, we see that $(\frac{dD}{dt})_{max}$ is also strongly affected by α, where this dependence can be approximated by the simple expression $\sim e^{0.6\lambda_+/\alpha}$.

5 Discussion

The main goal of the present paper was to provide a fully-analytical treatment of our epidemiological model with introduced social distancing, which predicts observables that are readily accessible in a large-scale epidemic. We accomplished this task by calculating these observables as explicit functions of time, expressed in closed-form: Eqs. (16) and (19). Particularly useful are the derived (approximate) expressions (18) and (21) for the detected cases and fatalities at saturation (i.e., at the end of an epidemic wave). We tested the model predictions against the observed COVID-19 data, obtaining a very good agreement (as illustrated in Fig. 2).

The obtained analytical results facilitate a better understanding of the influence of individual epidemiological parameters on COVID-19 observables. In particular, the effect of varying the detection efficacy ϵ (within reasonable boundaries) turned out to be exponentially smaller than the influence of the λ_+ value, as illustrated in Figs. 3 and 4. Since the λ_+ value is directly related to the basic reproduction number R_0, which characterizes the inherent biological transmission of the virus in an (initially) completely unprotected pop-
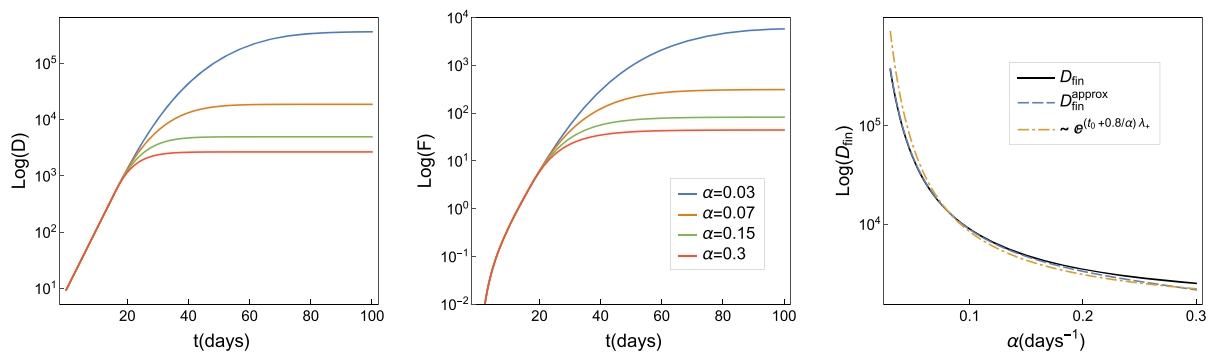
Fig. 5 The effect of social distancing strength α on the main observables. The time evolution of detected cases and fatalities are presented in the left and central plots, respectively. α values are indicated in the legend. The α dependence of detected cases at saturation is assessed in the right plot. D_{fin}, D_{fin}^{approx} and $\sim e^{0.8\lambda_+/\alpha}$ are denoted by the solid black, the dashed blue and dot-dashed orange curves, respectively. All plots are on log-linear scale

Fig. 6 The effect of initial slope of the infectious curve λ_+ and social distancing strength α on the maximum of detected cases per day $(\frac{dD}{dt})_{max}$ is shown on the left and right plots, respectively. $(\frac{dD}{dt})_{max}$ and approximate expressions are denoted by the solid black and dot-dashed orange curves, respectively. All plots are on a log-linear scale
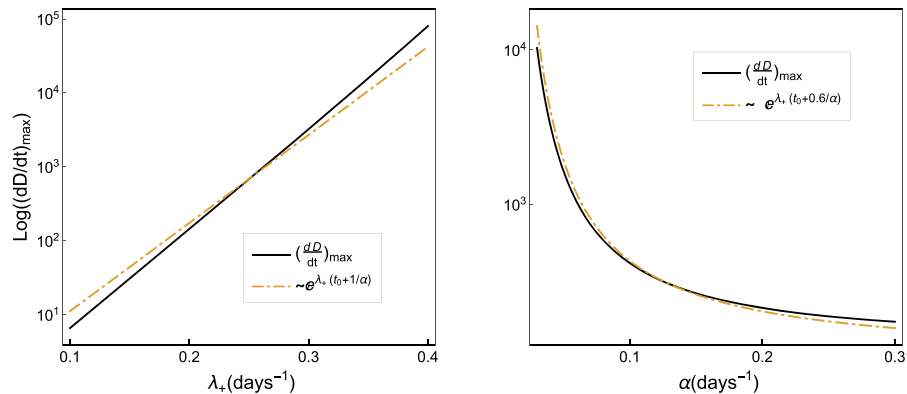
ulation (λ_+ and R_0 are roughly proportional, in realistic parameter ranges) [57], this conclusion has a simple and yet important interpretation. Namely, it means that medical, demographic, and environmental predispositions (determining R_0) [70,71] should be expected to strongly influence the behavior of the considered observables (detected cases and fatalities attributed to the virus) [72–74]. On the other hand, R_0 seems not to significantly impact the infection extinguishing time.

Our analysis has shown that the strength of the implemented social measures, quantified by α, effectively appears in the denominator in the exponent of the number of total COVID-19 casualties, as follows from Eq. (27). The impact of the social measures is thus, unsurprisingly, highly significant— as illustrated in Figs. 5 and 6.

Even more interesting is the interplay between t_0 (the timing of the introduction of measures) and α values in the asymptotic behavior of the COVID-19 observables.

Careful analysis of the functions for COVID-19 fatalities (18) and detected cases (21) at saturation, as well as the maximum of detected cases per day (24), revealed that this dependence is, in all three cases, effectively of the form: $e^{(t_0+\frac{1}{\alpha})\lambda_+}$ (see also Figs. 4 and 6). The significance of the value $t_\alpha = t_0 + \frac{1}{\alpha}$ has already been numerically recognized in [57], where this combination of parameters was named "protection time". Here we show that the total number of fatalities and detected COVID-19 cases for the entire infection wave does not depend on either t_0 or α individually, but only jointly, through the protection time t_α. The implications of this analytical result are striking: introducing very strict (and economically debilitating) social measures can have precisely the same effect (infected case-wise and mortality-wise) as implementing much weaker measures somewhat earlier.

For example, consider a decision to introduce weak-to-moderate social measures, corresponding to $\alpha =$

0.1, some t_0 days from the epidemic onset. If this decision is only one week postponed (i.e., measures put into practice at $t_0 + 7$), it would require far more restrictive policies, corresponding to $\alpha = 0.3$, to compensate for the delay and retain the same number of fatalities (according to our analysis [58] - $\alpha = 0.3$ corresponds to the strongest social measures that had been imposed in practice, in the first wave of COVID-19 pandemic).

"The sooner the better" conclusion regarding the introduction of social measures is hardly surprising [28–30] and does not require such a sophisticated analysis to reach. However, the analysis presented here provides us with additional insight that was not so obvious: even reasonably weak measures introduced quickly and without prolonged preparations seem to have much stronger mitigation potential than very strong measures introduced with hesitation and delay.

Furthermore, since the numbers of COVID-19 fatalities and detected cases in saturation depend upon the protection time t_α as $e^{t_\alpha \lambda_+}$, it is clear that the measures must be put into force sooner and/or be stronger (i.e., t_α lower) in populations with higher SARS-CoV-2 reproduction number R_0. While this conclusion is fairly natural, having this quantitative relation and combining it with machine learning techniques to estimate R_0 dependence upon demographic and environmental parameters [71] may substantially aid the policymaking process, in multiple ways. For example, by estimating how much sooner the measures must be implemented in areas with greater median age, higher prevalence of comorbidities, or higher pollution [70,71]. Also, to properly allocate medical resources according to this interplay of R_0, t_0, and α.

6 Conclusion

In this manuscript, we demonstrated that it is possible to carry out a full analytical treatment of a compartmental epidemiological model that takes into account the effects of social distancing measures. The model has shown a good agreement with publicly available data on COVID-19 case counts.

As a benefit of having analytical solutions to the model equations, we were able to point out simple quantitative relations between the model variables and epidemiological observables. Such relations provide insights into cause-effect connections that underlie the

epidemiological dynamics and are obscured in more standard, i.e., purely numerical, approaches.

Our analysis revealed a quantitatively expressible interplay between the strength of the social measures and the time of their introduction, showing that the two variables effectively combine into a single relevant parameter called protection time. This not only implies that stringent measures can be often substituted by more relaxed ones introduced at earlier times but provides a direct analytical expression to quantify this trade-off.

We emphasize that our model and its implications are not COVID-19 specific and should hold for any potential future epidemic. Many epidemiologists believe that outbursts of new infectious diseases (or even pandemics) are likely, possibly even in the near future [75]. Thus, our results might be even more useful in the future, i.e., in the early stages of some new pandemic, when vaccines or effective pharmaceutical treatments are still not at our disposal, but we can only count on well-timed and appropriately chosen control measures.

Author contributions Magdalena Djordjevic and Marko Djordjevic contributed to the study conception and design. Analytical calculations were performed by Magdalena Djordjevic, Bojana Ilic and Igor Salom. Numerical analysis was performed by Bojana Ilic, Magdalena Djordjevic and Marko Djordjevic. The first draft of the manuscript was written by Bojana Ilic and Igor Salom with the help of Magdalena Djordjevic and Marko Djordjevic. All authors read and approved the final manuscript.

Declarations

A Appendix

A.1 Analytical derivation of the number of fatalities

To assess the dynamics of COVID-19 infection, we employed the mechanistic model, defined by equations (1)-(8). In Ref. [58], we have already obtained the number of infectious individuals as a function of time (9).

Throughout the derivations, we will distinguish two-time regions: I) $t \leq t_0$ and II) $t > t_0$, and will denote the variables in these two regions accordingly.

First, we concentrate on deriving the expression for the time evolution of the number of fatalities. To this end, we start from Eqs. (7)-(8), which lead to a single equation (10). In region I, this second-order inhomogeneous differential equation, after taking into account the first term of Eq. (9) (i.e., $I_I(t) = I_0 e^{\lambda_+ t}$), reduces to:

$$\frac{d^2 F_I(t)}{dt^2} + (h+m)\frac{dF_I(t)}{dt} - m\epsilon\delta I_0 e^{\lambda_+ t} = 0. \quad (28)$$

If we assume $F_I(t=0) = 0$ and $F_I'(t=0) = 0$, the time-dependent fatalities for $t \leq t_0$ are given by:

$$F_I(t) = \frac{I_0 \epsilon \delta}{\lambda_+} \frac{m}{m+h}\left\{ -1 + \frac{\lambda_+}{h+m+\lambda_+}e^{-(h+m)t} \right.$$
$$\left. + \frac{h+m}{h+m+\lambda_+}e^{\lambda_+ t} \right\}. \quad (29)$$

In region II, for simplicity we shift $t - t_0 \rightarrow t$, and take into account that the expression for infectious now reads $I_{II}(t) = I_0 e^{\lambda_+ t_0}e^{-\frac{\gamma+\epsilon\delta+\sigma}{2}t}K\left(\frac{\gamma+\epsilon\delta-\sigma}{\alpha}, \frac{2\sqrt{e^{-\alpha t}\beta\sigma}}{\alpha}\right)$ $/K\left(\frac{\gamma+\epsilon\delta-\sigma}{\alpha}, \frac{2\sqrt{\beta\sigma}}{\alpha}\right)$ (the second term of Eq. (9)). Since $I_{II}(t)$ has this complex form, the further derivations are quite demanding. By substituting $t \rightarrow y = \frac{2\sqrt{e^{-\alpha t}\beta\sigma}}{\alpha}$, it can easily be verified that Eq. (10) is in region II reduced to the well-known second-order inhomogeneous Cauchy–Euler equation [76,77] $ax^2 y'' + bxy' + cy = g(x)$. After dividing thus obtained differential equation by y^2, we obtain

$$\frac{d^2 F_{II}}{dy^2} + \left[1 - \frac{2(h+m)}{\alpha}\right]\frac{1}{y}\frac{dF_{II}}{dy}$$
$$= Cy^{\frac{\gamma+\epsilon\delta+\sigma}{\alpha}-2}K\left(\frac{\gamma+\epsilon\delta-\sigma}{\alpha}, y\right), \quad (30)$$

where $C = \frac{4I_0\epsilon\delta m}{\alpha^2}\left(2\sqrt{\beta\sigma}/\alpha\right)^{-\frac{\gamma+\epsilon\delta+\sigma}{\alpha}}e^{\lambda_+ t_0}/K\left(\frac{\gamma+\epsilon\delta-\sigma}{\alpha}, \frac{2\sqrt{\beta\sigma}}{\alpha}\right)$.

Next, we apply the standard procedure for solving inhomogeneous differential equation given by Eq. (30): the full solution equals homogeneous plus particular solution $F_{II}(y) = F_{II,h}(y) + F_{II,p}(y)$. It is straightforward to show that auxiliary/characteristic equation yields the following simple form of homogeneous solution $F_{II,h}(y) = C_1 + C_2 y^{\frac{2(h+m)}{\alpha}}$ (where linearly independent solutions are $F_{II,1}(y) = 1$ and $F_{II,2}(y) = y^{\frac{2(h+m)}{\alpha}}$), while for obtaining particular solution $F_{II,p}(y)$ we used the Lagrange's method of variation of parameters [76]. More precisely, we assume that $F_{II,p}(y) = C_1(y) + C_2(y)y^{\frac{2(h+m)}{\alpha}}$, where again linearly independent solutions of the homogeneous equation are employed. The unknown functions C_i $(i = 1, 2)$ of variable y are sought for via the standard procedure

$$C_1(y) = -\int \frac{F_{II,2}(y)f(y)}{W}dy,$$
$$C_2(y) = \int \frac{F_{II,1}(y)f(y)}{W}dy, \quad (31)$$

where $f(y)$ denotes the right-hand side of Eq. (30), while Wronskian [76,77] is given by $W = F_{II,1}F_{II,2}' - F_{II,2}F_{II,1}' = \frac{2(h+m)}{\alpha}y^{\frac{2(h+m)}{\alpha}-1}$. This leads to:

$$C_1(t) = -\frac{C\alpha}{2(h+m)}\int_0^{\frac{2\sqrt{e^{-\alpha t}\beta\sigma}}{\alpha}} y^{\frac{\gamma+\epsilon\delta+\sigma}{\alpha}-1}$$
$$K\left(\frac{\gamma+\epsilon\delta-\sigma}{\alpha}, y\right)dy,$$
$$C_2(t) = \frac{C\alpha}{2(h+m)}\int_0^{\frac{2\sqrt{e^{-\alpha t}\beta\sigma}}{\alpha}} y^{\frac{\gamma+\epsilon\delta+\sigma-2(h+m)}{\alpha}-1}$$
$$K\left(\frac{\gamma+\epsilon\delta-\sigma}{\alpha}, y\right)dy. \quad (32)$$

In spite that the above form of the result will be more useful in what follows, we nevertheless provide also its full-fledged form:

$$C_1(t) = C_0\left[\left(\frac{\sqrt{\beta\sigma}}{\alpha}\right)^{\frac{\gamma+\epsilon\delta-\sigma}{\alpha}}e^{-(\gamma+\epsilon\delta)t}\Gamma\left(\frac{\gamma+\epsilon\delta}{\alpha}\right)\right.$$
$$\times {}_1\tilde{F}_2\left(\frac{\gamma+\epsilon\delta}{\alpha}; 1+\frac{\gamma+\epsilon\delta}{\alpha}, 1+\frac{\gamma+\epsilon\delta-\sigma}{\alpha}; \frac{e^{-\alpha t}\beta\sigma}{\alpha^2}\right)$$
$$- \left(\frac{\sqrt{\beta\sigma}}{\alpha}\right)^{-\frac{\gamma+\epsilon\delta-\sigma}{\alpha}}e^{-\sigma t}\Gamma\left(\frac{\sigma}{\alpha}\right)$$
$$\left.\times {}_1\tilde{F}_2\left(\frac{\sigma}{\alpha}; 1+\frac{\sigma}{\alpha}, 1+\frac{\sigma-\gamma-\epsilon\delta}{\alpha}; \frac{e^{-\alpha t}\beta\sigma}{\alpha^2}\right)\right]$$
$$\frac{\pi}{2}\csc\left[\frac{\pi(\gamma+\epsilon\delta-\sigma)}{\alpha}\right]$$
$$C_2(t) = -C_0\left[\left(\frac{\sqrt{\beta\sigma}}{\alpha}\right)^{\frac{\gamma+\epsilon\delta-\sigma}{\alpha}}e^{-(\gamma+\epsilon\delta)t}\Gamma\left(\frac{\gamma+\epsilon\delta-h-m}{\alpha}\right)\right.$$

$$\times {}_1\tilde{F}_2\left(\frac{\gamma+\epsilon\delta-h-m}{\alpha}; 1+\frac{\gamma+\epsilon\delta-h-m}{\alpha}, 1\right.$$
$$\left.+\frac{\gamma+\epsilon\delta-\sigma}{\alpha}; \frac{e^{-\alpha t}\beta\sigma}{\alpha^2}\right)$$
$$-\left(\frac{\sqrt{\beta\sigma}}{\alpha}\right)^{-\frac{\gamma+\epsilon\delta-\sigma}{\alpha}}e^{-\sigma t}\Gamma\left(\frac{\sigma-h-m}{\alpha}\right)$$
$$\times {}_1\tilde{F}_2\left(\frac{\sigma-h-m}{\alpha}; 1+\frac{\sigma-h-m}{\alpha}, 1\right.$$
$$\left.+\frac{\sigma-\gamma-\epsilon\delta}{\alpha}; \frac{e^{-\alpha t}\beta\sigma}{\alpha^2}\right)\Bigg]$$
$$\times\frac{\pi}{2}\csc\left[\frac{\pi(\gamma+\epsilon\delta-\sigma)}{\alpha}\right], \tag{33}$$

where $C_0 = \frac{I_0\epsilon\delta}{\alpha}\frac{m}{h+m}e^{\lambda_+ t_0}/\mathrm{K}\left(\frac{\gamma+\epsilon\delta-\sigma}{\alpha}, \frac{2\sqrt{\beta\sigma}}{\alpha}\right)$, while $_p\tilde{F}_q(a_1, a_2, ...a_p; b_1, b_2, ...b_q; z)$ denotes regularized generalized hypergeometric function [65]. The general solution of Eq. (30), when returned to variable t, has a form:

$$F_{II}(t) = C_1 + C_2 e^{-(h+m)t} + C_1(t)$$
$$+ C_2(t)\left(\frac{2\sqrt{\beta\sigma}}{\alpha}\right)^{\frac{2(h+m)}{\alpha}}e^{-(h+m)t}, \tag{34}$$

where the only unknown parameters are C_1 and C_2. In order to determine these constants we use the following boundary conditions: $F_{II}(0) = F_I(t_0)$ and $F'_{II}(0) = F'_I(t_0)$. After some cumbersome calculation steps we obtain the following expressions:

$$C_1 = I_0\epsilon\delta\frac{m}{(h+m)}\frac{e^{\lambda_+ t_0}-1}{\lambda_+}$$
$$- C_0\Bigg[\left(\frac{\sqrt{\beta\sigma}}{\alpha}\right)^{\frac{\gamma+\epsilon\delta-\sigma}{\alpha}}\Gamma\left(\frac{\gamma+\epsilon\delta}{\alpha}\right)$$
$$\times {}_1\tilde{F}_2\left(\frac{\gamma+\epsilon\delta}{\alpha}; 1+\frac{\gamma+\epsilon\delta}{\alpha}, 1\right.$$
$$\left.+\frac{\gamma+\epsilon\delta-\sigma}{\alpha}; \frac{\beta\sigma}{\alpha^2}\right)$$
$$-\left(\frac{\sqrt{\beta\sigma}}{\alpha}\right)^{-\frac{\gamma+\epsilon\delta-\sigma}{\alpha}}\Gamma\left(\frac{\sigma}{\alpha}\right)$$
$${}_1\tilde{F}_2\left(\frac{\sigma}{\alpha}; 1+\frac{\sigma}{\alpha}, 1+\frac{\sigma-\gamma-\epsilon\delta}{\alpha}; \frac{\beta\sigma}{\alpha^2}\right)\Bigg]\frac{\pi}{2}$$
$$\times\csc\left[\frac{\pi(\gamma+\epsilon\delta-\sigma)}{\alpha}\right] \tag{35}$$
$$C_2 = I_0\epsilon\delta\frac{m}{(h+m)}\frac{e^{-(h+m)t_0}-e^{\lambda_+ t_0}}{h+m+\lambda_+}$$

$$+ C_0\Bigg[\left(\frac{\sqrt{\beta\sigma}}{\alpha}\right)^{\frac{\gamma+\epsilon\delta-\sigma}{\alpha}}\Gamma\left(\frac{\gamma+\epsilon\delta-h-m}{\alpha}\right)$$
$$\times {}_1\tilde{F}_2\left(\frac{\gamma+\epsilon\delta-h-m}{\alpha}; 1+\frac{\gamma+\epsilon\delta-h-m}{\alpha}, 1\right.$$
$$\left.+\frac{\gamma+\epsilon\delta-\sigma}{\alpha}; \frac{\beta\sigma}{\alpha^2}\right)$$
$$-\left(\frac{\sqrt{\beta\sigma}}{\alpha}\right)^{-\frac{\gamma+\epsilon\delta-\sigma}{\alpha}}\Gamma\left(\frac{\sigma-h-m}{\alpha}\right)$$
$$\times {}_1\tilde{F}_2\left(\frac{\sigma-h-m}{\alpha}; 1+\frac{\sigma-h-m}{\alpha}, 1\right.$$
$$\left.+\frac{\sigma-\gamma-\epsilon\delta}{\alpha}; \frac{\beta\sigma}{\alpha^2}\right)\Bigg]\frac{\pi}{2}$$
$$\times\csc\left[\frac{\pi(\gamma+\epsilon\delta-\sigma)}{\alpha}\right] \tag{36}$$

Now, if we use the definition of regularized generalized hypergeometric functions, the above expressions can be significantly simplified and reduced to the form similar to Eq. (32). Namely [65]

$${}_1\tilde{F}_2(a_1; b_1, b_2; z) = \sum_{k=0}^{\infty}\frac{(a_1)_k z^k}{k!\Gamma(k+b_1)\Gamma(k+b_2)}, \tag{37}$$

where $(a_1)_0 = 1$, while for $k \geqslant 1$

$$(a_1)_k = a(a+1)...(a+k-1). \tag{38}$$

Let us first concentrate on C_1, where from Eq. (35) it follows that $z = \beta\sigma/\alpha^2$. By denoting $a_1 = (\gamma+\epsilon\delta)/\alpha$ and $a_2 = \sigma/\alpha$, it is straightforward to infer that the expression in the square brackets of Eq. (35) can be rewritten in a form:

$$\mathcal{I}_1 = z^{\frac{a_1-a_2}{2}}\Gamma(a_1)\,{}_1\tilde{F}_2(a_1; 1+a_1, 1+a_1-a_2; z)$$
$$- z^{\frac{a_2-a_1}{2}}\Gamma(a_2)\,{}_1\tilde{F}_2(a_2; 1+a_2, 1+a_2-a_1; z). \tag{39}$$

After multiplying the right-hand side by $z^{\frac{a_1+a_2}{2}}/z^{\frac{a_1+a_2}{2}}$ we obtain:

$$\mathcal{I}_1 = \frac{1}{z^{\frac{a_1+a_2}{2}}}\sum_{k=0}^{\infty}\Bigg[\frac{z^{k+a_1}}{k!(k+a_1)\Gamma(k+1+a_1-a_2)}$$
$$- \frac{z^{k+a_2}}{k!(k+a_2)\Gamma(k+1+a_2-a_1)}\Bigg], \tag{40}$$

where we made use of the fact that $\Gamma(n+1) = n\Gamma(n)$ and $\Gamma(a)(a)_k = \Gamma(a+k)$ (see Eq. (38)). To further simplify Eq. (40), we adopt the following notation $\mathcal{J}_1 = \sum_{k=0}^{\infty} \frac{z^{k+a_1}}{k!(k+a_1)\Gamma(k+1+a_1-a_2)}$ and differentiate it with respect to z:

$$\frac{\mathrm{d}\mathcal{J}_1}{\mathrm{d}z} = \sum_{k=0}^{\infty} \frac{(\sqrt{z})^{2k+2a_1-2}}{k!\Gamma(k+1+a_1-a_2)}. \tag{41}$$

As already mentioned, the main idea is to try to reduce Eq. (35) to a form similar to Eq. (32), i.e., to relate the above expression to modified Bessel functions, and the modified Bessel function of the first kind [64] is defined as:

$$\mathrm{I}_n(x) = \sum_{k=0}^{\infty} \frac{\left(\frac{x}{2}\right)^{2k+n}}{k!\Gamma(k+n+1)}. \tag{42}$$

By comparing Eqs. (41) and (42), we observe that their right-hand sides are of a similar form, if $x/2 \rightarrow \sqrt{z}$, $n \rightarrow a_1 - a_2$, that is:

$$\frac{\mathrm{d}\mathcal{J}_1}{\mathrm{d}z} = (\sqrt{z})^{a_1+a_2-2}\mathrm{I}_{a_1-a_2}(2\sqrt{z}). \tag{43}$$

Proceeding in a similar manner in the case of the remaining term in Eq. (40) $\mathcal{J}_2 = \sum_{k=0}^{\infty} \frac{z^{k+a_2}}{k!(k+a_2)\Gamma(k+1+a_2-a_1)}$ we arrive at:

$$\frac{\mathrm{d}\mathcal{J}_2}{\mathrm{d}z} = (\sqrt{z})^{a_1+a_2-2}\mathrm{I}_{a_2-a_1}(2\sqrt{z}). \tag{44}$$

Note, from Eq. (40), that $\mathcal{I}_1 = z^{-\frac{a_1+a_2}{2}}(\mathcal{J}_1 - \mathcal{J}_2)$.

By substituting integrated Eqs. (43) and (44) in Eq. (40), and thus obtained expression in Eq. (35), for C_1 we finally obtain:

$$C_1 = I_0\epsilon\delta\frac{m}{(h+m)}\frac{\mathrm{e}^{\lambda_+t_0}-1}{\lambda_+} + 2C_0\left(\frac{2\sqrt{\beta\sigma}}{\alpha}\right)^{-\frac{\gamma+\epsilon\delta+\sigma}{\alpha}}$$
$$\times \int_0^{\frac{2\sqrt{\beta\sigma}}{\alpha}} y^{\frac{\gamma+\epsilon\delta+\sigma}{\alpha}-1}\mathrm{K}\left(\frac{\gamma+\epsilon\delta-\sigma}{\alpha}, y\right)\mathrm{d}y. \tag{45}$$

Note that, in obtaining the above expression the identity [66,68] relating modified Bessel function of the first and the second kind $\mathrm{I}_{-n}(x) - \mathrm{I}_n(x) = \frac{2}{\pi}\sin(n\pi)\mathrm{K}_n(x)$ was used.

The remaining constant C_2 (see Eq. (36)) from fatality counts expression is simplified by applying the same procedure as in the case of C_1. To avoid redundant derivations (i.e., the repetition of the above calculations), we simply outline the final expression:

$$C_2 = I_0\epsilon\delta\frac{m}{(h+m)}\frac{\mathrm{e}^{-(h+m)t_0}-\mathrm{e}^{\lambda_+t_0}}{h+m+\lambda_+}$$
$$- 2C_0\left(\frac{2\sqrt{\beta\sigma}}{\alpha}\right)^{-\frac{\gamma+\epsilon\delta+\sigma-2(h+m)}{\alpha}}$$
$$\times \int_0^{\frac{2\sqrt{\beta\sigma}}{\alpha}} y^{\frac{\gamma+\epsilon\delta+\sigma-2(h+m)}{\alpha}-1}\mathrm{K}\left(\frac{\gamma+\epsilon\delta-\sigma}{\alpha}, y\right)\mathrm{d}y, \tag{46}$$

with the only distinction that, in the process of simplification, parameters a_1 and a_2 now read $(\gamma+\epsilon\delta-h-m)/\alpha$ and $(\sigma-h-m)/\alpha$, respectively.

Now that all terms of fatalities count (given by Eq. (34)) are determined, we note that all constants (C_1, C_2, $C_1(t)$ and $C_2(t)$) are still in their integral form. Since, for all countries that we consider it holds $2\sqrt{\beta\sigma}/\alpha \gg 1$, we may further simplify these integrals by utilizing Hankel's asymptotic expression [66]:

$$\mathrm{K}_n(x) \sim \sqrt{\frac{\pi}{2x}}e^{-x}\left(1+\mathcal{O}\left(\frac{1}{x}\right)\right), \tag{47}$$

which holds for large $x = 2\sqrt{\beta\sigma}/\alpha$.

Along these lines, we rewrite Eqs. (32, 45, 46):

$$C_1 \approx I_0\epsilon\delta\frac{m}{(h+m)}$$
$$\left[\frac{\mathrm{e}^{\lambda_+t_0}-1}{\lambda_+} + \frac{2}{\alpha}\left(\frac{2\sqrt{\beta\sigma}}{\alpha}\right)^{-\frac{\gamma+\epsilon\delta+\sigma}{\alpha}+\frac{1}{2}}\mathrm{e}^{\lambda_+t_0+\frac{2\sqrt{\beta\sigma}}{\alpha}}\right.$$
$$\left.\times \int_0^{\frac{2\sqrt{\beta\sigma}}{\alpha}} y^{\frac{\gamma+\epsilon\delta+\sigma}{\alpha}-\frac{3}{2}}e^{-y}\mathrm{d}y\right]$$

$$C_2 \approx I_0\epsilon\delta\frac{m}{(h+m)}\left[\frac{\mathrm{e}^{-(h+m)t_0}-\mathrm{e}^{\lambda_+t_0}}{h+m+\lambda_+}\right.$$
$$- \frac{2}{\alpha}\left(\frac{2\sqrt{\beta\sigma}}{\alpha}\right)^{-\frac{\gamma+\epsilon\delta+\sigma-2(h+m)}{\alpha}+\frac{1}{2}}$$
$$\left.\times \mathrm{e}^{\lambda_+t_0+\frac{2\sqrt{\beta\sigma}}{\alpha}}\int_0^{\frac{2\sqrt{\beta\sigma}}{\alpha}} y^{\frac{\gamma+\epsilon\delta+\sigma-2(h+m)}{\alpha}-\frac{3}{2}}e^{-y}\mathrm{d}y\right]$$

$$C_1(t) \approx -\frac{2I_0\epsilon\delta}{\alpha}\frac{m}{h+m}\left(\frac{2\sqrt{\beta\sigma}}{\alpha}\right)^{-\frac{\gamma+\epsilon\delta+\sigma}{\alpha}+\frac{1}{2}}\mathrm{e}^{\lambda_+t_0+\frac{2\sqrt{\beta\sigma}}{\alpha}}$$

$$\times \int_0^{\frac{2\sqrt{e^{-\alpha t}\beta\sigma}}{\alpha}} y^{\frac{\gamma+\epsilon\delta+\sigma}{\alpha}-\frac{3}{2}} e^{-y} dy$$

$$C_2(t) \approx \frac{2I_0\epsilon\delta}{\alpha}\frac{m}{h+m}\left(\frac{2\sqrt{\beta\sigma}}{\alpha}\right)^{-\frac{\gamma+\epsilon\delta+\sigma}{\alpha}+\frac{1}{2}} e^{\lambda_+ t_0 + \frac{2\sqrt{\beta\sigma}}{\alpha}}$$

$$\times \int_0^{\frac{2\sqrt{e^{-\alpha t}\beta\sigma}}{\alpha}} y^{\frac{\gamma+\epsilon\delta+\sigma-2(h+m)}{\alpha}-\frac{3}{2}} e^{-y} dy, \quad (48)$$

where we also used the same approximation given by Eq. (47) for modified Bessel function of the second kind contained in C and C_0. Note that the second terms of C_1 and $C_1(t)$ on one side, and the second terms of C_2 and $C_2(t)$ on the other have the same exponents (keep in mind that, according to Eq. (34), there is still a remaining factor $\left(2\sqrt{\beta\sigma}/\alpha\right)^{\frac{2(h+m)}{\alpha}}$ multiplying $C_2(t)$).

In Eq. (48), we encounter the lower incomplete gamma function [66] $\gamma(s,x) = \int_0^x t^{s-1}e^{-t}dt$, which we go about by utilizing [66]:

$$\gamma(s,x) = \Gamma(s) - \Gamma(s,x), \quad (49)$$

where $\Gamma(s,x) = \int_x^\infty t^{s-1}e^{-t}dt$ represents the upper incomplete gamma function [66].

Finally, upon implementing thus calculated constants of Eq. (48) in Eq. (34), and by taking into account Eq. (29), we obtain the expression (16) for the general solution of Eq. (10) at the entire t region.

A.2 Analytical derivation of detected cases

Next, we concentrate on the time evolution of detected counts. To this end, we make use of Eqs. (6) and (9), i.e.

$$D(t) = \epsilon\delta \int I(t)dt + C_i, \quad (50)$$

where C_i ($i = 3, 4$) stands for the constant of integration. In region I the integration of $I_I(t)$ (the first term in Eq. (9)) is straightforward and yields $D_I(t) = \frac{I_0\epsilon\delta}{\lambda_+}e^{\lambda_+ t} + C_3$, while C_3 is obtained from the initial conditions $D_I(t=0) = D_0 \equiv \frac{I_0\epsilon\delta}{\lambda_+}$, leading to:

$$D_I(t) = \frac{I_0\epsilon\delta}{\lambda_+}e^{\lambda_+ t}. \quad (51)$$

In region II, the integration is more demanding, due to the form of $I_{II}(t)$ (the second term of Eq. (9)). To

address this, we employ the following substitution of variable $t - t_0 \to x = \frac{2\sqrt{\beta\sigma}}{\alpha}e^{-\frac{\alpha(t-t_0)}{2}}$. Thus:

$$D_{II}(t) = -2C_0\frac{h+m}{m}\left(\frac{2\sqrt{\beta\sigma}}{\alpha}\right)^{-\frac{\gamma+\epsilon\delta+\sigma}{\alpha}}$$

$$\times \int_{\frac{2\sqrt{\beta\sigma}}{\alpha}}^{\frac{2\sqrt{e^{-\alpha(t-t_0)}\beta\sigma}}{\alpha}} x^{\frac{\gamma+\epsilon\delta+\sigma}{\alpha}-1}$$

$$K\left(\frac{\gamma+\epsilon\delta-\sigma}{\alpha}, x\right) dx + C_4. \quad (52)$$

Note that, as opposed to our previous notation during the derivation of $F_{II}(t)$, now we do not make use of the substitution $t - t_0 \to t$. Because of this, the boundary condition reads: $D_{II}(t_0) = D_I(t_0)$, which is used for determining the integration constant $C_4 = \frac{I_0\epsilon\delta}{\lambda_+}e^{\lambda_+ t_0}$. So, the expression for detected cases reads:

$$D(t) = \theta(t_0 - t)\frac{I_0\epsilon\delta}{\lambda_+}e^{\lambda_+ t} + \theta(t - t_0)$$

$$\left\{\frac{I_0\epsilon\delta}{\lambda_+}e^{\lambda_+ t_0} + C_0\frac{h+m}{m}\right.$$

$$\times \left[\left(\frac{\sqrt{\beta\sigma}}{\alpha}\right)^{-\frac{\gamma+\epsilon\delta-\sigma}{\alpha}}\Gamma\left(\frac{\sigma}{\alpha}\right)\right.$$

$$_1\tilde{F}_2\left(\frac{\sigma}{\alpha};1+\frac{\sigma}{\alpha},1+\frac{\sigma-\gamma-\epsilon\delta}{\alpha};\frac{\beta\sigma}{\alpha^2}\right)$$

$$-\left(\frac{\sqrt{\beta\sigma}}{\alpha}\right)^{\frac{\gamma+\epsilon\delta-\sigma}{\alpha}}\Gamma\left(\frac{\gamma+\epsilon\delta}{\alpha}\right)$$

$$\times\, _1\tilde{F}_2\left(\frac{\gamma+\epsilon\delta}{\alpha};1+\frac{\gamma+\epsilon\delta}{\alpha},1+\frac{\gamma+\epsilon\delta-\sigma}{\alpha};\frac{\beta\sigma}{\alpha^2}\right)$$

$$+\left(\frac{\sqrt{\beta\sigma}}{\alpha}\right)^{\frac{\gamma+\epsilon\delta-\sigma}{\alpha}}e^{-(\gamma+\epsilon\delta)(t-t_0)}\Gamma\left(\frac{\gamma+\epsilon\delta}{\alpha}\right)$$

$$\times\, _1\tilde{F}_2\left(\frac{\gamma+\epsilon\delta}{\alpha};1+\frac{\gamma+\epsilon\delta}{\alpha},1\right.$$

$$\left.+\frac{\gamma+\epsilon\delta-\sigma}{\alpha};\frac{e^{-\alpha(t-t_0)}\beta\sigma}{\alpha^2}\right)$$

$$-\left(\frac{\sqrt{\beta\sigma}}{\alpha}\right)^{-\frac{\gamma+\epsilon\delta-\sigma}{\alpha}}e^{-\sigma(t-t_0)}\Gamma\left(\frac{\sigma}{\alpha}\right)$$

$$\times\, _1\tilde{F}_2\left(\frac{\sigma}{\alpha};1+\frac{\sigma}{\alpha},1\right.$$

$$\left.\left.+\frac{\sigma-\gamma-\epsilon\delta}{\alpha};\frac{e^{-\alpha(t-t_0)}\beta\sigma}{\alpha^2}\right)\right]$$

$$\left.\frac{\pi}{2}\times\csc\left[\frac{\pi(\gamma+\epsilon\delta-\sigma)}{\alpha}\right]\right\}. \quad (53)$$

After performing the same algebraic manipulations of regularized generalized hypergeometric functions as in the previous Subsect. A.1, as well as applying Hankel's approximation (47), we obtain the expression (19) for the general solution of Eq. (11) at the entire t region.

Alternatively, the same expression (19) could be obtained more straightforwardly. Namely, the expression for the number of infectious individuals (Eq. (9)) can be simplified by utilizing Eq. (47):

$$
I(t) = \theta(t_0 - t) I_0 e^{\lambda_+ t} + \theta(t - t_0)
$$
$$
I_0 e^{\lambda_+ t_0 + \frac{2\sqrt{\beta\sigma}}{\alpha}} e^{-\frac{\alpha(t-t_0)}{2}\left(\frac{\gamma + \epsilon\delta + \sigma}{\alpha} - \frac{1}{2}\right)}
$$
$$
\times e^{-\frac{2\sqrt{e^{-\alpha(t-t_0)}\beta\sigma}}{\alpha}}. \tag{54}
$$

Now that $I(t)$ has been determined in the desired form, the detected counts can be calculated from Eq. (11). In region I, the derivation is straightforward (and therefore omitted) and leads to Eq. (51). In region II, the integration is more demanding, due to the form of $I_{II}(t) = I_0 e^{\lambda_+ t_0 + \frac{2\sqrt{\beta\sigma}}{\alpha}} e^{-\frac{\alpha(t-t_0)}{2}\left(\frac{\gamma + \epsilon\delta + \sigma}{\alpha} - \frac{1}{2}\right)} e^{-\frac{2\sqrt{e^{-\alpha(t-t_0)}\beta\sigma}}{\alpha}}$.

To address this, again we employ the following substitution of variable $t - t_0 \to x = \frac{2\sqrt{\beta\sigma}}{\alpha} e^{-\frac{\alpha(t-t_0)}{2}}$, resulting in the boundary condition $D_{II}(t_0) = D_I(t_0)$ (which is used for determining the integration constant C_4). In a similar manner as before, we again encounter the incomplete gamma functions [66]:

$$
D_{II}(t) = -\frac{2 I_0 \epsilon\delta}{\alpha} \left(\frac{2\sqrt{\beta\sigma}}{\alpha}\right)^{-\frac{\gamma + \epsilon\delta + \sigma}{\alpha} + \frac{1}{2}} e^{\frac{2\sqrt{\beta\sigma}}{\alpha} + \lambda_+ t_0}
$$
$$
\times \int_{\frac{2\sqrt{\beta\sigma}}{\alpha}}^{\frac{2\sqrt{e^{-\alpha(t-t_0)}\beta\sigma}}{\alpha}} x^{\frac{\gamma + \epsilon\delta + \sigma}{\alpha} - \frac{3}{2}} e^{-x} dx + C_4. \tag{55}
$$

The only difference compared to Eq. (48) is that now the lower boundary of integration is not zero but some positive real number. This integral is solved by applying the identity $\int_a^b x^{s-1} e^{-x} dx = \int_0^b x^{s-1} e^{-x} dx - \int_0^a x^{s-1} e^{-x} dx = \Gamma(s, a) - \Gamma(s, b)$. By combining this result with Eq. (51), we finally arrive at the expression (19) for the number of detected cases.

A.3 Simplified expressions for fatalities and detected cases

In this section, we show that certain terms in the expressions for fatalities and detected cases can be neglected (when epidemiological parameters are in realistic ranges), without significant loss of predictive precision. First, we start with Eq. (16) for fatality counts. We notice that for $t > t_0$ first two terms are much smaller than the remaining terms, due to $2\sqrt{\beta\sigma}/\alpha \gg 1$, and therefore can be neglected. Additionally, for the same reason all $\Gamma(s, 2\sqrt{\beta\sigma}/\alpha) \to \Gamma(s, \infty)$ are approximately equal to zero (i.e., the gamma integral is effectively $\int_\infty^\infty$). Therefore, instead of Eq. (16), the following formula can be safely used in practice:

$$
F_{simp}(t) \approx I_0 \epsilon\delta \frac{m}{h + m}
$$
$$
\left\{ \theta(t_0 - t)\left(\frac{e^{\lambda_+ t} - 1}{\lambda_+} + \frac{e^{-(h+m)t} - e^{\lambda_+ t}}{h + m + \lambda_+}\right) \right.
$$
$$
+ \theta(t - t_0) \frac{2}{\alpha} \left(\frac{2\sqrt{\beta\sigma}}{\alpha}\right)^{-\frac{\gamma + \epsilon\delta + \sigma}{\alpha} + \frac{1}{2}} e^{\lambda_+ t_0 + \frac{2\sqrt{\beta\sigma}}{\alpha}}
$$
$$
\times \left[\Gamma\left(\frac{\gamma + \epsilon\delta + \sigma}{\alpha} - \frac{1}{2}, \frac{2\sqrt{e^{-\alpha(t-t_0)}\beta\sigma}}{\alpha}\right)\right.
$$
$$
- \left(\frac{2\sqrt{e^{-\alpha(t-t_0)}\beta\sigma}}{\alpha}\right)^{\frac{2(h+m)}{\alpha}}
$$
$$
\times \Gamma\left(\frac{\gamma + \epsilon\delta + \sigma - 2(h+m)}{\alpha}\right.
$$
$$
\left.\left.\left. - \frac{1}{2}, \frac{2\sqrt{e^{-\alpha(t-t_0)}\beta\sigma}}{\alpha}\right)\right]\right\}. \tag{56}
$$

Continuing in the same manner, the simplified form of the number of detected cases is easily obtained:

$$
D_{simp}(t) \approx I_0 \epsilon\delta
$$
$$
\left[\theta(t_0 - t)\frac{e^{\lambda_+ t}}{\lambda_+} + \theta(t - t_0)\frac{2}{\alpha}\right.
$$
$$
\left(\frac{2\sqrt{\beta\sigma}}{\alpha}\right)^{-\frac{\gamma + \epsilon\delta + \sigma}{\alpha} + \frac{1}{2}}
$$
$$
\times e^{\lambda_+ t_0 + \frac{2\sqrt{\beta\sigma}}{\alpha}}
$$
$$
\left. \Gamma\left(\frac{\gamma + \epsilon\delta + \sigma}{\alpha} - \frac{1}{2}, \frac{2\sqrt{e^{-\alpha(t-t_0)}\beta\sigma}}{\alpha}\right)\right]. \tag{57}
$$

We have numerically tested and confirmed that the full-fledged (given by Eq. (16)) and simplified (given by Eq. (56)) fatality curves are practically overlapping (and the same for the detected cases).

A.4 Expressions for fatalities and detected cases at saturation

We will evaluate the saturation values of fatalities and detected counts, that is, their expressions in the limit of very large t. This means that we can concentrate only on $t > t_0$, i.e., region II, where we set $t \to \infty$. Building on the results of the previous section, from Eq. (56) we observe that, in this limit, the second term in the square brackets can be neglected, due to $e^{-(h+m)(t-t_0)} \to 0$. Likewise,

$$
\begin{aligned}
\Gamma\big(\frac{\gamma + \epsilon\delta + \sigma}{\alpha} &- \frac{1}{2}, \frac{2\sqrt{e^{-\alpha(t-t_0)}\beta\sigma}}{\alpha}\big) \\
&\to \Gamma\big(\frac{\gamma + \epsilon\delta + \sigma}{\alpha} - \frac{1}{2}, 0\big) \\
&\equiv \Gamma\big(\frac{\gamma + \epsilon\delta + \sigma}{\alpha} - \frac{1}{2}\big).
\end{aligned}
$$

Therefore, we obtain the expressions (17) and (20) for the saturation values.

A.5 Expressions for the epidemics peak and tipping points

Other important quantities characterizing infection dynamics during the first wave are epidemics peak time and inflection (tipping and turning) points, for which we here provide analytic expressions. Namely, the epidemics peak time is the moment when infected curve reaches its maximal value (i.e., $dI/dt = 0$), or equivalently $d^2D/dt^2 = 0$. The second derivative of Eq. (19) in region II (or equivalently Eq. (57) in the same region) yields:

$$
\begin{aligned}
\frac{d^2 D_{II}}{dt^2} &= I_0\epsilon\delta e^{\lambda_+ + t_0 + \frac{2\sqrt{\beta\sigma}}{\alpha}} \\
&e^{-\frac{\alpha(t-t_0)}{2}\big(\frac{\gamma + \epsilon\delta + \sigma}{\alpha} - \frac{1}{2}\big)}e^{-\frac{2\sqrt{e^{-\alpha(t-t_0)}\beta\sigma}}{\alpha}} \\
&\times \big(-\frac{\gamma + \epsilon\delta + \sigma}{2} + \frac{\alpha}{4} + \sqrt{e^{-\alpha(t-t_0)}\beta\sigma}\big).
\end{aligned}
\tag{58}
$$

In deriving the above expression, we made use of equality $d\Gamma(s, x)/dx = -x^{s-1}e^{-x}$, following from the definition of incomplete gamma functions [66]. Note that, in this subsection, we are interested in region II, where all relevant points lay. After equating the second derivative of D_{II} with zero, for the epidemics peak time, we obtain:

$$
t_{max} = t_0 + \frac{1}{\alpha}\ln\Big[\frac{16\beta\sigma}{(2(\gamma + \epsilon\delta + \sigma) - \alpha)^2}\Big].
\tag{59}
$$

By evaluating $\frac{dD}{dt}$ at $t = t_{max}$, we can straightforwardly obtain the maximum of detected cases per day, given by

$$
\begin{aligned}
\Big(\frac{dD}{dt}\Big)_{max} &= D_0\lambda_+ e^{\lambda_+\big(t_0 + \frac{2}{\alpha}\big) + \frac{1}{2}} \\
&\Big(\frac{4\sqrt{\beta\sigma}}{2(\gamma + \epsilon\delta + \sigma) - \alpha}\Big)^{\frac{1}{2} - \frac{\gamma + \epsilon\delta + \sigma}{\alpha}}.
\end{aligned}
\tag{60}
$$

Along the same lines, the epidemics inflection points are defined as $d^2I/dt^2 = 0$, or equivalently $d^3D/dt^3 = 0$:

$$
\begin{aligned}
\frac{d^3 D_{II}}{dt^3} &= I_0\epsilon\delta e^{\lambda_+ + t_0 + \frac{2\sqrt{\beta\sigma}}{\alpha}} e^{-\frac{\alpha(t-t_0)}{2}\big(\frac{\gamma + \epsilon\delta + \sigma}{\alpha} - \frac{1}{2}\big)} \\
&e^{-\frac{2\sqrt{e^{-\alpha(t-t_0)}\beta\sigma}}{\alpha}} \\
&\times \Big[\big(\frac{\gamma + \epsilon\delta + \sigma}{2} - \frac{\alpha}{4} - \sqrt{e^{-\alpha(t-t_0)}\beta\sigma}\big)^2 \\
&- \frac{\alpha}{2}\sqrt{e^{-\alpha(t-t_0)}\beta\sigma}\Big] \\
&= 0.
\end{aligned}
\tag{61}
$$

Eq. (61) has two solutions, which correspond to the infection tipping points

$$
t_{1,2} = t_0 + \frac{2}{\alpha}\ln\Big(\frac{2\sqrt{\beta\sigma}}{\gamma + \delta\epsilon + \sigma \mp \sqrt{\alpha\big(\gamma + \epsilon\delta + \sigma - \frac{\alpha}{4}\big)}}\Big).
\tag{62}
$$

The duration of the epidemic peak can then be defined as a difference between these two tipping points and is equal to:

$$
\Delta t_{peak} = \frac{4}{\alpha}\ln\Big(\frac{\gamma + \epsilon\delta + \sigma + \sqrt{\alpha(\gamma + \epsilon\delta + \sigma - \frac{\alpha}{4})}}{\gamma + \epsilon\delta + \sigma - \alpha/2}\Big).
\tag{63}
$$

References

1. Liu, X., Zheng, X., Balachandran, B.: COVID-19: data-driven dynamics, statistical and distributed delay models, and observations. Nonlinear Dyn. **101**, 1527–1543 (2020). https://doi.org/10.1007/s11071-020-05863-5

2. Mondal, J., Khajanchi, S.: Mathematical modeling and optimal intervention strategies of the COVID-19 outbreak. Nonlinear Dyn. (2022). https://doi.org/10.1007/s11071-022-07235-7

3. Zhou, B., Jiang, D., Dai, Y., Hayat, T.: Stationary distribution and density function expression for a stochastic SIQRS epidemic model with temporary immunity. Nonlinear Dyn. **105**, 931–955 (2021). https://doi.org/10.1007/s11071-020-06151-y

4. Han, C., Li, M., Haihambo, N., Babuna, P., Liu, Q., Zhao, X., Jaeger, C., Li, Y., Yang, S.: Mechanisms of recurrent outbreak of COVID-19: a model-based study. Nonlinear Dyn. **106**, 1169–1185 (2021). https://doi.org/10.1007/s11071-021-06371-w

5. Al-Darabsah, I.: Threshold dynamics of a time-delayed epidemic model for continuous imperfect-vaccine with a generalized nonmonotone incidence rate. Nonlinear Dyn. **101**, 1281–1300 (2020). https://doi.org/10.1007/s11071-020-05825-x

6. Zhai, S., Luo, G., Huang, T., Wang, X., Tao, J., Zhou, P.: Vaccination control of an epidemic model with time delay and its application to COVID-19. Nonlinear Dyn. **106**, 1279–1292 (2021). https://doi.org/10.1007/s11071-021-06533-w

7. Raza, A., Rafiq, M., Awrejcewicz, J., Ahmed, N., Mohsin, M.: Dynamical analysis of coronavirus disease with crowding effect, and vaccination: a study of third strain. Nonlinear Dyn. (2022). https://doi.org/10.1007/s11071-021-07108-5

8. Das, P., Upadhyay, R.K., Misra, A.K., Rihan, F.A., Das, P., Ghosh, D.: Mathematical model of COVID-19 with comorbidity and controlling using non-pharmaceutical interventions and vaccination. Nonlinear Dyn. **106**, 1213–1227 (2021). https://doi.org/10.1007/s11071-021-06517-w

9. Guan, G., Guo, Z.: Stability behavior of a two-susceptibility SHIR epidemic model with time delay in complex networks. Nonlinear Dyn. **106**, 1083–1110 (2021). https://doi.org/10.1007/s11071-021-06804-6

10. Das, P., Nadim, S.S., Das, S., Das, P.: Dynamics of COVID-19 transmission with comorbidity: a data driven modelling based approach. Nonlinear Dyn. **106**, 1197–1211 (2021). https://doi.org/10.1007/s11071-021-06324-3

11. Babajanyan, S.G., Cheong, K.H.: Age-structured SIR model and resource growth dynamics: a COVID-19 study. Nonlinear Dyn. **104**, 2853–2864 (2021). https://doi.org/10.1007/s11071-021-06384-5

12. Vilar, J.M.G., Saiz, L.: Reliably quantifying the evolving worldwide dynamic state of the COVID-19 outbreak from death records, clinical parametrization, and demographic data. Sci. Rep. **11**, 19952 (2021). https://doi.org/10.1038/s41598-021-99273-1

13. Vilar, J.M.G., Saiz, L.: Ascertaining the initiation of epidemic resurgences: an application to the COVID-19 second surges in Europe and the Northeast United States. R Soc. Open Sci. **8**, 210773 (2021). https://doi.org/10.1098/rsos.210773

14. Xu, L., Zhang, H., Xu, H., Yang, H., Zhang, L., Zhang, W., Gu, F., Lan, X.: The coSIR model predicts effective strategies to limit the spread of SARS-CoV-2 variants with low severity and high transmissibility. Nonlinear Dyn. **105**, 2757–2773 (2021). https://doi.org/10.1007/s11071-021-06705-8

15. Khyar, O., Allali, K.: Global dynamics of a multi-strain SEIR epidemic model with general incidence rates: application to COVID-19 pandemic. Nonlinear Dyn. **102**, 489–509 (2020). https://doi.org/10.1007/s11071-020-05929-4

16. Ahmed, N., Elsonbaty, A., Raza, A., Rafiq, M., Adel, W.: Numerical simulation and stability analysis of a novel reaction-diffusion COVID-19 model. Nonlinear Dyn. **106**, 1293–1310 (2021). https://doi.org/10.1007/s11071-021-06623-9

17. Di Giamberardino, P., Iacoviello, D., Papa, F., Sinisgalli, C.: A data-driven model of the COVID-19 spread among interconnected populations: epidemiological and mobility aspects following the lockdown in Italy. Nonlinear Dyn. **106**, 1239–1266 (2021). https://doi.org/10.1007/s11071-021-06840-2

18. Jia, Q., Li, J., Lin, H., Tian, F., Zhu, G.: The spatiotemporal transmission dynamics of COVID-19 among multiple regions: a modeling study in Chinese provinces. Nonlinear Dyn. **107**, 1313–1327 (2022). https://doi.org/10.1007/s11071-021-07001-1

19. Sun, G.Q., Wang, S.F., Li, M.T., Li, L., Zhang, J., Zhang, W., Jin, Z., Feng, G.L.: Transmission dynamics of COVID-19 in Wuhan, China: effects of lockdown and medical resources. Nonlinear Dyn. **101**, 1981–1993 (2020). https://doi.org/10.1007/s11071-020-05770-9

20. Zlatić, V., Barjašić, I., Kadović, A., Štefančić, H., Gabrielli, A.: Bi-stability of SUDR+K model of epidemics and test kits applied to COVID-19. Nonlinear Dyn. **101**, 1635–1642 (2020). https://doi.org/10.1007/s11071-020-05888-w

21. Pacheco, P.M.C.L., Savi, M.A., Savi, P.V.: COVID-19 dynamics considering the influence of hospital infrastructure: an investigation into Brazilian scenarios. Nonlinear Dyn. **106**, 1325–1346 (2021). https://doi.org/10.1007/s11071-021-06323-4

22. Li, T., Xiao, Y.: Complex dynamics of an epidemic model with saturated media coverage and recovery. Nonlinear Dyn. (2022). https://doi.org/10.1007/s11071-021-07096-6

23. Rai, R.K., Khajanchi, S., Tiwari, P.K., Venturino, E., Misra, A.K.: Impact of social media advertisements on the transmission dynamics of COVID-19 pandemic in India. J. Appl. Math. Comput. **68**, 19–44 (2022). https://doi.org/10.1007/s12190-021-01507-y

24. WHO report. URL https://www.who.int/emergencies/diseases/novel-coronavirus-2019/situation

25. Diekmann, O., Heesterbeek, H., Britton, T.: Mathematical tools for understanding infectious disease dynamics. Princeton University Press, Princeton, NJ, USA (2012)

26. Martcheva, M.: An introduction to mathematical epidemiology. Springer, Berlin, Germany (2015)

27. Keeling, M.J., Rohani, P.: Modeling infectious diseases in humans and animals. Princeton University Press, Princeton, NJ, USA (2011)

28. Alagoz, O., Sethi, A.K., Patterson, B.W., Churpek, M., Safdar, N.: Effect of Timing of and Adherence to Social Distancing Measures on COVID-19 Burden in the United States.

Ann. Intern. Med. **174**(1), 50–57 (2021). https://doi.org/10.7326/m20-4096

29. Oraby, T., Tyshenko, M.G., Maldonado, J.C., Vatcheva, K., Elsaadany, S., Alali, W.Q., Longenecker, J.C., Al-Zoughool, M.: Modeling the effect of lockdown timing as a COVID-19 control measure in countries with differing social contacts. Sci. Rep. **11**, 3354 (2021)

30. Dressler, D.D.: Social Distancing's Effects on COVID-19: Roles of Timing and Adherence. NEJM Journal Watch. https://www.jwatch.org/na52712/2020/11/03/social-distancings-effects-covid-19-roles-timing-and (2020)

31. Nande, A., Adlam, B., Sheen, J., Levy, M.Z., Hill, A.L.: Dynamics of COVID-19 under social distancing measures are driven by transmission network structure. PLoS Comput. Biol. **17**(2), e1008684 (2021). https://doi.org/10.1371/journal.pcbi.1008684

32. Benjamin, M.F., Brockmann, D.: Effective containment explains subexponential growth in recent confirmed COVID-19 cases in China. Science **368**, 742–746 (2020). https://doi.org/10.1126/science.abb4557

33. He, S., Peng, Y., Sun, K.: SEIR modeling of the COVID-19 and its dynamics. Nonlinear Dyn. **101**, 1667–1680 (2020). https://doi.org/10.1007/s11071-020-05743-y

34. Hametner, C., Kozek, M., Boehler, L., Wasserburger, A., Du, Z.P., Kölbl, R., Bergmann, M., Bachleitner-Hofmann, T., Jakubek, S.: Estimation of exogenous drivers to predict COVID-19 pandemic using a method from nonlinear control theory. Nonlinear Dyn. **106**, 1111–1125 (2021). https://doi.org/10.1007/s11071-021-06811-7

35. Carvalho, T., Cristiano, R., Rodrigues, D.S., Tonon, D.J.: Global analysis of a piecewise smooth epidemiological model of COVID-19. Nonlinear Dyn. **105**, 3763–3773 (2021). https://doi.org/10.1007/s11071-021-06801-9

36. Saha, S., Samanta, G.P., Nieto, J.J.: Epidemic model of COVID-19 outbreak by inducing behavioural response in population. Nonlinear Dyn. **102**, 455–487 (2020). https://doi.org/10.1007/s11071-020-05896-w

37. Huang, J., Qi, G.: Effects of control measures on the dynamics of COVID-19 and double-peak behavior in Spain. Nonlinear Dyn. **101**, 1889–1899 (2020). https://doi.org/10.1007/s11071-020-05901-2

38. Saikia, D., Bora, K., Bora, M.P.: COVID-19 outbreak in India: an SEIR model-based analysis. Nonlinear Dyn. **104**, 4727–4751 (2021). https://doi.org/10.1007/s11071-021-06536-7

39. Kwuimy, C.A.K., Nazari, F., Jiao, X., Rohani, P., Nataraj, C.: Nonlinear dynamic analysis of an epidemiological model for COVID-19 including public behavior and government action. Nonlinear Dyn. **101**, 1545–1559 (2020). https://doi.org/10.1007/s11071-020-05815-z

40. Kermack, W.O., McKendrick, A.G.: A contribution to the mathematical theory of epidemics. In: Proceedings of the Royal Society of London. Series A, Mathematical and Physical Sciences **115**, 700–721 (1927)

41. Friedman, A., Kao, C.Y.: Mathematical modeling of biological processes. Springer, Berlin, Germany (2014)

42. Newman, M.E.J.: The spread of epidemic disease on networks. Phys. Rev. E **66**, 016128 (2002). https://doi.org/10.1103/PhysRevE.66.016128

43. Schutz, G.M., Brandaut, M., Trimper, S.: Exact solution of a stochastic susceptible-infectious-recovered model. Phys. Rev. E **78**, 061132 (2008). https://doi.org/10.1103/PhysRevE.78.061132

44. Awawdeh, F., Adawi, A., Mustafa, Z.: Solutions of the SIR models of epidemics using HAM. Chaos Solitons Fractals **42**, 3047–3052 (2009). https://doi.org/10.1016/j.chaos.2009.04.012

45. Khan, H., Mohapatra, R.N., Vajravelu, K., Liao, S.J.: The explicit series solution of SIR and SIS epidemic models. Appl. Math. Comput. **38**, 653–669 (2009). https://doi.org/10.1016/j.amc.2009.05.051

46. Harko, T., Lobo, F.S.N., Mak, M.K.: Exact analytical solutions of the susceptible-infected-recovered (SIR) epidemic model and of the SIR model with equal death and birth rates. Appl. Math. Comput. **236**, 184 (2014). https://doi.org/10.1016/j.amc.2014.03.030

47. Barlow, N.S., Weinstein, S.J.: Accurate closed-form solution of the SIR epidemic model. Physica D **408**, 132540 (2020). https://doi.org/10.1016/j.physd.2020.132540

48. Carvalho, A.M., Goncalves, S.: An analytical solution for the Kermack–McKendrick model. Physica A **566**, 125659 (2021). https://doi.org/10.1016/j.physa.2020.125659

49. Sadurni, E., Luna-Acosta, G.: Exactly solvable SIR models, their extensions and their application to sensitive pandemic forecasting. Nonlinear Dyn. **103**, 2955–2971 (2021). https://doi.org/10.1007/s11071-021-06248-y

50. Kroeger, M., Schlickeiser, R.: Analytical solution of the SIR-model for the temporal evolution of epidemics. Part A: time-independent reproduction factor. J. Phys. A **53**, 505601 (2020). https://doi.org/10.1088/1751-8121/abc65d

51. Schlickeiser, R., Kroeger, M.: Analytical solution of the SIR-model for the temporal evolution of epidemics. Part B: semi-time case. J. Phys. A **54**, 175601 (2021). https://doi.org/10.1088/1751-8121/abed66

52. Weinstein, S.J., Holland, M.S., Rogers, K.E., Barlow, N.S.: Analytic solution of the SEIR epidemic model via asymptotic approximant. Physica D: Nonlinear Phenomena **411**, 132633 (2020). https://doi.org/10.1016/j.physd.2020.132633

53. Piovella, N.: Analytical solution of SEIR model describing the free spread of the COVID-19 pandemic. Chaos Solitons Fractals **140**, 110243 (2020). https://doi.org/10.1016/j.chaos.2020.110243

54. Miller, J.C.: A note on the derivation of epidemic final sizes. Bull. Math. Biol. **74**, 2125–2141 (2012). https://doi.org/10.1007/s11538-012-9749-6

55. Turkyilmazoglu, M.: Explicit formulae for the peak time of an epidemic from the SIR model. Physica D: Nonlinear Phenomena **422**, 132902 (2021). https://doi.org/10.1016/j.physd.2021.132902

56. Kroeger, M., Turkyilmazoglu, M., Schlickeiser, R.: Explicit formulae for the peak time of an epidemic from the SIR model. Which approximant to use? Physica D: Nonlinear Phenomena **425**, 132981 (2021). https://doi.org/10.1016/j.physd.2021.132981

57. Djordjevic, M., Rodic, A., Salom, I., Zigic, D., Milicevic, O., Ilic, B., Djordjevic, M.: A systems biology approach to COVID-19 progression in population. Adv. Protein. Chem. Struct. Biol. **127**, 291–314 (2021). https://doi.org/10.1016/bs.apcsb.2021.03.003

58. Djordjevic, M., Djordjevic, M., Ilic, B., Stojku, S., Salom, I.: Understanding infection progression under strong control measures through universal COVID-19 growth signatures. Glob. Chall. **5**, 2000101 (2021). https://doi.org/10.1002/gch2.202170051

59. Li, R., Pei, S., Chen, B., Song, Y., Zhang, T., Yang, W., Shaman, J.: Substantial undocumented infection facilitates the rapid dissemination of novel coronavirus (SARS-CoV-2). Science **368**, 489–493 (2020). https://doi.org/10.1126/science.abb3221

60. He, X., Lau, E.H.Y., Wu, P., Deng, X., Wang, J., Hao, X., Lau, Y.C., Wong, J.Y., Guan, Y., Tan, X., Mo, X., Chen, Y., Liao, B., Chen, W., Hu, F., Zhang, Q., Zhong, M., Wu, Y., Zhao, L., Zhang, F., Cowling, B.J., Li, F., Leung, G.M.: Temporal dynamics in viral shedding and transmissibility of COVID-19. Nat. Med. **26**, 672–675 (2020). https://doi.org/10.1038/s41591-020-0869-5

61. Bar-On, Y.M., Flamholz, A.I., Phillips, R., Milo, R.: Science forum: SARS-CoV-2 (COVID-19) by the numbers. eLife **9**, e57309 (2020)

62. Phillips, R., Kondev, J., Theriot, J., Garcia, H.: Physical biology of the cell. Garland Science, New York, NY, USA (2012)

63. Worldometer: COVID-19 coronavirus pandemic. https://www.worldometers.info/coronavirus/ (2020)

64. Bowman, F.: Introduction to bessel functions. Dover, New York NY, USA (1958)

65. Weisstein, E.W.: CRC concise encyclopedia of mathematics. Chapman & Hall, CRC Press, Boca Raton, FL, USA (2003)

66. Abramowitz, M., Stegun, I.A.: Handbook of Mathematical Functions. Dover Publications, New York, NY, USA (1972)

67. Markovic, S., Rodic, A., Salom, I., Milicevic, O., Djordjevic, M., Djordjevic, M.: COVID-19 severity determinants inferred through ecological and epidemiological modeling. One Health **13**, 100355 (2021). https://doi.org/10.1016/j.onehlt.2021.100355

68. Zwillinger, D.: CRC standard mathematical tables and formulae. CRC Press, Boca Raton, FL, USA (1995)

69. Sarkar, K., Khajanchi, S., Nieto, J.J.: Modeling and forecasting the COVID-19 pandemic in India. Chaos, Solitons Fractals **139**, 110049 (2020)

70. Salom, I., Rodic, A., Milicevic, O., Zigic, D., Djordjevic, M., Djordjevic, M.: Effects of demographic and weather parameters on COVID-19 basic reproduction number. Front. Ecol. Evol. **8**, 617841 (2021). https://doi.org/10.3389/fevo.2020.617841

71. Milicevic, O., Salom, I., Rodic, A., Markovic, S., Tumbas, M., Zigic, D., Djordjevic, M., Djordjevic, M.: PM2.5 as a major predictor of COVID-19 basic reproduction number in the USA. Environ. Res. **201**, 111526 (2021). https://doi.org/10.1016/j.envres.2021.111526

72. Djordjevic, M., Salom, I., Markovic, S., Rodic, A., Milicevic, O., Djordjevic, M.: Inferring the main drivers of SARS-CoV-2 global transmissibility by feature selection methods. GeoHealth **5**(9), e2021GH000432 (2021). https://doi.org/10.1029/2021GH000432

73. Tadic, B., Melnik, R.: Modeling latent infection transmissions through biosocial stochastic dynamics. PloS One **15**(10), e0241163 (2020). https://doi.org/10.1371/journal.pone.0241163

74. Tadic, B., Melnik, R.: Microscopic dynamics modeling unravels the role of asymptomatic virus carriers in SARS-CoV-2 epidemics at the interplay between biological and social factors. Comput. Biol. Med. **133**, 104422 (2021). https://doi.org/10.1016/j.compbiomed.2021.104422

75. Frieden, T.R., Buissonniere, M., McClelland, A.: The world must prepare now for the next pandemic. BMJ Glob. Health **6**, e005184 (2021). https://doi.org/10.1136/bmjgh-2021-005184

76. Boyce, W.E., DiPrima, R.C., Rosatone, L.: Elementary differential equations and boundary value problems. Wiley, Hoboken, NJ, USA (2012)

77. Kreyszig, E.: Advanced engineering mathematics. Wiley, Hoboken, NJ, USA (2006)

Publisher's Note Springer Nature remains neutral with regard to jurisdictional claims in published maps and institutional affiliations.

RHIC and LHC jet suppression in non-central collisions

Magdalena Djordjevic [a,*], Marko Djordjevic [b], Bojana Blagojevic [a]

[a] *Institute of Physics Belgrade, University of Belgrade, Serbia*
[b] *Faculty of Biology, University of Belgrade, Serbia*

ARTICLE INFO

ABSTRACT

Understanding properties of QCD matter created in ultra-relativistic heavy-ion collisions is a major goal of RHIC and LHC experiments. An excellent tool to study these properties is high-momentum hadron suppression of light and heavy flavor observables. Utilizing this tool requires accurate suppression predictions for different experiments, probes and experimental conditions, and their unbiased comparison with experimental data. With this goal, we here extend our dynamical energy loss formalism towards generating predictions for non-central collisions; the formalism takes into account both radiative and collisional energy loss, dynamical (as opposed to static) scattering centers, finite magnetic mass, running coupling and uses no free parameters in comparison with experimental data. Specifically, we here generate predictions for all available centrality ranges, for both LHC and RHIC experiments, and for four different probes (charged hadrons, neutral pions, D mesons and non-prompt J/ψ). We obtain good agreement with all available non-central data, and also generate predictions for suppression measurements that will soon become available. Finally, we discuss implications of the obtained good agreement with experimental data with different medium models that are currently considered.

1. Introduction

High-momentum hadron suppression [1] of light and heavy observables provides an excellent tool [2–4] for studying properties of QCD matter created in ultra-relativistic heavy ion collisions. Mapping these properties is also a major goal of RHIC and LHC experiments, which requires comparison of hadron suppression measurements with corresponding theoretical predictions. To ensure the unbiased comparison with experimental data, it is necessary to generate predictions for different experiments, experimental probes and experimental conditions, within the same theoretical model. With a major goal of generating these predictions, we developed dynamical energy loss formalism, that *i)* allows treating, at the same time, both light and heavy partons, *ii)* is computed in dynamical QCD medium (i.e. takes into account recoil of the medium constituents), *iii)* includes both collisional [5] and radiative [6,7] energy losses, computed within the *same* theoretical framework, *iv)* includes realistic finite size effects, i.e. the fact that experimentally created QCD medium has finite size, and that the jets are produced inside the medium, *v)* includes finite magnetic mass effects [8] and running coupling [9]. We further integrated this formalism into numerical procedure which also includes multi-gluon fluctuations [10], path length fluctuations [11]

and most up-to-date jet production [12,13] and fragmentation functions [14]; the procedure allows generating predictions with no free parameters used in comparison with experimental data.

We previously applied the computational procedure outlined above for generating predictions in *most central* collisions for a number of different probes at LHC [9]. These predictions showed a very good agreement with experimental data; however, a comprehensive comparison also requires generating predictions for non-central collisions at RHIC and LHC. With this goal, we here extend the formalism towards generating predictions for different centrality ranges. We consequently generate the suppression predictions for all available centrality ranges, for both RHIC and LHC experiments and for four different probes – specifically for charged hadrons, D mesons and non-prompt J/ψ at LHC and neutral pions at RHIC. Such comprehensive comparison allows testing some of important assumptions behind our current understanding of the created QCD matter, such as ranges of validity for different medium models.

2. Theoretical framework

The numerical procedure for calculating high-momentum hadron suppression for central collisions is outlined in detail in [9]. We below first briefly list the main steps in this procedure and then describe the extension of the procedure that is necessary for generating the predictions for non-central collisions:

* Corresponding author.

i) Energy loss calculations: Our model takes into account both radiative and collisional contributions to jet energy loss. Specifically, the radiative energy loss calculations present a state-of-the-art extension of a well-known DGLV model [15,16] towards a finite size dynamical medium [6,7], finite magnetic mass [8] and running coupling [9]. These extensions are further discussed below.

ii) Dynamical scattering centers: To calculate the radiative energy loss, we use finite size dynamical energy loss formalism. This formalism removes a ubiquitous assumption of static scattering centers [17] and takes into account that the medium constituents are in reality dynamical, i.e. moving particles; similarly, the unrealistic assumption of infinite medium is also removed. Calculations of the jet energy loss in dynamical medium are done by using two-hard-thermal-loop approach. In contrast to the static energy loss, where only the electric contribution appears in the final result, both electric and magnetic contributions appear in the dynamical case. This then directly leads to the question of finite magnetic mass, which we further discuss below.

iii) Magnetic mass: In pQCD energy loss calculations – including our (initial) dynamical energy loss formalism [6,7] – magnetic mass is taken to be zero. However, different non-perturbative approaches suggest a non-zero magnetic mass at RHIC and LHC (see e.g. [18–21]). To address this issue, we generalized the dynamical energy loss calculations to the case of finite magnetic mass. Introducing the finite magnetic mass is described in detail in [8], where the finite magnetic mass is introduced through generalized sum-rules.

iv) Running coupling: Introducing the running coupling is described in detail in [9]. One should note that the obtained result is infrared safe and moreover of a moderate value. There is consequently no need to introduce an artificial cutoff as is commonly done elsewhere with the running coupling.

v) Suppression procedure: We further integrated the energy loss formalism outlined above into a numerical procedure that includes: light and heavy flavor production [12,13], path-length [11] and multigluon [10] fluctuations, up-to-date fragmentation functions [14] for light and heavy flavor and the decay of heavy mesons to single electrons and J/ψ. In the calculations, as a start point we use an effective temperature of 304 MeV for 0–40% centrality Pb + Pb collisions at LHC (as extracted by ALICE [22]) and effective temperature of 221 MeV for 0–20% centrality Au + Au collisions at RHIC (as extracted by PHENIX [23]). The other parameter values are specified in the next section, while the details of the procedure are provided in [9]. Note that we use no free parameters in comparison with the data, i.e. all the parameters that we use correspond to standard literature values.

To extend the computational procedure outlined above to non-central collisions, we start by obtaining the path-length distributions for different centrality ranges from [24]. Furthermore, we determine the temperature for each centrality region according to [15] $T^3 \sim \frac{\frac{dN_g}{dy}}{V} \rightarrow T = c\left(\frac{\frac{dN_g}{dy}}{N_{part}}\right)^{1/3}$ (more details will be provided in [25]), where $\frac{dN_g}{dy}$ is gluon rapidity density, V is the volume of created medium, and we take that $V \sim N_{part}$ (number of participants for a given collision). Furthermore, c is a constant for a specific system/collider energy, and $\frac{\frac{dN_g}{dy}}{N_{part}}$ is directly proportional to experimentally measured charged particle multiplicity per participant pair $\left(\frac{\frac{dN_{ch}}{dy}}{N_{part}/2}\right)$, which is measured for both RHIC [26] and LHC [27] and across different centralities. The constants c can be fixed through ALICE measurement of effective temperature for 0–40% centrality at 2.76 TeV Pb + Pb collisions at LHC, and through PHENIX measurement of effective temperature for 0–20% centrality at 200 GeV Au + Au collisions at RHIC (see above).

3. Numerical results

In this section, we concentrate on 200 GeV Au + Au collisions at RHIC and 2.76 TeV Pb + Pb collisions at LHC, and present our suppression predictions for light and heavy flavor observables. We proceed by considering a QGP with $n_f = 2.5$ effective light quark flavors for RHIC and $n_f = 3$ for LHC. Perturbative QCD scale is taken to be $\Lambda_{QCD} = 0.2$ GeV. For the light quarks we assume that their mass is dominated by the thermal mass $M = \mu_E/\sqrt{6}$, where the temperature dependent Debye mass $\mu_E(T)$ is obtained from [28]. Magnetic mass μ_M is taken as $0.4\mu_E < \mu_M < 0.6\mu_E$ [18–21], and the gluon mass is $m_g = \mu_E/\sqrt{2}$ [29]. For the charm (bottom) mass we use $M = 1.2$ GeV ($M = 4.75$ GeV). Path-length distribution and temperatures for different centralities are computed according to the procedure outlined in the previous section. Parton production, fragmentation functions and decays, which are used in the numerical calculations, are specified in [9]. Note that, on each panel of every figure, the gray region corresponds to the range of $0.4 < \mu_M/\mu_E < 0.6$, where the upper (lower) boundary of each band corresponds to $\mu_M/\mu_E = 0.6$ ($\mu_M/\mu_E = 0.4$).

We start by generating predictions for momentum dependence of hadron suppression at LHC experiments, for different centrality regions, which are shown in Figs. 1 and 2. Each panel in these figures shows a fixed centrality region (0–5%, 5–10%, 10–20%, etc.) and for each of these centrality regions, momentum dependence of R_{AA} is shown. Fig. 1 shows predictions for charged hadron R_{AA} and their comparison with relevant ALICE and CMS experimental data at 2.76 TeV Pb + Pb collisions at LHC. In Fig. 2 predictions for D meson R_{AA} are shown; predictions for 0–10% and 30–50% are compared with the available ALICE data, where a very good agreement can also be seen. Note that predictions for 30–50% region were generated *before* the experimental data – that are now shown in the figure – became available [34]. The experimental data for the rest of the predictions (the other two panels in Fig. 2) are expected to become available soon.

In Fig. 3, we show equivalent predictions as in Figs. 1 and 2, but for RHIC measurements of neutral pions at 200 GeV Au + Au collisions. Each panel shows predictions for different (fixed) centrality bin, which are compared with experimental data. Similarly as for LHC measurements, we see a very good agreement between the theoretical predictions and RHIC data.

In Fig. 4, instead of fixing the centrality ranges (as in Figs. 1–3), we fix the momentum regions and explore how R_{AA} changes for different centrality values (i.e. number of participants). The predictions are generated for both RHIC and LHC experiments, and for various probes. Specifically, we compare our predictions with experimental data for neutral pions at RHIC and charged hadrons, D mesons and non-prompt J/ψ at LHC. One can see that we here also obtain a robust agreement with the experimental data.

4. Conclusions

We here generated suppression predictions for all available centrality ranges, for both RHIC and LHC, and for diverse experimental probes. These predictions were generated by the same theoretical formalism and within the same numerical procedure. Furthermore, all the predictions within the same experiment (i.e. within RHIC and within LHC) were generated with the same parameter set, which corresponds to standard literature values, and with no free parameters used in comparison with experimental data. We obtained good agreement of the theoretical predictions with the diverse experimental measurements, for all momentum ranges larger than 10 GeV.
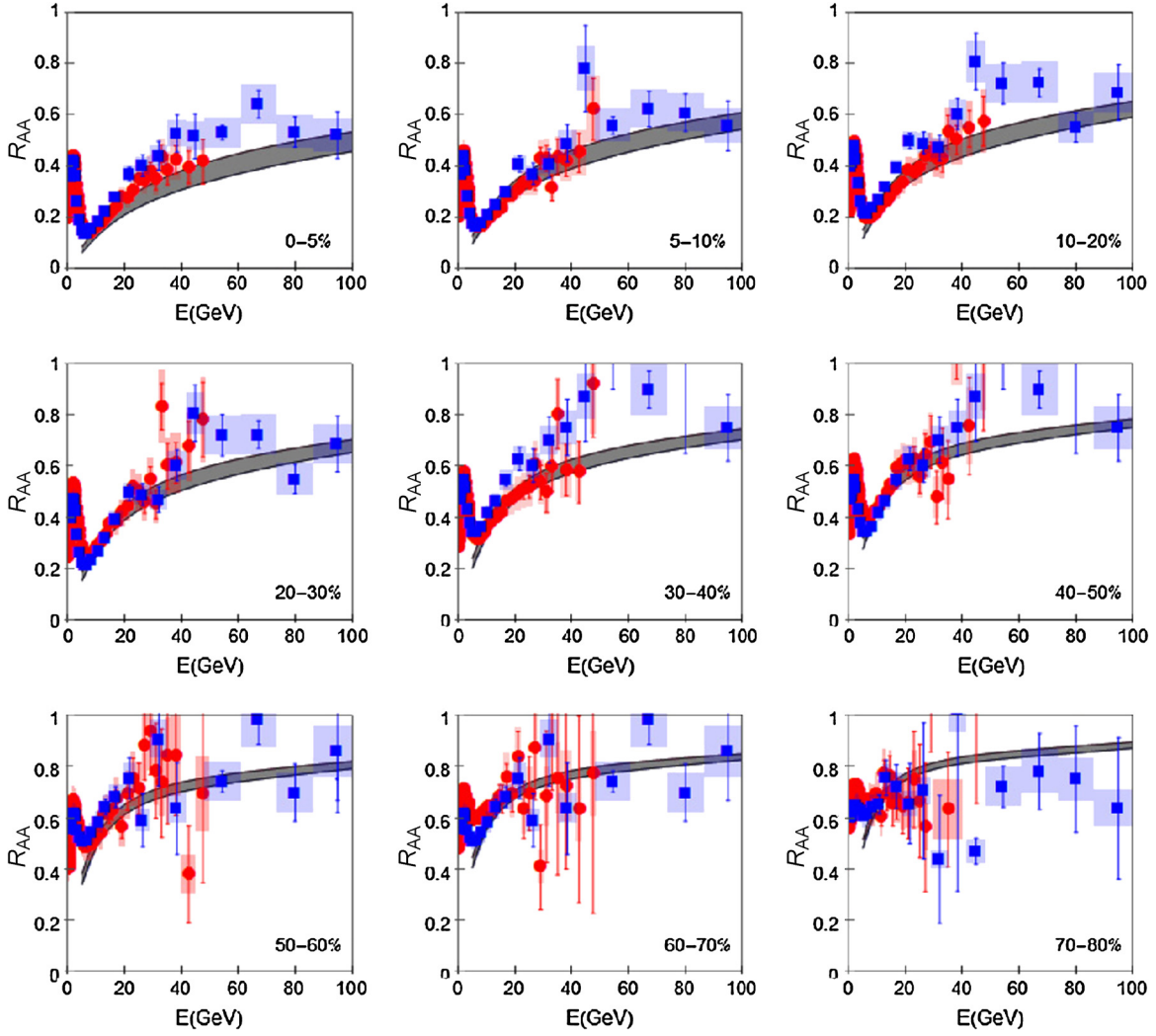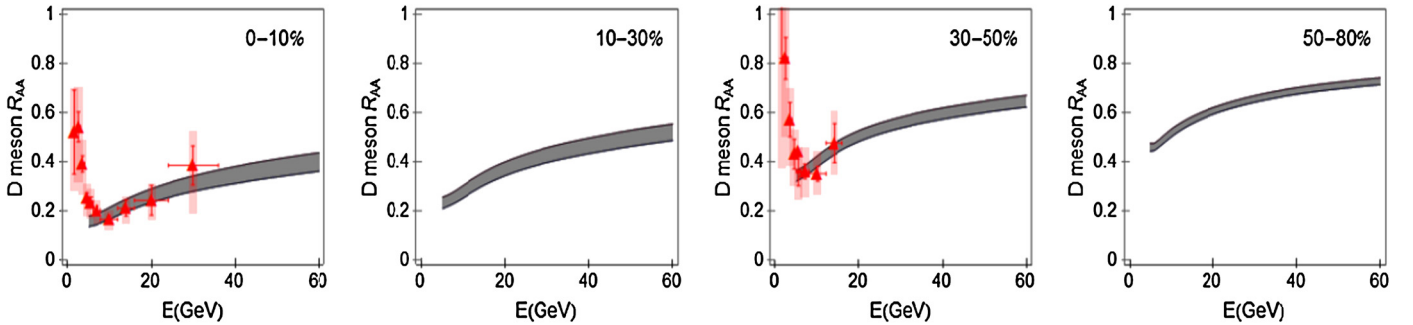
Fig. 1. Theory *vs.* experimental data for momentum dependence of charged hadron R_{AA} for different centrality bins at LHC. The panels show the comparison of charged hadron suppression predictions with experimentally measured R_{AA} for charged particles at 2.76 Pb + Pb collisions at LHC, for different (fixed) centrality ranges. Red circles and blue squares correspond to ALICE [30] and CMS [31] experimental data, respectively. In the lower right corner of each panel we denote the centrality for which the data and the predictions are presented. Note that, on the third and the fourth panels, CMS data for centrality bin 10–30% are shown. Similarly, on the fifth and the sixth panels, CMS data for centrality bin 30–50% are shown, on the seventh and the eight panels, CMS data for centrality bin 50–70% are shown, and on the ninth panel CMS data for 70–90% in centrality are shown.

Fig. 2. Theory *vs.* experimental data for momentum dependence of D meson R_{AA} for different centrality bins at LHC. The left panel shows the comparison of D meson suppression predictions with D meson R_{AA} at 0–7.5% central 2.76 Pb + Pb collisions at LHC [32] (the red triangles). The other three panels show the theoretical predictions for D meson R_{AA} for centrality bins 10–30%, 30–50% and 50–80%, respectively. In the third panel (30–50% centrality region), the predictions are compared with ALICE preliminary data [33] that recently became available.

The robust agreement discussed above has interesting implications for ranges of validity of different medium models, which are incorporated in different approaches to hadron suppression predictions. As discussed in the Introduction, our calculations employ state-of-the-art method for energy loss calculations and numerical

procedure for suppression calculations, but do not explicitly take into account the medium evolution (i.e. the evolution is taken into account through effective/average medium parameters). This is in contrast to a number of other approaches (see e.g. [39–42]), which simplify the energy loss to a various degree, in order to more
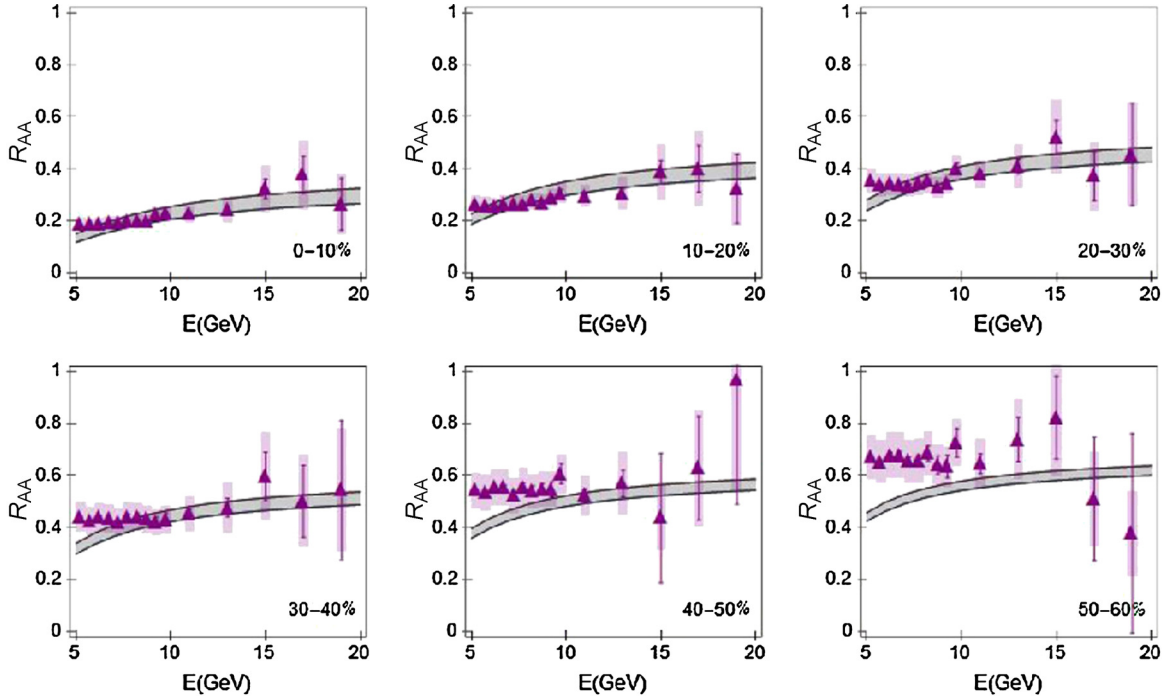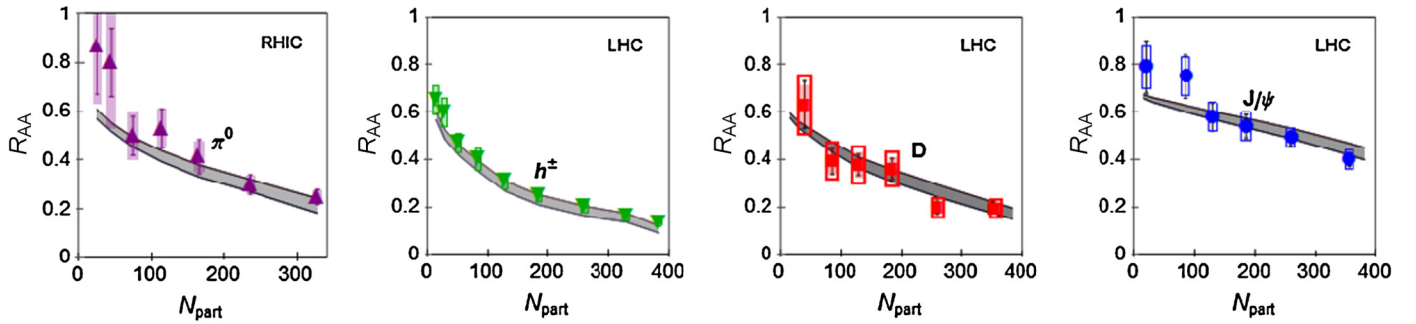
Fig. 3. Theory *vs.* experimental data for momentum dependence of neutral pion R_{AA} for different centrality bins at RHIC. The panels show the comparison of neutral pion suppression predictions with R_{AA} for neutral pions at 200 GeV Au + Au collisions at RHIC, for different (fixed) centrality regions. Purple triangles correspond to PHENIX [35] data. In the lower right corner of each panel we denote the centrality for which the data and the predictions are presented.

Fig. 4. Theory *vs.* experimental data for participant dependence of light and heavy flavor R_{AA} at RHIC and LHC. The first panel compares theoretical predictions with experimental data for participant dependence of π^0 R_{AA} [35] at 200 GeV Au + Au collisions at RHIC, where π^0 momentum is larger than 7 GeV. The second, third and fourth panels compare theoretical predictions with experimental data for participant dependence of, respectively, $h^{\pm}$ [36], D meson [37] and non-prompt J/ψ [38] R_{AA} at 2.76 TeV Pb + Pb collisions at LHC. The jet momentum ranges for the second, the third and the forth panels are, respectively, 6–12 GeV, 8–16 GeV and 6.5–30 GeV.

explicitly incorporate the evolving medium. Consequently, the obtained robust agreement with the experimental data above 10 GeV, strongly suggests that expansion of the medium does not play a major role in explaining *angular averaged* high momentum hadron suppression data. We hypothesize that the reason behind this result is that hard probes have a sufficiently large amount of energy, while the created medium is sufficiently short, so that the angular averaged suppression of the outcoming hadrons is only sensitive to the average properties of the created medium. This hypothesis is actually in line with previous work [43–47], which used different formalism – and explored lower centrality regions – but also obtained that angular averaged high momentum hadron suppression results are not sensitive to explicitly including the medium expansion. What however remains to be tested is validity of this simplification for jet energy ranges outside of those tested here, and whether the framework employed here can also reasonably explain angular differential suppression observables (such as high-momentum v_2); note that these observables are expected to be more sensitive to the medium evolution than the angular averaged

suppression studied here [46]. Such analysis could simplify theoretical predictions and facilitate intuitive understanding of complex experimental data.

Acknowledgements

References

[1] J.D. Bjorken, FERMILAB-PUB-82-059-THY, 1982, pp. 287, 292.
[2] N. Brambilla, et al., preprint, arXiv:hep-ph/0412158, 2004.
[3] M. Gyulassy, Lect. Notes Phys. 583 (2002) 37.
[4] D. d'Enterria, B. Betz, Lect. Notes Phys. 785 (2010) 285.
[5] M. Djordjevic, Phys. Rev. C 74 (2006) 064907.

[6] M. Djordjevic, Phys. Rev. C 80 (2009) 064909.

[7] M. Djordjevic, U. Heinz, Phys. Rev. Lett. 101 (2008) 022302.

[8] M. Djordjevic, M. Djordjevic, Phys. Lett. B 709 (2012) 229.

[9] M. Djordjevic, M. Djordjevic, Phys. Lett. B 734 (2014) 286.

[10] M. Gyulassy, P. Levai, I. Vitev, Phys. Lett. B 538 (2002) 282.

[11] S. Wicks, W. Horowitz, M. Djordjevic, M. Gyulassy, Nucl. Phys. A 784 (2007) 426.

[12] M. Cacciari, S. Frixione, N. Houdeau, M.L. Mangano, P. Nason, G. Ridolfi, J. High Energy Phys. 1210 (2012) 137.

[13] Z.B. Kang, I. Vitev, H. Xing, Phys. Lett. B 718 (2012) 482; R. Sharma, I. Vitev, B.W. Zhang, Phys. Rev. C 80 (2009) 054902.

[14] D. de Florian, R. Sassot, M. Stratmann, Phys. Rev. D 75 (2007) 114010.

[15] M. Gyulassy, P. Levai, I. Vitev, Nucl. Phys. B 594 (2001) 371.

[16] M. Djordjevic, M. Gyulassy, Nucl. Phys. A 733 (2004) 265.

[17] M. Gyulassy, X.N. Wang, Nucl. Phys. B 420 (1994) 583; X.N. Wang, M. Gyulassy, M. Plumer, Phys. Rev. D 51 (1995) 3436.

[18] Yu. Maezawa, et al., WHOT-QCD Collaboration, Phys. Rev. D 81 (2010) 091501; Yu. Maezawa, et al., WHOT-QCD Collaboration, PoS Lattice 194 (2008).

[19] A. Nakamura, T. Saito, S. Sakai, Phys. Rev. D 69 (2004) 014506.

[20] A. Hart, M. Laine, O. Philipsen, Nucl. Phys. B 586 (2000) 443.

[21] D. Bak, A. Karch, L.G. Yaffe, J. High Energy Phys. 0708 (2007) 049.

[22] M. Wilde, for theALICE Collaboration, Nucl. Phys. A 904–905 (2013) 573c.

[23] M. Csanad, arXiv:1101.1282.

[24] A. Dainese, Eur. Phys. J. C 33 (2004) 495.

[25] M. Djordjevic, M. Djordjevic, in preparation.

[26] S.S. Adler, et al., PHENIX Collaboration, Phys. Rev. C 71 (2005) 034908.

[27] K. Aamodt, et al., ALICE Collaboration, Phys. Rev. Lett. 106 (2011) 032301.

[28] A. Peshier, arXiv:hep-ph/0601119, 2006.

[29] M. Djordjevic, M. Gyulassy, Phys. Rev. C 68 (2003) 034914.

[30] B. Abelev, et al., ALICE Collaboration, arXiv:1208.2711.

[31] S. Chatrchyan, et al., CMS Collaboration, Eur. Phys. J. C 72 (2012) 1945.

[32] J. Otwinowski, for theALICE Collaboration, PoS ConfinementX 170 (2012).

[33] A. Festanti, for the ALICE Collaboration, Heavy-flavour production and nuclear modification factor in Pb–Pb collisions at $\sqrt{s_{NN}} = 2.76$ TeV with ALICE, oral presentation at Quark Matter 2014, Darmstadt, Germany.

[34] M. Djordjevic, Theoretical predictions of jet suppression: a systematic comparison, oral presentation at Quark Matter 2014, Darmstadt, Germany.

[35] A. Adare, et al., PHENIX Collaboration, Phys. Rev. C 87 (2013) 034911, arXiv:1204.1526.

[36] K. Aamodt, et al., ALICE Collaboration, Phys. Lett. B 720 (2013) 52.

[37] B. Abelev, et al., ALICE Collaboration, J. High Energy Phys. 9 (2012) 112.

[38] S. Chatrchyan, et al., CMS Collaboration, J. High Energy Phys. 5 (2012) 063.

[39] S.A. Bass, C. Gale, A. Majumder, C. Nonaka, G.-Y. Qin, T. Renk, J. Ruppert, Phys. Rev. C 79 (2009) 024901.

[40] B. Betz, M. Gyulassy, arXiv:1402.3419.

[41] Z. Xu, C. Greiner, Phys. Rev. C 71 (2005); Z. Xu, C. Greiner, Phys. Rev. C 76 (2007).

[42] P.B. Gossiaux, M. Nahrgang, M. Bluhm, T. Gousset, J. Aichelin, Nucl. Phys. A 904–905 (2013) 992c.

[43] T. Renk, J. Ruppert, C. Nonaka, S.A. Bass, Phys. Rev. C 75 (2007) 031902.

[44] D. Molnar, D. Sun, Nucl. Phys. A 910–911 (2013) 486–489.

[45] D. Molnar, D. Sun, arXiv:1405.4848.

[46] T. Renk, Phys. Rev. C 85 (2012) 044903.

[47] T. Renk, H. Holopainen, U. Heinz, C. Shen, Phys. Rev. C 83 (2011) 014910.

Importance of higher orders in opacity in quark-gluon plasma tomography

Stefan Stojku, Bojana Ilic, Igor Salom, and Magdalena Djordjevic[*]
Institute of Physics Belgrade, University of Belgrade, Serbia

We consider the problem of including a finite number of scattering centers in dynamical energy loss and classical DGLV formalism. Previously, either one or an infinite number of scattering centers were considered in energy loss models, while efforts to relax such approximations require a more conclusive and complete treatment. In reality, however, the number of scattering centers is generally estimated to be 4–5 at the BNL Relativistic Heavy Ion Collider (RHIC) and the CERN Large Hadron Collider (LHC), making the above approximations (*a priori*) inadequate and this theoretical problem significant for QGP tomography. We derived explicit analytical expressions for dynamical energy loss and DGLV up to the fourth order in opacity, resulting in complex, highly oscillatory, mathematical expressions. These expressions were then implemented into an appropriately generalized DREENA framework to calculate the effects of higher orders in opacity on a wide range of high-$p_\perp$ light and heavy flavor predictions. Results of extensive numerical analysis and interpretations of nonintuitive results are presented. We find that, for both RHIC and the LHC, higher-order effects on high-$p_\perp$ observables are small, and the approximation of a single scattering center is adequate for dynamical energy loss and DGLV formalisms.

I. INTRODUCTION

Quark-gluon plasma (QGP) [1–4] is a new form of matter consisting of quarks, antiquarks, and gluons that are no longer confined. It has been created in landmark experiments at the BNL Relativistic Heavy Ion Collider (RHIC) and the CERN Large Hadron Collider (LHC) (so-called little bangs), where heavy ions collide at ultrarelativistic energies [2,3]. Hard probes are one of the main tools for understanding and characterizing the QGP properties [2], where hard processes dominate interactions of these probes with QGP constituents. These interactions are dominantly described by energy loss, where radiative is one of the most important mechanisms at high transverse momentum $p_\perp$. The radiative energy loss can be analytically computed through pQCD approaches, typically under the assumption of the optically thick or optically thin medium [e.g., BDMPS-Z [5,6], ASW [7], (D)GLV [8,9], HT and HT-M [10,11], AMY [12], dynamical energy loss [13,14] and different applications and extensions of these methods] and tested against the experimental data.

Optically thick medium corresponds to the approximation of a jet experiencing infinite scatterings with medium constituents. While such an approximation would be adequate for QGP created in the early universe (big bang), little bangs are characterized by short, finite-size droplets of QCD matter. Another widely used approximation is an optically thin medium, assuming one scattering center. However, the medium created in little bangs is typically several femtometers in size (with mean free path $\lambda \approx 1$ fm), so considering

several scattering centers in energy loss calculations is needed. Thus, it is evident that both approaches represent two extreme limits to the realistic situations considered in RHIC and LHC experiments, and relaxing these approximations to the case of a finite number of scattering centers is necessary. Thus, relaxing such an approximation is a highly nontrivial problem, addressed in Ref. [8], with recently renewed interest [15–21]. Some of these approaches are analytically quite advanced, e.g., providing full expressions for a gluon radiation spectrum (or splitting functions) with relaxed soft-gluon approximation in DGLV formalism [19,20] or derivation of gluon emission spectrum with full resummation of multiple scatterings within the BDMPS-Z framework [15,17,18]. However, in our view, this issue requires a more conclusive and complete treatment. Namely, the importance of including higher orders in opacity effects on experimental observables is still not addressed. In relaxing this approximation, it is not only needed to estimate these effects on, e.g., the energy loss and gluon radiation spectrum, but also to implement these corrections in the numerical frameworks needed to generate predictions for high-$p_\perp$ observables measured at RHIC and the LHC experiments. Furthermore, most of these studies were done in massless quarks and gluons limit and/or use the approximation of an uncorrelated medium (i.e., where the spacings between collisions are considered to be mutually independent, see Ref. [21] for more details). Since we, *a priori*, do not know the magnitude of the effects of the inclusion of multiple scattering centers, nor how the mentioned approximations can influence this magnitude, we find it questionable to discuss higher-order corrections while ignoring the effects which might potentially overshadow or alter the final effects. For example, due to a finite-temperature medium, light quarks

*magda@ipb.ac.rs

and gluons gain mass in QGP, which can significantly numerically modify the importance of these effects on experimental observables.

In this study, we start from our dynamical energy loss formalism [13,14], computed under the approximation of an optically thin QCD medium, i.e., one scattering center. We use general expressions from Ref. [21] to relax this approximation to the case of finite number of scattering centers, where explicit analytical expressions up to the fourth order in opacity (scattering centers) are presented. These expressions are implemented in our (appropriately modified) DREENA-C [22] framework (which assumes a constant-temperature medium), enabling us to more straightforwardly estimate the effects of higher orders in opacity on high-$p_\perp$ R_{AA} and v_2 observables. Based on these results, we also provide estimates for the fully evolving medium, while a rigorous study in this direction is left for future work.

While the initial expressions taken from Ref. [21] were, strictly speaking, derived in the approximation of static scattering centers, we apply them here in the context of a dynamic QCD medium. Namely, by careful calculation, we have shown in Ref. [14] that—at least in the first order in opacity—the generalization from the static to dynamic medium eventually amounts to a mere appropriate replacement of the mean free path and effective potential in the final expressions. Following general arguments given in Ref. [8] and the expectations expressed in Ref. [21], we assume that the same prescription for progressing from static to dynamic medium remains valid in higher orders of opacity.

The outline of the paper is as follows: Sections II and III present the outline of theoretical and numerical frameworks used in this study, with more detailed analytical results presented in the Appendixes. In the Results section, we numerically analyze the effects of higher orders in opacity on the gluon radiation spectrum and high-$p_\perp$ R_{AA} and v_2 predictions. Intuitive explanations behind obtained results will be presented. This section will also analyze a special case of static QCD medium (extension of (D)GLV [8,9] to the finite number of scattering centers). The main results will be summarized in the last section.

II. THEORETICAL FRAMEWORK

In this study, we use our dynamical radiative energy loss [13,14] formalism, which has the following features: (i) QCD medium of *finite* size L and temperature T, which consists of dynamical (i.e., moving) partons, in a distinction to models with widely used static approximation and/or vacuum-like propagators [5,7,8,10]. (ii) Calculations based on generalized hard-thermal-loop approach [23,24], with naturally regulated infrared divergences [13,14,25]. (iii) Generalization towards running coupling [26] and finite magnetic mass [27].

However, as noted in the Introduction, this radiative energy loss is developed up to the first order in opacity. Thus, to improve the applicability of this formalism for QGP tomography, it is necessary to relax this approximation. To generalize the dynamical energy loss to finite number in scattering centers, we start from a closed-form expression—Eq. (46) from Ref. [21] and Eq. (20) from Ref. [9]—derived for static QCD medium [i.e., (D)GLV case [8,9]] but applicable for a generalized form of effective potential and mean free path λ [21]:

$$
x\frac{dN^{(n)}}{dx\,d^2\mathbf{k}} = \int_0^L dz_1 \cdots \int_{z_{n-1}}^L dz_n \int \prod_{i=1}^n \left(d^2\mathbf{q}_i \, \frac{v^2(\mathbf{q}_i) - \delta^2(\mathbf{q}_i)}{\lambda(z)} \right)
$$
$$
\times \frac{C_R \alpha_s(Q_k^2)}{\pi^2} \left(-2\,\mathbf{C}_{(1\cdots n)} \cdot \mathbf{B}_n \left[\cos\sum_{k=2}^n \omega_{(k\cdots n)}\Delta z_k - \cos\sum_{k=1}^n \omega_{(k\cdots n)}\Delta z_k \right] \right), \tag{1}
$$

where $|v_i(\mathbf{q}_i)|^2$ is defined as the normalized distribution of momentum transfers from the ith scattering center (i.e., "effective potential"), $\lambda(i)$ is the mean free path of the emitted gluon, C_R is the color Casimir of the jet. Note that, for consistency with our previous work, we denote transverse two-dimensional (2D) vectors as bold $\mathbf{p}$.

The running coupling is defined as in Ref. [26]:

$$
\alpha_s(Q^2) = \frac{4\pi}{(11 - 2/3 n_f)\ln(Q^2/\Lambda_{\mathrm{QCD}})}, \tag{2}
$$

where $Q_k^2 = (\mathbf{k}^2 + M^2 x^2 + m_g^2)/x$, appearing in Eq. (1) above is the off-shellness of the jet before gluon radiation [26].

$\omega_{(m\ldots n)}$ is the inverse of the formation time or the (longitudinal) momentum,

$$
\omega_{(m\ldots n)} = \frac{\chi^2 + (\mathbf{k} - \mathbf{q}_m - \cdots - \mathbf{q}_n)^2}{2xE}, \tag{3}
$$

where n is the final scatter, while m varies from the first up to the final scatter. $\chi^2 \equiv M^2 x^2 + m_g^2$, where x is the longitudinal momentum fraction of the quark jet carried away by the emitted gluon, M is the mass of the quark, $m_g = \mu_E/\sqrt{2}$ is the effective mass for gluons with hard momenta [25], and μ_E is the Debye mass (i.e., electric screening).

"Cascade" terms represent the shifting of the momentum of the radiated gluon due to momentum kicks from the medium:

$$
\mathbf{C}_{(i_1 i_2 \ldots i_m)} = \frac{(\mathbf{k} - \mathbf{q}_{i_1} - \mathbf{q}_{i_2} - \cdots - \mathbf{q}_{i_m})}{\chi^2 + (\mathbf{k} - \mathbf{q}_{i_1} - \mathbf{q}_{i_2} - \cdots - \mathbf{q}_{i_m})^2}. \tag{4}
$$

A special case of $\mathbf{C}$ without any momentum shifts is defined as the "hard" term:

$$
\mathbf{H} = \frac{\mathbf{k}}{\chi^2 + \mathbf{k}^2} \quad \text{and} \quad \mathbf{B}_i = \mathbf{H} - \mathbf{C}_i. \tag{5}
$$

In Refs. [13,14,27], we showed that, despite much more involved analytical calculations, at first order in opacity the

radiative energy loss in a dynamical medium has the same form as in the static medium, except for two straightforward substitutions in mean free path and effective potential:

$$\lambda_{\text{stat}} \rightarrow \lambda_{\text{dyn}}, \tag{6}$$

where

$$\lambda_{\text{stat}}^{-1} = 6 \frac{1.202}{\pi^2} \frac{1 + n_f/4}{1 + n_f/6} \lambda_{\text{dyn}}^{-1},$$

while the "dynamical mean free path" is given by $\lambda_{\text{dyn}}^{-1} = 3\alpha_s(Q_v^2)T$ [13,14], with $Q_v^2 = ET$ [26]. Running coupling $\alpha_s(Q_v^2)$ corresponds to the interaction between the jet and the virtual (exchanged) gluon, while E is the jet's energy.

$$\left[\frac{\mu_E^2}{\pi (\mathbf{q}^2 + \mu_E^2)^2} \right]_{\text{stat}} \rightarrow \left[\frac{\mu_E^2 - \mu_M^2}{\pi (\mathbf{q}^2 + \mu_E^2)(\mathbf{q}^2 + \mu_M^2)} \right]_{\text{dyn}}, \tag{7}$$

where μ_M is magnetic screening. Thus, we assume that Eq. (1) can also be used in our case, with the above modification of effective potential and mean free path. In Appendixes A and B, we use this general expression to derive an explicit expression for the gluon radiation spectrum for first, second, third, and fourth order in opacity ($dN_g^{(1)}/dx$, $dN_g^{(2)}/dx$, $dN_g^{(3)}/dx$, $dN_g^{(4)}/dx$, respectively).

III. NUMERICAL FRAMEWORK

To generate the results presented in this work, we used our (appropriately generalized, see below) DREENA-C framework. For completeness, we here give a brief outline of this framework, while a detailed description is presented in Ref. [22]. The quenched spectra of light and heavy quarks are calculated according to the generic pQCD convolution given by

$$\frac{E_f d^3\sigma}{dp_f^3} = \frac{E_i d^3\sigma(Q)}{dp_i^3} \otimes P(E_i \rightarrow E_f) \otimes D(Q \rightarrow H_Q). \tag{8}$$

Here, the indices i and f stand for "initial" and "final," respectively, while Q denotes initial high-energy parton (light quarks, heavy quarks, or gluons). $E_i d^3\sigma(Q)/dp_i^3$ is the initial momentum spectrum for the given parton, which is calculated according to Ref. [28], $P(E_i \rightarrow E_f)$ represents the energy loss probability for the given particle which was calculated within the dynamical energy loss formalism [13,14], which includes multigluon [29] and path-length fluctuations [22,30]. $D(Q \rightarrow H_Q)$ represents the fragmentation function of light and heavy partons into hadrons, where for light hadrons, D and B mesons, we use the DSS [31], BCFY [32], KLP [33] fragmentation functions, respectively. The geometry is averaged over by using path-length distributions, i.e., probability distributions of the path lengths of hard partons in Pb + Pb collisions, in the same way as in the original DREENA-C framework [22]. They are used as weight functions when integrating over the path-length in our numerical procedure.

We use the following parameters in the numerical procedure: $\Lambda_{\text{QCD}} = 0.2$ GeV and $n_f = 3$. The temperature-dependent Debye chromoelectric mass $\mu_E(T)$ has been extracted from Ref. [34]. For the mass of light quarks, we

take the thermal mass $M \approx \mu_E/\sqrt{6}$, and for the gluon mass, we use $m_g = \mu_E/\sqrt{2}$ [25]. The mass of the charm (bottom) quark is $M = 1.2$ GeV ($M = 4.75$ GeV). The magnetic and electric mass ratio is $0.4 < \mu_M/\mu_E < 0.6$ [35,36]. All the results presented in this paper are generated for the Pb + Pb collision system at $\sqrt{s_{NN}} = 5.02$ TeV.

As DREENA-C [22] does not include suppression from multiple scattering centers in the medium, we now upgrade this framework to include the second and third order in opacity contributions. We integrate the expressions obtained from (1) analytically for z_i (see Appendixes A and B), and then numerically for momenta $\mathbf{k}$ and $\mathbf{q}_i$ using the quasi-Monte Carlo method to obtain dN_g/dx up to third order in opacity. Also, to test the importance of multiple scattering centers on radiative energy loss, we exclude the collisional [37] contributions from the DREENA-C framework and only generate predictions for radiative energy loss. Appendixes A and B also include expressions for the fourth order in opacity. We implemented fourth order into DREENA-C, but as the resulting integrals are highly oscillatory, we could not reach convergence for this order using our available computational resources. Notably, this numerical complexity is significantly higher, estimated to be ≈ 2 orders of magnitude larger than for the third order (e.g., for the first order, we needed ≈ 25 CPU h; for the second order ≈ 2500 CPU h; for the third order $\approx 70\,000$ CPU h). Nevertheless, at specific points where we reached a convergence, we found the fourth-order contribution negligible, as expected from the results presented in the next section.

IV. RESULTS

In Fig. 1, the effect of higher orders in opacity on dN_g/dx as a function of x is shown for typical medium length $L = 5$ fm. In each plot, we use double axes for clarity: the lower axis corresponds to magnetic to electric mass ratio $\mu_M/\mu_E = 0.6$ (and the curves with the peak on the left side), while the upper axis corresponds to $\mu_M/\mu_E = 0.4$ (and the curves with the peak on the right side). Note that, in each case, maximum is reached for low values of x. We see that the importance of higher orders of opacity decreases with the increase of jet energy and mass. They also decrease with decreasing the size of the medium, as shown in Appendix C [equivalent figures for $L = 3$ fm (Fig. 6, left) and $L = 1$ fm (Fig. 6, right)]. For bottom quarks, higher-order effects are negligible independently of the jet momentum. In contrast, these effects are moderate for charm and light quarks and can influence the jet observables, as discussed below. Note that, due to color triviality, the results for light quarks show the (scaled) result for gluons, too. This holds up to the fact that, due to the indistinguishability of the radiated gluon from the gluon in the jet, the limits for subsequent integration of dN_g/dx with respect to x is performed from $x_{\text{lower}} = 0$ to $x_{\text{upper}} = 1/2$ (as opposed to $x_{\text{upper}} = 1$ for light quarks).

In Fig. 2, we show the effect of higher orders in opacity on radiative R_{AA} observable. Our computations have shown that the effect on v_2 is similar to the one on R_{AA} (see Fig. 8 in Appendix D). Thus, to avoid redundancy, we further concentrate only on R_{AA}.
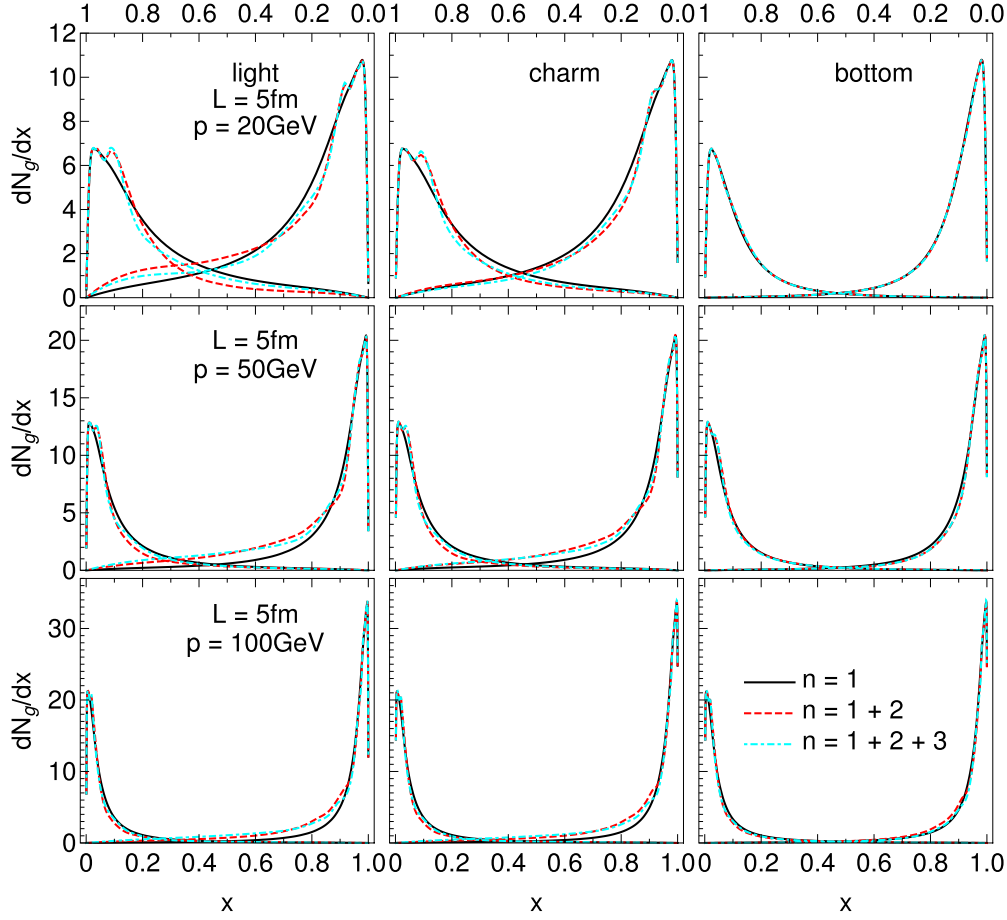
FIG. 1. Gluon radiation spectrum dN_g/dx as a function of x, for the typical medium length of $L = 5$ fm and various jet momenta. Different columns correspond to light, charm, and bottom quarks. Solid black curves show the first order in opacity results, red dashed curves show the results up to the second order, while cyan dot-dashed curves up to the third order in opacity. Curves with the peaks on the left (right) side of each of the plots correspond to the $\mu_M/\mu_E=0.6$ ($\mu_M/\mu_E = 0.4$) case, and the numerical values should be read off on the lower (upper) x axis.

We first observe that the effect on R_{AA} is smaller for more peripheral collisions. This is expected because the medium is shorter on average, so including multiple scattering centers becomes less important.

Furthermore, we find that higher orders in opacity are negligible for B mesons, while these effects increase with decreasing mass, as expected from Fig. 1. The reason behind this is the decrease in the gluon formation time with increasing jet mass. When the gluon formation time is short, the energy loss approaches the incoherent limit, where it was previously shown that the effects of higher orders in opacity are negligible [9]. Thus, our results are consistent with the previous findings. On the other hand, for large gluon formation time (massless quark and gluon limit), the higher orders in opacity effects become significant, also in general agreement with the previous findings [15]. In finite-temperature QGP (considered in this study), light quarks and gluons gain mass due to Debye screening, reducing the effects of higher orders in opacity on the energy loss, consistent with Fig. 2.

Unexpectedly, we also observe that, for different magnetic mass limiting cases, these effects on R_{AA} are opposite in sign: for $\mu_M/\mu_E = 0.6$, the inclusion of higher orders in opacity reduces energy loss (and, consequently, suppression). In

contrast, for $\mu_M/\mu_E = 0.4$, the effect is both opposite in sign and larger in magnitude. What is the reason behind these unexpected results?

To answer this question, we go back to the effective potential [27] $v(\mathbf{q})$ in dynamical QCD medium, which can be written in the following form:

$$v(\mathbf{q}) = v_L(\mathbf{q}) - v_T(\mathbf{q}), \tag{9}$$

where $v_L(\mathbf{q})$ is longitudinal (electric), and $v_T(\mathbf{q})$ is transverse (magnetic), contribution to the effective potential. The general expressions for the transverse and longitudinal contributions to the effective potentials are

$$
\begin{aligned}
v_L(\mathbf{q}) &= \frac{1}{\pi}\left(\frac{1}{(\mathbf{q}^2 + \mu_{pl}^2)} - \frac{1}{(\mathbf{q}^2 + \mu_E^2)} \right), \\
v_T(\mathbf{q}) &= \frac{1}{\pi}\left(\frac{1}{(\mathbf{q}^2 + \mu_{pl}^2)} - \frac{1}{(\mathbf{q}^2 + \mu_M^2)} \right),
\end{aligned}
\tag{10}
$$

where μ_E, μ_M, and $\mu_{pl} = \mu_E/\sqrt{3}$ are electric, magnetic, and plasmon masses, respectively. As seen from Eq. (9), this potential has two contributions: electric and magnetic, where the electric contribution is always positive due to $\mu_{pl} < \mu_E$. On
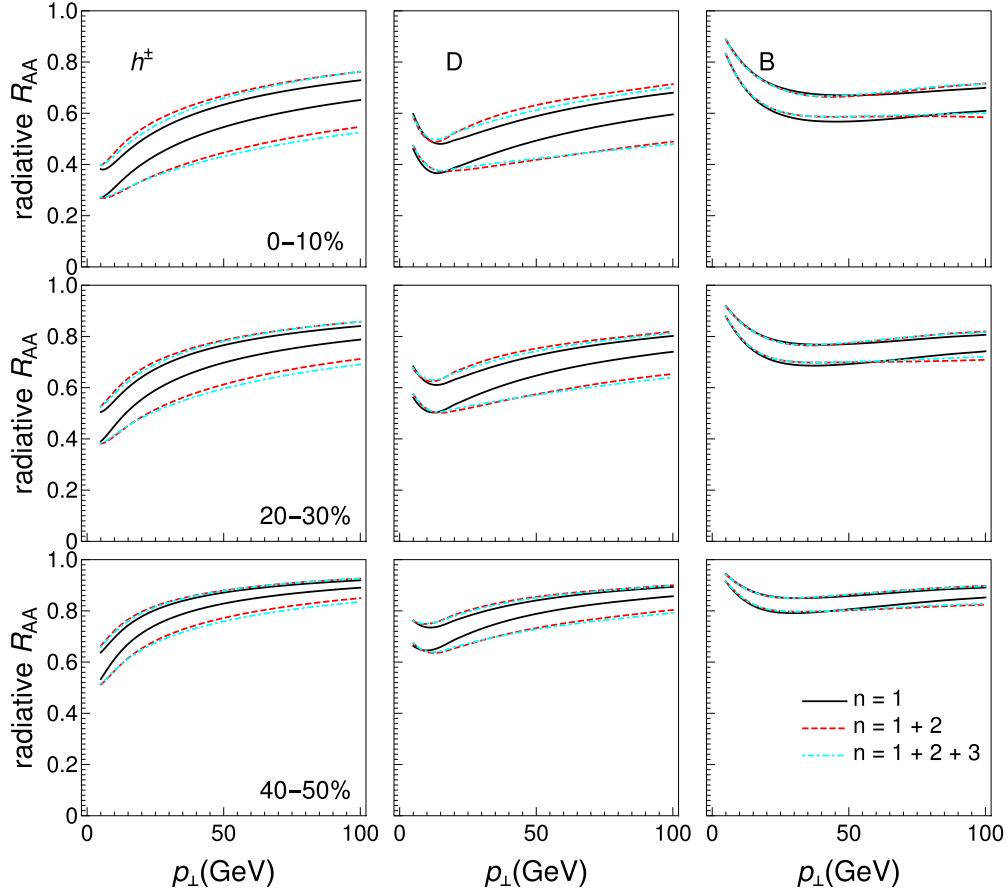
FIG. 2. Radiative R_{AA} results obtained within DREENA-C—the effects of different orders in opacity. The results are generated for the Pb + Pb collision system at $\sqrt{s_{NN}} = 5.02$ TeV, and all the other figures in the manuscript show the results for the same collision system and energy. Different columns correspond to charged hadrons, D and B mesons, while different rows show different centrality classes. Solid black curves show the first order in opacity results, red dashed curves show the results up to the second order, while cyan dot-dashed curves up to the third order in opacity. The upper (lower) boundary of each band corresponds to the $\mu_M/\mu_E = 0.6$ ($\mu_M/\mu_E = 0.4$) case.

the other hand, the magnetic contribution depends nontrivially on the value of magnetic mass. That is, for $\mu_M > \mu_{pl}$, we see that the magnetic contribution decreases the energy loss, while for $\mu_M < \mu_{pl}$ it increases the energy loss and consequently suppression, as shown in Fig. 2, which may intuitively explain the observed energy-loss behavior.

Furthermore, the Debye mass μ_E is well defined from lattice QCD, where the perturbative calculations are also consistent [34]. Thus, the electric potential is well defined in dynamical energy loss, and we can separately test the effect of higher orders in opacity on this contribution [by replacing $v(\mathbf{q})$ by $v_L(\mathbf{q})$ in the DREENA framework]. We surprisingly find it to be negligible, as shown in Fig. 3. Thus, higher orders in opacity essentially do not influence the electric contribution in a dynamical QCD medium, which is an interesting and intuitively unexpected result. That is, the higher orders mainly influence the magnetic contribution to energy loss (keeping the electric contribution unaffected), where the sign of the effect depends on the magnetic mass value. For example, as $\mu_M/\mu_E = 0.4$ is notably smaller than $\mu_{pl}/\mu_E = 1/\sqrt{3}$, the higher orders in opacity are significant for this limit and increase the suppression, in agreement with Fig. 2. On the

other hand, $\mu_M/\mu_E = 0.6$ is close to (but slightly larger than) μ_{pl}/μ_E, so higher orders in opacity are small for this magnetic mass limit and reduce the suppression, also in agreement with Fig. 2. Additionally, note that the most recent $2 + 1$ flavor lattice QCD results with physical quark masses further constrain the magnetic screening to $0.58 < \mu_M/\mu_E < 0.64$ [38]. Thus, for this range of magnetic screening, we conclude that the effects of higher orders in opacity are small in a dynamical QCD medium and can be safely neglected.

Furthermore, Fig. 3 raises another important question: as is well known, only electric contribution exist in the *static* QCD medium approximation [23,24] (although it has a different functional form compared to the electric contribution in dynamical QCD medium). That is, the magnetic contribution is inherently connected with the dynamic nature of the QCD medium. As most existing energy loss calculations assume (simplified) static QCD medium approximation, does this mean that higher orders in opacity can be neglected under such approximation?

We first note that this does not necessarily have to be the case, because the effective potential for electric contribution is significantly different in static compared with the dynamical
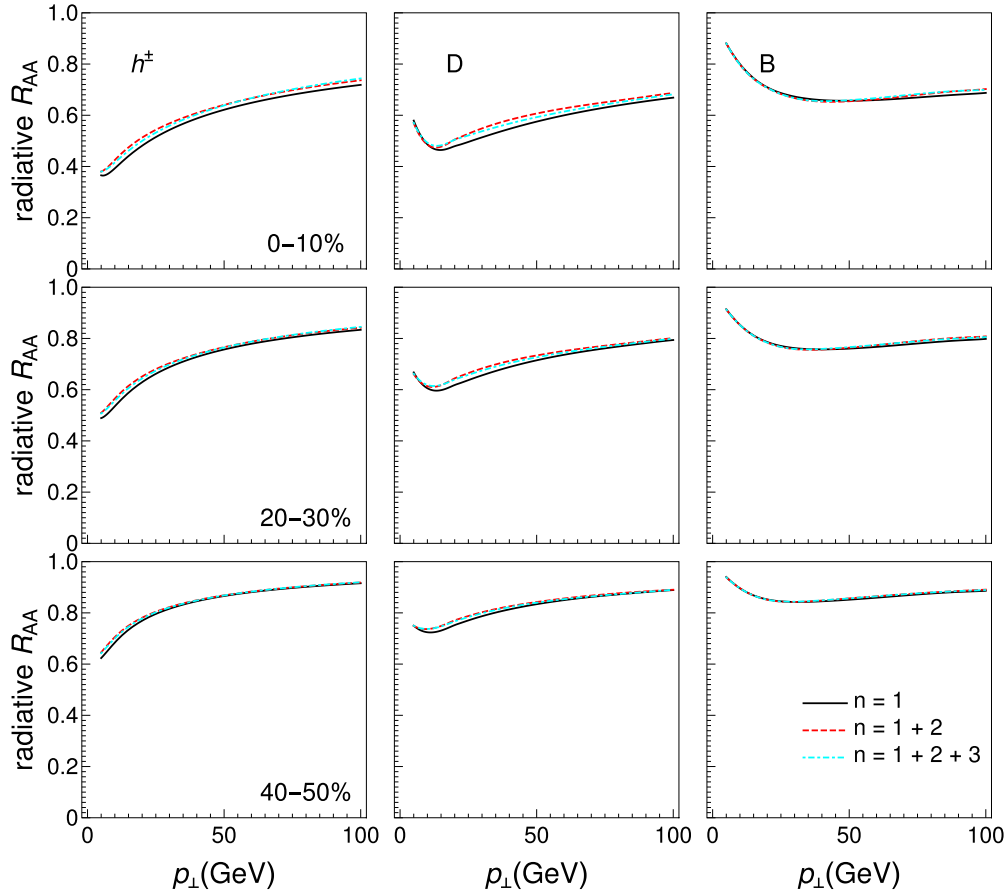
FIG. 3. R_{AA} results, obtained within DREENA-C when only electric contribution $v_L(\mathbf{q})$ to radiative energy loss is considered. Different columns correspond to charged hadrons, D and B mesons, while different rows show different centrality classes. Solid black curves show the first order in opacity results, red dashed curves show the results up to the second order, while cyan dot-dashed curves up to the third order in opacity.

medium. However, to address this question, we repeat the same analyses as above, this time assuming the static medium effective potential [left-hand side of Eq. (7)] and mean free path λ_{stat}. Figure 4 shows the effects of higher orders in opacity in static medium approximation. While larger than those in Fig. 3, we see that these effects are still small (i.e., less than 6%). Thus, for optically thin medium models with static approximation, we show that including multiple scattering centers has a small effect on the numerical results, i.e., these effects can also be neglected.

Finally, we ask how the inclusion of evolving medium would modify these results. Including higher-order effects in evolving medium is very demanding and out of the scope of this paper. However, it can be partially addressed by studying how higher-order effects depend on the temperature, which changes in the evolving medium. To address this, in Fig. 5, we focus on D meson R_{AA}, $\mu_M/\mu_E = 0.6$ (per agreement with Ref. [38]) and study the effects of higher orders in opacity for three different temperatures $T = 200, 400, 600$ MeV (which broadly covers the range of temperatures accessible at RHIC and the LHC). We find that the higher-order effects are largely independent of these values. Thus, we do not expect that including medium evolution will significantly influence

the results presented in this study, i.e., expect the effect of multiple scattering centers to remain small.

V. SUMMARY

In this paper, we generalized our dynamical energy loss and DGLV formalisms towards finite orders in opacity. For bottom quarks, we find that higher orders in opacity are insignificant due to short gluon formation time, i.e. the incoherent limit. For charm and light quarks, including second order in opacity is sufficient, i.e., the third order numerical results almost overlap with the second. Surprisingly, we also find that for limits of magnetic screening, $\mu_M/\mu_E = 0.4$ and $\mu_M/\mu_E = 0.6$, the effects on the R_{AA} are opposite in sign. That is, for $\mu_M/\mu_E = 0.6$ ($\mu_M/\mu_E = 0.4$), higher orders in opacity decrease (increase) the energy loss and subsequently suppression. The intuitive reason behind such behavior is the magnetic contribution to the dynamical energy loss. That is, while electric contribution remains almost insensitive to increases in the order of opacity, magnetic screening larger (smaller) than the plasmon mass value decreases (increases) the energy loss and suppression, in agreement with theoretical expectations. We also show that in the static QCD medium approximation, in
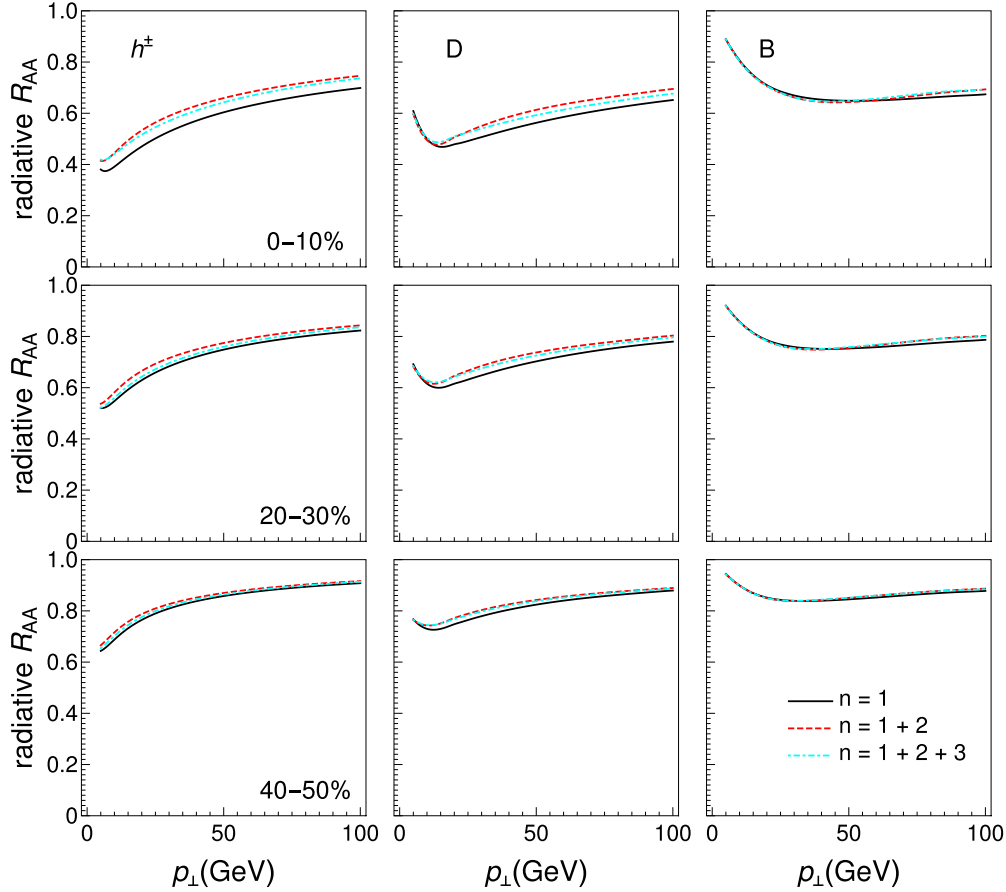
FIG. 4. Radiative R_{AA} results obtained within DREENA-C under the *static* medium approximation. Different columns correspond to charged hadrons, D and B mesons, while different rows show different centrality classes. Solid black curves show the first order in opacity results, red dashed curves show the results up to the second order, while cyan dot-dashed curves up to the third order in opacity.

which (per definition) only electric contribution remains, the effects of higher orders in opacity on high-$p_\perp$ observables are small and can be safely neglected. Thus, for static QCD
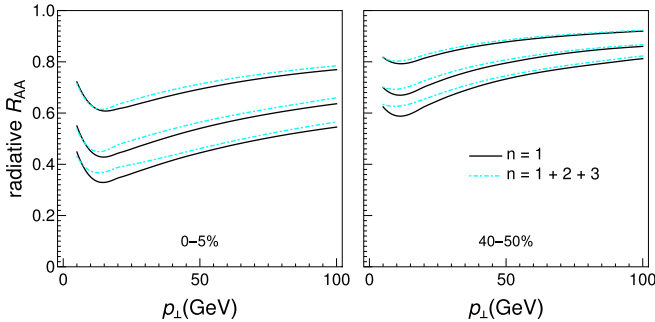

FIG. 5. D meson radiative R_{AA} results obtained within DREENA-C for different temperatures. The left panel corresponds to 0%–5% centrality, while the right panel corresponds to 40%–50% centrality. The values of temperature are $T = 200$ MeV (the uppermost curves), 400 MeV (the middle curves), and 600 MeV (the lowest curves). The solid black curves show the first order in opacity results, while cyan dot-dashed curves show the results up to the third order in opacity. The chromomagnetic and chromoelectric mass ratio is fixed at $\mu_M/\mu_E = 0.6$.

medium, the first order in opacity is an adequate approximation for finite-size QCD medium created at RHIC and the LHC. For dynamical energy loss, both the sign and the size of the effects depend on the magnetic screening, as outlined above. However, for most of the current estimates of magnetic screening [38], these effects remain less than 5%, so they can also be safely neglected.

The analyses presented here are obtained for a constant-temperature medium (and adequately generalized DREENA-C framework). However, we also tested how the effects of including multiple scatterers depend upon temperature and found this influence to be also small (affecting the radiative R_{AA} for less than 5%). Thus, we expect that including higher orders in opacity in the evolving medium will not change the qualitative results obtained here, but this remains to be rigorously tested in the future.

APPENDIX A: ANALYTICAL EXPRESSIONS FOR dN_g/dx: GENERAL FORM

The gluon radiation spectrum up to the fourth order in opacity contains the following terms, which are here given in detail:

$$
\left(\frac{dN_g}{dx}\right) = \left(\frac{dN_g^{(1)}}{dx}\right) + \left(\frac{dN_g^{(2)}}{dx}\right)_1 - \left(\frac{dN_g^{(2)}}{dx}\right)_2 + \left(\frac{dN_g^{(3)}}{dx}\right)_1 - \left(\frac{dN_g^{(3)}}{dx}\right)_2 - \left(\frac{dN_g^{(3)}}{dx}\right)_3 + \left(\frac{dN_g^{(3)}}{dx}\right)_4 + \left(\frac{dN_g^{(4)}}{dx}\right)_1
$$

$$
- \left(\frac{dN_g^{(4)}}{dx}\right)_2 - \left(\frac{dN_g^{(4)}}{dx}\right)_3 + \left(\frac{dN_g^{(4)}}{dx}\right)_4 - \left(\frac{dN_g^{(4)}}{dx}\right)_5 + \left(\frac{dN_g^{(4)}}{dx}\right)_6 + \left(\frac{dN_g^{(4)}}{dx}\right)_7 - \left(\frac{dN_g^{(4)}}{dx}\right)_8. \tag{A1}
$$

Numerical integrations with respect to the momentum $\mathbf{k}$ are performed over $0 < |\mathbf{k}| < 2Ex(1-x)$, and the ones with respect to momenta $\mathbf{q}_i$ are performed over $0 < |\mathbf{q}_i| < \sqrt{4ET}$ [39]. The integrations with respect to angles φ_i are performed over $0 < \varphi_i < 2\pi$. Under the constant-T approximation considered in this manuscript, the expressions presented below can be analytically integrated over z_i, significantly simplifying subsequent numerical calculations (see Appendix B).

In the expressions below, the following equations hold for $i, j \in \{1, 2, 3, 4\}$:

$$
\mathbf{k} \cdot \mathbf{q}_i = |\mathbf{k}||\mathbf{q}_i| \cos \varphi_i, \tag{A2}
$$

$$
\mathbf{q}_i \cdot \mathbf{q}_j = |\mathbf{q}_i||\mathbf{q}_j| \cos(\varphi_i - \varphi_j). \tag{A3}
$$

The first order in opacity term is given by

$$
\left(\frac{dN_g^{(1)}}{dx}\right) = \frac{4C_R}{\pi x} \int_0^L dz_1 \int \frac{d^2\mathbf{k}}{\pi} \int \frac{d^2\mathbf{q}_1}{\pi} \alpha_s(Q_k^2) \frac{1}{\lambda_{\mathrm{dyn}}} \frac{\mu_E^2 - \mu_M^2}{(\mathbf{q}_1^2 + \mu_E^2)(\mathbf{q}_1^2 + \mu_M^2)}
$$

$$
\times \frac{\chi^2[\mathbf{q}_1 \cdot (\mathbf{q}_1 - \mathbf{k})] + (\mathbf{q}_1 \cdot \mathbf{k})(\mathbf{k} - \mathbf{q}_1)^2}{(\chi^2 + \mathbf{k}^2)[\chi^2 + (\mathbf{k} - \mathbf{q}_1)^2]^2} \sin^2\left(\frac{\chi^2 + (\mathbf{k}^2 - \mathbf{q}_1)^2}{4xE} z_1\right). \tag{A4}
$$

After integration with respect to z_1, this expression reduces to the expression used to obtain dN_g/dx in the original DREENA-C framework [22].

The second order in opacity contains two terms, which are given by

$$
\left(\frac{dN_g^{(2)}}{dx}\right)_1 = \frac{4C_R}{\pi x} \int_0^L \int_{z_1}^L dz_1 dz_2 \int \frac{d^2\mathbf{k}}{\pi} \iint \frac{d^2\mathbf{q}_1}{\pi} \frac{d^2\mathbf{q}_2}{\pi} \alpha_s(Q_k^2) \frac{1}{\lambda_{\mathrm{dyn}}^2} \frac{\mu_E^2 - \mu_M^2}{(\mathbf{q}_1^2 + \mu_E^2)(\mathbf{q}_1^2 + \mu_M^2)} \frac{\mu_E^2 - \mu_M^2}{(\mathbf{q}_2^2 + \mu_E^2)(\mathbf{q}_2^2 + \mu_M^2)}
$$

$$
\times \frac{\chi^2[\mathbf{q}_2 \cdot (\mathbf{q}_1 + \mathbf{q}_2 - \mathbf{k})] + (\mathbf{q}_2 \cdot \mathbf{k})(\mathbf{k} - \mathbf{q}_2)^2 + (\mathbf{k} \cdot \mathbf{q}_1)[\mathbf{q}_2 \cdot (\mathbf{q}_2 - 2\mathbf{k})] + \mathbf{k}^2(\mathbf{q}_2 \cdot \mathbf{q}_1)}{(\chi^2 + \mathbf{k}^2)[\chi^2 + (\mathbf{k} - \mathbf{q}_2)^2][\chi^2 + (\mathbf{k} - \mathbf{q}_1 - \mathbf{q}_2)^2]}
$$

$$
\times \sin\left(\frac{\chi^2 + (\mathbf{k} - \mathbf{q}_1 - \mathbf{q}_2)^2}{4xE} z_1\right) \sin\left(\frac{\chi^2 + (\mathbf{k} - \mathbf{q}_1 - \mathbf{q}_2)^2}{4xE} z_1 + \frac{\chi^2 + (\mathbf{k} - \mathbf{q}_2)^2}{2xE} z_2\right), \tag{A5}
$$

$$
\left(\frac{dN_g^{(2)}}{dx}\right)_2 = \frac{4C_R}{\pi x} \int_0^L \int_{z_1}^L dz_1 dz_2 \int \frac{d^2\mathbf{k}}{\pi} \int \frac{d^2\mathbf{q}_2}{\pi} \alpha_s(Q_k^2) \frac{1}{\lambda_{\mathrm{dyn}}^2} \frac{\mu_E^2 - \mu_M^2}{(\mathbf{q}_2^2 + \mu_E^2)(\mathbf{q}_2^2 + \mu_M^2)}
$$

$$
\times \frac{\chi^2[\mathbf{q}_2 \cdot (\mathbf{q}_2 - \mathbf{k})] + (\mathbf{q}_2 \cdot \mathbf{k})(\mathbf{k} - \mathbf{q}_2)^2}{(\chi^2 + \mathbf{k}^2)[\chi^2 + (\mathbf{k} - \mathbf{q}_2)^2]^2} \sin\left(\frac{\chi^2 + (\mathbf{k} - \mathbf{q}_2)^2}{4xE} z_1\right) \sin\left[\frac{\chi^2 + (\mathbf{k} - \mathbf{q}_2)^2}{2xE}\left(\frac{z_1}{2} + z_2\right)\right]. \tag{A6}
$$

The third order in opacity contains four terms, which are given by

$$
\left(\frac{dN_g^{(3)}}{dx}\right)_1 = \frac{4C_R}{\pi x} \int_0^L \int_{z_1}^L \int_{z_2}^L dz_1 dz_2 dz_3 \int \frac{d^2\mathbf{k}}{\pi} \iiint \frac{d^2\mathbf{q}_1}{\pi} \frac{d^2\mathbf{q}_2}{\pi} \frac{d^2\mathbf{q}_3}{\pi}
$$

$$
\times \alpha_s(Q_k^2) \frac{1}{\lambda_{\mathrm{dyn}}^3} \frac{\mu_E^2 - \mu_M^2}{(\mathbf{q}_1^2 + \mu_E^2)(\mathbf{q}_1^2 + \mu_M^2)} \frac{\mu_E^2 - \mu_M^2}{(\mathbf{q}_2^2 + \mu_E^2)(\mathbf{q}_2^2 + \mu_M^2)} \frac{\mu_E^2 - \mu_M^2}{(\mathbf{q}_3^2 + \mu_E^2)(\mathbf{q}_3^2 + \mu_M^2)}
$$

$$
\times \frac{\chi^2[\mathbf{q}_3 \cdot (\mathbf{q}_1 + \mathbf{q}_2 + \mathbf{q}_3 - \mathbf{k})] + (\mathbf{q}_3 \cdot \mathbf{k})(\mathbf{k} - \mathbf{q}_3)^2 + [\mathbf{k} \cdot (\mathbf{q}_1 + \mathbf{q}_2)][\mathbf{q}_3 \cdot (\mathbf{q}_3 - 2\mathbf{k})] + \mathbf{k}^2[\mathbf{q}_3 \cdot (\mathbf{q}_1 + \mathbf{q}_2)]}{(\chi^2 + \mathbf{k}^2)[\chi^2 + (\mathbf{k} - \mathbf{q}_3)^2][\chi^2 + (\mathbf{k} - \mathbf{q}_1 - \mathbf{q}_2 - \mathbf{q}_3)^2]}
$$

$$
\times \sin\left(\frac{\chi^2 + (\mathbf{k} - \mathbf{q}_1 - \mathbf{q}_2 - \mathbf{q}_3)^2}{4xE} z_1\right)
$$

$$
\times \sin\left(\frac{\chi^2 + (\mathbf{k} - \mathbf{q}_1 - \mathbf{q}_2 - \mathbf{q}_3)^2}{4xE} z_1 + \frac{\chi^2 + (\mathbf{k} - \mathbf{q}_2 - \mathbf{q}_3)^2}{2xE} z_2 + \frac{\chi^2 + (\mathbf{k} - \mathbf{q}_3)^2}{2xE} z_3\right), \tag{A7}
$$

$$
\left(\frac{dN_g^{(3)}}{dx}\right)_2 = \frac{4C_R}{\pi x}\int_0^L\int_{z_1}^L\int_{z_2}^L dz_1 dz_2 dz_3 \int \frac{d^2\mathbf{k}}{\pi}\iint \frac{d^2\mathbf{q}_1}{\pi}\frac{d^2\mathbf{q}_3}{\pi}
$$

$$
\times\,\alpha_s(Q_k^2)\frac{1}{\lambda_{\mathrm{dyn}}^3}\frac{\mu_E^2-\mu_M^2}{(\mathbf{q}_1^2+\mu_E^2)(\mathbf{q}_1^2+\mu_M^2)}\frac{\mu_E^2-\mu_M^2}{(\mathbf{q}_3^2+\mu_E^2)(\mathbf{q}_3^2+\mu_M^2)}
$$

$$
\times\frac{\chi^2[\mathbf{q}_3\cdot(\mathbf{q}_1+\mathbf{q}_3-\mathbf{k})]+(\mathbf{q}_3\cdot\mathbf{k})(\mathbf{k}-\mathbf{q}_3)^2+(\mathbf{k}\cdot\mathbf{q}_1)[\mathbf{q}_3\cdot(\mathbf{q}_3-2\mathbf{k})]+\mathbf{k}^2(\mathbf{q}_3\cdot\mathbf{q}_1)}{(\chi^2+\mathbf{k}^2)[\chi^2+(\mathbf{k}-\mathbf{q}_3)^2][\chi^2+(\mathbf{k}-\mathbf{q}_1-\mathbf{q}_3)^2]}
$$

$$
\times\,\sin\left(\frac{\chi^2+(\mathbf{k}-\mathbf{q}_1-\mathbf{q}_3)^2}{4xE}z_1\right)\sin\left(\frac{\chi^2+(\mathbf{k}-\mathbf{q}_1-\mathbf{q}_3)^2}{4xE}z_1+\frac{\chi^2+(\mathbf{k}-\mathbf{q}_3)^2}{2xE}(z_2+z_3)\right), \tag{A8}
$$

$$
\left(\frac{dN_g^{(3)}}{dx}\right)_3 = \frac{4C_R}{\pi x}\int_0^L\int_{z_1}^L\int_{z_2}^L dz_1 dz_2 dz_3 \int \frac{d^2\mathbf{k}}{\pi}\iint \frac{d^2\mathbf{q}_2}{\pi}\frac{d^2\mathbf{q}_3}{\pi}\alpha_s(Q_k^2)\frac{1}{\lambda_{\mathrm{dyn}}^3}\frac{\mu_E^2-\mu_M^2}{(\mathbf{q}_2^2+\mu_E^2)(\mathbf{q}_2^2+\mu_M^2)}\frac{\mu_E^2-\mu_M^2}{(\mathbf{q}_3^2+\mu_E^2)(\mathbf{q}_3^2+\mu_M^2)}
$$

$$
\times\frac{\chi^2[\mathbf{q}_3\cdot(\mathbf{q}_2+\mathbf{q}_3-\mathbf{k})]+(\mathbf{q}_3\cdot\mathbf{k})(\mathbf{k}-\mathbf{q}_3)^2+(\mathbf{k}\cdot\mathbf{q}_2)[\mathbf{q}_3\cdot(\mathbf{q}_3-2\mathbf{k})]+\mathbf{k}^2(\mathbf{q}_3\cdot\mathbf{q}_2)}{(\chi^2+\mathbf{k}^2)[\chi^2+(\mathbf{k}-\mathbf{q}_3)^2](\chi^2+(\mathbf{k}-\mathbf{q}_2-\mathbf{q}_3)^2)}
$$

$$
\times\,\sin\left(\frac{\chi^2+(\mathbf{k}-\mathbf{q}_2-\mathbf{q}_3)^2}{4xE}z_1\right)\sin\left[\frac{\chi^2+(\mathbf{k}-\mathbf{q}_2-\mathbf{q}_3)^2}{2xE}\left(\frac{z_1}{2}+z_2\right)+\frac{\chi^2+(\mathbf{k}-\mathbf{q}_3)^2}{2xE}z_3\right], \tag{A9}
$$

$$
\left(\frac{dN_g^{(3)}}{dx}\right)_4 = \frac{4C_R}{\pi x}\int_0^L\int_{z_1}^L\int_{z_2}^L dz_1 dz_2 dz_3 \int \frac{d^2\mathbf{k}}{\pi}\int \frac{d^2\mathbf{q}_3}{\pi}\alpha_s(Q_k^2)\frac{1}{\lambda_{\mathrm{dyn}}^3}\frac{\mu_E^2-\mu_M^2}{(\mathbf{q}_3^2+\mu_E^2)(\mathbf{q}_3^2+\mu_M^2)}
$$

$$
\times\frac{\chi^2[\mathbf{q}_3\cdot(\mathbf{q}_3-\mathbf{k})]+(\mathbf{q}_3\cdot\mathbf{k})(\mathbf{k}-\mathbf{q}_3)^2}{(\chi^2+\mathbf{k}^2)[\chi^2+(\mathbf{k}-\mathbf{q}_3)^2]^2}\sin\left(\frac{\chi^2+(\mathbf{k}-\mathbf{q}_3)^2}{4xE}z_1\right)\sin\left[\frac{\chi^2+(\mathbf{k}-\mathbf{q}_3)^2}{2xE}\left(\frac{z_1}{2}+z_2+z_3\right)\right]. \tag{A10}
$$

The fourth order in opacity is given by eight terms, which are given by

$$
\left(\frac{dN_g^{(4)}}{dx}\right)_1 = \frac{4C_R}{\pi x}\int_0^L\int_{z_1}^L\int_{z_2}^L\int_{z_3}^L dz_1 dz_2 dz_3 dz_4 \int \frac{d^2\mathbf{k}}{\pi}\iiiint \frac{d^2\mathbf{q}_1}{\pi}\frac{d^2\mathbf{q}_2}{\pi}\frac{d^2\mathbf{q}_3}{\pi}\frac{d^2\mathbf{q}_4}{\pi}
$$

$$
\times\,\alpha_s(Q_k^2)\frac{1}{\lambda_{\mathrm{dyn}}^4}\frac{\mu_E^2-\mu_M^2}{(\mathbf{q}_1^2+\mu_E^2)(\mathbf{q}_1^2+\mu_M^2)}\frac{\mu_E^2-\mu_M^2}{(\mathbf{q}_2^2+\mu_E^2)(\mathbf{q}_2^2+\mu_M^2)}\frac{\mu_E^2-\mu_M^2}{(\mathbf{q}_3^2+\mu_E^2)(\mathbf{q}_3^2+\mu_M^2)}\frac{\mu_E^2-\mu_M^2}{(\mathbf{q}_4^2+\mu_E^2)(\mathbf{q}_4^2+\mu_M^2)}
$$

$$
\times\frac{\chi^2[\mathbf{q}_4\cdot(\mathbf{q}_1+\mathbf{q}_2+\mathbf{q}_3+\mathbf{q}_4-\mathbf{k})]+(\mathbf{q}_4\cdot\mathbf{k})(\mathbf{k}-\mathbf{q}_4)^2+[\mathbf{k}\cdot(\mathbf{q}_1+\mathbf{q}_2+\mathbf{q}_3)][\mathbf{q}_4\cdot(\mathbf{q}_4-2\mathbf{k})]+\mathbf{k}^2[\mathbf{q}_4\cdot(\mathbf{q}_1+\mathbf{q}_2+\mathbf{q}_3)]}{(\chi^2+\mathbf{k}^2)[\chi^2+(\mathbf{k}-\mathbf{q}_4)^2][\chi^2+(\mathbf{k}-\mathbf{q}_1-\mathbf{q}_2-\mathbf{q}_3-\mathbf{q}_4)^2]}
$$

$$
\times\,\sin\left(\frac{\chi^2+(\mathbf{k}-\mathbf{q}_1-\mathbf{q}_2-\mathbf{q}_3-\mathbf{q}_4)^2}{4xE}z_1+\frac{\chi^2+(\mathbf{k}-\mathbf{q}_2-\mathbf{q}_3-\mathbf{q}_4)^2}{2xE}z_2+\frac{\chi^2+(\mathbf{k}-\mathbf{q}_3-\mathbf{q}_4)^2}{2xE}z_3\right.
$$

$$
\left.+\frac{\chi^2+(\mathbf{k}-\mathbf{q}_4)^2}{2xE}z_4\right)\sin\left(\frac{\chi^2+(\mathbf{k}-\mathbf{q}_1-\mathbf{q}_2-\mathbf{q}_3-\mathbf{q}_4)^2}{4xE}z_1\right), \tag{A11}
$$

$$
\left(\frac{dN_g^{(4)}}{dx}\right)_2 = \frac{4C_R}{\pi x}\int_0^L\int_{z_1}^L\int_{z_2}^L\int_{z_3}^L dz_1 dz_2 dz_3 dz_4 \int \frac{d^2\mathbf{k}}{\pi}\iiint \frac{d^2\mathbf{q}_1}{\pi}\frac{d^2\mathbf{q}_2}{\pi}\frac{d^2\mathbf{q}_4}{\pi}
$$

$$
\times\,\alpha_s(Q_k^2)\frac{1}{\lambda_{\mathrm{dyn}}^4}\frac{\mu_E^2-\mu_M^2}{(\mathbf{q}_1^2+\mu_E^2)(\mathbf{q}_1^2+\mu_M^2)}\frac{\mu_E^2-\mu_M^2}{(\mathbf{q}_2^2+\mu_E^2)(\mathbf{q}_2^2+\mu_M^2)}\frac{\mu_E^2-\mu_M^2}{(\mathbf{q}_4^2+\mu_E^2)(\mathbf{q}_4^2+\mu_M^2)}
$$

$$
\times\frac{\chi^2[\mathbf{q}_4\cdot(\mathbf{q}_1+\mathbf{q}_2+\mathbf{q}_4-\mathbf{k})]+(\mathbf{q}_4\cdot\mathbf{k})(\mathbf{k}-\mathbf{q}_4)^2+[\mathbf{k}\cdot(\mathbf{q}_1+\mathbf{q}_2)][\mathbf{q}_4\cdot(\mathbf{q}_4-2\mathbf{k})]+\mathbf{k}^2[\mathbf{q}_4\cdot(\mathbf{q}_1+\mathbf{q}_2)]}{(\chi^2+\mathbf{k}^2)[\chi^2+(\mathbf{k}-\mathbf{q}_4)^2][\chi^2+(\mathbf{k}-\mathbf{q}_1-\mathbf{q}_2-\mathbf{q}_4)^2]}
$$

$$
\times\,\sin\left(\frac{\chi^2+(\mathbf{k}-\mathbf{q}_1-\mathbf{q}_2-\mathbf{q}_4)^2}{4xE}z_1+\frac{\chi^2+(\mathbf{k}-\mathbf{q}_2-\mathbf{q}_4)^2}{2xE}z_2+\frac{\chi^2+(\mathbf{k}-\mathbf{q}_4)^2}{2xE}(z_3+z_4)\right)
$$

$$
\times\,\sin\left(\frac{\chi^2+(\mathbf{k}-\mathbf{q}_1-\mathbf{q}_2-\mathbf{q}_4)^2}{4xE}z_1\right), \tag{A12}
$$

$$
\left(\frac{dN_g^{(4)}}{dx}\right)_3 = \frac{4C_R}{\pi x} \int_0^L \int_{z_1}^L \int_{z_2}^L \int_{z_3}^L dz_1 dz_2 dz_3 dz_4 \int \frac{d^2\mathbf{k}}{\pi} \iiint \frac{d^2\mathbf{q}_1}{\pi} \frac{d^2\mathbf{q}_3}{\pi} \frac{d^2\mathbf{q}_4}{\pi}
$$

$$
\times \alpha_s(Q_k^2) \frac{1}{\lambda_{\text{dyn}}^4} \frac{\mu_E^2 - \mu_M^2}{(\mathbf{q}_1^2 + \mu_E^2)(\mathbf{q}_1^2 + \mu_M^2)} \frac{\mu_E^2 - \mu_M^2}{(\mathbf{q}_3^2 + \mu_E^2)(\mathbf{q}_3^2 + \mu_M^2)} \frac{\mu_E^2 - \mu_M^2}{(\mathbf{q}_4^2 + \mu_E^2)(\mathbf{q}_4^2 + \mu_M^2)}
$$

$$
\times \frac{\chi^2[\mathbf{q}_4 \cdot (\mathbf{q}_1 + \mathbf{q}_3 + \mathbf{q}_4 - \mathbf{k})] + (\mathbf{q}_4 \cdot \mathbf{k})(\mathbf{k} - \mathbf{q}_4)^2 + [\mathbf{k} \cdot (\mathbf{q}_1 + \mathbf{q}_3)][\mathbf{q}_4 \cdot (\mathbf{q}_4 - 2\mathbf{k})] + \mathbf{k}^2[\mathbf{q}_4 \cdot (\mathbf{q}_1 + \mathbf{q}_3)]}{(\chi^2 + \mathbf{k}^2)[\chi^2 + (\mathbf{k} - \mathbf{q}_4)^2][\chi^2 + (\mathbf{k} - \mathbf{q}_1 - \mathbf{q}_3 - \mathbf{q}_4)^2]}
$$

$$
\times \sin\left(\frac{\chi^2 + (\mathbf{k} - \mathbf{q}_1 - \mathbf{q}_3 - \mathbf{q}_4)^2}{4xE} z_1 + \frac{\chi^2 + (\mathbf{k} - \mathbf{q}_3 - \mathbf{q}_4)^2}{2xE} (z_2 + z_3) + \frac{\chi^2 + (\mathbf{k} - \mathbf{q}_4)^2}{2xE} z_4\right)
$$

$$
\times \sin\left(\frac{\chi^2 + (\mathbf{k} - \mathbf{q}_1 - \mathbf{q}_3 - \mathbf{q}_4)^2}{4xE} z_1\right), \tag{A13}
$$

$$
\left(\frac{dN_g^{(4)}}{dx}\right)_4 = \frac{4C_R}{\pi x} \int_0^L \int_{z_1}^L \int_{z_2}^L \int_{z_3}^L dz_1 dz_2 dz_3 dz_4 \int \frac{d^2\mathbf{k}}{\pi} \iint \frac{d^2\mathbf{q}_1}{\pi} \frac{d^2\mathbf{q}_4}{\pi}
$$

$$
\times \alpha_s(Q_k^2) \frac{1}{\lambda_{\text{dyn}}^4} \frac{\mu_E^2 - \mu_M^2}{(\mathbf{q}_1^2 + \mu_E^2)(\mathbf{q}_1^2 + \mu_M^2)} \frac{\mu_E^2 - \mu_M^2}{(\mathbf{q}_4^2 + \mu_E^2)(\mathbf{q}_4^2 + \mu_M^2)}
$$

$$
\times \frac{\chi^2[\mathbf{q}_4 \cdot (\mathbf{q}_1 + \mathbf{q}_4 - \mathbf{k})] + (\mathbf{q}_4 \cdot \mathbf{k})(\mathbf{k} - \mathbf{q}_4)^2 + (\mathbf{k} \cdot \mathbf{q}_1)[\mathbf{q}_4 \cdot (\mathbf{q}_4 - 2\mathbf{k})] + \mathbf{k}^2(\mathbf{q}_4 \cdot \mathbf{q}_1)}{(\chi^2 + \mathbf{k}^2)[\chi^2 + (\mathbf{k} - \mathbf{q}_4)^2][\chi^2 + (\mathbf{k} - \mathbf{q}_1 - \mathbf{q}_4)^2]}
$$

$$
\times \sin\left(\frac{\chi^2 + (\mathbf{k} - \mathbf{q}_1 - \mathbf{q}_4)^2}{4xE} z_1\right) \sin\left(\frac{\chi^2 + (\mathbf{k} - \mathbf{q}_1 - \mathbf{q}_4)^2}{4xE} z_1 + \frac{\chi^2 + (\mathbf{k} - \mathbf{q}_4)^2}{2xE} (z_2 + z_3 + z_4)\right), \tag{A14}
$$

$$
\left(\frac{dN_g^{(4)}}{dx}\right)_5 = \frac{4C_R}{\pi x} \int_0^L \int_{z_1}^L \int_{z_2}^L \int_{z_3}^L dz_1 dz_2 dz_3 dz_4 \int \frac{d^2\mathbf{k}}{\pi} \iiint \frac{d^2\mathbf{q}_2}{\pi} \frac{d^2\mathbf{q}_3}{\pi} \frac{d^2\mathbf{q}_4}{\pi}
$$

$$
\times \alpha_s(Q_k^2) \frac{1}{\lambda_{\text{dyn}}^4} \frac{\mu_E^2 - \mu_M^2}{(\mathbf{q}_2^2 + \mu_E^2)(\mathbf{q}_2^2 + \mu_M^2)} \frac{\mu_E^2 - \mu_M^2}{(\mathbf{q}_3^2 + \mu_E^2)(\mathbf{q}_3^2 + \mu_M^2)} \frac{\mu_E^2 - \mu_M^2}{(\mathbf{q}_4^2 + \mu_E^2)(\mathbf{q}_4^2 + \mu_M^2)}
$$

$$
\times \frac{\chi^2[\mathbf{q}_4 \cdot (\mathbf{q}_2 + \mathbf{q}_3 + \mathbf{q}_4 - \mathbf{k})] + (\mathbf{q}_4 \cdot \mathbf{k})(\mathbf{k} - \mathbf{q}_4)^2 + [\mathbf{k} \cdot (\mathbf{q}_2 + \mathbf{q}_3)][\mathbf{q}_4 \cdot (\mathbf{q}_4 - 2\mathbf{k})] + \mathbf{k}^2[\mathbf{q}_4 \cdot (\mathbf{q}_2 + \mathbf{q}_3)]}{(\chi^2 + \mathbf{k}^2)[\chi^2 + (\mathbf{k} - \mathbf{q}_4)^2][\chi^2 + (\mathbf{k} - \mathbf{q}_2 - \mathbf{q}_3 - \mathbf{q}_4)^2]}
$$

$$
\times \sin\left[\frac{\chi^2 + (\mathbf{k} - \mathbf{q}_2 - \mathbf{q}_3 - \mathbf{q}_4)^2}{2xE} \left(\frac{z_1}{2} + z_2\right) + \frac{\chi^2 + (\mathbf{k} - \mathbf{q}_3 - \mathbf{q}_4)^2}{2xE} z_3 + \frac{\chi^2 + (\mathbf{k} - \mathbf{q}_4)^2}{2xE} z_4\right]
$$

$$
\times \sin\left(\frac{\chi^2 + (\mathbf{k} - \mathbf{q}_2 - \mathbf{q}_3 - \mathbf{q}_4)^2}{4xE} z_1\right), \tag{A15}
$$

$$
\left(\frac{dN_g^{(4)}}{dx}\right)_6 = \frac{4C_R}{\pi x} \int_0^L \int_{z_1}^L \int_{z_2}^L \int_{z_3}^L dz_1 dz_2 dz_3 dz_4 \int \frac{d^2\mathbf{k}}{\pi} \iint \frac{d^2\mathbf{q}_2}{\pi} \frac{d^2\mathbf{q}_4}{\pi}
$$

$$
\times \alpha_s(Q_k^2) \frac{1}{\lambda_{\text{dyn}}^4} \frac{\mu_E^2 - \mu_M^2}{(\mathbf{q}_2^2 + \mu_E^2)(\mathbf{q}_2^2 + \mu_M^2)} \frac{\mu_E^2 - \mu_M^2}{(\mathbf{q}_4^2 + \mu_E^2)(\mathbf{q}_4^2 + \mu_M^2)}
$$

$$
\times \frac{\chi^2[\mathbf{q}_4 \cdot (\mathbf{q}_2 + \mathbf{q}_4 - \mathbf{k})] + (\mathbf{q}_4 \cdot \mathbf{k})(\mathbf{k} - \mathbf{q}_4)^2 + (\mathbf{k} \cdot \mathbf{q}_2)[\mathbf{q}_4 \cdot (\mathbf{q}_4 - 2\mathbf{k})] + \mathbf{k}^2(\mathbf{q}_4 \cdot \mathbf{q}_2)}{(\chi^2 + \mathbf{k}^2)[\chi^2 + (\mathbf{k} - \mathbf{q}_4)^2][\chi^2 + (\mathbf{k} - \mathbf{q}_2 - \mathbf{q}_4)^2]}
$$

$$
\times \sin\left(\frac{\chi^2 + (\mathbf{k} - \mathbf{q}_2 - \mathbf{q}_4)^2}{4xE} z_1\right) \sin\left[\frac{\chi^2 + (\mathbf{k} - \mathbf{q}_2 - \mathbf{q}_4)^2}{2xE} \left(\frac{z_1}{2} + z_2\right) + \frac{\chi^2 + (\mathbf{k} - \mathbf{q}_4)^2}{2xE} (z_3 + z_4)\right], \tag{A16}
$$

$$
\left(\frac{dN_g^{(4)}}{dx}\right)_7 = \frac{4C_R}{\pi x} \int_0^L \int_{z_1}^L \int_{z_2}^L \int_{z_3}^L dz_1 dz_2 dz_3 dz_4 \int \frac{d^2\mathbf{k}}{\pi} \iint \frac{d^2\mathbf{q}_3}{\pi} \frac{d^2\mathbf{q}_4}{\pi}
$$

$$
\times \, \alpha_s(Q_k^2) \frac{1}{\lambda_{\mathrm{dyn}}^4} \frac{\mu_E^2 - \mu_M^2}{(\mathbf{q}_3^2 + \mu_E^2)(\mathbf{q}_3^2 + \mu_M^2)} \frac{\mu_E^2 - \mu_M^2}{(\mathbf{q}_4^2 + \mu_E^2)(\mathbf{q}_4^2 + \mu_M^2)}
$$

$$
\times \, \frac{\chi^2[\mathbf{q}_4 \cdot (\mathbf{q}_3 + \mathbf{q}_4 - \mathbf{k})] + (\mathbf{q}_4 \cdot \mathbf{k})(\mathbf{k} - \mathbf{q}_4)^2 + (\mathbf{k} \cdot \mathbf{q}_3)[\mathbf{q}_4 \cdot (\mathbf{q}_4 - 2\mathbf{k})] + \mathbf{k}^2(\mathbf{q}_4 \cdot \mathbf{q}_3)}{(\chi^2 + \mathbf{k}^2)[\chi^2 + (\mathbf{k} - \mathbf{q}_4)^2][\chi^2 + (\mathbf{k} - \mathbf{q}_3 - \mathbf{q}_4)^2]}
$$

$$
\times \, \sin\left(\frac{\chi^2 + (\mathbf{k} - \mathbf{q}_3 - \mathbf{q}_4)^2}{4xE} z_1\right) \sin\left[\frac{\chi^2 + (\mathbf{k} - \mathbf{q}_3 - \mathbf{q}_4)^2}{2xE}\left(\frac{z_1}{2} + z_2 + z_3\right) + \frac{\chi^2 + (\mathbf{k} - \mathbf{q}_4)^2}{2xE} z_4\right], \tag{A17}
$$

$$
\left(\frac{dN_g^{(4)}}{dx}\right)_8 = \frac{4C_R}{\pi x} \int_0^L \int_{z_1}^L \int_{z_2}^L \int_{z_3}^L dz_1 dz_2 dz_3 dz_4 \int \frac{d^2\mathbf{k}}{\pi} \int \frac{d^2\mathbf{q}_4}{\pi}
$$

$$
\times \, \alpha_s(Q_k^2) \frac{1}{\lambda_{\mathrm{dyn}}^4} \frac{\mu_E^2 - \mu_M^2}{(\mathbf{q}_4^2 + \mu_E^2)(\mathbf{q}_4^2 + \mu_M^2)} \frac{\chi^2[\mathbf{q}_4 \cdot (\mathbf{q}_4 - \mathbf{k})] + (\mathbf{q}_4 \cdot \mathbf{k})(\mathbf{k} - \mathbf{q}_4)^2}{(\chi^2 + \mathbf{k}^2)[\chi^2 + (\mathbf{k} - \mathbf{q}_4)^2]^2}
$$

$$
\times \, \sin\left(\frac{\chi^2 + (\mathbf{k} - \mathbf{q}_4)^2}{4xE} z_1\right) \sin\left[\frac{\chi^2 + (\mathbf{k} - \mathbf{q}_4)^2}{2xE}\left(\frac{z_1}{2} + z_2 + z_3 + z_4\right)\right]. \tag{A18}
$$

APPENDIX B: ANALYTICAL EXPRESSIONS FOR dN_g/dx WITHIN DREENA-C

Within the DREENA-C framework, under the assumption of constant medium temperature, we can explicitly perform analytical integrations for z_i, where $(i = 1, 2, 3, 4)$. $\omega_{(m\ldots n)}$ coefficients are defined in the Theoretical Framework section. The expression for the first order in opacity then became

$$
\left(\frac{dN_g^{(1)}}{dx}\right) = \frac{2C_R}{\pi x} \int \frac{d^2\mathbf{k}}{\pi} \int \frac{d^2\mathbf{q}_1}{\pi} \alpha_s(Q_k^2) \frac{L}{\lambda_{\mathrm{dyn}}} \frac{\mu_E^2 - \mu_M^2}{(\mathbf{q}_1^2 + \mu_E^2)(\mathbf{q}_1^2 + \mu_M^2)} \frac{\chi^2[\mathbf{q}_1 \cdot (\mathbf{q}_1 - \mathbf{k})] + (\mathbf{q}_1 \cdot \mathbf{k})(\mathbf{k} - \mathbf{q}_1)^2}{(\chi^2 + \mathbf{k}^2)[\chi^2 + (\mathbf{k} - \mathbf{q}_1)^2]^2}\left(1 - \frac{\sin(L\omega_{(1)})}{L\omega_{(1)}}\right),
$$

$$\tag{B1}$$

The expressions for higher orders in opacity became

$$
\left(\frac{dN_g^{(2)}}{dx}\right)_1 = \frac{2C_R}{\pi x} \int \frac{d^2\mathbf{k}}{\pi} \iint \frac{d^2\mathbf{q}_1}{\pi} \frac{d^2\mathbf{q}_2}{\pi} \alpha_s(Q_k^2) \frac{1}{\lambda_{\mathrm{dyn}}^2} \frac{\mu_E^2 - \mu_M^2}{(\mathbf{q}_1^2 + \mu_E^2)(\mathbf{q}_1^2 + \mu_M^2)} \frac{\mu_E^2 - \mu_M^2}{(\mathbf{q}_2^2 + \mu_E^2)(\mathbf{q}_2^2 + \mu_M^2)}
$$

$$
\times \, \frac{\chi^2[\mathbf{q}_2 \cdot (\mathbf{q}_1 + \mathbf{q}_2 - \mathbf{k})] + (\mathbf{q}_2 \cdot \mathbf{k})(\mathbf{k} - \mathbf{q}_2)^2 + (\mathbf{k} \cdot \mathbf{q}_1)[\mathbf{q}_2 \cdot (\mathbf{q}_2 - 2\mathbf{k})] + \mathbf{k}^2(\mathbf{q}_2 \cdot \mathbf{q}_1)}{(\chi^2 + \mathbf{k}^2)[\chi^2 + (\mathbf{k} - \mathbf{q}_2)^2][\chi^2 + (\mathbf{k} - \mathbf{q}_1 - \mathbf{q}_2)^2]}
$$

$$
\times \, \frac{1}{\omega_{(2)}}\left(\frac{\omega_{(2)} \cos[(\omega_{(2)} + \omega_{(12)})]}{(\omega_{(2)} + \omega_{(12)})\omega_{(12)}} + L \sin(L\omega_{(2)}) - \frac{(\omega_{(2)} - \omega_{(12)}) \cos(L\omega_{(2)})}{\omega_{(2)}\omega_{(12)}} - \frac{\omega_{(12)}}{\omega_{(2)}(\omega_{(2)} + \omega_{(12)})}\right), \tag{B2}
$$

$$
\left(\frac{dN_g^{(2)}}{dx}\right)_2 = \frac{2C_R}{\pi x} \int \frac{d^2\mathbf{k}}{\pi} \int \frac{d^2\mathbf{q}_2}{\pi} \alpha_s(Q_k^2) \frac{1}{\lambda_{\mathrm{dyn}}^2} \frac{\mu_E^2 - \mu_M^2}{(\mathbf{q}_2^2 + \mu_E^2)(\mathbf{q}_2^2 + \mu_M^2)}
$$

$$
\times \, \frac{\chi^2[\mathbf{q}_2 \cdot (\mathbf{q}_2 - \mathbf{k})] + (\mathbf{q}_2 \cdot \mathbf{k})(\mathbf{k} - \mathbf{q}_2)^2}{(\chi^2 + \mathbf{k}^2)[\chi^2 + (\mathbf{k} - \mathbf{q}_2)^2]^2} \frac{\sin(L\omega_{(2)})[L\omega_{(2)} - \sin(L\omega_{(2)})]}{\omega_{(2)}^2}, \tag{B3}
$$

$$
\left(\frac{dN_g^{(3)}}{dx}\right)_1 = \frac{2C_R}{\pi x} \int \frac{d^2\mathbf{k}}{\pi} \iiint \frac{d^2\mathbf{q}_1}{\pi} \frac{d^2\mathbf{q}_2}{\pi} \frac{d^2\mathbf{q}_3}{\pi} \alpha_s(Q_k^2) \frac{1}{\lambda_{\mathrm{dyn}}^3} \frac{\mu_E^2 - \mu_M^2}{(\mathbf{q}_1^2 + \mu_E^2)(\mathbf{q}_1^2 + \mu_M^2)} \frac{\mu_E^2 - \mu_M^2}{(\mathbf{q}_2^2 + \mu_E^2)(\mathbf{q}_2^2 + \mu_M^2)} \frac{\mu_E^2 - \mu_M^2}{(\mathbf{q}_3^2 + \mu_E^2)(\mathbf{q}_3^2 + \mu_M^2)}
$$

$$
\times \, \frac{\chi^2[\mathbf{q}_3 \cdot (\mathbf{q}_1 + \mathbf{q}_2 + \mathbf{q}_3 - \mathbf{k})] + (\mathbf{q}_3 \cdot \mathbf{k})(\mathbf{k} - \mathbf{q}_3)^2 + [\mathbf{k} \cdot (\mathbf{q}_1 + \mathbf{q}_2)][\mathbf{q}_3 \cdot (\mathbf{q}_3 - 2\mathbf{k})] + \mathbf{k}^2[\mathbf{q}_3 \cdot (\mathbf{q}_1 + \mathbf{q}_2)]}{(\chi^2 + \mathbf{k}^2)[\chi^2 + (\mathbf{k} - \mathbf{q}_3)^2][\chi^2 + (\mathbf{k} - \mathbf{q}_1 - \mathbf{q}_2 - \mathbf{q}_3)^2]}
$$

$$
\times \, \left\{ \frac{\omega_{(3)}\omega_{(123)} + 2\omega_{(23)}\omega_{(123)} - \omega_{(23)}^2 - \omega_{(3)}\omega_{(23)}}{\omega_{(23)}^2(\omega_{(3)} + \omega_{(23)})^2 \omega_{(123)}} \sin[L(\omega_{(3)} + \omega_{(23)})] - \frac{\omega_{(123)} \sin(L\omega_{(3)})}{\omega_{(3)}\omega_{(23)}^2(\omega_{(23)} + \omega_{(123)})} \right.
$$

$$
\left. + \, \frac{\sin[L(\omega_{(3)} + \omega_{(23)} + \omega_{(123)})]}{\omega_{(123)}(\omega_{(23)} + \omega_{(123)})(\omega_{(3)} + \omega_{(23)} + \omega_{(123)})} - \frac{L \cos[L(\omega_{(3)} + \omega_{(23)})]}{\omega_{(23)}(\omega_{(3)} + \omega_{(23)})} \right\}, \tag{B4}
$$

$$\left(\frac{dN_g^{(3)}}{dx}\right)_2 = \frac{C_R}{\pi x}\int \frac{d^2\mathbf{k}}{\pi}\iint \frac{d^2\mathbf{q}_1}{\pi}\frac{d^2\mathbf{q}_3}{\pi}\alpha_s(Q_k^2)\frac{1}{\lambda_{\text{dyn}}^3}\frac{\mu_E^2-\mu_M^2}{(\mathbf{q}_1^2+\mu_E^2)(\mathbf{q}_1^2+\mu_M^2)}\frac{\mu_E^2-\mu_M^2}{(\mathbf{q}_3^2+\mu_E^2)(\mathbf{q}_3^2+\mu_M^2)}$$

$$\times\frac{\chi^2[\mathbf{q}_3\cdot(\mathbf{q}_1+\mathbf{q}_3-\mathbf{k})]+(\mathbf{q}_3\cdot\mathbf{k})(\mathbf{k}-\mathbf{q}_3)^2+(\mathbf{k}\cdot\mathbf{q}_1)[\mathbf{q}_3\cdot(\mathbf{q}_3-2\mathbf{k})]+\mathbf{k}^2(\mathbf{q}_3\cdot\mathbf{q}_1)}{(\chi^2+\mathbf{k}^2)[\chi^2+(\mathbf{k}-\mathbf{q}_3)^2][\chi^2+(\mathbf{k}-\mathbf{q}_1-\mathbf{q}_3)^2]}$$

$$\times\left(\frac{\left(\frac{3\omega_{(13)}}{2}-\omega_{(3)}\right)\sin(2L\omega_{(3)})}{\omega_{(3)}^3\omega_{(13)}}-\frac{2\omega_{(13)}\sin(L\omega_{(3)})}{\omega_{(3)}^3(\omega_{(3)}+\omega_{(13)})}+\frac{\sin\left[2L\left(\omega_{(3)}+\frac{\omega_{(13)}}{2}\right)\right]}{\left(\omega_{(3)}+\frac{\omega_{(13)}}{2}\right)\omega_{(13)}(\omega_{(3)}+\omega_{(13)})}-\frac{L\cos(2L\omega_{(3)})}{\omega_{(3)}^2}\right),$$

(B5)

$$\left(\frac{dN_g^{(3)}}{dx}\right)_3 = \frac{2C_R}{\pi x}\int \frac{d^2\mathbf{k}}{\pi}\iint \frac{d^2\mathbf{q}_2}{\pi}\frac{d^2\mathbf{q}_3}{\pi}\alpha_s(Q_k^2)\frac{1}{\lambda_{\text{dyn}}^3}\frac{\mu_E^2-\mu_M^2}{(\mathbf{q}_2^2+\mu_E^2)(\mathbf{q}_2^2+\mu_M^2)}\frac{\mu_E^2-\mu_M^2}{(\mathbf{q}_3^2+\mu_E^2)(\mathbf{q}_3^2+\mu_M^2)}$$

$$\times\frac{\chi^2[\mathbf{q}_3\cdot(\mathbf{q}_2+\mathbf{q}_3-\mathbf{k})]+(\mathbf{q}_3\cdot\mathbf{k})(\mathbf{k}-\mathbf{q}_3)^2+(\mathbf{k}\cdot\mathbf{q}_2)[\mathbf{q}_3\cdot(\mathbf{q}_3-2\mathbf{k})]+\mathbf{k}^2(\mathbf{q}_3\cdot\mathbf{q}_2)}{(\chi^2+\mathbf{k}^2)[\chi^2+(\mathbf{k}-\mathbf{q}_3)^2](\chi^2+(\mathbf{k}-\mathbf{q}_2-\mathbf{q}_3)^2)}$$

$$\times\left(\frac{\sin\left[2L\left(\frac{\omega_{(3)}}{2}+\omega_{(23)}\right)\right]}{4\omega_{(23)}^2\left(\frac{\omega_{(3)}}{2}+\omega_{(23)}\right)}-\frac{\sin(L\omega_{(3)})}{2\omega_{(23)}^2\omega_{(3)}}+\frac{\frac{\sin[L(\omega_{(3)}+\omega_{(23)})]}{\omega_{(3)}+\omega_{(23)}}-L\cos[L(\omega_{(3)}+\omega_{(23)})]}{\omega_{(23)}(\omega_{(3)}+\omega_{(23)})}\right),$$

(B6)

$$\left(\frac{dN_g^{(3)}}{dx}\right)_4 = \frac{C_R}{\pi x}\int \frac{d^2\mathbf{k}}{\pi}\int \frac{d^2\mathbf{q}_3}{\pi}\alpha_s(Q_k^2)\frac{1}{\lambda_{\text{dyn}}^3}\frac{\mu_E^2-\mu_M^2}{(\mathbf{q}_3^2+\mu_E^2)(\mathbf{q}_3^2+\mu_M^2)}\frac{\chi^2[\mathbf{q}_3\cdot(\mathbf{q}_3-\mathbf{k})]+(\mathbf{q}_3\cdot\mathbf{k})(\mathbf{k}-\mathbf{q}_3)^2}{(\chi^2+\mathbf{k}^2)[\chi^2+(\mathbf{k}-\mathbf{q}_3)^2]^2}$$

$$\times\frac{1}{\omega_{(3)}^2}\left(-\frac{\sin(L\omega_{(3)})}{\omega_{(3)}}+\frac{\sin(2L\omega_{(3)})}{2\omega_{(3)}}+\frac{\sin(3L\omega_{(3)})}{3\omega_{(3)}}-L\cos(2L\omega_{(3)})\right),$$

(B7)

$$\left(\frac{dN_g^{(4)}}{dx}\right)_1 = \frac{2C_R}{\pi x}\int \frac{d^2\mathbf{k}}{\pi}\iiiint \frac{d^2\mathbf{q}_1}{\pi}\frac{d^2\mathbf{q}_2}{\pi}\frac{d^2\mathbf{q}_3}{\pi}\frac{d^2\mathbf{q}_4}{\pi}$$

$$\times\alpha_s(Q_k^2)\frac{1}{\lambda_{\text{dyn}}^4}\frac{\mu_E^2-\mu_M^2}{(\mathbf{q}_1^2+\mu_E^2)(\mathbf{q}_1^2+\mu_M^2)}\frac{\mu_E^2-\mu_M^2}{(\mathbf{q}_2^2+\mu_E^2)(\mathbf{q}_2^2+\mu_M^2)}\frac{\mu_E^2-\mu_M^2}{(\mathbf{q}_3^2+\mu_E^2)(\mathbf{q}_3^2+\mu_M^2)}\frac{\mu_E^2-\mu_M^2}{(\mathbf{q}_4^2+\mu_E^2)(\mathbf{q}_4^2+\mu_M^2)}$$

$$\times\frac{\chi^2[\mathbf{q}_4\cdot(\mathbf{q}_1+\mathbf{q}_2+\mathbf{q}_3+\mathbf{q}_4-\mathbf{k})]+(\mathbf{q}_4\cdot\mathbf{k})(\mathbf{k}-\mathbf{q}_4)^2+[\mathbf{k}\cdot(\mathbf{q}_1+\mathbf{q}_2+\mathbf{q}_3)][\mathbf{q}_4\cdot(\mathbf{q}_4-2\mathbf{k})]+\mathbf{k}^2[\mathbf{q}_4\cdot(\mathbf{q}_1+\mathbf{q}_2+\mathbf{q}_3)]}{(\chi^2+\mathbf{k}^2)[\chi^2+(\mathbf{k}-\mathbf{q}_4)^2][\chi^2+(\mathbf{k}-\mathbf{q}_1-\mathbf{q}_2-\mathbf{q}_3-\mathbf{q}_4)^2]}$$

$$\times\left\{-\frac{L\sin[L(\omega_{(4)}+\omega_{(34)}+\omega_{(234)})]}{\omega_{(234)}(\omega_{(34)}+\omega_{(234)})(\omega_{(4)}+\omega_{(34)}+\omega_{(234)})}\right.$$

$$-\frac{\cos[L(\omega_{(4)}+\omega_{(34)}+\omega_{(234)}+\omega_{(1234)})]}{\omega_{(1234)}(\omega_{(234)}+\omega_{(1234)})(\omega_{(34)}+\omega_{(234)}+\omega_{(1234)})(\omega_{(4)}+\omega_{(34)}+\omega_{(234)}+\omega_{(1234)})}$$

$$+\frac{F_{41}}{\omega_{(234)}^2(\omega_{(34)}+\omega_{(234)})^2(\omega_{(4)}+\omega_{(34)}+\omega_{(234)})^2\omega_{(1234)}}\cos[L(\omega_{(4)}+\omega_{(34)}+\omega_{(234)})]$$

$$+\frac{\omega_{(1234)}\cos[L(\omega_{(4)}+\omega_{(34)})]}{\omega_{(34)}(\omega_{(4)}+\omega_{(34)})\omega_{(234)}^2(\omega_{(234)}+\omega_{(1234)})}-\frac{\omega_{(1234)}\cos(L\omega_{(4)})}{\omega_{(4)}\omega_{(34)}(\omega_{(34)}+\omega_{(234)})^2(\omega_{(34)}+\omega_{(234)}+\omega_{(1234)})}$$

$$\left.+\frac{\omega_{(1234)}}{\omega_{(4)}(\omega_{(4)}+\omega_{(34)})(\omega_{(4)}+\omega_{(34)}+\omega_{(234)})^2(\omega_{(4)}+\omega_{(34)}+\omega_{(234)}+\omega_{(1234)})}\right\},$$

(B8)

where $F_{41} = (\omega_{(34)} + \omega_{(234)})[(\omega_{(4)} + \omega_{(34)})(\omega_{(234)} - \omega_{(1234)}) + \omega_{(234)}^2 - 3\omega_{(234)}\omega_{(1234)}] - \omega_{(4)}\omega_{(234)}\omega_{(1234)}$,

$$\left(\frac{dN_g^{(4)}}{dx}\right)_2 = \frac{C_R}{\pi x} \int \frac{d^2\mathbf{k}}{\pi} \iiint \frac{d^2\mathbf{q}_1}{\pi} \frac{d^2\mathbf{q}_2}{\pi} \frac{d^2\mathbf{q}_4}{\pi}$$

$$\times \alpha_s(Q_k^2) \frac{1}{\lambda_{\mathrm{dyn}}^4} \frac{\mu_E^2 - \mu_M^2}{(\mathbf{q}_1^2 + \mu_E^2)(\mathbf{q}_1^2 + \mu_M^2)} \frac{\mu_E^2 - \mu_M^2}{(\mathbf{q}_2^2 + \mu_E^2)(\mathbf{q}_2^2 + \mu_M^2)} \frac{\mu_E^2 - \mu_M^2}{(\mathbf{q}_4^2 + \mu_E^2)(\mathbf{q}_4^2 + \mu_M^2)}$$

$$\times \frac{\chi^2[\mathbf{q}_4 \cdot (\mathbf{q}_1 + \mathbf{q}_2 + \mathbf{q}_4 - \mathbf{k})] + (\mathbf{q}_4 \cdot \mathbf{k})(\mathbf{k} - \mathbf{q}_4)^2 + [\mathbf{k} \cdot (\mathbf{q}_1 + \mathbf{q}_2)][\mathbf{q}_4 \cdot (\mathbf{q}_4 - 2\mathbf{k})] + \mathbf{k}^2[\mathbf{q}_4 \cdot (\mathbf{q}_1 + \mathbf{q}_2)]}{(\chi^2 + \mathbf{k}^2)[\chi^2 + (\mathbf{k} - \mathbf{q}_4)^2][\chi^2 + (\mathbf{k} - \mathbf{q}_1 - \mathbf{q}_2 - \mathbf{q}_4)^2]}$$

$$\times \left\{ \frac{2[\omega_{(24)}(2\omega_{(4)}^2 + 3\omega_{(24)}\omega_{(4)} + \omega_{(24)}^2) - (2\omega_{(4)}^2 + 6\omega_{(24)}\omega_{(4)} + 3\omega_{(24)}^2)\omega_{(124)}]\cos[L(2\omega_{(4)} + \omega_{(24)})]}{\omega_{(24)}^2(\omega_{(4)} + \omega_{(24)})^2(2\omega_{(4)} + \omega_{(24)})^2\omega_{(124)}} \right.$$

$$- \frac{2\cos[L(2\omega_{(4)} + \omega_{(24)} + \omega_{(124)})]}{\omega_{(124)}(\omega_{(24)} + \omega_{(124)})(\omega_{(4)} + \omega_{(24)} + \omega_{(124)})(2\omega_{(4)} + \omega_{(24)} + \omega_{(124)})} + \frac{\omega_{(124)}\cos(2L\omega_{(4)})}{\omega_{(4)}^2\omega_{(24)}^2(\omega_{(24)} + \omega_{(124)})}$$

$$- \frac{2L\sin[L(2\omega_{(4)} + \omega_{(24)})]}{\omega_{(24)}(\omega_{(4)} + \omega_{(24)})(2\omega_{(4)} + \omega_{(24)})} - \frac{2\omega_{(124)}\cos(L\omega_{(4)})}{\omega_{(4)}^2(\omega_{(4)} + \omega_{(24)})^2(\omega_{(4)} + \omega_{(24)} + \omega_{(124)})}$$

$$\left. + \frac{\omega_{(124)}}{\omega_{(4)}^2(2\omega_{(4)} + \omega_{(24)})^2(2\omega_{(4)} + \omega_{(24)} + \omega_{(124)})} \right\}, \tag{B9}$$

$$\left(\frac{dN_g^{(4)}}{dx}\right)_3 = \frac{C_R}{2\pi x} \int \frac{d^2\mathbf{k}}{\pi} \iiint \frac{d^2\mathbf{q}_1}{\pi} \frac{d^2\mathbf{q}_3}{\pi} \frac{d^2\mathbf{q}_4}{\pi}$$

$$\times \alpha_s(Q_k^2) \frac{1}{\lambda_{\mathrm{dyn}}^4} \frac{\mu_E^2 - \mu_M^2}{(\mathbf{q}_1^2 + \mu_E^2)(\mathbf{q}_1^2 + \mu_M^2)} \frac{\mu_E^2 - \mu_M^2}{(\mathbf{q}_3^2 + \mu_E^2)(\mathbf{q}_3^2 + \mu_M^2)} \frac{\mu_E^2 - \mu_M^2}{(\mathbf{q}_4^2 + \mu_E^2)(\mathbf{q}_4^2 + \mu_M^2)}$$

$$\times \frac{\chi^2[\mathbf{q}_4 \cdot (\mathbf{q}_1 + \mathbf{q}_3 + \mathbf{q}_4 - \mathbf{k})] + (\mathbf{q}_4 \cdot \mathbf{k})(\mathbf{k} - \mathbf{q}_4)^2 + [\mathbf{k} \cdot (\mathbf{q}_1 + \mathbf{q}_3)][\mathbf{q}_4 \cdot (\mathbf{q}_4 - 2\mathbf{k})] + \mathbf{k}^2[\mathbf{q}_4 \cdot (\mathbf{q}_1 + \mathbf{q}_3)]}{(\chi^2 + \mathbf{k}^2)[\chi^2 + (\mathbf{k} - \mathbf{q}_4)^2][\chi^2 + (\mathbf{k} - \mathbf{q}_1 - \mathbf{q}_3 - \mathbf{q}_4)^2]}$$

$$\times \left\{ -\frac{2L\sin[L(\omega_{(4)} + 2\omega_{(34)})]}{\omega_{(34)}^2(\omega_{(4)} + 2\omega_{(34)})} - \frac{4\cos[L(\omega_{(4)} + 2\omega_{(34)} + \omega_{(134)})]}{\omega_{(134)}(\omega_{(34)} + \omega_{(134)})(2\omega_{(34)} + \omega_{(134)})(\omega_{(4)} + 2\omega_{(34)} + \omega_{(134)})} \right.$$

$$+ \frac{[2\omega_{(34)}(\omega_{(4)} + 2\omega_{(34)}) - (3\omega_{(4)} + 8\omega_{(34)})\omega_{(134)}]\cos[L(\omega_{(4)} + 2\omega_{(34)})]}{\omega_{(34)}^3(\omega_{(4)} + 2\omega_{(34)})^2\omega_{(134)}} - \frac{\omega_{(134)}\cos(L\omega_{(4)})}{\omega_{(4)}\omega_{(34)}^3(2\omega_{(34)} + \omega_{(134)})}$$

$$\left. + \frac{4\omega_{(134)}}{(\omega_{(4)} + \omega_{(34)})}\left(\frac{\cos[L(\omega_{(4)} + \omega_{(34)})]}{\omega_{(34)}^3(\omega_{(34)} + \omega_{(134)})} + \frac{1}{\omega_{(4)}(\omega_{(4)} + 2\omega_{(34)})^2(\omega_{(4)} + 2\omega_{(34)} + \omega_{(134)})}\right) \right\}, \tag{B10}$$

$$\left(\frac{dN_g^{(4)}}{dx}\right)_4 = \frac{C_R}{3\pi x} \int \frac{d^2\mathbf{k}}{\pi} \iint \frac{d^2\mathbf{q}_1}{\pi} \frac{d^2\mathbf{q}_4}{\pi} \alpha_s(Q_k^2) \frac{1}{\lambda_{\mathrm{dyn}}^4} \frac{\mu_E^2 - \mu_M^2}{(\mathbf{q}_1^2 + \mu_E^2)(\mathbf{q}_1^2 + \mu_M^2)} \frac{\mu_E^2 - \mu_M^2}{(\mathbf{q}_4^2 + \mu_E^2)(\mathbf{q}_4^2 + \mu_M^2)}$$

$$\times \frac{\chi^2[\mathbf{q}_4 \cdot (\mathbf{q}_1 + \mathbf{q}_4 - \mathbf{k})] + (\mathbf{q}_4 \cdot \mathbf{k})(\mathbf{k} - \mathbf{q}_4)^2 + (\mathbf{k} \cdot \mathbf{q}_1)[\mathbf{q}_4 \cdot (\mathbf{q}_4 - 2\mathbf{k})] + \mathbf{k}^2(\mathbf{q}_4 \cdot \mathbf{q}_1)}{(\chi^2 + \mathbf{k}^2)[\chi^2 + (\mathbf{k} - \mathbf{q}_4)^2][\chi^2 + (\mathbf{k} - \mathbf{q}_1 - \mathbf{q}_4)^2]}$$

$$\times \frac{1}{\omega_{(4)}^3}\left\{ -\frac{6\omega_{(4)}^3\cos[L(3\omega_{(4)} + \omega_{(14)})]}{\omega_{(14)}(\omega_{(4)} + \omega_{(14)})(2\omega_{(4)} + \omega_{(14)})(3\omega_{(4)} + \omega_{(14)})} + \left(\frac{1}{\omega_{(14)}} - \frac{11}{6\omega_{(4)}}\right)\cos(3L\omega_{(4)}) \right.$$

$$\left. -L\sin(3L\omega_{(4)}) - \frac{3\omega_{(14)}\cos(L\omega_{(4)})}{4\omega_{(4)}^2 + 2\omega_{(14)}\omega_{(4)}} + \frac{3\omega_{(14)}\cos(2L\omega_{(4)})}{(\omega_{(4)} + \omega_{(14)})\omega_{(4)}} + \frac{\omega_{(14)}}{9\omega_{(4)}^2 + 3\omega_{(14)}\omega_{(4)}} \right\}, \tag{B11}$$

$$\left(\frac{dN_g^{(4)}}{dx}\right)_5 = \frac{C_R}{\pi x}\int \frac{d^2\mathbf{k}}{\pi}\iiint \frac{d^2\mathbf{q}_2}{\pi}\frac{d^2\mathbf{q}_3}{\pi}\frac{d^2\mathbf{q}_4}{\pi}$$

$$\times \alpha_s(Q_k^2)\frac{1}{\lambda_{\rm dyn}^4}\frac{\mu_E^2-\mu_M^2}{(\mathbf{q}_2^2+\mu_E^2)(\mathbf{q}_2^2+\mu_M^2)}\frac{\mu_E^2-\mu_M^2}{(\mathbf{q}_3^2+\mu_E^2)(\mathbf{q}_3^2+\mu_M^2)}\frac{\mu_E^2-\mu_M^2}{(\mathbf{q}_4^2+\mu_E^2)(\mathbf{q}_4^2+\mu_M^2)}$$

$$\times \frac{\chi^2[\mathbf{q}_4\cdot(\mathbf{q}_2+\mathbf{q}_3+\mathbf{q}_4-\mathbf{k})]+(\mathbf{q}_4\cdot\mathbf{k})(\mathbf{k}-\mathbf{q}_4)^2+[\mathbf{k}\cdot(\mathbf{q}_2+\mathbf{q}_3)][\mathbf{q}_4\cdot(\mathbf{q}_4-2\mathbf{k})]+\mathbf{k}^2[\mathbf{q}_4\cdot(\mathbf{q}_2+\mathbf{q}_3)]}{(\chi^2+\mathbf{k}^2)[\chi^2+(\mathbf{k}-\mathbf{q}_4)^2][\chi^2+(\mathbf{k}-\mathbf{q}_2-\mathbf{q}_3-\mathbf{q}_4)^2]}$$

$$\times \frac{1}{\omega_{(234)}^2}\left(\frac{2\omega_{(234)}^3}{\omega_{(4)}(\omega_{(4)}+\omega_{(34)})(\omega_{(4)}+\omega_{(34)}+\omega_{(234)})^2(\omega_{(4)}+\omega_{(34)}+2\omega_{(234)})}+\frac{\cos[L(\omega_{(4)}+\omega_{(34)})]}{\omega_{(34)}(\omega_{(4)}+\omega_{(34)})}\right.$$

$$-\frac{2\omega_{(234)}^3\cos(L\omega_{(4)})}{\omega_{(4)}\omega_{(34)}(\omega_{(34)}+\omega_{(234)})^2(\omega_{(34)}+2\omega_{(234)})}-\frac{2L\omega_{(234)}\sin[L(\omega_{(4)}+\omega_{(34)}+\omega_{(234)})]}{(\omega_{(34)}+\omega_{(234)})(\omega_{(4)}+\omega_{(34)}+\omega_{(234)})}$$

$$\left.-\frac{\cos[L(\omega_{(4)}+\omega_{(34)}+2\omega_{(234)})]}{(\omega_{(34)}+2\omega_{(234)})(\omega_{(4)}+\omega_{(34)}+2\omega_{(234)})}-\frac{2\omega_{(234)}(\omega_{(4)}+2\omega_{(34)}+2\omega_{(234)})\cos[L(\omega_{(4)}+\omega_{(34)}+\omega_{(234)})]}{(\omega_{(34)}+\omega_{(234)})^2(\omega_{(4)}+\omega_{(34)}+\omega_{(234)})^2}\right),$$

$$\tag{B12}$$

$$\left(\frac{dN_g^{(4)}}{dx}\right)_6 = \frac{C_R}{\pi x}\int \frac{d^2\mathbf{k}}{\pi}\iint \frac{d^2\mathbf{q}_2}{\pi}\frac{d^2\mathbf{q}_4}{\pi}\alpha_s(Q_k^2)\frac{1}{\lambda_{\rm dyn}^4}\frac{\mu_E^2-\mu_M^2}{(\mathbf{q}_2^2+\mu_E^2)(\mathbf{q}_2^2+\mu_M^2)}\frac{\mu_E^2-\mu_M^2}{(\mathbf{q}_4^2+\mu_E^2)(\mathbf{q}_4^2+\mu_M^2)}$$

$$\times \frac{\chi^2[\mathbf{q}_4\cdot(\mathbf{q}_2+\mathbf{q}_4-\mathbf{k})]+(\mathbf{q}_4\cdot\mathbf{k})(\mathbf{k}-\mathbf{q}_4)^2+(\mathbf{k}\cdot\mathbf{q}_2)[\mathbf{q}_4\cdot(\mathbf{q}_4-2\mathbf{k})]+\mathbf{k}^2(\mathbf{q}_4\cdot\mathbf{q}_2)}{(\chi^2+\mathbf{k}^2)[\chi^2+(\mathbf{k}-\mathbf{q}_4)^2][\chi^2+(\mathbf{k}-\mathbf{q}_2-\mathbf{q}_4)^2]}$$

$$\times \left\{\frac{\omega_{(24)}}{8\omega_{(4)}^2(\omega_{(4)}+\frac{\omega_{(24)}}{2})^2(\omega_{(4)}+\omega_{(24)})}-\frac{L\sin[L(2\omega_{(4)}+\omega_{(24)})]+\frac{(\frac{3\omega_{(4)}}{2}+\omega_{(24)})\cos[2L(\omega_{(4)}+\frac{\omega_{(24)}}{2})]}{(\omega_{(4)}+\frac{\omega_{(24)}}{2})(\omega_{(4)}+\omega_{(24)})}}{(\omega_{(4)}+\frac{\omega_{(24)}}{2})(\omega_{(4)}+\omega_{(24)})\omega_{(24)}}\right.$$

$$\left.+\frac{(\frac{\cos(2L\omega_{(4)})}{2\omega_{(4)}}-\frac{\omega_{(4)}\cos[2L(\omega_{(4)}+\omega_{(24)})]}{4(\frac{\omega_{(4)}}{2}+\omega_{(24)})(\omega_{(4)}+\omega_{(24)})})}{\omega_{(4)}\omega_{(24)}^2}-\frac{\omega_{(24)}\cos(L\omega_{(4)})}{\omega_{(4)}^2(\frac{\omega_{(4)}}{2}+\omega_{(24)})(\omega_{(4)}+\omega_{(24)})^2}\right\},$$

$$\tag{B13}$$

$$\left(\frac{dN_g^{(4)}}{dx}\right)_7 = \frac{C_R}{2\pi x}\int \frac{d^2\mathbf{k}}{\pi}\iint \frac{d^2\mathbf{q}_3}{\pi}\frac{d^2\mathbf{q}_4}{\pi}\alpha_s(Q_k^2)\frac{1}{\lambda_{\rm dyn}^4}\frac{\mu_E^2-\mu_M^2}{(\mathbf{q}_3^2+\mu_E^2)(\mathbf{q}_3^2+\mu_M^2)}\frac{\mu_E^2-\mu_M^2}{(\mathbf{q}_4^2+\mu_E^2)(\mathbf{q}_4^2+\mu_M^2)}$$

$$\times \frac{\chi^2[\mathbf{q}_4\cdot(\mathbf{q}_3+\mathbf{q}_4-\mathbf{k})]+(\mathbf{q}_4\cdot\mathbf{k})(\mathbf{k}-\mathbf{q}_4)^2+(\mathbf{k}\cdot\mathbf{q}_3)[\mathbf{q}_4\cdot(\mathbf{q}_4-2\mathbf{k})]+\mathbf{k}^2(\mathbf{q}_4\cdot\mathbf{q}_3)}{(\chi^2+\mathbf{k}^2)[\chi^2+(\mathbf{k}-\mathbf{q}_4)^2][\chi^2+(\mathbf{k}-\mathbf{q}_3-\mathbf{q}_4)^2]}$$

$$\times \left\{\frac{1}{\omega_{(34)}^2(\frac{\omega_{(4)}}{2}+\omega_{(34)})}\left(\frac{2\omega_{(34)}^3}{\omega_{(4)}(\omega_{(4)}+\omega_{(34)})(\omega_{(4)}+2\omega_{(34)})(\omega_{(4)}+3\omega_{(34)})}-\frac{(\frac{\omega_{(4)}}{2}+2\omega_{(34)})\cos[L(\omega_{(4)}+2\omega_{(34)})]}{(\omega_{(4)}+2\omega_{(34)})\omega_{(34)}}\right.\right.$$

$$\left.\left.-L\sin[L(\omega_{(4)}+2\omega_{(34)})]-\frac{(\frac{\omega_{(4)}}{2}+\omega_{(34)})(\frac{\cos(L\omega_{(4)})}{\omega_{(4)}}-\frac{6\cos[L(\omega_{(4)}+\omega_{(34)})]}{\omega_{(4)}+\omega_{(34)}}+\frac{2\cos[L(\omega_{(4)}+3\omega_{(34)})]}{\omega_{(4)}+3\omega_{(34)}})}{3\omega_{(34)}}\right)\right\},$$

$$\tag{B14}$$

$$\left(\frac{dN_g^{(4)}}{dx}\right)_8 = \frac{C_R}{3\pi x}\int \frac{d^2\mathbf{k}}{\pi}\int \frac{d^2\mathbf{q}_4}{\pi}\alpha_s(Q_k^2)\frac{1}{\lambda_{\rm dyn}^4}\frac{\mu_E^2-\mu_M^2}{(\mathbf{q}_4^2+\mu_E^2)(\mathbf{q}_4^2+\mu_M^2)}\frac{\chi^2\mathbf{q}_4\cdot(\mathbf{q}_4-\mathbf{k})+(\mathbf{q}_4\cdot\mathbf{k})(\mathbf{k}-\mathbf{q}_4)^2}{(\chi^2+\mathbf{k}^2)[\chi^2+(\mathbf{k}-\mathbf{q}_4)^2]^2}$$

$$\times \frac{1}{\omega_{(4)}^3}\left(\frac{1}{12\omega_{(4)}}-L\sin(3L\omega_{(4)})-\frac{\cos(L\omega_{(4)})}{2\omega_{(4)}}+\frac{3\cos(2L\omega_{(4)})}{2\omega_{(4)}}-\frac{5\cos(3L\omega_{(4)})}{6\omega_{(4)}}-\frac{\cos(4L\omega_{(4)})}{4\omega_{(4)}}\right).$$

$$\tag{B15}$$

APPENDIX C: dN_g/dx RESULTS FOR $L = 3$ AND $L = 1$

In this section, we show dN_g/dx as a function of x for medium lengths $L = 3\,fm$ [Fig. (6)] and $L = 1\,fm$ [Fig. (7)].

FIG. 6. Gluon radiation spectrum dN_g/dx as a function of x, for the medium length of $L = 3$ fm and various jet momenta. The panel on the left (right) side shows the result for $\mu_M/\mu_E = 0.4$ (0.6). The figure caption is the same as for Fig. 1.
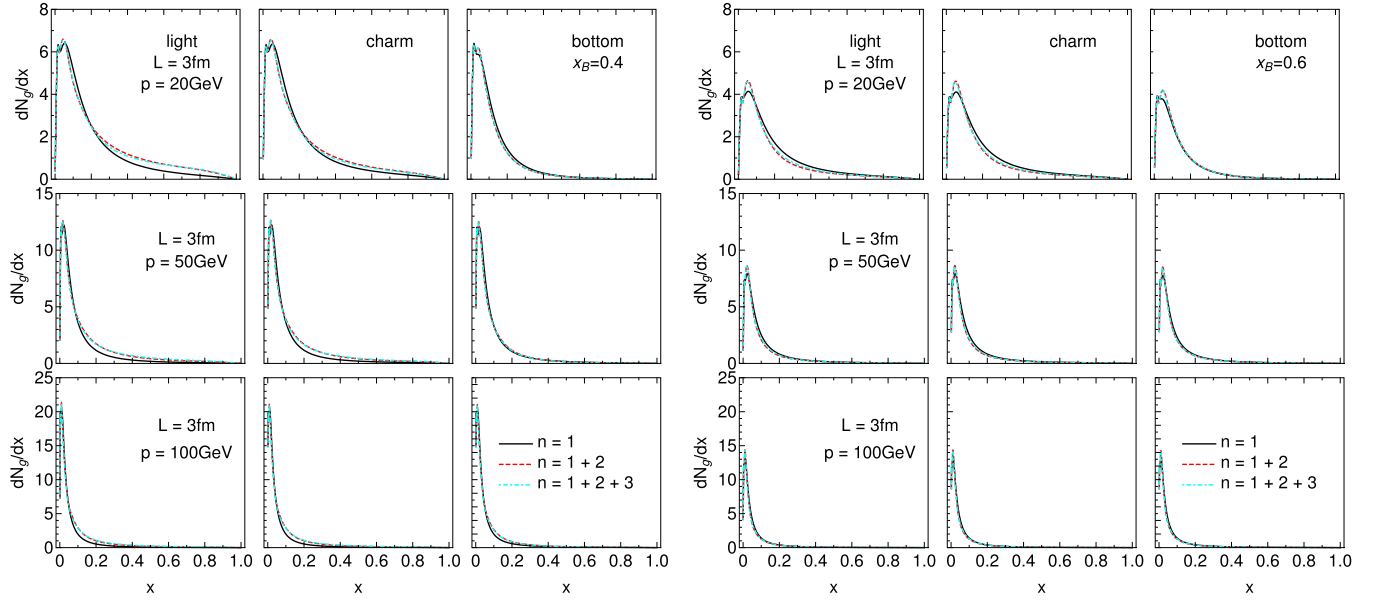

FIG. 7. Gluon radiation spectrum dN_g/dx as a function of x, for the medium length of $L = 1$ fm and various jet momenta. The panel on the left (right) side shows the result for $\mu_M/\mu_E = 0.4$ (0.6). The figure caption is the same as for Fig. 1.
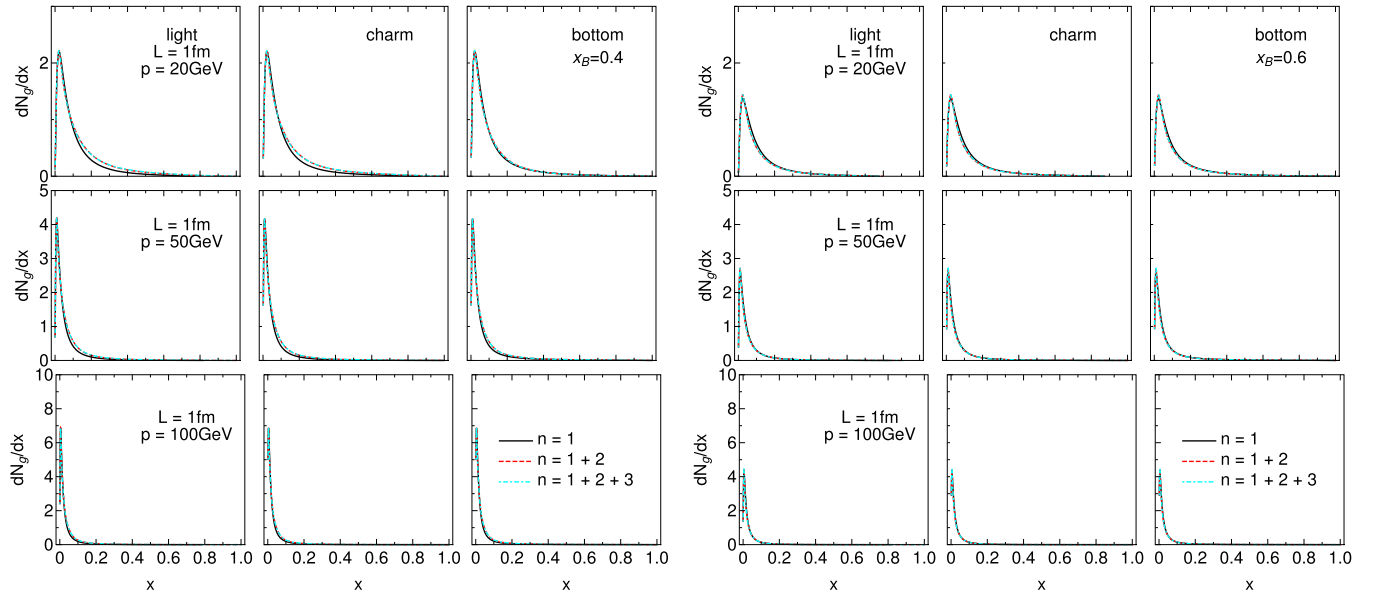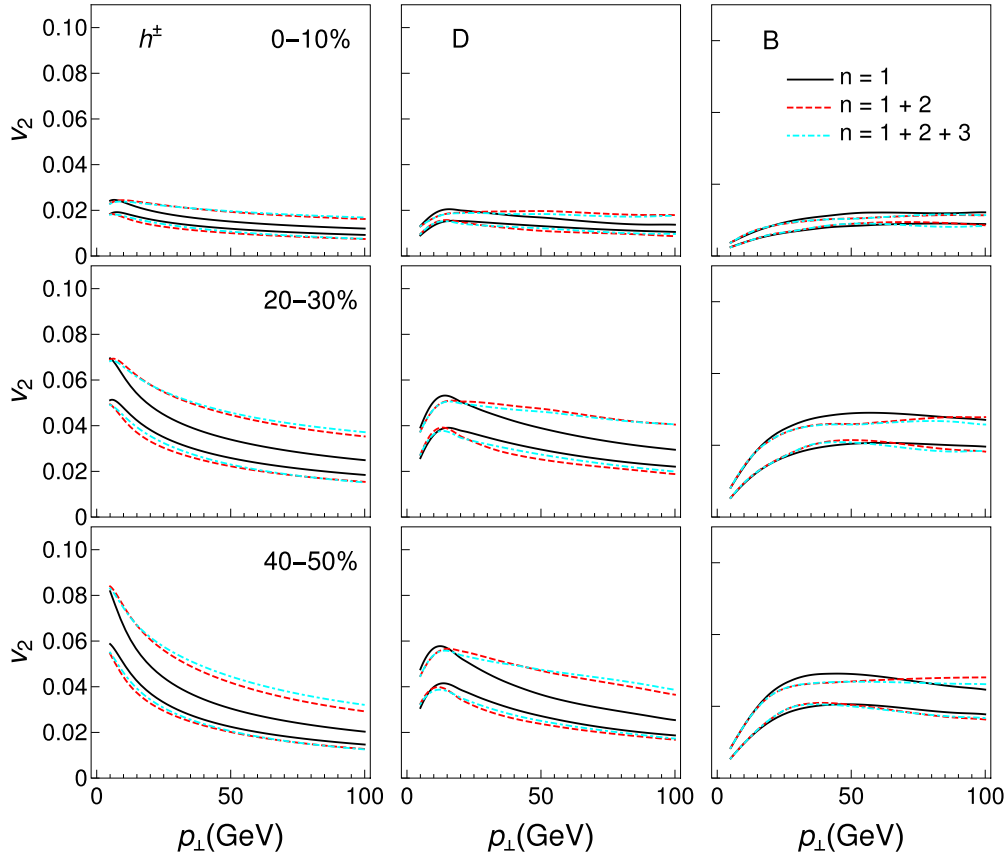
FIG. 8. v_2 results obtained within DREENA-C – the effects of different orders in opacity. Different columns correspond to charged hadrons, D, and B mesons, while different rows show different centrality classes. Only radiative energy loss is taken into account. Solid black curves show the first order in opacity results, red dashed curves show the results up to the second order, while cyan dot-dashed curves up to the third order in opacity. The lower (upper) boundary of each band corresponds to the $\mu_M/\mu_E = 0.6$ ($\mu_M/\mu_E = 0.4$) case.

APPENDIX D: v_2 RESULTS UP TO THIRD ORDER IN OPACITY

We here show the results for v_2 up to the third order in opacity (Fig. 8). Note that here the lower (upper) boundary of each band corresponds to the $\mu_M/\mu_E = 0.6$ ($\mu_M/\mu_E = 0.4$) case (opposite with respect to R_{AA} results). We observe the same behavior as for R_{AA}.

---

[1] E. V. Shuryak, Nucl. Phys. A **750**, 64 (2005); Rev. Mod. Phys. **89**, 035001 (2017).
[2] M. Gyulassy and L. McLerran, Nucl. Phys. A **750**, 30 (2005).
[3] B. Jacak and P. Steinberg, Phys. Today **63**(5), 39 (2010).
[4] B. Müller, J. Schukraft, and B. Wyslouch, Annu. Rev. Nucl. Part. Sci. **62**, 361 (2012).
[5] R. Baier, Y. Dokshitzer, A. Mueller, S. Peigne, and D. Schiff, Nucl. Phys. B **484**, 265 (1997).
[6] B. Zakharov, JETP Lett. **63**, 952 (1996); **65**, 615 (1997).
[7] N. Armesto, C. A. Salgado, and U. A. Wiedemann, Phys. Rev. D **69**, 114003 (2004).
[8] M. Gyulassy, P. Levai, and I. Vitev, Nucl. Phys. B **594**, 371 (2001).
[9] M. Djordjevic and M. Gyulassy, Nucl. Phys. A **733**, 265 (2004).

[10] W. Xin-Nian and X. Guo, Nucl. Phys. A **696**, 788 (2001).
[11] A. Majumder and M. Van Leeuwen, Prog. Part. Nucl. Phys. **66**, 41 (2011).
[12] P. Arnold, G. D. Moore, and L. G. Yaffe, J. High Energy Phys. 11 (2001) 057; 12 (2001) 009.
[13] M. Djordjevic, Phys. Rev. C **80**, 064909 (2009).
[14] M. Djordjevic and U. Heinz, Phys. Rev. Lett. **101**, 022302 (2008).
[15] C. Andres, L. Apolinário, and F. Dominguez, J. High Energy Phys. 07 (2020) 114.
[16] C. Andres, F. Dominguez, and M. Gonzalez Martinez, J. High Energy Phys. 03 (2021) 102.
[17] Y. Mehtar-Tani, J. High Energy Phys. 07 (2019) 057.
[18] Y. Mehtar-Tani and K. Tywoniuk, J. High Energy Phys. 06 (2020) 187.

[19] M. D. Sievert and I. Vitev, Phys. Rev. D **98**, 094010 (2018).

[20] M. D. Sievert, I. Vitev, and B. Yoon, Phys. Lett. B **795**, 502 (2019).

[21] S. Wicks, arXiv:0804.4704.

[22] D. Zigic, I. Salom, J. Auvinen, M. Djordjevic, and M. Djordjevic, J. Phys. G **46**, 085101 (2019).

[23] J. I. Kapusta, *Finite-Temperature Field Theory* (Cambridge University Press, Cambridge, 1989).

[24] M. Le Bellac, *Thermal Field Theory* (Cambridge University Press, Cambridge, 1996).

[25] M. Djordjevic and M. Gyulassy, Phys. Rev. C **68**, 034914 (2003).

[26] M. Djordjevic and M. Djordjevic, Phys. Lett. B **734**, 286 (2014).

[27] M. Djordjevic, Phys. Lett. B **709**, 229 (2012).

[28] Z. B. Kang, I. Vitev, and H. Xing, Phys. Lett. B **718**, 482 (2012); R. Sharma, I. Vitev, and B. W. Zhang, Phys. Rev. C **80**, 054902 (2009).

[29] M. Gyulassy, P. Levai, and I. Vitev, Phys. Lett. B **538**, 282 (2002).

[30] S. Wicks, W. Horowitz, M. Djordjevic, and M. Gyulassy, Nucl. Phys. A **784**, 426 (2007).

[31] D. de Florian, R. Sassot, and M. Stratmann, Phys. Rev. D **75**, 114010 (2007).

[32] M. Cacciari and P. Nason, J. High Energy Phys. 09 (2003) 006; E. Braaten, K.-M. Cheung, S. Fleming, and T. C. Yuan, Phys. Rev. D **51**, 4819 (1995).

[33] V. G. Kartvelishvili, A. K. Likhoded, and V. A. Petrov, Phys. Lett. B **78**, 615 (1978).

[34] A. Peshier, arXiv:hep-ph/0601119.

[35] Y. Maezawa, S. Aoki, S. Ejiri, T. Hatsuda, N. Ishii, K. Kanaya, N. Ukita, and T. Umeda (WHOT-QCD Collaboration), Phys. Rev. D **81**, 091501(R) (2010).

[36] A. Nakamura, T. Saito, and S. Sakai, Phys. Rev. D **69**, 014506 (2004).

[37] M. Djordjevic, Phys. Rev. C **74**, 064907 (2006).

[38] S. Borsányi, Z. Fodor, S. D. Katz, A. Pásztor, K. K. Szabó, and C. Török, J. High Energy Phys. 04 (2015) 138.

[39] M. Djordjevic, M. Gyulassy, and S. Wicks, Phys. Rev. Lett. **94**, 112301 (2005).

Understanding mass hierarchy in collisional energy loss through heavy flavor data

Bojana Ilic ⊙* and Magdalena Djordjevic ⊙
Institute of Physics Belgrade, University of Belgrade, 11000 Belgrade, Serbia

While experimental observations, such as the mass hierarchy effect, are attributed and analyzed within radiative models, their interpretation crucially depends on collisional energy loss contribution, which is often neglected in such analyses. To our knowledge, there are neither an established (direct) simple relation between collisional energy loss and heavy quark mass nor an observable that quantifies this effect. On the other hand, the upcoming high-luminosity measurements at the BNL Relativistic Heavy Ion Collider (RHIC) and the CERN Large Hadron Collider (LHC) will generate heavy flavor data with unprecedented precision, providing an opportunity to utilize high-$p_\perp$ heavy flavor data to analyze the interaction mechanisms in the quark-gluon plasma. To this end, we employ a recently developed DREENA framework based on our dynamical energy loss formalism to study the mass hierarchy in heavy flavor suppression. We present (i) an analytical derivation of a direct relation between collisional suppression/energy loss and heavy quark mass; (ii) a novel observable sensitive only to the collisional energy loss mechanism to be tested by future high-precision experiments, and (iii) analytical and numerical extraction of the mass hierarchy in collisional energy losses through this observable.

I. INTRODUCTION

For over two decades, ultrarelativistic heavy-ion collisions at the BNL Relativistic Heavy Ion Collider (RHIC) and the CERN Large Hadron Collider (LHC) have been aiming to create and understand the features of the new form of matter, the quark-gluon plasma [1–4] (QGP). The rare high-$p_\perp$ partons, while traversing the medium, interact with the QGP bulk and lose energy, which results in jet quenching [5]. The jet quenching is recognized as one of the most important probes of the QGP medium, with a crucial role in the QGP discovery [6]. Today, joint theoretical and experimental effort is necessary for providing unbiased insight into the nature of parton-medium interactions and, consequently, the QGP features. Within this, an important goal is the search for adequate effect and an observable for characterizing the appropriate energy loss mechanisms.

Due to the prevailing opinion that a gluon's bremsstrahlung is the dominant mechanism of high-$p_\perp$ parton energy loss [7–14], many experimental observations [15] are attributed to and analyzed within radiative models. On the other hand, in the intermediate-$p_\perp$ regime ($p_\perp \lesssim 10$ GeV) it is considered that, due to the dead-cone effect [16], elastic interactions prevail for heavy flavor [17–22]. Moreover, in [23–28], it was shown that for the charm and bottom quarks the collisional energy loss is comparable to, or even larger than, radiative energy loss.

A major research goal has been to understand the mass hierarchy in parton energy loss. In the case of inelastic scattering, it is known as the dead-cone effect [16], which reflects in gluon radiation suppression of the heavy (i.e., bottom) quarks compared to the light quarks at small angles. While the dead-cone effect is extensively studied, both analytically and numerically, within different radiative energy loss models [9,29–32] (see also Refs. [33,34], for more generalized study of this effect), the mass hierarchy in collisional energy loss has not been addressed. Within this, specific challenges are (i) the search for an observable which can disentangle collisional from radiative energy loss and (ii) analytical derivation of a direct relation between collisional suppression/energy loss and heavy quark mass. With this goal in mind, we here propose, through analytical and numerical analysis within our DREENA-C framework [35], a novel observable sensitive to the mass hierarchy in collisional energy loss of high-$p_\perp$ particles. Further, we demonstrate that our estimate for mass hierarchy in collisional energy loss is qualitatively and quantitatively in good agreement with the existing (scarce) experimental data. While current error bars at the RHIC and the LHC are large, we expect that the upcoming high-precision measurements will be able to directly extract mass dependence in collisional energy loss from the data.

II. COMPUTATIONAL FRAMEWORK

For generating predictions, we employ our fully optimized DREENA-C [35] (Dynamical Radiative and Elastic ENergy loss Approach, where C stands for constant/average

*Corresponding author: bojanab@ipb.ac.rs

temperature profile) framework. We opt for DREENA-C instead of hydrodynamically-wise more upgraded versions DREENA-B [36] (Bjorken [37] medium expansion) and -A (Adaptive, i.e., arbitrary temperature profile) [38], to avoid unnecessary complications stemming from subtleties of medium evolution and consequently allow analytical derivations. This can be done without significant loss of accuracy, as we previously demonstrated that energy-loss-sensitive observable R_{AA} (considered in this study) is practically unaffected by the medium evolution model (for details, see Sec. III).

The framework consists of (i) initial quark momentum distribution [39] and (ii) energy loss probability rooted in the dynamical energy loss formalism [24,40,41], which comprises multigluon and path-length fluctuations. Multigluon fluctuations are introduced according to Refs. [41,42] for radiative and [17,23] for collisional energy loss. The path-length fluctuations [23] are calculated following the procedure provided in [35,43]. The average temperature for each centrality bin is evaluated following the procedure outlined in Refs. [35,44]. It is worth noting that our predictions are valid for $p_\perp \gtrsim 7$ GeV.

The medium modified distribution of high-$p_\perp$ heavy flavor particles is obtained by utilizing the generic pQCD convolution formula [23,41]:

$$\frac{E_f d^3\sigma_f}{dp_f^3} = \frac{E_i d^3\sigma_i(Q)}{dp_i^3} \otimes P(E_i \to E_f), \quad (1)$$

where subscripts i and f stand for *initial* and *final* quantities, while $\frac{E_i d^3\sigma_i}{dp_i^3}$ denotes the initial heavy quark distribution computed according to [39]. $P(E_i \to E_f)$ represents energy loss probability, based on the dynamical energy loss formalism (see below). In contrast to Refs. [23,41], Eq. (1) does not include the fragmentation function ($D(Q \to H_Q)$) for both charm and beauty (into D and B mesons), as D/B suppression presents clear (genuine) charm/bottom probe's suppression [45–47]. Also, when providing predictions for b quark observables, we compare with indirect, nonprompt J/ψ total R_{AA}, due to its broader availability. This is legit, since due to the interplay of collisional and radiative energy losses, B meson suppression is almost independent of $p_\perp$ [32] (in the relevant region), so the fragmentation/decay functions will not play a notable role for different types of b quark observables.

DREENA-C [35] is based on our dynamical energy loss formalism [24,40,41], which includes several realistic features: (i) The QCD medium is of finite size and finite temperature. (ii) The medium consists of dynamical (i.e., moving) as opposed to static partons, which allows the longitudinal momentum exchange with the medium constituents; this is contrary to the medium models with widely applied vacuumlike propagators and/or static approximation [8–13]. (iii) Calculations are based on a generalized hard-thermal-loop approach [48], where infrared divergences are naturally regulated [24,40]. (iv) Both collisional [24] and radiative [40] energy loss are consistently included in the same theoretical framework (see also [49]), with the same/consistent approximations and the same constants corresponding to standard literature values (e.g., T-dependent Debye mass, number of flavors, etc.). These two contributions do not overlap or interfere, as different kinematic regions contribute to these energy

losses [50]. (v) Finite parton mass [29] is incorporated, broadening the formalism applicability from light toward heavy flavor. (vi) There are generalizations toward running coupling [41], finite magnetic mass [51], and beyond-soft-gluon approximation [52]. In Ref. [25] we demonstrated that all these features are necessary for reliable suppression predictions.

High-$p_\perp$ R_{AA} predictions, generated with DREENA-C for a large amount of experimental data at the RHIC and the LHC, show a good agreement [35,41,44] with the existing data; they explain puzzling observations (such as the heavy-flavor puzzle [46,53]) and provide nonintuitive predictions for the upcoming experiments [32,54,55] (some of which were subsequently confirmed by data [56]). Consequently, our framework/formalism can adequately describe high-$p_\perp$ parton-medium interactions, and it presents a suitable framework for study conveyed in this paper. Furthermore, we use no fitting parameters in generating predictions, i.e., all the parameters correspond to standard literature values, stated in [35]. To name the most relevant ones for this study the charm (bottom) mass is $M_c = 1.2$ GeV ($M_b = 4.75$ GeV). Different nonperturbative calculations [57,58] indicate chromomagnetic to chromoelectric mass ratio in the range $0.4 < \frac{\mu_B}{\mu_E} < 0.6$ for RHIC and LHC. We here opt for $\frac{\mu_B}{\mu_E} = 0.4$, while we checked that introducing a larger value has a negligible impact on our predictions.

III. RESULTS AND DISCUSSION

In this section, we start with comparing patterns in energy loss of charm and bottom quarks within the DREENA-C framework [35]. From the left plot of Fig. 1, we reproduce the dead-cone effect, i.e., mass hierarchy in radiative energy loss. Namely, we see that the bottom quark, due to larger mass, loses significantly less energy compared to the charm quark [31–34]. This is especially pronounced at lower $p_\perp \approx 10$ GeV, where M_b is comparable to the transverse momentum (i.e., energy, since we focus on midrapidity). This difference in $\frac{\Delta E_{\rm rad}}{E}$ between bottom and charm decreases with increasing transverse momentum, which can be attributed to the fact that for both flavors the mass becomes negligible compared to their $p_\perp$. Thus, already at $p_\perp \approx 50$ GeV, these two curves approach each other in accordance with [54]. Though we primarily show centrality bin 30–40%, the results are the same regardless of the selected centrality range and therefore omitted.

For collisional energy loss, shown in the right plot of Fig. 1, we observe a qualitatively similar tendency. That is, we obtain clear mass hierarchy in $\frac{\Delta E_{\rm coll}}{E}$ (see also, e.g., [24,59–62]), with heavier quark encountering notably smaller collisional energy loss at $p_\perp \approx 10$. Compared to the fractional radiative energy loss, this effect is less pronounced (and disappears faster with increasing $p_\perp$), but it is an important observation.

To quantify this effect on the experimental observables, we recall that R_{AA} is well suited for our study, as it is susceptible to energy loss [25] while being practically insensitive to the details of medium evolution (contrary to, e.g., elliptic flow) [35,36,63–65]. Therefore, it is reasonable to assume that an adequate observable should be a function of R_{AA}. In particular, we will further analyze $1 - R_{AA}$, as this observable carries more direct information on the parton energy loss than
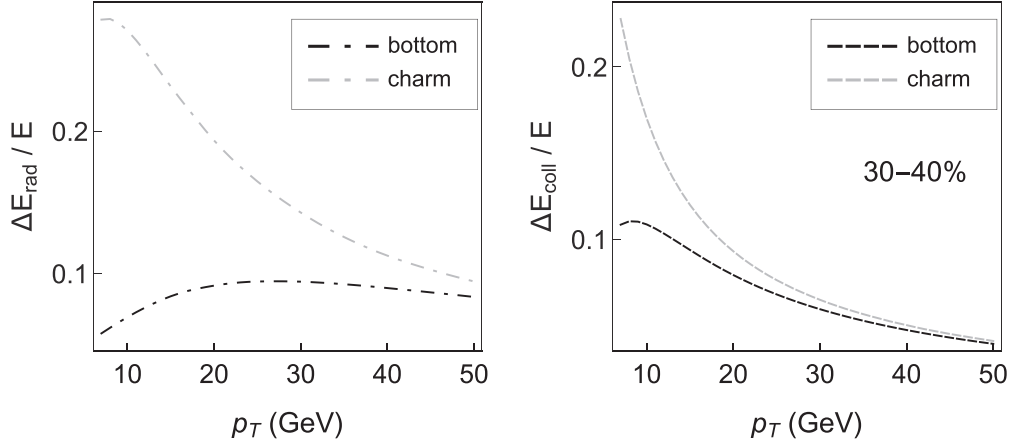
FIG. 1. The mass hierarchy in fractional energy losses. Heavy quark fractional energy loss as a function of $p_\perp$, when only radiative (the left plot) and only collisional (the right plot) energy loss mechanism is assumed. The selected centrality bin is 30–40%. Black (gray) curves correspond to bottom (charm) quark.

commonly used R_{AA} [63]. To this end, in Fig. 2, we compare $1 - R_{AA}$ bottom to charm ratios, when *total* (radiative and collisional) energy losses are accounted for. In the same plot, we also separately consider the $1 - R_{AA}$ ratio, resulting from only *collisional* and only *radiative* energy loss scenarios. The predictions for all considered centrality ranges are displayed.

Figure 2 contains a large number of curves, which makes it overcrowded and may obscure some important observations. Therefore, an inset corresponding only to 30–40% centrality is added for transparency. Note that the choice of centrality does not influence the conclusion, as we checked that we

observe the same for other centralities. The inset provides a somewhat unexpected insight. That is, we observe that the $1 - R_{AA}^{\rm coll}$ bottom to charm ratio is practically overlapping with the $1 - R_{AA}^{\rm tot}$ ratio. Furthermore, the *total* (and likewise the *collisional*) ratio is notably larger than the $1 - R_{AA}^{\rm rad}$ bottom to charm ratio. As expected, the suppression curve corresponding to the *total* energy loss is in between the *collisional* and *radiative* energy loss scenarios. It is, however, surprising that the *total* energy loss curve closely follows the *collisional* energy loss curve, i.e., that the *radiative* contribution is negligible. Consequently, this figure demonstrates that the $1 - R_{AA}$ ratio for heavy flavor is dominantly driven by the *collisional* contribution. Note also that the bottom to charm ratio is smaller than 1 at lower $p_\perp$, and increases with increasing $p_\perp$ (toward 1). This implies that $R_{AA}^{b,{\rm coll}} > R_{AA}^{c,{\rm coll}}$, which might reflect mass ordering in collisional energy loss for heavy flavors that we further explore.

To analytically analyze what is reflected by the ratio in Fig. 2, we start from the definition of high-$p_\perp$ particle suppression, assuming only collisional interactions within the QGP. To obtain the final particle spectrum ($d\sigma^f/dp_\perp^2$) at midrapidity, the standard procedure [66] is a convolution of the initial parton momentum distribution ($d\sigma^i(p_\perp + \epsilon)/dp_\perp^2$) with the energy loss probability ($D(\epsilon)$) in the final stage [27]. The assumption that energy loss of a high-$p_\perp$ heavy flavor is small (i.e., $\epsilon \ll p_\perp$) allows Taylor expansion:

$$
\begin{aligned}
\frac{d\sigma^f}{dp_\perp^2} &= \int d\epsilon\, D(\epsilon) \frac{d\sigma^i(p_\perp + \epsilon)}{dp_\perp^2} \\
&= \int d\epsilon\, D(\epsilon) \frac{d\sigma^i(p_\perp)}{dp_\perp^2} \\
&\quad + \int d\epsilon\, D(\epsilon) \frac{\epsilon}{1!} \frac{d}{dp_\perp}\left(\frac{d\sigma^i(p_\perp)}{dp_\perp^2}\right) \\
&\quad + \cdots \\
&\simeq \frac{d\sigma^i}{dp_\perp^2} + \Delta E_{\rm coll} \frac{d}{dp_\perp}\left(\frac{d\sigma^i}{dp_\perp^2}\right).
\end{aligned} \tag{2}
$$
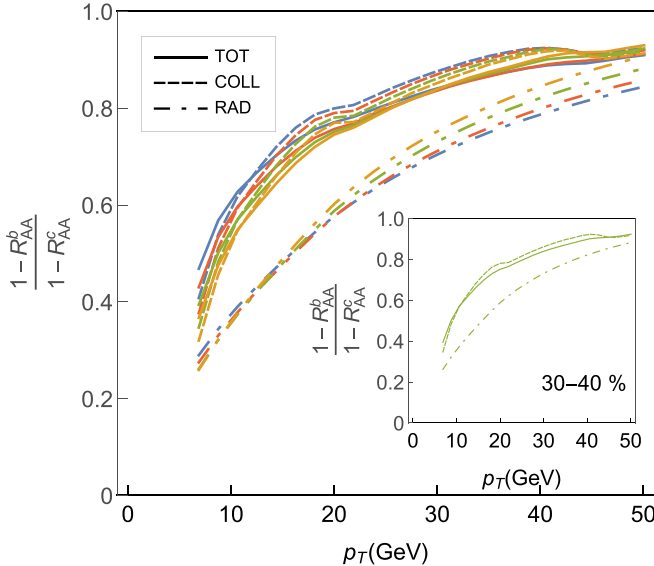
FIG. 2. Comparison of $1 - R_{AA}$ bottom to charm ratios for *total, collisional*, and *radiative* suppressions, generated with the DREENA-C [35] framework. For clarity, 30–40% centrality is presented in the inset. Full, dashed, and dot-dashed curves denotes *total, collisional*, and *radiative* cases, respectively, as indicated in the legend. The blue, red, green, and orange curves correspond to 10–20%, 20–30%, 30–40%, and 40–50% centrality bins, respectively.
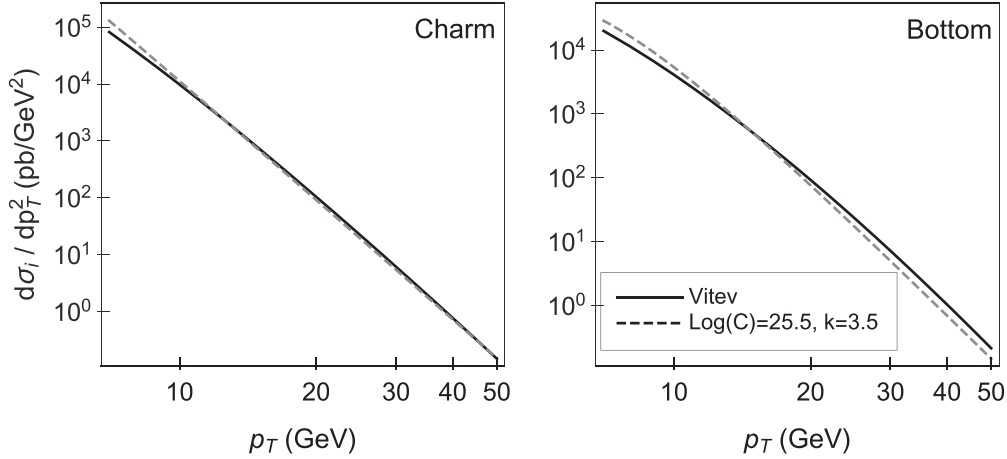
FIG. 3. Mass parametrization of transverse momentum distributions for charm and bottom. Charm and bottom initial distributions are presented on the left and the right plots, respectively, as a function of $p_\perp$. On each plot, full black curve corresponds to the distribution, computed at next to leading order according to [39], while gray dashed curve represents our mass-dependent fitted distribution, based on Eq. (3).

Here, we use that the probability $\int d\epsilon\, D(\epsilon) = 1$, as well as the fact that the total collisional energy loss of a parton in the medium is given by $\Delta E_{\text{coll}} = \int d\epsilon\, D(\epsilon)\epsilon$.

Furthermore, we assume that initial $p_\perp$ distribution of a heavy parton can be parameterized as [17]

$$\frac{d\sigma^i}{dp_\perp^2} = \frac{C}{(p_\perp^2 + M^2)^k},\tag{3}$$

where constants C and k should be the same for the charm and bottom quarks. Indeed, for the initial distributions used [39], we explicitly verified this equality in Fig. 3, where our numerical analysis yields consistent values for both heavy partons ($\ln(C) \simeq 25.5$, $k \simeq 3.5$).

After taking the derivative of Eq. (3) with respect to $p_\perp$, Eq. (2) straightforwardly reduces to

$$\frac{d\sigma^f}{dp_\perp^2} \simeq \frac{d\sigma^i}{dp_\perp^2}\left(1 - 2k\,\frac{p_\perp}{E}\,\frac{\Delta E_{\text{coll}}}{E}\right),\tag{4}$$

where $E = \sqrt{p_\perp^2 + M^2}$. Since the parton's suppression [10] is defined as [17] $R_{AA} = \frac{d\sigma^f/dp_\perp^2}{d\sigma^i/dp_\perp^2}$, we finally obtain

$$1 - R_{AA} \simeq 2k\,\frac{p_\perp}{E}\,\frac{\Delta E_{\text{coll}}}{E}.\tag{5}$$

To extract the analytic dependence of $1 - R_{AA}$ on the mass of the heavy quark, we need to analyze the mass dependence of collisional energy loss analytically. Since our energy loss expression [24] is highly nontrivial and not analytically tractable, we opt for a more straightforward Thoma-Gyulassy [67] result, which is moreover in a (reasonably) good agreement with our result [24] (in the $p_\perp$ range of concern). After algebraic manipulation, we obtain that the proportionality between fractional collisional energy loss and the parton's mass is represented by (see Eq. (A3) in the Appendix)

$$\frac{\Delta E_{\text{coll}}}{E} \sim \frac{1}{p_\perp}\left(1 - \frac{M^2}{p_\perp^2}\ln\frac{2p_\perp}{M}\right).\tag{6}$$

Along the same lines, from Eq. (5), we obtain that the mass dependence of $1 - R_{AA}$ is represented by (see Eq. (A7) in the Appendix)

$$1 - R_{AA} \sim \frac{2k}{p_\perp}\left[1 - \frac{M^2}{p_\perp^2}\left(\ln 2 + \frac{1}{2}\right) + \left(\frac{M}{p_\perp}\right)^{\frac{M}{p_\perp}+1} - \frac{M}{p_\perp}\right].\tag{7}$$

Surprisingly, further numerical consideration revels that the dominant mass term acquires the form

$$1 - R_{AA} \sim \frac{2k}{p_\perp}\left(1 - \frac{M}{p_\perp}\right).\tag{8}$$

We further form bottom to charm $1 - R_{AA}$ ratio, so that a common factor $\frac{2k}{p_\perp}$ is canceled, leading to

$$\frac{1 - R_{AA}^b}{1 - R_{AA}^c} \simeq \frac{1 - \frac{M_b}{p_\perp}}{1 - \frac{M_c}{p_\perp}}.\tag{9}$$

Thus, we obtain that the $1 - R_{AA}$ ratio for heavy flavor is surprisingly simple, depends only on the mass and momentum of heavy quarks, and is independent of the considered centrality.

To test the centrality independence, we go back to Fig. 2. We see that *total* and *collisional* $1 - R_{AA}$ bottom to charm ratios are nearly indistinguishable regardless of the centrality bin; i.e., as predicted, they do not depend on the collision centrality.

Finally, in Fig. 4, DREENA-C [35] predictions of *total* $1 - R_{AA}$ bottom to charm ratios are compared with our analytical estimate, presented on the right-hand side of Eq. (9). From this figure, we observe a good agreement between our predictions and $\frac{1 - M_b/p_\perp}{1 - M_c/p_\perp}$ for all considered centralities. This implies the validity of the analysis presented here. A small disagreement could be attributed to the fact that our estimate originates only from the collisional energy loss/suppression expression and is in agreement with Fig. 2.

Furthermore, Fig. 4 also provides experimental CMS Collaboration data [68,69] for the $1 - R_{AA}$ ratio between
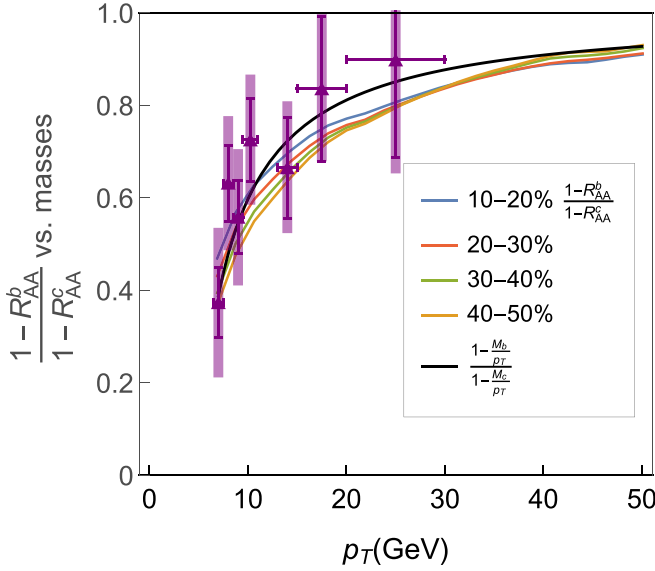
FIG. 4. Quantifying the mass hierarchy in collisional energy loss. $1 - R_{AA}$ bottom to charm ratios for *total* suppression at 10–20% (blue curve), 20–30% (red curve), 30–40% (green curve), and 40–50% (orange curve) as a function of $p_\perp$. The predictions are generated within our full-fledged DREENA-C [35] suppression numerical procedure and compared with the $1 - R_{AA}$ ratio of nonprompt J/ψ at 30–100% (CMS [68]) and average D^0, D^+, D^{*+} at 30–50% (ALICE [69]) 5.02 TeV Pb+Pb collisions (purple triangles). The black curve corresponds to the extracted mass dependence (see Eq. (9)).

nonprompt J/ψ on one side, and average D mesons on the other side. Due to the lack of experimental data in the same centrality bins for b and c probes at 5.02 TeV Pb+Pb collisions, and for consistency throughout the paper, we choose overlapping bins: 30–100% for nonprompt J/ψ, while 30–50% for average D mesons. From this figure, we observe qualitatively and quantitatively good agreement between (i) the data and our predictions, supporting the validity of the DREENA-C framework used in this study, and (ii) the data and our analytical mass estimate, confirming the adequacy of the proposed observable given by Eq. (9), and justifying the applied approximations (see the Appendix). As the error bars are quite large, our study also implies a need for higher precision data for a more satisfactory test of the proposed observable. Furthermore, suppression measurements for both B (or nonprompt J/ψ) and D mesons in the same centrality bins are needed for extracting the mass hierarchy in collisional energy loss from the data.

IV. CONCLUSIONS AND OUTLOOK

One of the inherent characteristics of parton's energy loss is the apparent flavor dependence. Inspired by the dead-cone effect [16] in radiative energy loss and experimentally observed [15] mass ordering in nonprompt J/ψ (B) and D meson suppressions, we addressed the mass hierarchy in heavy flavor suppression. We found that the $1 - R_{AA}$ ratio for heavy flavor reflects the mass hierarchy in the collisional energy loss, which is a nontrivial and important result.

While the dead-cone effect is extensively studied within different radiative energy loss models [9,29–32], the mass hierarchy in collisional energy loss was not previously addressed. To our knowledge, no direct relationship between collisional energy loss and heavy quark mass is established. To this end, the analytical results provided here yielded a simple relation between collisional suppression/energy loss and heavy quark mass. Also, through joint numerical and analytical analysis within our DREENA framework [35], we proposed a novel observable for straightforwardly extracting the mass hierarchy in collisional energy loss through heavy flavor data, to be more rigorously tested by future high-precision experiments. It is based on one of the most common jet quenching observables, the high-$p_\perp$ R_{AA}, and is independent of the collision centrality, collision system (size), and collision energy, and therefore has general applicability for both RHIC and LHC.

As an outlook, the analysis provides specific guidelines on where future experimental efforts regarding this aim should be focused. For instance, the mass hierarchy is more pronounced at lower $p_\perp$. This momentum region is experimentally accessible for both RHIC and LHC in the upcoming high-luminosity experiments, so data from both experiments can be used to test this observable. Furthermore, it is undoubtedly useful to provide B meson suppression data. Finally, the suppression measurement of both B (or nonprompt J/ψ, nonprompt D) and D mesons in the same centrality bins would be beneficial for readily extracting mass hierarchy in collisional energy loss from the data.

APPENDIX: APPROXIMATION OF COLLISIONAL ENERGY LOSS AND $1 - R_{AA}$

In this Appendix, we first simplify the analytically tractable collisional energy loss from [67], by assuming $M/p_\perp \ll 1$. We start from

$$\frac{\Delta E_{\text{coll}}}{E} \sim \frac{1}{E v^2}\left(v + \frac{v^2 - 1}{2} \ln \frac{1+v}{1-v}\right), \quad \text{(A1)}$$

where $v = p_\perp/\sqrt{p_\perp^2 + M^2}$ denotes magnitude of the velocity of initial parton ($\vec{v}$). We Taylor expand Eq. (A1) for $M/p_\perp \ll 1$. Starting from $v \simeq 1 - \frac{M^2}{2p_\perp^2}$ ($\frac{1}{(1+x)^{\frac{1}{2}}} \simeq 1 - \frac{x}{2}$), first we obtain

$$\frac{\Delta E_{\text{coll}}}{E} \sim \frac{1}{p_\perp} \frac{1}{\sqrt{1 + \frac{M^2}{p_\perp^2}}}\left(1 + \frac{M^2}{p_\perp^2}\right)$$
$$\times \left[1 - \frac{M^2}{2p_\perp^2} - \frac{M^2}{2p_\perp^2\left(1 + \frac{M^2}{p_\perp^2}\right)} \ln\left(\frac{4p_\perp^2}{M^2} - 1\right)\right].$$
$$\text{(A2)}$$

To further simplify the above expression, we frequently use the same Taylor expansion $(1 + x)^{-n} \simeq 1 - nx$, as well as

$4p_\perp^2/M^2 \gg 1$, while keeping the leading terms in $M/p_\perp$ expansion. Thus, Eq. (A2) reduces to

$$\frac{\Delta E_{\text{coll}}}{E} \sim \frac{1}{p_\perp}\left(1 - \frac{M^2}{p_\perp^2}\ln\frac{2p_\perp}{M}\right). \tag{A3}$$

Here we encounter nontrivial term $x^2 \ln x$, where $x = \frac{M}{p_\perp}$, for which we are seeking the approximation for small x. We start from the similar expression $x \ln x$, and apply the trick of raising the expression into the exponent

$$e^{x \ln x} = x^x, \tag{A4}$$

where we use the logarithm rules. Note, however, that $\lim_{x\to0} x \ln x = \lim_{x\to0}\frac{\ln x}{1/x} = \lim_{x\to0}\frac{1/x}{-1/x^2} = 0$, where we applied L'Hôpital's rule [70]. Since the exponent in Eq. (A4) is close to zero, we may Taylor expand the left-hand side of this equation, which leads to $x \ln (x) \simeq x^x - 1$. Likewise,

$$x^2 \ln (x) \simeq x^{x+1} - x. \tag{A5}$$

By substituting Eq. (A5) in Eq. (A3) we obtain

$$\frac{\Delta E_{\text{coll}}}{E} \sim \frac{1}{p_\perp}\left[1 - \frac{M^2}{p_\perp^2}\ln 2 + \left(\frac{M}{p_\perp}\right)^{\frac{M}{p_\perp}+1} - \frac{M}{p_\perp}\right]. \tag{A6}$$

Next we substitute Eq. (A6) in Eq. (5) resulting in

$$1 - R_{AA} \sim 2k\frac{1}{\sqrt{p_\perp^2 + M^2}}$$
$$\times \left[1 - \frac{M^2}{p_\perp^2}\ln 2 + \left(\frac{M}{p_\perp}\right)^{\frac{M}{p_\perp}+1} - \frac{M}{p_\perp}\right]$$
$$= \frac{2k}{p_\perp}\left[1 - \frac{M^2}{p_\perp^2}\left(\ln 2 + \frac{1}{2}\right) + \left(\frac{M}{p_\perp}\right)^{\frac{M}{p_\perp}+1} - \frac{M}{p_\perp}\right], \tag{A7}$$

where in the second line of this equation, we again utilized $\frac{1}{(1+x^2)^{\frac{1}{2}}} \simeq 1 - \frac{x^2}{2}$.

This expression can be further simplified, since we explicitly checked that the second and third terms in Eq. (A7), on one side, are of an opposite sign, and that their sum is much smaller compared to the remaining terms on the other side. Finally, we obtain a simple proportionality:

$$1 - R_{AA} \sim \frac{2k}{p_\perp}\left(1 - \frac{M}{p_\perp}\right). \tag{A8}$$

[1] M. Gyulassy and L. McLerran, Nucl. Phys. A **750**, 30 (2005).
[2] E. V. Shuryak, Nucl. Phys. A **750**, 64 (2005); Rev. Mod. Phys. **89**, 035001 (2017).
[3] C. V. Johnson and P. Steinberg, Phys. Today **63**(5), 29 (2010).
[4] B. Jacak and P. Steinberg, Phys. Today **63**(5), 39 (2010).
[5] J. D. Bjorken, Report No. FERMILAB-PUB-82-059-THY, 1982 (unpublished), p. 287.
[6] J. Adams *et al.* (STAR Collaboration), Phys. Rev. Lett. **91**, 072304 (2003); C. Adler *et al.* (STAR Collaboration), *ibid.* **90**, 082302 (2003).
[7] B. G. Zakharov, JETP Lett. **70**, 176 (1999); **73**, 49 (2001).
[8] R. Baier, Y. Dokshitzer, A. Mueller, S. Peigne, and D. Schiff, Nucl. Phys. B **484**, 265 (1997).
[9] N. Armesto, C. A. Salgado, and U. A. Wiedemann, Phys. Rev. D **69**, 114003 (2004).
[10] C. A. Salgado and U. A. Wiedemann, Phys. Rev. D **68**, 014008 (2003).
[11] M. Gyulassy, P. Levai, and I. Vitev, Nucl. Phys. B **594**, 371 (2001).
[12] P. B. Arnold, G. D. Moore, and L. G. Yaffe, J. High Energy Phys. 06 (2002) 030.
[13] X. N. Wang and X. F. Guo, Nucl. Phys. A **696**, 788 (2001).
[14] A. Majumder and C. Shen, Phys. Rev. Lett. **109**, 202301 (2012).
[15] A. M. Sirunyan *et al.* (CMS Collaboration), Phys. Lett. B **782**, 474 (2018).
[16] Y. L. Dokshitzer and D. E. Kharzeev, Phys. Lett. B **519**, 199 (2001).
[17] G. D. Moore and D. Teaney, Phys. Rev. C **71**, 064904 (2005).
[18] B. Svetitsky, Phys. Rev. D **37**, 2484 (1988).
[19] P. B. Gossiaux and J. Aichelin, J. Phys. G **36**, 064028 (2009).
[20] H. van Hees and R. Rapp, Phys. Rev. C **71**, 034907 (2005); H. van Hees, V. Greco, and R. Rapp, *ibid.* **73**, 034913 (2006).

[21] Y. Akamatsu, T. Hatsuda, and T. Hirano, Phys. Rev. C **79**, 054907 (2009).
[22] D. Molnar, Eur. Phys. J. C **49**, 181 (2007).
[23] S. Wicks, W. Horowitz, M. Djordjevic, and M. Gyulassy, Nucl. Phys. A **784**, 426 (2007).
[24] M. Djordjevic, Phys. Rev. C **74**, 064907 (2006).
[25] B. Blagojevic and M. Djordjevic, J. Phys. G **42**, 075105 (2015).
[26] M. H. Thoma, Phys. Lett. B **273**, 128 (1991).
[27] M. G. Mustafa, Phys. Rev. C **72**, 014905 (2005).
[28] M. G. Mustafa and M. H. Thoma, Acta Phys. Hung. A **22**, 93 (2005).
[29] M. Djordjevic and M. Gyulassy, Nucl. Phys. A **733**, 265 (2004).
[30] B. W. Zhang, E. Wang, and X. N. Wang, Phys. Rev. Lett. **93**, 072301 (2004).
[31] M. Djordjevic and U. Heinz, Phys. Rev. C **77**, 024905 (2008).
[32] M. Djordjevic, Phys. Lett. B **763**, 439 (2016).
[33] R. Abir, C. Greiner, M. Martinez, M. G. Mustafa, and J. Uphoff, Phys. Rev. D **85**, 054012 (2012).
[34] R. Abir, U. Jamil, M. G. Mustafa, and D. K. Srivastava, Phys. Lett. B **715**, 183 (2012).
[35] D. Zigic, I. Salom, J. Auvinen, M. Djordjevic and M. Djordjevic, J. Phys. G **46**, 085101 (2019).
[36] D. Zigic, I. Salom, J. Auvinen, M. Djordjevic, and M. Djordjevic, Phys. Lett. B **791**, 236 (2019).
[37] J. D. Bjorken, Phys. Rev. D **27**, 140 (1983).
[38] D. Zigic, I. Salom, J. Auvinen, P. Huovinen and M. Djordjevic, arXiv:2110.01544.
[39] Z. B. Kang, I. Vitev, and H. Xing, Phys. Lett. B **718**, 482 (2012); R. Sharma, I. Vitev, and B. W. Zhang, Phys. Rev. C **80**, 054902 (2009).
[40] M. Djordjevic, Phys. Rev. C **80**, 064909 (2009); M. Djordjevic and U. Heinz, Phys. Rev. Lett. **101**, 022302 (2008).

[41] M. Djordjevic and M. Djordjevic, Phys. Lett. B **734**, 286 (2014).

[42] M. Gyulassy, P. Levai, and I. Vitev, Phys. Lett. B **538**, 282 (2002).

[43] A. Dainese, Eur. Phys. J. C **33**, 495 (2004).

[44] M. Djordjevic, M. Djordjevic, and B. Blagojevic, Phys. Lett. B **737**, 298 (2014).

[45] M. Djordjevic, M. Gyulassy, R. Vogt, and S. Wicks, Phys. Lett. B **632**, 81 (2006).

[46] M. Djordjevic, Phys. Rev. Lett. **112**, 042302 (2014).

[47] M. Djordjevic and M. Djordjevic, Phys. Rev. C **90**, 034910 (2014).

[48] J. I. Kapusta, *Finite-Temperature Field Theory* (Cambridge University Press, Cambridge, 1989).

[49] G. Y. Qin, J. Ruppert, C. Gale, S. Jeon, G. D. Moore, and M. G. Mustafa, Phys. Rev. Lett. **100**, 072301 (2008).

[50] M. Djordjevic, Nucl. Phys. A **783**, 197 (2007).

[51] M. Djordjevic, Phys. Lett. B **709**, 229 (2012).

[52] B. Blagojevic, M. Djordjevic and M. Djordjevic, Phys. Rev. C **99**, 024901 (2019).

[53] M. Djordjevic, Phys. Rev. C **85**, 034904 (2012).

[54] M. Djordjevic, B. Blagojevic, and L. Zivkovic, Phys. Rev. C **94**, 044908 (2016).

[55] M. Djordjevic and M. Djordjevic, Phys. Rev. C **92**, 024918 (2015).

[56] V. Khachatryan *et al.* (CMS Collaboration), J. High Energy Phys. 04 (2017) 039; S. Acharya *et al.* (ALICE Collaboration), *ibid.* 11 (2018) 013

[57] A. Nakamura, T. Saito, and S. Sakai, Phys. Rev. D **69**, 014506 (2004).

[58] Y. Maezawa, S. Aoki, S. Ejiri, T. Hatsuda, N. Ishii, K. Kanaya, N. Ukita, and T. Umeda (WHOT-QCD Collaboration), Phys. Rev. D **81**, 091501(R) (2010).

[59] T. Lang, H. van Hees, G. Inghirami, J. Steinheimer, and M. Bleicher, Phys. Rev. C **93**, 014901 (2016).

[60] P. B. Gossiaux, J. Aichelin, T. Gousset, M. Nahrgang, V. Ozvenchuk, and K. Werner, Nucl. Phys. A **931**, 581 (2014).

[61] R. S. Kolevatov, arXiv:0812.0691; R. Kolevatov and U. A. Wiedemann, arXiv:0812.0270.

[62] A. Ayala, J. Magnin, L. M. Montano, and E. Rojas, Phys. Rev. C **77**, 044904 (2008).

[63] M. Djordjevic, D. Zigic, M. Djordjevic, and J. Auvinen, Phys. Rev. C **99**, 061902(R) (2019).

[64] T. Renk, Phys. Rev. C **85**, 044903 (2012).

[65] D. Molnar and D. Sun, Nucl. Phys. A **932**, 140 (2014); **910-911**, 486 (2013).

[66] R. Baier, Y. L. Dokshitzer, A. H. Mueller, and D. Schiff, J. High Energy Phys. 09 (2001) 033.

[67] M. H. Thoma and M. Gyulassy, Nucl. Phys. B **351**, 491 (1991).

[68] A. M. Sirunyan *et al.* (CMS Collaboration), Eur. Phys. J. C **78**, 509 (2018).

[69] S. Acharya *et al.* (ALICE Collaboration), J. High Energy Phys. 10 (2018) 174.

[70] *Handbook of Mathematical Functions with Formulas, Graphs, and Mathematical Tables*, edited by M. Abramowitz and I. A. Stegun (Dover, New York, 1972), p. 13.

Understanding Infection Progression under Strong Control Measures through Universal COVID-19 Growth Signatures

Magdalena Djordjevic,* Marko Djordjevic,* Bojana Ilic, Stefan Stojku, and Igor Salom

Widespread growth signatures in COVID-19 confirmed case counts are reported, with sharp transitions between three distinct dynamical regimes (exponential, superlinear, and sublinear). Through analytical and numerical analysis, a novel framework is developed that exploits information in these signatures. An approach well known to physics is applied, where one looks for common dynamical features, independently from differences in other factors. These features and associated scaling laws are used as a powerful tool to pinpoint regions where analytical derivations are effective, get an insight into qualitative changes of the disease progression, and infer the key infection parameters. The developed framework for joint analytical and numerical analysis of empirically observed COVID-19 growth patterns can lead to a fundamental understanding of infection progression under strong control measures, applicable to outbursts of both COVID-19 and other infectious diseases.

COVID-19 pandemic introduced unprecedented worldwide social distancing measures.[1] While interventions such as quarantine or vaccination have been extensively studied in quantitative epidemiology, effects of social distancing are not well understood,[2–4] and when addressed, they have been studied only numerically. Unique opportunity to understand these effects has been provided by COVID-19 tracing through confirmed case counts, active cases and fatalities, in a variety of countries with different demographic and environmental conditions.[5,6] We here show that focusing on analytical and numerical derivations in distinct epidemics growth regimes, is

a novel and effective approach in revealing infection progression mechanisms that may be a valuable alternative to detailed numerical simulations.

We start by introducing our COVID-19 dynamics model. We then extract COVID-19 count data[7] and select those countries that systematically trace not only confirmed cases and fatalities, but also active cases (Andorra, Austria, Czechia, Croatia, Cuba, Germany, Israel, New Zealand, Switzerland and Turkey), which allows tight constraint of numerical analysis. We observe three characteristic growth regimes in confirmed case counts, show that our model is well constrained by these regimes for a wide range of countries, and provide an intuitive explanation behind the emergence of such regimes. Our analytical results

for the characteristic (inflection and maximum) points of the infective curve will allow to i) explain the nearly constant value of the scaling exponent in the superlinear regime of confirmed counts; ii) understand the relation between the duration of this regime and strength of social distancing; iii) pinpoint changes in the reproduction number from outburst to extinguishing the infection, and iv) constrain the main parameter quantifying the effect of social distancing by analyzing scaling of the infection growth with time in the sublinear regime. The obtained constraints provide a basis for successful analysis of countries that did not continuously track the active cases (here demonstrated for France, Italy, Spain, United Kingdom, and Serbia). We will finally present the key infection parameters inferred through combined analytical and numerical analysis.

We develop a mechanistic model (nonlinear and nonhomogeneous), which takes into account gradual introduction of social distancing (as relevant for most countries' response), in addition to other important infection progression mechanisms. We start from standard compartments for epidemiological models, that is, susceptible (S), exposed (E), infective (I), and recovered (R).[2–4] To account for social distancing and observable quantities, we introduce additional compartments: protected (P)—where individuals effectively move from susceptible category due to social distancing; total number of diagnosed (confirmed and consequently quarantined) cases (D), active cases (A), and fatalities (F). D, A, and F correspond to directly observable (measured) quantities, but are indirect observables of I, as only part of infective individuals gets diagnosed, due to a large number of mild/asymptomatic cases.[8]

Dr. M. Djordjevic, Dr. B. Ilic, S. Stojku, Dr. I. Salom
Institute of Physics Belgrade
University of Belgrade
Belgrade 11080, Serbia
E-mail: magda@ipb.ac.rs

Prof. M. Djordjevic
Quantitative Biology Group
Faculty of Biology
University of Belgrade
Belgrade 11000, Serbia
E-mail: dmarko@bio.bg.ac.rs

The ORCID identification number(s) for the author(s) of this article can be found under https://doi.org/10.1002/gch2.202000101.

**ADVANCED
SCIENCE NEWS**

www.advancedsciencenews.com
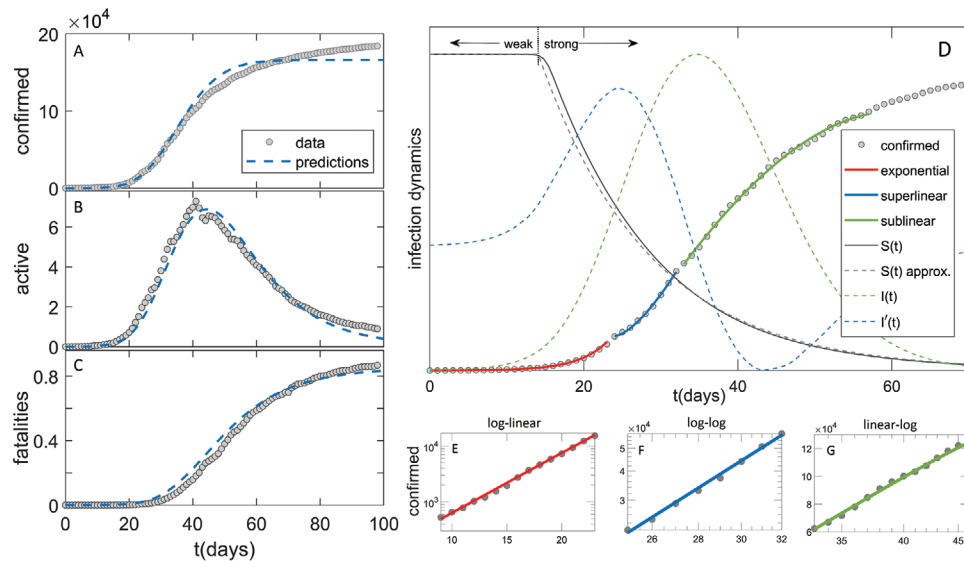
**Global
Challenges**

www.global-challenges.com

Figure 1. Comparison of the model (dashed blue curves) with the data in the case of Germany (grey circles) for A) confirmed case counts, B) active cases, C) fatalities. D) Exponential, superlinear, and sublinear fit to confirmed case data, is shown. Arrows "weak" and "strong" indicate, respectively, the regions with a small and large magnitude of social distancing. The full grey curve denotes susceptibles ($S(t)$), where the dashed grey curve shows an approximation to $S(t)$. The dashed green curve denotes the number of infectious cases ($I(t)$), where the dashed blue curve is $I'(t)$, whose maxima indicate $I(t)$ inflection points. The confirmed case counts in the three regimes are shown on E) log–linear, F) log–log and G) linear–log scale.

We implement the model deterministically, as COVID-19 count numbers are very high wherever reasonable testing capacities are employed. This makes model analytically tractable, and allows robust parameter inference through combination of analytically derived expressions and tightly constrained numerical analysis, as we show below. Our analysis is applied separately to each country, as the effect of social distancing, initial numbers of infected and exposed cases, diagnosis/detection efficiency and transmission rates may be different. However, within a given country, we do not take into account different heterogeneities–demographic, spatial, population activity, or seasonality effects.[2,9,10] Alternatively, global dynamical properties of the outbreak can be analyzed in a probabilistic framework employing partial differential equations in an age-structured model.[11,12] These can readily be included in our model, but would lead to model structure which is not analytically tractable, so these extensions are left for future work.

Given this, the model equations are:

$$dS/dt = -\beta IS/N - dP/dt; \quad dP/dt = \alpha/(1+(t_0/t)^n)S \quad (1)$$

$$dE/dt = \beta IS/N - \sigma E; \quad dI/dt = \sigma E - \gamma I - \varepsilon\delta I; \quad dR/dt = \gamma I \quad (2)$$

$$dD/dt = \varepsilon\delta I; \quad dA/dt = \varepsilon\delta I - hA - mA; \quad dF/dt = mA \quad (3)$$

where N is the total population number; β-the transmission rate; σ-inverse of the latency period; γ-inverse of the infectious period; δ-inverse of the detection/diagnosis period; ε-detection efficiency; h—the recovery rate; m-the mortality rate. Social distancing is included through Equation (1) (second equation), which represents the rate at which the

population moves (on average) from susceptible to protected category. The term $\frac{\alpha}{1+(t_0/t)^n}$ corresponds to a sigmoidal dependence (similar to Fermi–Dirac function, in quantitative biology known as the Hill function[13]). Time t_0 determines the half-saturation, so that well before t_0 the social distancing is negligible, while well after t_0 the rate of transition to the protected category approaches α. Parameter n (the Hill constant) determines how rapidly the social distancing is introduced, that is, large n leads to rapid transition from OFF to ON state, and vice versa.[13] Equation (3) considers that only a fraction of the infected is diagnosed, so that $\varepsilon\delta I$ takes into account the diagnosis and the subsequent quarantine process.

To make the problem analytically tractable, we approximate the Hill function in the first relation of Equation (1) by unit step function, so that after t_0 the second term in Equation (1) becomes $-\alpha S$ and dominates over the first term, that is, $S(t) \approx e^{-\alpha t}$. We checked that this approximation agrees well with full-fledged numerical simulations (**Figure 1**D and Supporting Information). In all comparisons with analytical results, numerical analysis is done with the full model, allowing an independent check of both analytical derivations and employed approximations. Under this assumption, Equations (1) and (2) reduce to:

$$\frac{d^2 I(t)}{dt^2} + (\gamma + \varepsilon\delta + \sigma)\frac{dI(t)}{dt} = \sigma\left\{\beta[\theta(t_0-t) + e^{-(t-t_0)\alpha}\theta(t-t_0)] - (\gamma+\varepsilon\delta)\right\}I(t)$$

$$(4)$$

We next introduce two time regions: I) $t \leq t_0$ and II) $t > t_0$ and solve Equations (4) separately within these regions, where corresponding solutions are denoted as $I_I(t)$ and $I_{II}(t)$. As in the above expressions $\gamma + \varepsilon\delta$ always appear together, we further denote $\gamma + \varepsilon\delta \rightarrow \gamma$.

**ADVANCED
SCIENCE NEWS**

www.advancedsciencenews.com

**Global
Challenges**

www.global-challenges.com

For $I_1(t)$, we take $I(t=0) \equiv I_0$, and restrict to dominant (positive) Jacobian eigenvalue, leading to the exponential regime:

$$I_1(t) = I_0 e^{\frac{1}{2}[-(\gamma+\sigma)+\sqrt{(\gamma-\sigma)^2+4\beta\sigma}]t} \tag{5}$$

By shifting $t - t_0 \to t$, $I_{II}(t)$ is determined by

$$\frac{d^2 I_{II}(t)}{dt^2} + (\gamma+\sigma)\frac{dI_{II}(t)}{dt} = \sigma(\beta e^{-\alpha t} - \gamma)I_{II}(t) \tag{6}$$

Equation (6) is highly nontrivial, due to variable coefficient $(\sigma\beta e^{-\alpha t})$. By substituting variable $t \to x = \frac{-2i\sqrt{\beta\sigma}}{\alpha}e^{-\frac{\alpha t}{2}}$ it can be shown that Equation (6) reduces to transformed form of Bessel differential equation:[14]

$$x^2\frac{d^2\gamma}{dx^2} + (1-2\alpha_1)x\frac{d\gamma}{dx} + (\beta_1^2\gamma_1^2 x^{2\gamma_1} + \alpha_1^2 - \nu^2\gamma_1^2)\gamma = 0 \tag{7}$$

whose general solution for noninteger ν is given by:

$$\gamma(x) = x^{\alpha_1}\left[C_1 J(\nu, \beta_1 x^{\gamma_1}) + C_2 J(-\nu, \beta_1 x^{\gamma_1})\right] \tag{8}$$

where $J(\nu, x)$ represents Bessel function of the first kind, and C_1, C_2 are arbitrary constants. In our case $\alpha_1 = \frac{\gamma+\sigma}{\alpha}$, $\gamma_1 = \beta_1 = 1$, while $\nu = \frac{\gamma-\sigma}{\alpha}$ is indeed noninteger. If we return to t variable, taking into account the following relation between standard and modified ($I(\nu, x)$) Bessel functions of the first kind:[15,16] $I(\nu, x) = i^{-\nu}J(\nu, ix)$, the general solution of Equation (6) reads:

$$I_{II}(t) = \left(\frac{\beta\sigma}{\alpha^2}e^{-\alpha t}\right)^{\frac{\gamma+\sigma}{2\alpha}}\left\{C_1(-1)^{\frac{\gamma}{\alpha}}I\left(\frac{\gamma-\sigma}{\alpha}, \frac{2\sqrt{e^{-\alpha t}\beta\sigma}}{\alpha}\right)\Gamma\left(1+\frac{\gamma-\sigma}{\alpha}\right)\right.$$
$$\left.+C_2(-1)^{\frac{\sigma}{\alpha}}I\left(-\frac{\gamma-\sigma}{\alpha}, \frac{2\sqrt{e^{-\alpha t}\beta\sigma}}{\alpha}\right)\Gamma\left(1-\frac{\gamma-\sigma}{\alpha}\right)\right\} \tag{9}$$

To determine C_1, C_2, we use the following boundary conditions: $I_{II}(0) = I_1(t_0)$ and $I_{II}'(0) = I_1'(t_0)$, where the first derivative in region II has the following expression:

$$I_{II}'(0) = \left(\frac{\beta\sigma}{\alpha^2}\right)^{\frac{\gamma+\sigma}{2\alpha}}\left\{C_1(-1)^{\frac{\alpha+\gamma}{\alpha}}\Gamma\left(1+\frac{\gamma-\sigma}{\alpha}\right)\right.$$
$$\left[\gamma I\left(\frac{\gamma-\sigma}{\alpha}, \frac{2\sqrt{\beta\sigma}}{\alpha}\right) + \sqrt{\beta\sigma}I\left(1+\frac{\gamma-\sigma}{\alpha}, \frac{2\sqrt{\beta\sigma}}{\alpha}\right)\right]$$
$$+C_2(-1)^{\frac{\alpha+\sigma}{\alpha}}\Gamma\left(1-\frac{\gamma-\sigma}{\alpha}\right) \tag{10}$$
$$\left.\left[\sigma I\left(-\frac{\gamma-\sigma}{\alpha}, \frac{2\sqrt{\beta\sigma}}{\alpha}\right) + \sqrt{\beta\sigma}I\left(1-\frac{\gamma-\sigma}{\alpha}, \frac{2\sqrt{\beta\sigma}}{\alpha}\right)\right]\right\}$$

In obtaining the expression above, the following identities were frequently used:[15,16]

$$\frac{dI(\nu, x)}{dx} = I(\nu-1, x) - \frac{\nu}{x}I(\nu, x); \quad I(\nu-1, x) - I(\nu+1, x) = \frac{2\nu I(\nu, x)}{x} \tag{11}$$

After derivations, where the following relation[16]

$$I(\nu+1, x)I(-\nu, x) - I(\nu, x)I(-\nu-1, x) = \frac{2\sin(\pi\nu)}{\pi x} \tag{12}$$

together with $\sin((\nu\pm 1)\pi) = -\sin(\nu\pi)$ and the identity relating modified Bessel function of the first and second kind $K(\nu, x) = \frac{\pi}{2}\frac{I(-\nu, x) - I(\nu, x)}{\sin\nu\pi}$ are used,[15,16] we finally obtain a surprisingly simple result:

$$I_{II}(t) = I_1(t_0)e^{-\frac{\gamma+\sigma}{2}t}\frac{K\left(\frac{\gamma-\sigma}{\alpha}, \frac{2\sqrt{e^{-\alpha t}\beta\sigma}}{\alpha}\right)}{K\left(\frac{\gamma-\sigma}{\alpha}, \frac{2\sqrt{\beta\sigma}}{\alpha}\right)} \tag{13}$$

where $K(\nu, x)$ is the modified Bessel function of the second kind.

At maximum and inflection points, $I_{II}' = 0$ and $I_{II}'' = 0$, respectively. After extensive simplification of the results, this leads to ($\gamma = R_{0,\text{free}}e^{-\alpha t}$, where $R_{0,\text{free}} = \beta/\gamma$ is the basic reproduction number in the absence of social distancing:[6,17])

$$\sqrt{\gamma}K\left(\frac{\gamma-\sigma}{\alpha}+1, \frac{2\sqrt{\gamma\sigma}}{\alpha}\sqrt{\gamma}\right) = \sqrt{\frac{\gamma}{\sigma}}K\left(\frac{\gamma-\sigma}{\alpha}, \frac{2\sqrt{\gamma\sigma}}{\alpha}\sqrt{\gamma}\right) \tag{14}$$

$$\sqrt{\gamma}K\left(\frac{\gamma-\sigma}{\alpha}+1, \frac{2\sqrt{\gamma\sigma}}{\alpha}\sqrt{\gamma}\right) = \sqrt{\frac{\gamma}{\sigma}}\frac{\left(\frac{\gamma}{\sigma}+\gamma\right)}{\left(\frac{\gamma}{\sigma}+1\right)}K\left(\frac{\gamma-\sigma}{\alpha}, \frac{2\sqrt{\gamma\sigma}}{\alpha}\sqrt{\gamma}\right) \tag{15}$$

Equations (14) and (15) have to be solved numerically, but, as γ and σ are constants, we, interestingly, obtain that solutions will depend only on α. Since, for the analysis of superlinear and sublinear regimes, only the left inflection point and the maximum are important, we will further omit the second solution of Equation (15) (Equation (14) has one solution), and denote $\gamma_i = f_{i1}(\alpha) \equiv f_i(\alpha)$, $\gamma_m = f_m(\alpha)$ (these two solutions are presented as upper and lower curves on **Figure 2**C, respectively), so that the effective reproduction numbers at inflection and maximum points ($R_{e,i}$ and $R_{e,m}$) are:

$$R_{e,i} \equiv R_{0,\text{free}}e^{-\alpha t_i} = f_i(\alpha),$$
$$R_{e,m} \equiv R_{0,\text{free}}e^{-\alpha t_m} = f_m(\alpha). \tag{16}$$

From this follows the length of superlinear regime (between inflection and maximum points):

$$\Delta t \equiv t_m - t_i = \frac{1}{\alpha}\ln\left(\frac{f_i(\alpha)}{f_m(\alpha)}\right) \tag{17}$$

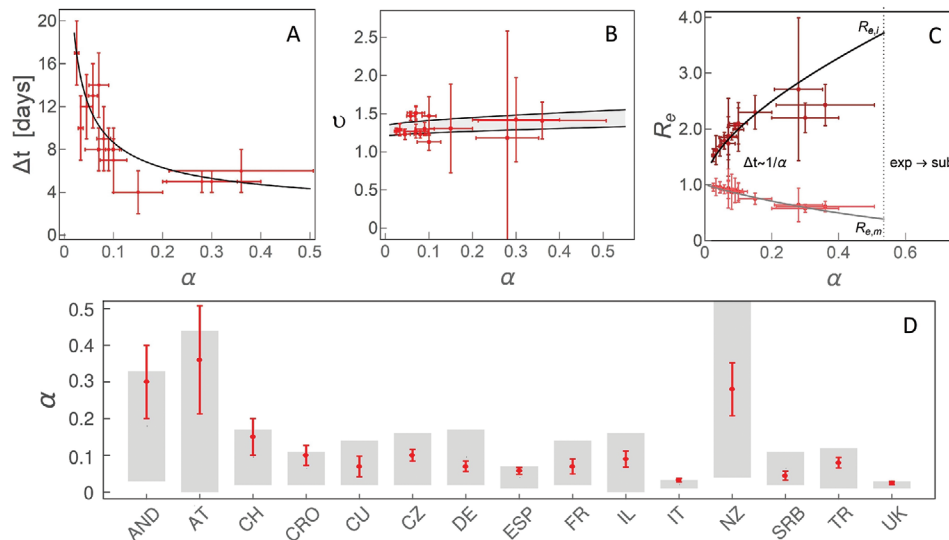We further Taylor expand $I_{II}(t)$ around the inflection point:

Figure 2. The dependence on the effective social distancing strength (α) of A) Δt, the duration of the superlinear regime, B) υ, the scaling exponent of the superlinear regime, C) R_e, effective reproduction number at the left inflection point ($R_{e,i}$) and the maximum ($R_{e,m}$) of $I(t)$. $\Delta t \approx 1/\alpha$ indicates that the time, in which the change from $R_{e,i}$ to $R_{e,m}$ is exhibited, is approximately inversely proportional to α. "exp $\rightarrow$ sub" indicates the region of α where we predict a direct transition from exponential to sublinear growth. D) Comparison of α constrained from analytical derivations (the grey bands) and numerical analysis, with countries indicated on the horizontal axis by their abbreviations. Results obtained by independent numerical analysis are presented by red dots with corresponding errorbars.

$$I_{\mathrm{II}}(t) = I_{\mathrm{I}}(t_0)e^{\frac{\gamma+\sigma}{2}t_i}\frac{K\left(\frac{\gamma-\sigma}{\alpha},\frac{2\sqrt{\gamma\sigma}}{\alpha}\sqrt{f_i(\alpha)}\right)}{K\left(\frac{\gamma-\sigma}{\alpha},\frac{2\sqrt{\beta\sigma}}{\alpha}\right)} \tag{18}$$
$$\left[1-\frac{\gamma\sigma}{\gamma+\sigma}(1-f_i(\alpha))(t-t_i)+\mathcal{O}\left((t-t_i)^2\right)\right]$$

In the superlinear regime $D(t) \approx (t-t_s)^{\upsilon}$, where υ is the scaling exponent and t_s marks the beginning of this regime. By Taylor expanding $D(t)$ around t_i, using Equations (18) and (3):

$$\upsilon = 1 + \frac{1}{k\alpha}\frac{\gamma\sigma}{\gamma+\sigma}[f_i(\alpha)-1]\ln\left(\frac{f_i(\alpha)}{f_m(\alpha)}\right) \tag{19}$$

which is always larger than 1, as expected for the superlinear regime. As t_i is localized toward the beginning of the regime, we estimate $t_i - t_s \approx \frac{\Delta t}{k}$, where $k \approx 3, 4$.

Finally, to provide analytical constrain on α, we Taylor expand $I_{II}(t)$ around the maximum:

$$I_{\mathrm{II}}(t) = I_{\mathrm{I}}(t_0)e^{-\frac{\gamma+\sigma}{2}t_m}\frac{K\left(\frac{\gamma-\sigma}{\alpha},\frac{2\sqrt{\gamma\sigma}}{\alpha}\sqrt{f_m(\alpha)}\right)}{K\left(\frac{\gamma-\sigma}{\alpha},\frac{2\sqrt{\beta\sigma}}{\alpha}\right)} \tag{20}$$
$$\left[1-\frac{\gamma\sigma}{2}(1-f_m(\alpha))(t-t_m)^2+\mathcal{O}\left((t-t_m)^3\right)\right]$$

As $f_m(\alpha) < 0$, we see that the quadratic term in Equation (20) is always negative, that is, $D(t)$ curve enters sublinear regime around maximum of the infection. By fitting $D(t)$

to $c + d(t-t_m) - f(t-t_m)^3$ in this regime, and by using Equation (20) together with Equation (3), we obtain:

$$\frac{f}{d} = \frac{\gamma\sigma}{6}[1-f_m(\alpha)] \tag{21}$$

which allows to directly constrain α.

We first numerically analyze outburst dynamics in the countries that continuously updated[18] three observable categories (D, A, and F). For a large majority of countries active cases were either not tracked or were not continuously updated, so the analysis is done for ten countries listed in the outline above.

In the exponential regime, the analytical closed-form solution is given by Equation (5). From this, and the initial slope of $\ln(D)$ curve (once the number of counts are out of the stochastic regime), β can be directly determined, while the corresponding eigenvector sets the ratio of I_0 to E_0. The intercept of the initial exponential growth of D at $t = 0$ sets the product of I_0 and $\varepsilon\delta$. h and m can also be readily constrained, as from Equation (3), they depend only on integrals of the corresponding counts; here note that $\mathrm{d}(D-A-F)/\mathrm{d}t = hA$. Also,[17,19,20] $\sigma = 1/3$ day^{-1} and $\gamma = 1/4$ day^{-1}, characterize fundamental infectious process, which we assume not to change between different countries.

Only parameters related with the intervention measures ($\alpha, t_0, n, \varepsilon\delta$) are left to be inferred numerically, leading to tightly constrained numerical results. For this, we individually performed joint fit to all three observable quantities (A, D, F) for each country. The errors are estimated through Monte-Carlo[21,22] simulations, assuming that count numbers follow Poisson distribution.

Representative numerical results are shown in Figure 1 for Germany, while other countries are shown in the Supporting

**ADVANCED
SCIENCE NEWS**
www.advancedsciencenews.com

**Global
Challenges**
www.global-challenges.com

Information. In Figure 1A–C (and Supporting Information) we see a good agreement of our numerical analysis with all three classes of the case counts. In Figure 1D, we see sharp transitions between the three growth patterns indicated in the figure: i) exponential growth, observed as a straight line in log–linear plot in Figure 1E; ii) superlinear growth, a straight line in log–log plot in Figure 1F; iii) sublinear growth, a straight line in linear–log plot in Figure 1G.

Transition between the growth patterns can be qualitatively understood from Equation (3), and $I(t)$ curve in Figure 1D. The exponential growth has to break after the inflection point of $I(t)$, that is, once the maximum of its first derivative ($I'(t)$ in Figure 1D) is reached. In the superlinear regime, confirmed counts case ($D(t)$) curve is convex ($D''(t) > 0$), so this regime breaks once $I'(t)$ (dashed blue curve) becomes negative. Equivalently, $D(t)$ curve becomes concave (enters sublinear regime) once the maximum of the $I(t)$ is reached. Note that the growth of $D(t)$ can reemerge if the social distancing measures are alleviated. Our model can account for this by allowing transition from protected back to susceptible category, which is out of the scope of this study, but may improve the agreement with the data at later times (see Figure 1A–C). In addition to this numerical/intuitive understanding, we also showed that we analytically reproduce the emergence of these growth regimes (Equations (6), (14), (15)). Can we also analytically derive the parameters that characterize these regimes?

The exponential regime is straightforward to explain, as described above. The superlinear regime is in between the left inflection point and the maximum of $I(t)$, so that infective numbers grow, but with a decreasing rate. While the derivations are straightforward in the exponential regime, they are highly non-trivial during the subsequent subexponential (superlinear and sublinear) growth. As the superlinear regime spans the region between the left inflection point ($t_i, I''(t_i) = 0$) and the maximum ($t_m, I'(t_m) = 0$), its duration is $\Delta t = t_m - t_i$ given by Equation (17), with $\approx 1/\alpha$ dependence, so that weak measures lead to protracted superlinear growth (see Figure 2A). This tendency is also confirmed by independent numerical analysis in Figure 2A, where for each individual country we numerically infer α and extract the length of the superlinear regime. Therefore, the duration of the superlinear regime indicates the effectiveness of introduced social distancing.

The scaling exponent υ of the superlinear regime is given by Equation (19), and shown in Figure 2B, where we predict that all countries are roughly in the same range of $1.2 < \upsilon < 1.5$ (surprisingly, weakly dependent on α), despite significant differences in the applied measures, demographic and environmental factors. This result is (independently from our model) confirmed from case count numbers (the slope in Figure 1F, and equivalently for other countries, see Figure 2B).

How the effective reproduction number R_e changes during this regime, that is, between the left inflection point and the maximum of $I(t)$? R_e quantifies the average number of secondary cases per infectious case, so that $R_e > 1$ signifies disease outburst, while for $R_e < 1$ the disease starts to be eliminated from the population.[17] The Equation (16) provides expressions for $R_{e,i}$ (at the inflection point) and $R_{e,m}$ (at the maximum). Interestingly, from Figure 2C, we observe that $R_{e,i}$ and $R_{e,m}$

do not depend on $R_{0,\text{free}}$ and are, respectively, significantly larger and smaller than 1, which shows that transition from infection outburst to extinguishing happens during the superlinear growth. Consequently, the steepness of R_e change over the superlinear regime significantly increases (larger change over smaller time interval, see Figure 2C) with the measure strength.

Finally, in the sublinear regime, in a wide vicinity of $I(t)$ maximum (which marks the beginning of the sublinear growth) leading non-linear term of $D(t)$ is cubic ($\approx t^3$, with negative prefactor). This is consistent with the expansion of $I(t)$ around t_m, which has leading negative quadratic (t^2) dependence (see Equations (3) and (20)). The ratio between the prefactors in $D(t)$ expansion is given by Equation (21), from which we see that α can be directly constrained, as shown in Figure 2D. For the ten countries with consistent tracking of $D, A,$ and F, we independently numerically determined α and compared it with analytical results coming from Equation (21), obtaining an excellent agreement between our derivations and numerical results. The obtained α values should be understood as an effective epidemic containment measure—that is, estimating the true result of the introduced measures, which can be used to evaluate the practical effectiveness of the official policies.

To demonstrate how constraining α can aid numerical analysis in the cases when A is not continuously tracked, we next analyze five additional countries listed in the outline above, so that altogether our study covers majority of COVID-19 hotspots, which (at the time of this analysis) are close to saturation in confirmed counts. Furthermore, in the specific cases of UK and Italy, where we analytically obtained both very low and very constrained α ($0.01 < \alpha < 0.04$), we chose five times larger parameter span in α in the numerical analysis, to confirm that these low values are indeed preferred by the exhaustive numerical search. For example, the finally obtained α for Italy (0.033 ± 0.005) and UK (0.025 ± 0.005), together with previously obtained agreements shown in Figure 2A–C, strongly confirm that the observed growth patterns provide invaluable information for successful analysis of the infection progression data.

To further illustrate this, the synergy of analytical derivations and numerical analysis presented above enables us to, directly from the publicly available data, infer key infection parameters necessary to assess epidemics risks (provided in Table S1, Supporting Information). We estimate these parameters by the same model/analysis, for a number of diverse countries, allowing their direct comparison. In **Figure 3**, we show together case fatality rate (CFR), infected fatality rate (IFR) and infection attack rate (AR).[17,24] CFR is the number of fatalities per confirmed cases. CFR can, in principle, be inferred directly from the data, but since different countries are in different phases of infection, we project forward the number of confirmed cases until a saturation is reached for each country, from which we calculate CFR. IFR (crucial parameter for assessing the risks for infection progression under different scenarios) is the number of fatalities per total number of infected cases, which is a genuine model estimate, due to the unknown total number of infected cases. AR (necessary for understanding the virus recurrence risk) is also determined from our model and provides an estimate of the fraction of the total population that got infected and possibly resistant.
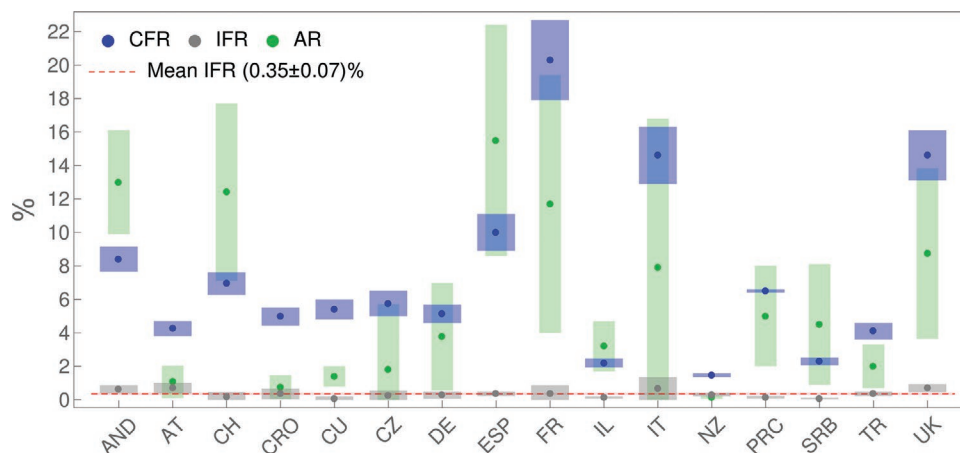
Figure 3. CFR, IFR, and AR, inferred for countries whose abbreviations are indicated on the horizontal axis, are denoted, respectively, by blue, grey, and green dots, with errorbars indicated by corresponding bands. The dashed red horizontal line stands for IFR consistent with a mean value (indicated in the legend). Values for PRC are from ref. [23].

From Figure 3, we see that CFR takes very different values for different countries, from below 2% (New Zealand) to above 20% (France). On the other hand, IFR is consistent with a constant value (the dashed red line in the figure) of $\approx 0.3 - 0.4\%$. In distinction to IFR, AR also takes diverse values for different countries, ranging from $\approx 1\%$ to as high as $\approx 15\%$ (though with large errorbars). Although diverse, these AR values are well bellow the classical herd immunity threshold of 60–70%

To summarize, we here developed a novel quantitative framework through which we showed that: i) The emergence of three distinct growth regimes in COVID-19 case counts can be reproduced both analytically and numerically. ii) Typically, a brief superlinear regime is characterized by a sharp transition from outburst to extinguishing the infection, where effective reproduction number changes from much larger to much smaller than one; more effective measures lead to shorter superlinear growth, and to a steeper change of the effective reproduction number. iii) Scaling exponent of the superlinear regime is surprisingly uniform for countries with diverse environmental and demographic factors and epidemics containment policies; this highly non-trivial empirical result is well reproduced by our model. iv) Scaling prefactors in the sublinear regime contain crucial information for analytically constraining infection progression parameters, so that they can be straightforwardly extracted through numerical analysis. Interestingly, we found that the number of COVID-19 fatalities per total number of infected is highly uniform across diverse analyzed countries, in distinction to other (highly variable) infection parameters, and about twice higher than commonly quoted for influenza (0.3–0.4% compared to 0.1–0.2%), which may be valuable for direct assessment of the epidemics risks.

While state-of-the-art approach in epidemiological modeling uses computationally highly demanding numerical simulations, the results above demonstrate a shift of paradigm toward simpler, but analytically tractable models, that can both explain common dynamical features of the system and be used for straightforward and highly constrained parameter inference. This shift is based on a novel framework that relates universal growth patterns with characteristic points of the infective curve, followed by analytical derivations in the vicinity of these points, in an approach akin to those in a number of

physics problems. The framework presented here can be, in principle, further extended toward, for example, including stochastic effects or different heterogeneities such as age-structure. However, these are non-trivial tasks, and it remains to be seen to what extent the analytical results can be obtained in those more complex models. Overall, as our approach does not depend on any COVID-19 specifics, the developed framework can also be readily applied to potential outbursts of future infections.

Supporting Information

Supporting Information is available from the Wiley Online Library or from the author.

Acknowledgements

Conflict of Interest

The authors declare no conflict of interest.

Data Availability Statement

The data used in this study are openly available in Worldometer at https://www.worldometers.info/coronavirus/, reference number [7]. Parameters inferred through the analysis are available in the supplementary material of this article.

Keywords

**ADVANCED
SCIENCE NEWS**

www.advancedsciencenews.com

Global
Challenges

www.global-challenges.com

[1] WHO report. https://www.who.int/emergencies/diseases/novel-coronavirus-2019/situation.

[2] O. Diekmann, H. Heesterbeek, T. Britton, *Mathematical Tools for Understanding Infectious Disease Dynamics*, Princeton University Press, Princeton, NJ **2012**.

[3] M. Martcheva, *An Introduction to Mathematical Epidemiology*, Springer, Berlin **2015**.

[4] M. J. Keeling, P. Rohani, *Modeling Infectious Diseases in Humans and Animals*, Princeton University Press, Princeton, NJ **2011**.

[5] H. Tian, Y. Liu, Y. Li, C. H. Wu, B. Chen, U. G. Kraemer, B. Li, J. Cai, B. Xu, Q. Yang, B. Wang, P. Yang, Y. Cui, Y. Song, P. Zheng, Q. Wang, O. N. Bjornstad, R. Yang, B. T. Grenfell, O. G. Pybus, C. Dye, *Science* **2020**, *368*, 638.

[6] G. Chowell, L. Sattenspiel, S. Bansal, C. Viboud, *Physics of Life Reviews* **2016**, *18*, 66.

[7] Worldometer **2020**. *COVID-19 Coronavirus Pandemic*. https://www.worldometers.info/coronavirus/ (accessed: June 2020).

[8] M. Day, *BMJ: British Medical Journal* **2020**, *368*, m1165.

[9] G. N. Wong, Z. J. Weiner, A. V. Tkachenko, A. Elbanna, S. Maslov, N. Goldenfeld, *arXiv:200602036*, **2020**.

[10] J. R. Dormand, P. J. Prince, *J. Comput. Appl. Math.* **1980**, *6*, 19.

[11] J. M. Vilar, L. Saiz. medRxiv 2020.11.26.20239434, **2020**.

[12] N. C. Grassly, C. Fraser, *Nat. Rev. Microbiol.* **2008**, *6*, 477.

[13] R. Phillips, J. Kondev, J. Theriot, H. Garcia, *Physical Biology of the Cell*, Garland Science, New York, NY **2012**.

[14] F. Bowman, *Introduction to Bessel Functions*, Dover Publications, New York, NY **1958**.

[15] D. Zwillinger, *Standard Mathematical Tables and Formulae*, CRC Press, Boca Raton, FL **1995**.

[16] M. Abramowitz, T. A. Stegun, *Handbook of Mathematical Functions* (Ed: M. Abramowitz), Dover Publications, New York, NY **1972**.

[17] Y. M. Bar-On, A. I. Flamholz, R. Phillips, R. Milo, *eLife* **2020**, *9*, e57309.

[18] E. Dong, H. Du, L. Gardner, *Lancet Infect. Dis.* **2020**, *20*, 533.

[19] R. Li, S. Pei, B. Chen, Y. Song, T. Zhang, W. Yang, J. Shaman, *Science* **2020**, *368*, 489.

[20] X. He, E. H. Y. Lau, P. Wu, X. Deng, J. Wang, X. Hao, Y. C. Lau, J. Y. Wong, Y. Guan, X. Tan, X. Mo, Y. Chen, B. Liao, W. Chen, F. Hu, Q. Zhang, M. Zhong, Y. Wu, L. Zhao, F. Zhang, B. J. Cowling, F. Li, G. M. Leung, *Nat. Med.* **2020**, *26*, 672.

[21] W. H. Press, B. P. Flannery, S. A. Teukolsky, W. T. Vetterling, *Numerical Recipes: The Art of Scientific Computing*, Cambridge University Press, Cambridge **1986**.

[22] R. W. Cunningham, *Comput. Phys.* **1993**, *7*, 570.

[23] M. Djordjevic, M. Djordjevic, I. Salom, A. Rodic, D. Zigic, O. Milicevic, B. Ilic, *arXiv:2005.09630*, **2020**.

[24] S. Eubank, I. Eckstrand, B. Lewis, S. Venkatramanan, M. Marathe, C. L. Barrett, *Bull. Math. Biol.* **2020**, *82*, 1.

[25] T. Britton, F. Ball, P. Trapman, *arXiv:2005.03085*, **2020**.

[26] F. P. Havers, C. Reed, T. Lim, J. M. Montgomery, J. D. Klena, A. J. Hall, A. M. Fry, D. L. Cannon, C.-F. Chiang, A. Gibbons, I. Krapiunaya, M. Morales-Betoulle, K. Roguski, M. Ata Ur Rasheed, B. Freeman, S. Lester, L. Mills, D. S. Carroll, S. M. Owen, J. A. Johnson, V. Semenova, C. Blackmore, D. Blog, S. J. Chai, A. Dunn, J. Hand, S. Jain, S. Lindquist, R. Lynfield, S. Pritchard, et al., *JAMA Intern. Med.* **2020**, *180*, 1576.

Extracting the temperature dependence in high-$p_\perp$ particle energy loss

Stefan Stojku [ORCID],[1] Bojana Ilic [ORCID],[1] Marko Djordjevic [ORCID],[2] and Magdalena Djordjevic [ORCID][1,*]

[1]*Institute of Physics Belgrade, University of Belgrade, Belgrade, Serbia*
[2]*Faculty of Biology, University of Belgrade, Belgrade, Serbia*

The suppression of high-$p_\perp$ particles is one of the main signatures of parton energy loss during its passing through the quark-gluon plasma medium, and is reasonably reproduced by different theoretical models. However, a decisive test of the reliability of a certain energy-loss mechanism, apart from its path length, is its temperature dependence. Despite its importance and comprehensive dedicated studies, this issue is still awaiting more stringent constraints. To this end, we here propose a novel observable to extract the temperature-dependence exponent of a high-$p_\perp$ particle's energy loss, based on R_{AA}. More importantly, by combining analytical arguments, full-fledged numerical calculations, and comparison with experimental data, we argue that this observable is highly suited for testing the long-standing $\Delta E/E \propto L^2 T^3$ paradigm. The anticipated significant reduction of experimental errors will allow direct extraction of temperature dependence, by considering different centrality pairs in $A + A$ collisions (irrespective of the nucleus size) in the high-$p_\perp$ region. Overall, our results imply that this observable, which reflects the underlying energy-loss mechanism, is very important to distinguish between different theoretical models.

I. INTRODUCTION

The main goal of the ultrarelativistic heavy-ion program [1–4] at the Relativistic Heavy Ion Collider (RHIC) and the Large Hadron Collider (LHC) is inferring the features of the created novel form of matter—quark-gluon plasma (QGP) [5,6]—which provides an insight into the nature of the hottest and densest known medium. Energy loss of rare high-$p_\perp$ partons traversing the medium is considered to be one of the crucial probes [7] of the medium properties, which also had a decisive role in QGP discovery [8]. Comparison of predictions stemming from different energy-loss models with experimental data tests our understanding of the mechanisms underlying the jet-medium interactions, thereby illuminating the QGP properties. Within this, an important goal involves a search for adequate observables for distinguishing the energy-loss mechanisms.

Connected to this, it is known that the temperature (T) dependence of the energy-loss predictions may be related to the underlying energy-loss mechanisms; e.g., pQCD *radiative* energy loss (Baier-Dokshitzer-Mueller-Peigne-Schiff (BDMPS) and Armesto-Salgado-Wiedemann (ASW) [9–11], Gyulassy-Levai-Vitev (GLV) [12], light-cone path integral (LCPI) [13] and Arnold-Moore-Yaffe (AMY) [14], higher-twist (HT) [15], and some of their extensions [16–20]) is typically considered to have cubic T dependence (T^3, stemming from entropy, or energy density dependence), while *collisional* energy loss [7,21–23] is generally considered to be proportional to T^2. Additionally, anti-de Sitter/conformal field

theory (AdS/CFT)-motivated jet-energy-loss models [24,25] display even quartic (T^4) dependence on temperature. The different functional dependences on T found in these models are the results of the considered energy-loss mechanism (elastic or inelastic), different treatment of the QCD medium (finite or infinite size), and inclusion or omission of finite temperature effects (i.e., application of temperature-modified or vacuumlike propagators). Therefore, assessing the accurate temperature dependence is important for disentangling relevant effects for adequate description of leading parton energy loss, and consequently for understanding the QGP properties.

For a comprehensive study on temperature (and path-length) dependence of different energy-loss models we refer the reader to Ref. [18]. However, even this systematic study could not single out local T dependence, as the attempt to simultaneously describe high-$p_\perp$ R_{AA} and v_2 data within these models requires some more rigorous physical justifications. Moreover, the current error bars at the RHIC and the LHC are still too large to resolve between different energy-loss models. Having this in mind, we here propose a novel observable to extract the scaling of a high-$p_\perp$ particle's energy loss on the local temperature. Note that, for extracting the exact value of the temperature-dependence exponent, this new observable relies on the previously extracted value of the path-length dependence coefficient [26]. We expect that this observable will allow direct extraction of T dependence from the data in the upcoming high-luminosity third run at the LHC, where the error bars are expected to notably decrease.

We also propose high-$p_\perp$ $h^\pm$ as the most suitable probe for this paper, as the experimental data for $h^\pm$ R_{AA} are more abundant and with smaller error bars, compared to heavier hadrons for all centrality classes, where this is also expected

to hold in the future. Therefore, in this paper, we concentrate on $h^\pm$ in 5.02-TeV Pb + Pb collisions at the LHC, with the goal to elucidate this new observable, and test its robustness to medium evolution and colliding system size. By combining full-fledged numerical predictions and scaling arguments within our dynamical radiative and elastic energy-loss approach (DREENA) [27,28] framework, this new observable yields the value of the temperature-dependence exponent, which is in accordance with our previous estimate [29]. More importantly, we utilize this observable to question the long-standing $\Delta E/E \propto L^2 T^3$ paradigm, used in a wide range of theoretical models [9–12,15–20].

II. THEORETICAL FRAMEWORK

In this paper, we use our state-of-the-art dynamical energy-loss formalism [30–32], which includes several unique features in modeling jet-medium interactions: (1) calculations within the finite temperature field theory and generalized hard-thermal-loop approach [33] (contrary to many models

which apply vacuumlike propagators [9,10,12,15]), so that infrared divergences are naturally regulated in a highly nontrivial manner; (2) finite size of created QGP; (3) the QCD medium consisting of dynamical (moving) as opposed to static scattering centers, which allows the longitudinal momentum exchange with the medium constituents; (4) both radiative [30,31] and collisional [32] contributions calculated within the same theoretical framework; (5) the inclusion of a finite parton's mass [34], making the formalism applicable to both light and heavy flavor; and (6) the generalization to a finite magnetic mass [35], running coupling [36], and beyond soft-gluon approximation [37]. Note, however, that in Ref. [37] we obtained that the effect of relaxing the soft-gluon approximation on (fractional radiative energy loss and) R_{AA} is negligible, and thus can be omitted without losing the reliability of the obtained results. Therefore, to avoid unnecessary involvement of already complex expressions we here apply their soft-gluon equivalents.

The analytical expression for the single gluon radiation spectrum reads [27,30,35,36]

$$\frac{dN_{\rm rad}}{dx d\tau} = \frac{C_2(G)C_R}{\pi} \frac{1}{x} \int \frac{d^2\mathbf{q}}{\pi} \frac{d^2\mathbf{k}}{\pi} \frac{\mu_E^2(T) - \mu_M^2(T)}{[\mathbf{q}^2 + \mu_E^2(T)][\mathbf{q}^2 + \mu_M^2(T)]} T \alpha_s(ET) \alpha_s\left(\frac{\mathbf{k}^2 + \chi(T)}{x}\right)$$

$$\times \left[1 - \cos\left(\frac{(\mathbf{k} + \mathbf{q})^2 + \chi(T)}{xE^+}\tau\right)\right] \frac{2(\mathbf{k} + \mathbf{q})}{(\mathbf{k} + \mathbf{q})^2 + \chi(T)} \left[\frac{\mathbf{k} + \mathbf{q}}{(\mathbf{k} + \mathbf{q})^2 + \chi(T)} - \frac{\mathbf{k}}{\mathbf{k}^2 + \chi(T)}\right], \quad (1)$$

where $\mathbf{k}$ and $\mathbf{q}$ denote transverse momenta of radiated and exchanged gluons, respectively; $C_2(G) = 3$ and $C_R = 4/3$ ($C_R = 3$) for the quark (gluon) jet; while $\mu_E(T)$ and $\mu_M(T)$ are electric (Debye) and magnetic screening masses, respectively. The temperature-dependent Debye mass [27,38] is obtained by self-consistently solving Eq. (5) from Ref. [27]. α_s is the (temperature-dependent) running coupling [27,36,39], E is

the initial parton energy, while $\chi(T) = M^2 x^2 + m_g^2(T)$, where x is the longitudinal momentum fraction of the initial parton carried away by the emitted gluon. M is the mass of the propagating parton, while the gluon mass is considered to be equal to its asymptotical mass $m_g = \mu_E/\sqrt{2}$ [40].

The analytical expression for collisional energy loss per unit length is given by the following expression [27,32]:

$$\frac{dE_{\rm coll}}{d\tau} = \frac{2C_R}{\pi v^2} \alpha_s(ET) \alpha_s(\mu_E^2(T)) \int_0^\infty n_{\rm eq}(|\vec{\mathbf{k}}|, T) d|\vec{\mathbf{k}}|$$

$$\times \left[\int_0^{|\vec{\mathbf{k}}|/(1+v)} d|\vec{\mathbf{q}}| \int_{-v|\vec{\mathbf{q}}|}^{v|\vec{\mathbf{q}}|} \omega d\omega + \int_{|\vec{\mathbf{k}}|/(1+v)}^{|\vec{\mathbf{q}}|_{\rm max}} d|\vec{\mathbf{q}}| \int_{|\vec{\mathbf{q}}|-2|\vec{\mathbf{k}}|}^{v|\vec{\mathbf{q}}|} \omega d\omega\right]$$

$$\times \left[|\Delta_L(q, T)|^2 \frac{(2|\vec{\mathbf{k}}| + \omega)^2 - |\vec{\mathbf{q}}|^2}{2} + |\Delta_T(q, T)|^2 \frac{(|\vec{\mathbf{q}}|^2 - \omega^2)[(2|\vec{\mathbf{k}}| + \omega)^2 + |\vec{\mathbf{q}}|^2]}{4|\vec{\mathbf{q}}|^4}(v^2|\vec{\mathbf{q}}|^2 - \omega^2)\right], \quad (2)$$

where $n_{\rm eq}(|\vec{\mathbf{k}}|, T) = \frac{N}{e^{|\vec{\mathbf{k}}|/T} - 1} + \frac{N_f}{e^{|\vec{\mathbf{k}}|/T} + 1}$ is the equilibrium momentum distribution [22] including gluons, quarks, and antiquarks. k is the four-momentum of the incoming medium parton, v is the velocity of the initial jet, and $q = (\omega, \vec{\mathbf{q}})$ is the four-momentum of the exchanged gluon. $|\vec{\mathbf{q}}|_{\rm max}$ is provided in Ref. [32], while $\Delta_T(q, T)$ and $\Delta_L(q, T)$ are effective transverse and longitudinal gluon propagators given by Eqs. (3) and (4) from Ref. [27].

Despite the very complicated temperature dependence of Eqs. (1) and (2), in Ref. [29] it was obtained that our dynamical energy-loss formalism [36] (which accommodates

some unique jet-medium effects mentioned above) has an exceptional feature of near linear T dependence. That is, while T^3 dependence for radiative energy loss is widely used [9–12,14–20], from Eq. (1) it is evident that this simplified relation is reproduced with approximations using vacuum gluon propagators (leading to the absence of $m_g(T)$ from the χ expression) and neglecting running coupling. It is straightforward to show that in that case leading T dependence is $\frac{\Delta E_{\rm rad}}{E} \propto \mu_E^2 T \propto T^3$ ($\mu_E \propto T$). However, Eq. (1) clearly demonstrates that a more realistic T dependence is far from cubic, where in Ref. [29] it was shown that asymptotic T dependence

of our full radiative energy loss is between linear and quadratic.

Additionally, commonly overlooked (due to being smaller compared to radiative at high $p_\perp$) collisional energy loss must not be neglected in suppression predictions [41]. Moreover, widely used dominant T^2 dependence of collisional energy loss [7,21–23] can also be shown to be a consequence of (i) using tree-level diagrams, and consequently introducing artificial cutoffs to nonphysically regulate ultraviolet (and infrared) divergencies (e.g., in Ref. [7]) in the hard momentum transfer sector [22]; or (ii) considering only soft momentum exchange [21]. That is, it is straightforward to show that Eq. (2) recovers leading T^2 dependence from Ref. [21] if (1) only the soft gluon sector is considered, with the upper limit of integration artificially set to $|\vec{q}|_{\max}$; (2) only forward emission is accounted for ($\omega > 0$); and (3) running coupling is neglected. Accordingly, in Ref. [29] it was demonstrated that complex T dependence of our *collisional energy loss* (Eq. (2)) reduces not to commonly considered quadratic, but rather to nearly linear dependence for asymptotically large $p_\perp$. Therefore, a state-of-the-art energy-loss model leads to a much slower growth of the energy loss with temperature compared to the common paradigm, where the widely assumed faster growth can be reproduced only through quite drastic simplifying assumptions.

Since the goal of this paper is the extraction of the temperature-dependence exponent of the energy loss, this paper will furthermore provide an opportunity to test our dynamical energy-loss formalism on a more basic level.

III. NUMERICAL FRAMEWORK

In this paper, the predictions are generated within our fully optimized DREENA [27,28] numerical framework, comprising (i) initial parton momentum distribution [42]; (ii) energy-loss probability based on our dynamical energy-loss formalism [30–32] (discussed in the previous section), which includes multigluon [43] and path-length fluctuations [44], where the path-length fluctuations are calculated according to the procedure provided in Ref. [45] (see also Ref. [28]); and (iii) fragmentation functions [46]. In this paper, we will primarily use two implementations of this framework: (i) DREENA-C, where C corresponds to constant temperature medium; and (ii) DREENA-B, where B corresponds to one-dimensional (1D) Bjorken QGP evolution [7].

In the first part of our paper, using the DREENA-C framework, the average temperature is obtained according to the procedure described in Refs. [28,47], which we briefly outline here. For each centrality region in 5.02-TeV Pb + Pb collisions, the average temperature is estimated through $T^3 \sim \frac{\frac{dN_g}{dy}}{A_\perp L}$ [12,48], where $A_\perp$ is the overlap area. $\frac{dN_g}{dy}$ is gluon rapidity density, and is shown to be directly proportional to charged particle multiplicity $\frac{dN_{ch}}{d\eta}$, which is measured for all relevant centralities in 5.02-TeV Pb + Pb collisions at the LHC [49]. Thus, the required expression reads $T = c(\frac{\frac{dN_{ch}}{d\eta}}{A_\perp L})^{\frac{1}{3}}$, where constant c can be fixed by effective temperature for 0–20% 2.76-TeV Pb+Pb collisions at LHC [50], leading to, e.g., the average medium temperature of 348 MeV [47,50] in most central 5.02-TeV Pb + Pb collisions at the LHC.

In the second part of this paper, where we use the DREENA-B framework to test the sensitivity of the obtained results, the initial temperature (T_0) for each centrality is estimated in accordance with Ref. [27]. That is, for each centrality class, T_0 is determined in accordance with $T_0 \sim (\frac{\frac{dN_{ch}}{d\eta}}{A_\perp})^{\frac{1}{3}}$ [51]. As a starting point, $T_0 = 500$ MeV in most central 5.02-TeV Pb + Pb collisions at the LHC is estimated from the average medium temperature of 348 MeV [47,50] in these collisions (see above), and a QCD transition temperature of $T_c \approx 155$ MeV [52]. By knowing T_0 in the most central 5.02-TeV Pb + Pb collision, based on the expression above, it is straightforward to obtain T_0s for different centralities. In both studies, the average path lengths (L) for different centrality classes have been calculated by integrating the path-length distributions [28] which were obtained by following the procedure outlined in Ref. [45], with an additional hard-sphere restriction $r < R_A$ in the Woods-Saxon nuclear density distribution to regulate the path lengths in the peripheral collisions.

In generating numerical predictions, all the parameters correspond to standard literature values, i.e., we use no fitting parameters. We consider a QGP with $n_f = 3$ and $\Lambda_{QCD} = 0.2$ GeV. For the light quarks we assume that their mass is dominated by the thermal mass $M \approx \mu_E/\sqrt{6}$. The magnetic to electric mass ratio is assumed to be $0.4 < \mu_M/\mu_E < 0.6$ [53,54].

IV. RESULTS AND DISCUSSION

In this section, we first address the choice of the suitable observable for extracting energy-loss temperature dependence. For this purpose, an observable which is sensitive only to the details of jet-medium interactions (to facilitate extraction of T dependence), rather than the subtleties of medium evolution (to avoid unnecessary complications and ensure robustness), would be optimal. R_{AA} has such features, since it was previously reported that it is very sensitive to energy-loss effects [41] and the average medium properties, while being practically insensitive to the details of medium evolution (as opposed to v_2) [26–28,55,56]. Therefore, it is plausible that the appropriate observable should be closely related to R_{AA}.

Our theoretical and numerical approaches described above (where the dynamical energy loss explicitly depends on T) are implemented in a fully optimized DREENA framework [27,28], which makes it suitable for this paper. To more easily interpret the obtained results, we start from a constant T medium, i.e., DREENA-C [28]. In this framework, the local temperature becomes the average (constant) temperature— this makes the extraction of the temperature dependence straightforward, which is the main advantage of that framework. To confirm that, through such procedure, we indeed extracted the local temperature dependence, we will use DREENA-B [27] as a crosscheck, as this more complex model incorporates medium evolution through 1D Bjorken longitudinal expansion [7]. We here exploit that DREENA-C and DREENA-B are analytically tractable, allowing us to derive the appropriate scaling behavior. Finally, as a check of sensitivity of our proposed observable to the details of the medium evolution we employ our DREENA-A framework ("A" stands

for "adaptive"), which employs state-of-the-art full three- plus one-dimensional (3+1D) hydrodynamical evolution.

With the intention of extracting simple functional dependence on T (of the otherwise analytically and numerically quite complex dependence of the fractional energy loss; see Eqs. (1) and (2)), we first provide the scaling arguments within the DREENA-C [28] framework. These scaling (analytical) arguments will then be followed by a full-fledged numerical analysis. Namely, in Refs. [26–28,43] it was shown that, at very large values of transverse momentum $p_\perp$ and/or in peripheral collisions, the following estimates can be made:

$$\Delta E/E \approx \eta T^a L^b,$$
$$R_{AA} \approx 1 - \xi T^a L^b, \quad (3)$$

where η denotes a proportionality factor, depending on initial parton transverse momentum and its flavor, while $\xi = (n - 2)\eta/2$, where n is the steepness of a power-law fit to the initial transverse momentum distribution, i.e., $d\sigma/dp_\perp^2 \propto p_\perp^{-n}$. T and L denote the average temperature (of the QCD medium) along the jet path and the average path length traversed by the energetic parton. The scaling factors for temperature and path-length energy-loss dependence are denoted as a and b, respectively.

We next formulate the quantity R_{AA}^T, with the goal to isolate the temperature dependence:

$$R_{AA}^T = \frac{1 - R_{AA}}{1 - R_{AA}^{\text{ref}}}, \quad (4)$$

which presents the $(1 - R_{AA})$ ratio for a pair of two different centrality classes. The centrality class that corresponds to R_{AA}^{ref} (i.e., the quantity in the denominator) is denoted as the referent centrality, and is always lower (corresponding to a more central collision) than centrality in the numerator. We term this new quantity, given by Eq. (4), as a *temperature-dependent suppression ratio* (R_{AA}^T), which we will further elucidate below.

Namely, by using Eq. (3), it is straightforward to isolate average T and average path-length dependence of R_{AA}^T:

$$R_{AA}^T = \frac{1 - R_{AA}}{1 - R_{AA}^{\text{ref}}} \approx \frac{\xi T^a L^b}{\xi T_{\text{ref}}^a L_{\text{ref}}^b} = \left(\frac{T}{T_{\text{ref}}}\right)^a \left(\frac{L}{L_{\text{ref}}}\right)^b, \quad (5)$$

which in logarithmic form reads

$$\ln\left(R_{AA}^T\right) = \ln\left(\frac{1 - R_{AA}}{1 - R_{AA}^{\text{ref}}}\right) \approx a \ln\left(\frac{T}{T_{\text{ref}}}\right) + b \ln\left(\frac{L}{L_{\text{ref}}}\right). \quad (6)$$

However, the remaining dependence of the newly defined quantity on the path length is undesired for the purpose of this paper. So, in order to make use of the previous equation, we first test how the two terms on the right-hand side of Eq. (6) are related. To this end, in Fig. 1 we plot $\ln(L/L_{\text{ref}})$ against $\ln(T/T_{\text{ref}})$ for several combinations of centralities, as denoted in the caption of Fig. 1.

Conveniently, Fig. 1 shows a linear dependence $\ln(L/L_{\text{ref}}) \approx k \ln(T/T_{\text{ref}})$, with $k \approx 1.86$. This leads to a simple relation:

$$\ln\left(R_{AA}^T\right) \approx (a + kb) \ln\left(\frac{T}{T_{\text{ref}}}\right), \quad (7)$$
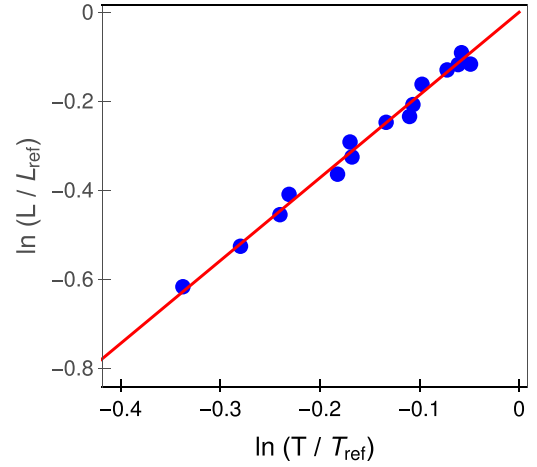

FIG. 1. $\ln(L/L_{\text{ref}})$ vs $\ln(T/T_{\text{ref}})$ in 5.02-TeV Pb+Pb collisions at the LHC for various centrality pairs. The *referent centralities* (for quantities in denominators) acquire one of the values 5–10, 10–20, 20–30, 30–40, or 40–50%, while the centralities in the numerator are always higher (the highest one being 50–60%). The solid red line corresponds to the linear fit to the calculated points.

so that with $f = a + kb$

$$R_{AA}^T \approx \left(\frac{T}{T_{\text{ref}}}\right)^f, \quad (8)$$

where this simple form facilitates extraction of a.

In Eq. (8), R_{AA}^T depends solely on T and effectively the temperature-dependence exponent a (as k and b [26] are known), which justifies the use of the "temperature-sensitive" term with this new quantity. Therefore, here we propose R_{AA}^T, given by Eq. (4), as a new observable, which is highly suitable for the purpose of this paper. Note, however, that this coupled dependence of R_{AA}^T on a and b exponents has its advantage, since it allows using this new observable to shed light on the underlying energy-loss mechanisms, by differentiating between various energy-loss models on both their T and L dependences.

The proposed extraction method is the following: We use our full-fledged DREENA-C numerical procedure to generate predictions for R_{AA} and thereby for the left-hand side of Eq. (8). Calculation of average T is already outlined in the previous section and described in detail above. We will generate the predictions with a full-fledged procedure, where we expect asymptotic scaling behavior (given by Eq. (8)) to be valid at high $p_\perp \approx 100$ GeV. Having in mind that values of k and b parameters have been extracted earlier, the temperature-dependence exponent a in the very high-$p_\perp$ limit can then be estimated from the slope (f) of a $\ln(R_{AA}^T)$ vs $\ln(T/T_{\text{ref}})$ linear fit, done for a variety of centrality pairs.

However, before embarking on this task, we first verify whether our predictions of R_{AA}^T for different centrality classes, based on the full-fledged DREENA-C framework, are consistent with the available experimental data. In Fig. 2 we compare our R_{AA}^T vs $p_\perp$ predictions for charged hadrons with corresponding 5.02-TeV Pb + Pb LHC data from A Large Ion Collider Experiment (ALICE) [57], Compact Muon Solenoid
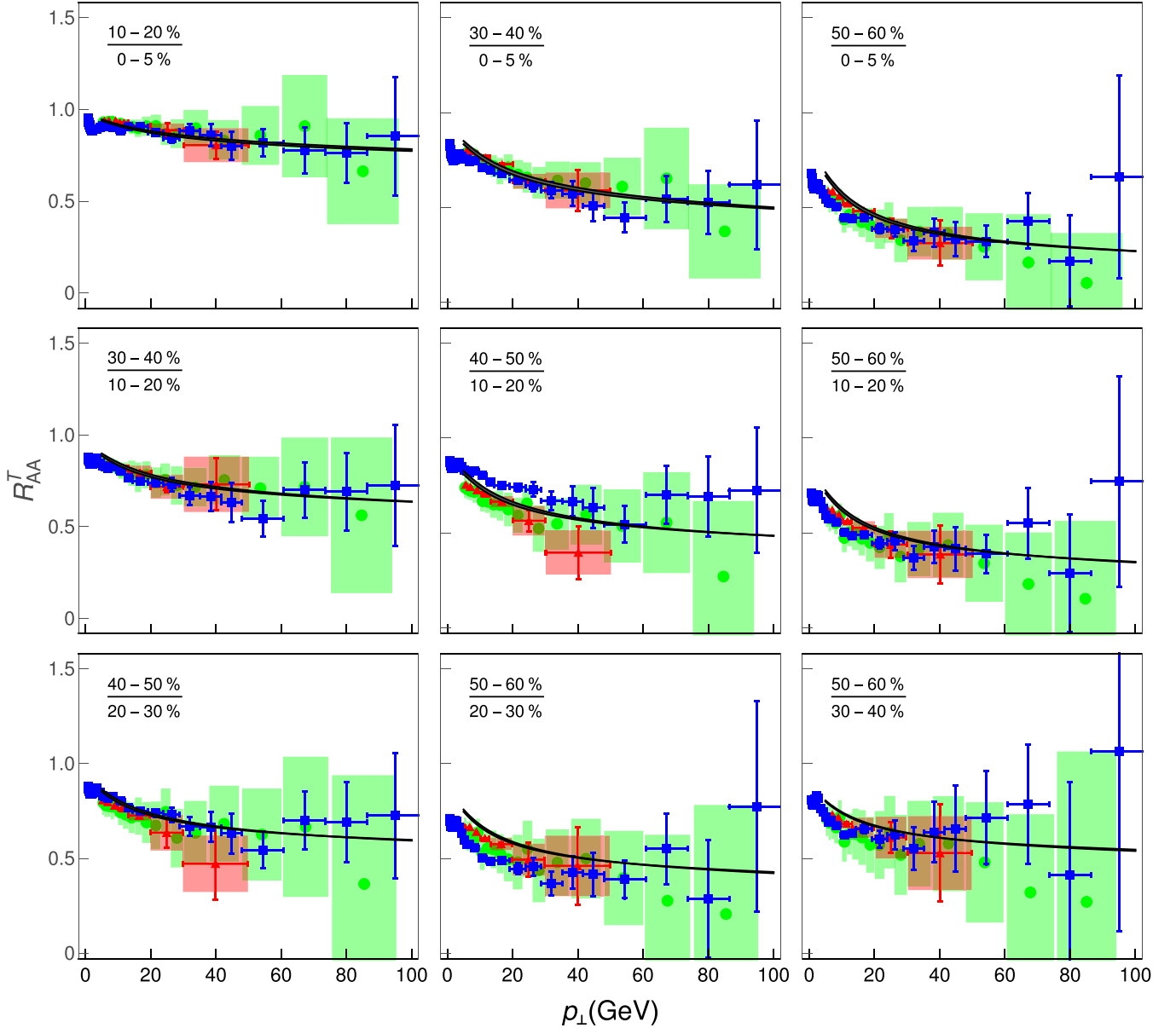
FIG. 2. Charged hadron R_{AA}^T for different pairs of centrality classes as a function of $p_\perp$. The predictions generated within our full-fledged suppression numerical procedure DREENA-C [28] (black curves with corresponding gray bands) are compared with ALICE [57] (red triangles), CMS [58] (blue squares), and ATLAS [59] (green circles) data. The lower (upper) boundary of each band corresponds to $\mu_M/\mu_E = 0.6$ ($\mu_M/\mu_E = 0.4$). Centrality pairs are indicated in the upper-left corner of each plot.

(CMS) [58], and A Toroidal LHC ApparatuS (ATLAS) [59], for different centrality pairs as indicated in the upper-left corner of each plot. Despite the large error bars, for all centrality pairs we observe consistency between our DREENA-C predictions and experimental data, in the $p_\perp$ region where our formalism is applicable ($p_\perp \gtrsim 10$ GeV). Moreover, we also notice the flattening of each curve with increasing $p_\perp$ (≈ 100 GeV), confirming that the expecting saturating (limiting) behavior is reached.

Furthermore, based on the analytical relation provided by Eq. (7), we expect linear functional dependence between $\ln R_{AA}^T$ and $\ln(T/T_{ref})$, which we test in Fig. 3. Note that all quantities throughout the paper are determined at $p_\perp = 100$ GeV, and by calculating R_{AA}^T for various centrality pairs

(see figure captions) within the full-fledged DREENA procedure. Remarkably, from Fig. 3, we observe that $\ln(R_{AA}^T)$ and $\ln(T/T_{ref})$ are indeed linearly related, which confirms the validity of our scaling arguments at high $p_\perp$ and the proposed procedure.

Linear fit to calculated points in Fig. 3 leads to the proportionality factor $f = a + kb = 3.79 \approx 4$. This small value of f would lead to k smaller than 1 *if* (commonly assumed) $a = 3$ and $b = 2$ are used. Such k value seems, however, implausible, as it would require (T/T_{ref}) to change more slowly with centrality compared to (L/L_{ref}).

More importantly, the temperature exponent can now be extracted ($b \approx 1.4$ as estimated in Ref. [26]), leading to $a \approx 1.2$. This indicates that temperature dependence of energetic
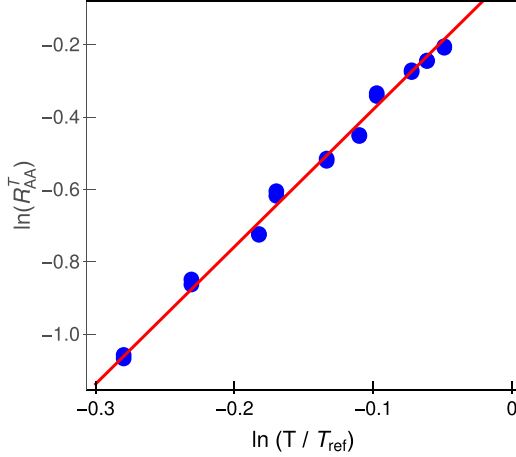
FIG. 3. $\ln(R_{AA}^T)$ vs $\ln(T/T_{ref})$ relation. $\ln(R_{AA}^T)$ and $\ln(T/T_{ref})$ are calculated from the full-fledged DREENA-C framework [28], for $h^\pm$ at $p_\perp = 100$ GeV in 5.02-TeV Pb+Pb collisions at the LHC for different centrality pairs. The referent centrality values are 10–20, 20–30, 30–40, and 40–50%, while their counterpart values are always higher, with the highest being equal to 50–60%. The red solid line corresponds to the linear fit to the values. Remaining parameters are the same as in Fig. 2.

particle energy loss (at very high $p_\perp$) is close to linear (see Eq. (3)), that is, certainly not quadratic or cubic, as commonly considered. This is in accordance with previously reported dependence of fractional dynamical energy loss on T somewhere between linear and quadratic [29], and as opposed to commonly used pQCD estimate $a = 3$ for radiative [9–12,14–20] (or even $a = 2$ for collisional [7,21–23]) energy loss.

The extraction of T dependence, together with previously estimated path-length dependence [26], within the DREENA framework, allows utilizing this new observable R_{AA}^T in discriminating between energy-loss models, with the aim of better understanding QGP properties. To this end, in Fig. 4, we (i) test sensitivity of R_{AA}^T on different medium evolutions (constant temperature, 1D Bjorken [60], and full 3+1D hydrodynamics [61]) and (ii) compare the asymptote derived from this study $((T/T_{ref})^{1.2}(L/L_{ref})^{1.4})$, with the commonly used estimate of $(T/T_{ref})^3(L/L_{ref})^2$.

Several conclusions can be drawn from Fig. 4.

(i) With respect to different models of QGP expansion, we see that, as expected, obtained R_{AA}^T results are similar, i.e., not very sensitive to the details of the medium evolution. As in DREENA-C (and DREENA-B; see the next subsection) the temperature dependence can be analytically tracked (which is, however, not possible in more complex DREENA-A), this result additionally confirms that the DREENA-C framework is suitable for the extraction of energy-loss temperature dependence.

(ii) Ideally, the T dependence exponent could be directly extracted from experimental data, by fitting a straight line to the very high-$p_\perp$ part (≈ 100 GeV) of R_{AA}^T for practically any centrality pair (upon L the dependence exponent is determined following Ref. [26]). However, the fact that data from different experiments (ALICE, CMS, and ATLAS) are not ideally consistent, and that the error bars are quite sizable,

currently prevents such direct extraction. The error bars in the upcoming high-luminosity third run at the LHC are, however, expected to significantly decrease, which would enable the direct extraction of the exponent a from the data.

(iii) Finally, Fig. 4 also indicates that widely considered energy-loss dependence T^3L^2 may be inconsistent with the experimental data. Future increase in measurements precision could provide confidence in this observation and resolve the exact form of these dependencies from the data, through our proposed observable. This discriminative power of the R_{AA}^T quantity highlights its importance in understanding the underlying energy-loss mechanisms in QGP.

A. Effects of medium evolution

While in Fig. 4 we showed that R_{AA}^T results are robust with respect to the medium evolution, the analytical procedure for extracting temperature dependence is different in DREENA-C and DREENA-B frameworks. A comparison of scaling factors extracted from these two procedures can be used to test reliability of the proposed procedure. In this subsection, we consequently utilize the DREENA-B framework [27], where medium evolution is introduced through Bjorken 1D hydrodynamical expansion [60], i.e., there is the following functional dependence of T on path length:

$$T = T_0 \left(\frac{\tau_0}{l} \right)^{1/3}, \qquad (9)$$

where T_0 and $\tau_0 = 0.6$ fm [62,63] denote initial temperature and thermalization time of the QGP.

Proceeding in a similar manner as in constant medium case, R_{AA}^T (given by Eq. (4)) in the evolving medium (for coupled local T and l, where l stands for traversed path length) reads

$$R_{AA}^T = \frac{\int_0^L T^a l^{b-1} dl}{\int_0^{L_{ref}} (T_{ref})^a (l_{ref})^{b-1} dl_{ref}} = \frac{T_0^a \tau_0^{a/3} \int_0^L \frac{l^{b-1}}{l^{a/3}} dl}{T_{0,ref}^a \tau_0^{a/3} \int_0^{L_{ref}} \frac{(l_{ref})^{b-1}}{(l_{ref})^{a/3}} dl_{ref}}$$

$$= \left(\frac{T_0}{T_{0,ref}} \right)^a \left(\frac{L}{L_{ref}} \right)^{b-\frac{a}{3}}, \qquad (10)$$

where we used Eq. (9). Again, we assess whether there is a simple relation between logarithms of the (now initial) temperature ratio and average path-length ratio for different centrality pairs. Similarly to the constant T case, from Fig. 5 we infer linear dependence between these two quantities, where the slope coefficient now acquires the value $\kappa \approx 1.3$. Thus, we may write

$$\frac{L}{L_{ref}} = \left(\frac{T_0}{T_{0,ref}} \right)^\kappa \Rightarrow \frac{T_0}{T_{0,ref}} = \left(\frac{L}{L_{ref}} \right)^{1/\kappa}, \qquad (11)$$

which ensures that the R_{AA}^T quantity has a very simple form, depending only on average path length and exponents a, b, and κ:

$$R_{AA}^T = \left(\frac{L}{L_{ref}} \right)^{\frac{a}{\kappa} + b - \frac{a}{3}}. \qquad (12)$$

If we substitute the value of $a \approx 1.2$ obtained in the constant T medium case, previously estimated $b \approx 1.4$ [26], and
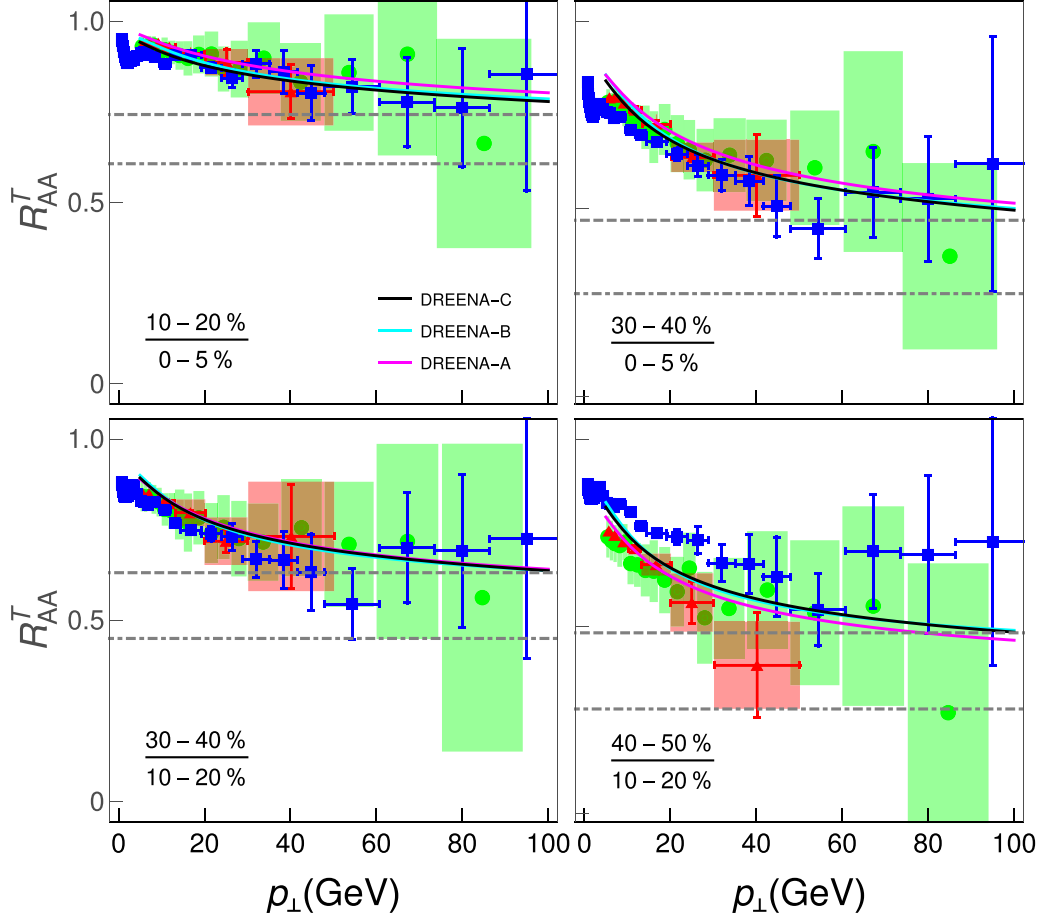
FIG. 4. The discriminative power of the R_{AA}^T quantity in resolving the energy-loss mechanism. Four panels in Fig. 2 are extended to include comparison of our asymptotic scaling behavior $(T/T_{\mathrm{ref}})^{1.2}(L/L_{\mathrm{ref}})^{1.4}$ (gray dashed horizontal line) with common assumption $(T/T_{\mathrm{ref}})^3(L/L_{\mathrm{ref}})^2$ (gray dot-dashed horizontal line). The figure also shows comparison of R_{AA}^Ts obtained by three different numerical frameworks: constant temperature DREENA-C (black curve), 1D Bjorken expansion DREENA-B [27] (cyan curve), and full 3+1D hydrodynamics evolution [61] DREENA-A (magenta curve). The remaining labeling is the same as in Fig. 2.
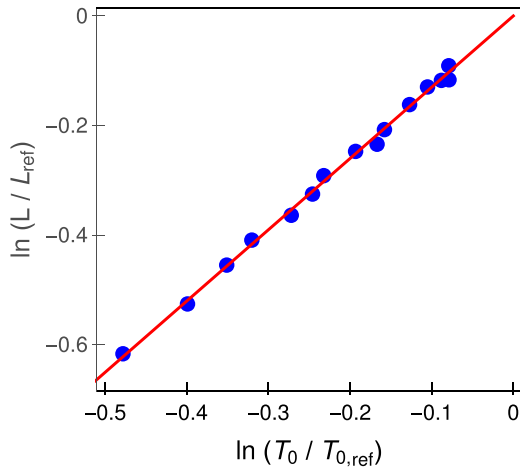

FIG. 5. $\ln(L/L_{\mathrm{ref}})$ vs $\ln(T_0/T_{0,\mathrm{ref}})$ for various pairs of centralities in evolving medium. The assumed centrality pairs are the same as in Fig. 1. The red solid line corresponds to the linear fit to the values.

here inferred $\kappa \approx 1.3$, we arrive at the following estimate:

$$R_{AA}^T = \left(\frac{L}{L_{\mathrm{ref}}}\right)^{1.93} \Rightarrow \ln(R_{AA}^T) = 1.93 \ln\left(\frac{L}{L_{\mathrm{ref}}}\right). \quad (13)$$

This equation is quite suitable for testing the robustness of the procedure for extracting the exponent a to inclusion of the evolving medium. Namely, value 1.93 in Eq. (13) stems from coefficient a, which is extracted from the constant T medium case. On the other hand, if we plot $\ln(R_{AA}^T)$, generated by full-fledged DREENA-B calculations (i.e., in the evolving medium) which are *fundamentally different* from DREENA-C, against $\ln(L/L_{\mathrm{ref}})$ for a variety of centrality pairs, again we observe a linear dependence (see Fig. 6). Furthermore, a linear fit to the values surprisingly yields the exact same slope coefficient value of 1.93 (see also Table I).

Consequently, the procedure of extracting the temperature-dependence exponent, introduced first in the case of the constant T medium, is applicable to the expanding medium as well. Moreover, the fact that the same coefficient a is obtained through two different procedures leads us to conclude that (i) for the purpose of this paper the DREENA-C framework
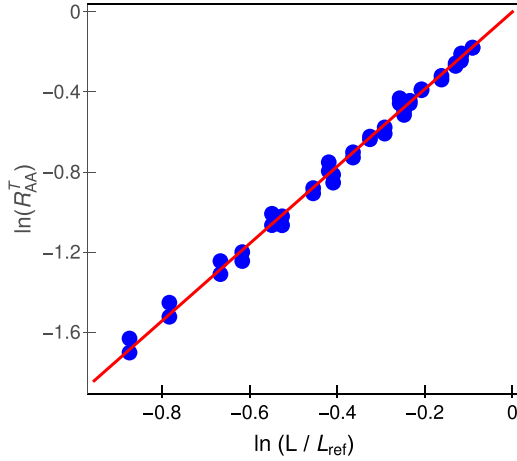
FIG. 6. Testing the validity of our procedure for temperature-dependence extraction in the case of the expanding QCD medium. $\ln(R_{AA}^T)$ vs $\ln(L/L_{ref})$ for $h^\pm$ at $p_\perp = 100$ GeV for different pairs of centrality classes is plotted. Suppression predictions are obtained from full-fledged DREENA-B [27] calculations. Referent centrality values are 5–10, 10–20, 20–30, 30–40, 40–50, and 50–60%, while their counterpart values are always higher, with the highest being 60–70%. The red solid line corresponds to the linear fit to the values.

(assuming a constant temperature medium) is sufficient and (ii) the same energy-loss scaling holds in an evolving medium (i.e., for local temperature) as well. The displayed consistency of the results provides confidence in the general applicability of our procedure (suggesting robustness to the applied model of the bulk medium) and supports the reliability of the value of extracted T dependence exponent $a \approx 1.2$.

It is worth noting that the definition of R_{AA}^T relies on the fact that we assume that $R_{AA} = 1$ if no energy loss is encountered. Related to this, we do not study the effect of (nuclear) parton distribution function differences on R_{AA}, as it is generally studied under initial-state effects. However, it is known that initial-state effects have a sizable impact only on the low- and moderate-$p_\perp$ sector (lower than 6 GeV) [64–70]. Since our numerical predictions are generated above 8–10 GeV and the temperature dependence is extracted at very high-$p_\perp$ values ($p_\perp \sim 100$ GeV), these effects will be negligible in this $p_\perp$ region, and should not influence the results obtained in our paper.

B. Effects of colliding system size

We below extend our analysis to smaller colliding systems in order to assess generality of the conclusions presented

TABLE I. Inferred temperature-dependence exponent across different frameworks.

Framework	Temperature dependence exponent
DREENA-C	$a \approx 1.2$
DREENA-B	Consistent with $a \approx 1.2$
DREENA-A	Not analytically tractable

above. Smaller colliding systems, such as Xe + Xe, Kr + Kr, Ar + Ar, and O + O, are important to gradually resolve the issue of QGP formation in small systems (such as pA), and (except Xe + Xe, which is already in a run) are expected to be a part of the future heavy-ion program at the LHC [71].

As already discussed in Ref. [26], for this analysis within the DREENA-C framework [28] (which we employ here for simplicity, since the robustness of the procedure to the evolving medium was demonstrated above) note that R_{AA} depends on (i) initial high-$p_\perp$ parton distribution, (ii) medium average T, and (iii) path-length distribution. For different colliding systems (probably at slightly different $\sqrt{s_{NN}} = 5.44$ TeV compared to the Pb + Pb system) we employ the same high-$p_\perp$ distributions, since in Ref. [29] it was shown that for almost twofold increase of the collision energy (from 2.76 to 5.02 TeV) the change in corresponding initial distributions results in a negligible change (approximately 5%) in suppression.

Regarding the average temperature, one should note that T is directly proportional to the charged particle multiplicity, while inversely proportional to the size of the overlap area and average medium size [26,28,47,48], i.e., $T \propto (\frac{dN_{ch}/d\eta}{A_\perp L})^{1/3}$. The transition to smaller colliding systems, for a certain fixed centrality class, leads to the following scaling: $A_\perp \propto A^{2/3}$, $L \propto A^{1/3}$ [72,73], and $dN_{ch}/d\eta \propto N_{part} \propto A$ [74,75], where A denotes atomic mass. This leads to $T \sim (\frac{A}{A^{\frac{2}{3}}A^{\frac{1}{3}}})^{1/3} \sim$ const, that is, we expect that average temperature does not change, when transitioning from large Pb + Pb to smaller systems, for a fixed centrality class. Lastly, path-length distributions for smaller systems and each centrality class are obtained in the same manner as for Pb+Pb [28], and are the same as in Pb + Pb collisions up to a rescaling factor of $A^{1/3}$.

By denoting all quantities related to smaller systems with a tilde, with Pb + Pb quantities denoted as before, it is straightforward to show that the temperature sensitive suppression ratio for smaller systems satisfies

$$
\begin{aligned}
\widetilde{R}_{AA}^T &= \frac{1 - \widetilde{R}_{AA}}{1 - \widetilde{R}_{AA}^{ref}} \approx \frac{\widetilde{T}^a \widetilde{L}^b}{\widetilde{T}_{ref}^a \widetilde{L}_{ref}^b} \approx \frac{T^a L^b}{T_{ref}^a L_{ref}^b} \frac{(\widetilde{A}/A)^{b/3}}{(\widetilde{A}/A)^{b/3}} \\
&= \frac{1 - R_{AA}}{1 - R_{AA}^{ref}} = R_{AA}^T,
\end{aligned}
\tag{14}
$$

where we used $\widetilde{T} = T$ and $\widetilde{L}/L = (\widetilde{A}/A)^{1/3}$.

To validate equality of R_{AA}^Ts for different system sizes, predicted by analytical scaling behavior (Eq. (14)), in Fig. 7 we compare our full-fledged R_{AA}^T predictions for $h^\pm$ in the Pb + Pb system with those for smaller colliding systems. We observe that, practically irrespective of system size, R_{AA}^T exhibits the same asymptotical behavior at high $p_\perp$. This not only validates our scaling arguments, but also demonstrates the robustness of the new observable R_{AA}^T to system size. Consequently, since for fixed centrality range T should remain the same for all these colliding systems, we obtained that temperature-dependence exponent a should be the same independently of the considered colliding system (see Fig. 3). Therefore, the proposed procedure for extracting the
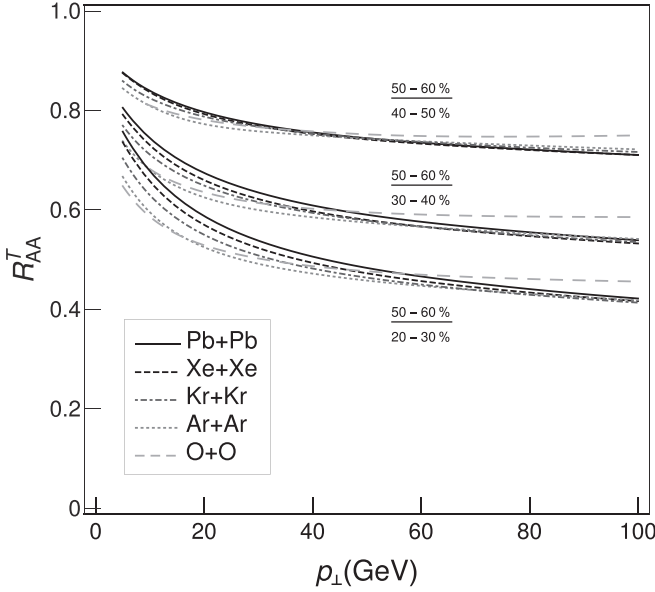
FIG. 7. Dependence of R_{AA}^T on a system size as a function of $p_\perp$. Predictions for $h^\pm$ generated within the full-fledged DREENA-C [28] suppression numerical procedure are compared for different colliding systems: Pb+Pb, Xe + Xe, Kr + Kr, Ar + Ar, and O + O (for lines specification see legend). For clarity, the results are shown only for three centrality pairs, as specified in the plot, although checked for all available centrality classes. The magnetic to electric mass ratio is fixed to $\mu_M/\mu_E = 0.4$.

V. CONCLUSIONS AND OUTLOOK

One of the main signatures of the high-$p_\perp$ particle's energy loss, apart from its path length, is its temperature dependence. Although extensive studies on both issues were performed, not until recently was the path-length dependence resolution suggested [26]. Here we proposed a new simple observable for extracting temperature dependence of the energy loss, based on one of the most common jet quenching observables—the high-$p_\perp$ suppression. By combining full-fledged numerical calculations with asymptotic scaling behavior, we surprisingly obtained that temperature dependence is nearly linear, i.e., far from quadratic or cubic, as commonly assumed. Further, we verified its robustness and reliability on colliding system size and evolving QGP medium. Moreover, we demonstrated that the same observable, due to its joint dependence on T and L exponents, can be utilized to discriminate between different energy-loss models on *both* their *temperature* and *path-length* dependence bases. Comparison with the experimental data also indicated a need for revising the long-standing $\Delta E/E \propto L^2 T^3$ paradigm.

As an outlook, the expected substantial decrease of error bars in the upcoming third run measurements at the LHC will allow direct extraction of the temperature-dependence exponent from high-$p_\perp$ data of this observable. This will provide a resolving power to temperature/path-length [26] dependence of the energy loss and test our understanding of the underlying QGP physics.

temperature dependence of the energy loss is also robust to the collision system size. As a small exception, the O + O system exhibits a slight departure from the remaining systems at high $p_\perp$, which might be a consequence of the fact that this system is significantly smaller than other systems considered here.

[1] M. Gyulassy and L. McLerran, Nucl. Phys. A **750**, 30 (2005).

[2] E. V. Shuryak, Nucl. Phys. A **750**, 64 (2005).

[3] C. V. Johnson and P. Steinberg, Phys. Today **63**(5), 29 (2010).

[4] B. Jacak and P. Steinberg, Phys. Today **63**(5), 39 (2010).

[5] J. C. Collins and M. J. Perry, Phys. Rev. Lett. **34**, 1353 (1975).

[6] G. Baym and S. A. Chin, Phys. Lett. B **62**, 241 (1976).

[7] J. D. Bjorken, FERMILAB-PUB-82-059-THY, 287 (1982).

[8] J. Adams *et al.* (STAR Collaboration), Phys. Rev. Lett. **91**, 072304 (2003); C. Adler *et al.* (STAR Collaboration), *ibid.* **90**, 082302 (2003).

[9] R. Baier, Y. Dokshitzer, A. Mueller, S. Peigne, and D. Schiff, Nucl. Phys. B **484**, 265 (1997).

[10] N. Armesto, C. A. Salgado, and U. A. Wiedemann, Phys. Rev. D **69**, 114003 (2004).

[11] C. A. Salgado and U. A. Wiedemann, Phys. Rev. D **68**, 014008 (2003).

[12] M. Gyulassy, P. Levai, and I. Vitev, Nucl. Phys. B **594**, 371 (2001).

[13] B. G. Zakharov, JETP Lett. **70**, 176 (1999); **73**, 49 (2001).

[14] P. B. Arnold, G. D. Moore, and L. G. Yaffe, J. High Energy Phys. 06 (2002) 030.

[15] X. N. Wang and X. F. Guo, Nucl. Phys. A **696**, 788 (2001).

[16] C. Andres, N. Armesto, M. Luzum, C. A. Salgado, and P. Zurita, Eur. Phys. J. C **76**, 475 (2016).

[17] B. Betz and M. Gyulassy, Phys. Rev. C **86**, 024903 (2012).

[18] B. Betz and M. Gyulassy, J. High Energy Phys. 08 (2014) 090; 10 (2014) 043.

[19] J. Noronha-Hostler, B. Betz, J. Noronha, and M. Gyulassy, Phys. Rev. Lett. **116**, 252301 (2016).

[20] A. Majumder and C. Shen, Phys. Rev. Lett. **109**, 202301 (2012).

[21] M. H. Thoma and M. Gyulassy, Nucl. Phys. B **351**, 491 (1991).

[22] E. Braaten and M. H. Thoma, Phys. Rev. D **44**, 1298 (1991); **44**, 2625(R) (1991).

[23] Y. He, T. Luo, X.-N. Wang, and Y. Zhu, Phys. Rev. C **91**, 054908 (2015); **97**, 019902(E) (2018).

[24] C. Nonaka and S. A. Bass, Phys. Rev. C **75**, 014902 (2007).

[25] C. Marquet and T. Renk, Phys. Lett. B **685**, 270 (2010).

[26] M. Djordjevic, D. Zigic, M. Djordjevic, and J. Auvinen, Phys. Rev. C **99**, 061902(R) (2019).

[27] D. Zigic, I. Salom, M. Djordjevic, and M. Djordjevic, Phys. Lett. B **791**, 236 (2019).

[28] D. Zigic, I. Salom, J. Auvinen, M. Djordjevic, and M. Djordjevic, J. Phys. G **46**, 085101 (2019).

[29] M. Djordjevic and M. Djordjevic, Phys. Rev. C **92**, 024918 (2015).

[30] M. Djordjevic, Phys. Rev. C **80**, 064909 (2009).

[31] M. Djordjevic and U. Heinz, Phys. Rev. Lett. **101**, 022302 (2008).

[32] M. Djordjevic, Phys. Rev. C **74**, 064907 (2006).

[33] J. I. Kapusta, *Finite-Temperature Field Theory* (Cambridge University, Cambridge, England, 1989).

[34] M. Djordjevic and M. Gyulassy, Nucl. Phys. A **733**, 265 (2004).

[35] M. Djordjevic, Phys. Lett. B **709**, 229 (2012).

[36] M. Djordjevic and M. Djordjevic, Phys. Lett. B **734**, 286 (2014).

[37] B. Blagojevic, M. Djordjevic, and M. Djordjevic, Phys. Rev. C **99**, 024901 (2019).

[38] A. Peshier, arXiv:hep-ph/0601119.

[39] R. Field, *Applications of Perturbative QCD* (Perseus, Cambridge, MA, 1995).

[40] M. Djordjevic and M. Gyulassy, Phys. Rev. C **68**, 034914 (2003).

[41] B. Blagojevic and M. Djordjevic, J. Phys. G **42**, 075105 (2015).

[42] Z. B. Kang, I. Vitev, and H. Xing, Phys. Lett. B **718**, 482 (2012); R. Sharma, I. Vitev, and B. W. Zhang, Phys. Rev. C **80**, 054902 (2009).

[43] M. Gyulassy, P. Levai, and I. Vitev, Phys. Lett. B **538**, 282 (2002).

[44] S. Wicks, W. Horowitz, M. Djordjevic, and M. Gyulassy, Nucl. Phys. A **784**, 426 (2007).

[45] A. Dainese, Eur. Phys. J. C **33**, 495 (2004).

[46] D. de Florian, R. Sassot, and M. Stratmann, Phys. Rev. D **75**, 114010 (2007).

[47] M. Djordjevic, M. Djordjevic, and B. Blagojevic, Phys. Lett. B **737**, 298 (2014).

[48] J. Xu, A. Buzzatti, and M. Gyulassy, J. High Energy Phys. 08 (2014) 063.

[49] J. Adam *et al.* (ALICE Collaboration), Phys. Rev. Lett. **116**, 222302 (2016).

[50] J. Adam *et al.* (ALICE Collaboration), Phys. Lett. B **754**, 235 (2016); M. Wilde (for the ALICE Collaboration), Nucl. Phys. A **904–905**, 573c (2013).

[51] M. Djordjevic, M. Gyulassy, R. Vogt, and S. Wicks, Phys. Lett. B **632**, 81 (2006).

[52] A. Bazavov *et al.* (HotQCD Collaboration), Phys. Rev. D **90**, 094503 (2014).

[53] Y. Maezawa, S. Aoki, S. Ejiri, T. Hatsuda, N. Ishii, K. Kanaya, N. Ukita, and T. Umeda (WHOT-QCD Collaboration), Phys. Rev. D **81**, 091501(R) (2010).

[54] A. Nakamura, T. Saito, and S. Sakai, Phys. Rev. D **69**, 014506 (2004).

[55] T. Renk, Phys. Rev. C **85**, 044903 (2012).

[56] D. Molnar and D. Sun, Nucl. Phys. A **932**, 140 (2014); **910–911**, 486 (2013).

[57] S. Acharya *et al.* (ALICE Collaboration), J. High Energy Phys. 11 (2018) 013.

[58] V. Khachatryan *et al.* (CMS Collaboration), J. High Energy Phys. 04 (2017)039.

[59] (ATLAS Collaboration), ATLAS-CONF-2017-012 (2017).

[60] J. D. Bjorken, Phys. Rev. D **27**, 140 (1983).

[61] E. Molnar, H. Holopainen, P. Huovinen, and H. Niemi, Phys. Rev. C **90**, 044904 (2014).

[62] P. F. Kolb and U. W. Heinz, Hydrodynamic description of ultra-relativistic heavy ion collisions, in *Quark-Gluon Plasma*, edited by R. C. Hwa and X.-N. Wang (World Scientific, Singapore, 2004), Vol. 3, p. 634.

[63] J. E. Bernhard, J. S. Moreland, and S. A. Bass, Nucl. Phys. A **967**, 293 (2017).

[64] M. R. Adams *et al.*, Phys. Rev. Lett. **68**, 3266 (1992).

[65] V. Barone and M. Genovese, Phys. Lett. B **412**, 143 (1997).

[66] A. Dainese (ALICE Collaboration), Czech. J. Phys. **55**, B367 (2005).

[67] S. Cao, G.-Y. Qin, and S. A. Bass, Phys. Rev. C **92**, 024907 (2015).

[68] J. W. Cronin, H. J. Frisch, M. J. Shochet, J. P. Boymond, P. A. Piroue, and R. L. Sumner, Phys. Rev. D **11**, 3105 (1975).

[69] M. Lev and B. Petersson, Z. Phys. C **21**, 155 (1983).

[70] A. Krzywicki, J. Engels, B. Petersson, and U. Sukhatme, Phys. Lett. B **85**, 407 (1979).

[71] Z. Citron, A. Dainese, J. F. Grosse-Oetringhaus, J. M. Jowett, Y. J. Lee, U. A. Wiedemann, M. Winn, A. Andronic, F. Bellini, and E. Bruna, CERN Yellow Rep. Monogr. **7**, 1159 (2019).

[72] G. Giacalone, J. Noronha-Hostler, M. Luzum, and J. Y. Ollitrault, Phys. Rev. C **97**, 034904 (2018).

[73] C. Loizides, J. Kamin, and D. d'Enterria, Phys. Rev. C **97**, 054910 (2018).

[74] K. J. Eskola, H. Niemi, R. Paatelainen, and K. Tuominen, Phys. Rev. C **97**, 034911 (2018).

[75] S. Acharya *et al.* (ALICE Collaboration), Phys. Lett. B **790**, 35 (2019).

A systems biology approach to COVID-19 progression in population

Magdalena Djordjevic[a], Andjela Rodic[b], Igor Salom[a], Dusan Zigic[a], Ognjen Milicevic[c], Bojana Ilic[a], and Marko Djordjevic[b,*]

[a]Institute of Physics Belgrade, University of Belgrade, Belgrade, Serbia
[b]Computational Systems Biology Group, Faculty of Biology, University of Belgrade, Belgrade, Serbia
[c]Department for Medical Statistics and Informatics, Faculty of Medicine, University of Belgrade, Belgrade, Serbia
*Corresponding author: e-mail address: dmarko@bio.bg.ac.rs

Contents

Abstract

A number of models in mathematical epidemiology have been developed to account for control measures such as vaccination or quarantine. However, COVID-19 has brought unprecedented social distancing measures, with a challenge on how to include these in a manner that can explain the data but avoid overfitting in parameter inference. We here develop a simple time-dependent model, where social distancing effects are introduced analogous to coarse-grained models of gene expression control in systems biology. We apply our approach to understand drastic differences in COVID-19 infection and fatality counts, observed between Hubei (Wuhan) and other Mainland China provinces. We find that these unintuitive data may be explained through an interplay of differences in transmissibility, effective protection, and detection efficiencies between Hubei and other provinces. More generally, our results demonstrate that regional differences may drastically shape infection outbursts. The obtained results demonstrate the applicability of our developed method to extract key infection parameters directly from publically available data so that it can be globally applied to outbreaks of COVID-19

in a number of countries. Overall, we show that applications of uncommon strategies, such as methods and approaches from molecular systems biology research to mathematical epidemiology, may significantly advance our understanding of COVID-19 and other infectious diseases.

1. Introduction

As the novel COVID-19 disease caused by the SARS–CoV-2 virus took the world by a storm, the new pandemic quickly gained priority in scientific research in a wide range of biological and medical science disciplines. Despite that their prior expertise was in unrelated research fields, many researchers have successfully adapted their approaches and methods to examine various aspects of this viral infection and, thus, contributed to finding the necessary solutions. The systems biology community is not an exception (Alon, Mino, & Yashiv, 2020; Bar-On, Flamholz, Phillips, & Milo, 2020; Djordjevic, Djordjevic, Ilic, Stojku, & Salom, 2021; Eilersen & Sneppen, 2020; Karin et al., 2020; Saad-Roy et al., 2021; Vilar & Saiz, 2020; Wong et al., 2020): those involved in modeling the dynamics of biological systems at the molecular and cellular level can directly apply the similar methodology in epidemiological studying of the virus spread—and this exactly is the central point of the present paper. In particular, dynamic models of biochemical reaction networks, in which the reaction kinetics follow the law of mass action, are analogous to compartmental epidemiological models which, instead of concentrations of chemical species, track the prevalence of individuals in defined population classes over time (Voit, Martens, & Omholt, 2015). Moreover, gene expression dynamics is usually a result of the interplay between the changing rate of cell growth, on which the global physiological rates of molecule synthesis and degradation depend, and complex transcription regulation (Djordjevic, Rodic, & Graovac, 2019). Therefore, modeling dynamics of gene circuits implies combining kinetic models, often relying on the law of mass action, with appropriate non-linear functions describing the regulation part. In the case of the COVID-19 epidemic, one can note that the virus transmission in a population, driven by the biological capacity of the particular virus in the given environment, is coupled with strong, time–dependent regulation, represented by the epidemic mitigation measures imposed by governments. These similarities between the modeled systems may facilitate the application of

the systems biology techniques to the epidemiology field of research. In this paper, we will show how such an approach can be used to assess the basic parameters of the COVID-19 epidemic progression in a given population. In particular, we will use the analogy outlined above to study the COVID-19 spread in Mainland China and test the hypothesis about possible reasons for the uneven disease spread in China provinces.

Our interest in Mainland China infection progression comes from Fig. 1. The progression seems highly intriguing, as Hubei (with only 4% of China population) shows an order of magnitude larger number of detected infection cases (Fig. 1A) and two orders of magnitude higher fatalities (Fig. 1B) compared to the *total* sum in all other Mainland China provinces. The epidemic was unfolding well before the Wuhan closure (with the reported symptom onset of the first patient on December 1, 2019) and within the period of huge population movement, which started 2 weeks before January 25 (the Chinese Lunar New Year) (Chen, Yang, Yang, Wang, & Bärnighausen, 2020). As a rough baseline, a modeling study of the infection spread from Wuhan (Wu, Leung, & Leung, 2020) estimated more than 10^5 new cases per day in Chongqing alone—instead, the actual (reported) peak number for *all* Mainland China provinces outside Hubei was just 831.
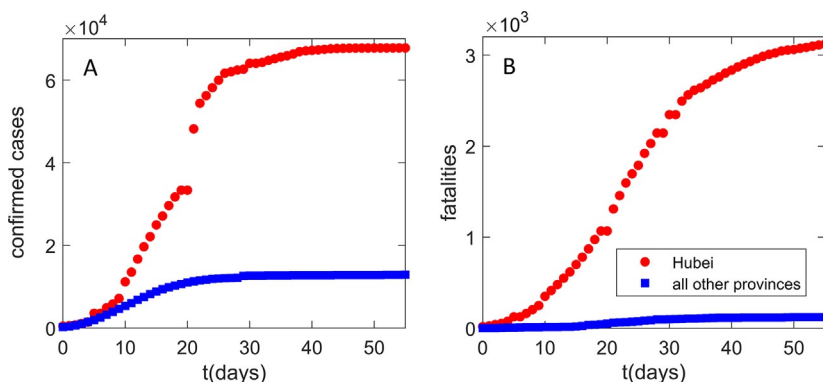
Fig. 1 Infection and fatality counts for Hubei vs all other provinces. The number of (A) detected infections, (B) fatality cases. Zero on the horizontal axis corresponds to the time from which the data (Hu et al., 2020) are taken (January 23), which also coincides with the Wuhan closure. Red circles correspond to the observed Hubei counts. Blue squares correspond to the sum of the number of counts for all other provinces. The figure illustrates a puzzling difference in the number of counts between Hubei alone and the sum of all other Mainland China provinces.

Consequently, it is a notable challenge for computational modeling to understand drastic differences in COVID-19 infection and fatality counts observed between Hubei (Wuhan) and other Mainland China provinces. These drastic differences may be a consequence of an interplay between the virus transmissibility (influenced by environmental and demographic factors) and the effectiveness of the protection measures. Both can significantly change between different provinces (more generally different countries/regions), and the model has to infer this from available data (commonly the number of confirmed cases, publicly available for a large number of countries/regions).

The study presented here will therefore demonstrate the usefulness of the systems biology approach to the analysis of non-trivial COVID-19 data from China. In particular, the developed method will allow us to analyze the puzzling differences in dynamics trajectories in Mainland China provinces, and it will also turn out to be more generally applicable for understanding regional differences in outburst dynamics. The surprising differences in COVID-19 progression in different provinces may put strong constraints on the underlying infection progression parameters and allow us to understand:

i. What interplay between the inherent disease transmissibility and the effects of social distancing is responsible for the large difference in the count numbers between Hubei and the rest of Mainland China? Addressing this question in a proper way would make easier to comprehend how regional differences may shape the infection outbursts, which is important both locally (for explaining this puzzle), and more generally in the context of global COVID-19 pandemics progression.

ii. What is the Infected Fatality Rate (IFR, the number of fatalities per total number of *infected* cases) in China? Case Fatality Rate (CFR, the number of fatalities per *confirmed/detected* cases) can be obtained directly from the data but is highly sensitive to the testing coverage. IFR is a more fundamental mortality parameter, as it does not depend on the testing coverage, but is however much harder to determine, due to the unknown number of infected cases.

Addressing these questions allows understanding both the different response policies, and the inherent risks posed by the pandemics and will enable future cross-country comparisons. The developed methodology (i) demonstrates the usefulness of applying transdisciplinary expertise to efficiently analyze problems of nationwide importance, (ii) allows to readily analyze future

outbreaks of COVID-19 and other infectious diseases, as it depends only on inference from straightforward and publically available data.

2. An overview of compartmental models of epidemic progression

In epidemiology, for practical and ethical reasons, it is fairly impossible to conduct scientific experiments in controlled conditions in order to investigate the spread of the disease in the human population (Brauer, 2008). Therefore, epidemiologists usually resort to collecting data from clinical reports on the observed situation in the field and, then, using mathematical models to interpret these data, i.e., to infer the principles underlying the process of disease spreading. These principles may point to potentially successful control strategies, as well as to the probable future status of the disease in the population. Epidemiological data can often be incomplete or inaccurate due to poorly controlled or non-standardized collection methods, which significantly complicates modeling. However, even a qualitative agreement of the model with the data can provide useful information of great practical importance. Hence, model predictions are widely used for making various estimates and answering important questions about the seriousness of the epidemic consequences. For example, how many people will be infected, require treatment, or die, or how many patients should the public health facilities expect at any given time? Also, how long will the epidemic last? To what extent could quarantine and self-isolation of the infected contribute to mitigating the effects of the epidemic? Model predictions guide the development of strategies to control the epidemic spread, including vaccination programs.

When the goal is to discover the general principles of epidemic progression, simple mathematical models, which can be solved and analyzed with a "pencil on paper," are a logical choice as they give insight into the properties of the examined process despite failing to reproduce it in detail. In 1927, Kermack and McKendrick formulated a simple model that predicted behavior similar to that observed in numerous epidemics (Kermack & McKendrick, 1927). It was a type of compartmental model describing the infection spread in a population by analogy with a system of vessels connected by pipes through which a fluid flows. Namely, the population is divided into compartments, and assumptions are made about the nature and the rate of the flow between them. The structure of the compartmental

model—which sections and how many of them it will contain and how they will be connected—depends on the characteristics of transmission of a given infectious disease and whether the past disease provides immunity to re-infections or not. The model set by these two scientists is known as SIR (from **S**usceptible–**I**nfected–**R**ecovered). It divides the population into three classes which correspond to compartments (Fig. 2): Susceptible (S) class includes healthy individuals susceptible to infection, which have never been exposed to the virus; Those who are infected and can infect others belong to the Infected (I) class; Recovered (R) class encompasses those who are excluded from the population, either by quarantining the infected, or by acquiring immunity through recovery from disease or immunization, or by the death of the infected (Brauer, 2008).

Mathematically, this model is represented by a system of ordinary differential equations. The time derivative of the number of individuals in a compartment, i.e., the rate of their change, is given by the difference between the rates at which the compartment is filled and emptied. Analogous to the processes in which chemical species (e.g., proteins) are degraded or converted into others within a biochemical reaction network (Ingalls, 2013), the rate of transition of individuals from one compartment to another follows the law of mass action. For example, a person moves from compartment S to compartment I at the rate which is proportional to the product of the S and I, as the encounter with an infected person enables virus transmission to the susceptible one (Voit et al., 2015).

By formulating such (or similar) models, one assumes that the epidemic is a deterministic process. Namely, the state of the population at all times is completely determined by its previous state and the rules described by the model. This is a reasonable approximation in cases where the numbers of individuals in the compartments are large, i.e., in a commonly considered

Fig. 2 Schematic representation of the SIR model. Rectangles denote model compartments containing susceptible (S), infected (I), and recovered (R) individuals in the population of size N. Permitted directions of flow between compartments are denoted by arrows, with the rates of flow indicated above them. The rates are expressed according to the law of mass action, where κ_1 and κ_2 are the rate constants. The dashed curve corresponds to bimolecular reaction, where newly infected are generated through interactions (contacts) between susceptible and already infected individuals.

deterministic range (>10). Such approximation (i.e., deterministic modeling) is well suited for the spread of COVID-19, which is up to now known for a large number of individuals in all compartments.

3. Systems biology approach to compartmental modeling of the COVID-19 epidemic

The above-introduced SIR model is likely the simplest compartmental model in mathematical epidemiology and many subsequent models are derivatives of this basic form. Among others, these extensions have also been developed toward including control measures such as vaccination or quarantine (Diekmann, Heesterbeek, & Britton, 2012; Keeling & Rohani, 2011; Martcheva, 2015). However, COVID-19 brought a challenge to account for previously unprecedented social distancing measures, taken by most countries. When included, these effects have been, up to now, accounted for by the direct changes in the transmissibility term (Chowell, Sattenspiel, Bansal, & Viboud, 2016; Tian et al., 2020), which, however, corresponds to introducing a phenomenological dependence in otherwise mechanistic models. That is, to be included consistently in the model, social distancing should move individuals from one compartment to the other, just as vaccination and quarantine are usually implemented. On the other hand, it is necessary to construct a minimal mechanistic model in terms of the ability to explain the data with the smallest number of parameters, so that relevant infection progression properties can be inferred without overfitting. With this goal in mind, we used our systems biology background to develop a minimal model that accounts for all the main qualitative features of the SARS-CoV-2 infection spread under epidemic mitigation measures. As outlined above, we opt for a deterministic model due to the robust and computationally less demanding parameter inference (Wilkinson, 2018).

To describe the COVID-19 epidemic, we developed SPEIRD model depicted schematically in Fig. 3. It assumes that healthy persons susceptible to infection (S), can be infected, but in the case of this (and many other) viruses they do not immediately become contagious to other people, but first spend some time in the compartment E (**E**xposed to the virus) and then develop symptoms and pass to the compartment I. Infected persons can either recover at home, moving to the compartment R, or they can be diagnosed with SARS-CoV-2 virus infection (**A**ctive detected cases). A (Active) cases can, further, either become healed (H) or die from the disease (F). To consistently implement the social distancing within this model structure, we
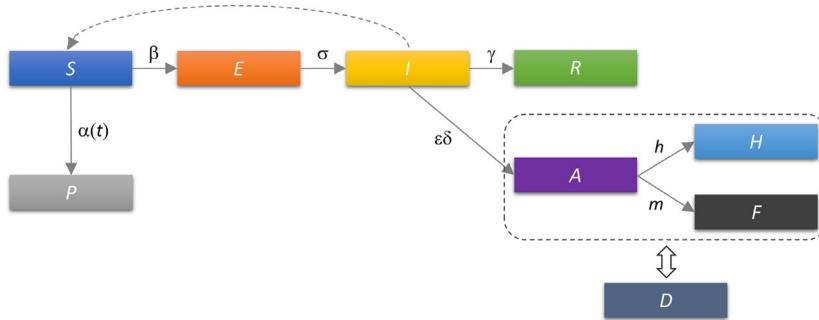
Fig. 3 Schematic representation of the SPEIRD model. Compartments and the transition rates are as indicated in the text, where transitions between different compartments are marked by arrows. The time-dependent transition rate from susceptible to protected category $\alpha(t)$ is indicated by the solid arrow. The infected can transition to the recovered category either without being diagnosed (transition to R), or being diagnosed and then transitioning to confirmed healed or fatality cases. The dashed rectangle indicates that A, H, and F categories in the starting model are substituted for the cumulative case counts (D), which removes h and m from the analysis, where D is fitted to the observed data.

included a compartment P (**P**rotected) in the model, which contains susceptible persons who are protected from exposure to the virus as a result of the epidemic mitigation measures, such as self-imposed isolation, social distancing, and advised changes in individual behavior.

The following differential equations describe how different categories change with time:

$$dS/dt = -\beta \cdot I \cdot S/N - \alpha(t) \cdot S \tag{1}$$
$$dE/dt = \beta \cdot I \cdot S/N - \sigma \cdot E \tag{2}$$
$$dI/dt = \sigma \cdot E - \gamma \cdot I - \varepsilon \cdot \delta \cdot I \tag{3}$$
$$dA/dt = \varepsilon \cdot \delta \cdot I - h \cdot A - m \cdot A \tag{4}$$
$$dH/dt = h \cdot A \tag{5}$$
$$dF/dt = m \cdot A \tag{6}$$

where β is the infection rate in a fully susceptible population; $\alpha(t)$, the time–dependent protection rate, i.e., the rate at which the population moves from susceptible to the protected category, quantifying the impact of the social protection measures; σ, the inverse of the exposed period; γ, the inverse of the infectious period; δ, the inverse of the period of the infection diagnosis; ε, the detection efficiency; h, the healing rate of diagnosed cases; m, the mortality rate.

The probability that an infected person will meet a susceptible person is proportional to S/N, where N is the total number of individuals in the population. The rate at which individuals move from S to E is obtained when the product of I and S/N is multiplied by the infection rate, β, which quantifies the efficiency of transmission of a particular virus in the population with certain demographic characteristics and meteorological conditions, and it does not depend on epidemic suppression measures. Thus, β is a characteristic of the virus, the population, and the external conditions in which the virus is transmitted. Since the compartment S is being emptied, the corresponding rate in the first equation is specified with the minus sign.

S also decays by moving the individuals to P with a protection rate that may vary with time. While mitigation measures are commonly accounted for by models with time-independent terms (Martcheva, 2015), we note that the social distancing term should depend on time, as this measure is introduced at a certain point in epidemics and may also evolve gradually. We denote the time point (more specifically, the date) of the onset of the social distancing measures in the examined population with t_0. The protection rate $\alpha(t)$ is then taken as 0 before t_0 and a constant value α afterwards.

One may notice a direct parallel between the model outlined above, and e.g., modeling gene expression regulation in systems biology with a step function that approximates the activity of a promoter to which repressor proteins are highly cooperatively bound: the promoter is initially silenced and upon receiving a signal which leads to the abrupt removal of repression, promoter activity rises sharply to its maximum value. We notice that the step function is a satisfactory approximation of the dynamics of social distancing, i.e., it may not be necessary to further increase the number of parameters by applying the Hill function (which describes a more gradual activation), since governments quickly introduced these measures, together with their effective implementation. Note however that in (Djordjevic et al., 2021) we introduced a more complex model with Hill function, and provided analytical results for key properties of this model.

Compartment E is filled by infecting the susceptibles and emptied by moving the individuals to I, with the rate σ representing the inverse value of the latent period during which the person is not contagious. While compartment I is filled with individuals from E, it is depleted through two channels. Individuals move to R with the rate γ, which is the inverse of the period of contagiousness, and to A with the rate δ, which is the inverse of the time required for diagnosis, multiplied by ε, reflecting that only a fraction (likely small due to many asymptomatic infections) of the total infected are

detected. Note that case detection reduces the number of individuals in I that can infect susceptibles: the model assumes that the detected cases are quarantined and thus isolated from the general population. The numbers in compartments A, H, and F change following the same logic described for the other compartments.

We can further simplify the analysis by looking at the total number of detected cases (D), which is the sum of A, H, and F. By adding the Eqs. (4)–(6), we obtain:

$$dD/dt = \varepsilon \cdot \delta \cdot I, \tag{7}$$

and thus lose two parameters, h and m. The total number of detected cases in time is a measurable quantity from which we can determine the dynamics of other model compartments since this is the data that is available for various different regions and countries. Thereby, we assume that before t_0 social distancing does not take effect, and the measures introduced at t_0 will take effect on $D \sim 10$ days later, as this is about the time that elapses between infection and detection/diagnosis (Feng et al., 2020). Consequently, for the first $t_0 + 10$ days, the D curve reflects disease transmission without epidemic suppression measures.

3.1 Virus transmission in the early stages of epidemics

We will now focus on the dynamics of the infection spread at the very beginning of the epidemic, i.e., on the period before the introduction and practice of any control measures (Salom et al., 2021). Regarding the model, we assume that there is no social distancing (no transition from S to P), there is no quarantine, and almost the entire population consists of people susceptible to infection, so S/N = 1. This gives us an even simpler mathematical model which appears to be very useful because it allows analytical derivation of the expressions we need. Our system of Eqs. (1)–(3) and (7) is reduced to two linear differential equations that we can write in matrix form

$$\frac{d}{dt}\begin{pmatrix} E \\ I \end{pmatrix} = \begin{pmatrix} -\sigma & \beta \\ \sigma & -\gamma \end{pmatrix}\begin{pmatrix} E \\ I \end{pmatrix} = A\begin{pmatrix} E \\ I \end{pmatrix}, \tag{8}$$

determine the eigenvalues and eigenvectors of the matrix and, subsequently, the solutions of the system, $E(t)$ and $I(t)$. Specifically, the cumulative number of infected in time, $I(t)$, is obtained according to the following equation:

$$I(t) = C_1 \exp(\lambda_+ t) + C_2 \exp(\lambda_- t), \tag{9}$$

where λs are eigenvalues of the matrix. Since one of the eigenvalues, here denoted by λ_-, is negative, the corresponding term of the Eq. (9) will decrease over time, and $I(t)$ will be effectively described by the first term, already after few days from the epidemic outbreak (Salom et al., 2021). We can further derive this equation for the dependence of the logarithm of the number of detected cases in time:

$$\log\left(D(t)\right) = \log\left(\varepsilon \cdot \delta \cdot I(0)/\lambda_+\right) + \lambda_+ \cdot t \tag{10}$$

This is the straight line equation whose slope is given by the value of λ_+ (the dominant, positive eigenvalue of the matrix in Eq. (8)).

Once we know λ_+, we can calculate the value of the so-called basic reproduction number, $R_{0,\text{free}}$, by fixing mean values of the latency period and the infectivity period ($\gamma = 0.4\ \text{days}^{-1}$, $\sigma = 0.2\ \text{days}^{-1}$), which are known from the literature and characterize the fundamental infection processes (Kucharski et al., 2020; Li et al., 2020):

$$R_{0,\text{free}} = \frac{\beta}{\gamma} = 1 + \frac{\lambda_+(\gamma + \sigma) + \lambda_+^2}{\gamma\sigma} \tag{11}$$

$R_{0,\text{free}}$ is an important epidemiological parameter that characterizes the inherent biological transmission of the virus in a completely unprotected population. In particular, it is the mean number of secondarily infected by one infected person introduced in a completely susceptible population. It depends on the biology of the specific virus, as well as the demographic characteristics of the population and the environmental conditions, while it does not depend on the applied infection control measures (Brauer, 2008). In Salom et al. (2021) we utilized a bioinformatics analysis, akin to those often used to understand complex data in systems biology, to pinpoint demographic and meteorological factors that affect $R_{0,\text{free}}$ (i.e., inherent virus transmissibility in population). This furthermore underlines that a rich array of techniques developed and/or widely used within systems biology can be successfully employed within infectious disease modeling.

4. Parameter analysis and inference

$R_{0,\text{free}}$, α, t_0, two initial conditions (I_0 and E_0), and the detection efficiency ε, are unknown and may differ between the provinces. Is it possible to determine these unknown parameters from different properties of the D curve? Early in the infection, almost the entire population is susceptible ($S \approx N$), so Eqs. (2) and (3) become linear, and decoupled from the rest of the

system, as discussed in the previous section. This sets the ratio of I_0 to E_0, through the eigenvector components with the dominant (positive) eigenvalue of the Jacobian for this subsystem. This eigenvalue, corresponding to the initial slope of the $log(D)$ curve, sets the value of λ_+ and subsequently, of $R_{0,\text{free}}$ (see Eq. 11). From Eq. (7) one can see that the product of I_0 and $\varepsilon \cdot \delta$ is set by dD/dt at the initial time ($t = 0$). Later dynamics of the D curve is determined solely by the combination $t_\alpha = t_0 + 1/\alpha$ (which we denote as protection time), setting the time at which $\sim \frac{1}{2}$ of the population moves to the protected category. We also numerically checked this, and confirmed that t_0 can be lowered at the expense of increasing $1/\alpha$, without affecting the fit quality. We allowed for t_0 to vary in reasonable proximity of January 23, as the social distancing was generally introduced close to Wuhan closure (e.g., on that date, all major events in Beijing were canceled) (Chen et al., 2020; Du et al., 2020), but we cannot be sure when the measures effectively took place. Our inferred t_0 values are within a week from Wuhan closure, appearing as reasonable. The remaining independent parameter (I_0) is then left to be determined from D curve properties at the late infection stage, such as its saturation time. The number of characteristic dynamics features is thus at least equal to the number of fit parameters, leading to constrained numerical analysis, so that overfitting is not expected. For few provinces, we however observed that I_0 can be decreased compared to the best fit value, without noticeably affecting the fit quality. For these provinces, we chose the lowest I_0 value that still leads to a comparably good fit. This allows obtaining the most conservative (i.e., as high as possible while still consistent with data) IFR estimate, as the reported fatality counts for provinces other than Hubei is surprisingly low.

Parameter inference and uncertainties are estimated separately for each province. However, within a given province, demographic, special, or population activity (network effects) heterogeneities (Britton, Ball, & Trapman, 2020; Diekmann et al., 2012), or seasonality effects (Wong et al., 2020), are not taken into account. These are potentially important, particularly for projections (longer-term predictions of infection dynamics under different scenarios), and can be readily included in our model. Such extensions would however complicate parameter inference, due to an increase in parameter number, as this may either lead to overfitting or require special/additional data that may be available only for a limited number of countries/regions (which would limit the generality of our proposed method). A more complex model structure may also obscure a straightforward relationship between the model parameters and distinct dynamical features of the

confirmed case count curve analyzed above. While the inclusion of additional effects is left for future work, we here employ the model structure and parameter inference introduced above on widely available case count data, as proof of the principle for the generality of our proposed approach. Moreover, a major advantage of our approach is that it allows consistent analysis for all provinces with the same model, numerical procedure, and parameter set, allowing an objective comparison of the obtained results.

Our model was numerically solved by the Runge-Kutta method (Dormand & Prince, 1980) for each parameter combination. Parameter values were inferred by exhaustive search over a wide parameter range, to avoid reaching a local minimum of the objective function (R^2). To infer the unknown parameters, we fit (by minimizing R^2) the model to the observed total number of detected D for each province. As an alternative to exhaustive search, some of many optimization techniques used in epidemics modeling, such as the Markov chain Monte Carlo (MCMC) approach, can be used instead (Keeling & Rohani, 2011; Wong et al., 2020)—exhaustive search is however straightforward, guarantees that the global minimum is reached, and is in this case not computationally demanding. Errors were estimated through Monte-Carlo simulations (Press, Flannery, Teukolsky, & Vetterling, 1986), individually for each province with the assumption that count numbers follow the Poisson distribution. Monte-Carlo simulations were found as the most reliable estimate of the fit parameter uncertainties for a non-linear fit (Cunningham, 1993). This also serves as an independent check for overfitting, as in that case, data point perturbations would lead to large parameter uncertainties. We find no indication of this in the results reported below, as the inferred uncertainties (consistently indicated with all results) are reasonably small. In particular, the differences in the inferred parameter values, which are relevant for the reported results/conclusions, are statistically highly significant. P values for extracted parameter differences between provinces are estimated by the t-test.

5. Analysis of COVID-19 transmission in China

We used our SPEIRD model with the parameter inference described above, to analyze all Mainland China provinces, except Tibet, where only one COVID-19 case was reported. Parameters were estimated separately for each of the 30 provinces by the same model and parameter set, which enables an impartial comparison of the results presented below. To allow

for a straightforward comparison of the infection progression between different provinces, the starting date (i.e., $t = 0$) in our analysis is the same for all the provinces and corresponds to January 23 (when the data for all the provinces became publically available and continuously tracked (Hu et al., 2020)).

In Fig. 4A and B, we show that our model can robustly explain the observed D, in the cases of large outburst (Hubei on Fig. 4A), as well as for all other provinces, where D is in the range from intermediate (e.g., Guangdong) to low (e.g., Inner Mongolia). Provinces in Fig. 2B were selected to cover the entire range of observed D (from lower to higher counts), while comparably good fits were obtained for other provinces, which were all included in the further analysis. Our method is also robust to data perturbations (which might be frequent), e.g., in the case of Hubei (Wuhan), a large number of counts was added on February 12, based on clinical diagnosis (CT scan) (Feng et al., 2020), which is apparent as a discontinuity in observed D in Fig. 4A. The model however interpolates this discontinuity, finding a reasonable description of the overall data.

We backpropagated the dynamics inferred for Hubei, to estimate that January 5 (± 4 days) was the onset of the infection's exponential growth in the population (not to be confused with the appearance of first infections, which likely happened in December (Feng et al., 2020)). This agrees well with (Feng et al., 2020) (cf. Fig. 3A), which tracked cases according to their symptom onset (shifted for $\sim$12 days with respect to detection/diagnosis, cf. Fig. 3B), and coincides with WHO reports on social media that there is a cluster of pneumonia cases—with no deaths—in Wuhan (WHO, 2020). Since our analysis does not directly use any information before January 23, this agreement provides confidence in our I_0 estimate. Note that we infer I_0 separately for each province of interest, through which we also take into account different times of the infection onset in different provinces (so that earlier onset time would generally lead to a larger number of infected on January 23).

Key parameters inferred from our analysis are summarized in Fig. 4C–F, with individual results and errors for all the provinces shown in Table 1. Fig. 4C shows the distribution of $R_{0,\text{free}}$. Note that $R_{0,\text{free}}$ might depend on demographic (population density, etc.) and climate factors (temperature, humidity…), which are not controllable, but are unrelated to the applied social distancing measures (see above). It is known that the R_0 value can strongly depend on the model, e.g., the number of introduced compartments (Keeling & Rohani, 2011); accordingly, a wide range of R_0 values
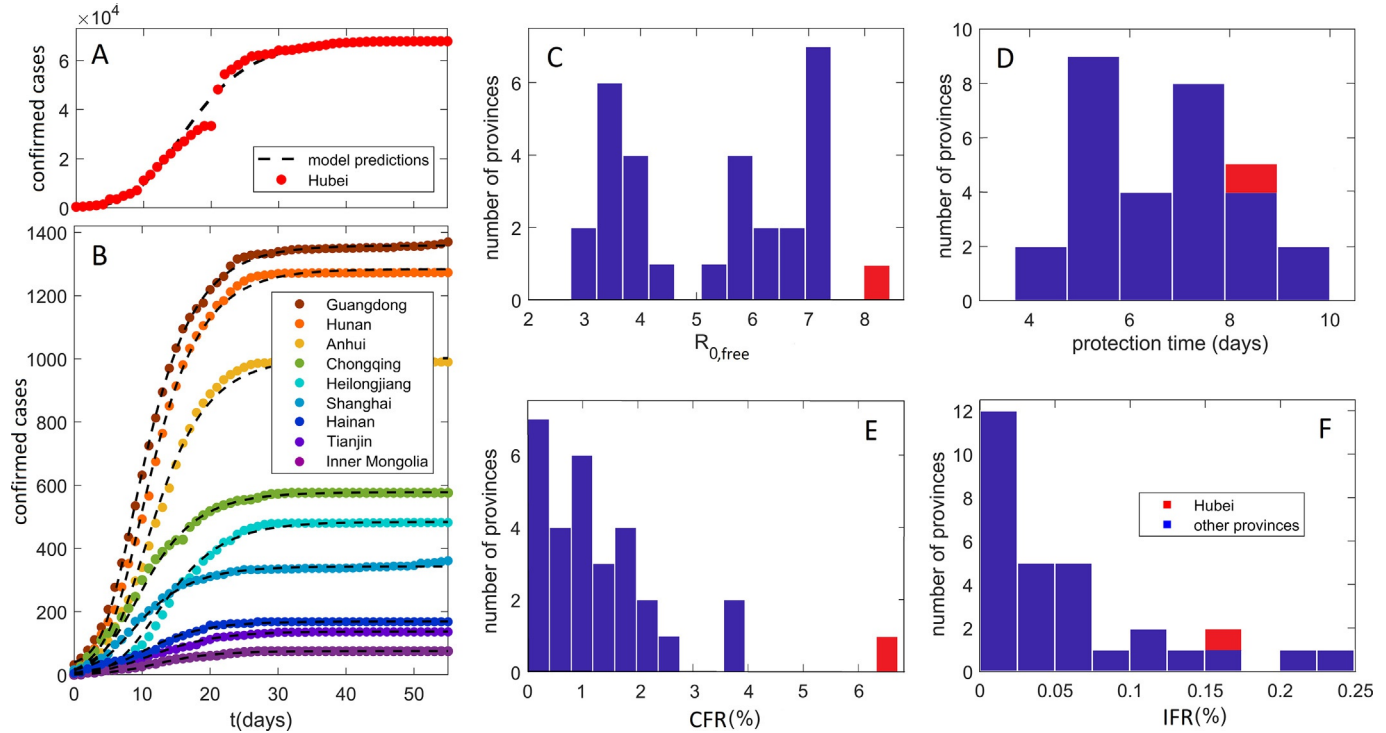
Fig. 4 Model predictions: comparison with data and key parameter estimates. Predictions (compared to data) of detected infection counts for (A) Hubei, (B) other Mainland China provinces. Zeros on the horizontal axis correspond to January 23, which is the initial time in our numerical analysis for all the provinces. The observed counts are shown by dots and our model predictions by dashed curves. Names of the provinces are indicated in the legend, with provinces selected to cover the full range of the observed total detected counts. The distribution with respect to provinces of (C) the basic reproduction number in the absence of social distancing, $R_{0,free}$, (D) the protection time t_α. (E) Case Fatality Rate, calculated directly from the reported data. (F) Infected Fatality Rate. The values for Hubei are indicated by the red bars.

Table 1 Inferred COVID-19 infection progression parameters for Mainland China provinces

Province	t_α (days)	R_0	E_0	I_0	IFR (%)	CFR (%)	Detected (%)
Anhui	6.6 ± 0.5	5.5 ± 0.8	920 ± 30	220 ± 20	0.04 ± 0.02	0.6 ± 0.3	6 ± 3
Beijing	7.9 ± 0.5	3.5 ± 0.4	610 ± 20	180 ± 10	0.12 ± 0.05	1.7 ± 0.7	7 ± 3
Chongqing	7.0 ± 0.2	3.5 ± 0.2	1900 ± 40	560 ± 20	0.04 ± 0.03	1.0 ± 0.5	4 ± 2
Fujian	3.7 ± 0.4	7 ± 2	1660 ± 40	360 ± 20	0.007 ± 0.003	0.3 ± 0.4	2 ± 1
Gansu	5 ± 1	6 ± 3	630 ± 20	150 ± 10	0.03 ± 0.04	1 ± 1	2 ± 3
Guangdong	5.0 ± 0.1	7 ± 1	1360 ± 40	290 ± 20	0.04 ± 0.01	0.6 ± 0.2	7 ± 2
Guangxi	7 ± 1	3.8 ± 0.8	1000 ± 30	290 ± 20	0.02 ± 0.02	0.8 ± 0.6	3 ± 3
Guizhou	8.1 ± 0.6	7 ± 1	53 ± 7	11 ± 3	0.06 ± 0.03	1 ± 1	4 ± 2
Hainan	7.6 ± 0.8	3.3 ± 0.7	300 ± 20	90 ± 10	0.21 ± 0.09	4 ± 2	6 ± 3
Hebei	6.0 ± 0.6	7 ± 2	240 ± 20	52 ± 7	0.11 ± 0.03	1.8 ± 0.8	6 ± 2
Heilongjiang	7 ± 1	6 ± 2	260 ± 20	59 ± 7	0.15 ± 0.07	2.9 ± 0.9	5 ± 3
Henan	7.0 ± 0.3	4.5 ± 0.5	1780 ± 40	460 ± 20	0.09 ± 0.04	1.7 ± 0.4	5 ± 2
Hubei	8.3 ± 0.2	8.2 ± 0.4	$31,900\pm400$	6600 ± 200	0.15 ± 0.09	6.5 ± 0.1	2 ± 2
Hunan	5.1 ± 0.1	6.8 ± 0.8	1430 ± 40	310 ± 20	0.02 ± 0.01	0.4 ± 0.2	5 ± 2
I. Mongolia	10.0 ± 0.8	2.8 ± 0.4	940 ± 30	300 ± 20	0.01 ± 0.03	1 ± 1	1 ± 3
Jiangsu	5.5 ± 0.5	7 ± 2	500 ± 20	110 ± 10	0 ± 0	0 ± 0	6 ± 2

	t_α	$R_{0,\text{free}}$	E_0	I_0	IFR	CFR	detected %
Jiangxi	7.0 ± 0.2	5.6 ± 0.9	890 ± 30	210 ± 10	0.005 ± 0.002	0.1 ± 0.1	5 ± 2
Jilin	10.0 ± 0.7	4.0 ± 0.8	270 ± 20	76 ± 9	0.02 ± 0.02	1 ± 1	1 ± 2
Liaoning	7 ± 1	2.9 ± 0.7	1240 ± 40	390 ± 20	0.02 ± 0.04	2 ± 2	1 ± 2
Ningxia	5.3 ± 0.9	7 ± 3	72 ± 9	15 ± 4	0 ± 0	0 ± 0	6 ± 23
Qinghai	6.1 ± 0.6	4.0 ± 0.5	2260 ± 50	640 ± 30	0 ± 0	0 ± 0	0 ± 2
Shaanxi	5.2 ± 0.5	6 ± 1	380 ± 20	90 ± 10	0.07 ± 0.03	1.3 ± 0.8	6 ± 2
Shandong	9 ± 1	3.5 ± 0.5	900 ± 30	260 ± 20	0.06 ± 0.01	1.0 ± 0.4	6 ± 1
Shanghai	5.0 ± 0.4	6 ± 1	1570 ± 40	370 ± 20	0.02 ± 0.02	0.8 ± 0.5	2 ± 3
Shanxi	5.2 ± 0.5	6 ± 2	1600 ± 40	370 ± 20	0 ± 0	0 ± 0	1 ± 2
Sichuan	7.7 ± 0.8	3.7 ± 0.5	990 ± 30	280 ± 20	0.03 ± 0.02	0.6 ± 0.3	5 ± 3
Tianjin	7 ± 2	4 ± 2	170 ± 10	46 ± 7	0.14 ± 0.06	2 ± 1	7 ± 3
Xinjiang	7.3 ± 0.9	6 ± 1	42 ± 7	10 ± 3	0.25 ± 0.09	3 ± 2	8 ± 2
Yunnan	4.0 ± 0.2	7 ± 2	360 ± 20	76 ± 9	0.06 ± 0.03	1.2 ± 0.9	5 ± 2
Zhejiang	5.0 ± 0.1	7.2 ± 0.8	1340 ± 40	290 ± 20	0.005 ± 0.002	0.1 ± 0.1	7 ± 3

t_α, protection time; $R_{0,\text{free}}$, basic reproduction number; E_0, initial exposed; I_0, initial infected; *IFR*, Infected Fatality Rate; *CFR*, Case Fatality Rate; *detected %*, fraction of the infected population that has been detected. Error of the quantities correspond to one standard deviation.

were reported for China in the literature (Sanche et al., 2020; Wu, Leung, Bushman, et al., 2020). Consequently, a clear advantage of our study is that parameters for all China provinces were determined from the same model and data set, which allows direct comparisons. Our obtained average $R_{0,\text{free}}$ for provinces outside of Hubei is 5.3 ± 0.3, in a reasonable agreement with a recent estimate (≈ 5.7) (Sanche et al., 2020). Furthermore, we observe that $R_{0,\text{free}}$ for Hubei is a far outlier with a value of 8.2 ± 0.4, which is notably larger than for other provinces with $p \sim 10^{-11}$. This then strongly suggests that demographic and climate factors that determine $R_{0,\text{free}}$, played a decisive role in a large outburst in Hubei vs other provinces, which we further address below.

The distribution of protection time t_α for the provinces is shown in Fig. 4D, with the value for Hubei indicated in red. The mean for the other provinces is 6.6 ± 0.2 days. That is, we observe that the suppression measures were efficiently implemented, with $\sim \frac{1}{2}$ of the population moving to the protected category within a week from Wuhan closure. The protection time for Hubei of 8.3 ± 0.2 days was longer, which is statistically significant at the $p \sim 10^{-11}$ level. The estimated less efficient protection in the case of Hubei may also be an important contributing factor in the surprising difference in Hubei vs other provinces, which we further investigate below.

CFR distribution, based on the fatality numbers reported for Hubei and other provinces is shown in Fig. 4E. These numbers are not based on the model predictions, i.e., can be straightforwardly obtained by dividing the total number of fatalities by the total number of detected cases. CFR for other provinces with a mean of $1.2 \pm 0.4\%$ is significantly smaller compared to CFR for Hubei, which was 4.6% before the correction on April 17, and 6.5% after the correction (with 1290 fatalities added to Wuhan). This large difference in CFR between Hubei and other provinces further accentuates the differences noted in Fig. 1.

IFR is harder to determine than CFR, as a majority of COVID-19 infections correspond to asymptomatic or mild cases that are by large not diagnosed (Day, 2020). We consequently calculate IFR as the total number of fatalities divided by the total number of infections (cumulative incidence) for the entire outburst, where cumulative incidence is estimated from our model. As the infections precede fatalities, both the total number of fatalities and the cumulative incidence in our estimate correspond to the entire outburst, so that all the infections had a sufficient time to recover or lead to fatalities—this is directly feasible for the provinces in China, where all detected case counts reached saturation. Note that IFR calculated in this

way corresponds to an averaged quantity so that it does not capture possible time-dependent change over the outburst interval (in fact, for Wuhan it is known that the fatality rate was larger at the very beginning of the outburst). Nevertheless, the estimated IFR's present a reasonable measure of COVID-19 mortality across China provinces.

IFR distribution, which provides a much less biased measure of the infection mortality, is shown in Fig. 4F. In distinction to CFR, estimated IFR shows a much smaller difference between Hubei ($0.15 \pm 0.09\%$) and other provinces ($0.056 \pm 0.007\%$). Therefore, while Hubei is a clear outlier with respect to CFR, we observe similar IFR values for all Mainland China provinces, where few provinces have even higher IFR than Hubei. The ratio of IFR to CFR equals the fraction of all infected that got detected (*detection coverage*). We estimate that the mean detection coverage for all provinces except Hubei is higher than detection coverage for Hubei ($4.5 \pm 0.9\%$ vs $2 \pm 2\%$). This difference is responsible for a decrease by a factor of two from CFR to IFR for Hubei, compared to the other provinces, and consequently for more uniform mortality estimates at the IFR level. Xinjiang has the highest IFR of $0.25 \pm 0.09\%$ so that Hubei is not an outlier anymore. Estimated IFR's of up to 0.3% in China provinces are in general agreement with the estimates reported elsewhere (see e.g., (Bar-On et al., 2020; Djordjevic et al., 2021; Mizumoto, Kagaya, & Chowell, 2020)).

In Fig. 5A, two key infection progression parameters are plotted against each other: protection time t_α vs basic reproduction number $R_{0,\text{free}}$. Unexpectedly, there is a high negative correlation, with Pearson correlation coefficient $R = -0.70$, which is statistically highly significant $p \sim 10^{-5}$, where these two are a priori unrelated (see above). Actually, stronger social distancing measures—which by definition are not included in $R_{0,\text{free}}$— would lead to a decrease in *effective* transmissibility. This would then lead to a tendency of transmissibility to positively correlate with t_α, oppositely from the strong negative correlation observed in Fig. 5A. Therefore, higher basic reproduction number is genuinely related to a shorter protection time (larger effect of the suppression measures). Intuitively, this could be understood as a negative feedback loop, commonly observed in systems biology (Alon, 2019; Phillips, Kondev, Theriot, & Garcia, 2012), where larger $R_{0,\text{free}}$ leads to steeper initial growth in the infected numbers, which may elicit stronger measures and better observing of these measures by the population faced with a more serious outbreak. Interestingly, similar negative feedback was also obtained in the context of epidemics research other than COVID-19 (Wang, Andrews, Wu, Wang, & Bauch, 2015).
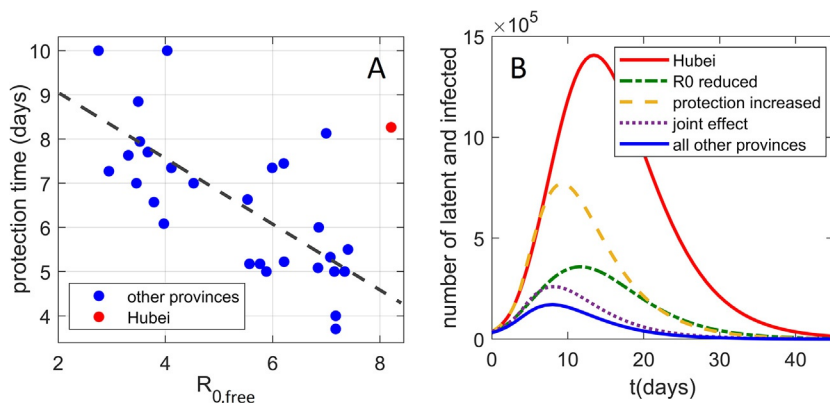
Fig. 5 The interplay of transmissibility and effective social distancing. (A) The correlation plot of t_α vs $R_{0,\text{free}}$ for all provinces, where the point corresponding to Hubei is marked in red. (B) The effect (on the Hubei dynamics of infected and latent cases) of reducing $R_{0,\text{free}}$ and t_α to the mean values of other Mainland China provinces. Both the unperturbed Hubei dynamics and the sum of infected and latent cases for all other provinces are included as references.

The two main properties of the Hubei outburst are therefore higher $R_{0,\text{free}}$ and t_α compared to other provinces. In Fig. 5B, we investigate how these two properties separately affect the Wuhan outburst for latent and infected cases, where unperturbed Hubei dynamics is shown by the red full curve. We first reduce only $R_{0,\text{free}}$ from the Hubei value, to the mean value for all other provinces (the dash-dotted green curve). We see that this reduction substantially lowers the peak of the curve, though it still remains wide. Next, instead of decreasing $R_{0,\text{free}}$, we decrease the protection time t_α to the mean value for all other provinces (dashed orange curve). While reducing t_α also significantly lowers the peak of the curve, its main effect is in narrowing the curve, i.e., reducing the outburst time. Finally, when $R_{0,\text{free}}$ and t_α are jointly reduced, we obtain the (dotted purple) curve that is both significantly lower and narrower than the original Hubei progression. This curve comes quite close to the curve that presents the sum of all other provinces (full blue curve)—the dotted curve remains somewhat above this sum, mainly because the initial number of latent and infected cases is somewhat higher for Hubei compared to the sum of all other provinces. This synergy between the transmissibility and the control measures will be further discussed below.

6. Conclusions

In this study, we applied a systems biology approach to develop a novel method of COVID-19 transmission dynamics. The model includes (time–dependent) social distancing measures in a simple manner, consistent with the compartmental mechanistic nature of the underlying process. The model has a major advantage that it is independent of the specific transmission process considered, and requires only commonly available count data as an input. The model allows extracting key infection parameters from the data that are readily available and publicly accessible (both for China and other countries), so that, in a nutshell, our approach is of wide applicability. To our best knowledge, such parameters (necessary to assess any future COVID-19 risks), were not extracted by other computational approaches.

The developed method is subsequently applied to the problem that appears highly non–trivial, i.e., to understand the puzzle created by the drastic differences in the infection and fatality counts between Hubei and the rest of Mainland China. The goal was to determine if it is possible to consistently explain such drastic differences by the same model, and what are the resulting numerical estimates and conclusions. We found that Hubei was a suitable ground for infection transmission, being an outlier with respect to two key infection progression parameters: having significantly larger $R_{0,\text{free}}$, and a longer time needed to move a sizable fraction of the population from susceptible to a protected category. While stricter measures were formally introduced in Hubei, the initial phase of the outburst put a large strain on the system, arguably leading to less effective measures compared to other provinces.

The fact that the initial epidemic in Hubei was not followed by similar outbursts in the rest of Mainland China may be understood as a serendipitous interplay of the two factors noted above. While both smaller $R_{0,\text{free}}$ and lower half–protection time (more efficient measures) significantly suppress the infection curve, their effect is also qualitatively different. While lowering $R_{0,\text{free}}$ more significantly suppresses the peak, decreasing the half–protection time significantly reduces the outburst duration. Consequently, the synergy of these two effects appears to lead to drastically suppressed infection dynamics in other Mainland China provinces compared to Hubei. The number of detected (diagnosed) cases in the entire Mainland China is, therefore, though unintuitive, well consistent with the model, and is explainable by a seemingly reasonable combination of circumstances. Our obtained

negative feedback between transmissibility and effects of social distancing may be understood in terms of larger transmissibility triggering more stringent social distancing measures, where a similar conclusion was also obtained through entirely different means (a combination of real-time human mobility data and regression analysis) (Kraemer et al., 2020).

In summary, we showed that unintuitive dissimilarity in the infection progression for Hubei vs other Mainland China provinces is consistent with our model, and can be attributed to the interplay of transmissibility and effective protection, demonstrating that regional differences may drastically shape the infection outbursts. This also shows that comparisons in terms of the confirmed cases, or fatality counts (even when normalized for population size), between COVID-19 and other infectious diseases, or between different regions for COVID-19, are not feasible, and that parameter inference from quantitative models (individually for different affected regions) is necessary. Consequently, this paper illustrates that utilization of uncommon strategies, such as systems biology application to mathematical epidemiology, may significantly advance our understanding of COVID-19 and other infectious diseases.

Acknowledgment

References

Alon, U. (2019). *An introduction to systems biology: Design principles of biological circuits*. CRC press.

Alon, U., Mino, R., & Yashiv, E. (2020). *10–4: How to reopen the economy by exploiting the coronavirus's weak spot*. The New York Times.

Bar-On, Y. M., Flamholz, A., Phillips, R., & Milo, R. (2020). Science forum: SARS-CoV-2 (COVID-19) by the numbers. *eLife, 9,* e57309.

Brauer, F. (2008). Compartmental models in epidemiology. In *Mathematical epidemiology* (pp. 19–79). Springer.

Britton, T., Ball, F., & Trapman, P. (2020). A mathematical model reveals the influence of population heterogeneity on herd immunity to SARS-CoV-2. *Science, 369*(6505), 846–849.

Chen, S., Yang, J., Yang, W., Wang, C., & Bärnighausen, T. (2020). COVID-19 control in China during mass population movements at New Year. *The Lancet, 395*(10226), 764–766.

Chowell, G., Sattenspiel, L., Bansal, S., & Viboud, C. (2016). Mathematical models to characterize early epidemic growth: A review. *Physics of Life Reviews, 18,* 66–97.

Cunningham, R. W. (1993). Comparison of three methods for determining fit parameter uncertainties for the Marquardt Compromise. *Computers in Physics,* 7(5), 570–576.

Day, M. (2020). Covid-19: Identifying and isolating asymptomatic people helped eliminate virus in Italian village. *British Medical Journal, 368*(m1165)(Online).

Diekmann, O., Heesterbeek, H., & Britton, T. (2012). Mathematical tools for understanding infectious disease dynamics. In (Vol. 7). Princeton University Press.

Djordjevic, M., Djordjevic, M., Ilic, B., Stojku, S., & Salom, I. (2021). Understanding infection progression under strong control measures through universal COVID-19 growth strategies. *Global Challenges*, *5*, 2000101.

Djordjevic, M., Rodic, A., & Graovac, S. (2019). From biophysics to 'omics and systems biology. *European Biophysics Journal*, *48*(5), 413–424.

Dormand, J. R., & Prince, P. J. (1980). A family of embedded Runge-Kutta formulae. *Journal of Computational and Applied Mathematics*, *6*(1), 19–26.

Du, Z., Xu, X., Wang, L., Fox, S. J., Cowling, B. J., Galvani, A. P., et al. (2020). Effects of proactive social distancing on COVID-19 outbreaks in 58 cities, China. *Emerging Infectious Diseases*, *26*(9), 2267.

Eilersen, A., & Sneppen, K. (2020). Cost–benefit of limited isolation and testing in COVID-19 mitigation. *Scientific Reports*, *10*(1), 1–7.

Feng, Z., et al. (2020). The epidemiological characteristics of an outbreak of 2019 novel coronavirus diseases (COVID-19)—China, 2020. *China CDC Weekly*, *2*(8), 113–122.

Hu, T., Weihe, W. G., Zhu, X., Shao, Y., Liu, L., Du, J., et al. (2020). Building an open resources repository for COVID-19 research. *Data and Information Management*, *4*(3), 130–147.

Ingalls, B. P. (2013). *Mathematical modeling in systems biology: An introduction*. MIT Press.

Karin, O., Bar-On, Y. M., Milo, T., Katzir, I., Mayo, A., Korem, Y., et al. (2020). Cyclic exit strategies to suppress COVID-19 and allow economic activity. *medRxiv* 2020.04.04.20053579.

Keeling, M. J., & Rohani, P. (2011). *Modeling infectious diseases in humans and animals*. Princeton University Press.

Kermack, W. O., & McKendrick, A. G. (1927). A contribution to the mathematical theory of epidemics. *Proceedings of the Royal Society of London Series A, Containing Papers of a Mathematical and Physical Character*, *115*(772), 700–721.

Kraemer, M. U., Yang, C.-H., Gutierrez, B., Wu, C.-H., Klein, B., Pigott, D. M., et al. (2020). The effect of human mobility and control measures on the COVID-19 epidemic in China. *Science*, *368*(6490), 493–497.

Kucharski, A. J., Russell, T. W., Diamond, C., Liu, Y., Edmunds, J., Funk, S., et al. (2020). Early dynamics of transmission and control of COVID-19: A mathematical modelling study. *The Lancet Infectious Diseases*, *20*(5), 553–558.

Li, Q., Guan, X., Wu, P., Wang, X., Zhou, L., Tong, Y., et al. (2020). Early transmission dynamics in Wuhan, China, of novel coronavirus–infected pneumonia. *New England Journal of Medicine*, *382*(13), 1199–1207.

Martcheva, M. (2015). An introduction to mathematical epidemiology. In (Vol. 61)Springer.

Mizumoto, K., Kagaya, K., & Chowell, G. (2020). Early epidemiological assessment of the transmission potential and virulence of coronavirus disease 2019 (COVID-19) in Wuhan City, China, January–February, 2020. *BMC Medicine*, *18*(1), 1–9.

Phillips, R., Kondev, J., Theriot, J., & Garcia, H. (2012). *Physical biology of the cell*. Garland Science.

Press, W. H., Flannery, B. P., Teukolsky, S. A., & Vetterling, W. T. (1986). *Numerical recipes: The art of scientific computing*. Cambridge: Cambridge University Press.

Saad-Roy, C. M., Grenfell, B. T., Levin, S. A., Pellis, L., Stage, H. B., van den Driessche, P., et al. (2021). Superinfection and the evolution of an initial asymptomatic stage. *Royal Society Open Science*, *8*(1), 202212.

Salom, I., Rodic, A., Milicevic, O., Zigic, D., Djordjevic, M., & Djordjevic, M. (2021). Effects of demographic and weather parameters on COVID-19 basic reproduction number. *Frontiers in Ecology and Evolution*, *8*, 617841.

Sanche, S., Lin, Y. T., Xu, C., Romero-Severson, E., Hengartner, N., & Ke, R. (2020). High contagiousness and rapid spread of severe acute respiratory syndrome coronavirus 2. *Emerging Infectious Diseases*, *26*(7), 1470–1477.

Tian, H., Liu, Y., Li, Y., Wu, C.-H., Chen, B., Kraemer, M. U., et al. (2020). An investigation of transmission control measures during the first 50 days of the COVID-19 epidemic in China. *Science*, *368*(6491), 638–642.

Vilar, J. M., & Saiz, L. (2020). The evolving worldwide dynamic state of the COVID-19 outbreak. *medRxiv*.

Voit, E., Martens, H., & Omholt, S. (2015). 150 years of the mass action law. *PLoS Computational Biology*, *11*(1), e1004012.

Wang, Z., Andrews, M. A., Wu, Z.-X., Wang, L., & Bauch, C. T. (2015). Coupled disease–behavior dynamics on complex networks: A review. *Physics of Life Reviews*, *15*, 1–29.

WHO. (2020). *WHO timeline—COVID-19*. https://www.who.int/news-room/detail/27-04-2020-who-timeline—covid-19: World Health Organization.

Wilkinson, D. J. (2018). *Stochastic modelling for systems biology* (3rd ed.). London: Chapman and Hall/CRC.

Wong, G. N., Weiner, Z. J., Tkachenko, A. V., Elbanna, A., Maslov, S., & Goldenfeld, N. (2020). Modeling COVID-19 dynamics in Illinois under nonpharmaceutical interventions. *Physical Review X*, *10*(4), 041033.

Wu, J. T., Leung, K., Bushman, M., Kishore, N., Niehus, R., de Salazar, P. M., et al. (2020). Estimating clinical severity of COVID-19 from the transmission dynamics in Wuhan, China. *Nature Medicine*, *26*(4), 506–510.

Wu, J. T., Leung, K., & Leung, G. M. (2020). Nowcasting and forecasting the potential domestic and international spread of the 2019-nCoV outbreak originating in Wuhan, China: A modelling study. *The Lancet*, *395*(10225), 689–697.

Exploring the initial stages in heavy-ion collisions with high-$p_\perp$ theory and data

Dusan Zigic,[1] Bojana Ilic ⬤,[1] Marko Djordjevic ⬤,[2] and Magdalena Djordjevic ⬤[1,*]

[1]*Institute of Physics Belgrade, University of Belgrade, 11080 Belgrade, Serbia*
[2]*Faculty of Biology, University of Belgrade, 11000 Belgrade, Serbia*

Traditionally, the low-$p_\perp$ sector is used to infer the features of initial stages before quark-gluon plasma thermalization. On the other hand, a recently acquired wealth of high-$p_\perp$ experimental data paves the way to utilize the high-$p_\perp$ particles' energy loss in exploring the initial stages. We here study how four different commonly considered initial-stage scenarios—which have the same temperature profile after thermalization, but differ in the "temperature" profile before thermalization—affect predictions of high-$p_\perp$ R_{AA} and v_2 observables. Contrary to common expectations, we obtain that high-$p_\perp$ v_2 is insensitive to the initial stages of medium evolution, being unable to discriminate between different conditions. On the other hand, R_{AA} is sensitive to these conditions; however, within the current error bars, the sensitivity is not sufficient to distinguish between different initial stages. Moreover, we also reconsider the validity of the widely used procedure of fitting the energy loss parameters, individually for different initial-stage cases, to reproduce the experimentally observed R_{AA}. We here find that previously reported sensitivity of v_2 to different initial states is mainly a consequence of the R_{AA} fitting procedure, which may lead to incorrect conclusions. On the other hand, if a global property, in particular the same average temperature, is imposed to tested temperature profiles, high sensitivity of high-$p_\perp$ v_2 is again obtained. We show, however, that this sensitivity would be a consequence of differences not in initial stages but rather in final stages. Consequently, the simultaneous study of high-$p_\perp$ R_{AA} and v_2, with consistent energy loss parametrization and stringently controlled temperature profiles, is necessary to assess sensitivity of different variables to differences in initial and final stages.

I. INTRODUCTION

It is by now firmly confirmed that a new state of matter—the quark-gluon plasma (QGP) [1,2], in which quarks, antiquarks and gluons are deconfined—is formed at the Relativistic Heavy Ion Collider (RHIC) and the Large Hadron Collider (LHC). Rare high transverse momentum (high-$p_\perp$) particles, which are created immediately upon collision, are sensitive to all stages of QGP evolution, and are considered to be excellent probes [3–6] of this extreme form of matter. As these probes traverse the QGP, they lose energy, which is commonly assessed through high-$p_\perp$ angular averaged (R_{AA}) [7–14] and high-$p_\perp$ angular differential (v_2) [15–19] nuclear modification factors.

Commonly, high-$p_\perp$ particles are used to study the nature of jet-medium interactions, while low-$p_\perp$ particles are used to infer the bulk QGP properties. Accordingly, the scarce knowledge of the features of initial stages before QGP thermalization ($\tau < \tau_0$) was mostly inferred by utilizing data from the low-$p_\perp$ sector [20–22] ($p_\perp \lesssim 5$ GeV). However, since

high-$p_\perp$ partons effectively probe QGP properties, which in turn depend on initial stages, the idea of utilizing high-$p_\perp$ theory and data in exploring the initial stages emerged. This idea acquired an additional boost, since a wealth of precision high-$p_\perp$ R_{AA} [7–12] and v_2 [15–19] data have recently become available. Thus, the main goal of this paper is to assess to what extent and through what observables the initial stages of QGP evolution can be restrained by exploiting the energy loss of high-$p_\perp$ particles in the evolving medium.

While clarifying these issues is clearly intriguing, the results of current theoretical studies on this subject are either inconclusive or questionable [23–25] as, e.g., the energy loss parameters are fitted to reproduce the experimentally observed high-$p_\perp$ R_{AA} data individually for different analyzed initial stages. The energy loss parametrization should, however, clearly be a property of high-$p_\perp$ parton interactions with the medium, rather than of individual temperature profiles. Consequently, to more rigorously study this issue, one needs a high control on both the energy loss and the analyzed temperature (T) profiles. To achieve this, we here use our state-of-the-art dynamical energy loss formalism, embedded in Bjorken one-dimensional (1D) medium evolution [26] (DREENA-B framework). While Bjorken 1D medium evolution is not a full bulk QGP evolution model, for this particular study it has a major advantage, as it allows one to analytically introduce different evolutions before thermalization, with the same evolution after thermalization, which therefore allows one to clearly isolate only the effects of different initial stages (which would not be possible with full hydrodynamics models).

Consequently, we will here consider the effects on high-$p_\perp$ R_{AA} and v_2 predictions of four common initial-stage cases [23], which have the same T profiles after thermalization, but differ in T profiles before the thermalization.

Furthermore, we recently demonstrated that the DREENA-B framework [27] is able to accurately reproduce both high-$p_\perp$ R_{AA} and v_2 data for diverse colliding systems and energies (Pb + Pb at 2.76 and 5.02 TeV and Xe + Xe at 5.44 TeV), for both light and heavy flavors ($h^\pm$, B, D) and all available centralities, without introducing new phenomena [28,29]. This is distinct from many other formalisms, which employ more advanced medium evolution models, but contain simplified energy loss models, which have a tendency to underestimate v_2 relative to the experimental data; this is widely known as the v_2 puzzle [30,31]. Moreover, we recently obtained that going from 1D Bjorken to full 3+1D hydrodynamics evolution [32] does not significantly change the agreement between our predictions and experimental data, strongly suggesting that, for high-$p_\perp$ data, accurate energy loss description is more important than the medium evolution. Consequently, for this study, using 1D Bjorken evolution has a major advantage of tight control over the temperature profiles used to mimic different initial states, while, at the same time, providing a reasonably realistic description of the data within our model.

The paper is organized as follows. In Sec. II, theoretical and computational frameworks are outlined. In Sec. III, we first assess the sensitivity of R_{AA} and v_2 to the aforementioned initial stages. We then adopt the approach of fitting initial temperature (T_0) to reproduce the same R_{AA} in all cases, and then assess the effect of thus obtained "modified" temperature profiles on R_{AA} and v_2. We finally reexamine the validity of the widely used procedure [23–25] of fitting the energy loss parameters for different initial-stage cases to reproduce the same R_{AA}. For all these studies, we analytically pinpoint the origin of the obtained results. Our conclusions are presented in Sec. IV.

II. THEORETICAL AND COMPUTATIONAL FRAMEWORKS

To obtain the medium modified distribution of high-$p_\perp$ light and heavy flavor particles, the generic pQCD convolution formula [33,34] is utilized:

$$\frac{E_f d^3\sigma}{d p_f^3} = \frac{E_i d^3\sigma(Q)}{d p_i^3} \otimes P(E_i \to E_f) \otimes D(Q \to H_Q), \quad (1)$$

where indexes f and i refer to the final hadron (H_Q) and initial parton (Q), respectively. $\frac{E_i d^3\sigma(Q)}{d p_i^3}$ denotes the parton initial momentum distribution, calculated according to [35]. $P(E_i \to E_f)$ represents the energy loss probability based on our dynamical energy loss formalism (see below). $D(Q \to H_Q)$ stands for the fragmentation function of a parton into a hadron (H_Q), where for the light hadrons and D and B mesons we apply fragmentation functions of de Florian, Sassot, and Stratmann (DSS) [36], Braaten, Cheung, Fleming, and Yuan (BCFY) [37], and Kartvelishvili, Likhoded, and Petrov (KLP) [38], respectively.

The dynamical energy loss formalism [39–41] includes several unique features in modeling jet-medium interactions, whereby we previously showed [42] that all the ingredients are important for accurately describing experimental data: (1) The finite size QCD medium, that consists of dynamical (moving) as opposed to static scattering centers, which allows longitudinal momentum exchange with the medium constituents. (2) The calculations are done within the finite temperature generalized hard-thermal-loop approach [43], so that infrared divergences are naturally regulated in a highly nontrivial manner, contrary to many models which apply tree-level (vacuumlike) propagators [44–47]. (3) Both radiative [40,41] and collisional [39] contributions are calculated within the same theoretical framework. (4) The generalizations to a finite magnetic mass [48], running coupling [33], and beyond the soft-gluon approximation [49] are performed. In this paper, for the magnetic to electric mass ratio we assume the value $\mu_M/\mu_E = 0.5$, since various nonperturbative [50,51] approaches reported it to be in the range 0.4–0.6. (5) The energy loss probability comprises also multigluon [52] and path-length [34] fluctuations. The path-length fluctuations are calculated according to the procedure presented in [53], and are provided in Ref. [54].

As outlined in Ref. [27], the analytical expression for a single gluon radiation spectrum, in an evolving medium, reads

$$\frac{dN_{\text{rad}}}{dx\,d\tau} = \frac{C_2(G)C_R}{\pi}\frac{1}{x}\int \frac{d^2\mathbf{q}}{\pi}\frac{d^2\mathbf{k}}{\pi}\frac{\mu_E^2(T) - \mu_M^2(T)}{[\mathbf{q}^2 + \mu_E^2(T)][\mathbf{q}^2 + \mu_M^2(T)]}T\alpha_s(ET)\alpha_s\left(\frac{\mathbf{k}^2 + \chi(T)}{x}\right)$$

$$\times \left[1 - \cos\left(\frac{(\mathbf{k}+\mathbf{q})^2 + \chi(T)}{xE^+}\tau\right)\right]\frac{2(\mathbf{k}+\mathbf{q})}{(\mathbf{k}+\mathbf{q})^2 + \chi(T)}\left[\frac{\mathbf{k}+\mathbf{q}}{(\mathbf{k}+\mathbf{q})^2 + \chi(T)} - \frac{\mathbf{k}}{\mathbf{k}^2 + \chi(T)}\right], \quad (2)$$

where $\mathbf{k}$ and $\mathbf{q}$ denote transverse momenta of radiated and exchanged gluons, respectively, $C_2(G) = 3$, $C_R = 4/3$ ($C_R = 3$) for the quark (gluon) jet, while $\mu_E(T)$ and $\mu_M(T)$ are electric (Debye) and magnetic screening masses, respectively. Temperature dependent Debye mass [55] is obtained by self-consistently solving Eq. (5) from Ref. [27]. α_s is the (temperature dependent) running coupling [56], E is the initial jet energy, while $\chi(T) = M^2 x^2 + m_g^2(T)$, where x is the longitudinal momentum fraction of the jet carried away by the emitted gluon, M is the mass of the quark ($M_{u,d,s} \approx \mu_E(T)/\sqrt{6}$, i.e., the thermal mass, whereas $M_c = 1.2$ GeV and $M_b = 4.75$ GeV) or gluon jet, and $m_g(T) = \mu_E(T)/\sqrt{2}$ [57] is the effective gluon mass in finite temperature QCD medium. Note that for all parameters we use standard literature values, i.e., we do not include additional fitting parameters when comparing our predictions with experimental data.

The analytical expression for the collisional energy loss per unit length in the evolving medium is given by [27]

$$
\frac{dE_{\text{coll}}}{d\tau} = \frac{2C_R}{\pi v^2} \alpha_s(ET) \alpha_s\big(\mu_E^2(T)\big) \int_0^\infty n_{\text{eq}}(|\vec{\mathbf{k}}|, T) d|\vec{\mathbf{k}}| \left[\int_0^{|\vec{\mathbf{k}}|/(1+v)} d|\vec{\mathbf{q}}| \int_{-v|\vec{\mathbf{q}}|}^{v|\vec{\mathbf{q}}|} \omega d\omega + \int_{|\vec{\mathbf{k}}|/(1+v)}^{|\vec{\mathbf{q}}|_{\text{max}}} d|\vec{\mathbf{q}}| \int_{|\vec{\mathbf{q}}|-2|\vec{\mathbf{k}}|}^{v|\vec{\mathbf{q}}|} \omega d\omega \right]
$$

$$
\times \left[|\Delta_L(q,T)|^2 \frac{(2|\vec{\mathbf{k}}| + \omega)^2 - |\vec{\mathbf{q}}|^2}{2} + |\Delta_T(q,T)|^2 \frac{(|\vec{\mathbf{q}}|^2 - \omega^2)[(2|\vec{\mathbf{k}}| + \omega)^2 + |\vec{\mathbf{q}}|^2]}{4|\vec{\mathbf{q}}|^4} (v^2|\vec{\mathbf{q}}|^2 - \omega^2) \right], \tag{3}
$$

where $n_{\text{eq}}(|\vec{\mathbf{k}}|, T) = \frac{N}{e^{|\vec{\mathbf{k}}|/T}-1} + \frac{N_f}{e^{|\vec{\mathbf{k}}|/T}+1}$ is the equilibrium momentum distribution [58] comprising gluons, quarks, and antiquarks ($N = 3$ and $N_f = 3$ are the numbers of colors and flavors, respectively). k is the four-momentum of the incoming medium parton, v is velocity of the initial jet, and $q = (\omega, \vec{\mathbf{q}})$ is the four-momentum of the exchanged gluon. $|\vec{\mathbf{q}}|_{\text{max}}$ is provided in Ref. [39], while $\Delta_T(T)$ and $\Delta_L(T)$ are effective transverse and longitudinal gluon propagators given by Eqs. (3) and (4) in Ref. [27].

One of the assets of our energy loss formalism is the fact that energy loss explicitly depends on T, which makes it naturally suited for examining the QGP properties via implementation of various temperature profiles. In this paper, the temperature dependence on proper time (τ) is taken according to the ideal hydrodynamical 1D Bjorken expansion [26] $T(\tau) \sim \sqrt[3]{(\tau_0/\tau)}$, with thermalization time $\tau_0 = 0.6$ fm [59,60]. The initial QGP temperature T_0 for the chosen centrality bin is not a free parameter, i.e., it is constrained starting from the ALICE effective temperature [61] and following the numerical procedure outlined in Ref. [62]. In this paper, we will concentrate on mid-central 30–40% centrality region at 5.02 TeV Pb + Pb at the LHC, which corresponds to $T_0 = 391$ MeV [27]. However, we performed an extensive study on all centrality regions (as in [27]), and checked that the results and conclusions obtained here are the same irrespectively of the centrality region (results not shown for brevity). The QGP transition temperature is considered to be $T_C \approx 160$ MeV [63].

The DREENA-B framework is applied to generate predictions for two main high-$p_\perp$ observables: R_{AA} and v_2. R_{AA} is defined as the ratio of the quenched $A + A$ spectrum to the $p + p$ spectrum, scaled by the number of binary collisions N_{bin}:

$$
R_{\text{AA}}(p_T) = \frac{dN_{\text{AA}}/dp_T}{N_{\text{bin}}dN_{pp}/dp_T}; \tag{4}
$$

while for intuitive understanding of the underlying effects we also use [54]

$$
R_{\text{AA}} \approx \frac{R_{\text{AA}}^{\text{in}} + R_{\text{AA}}^{\text{out}}}{2}, \tag{5}
$$

where $R_{\text{AA}}^{\text{in}}$ and $R_{\text{AA}}^{\text{out}}$ denote in-plane and out-of-plane nuclear modification factors, respectively. The expression for the high-$p_\perp$ elliptic flow is derived in [23] (see also [54,64,65]), under the assumption of negligible higher harmonics at high $p_\perp \gtrsim 10$ GeV, leading to

$$
v_2 \approx \frac{1}{2} \frac{R_{\text{AA}}^{\text{in}} - R_{\text{AA}}^{\text{out}}}{R_{\text{AA}}^{\text{in}} + R_{\text{AA}}^{\text{out}}}. \tag{6}
$$

The advantage of using Eq. (6) for high-$p_\perp$ predictions is that it is computationally significantly less demanding than the commonly used v_2 expression (see, e.g., Eq. (1) from [15]). However, to explicitly verify its applicability, we checked that, for average temperature profiles, Eq. (6) will lead to the same result (up to less than 1% difference) as the commonly used azimuthally dependent expression.

We also note that the approach to experimentally infer v_2 (see, e.g., Eq. (16) in [15]) is different from the above-mentioned theoretical approaches. However, that approach could lead to different v_2 predictions only if event-by-event fluctuations are considered (which we do not do in this study). We also note that the importance of event-by-event fluctuations in adequately addressing high-$p_\perp$ v_2 is currently an open question; i.e., in [30], it was proposed that event-by-event fluctuations may increase the high-$p_\perp$ v_2, while this was not supported by two subsequent independent studies [29,66].

III. RESULTS AND DISCUSSION

In the first part of this section we address how different initial stages (before the thermalization time τ_0) affect our predictions of high-$p_\perp$ R_{AA} and v_2. To this end, we consider the following four common cases of initial stages [23], which assume the same 1D Bjorken hydro temperature (T) profile [26] upon thermalization (for $\tau \geqslant \tau_0$), but have different T profiles before the thermalization (for $\tau < \tau_0$):

(a) $T = 0$, the so-called *free-streaming case*, which corresponds to neglecting interactions (i.e., energy loss) before the QGP thermalization.

(b) The *linear case*, corresponding to linearly increasing T with time from transition temperature ($T_C = 160$ MeV at $\tau_C = 0.25$ fm) to the initial temperature T_0.

(c) The *constant case*, $T = T_0$.

(d) The *divergent case*, corresponding to 1D Bjorken expansion from $\tau = 0$.

These initial stages are depicted in Fig. 1, and it is clear that (a)–(d) case ordering corresponds to gradually increasing prethermal interactions. Note that we use this classification (a)–(d) consistently throughout the paper to denote initial stages (for $\tau < \tau_0$), as well as for the entire evolution. Also, note that in this part of the study we will include experimental data for comparison with our predictions. However, to allow better visualization of our obtained numerical results, in the other two parts of the study we will omit the comparison with the data, as the error bars are large and the data remain the same. Intuitively, one would expect that introducing these prethermal interactions would increase the energy loss
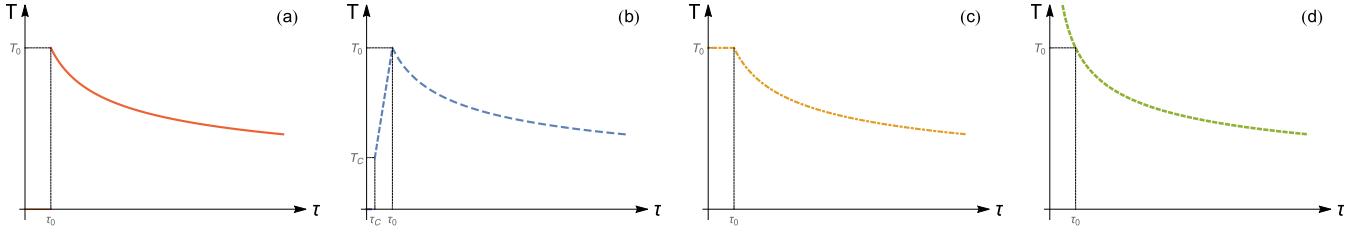
FIG. 1. Four temperature evolution profiles, which differ at the initial stages. At $\tau \geqslant \tau_0$, all profiles assume the same temperature dependence on the proper time (1D Bjorken [26]). At the initial stage, i.e., for $0 < \tau < \tau_0$, the temperature is considered to be (a) equal to zero; (b) increasing linearly from T_C to T_0 between τ_C and τ_0, otherwise zero; (c) constant and equal to T_0; and (d) a continuous function of τ matching the dependence for $\tau \geqslant \tau_0$. Note that, in each panel, T_0 has the same value at τ_0.

compared to the commonly considered free-streaming case, and consequently lead to smaller R_{AA}. In Fig. 2 we indeed observe that R_{AA} is sensitive to the initial stages for all types of particles. That is, as expected, we see that the suppression progressively increases from case (a) to case (d). However, these differences are not very large, and the current error bars at the LHC do not allow distinguishing between these scenarios, as can be seen in Fig. 2 (left).

In contrast to R_{AA}, the effect of initial stages on v_2 is intuitively less clear, as this observable nontrivially depends on the energy loss or R_{AA}'s (see Eq. (6)). From Fig. 3, we surprisingly infer that v_2 is insensitive to the presumed initial stage for all types of particles (in distinction to the results obtained in [24]), so that v_2 is unable to distinguish between different initial-stage scenarios.

To quantitatively understand this unexpected observation, in Fig. 4 we show transverse momentum dependence of R_{AA}^{in}, R_{AA}^{out}, and R_{AA} in $i = b, c, d$ cases relative to the baseline case (a) for charged hadrons. The conclusions for heavy particles are the same and therefore omitted. We distinguish three sets of curves, which correspond to the ratio of R_{AA}'s in linear (b), constant (c), and divergent (d) cases relative to the free-streaming (a) case. Note that the free-streaming case is used

as a baseline, as it corresponds to the most commonly used scenario, both in low- and high-$p_\perp$ calculations.

Each set of curves in Fig. 4 contains three lines, representing proportionality functions $\gamma(p_\perp)$, which are defined as follows:

$$\gamma_{ia}^{in} = \frac{R_{AA,i}^{in}}{R_{AA,a}^{in}}, \quad \gamma_{ia}^{out} = \frac{R_{AA,i}^{out}}{R_{AA,a}^{out}}, \quad \gamma_{ia} = \frac{R_{AA,i}}{R_{AA,a}}, \quad (7)$$

where $i = b, c, d$ denotes the corresponding cases from Fig. 1. From Fig. 4 we see that for the same i (i.e., within the same set of curves (b), (c), or (d)) the proportionality functions $\gamma_{ia}(p_\perp)$ are practically identical for the relations involving in-plane, out-of-plane, and angular averaged R_{AA}'s:

$$\gamma_{ia}^{in} \approx \gamma_{ia}^{out} \approx \gamma_{ia}. \quad (8)$$

Note also that $\gamma_{ia} < 1$, while γ_{ia}s from distinct sets significantly differ from one another (i.e., for $i \neq j \rightarrow \gamma_{ia}(p_\perp) \neq \gamma_{ja}(p_\perp)$).

Consequently, by implementing Eq. (7) in Eq. (6) and acknowledging Eq. (8), we obtain

$$v_{2,i} \approx \frac{1}{2} \frac{\gamma_{ia}(R_{AA,a}^{in} - R_{AA,a}^{out})}{\gamma_{ia}(R_{AA,a}^{in} + R_{AA,a}^{out})} = v_{2,a}, \quad (9)$$
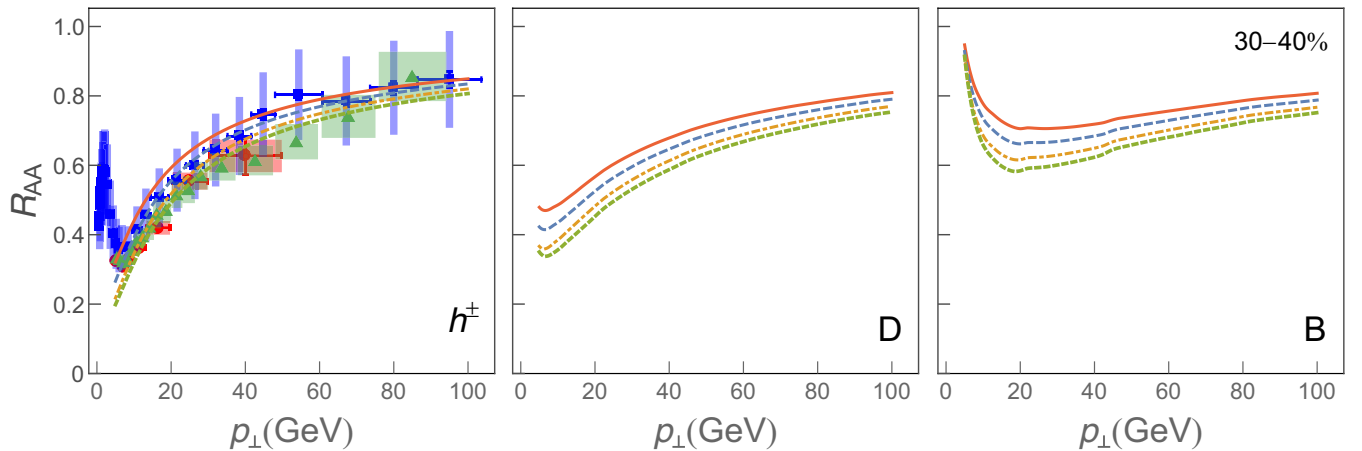

FIG. 2. R_{AA} dependence on $p_\perp$ for four different initial stages depicted in Fig. 1 is shown for charged particles (left panel), D mesons (central panel) and B mesons (right panel). For charged hadrons, the predictions are compared with 5.02 TeV Pb + Pb ALICE [7] (red circles), ATLAS [8] (green triangles), and CMS [9] (blue squares) $h^\pm$ R_{AA} experimental data. In each panel, temperature profiles from Fig. 1 are represented by a full red curve (case (a)), by a dashed blue curve (case (b)), by a dot-dashed orange curve (case (c)), and by dotted green curve (case (d)). The results correspond to the centrality bin 30–40%, and $\mu_M/\mu_E = 0.5$.
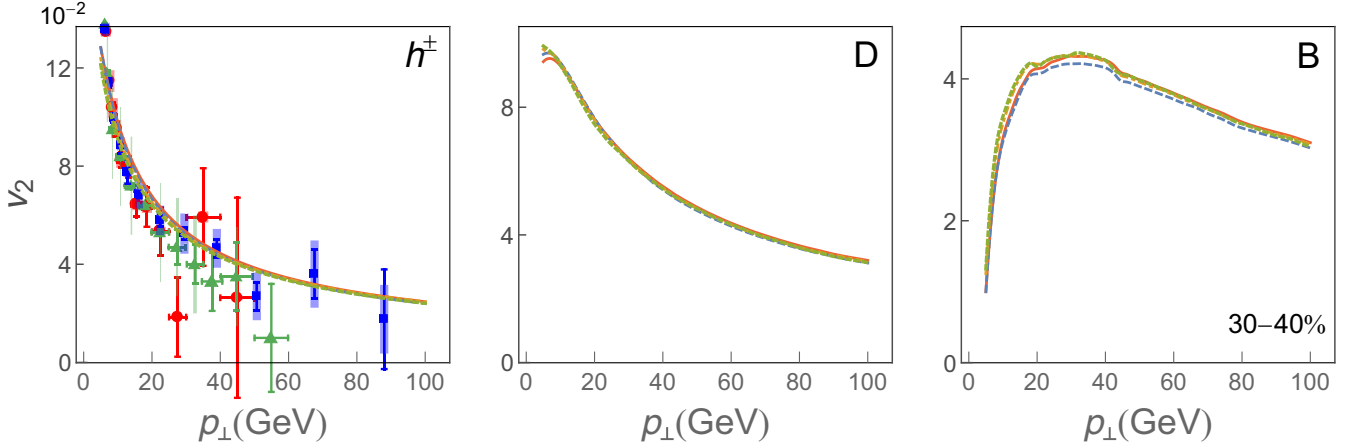
FIG. 3. v_2 dependence on $p_\perp$ for four different initial stages depicted in Fig. 1. Left, central, and right panels correspond to charged hadrons, D mesons and B mesons, respectively. For charged hadrons, the predictions are compared with 30–40% centrality 5.02 TeV Pb + Pb ALICE [15] (red circles), ATLAS [16] (green triangles), and CMS [17] (blue squares) $h^\pm$ v_2 experimental data. The labeling and remaining parameters are the same as in Fig. 2.

for any choice of $i = b, c, d$, as observed in Fig. 3. Therefore, we here showed that initial stages alone do not affect v_2, i.e., they affect only R_{AA}. R_{AA} susceptibility to the initial stages is in qualitative agreement with papers [27,67,68], where R_{AA} is shown to be only sensitive to the averaged properties of the evolving medium, i.e., average temperature $(\overline{T})$. Since R_{AA} is proportional to $\overline{T}$, and since for all four initial-stage cases (a)–(d) the $\overline{T}$ value is different $(\overline{T}_a < \overline{T}_b < \overline{T}_c < \overline{T}_d)$, it is evident that R_{AA} will be different in these cases.

The fact that R_{AA} depends on the average temperature of the medium, motivates us to further explore the case in which we modify the above temperature profiles to reproduce the same average temperature. This is equivalent to reevaluating the initial temperatures for different cases from Fig. 1, and, based on the reasoning above, it is evident that new initial temperatures should satisfy the following ordering: $T_{0,d'} < T_{0,c'} < T_{0,b'} < T_{0,a'}$. This leads to T profiles, which do not differ only at early times $(\tau < \tau_0)$, but represent *different evolutions altogether*. These new evolutions, that are illustrated in Fig. 5 (which is a counterpart of Fig. 1 for the second

FIG. 4. Transverse momentum dependence of in-plane (dashed), out-of-plane (dot-dashed), and angular averaged (full curves) R_{AA} relative to the free-streaming (a) case for charged hadrons. Blue (upper), orange (middle), and green (lower) sets of curves correspond, respectively, to (b), (c) and (d) cases. The remaining parameters are the same as in Fig. 2.
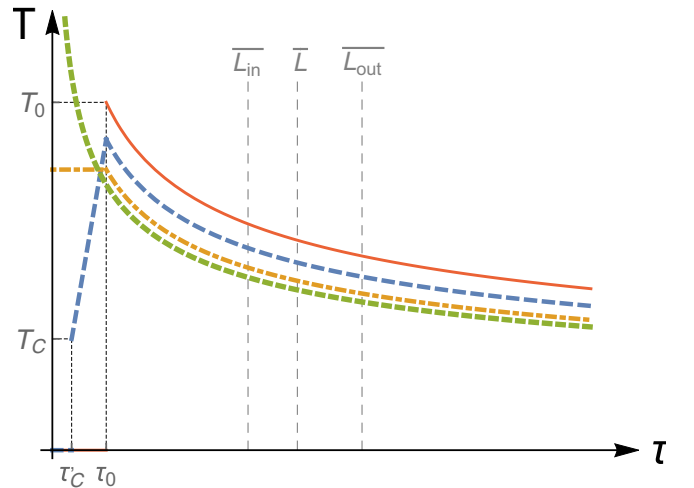
FIG. 5. Temperature dependence on the proper time in the setup with the same average temperatures. The labeling is the same as in Fig. 1, apart from the fact that initial temperatures $(T_0$'s) now differ in these four cases. As in Fig. 1, $T_C = 160$ MeV, $\tau_0 = 0.6$ fm, and $\tau_C' = 0.27$ fm. Vertical gray dashed lines correspond to average in-medium path length $(\overline{L})$, and to the path lengths along in-plane $(\overline{L}_{in})$ and out-of-plane $(\overline{L}_{out})$ directions, as labeled in the figure.
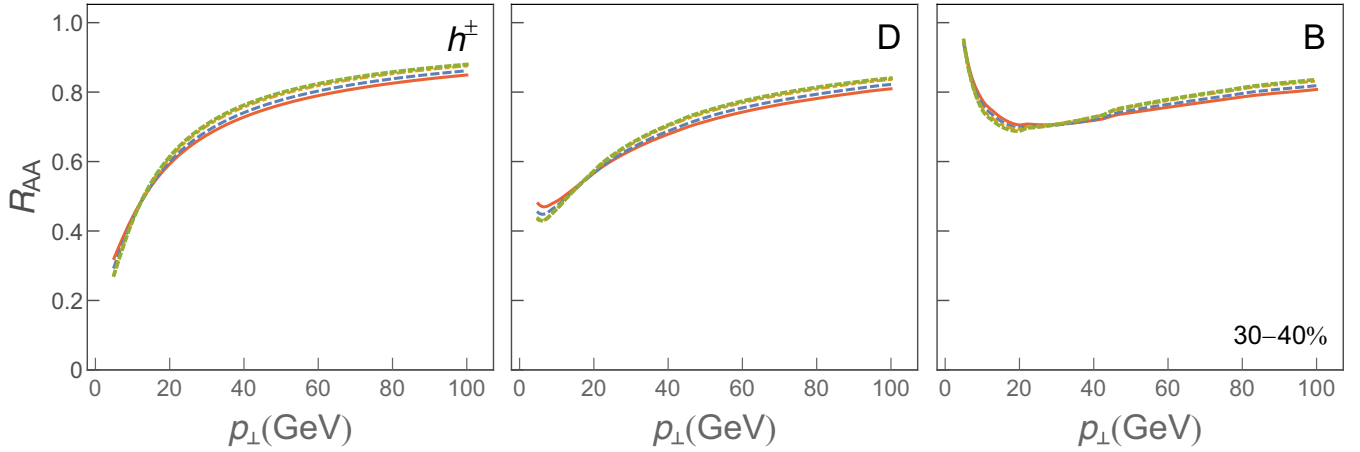
FIG. 6. R_{AA} dependence on $p_\perp$ for four different medium evolutions depicted in Fig. 5. Left, central, and right panels correspond to charged hadrons, D mesons, and B mesons, respectively. In each panel, the T profile corresponding to the case (a′) from Fig. 5 is represented by a full red curve, case (b′) by a dashed blue curve, case (c′) by a dot-dashed orange curve, and case (d′) by a dotted green curve. The results correspond to the centrality bin 30–40%, and $\mu_M/\mu_E = 0.5$.

part of this section), are denoted as (a′)–(d′) and referred to as "modified" T profiles ((a) ≡ (a′)).

In this second T-profiles setup, we first verify from Fig. 6 that R_{AA}s in all four cases practically overlap, as expected. We next address how these modified evolution cases (a′)–(d′) affect v_2. From Fig. 7 we see that v_2 is now very sensitive to the transition from the free-streaming case to other modified T profiles. More accurately, for all types of particles, the lowest v_2 is observed in the modified divergent case, while the highest v_2 is observed in the free-streaming case.

The observation from Fig. 7 leads to the following two questions: (i) Why is v_2 altered by these modified T profiles (a′)–(d′)? (ii) Are these discrepancies a consequence of different initial stages? To answer these questions, we first note that, within this setup, the differences between v_2 (observed in Fig. 7) are proportional to $R_{AA}^{in} - R_{AA}^{out}$, as the denominator in Eq. (6) (as a starting premise) remains practically unchanged (see Fig. 6). The transverse momentum dependence of $R_{AA}^{in} -$

R_{AA}^{out} is further shown in Fig. 8 for charged hadrons (as results for D and B mesons will lead to the same conclusion). We see a clear hierarchy, i.e., the largest $R_{AA}^{in} - R_{AA}^{out}$ for free streaming, descending towards the divergent case. To quantitatively understand this observation, we note that for R_{AA}^{in} the high-$p_\perp$ probes traverse, on average, the medium up to $\overline{L}_{in}$, while for R_{AA}^{out} the medium is traversed up to $\overline{L}_{out}$. Consequently, if we refer to Fig. 5, $R_{AA}^{in} - R_{AA}^{out}$ comes from the T-profile difference in the time region between $\overline{L}_{in}$ and $\overline{L}_{out}$, i.e., *upon thermalization*. Since in this region $\overline{T}_{d'} < \overline{T}_{c'} < \overline{T}_{b'} < \overline{T}_{a'}$ holds, $R_{AA}^{in} - R_{AA}^{out}$ is the largest for the free-streaming case and the smallest for the divergent case, as observed in Fig. 8, and in agreement with v_2 ordering in Fig. 7. This therefore provides clarification of why $R_{AA}^{in} - R_{AA}^{out}$, and consequently v_2, is affected by these four different QGP evolution profiles, and that this difference originates primarily from the interactions of high-$p_\perp$ partons with *thermalized QGP* and *not the initial stages*. This agrees with the first part of this section
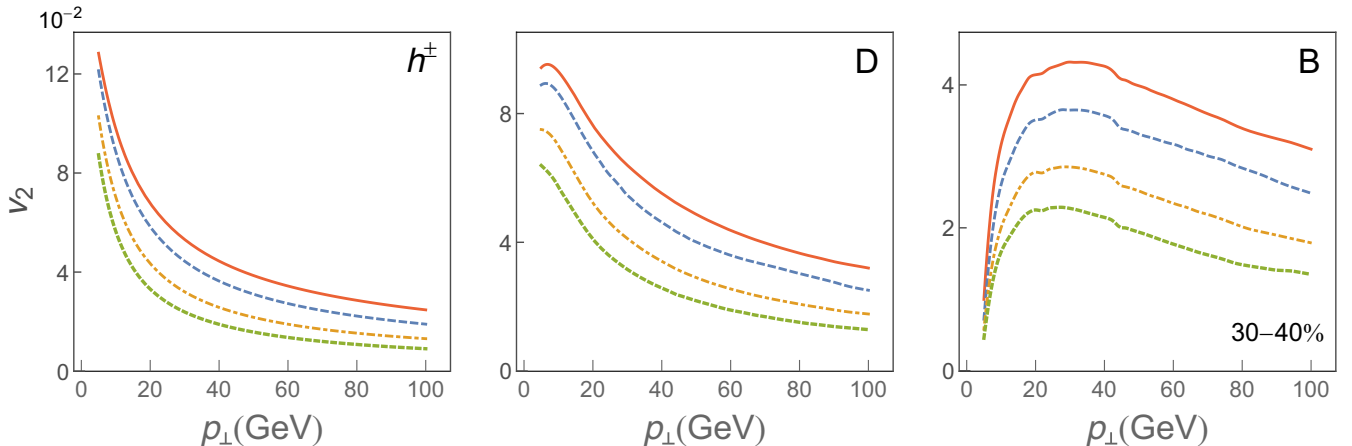

FIG. 7. v_2 dependence on $p_\perp$ for four different medium evolutions depicted in Fig. 5. Left, central, and right panels correspond to charged hadrons, D mesons, and B mesons, respectively. The labeling and remaining parameters are the same as in Fig. 6.
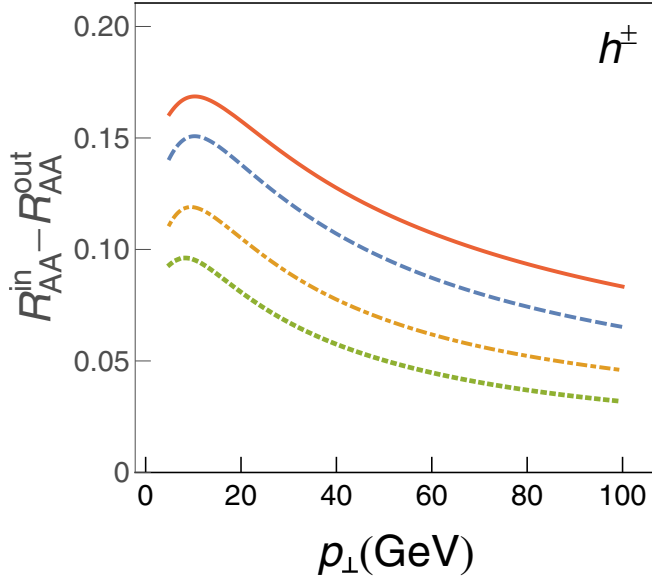
FIG. 8. $R_{\mathrm{AA}}^{\mathrm{in}} - R_{\mathrm{AA}}^{\mathrm{out}}$ dependence on $p_\perp$ for charged hadrons. The labeling and remaining parameters are the same as in Fig. 6.

TABLE I. Fitting factors values.

T profile case	C_i^{fit}
Free-streaming case (a)	1
Linear case (b)	0.87
Constant case (c)	0.74
Divergent case (d)	0.67

(Figs. 2 and 3), where we showed and explained insensitivity of v_2 to different initial stages. It is worth emphasizing that, contrary to the first part of this section, in the second part we tested the effects on R_{AA} and v_2 not from distinctive initial stages but instead from four entirely different evolutions of the QCD medium (related by the same global property, i.e., average temperature).

In the final, third part of this section we adopt a commonly used approach, in which the energy loss is fitted through change of multiplicative fitting factor in the energy loss, to reproduce the desired high-$p_\perp$ R_{AA}, e.g., the one that best fits the experimental data (see, e.g., [24,30,65,69–71]). To this end, we use the same four T profiles from the first part of

this section (Fig. 1), while in our full-fledged calculations (see Sec. II) we introduce an additional multiplicative fitting factor (free parameter) C_i^{fit}, $i = b, c, d$. C_i^{fit} is then estimated for each initial-stage case as a best fit to the free-streaming R_{AA} (see Table I). Thus-obtained R_{AA}s are shown in the left panel of Fig. 9 only for the representative case of $h^\pm$, as the same conclusions stand for both light and heavy flavor hadrons. From the left panel of this figure we observe practically overlapping R_{AA}s in all (a)–(d) cases, as anticipated, which is obtained by decreasing C_i^{fit} consistently from the free-streaming to the divergent case (each $C_i^{\mathrm{fit}} \leqslant 1$) in order to *compensate* for the higher energy losses in the corresponding cases compared to the case (a).

The effect of different T profiles from Fig. 1 after introduction of multiplicative fitting factor C_i^{fit} in the full-fledged numerical procedure on v_2 is depicted in the right panel of Fig. 9, where we see that elliptic flow in (a)–(d) cases notably differs; i.e., it is the highest in the free-streaming case while it is the lowest in the divergent case. Based on this observation, one could naively infer that initial stages, i.e., the $\tau < \tau_0$ region (the only region in which T profiles differ), have a significant effect on v_2, as recently observed by an alternative approach [24].

However, this kind of reasoning is inconsistent with our analysis outlined in the first two parts of this section, as well as with intuitive expectation that introduction of the
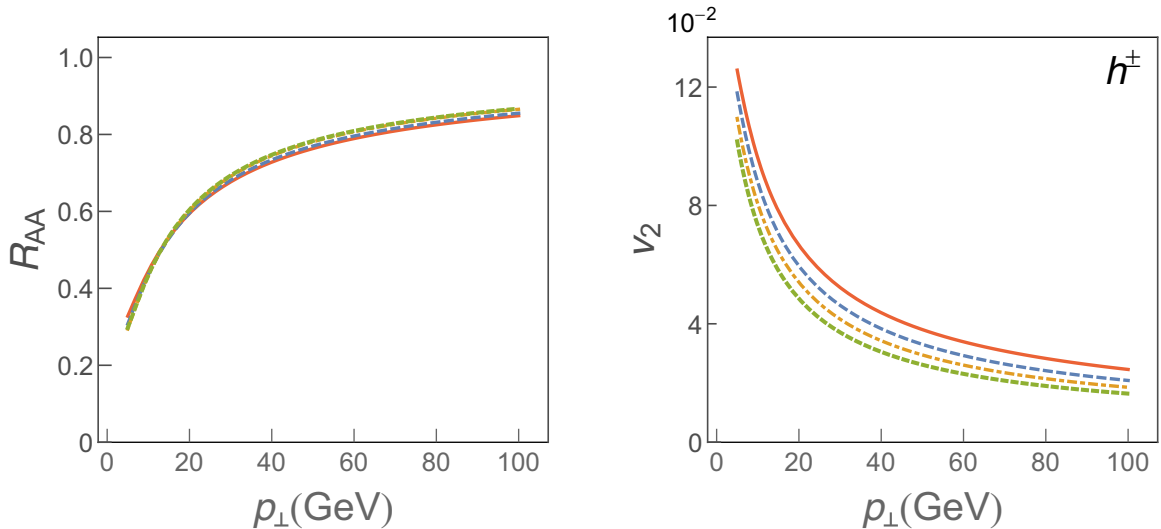

FIG. 9. R_{AA} (left panel) and v_2 (right panel) dependence on $p_\perp$ for charged hadrons, when an additional energy loss multiplicative factor is introduced to reproduce the free-streaming R_{AA}, in four different initial-stage cases depicted in Fig. 1. The labeling and remaining parameters are the same as in Fig. 2.
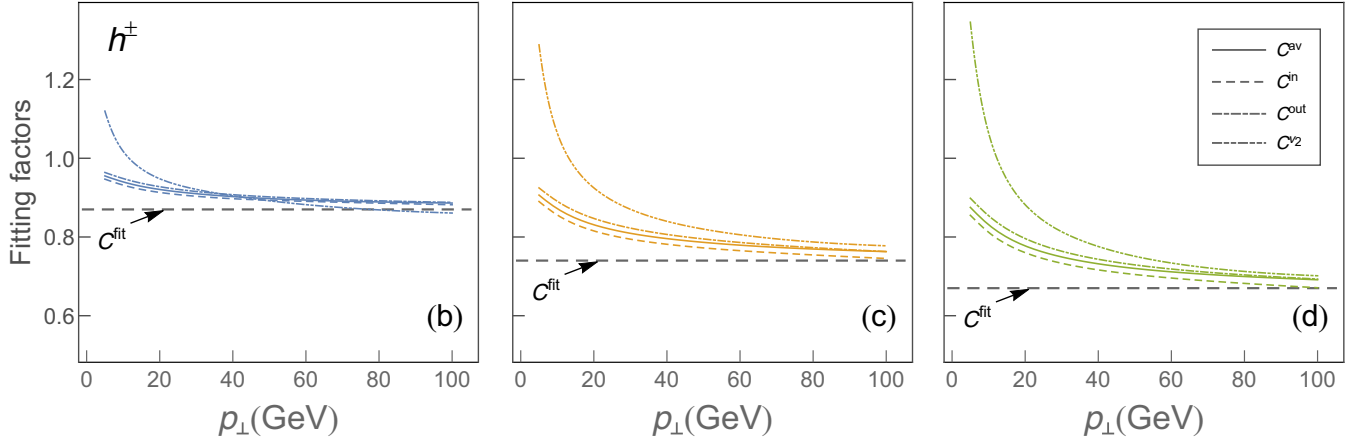
FIG. 10. Comparison of four fitting factors defined by Eq. (16) with the C_i^{fit} value, obtained from full-fledged numerical procedure, in *linear* (b) (left), *constant* (c) (central) and *divergent* (d) (right panel) cases. C factors represented by full, long-dashed, dot-dashed, and dot-dot-dashed curves correspond to $h^{\pm}$ angular averaged, in-plane, and out-of-plane R_{AA} and v_2 cases, respectively. The horizontal gray dashed line represents the energy loss fitted value C_i^{fit}. The results correspond to the centrality bin 30–40%, and $\mu_M/\mu_E = 0.5$.

energy loss at the initial stage affects R_{AA}. To quantitatively understand this result, we introduce asymptotic scaling behavior [27,54,72]. That is, for higher $p_{\perp}$ of the initial jet, and for higher centralities (where fractional energy loss is expected to be small), we can make the following estimates:

$$\Delta E/E \approx \chi \overline{T}^m \overline{L}^n, \quad R_{\text{AA}} \approx 1 - \frac{l-2}{2}\frac{\Delta E}{E} = 1 - \xi \overline{T}^m \overline{L}^n,$$
$$\tag{10}$$

where m, n are proportionality factors, $\overline{T}$ is the average temperature of the QGP, $\overline{L}$ denotes the average path length traversed by the jet, χ is a proportionality factor (that depends on $p_{\perp}$ and flavor of the jet). $\xi = \frac{l-2}{2}\chi$, where l is the steepness of a power law fit to the transverse momentum distribution.

If $\Delta E/E$ is fitted by additional multiplicative factor C, the new $R_{\text{AA}}^{\text{fit}}$ becomes

$$R_{\text{AA},i}^{\text{fit}} \approx 1 - C_i \xi \overline{T}_i^m \overline{L}_i^n \approx 1 - C_i(1 - R_{\text{AA},i}), \tag{11}$$

where $i = b, c, d$ and C_i ($C_i < 1, \forall i$) denotes the fitting factor, and the last part of Eq. (11) is obtained by using Eq. (10), leading to

$$C_i \approx \frac{1 - R_{\text{AA},i}^{\text{fit}}}{1 - R_{\text{AA},i}}. \tag{12}$$

We note that Eq. (12) is applicable to the average, in-plane and out-of-plane R_{AA}s, since the same fitting factor is consistently applied in all three cases. By imposing the condition (which quantifies the equivalence of fitted R_{AA} in (b)–(d) cases to the free-streaming case)

$$R_{\text{AA},i}^{\text{fit}} = R_{\text{AA},a}, \tag{13}$$

and by applying Eqs. (5)–(8) and (13), together with Eqs. (10) and (11) and their in-plane and out-of-plane analogs, we obtain

$$\begin{aligned} v_{2,i}^{\text{fit}} &\approx \frac{1}{2}\frac{C_i\left(R_{\text{AA},i}^{\text{in}} - R_{\text{AA},i}^{\text{out}}\right)}{2R_{\text{AA},a}} = \frac{1}{2}\frac{C_i\gamma_{ia}\left(R_{\text{AA},a}^{\text{in}} - R_{\text{AA},a}^{\text{out}}\right)}{R_{\text{AA},a}^{\text{in}} + R_{\text{AA},a}^{\text{out}}} \\ &= C_i\gamma_{ia}v_{2,a}, \end{aligned} \tag{14}$$

which can also be written as

$$C_i \approx \frac{v_{2,i}^{\text{fit}}}{\gamma_{ia}v_{2,a}}. \tag{15}$$

From Eq. (14), we see that decrease of v_2^{fit} in (b)–(d) cases compared to (a) is a result of a fitting factor $C_i(p_{\perp})$ (which is smaller than 1), as well as the proportionality function $\gamma_i(p_{\perp})$ (also smaller than 1). However, note that Eq. (14) describes asymptotic behavior at very high $p_{\perp}$, where, as shown earlier, γs approach 1. Consequently, the diminishing of elliptic flow compared to the case (a) is predominantly due to a decrease of the *artificially imposed fitting factor C*. Therefore, we obtain that, contrary to [24], *initial stages are not* mainly responsible for the obtained differences (the right panel of Fig. 9) in the v_2^{fit} curves for different T profiles. Moreover, this argument, as well as the obtained inconsistency of the results in this and the first two parts of the paper, implies that application of multiple fitting procedure for each different initial stage may result in incorrect energy loss estimates and in misinterpreting the underlying physics.

To asses if this qualitative conclusion indeed holds, i.e., that v_2 susceptibility observed in Fig. 9 (as well as in [24]) is indeed mainly a consequence of a fitting factor in the energy loss, in Fig. 10 we check the consistency of Eqs. (12) and (15) with the full-fledged numerical calculations. That is, a nontrivial consequence of Eqs. (12) and (15) is that C_i factors for the average, in-plane, and out-of-plane R_{AA}'s (Eq. (12)) and v_2 (Eq. (15)), should be the same in high-$p_{\perp}$ limit, and moreover overlap with C_i^{fit} in this limit. To this end, we define the C factors (originating from Eqs. (12) and (15))

$$C_i^{\text{in}} = \frac{1 - R_{\text{AA},i}^{\text{in,fit}}}{1 - R_{\text{AA},i}^{\text{in}}}, \quad C_i^{\text{out}} = \frac{1 - R_{\text{AA},i}^{\text{out,fit}}}{1 - R_{\text{AA},i}^{\text{out}}},$$

$$C_i^{av} = \frac{1 - R_{\text{AA},i}^{\text{fit}}}{1 - R_{\text{AA},i}}, \quad C_i^{v_2} = \frac{1}{\gamma_{ia}}\frac{v_{2,i}^{\text{fit}}}{v_{2,a}} \tag{16}$$

and compare them with C_i^{fit}, for each separate initial-stages case, $i = b, c, d$. Note that, while terms themselves on the right-hand side of each expression in Eq. (16) are obtained from Eqs. (12) and (15) in the high-$p_\perp$ limit (and consequently are expected to overlap in this limit, if our analytical estimate is valid), we calculate C_i^{fit}, and the terms on the right-hand side of each expression in Eq. (16), through full-fledged numerical procedure. We indeed observe that, for each i and at high-$p_\perp$, C_i^{in}, C_i^{out}, C_i^{av}, and $C_i^{v_2}$ factors are practically overlapping, and approach the value C_i^{fit}. Consequently, this highly nontrivial observation confirms that our qualitative conclusion is valid, and that v_2 susceptibility in this case is indeed mainly a consequence of an additionally introduced fitting factor.

IV. CONCLUSIONS

Traditionally, the features of initial stages before QGP thermalization are explored through comparison of bulk medium simulations and low-$p_\perp$ data. On the other hand, the recent abundance of high-$p_\perp$ experimental data motivates exploiting the high-$p_\perp$ energy loss in studying the initial stages. We here utilized state-of-the-art dynamical energy loss embedded in analytical 1D Bjorken medium expansion (DREENA-B framework), which allowed us to tightly control the analyzed temperature profiles. In particular, we considered four temperature profiles, which are identical after thermalization but are different before thermalization, corresponding to four commonly considered initial-stage cases. This allowed us to study the effects of different initial-stage cases on high-$p_\perp$

R_{AA} and v_2 predictions, under highly controlled conditions, by combining full-fledged numerical results and analytical estimates used to interpret the experimental results.

We found that high-$p_\perp$ R_{AA} is sensitive to the prethermalized stages of the medium evolution; however, within the current error bars, the sensitivity is not sufficient to distinguish between different scenarios. On the other hand, the high-$p_\perp$ v_2 is unexpectedly insensitive to the initial stages. We furthermore found that previously reported sensitivity [24] of high-$p_\perp$ v_2 to initial stages is mainly a consequence of the fitting procedure in which the parameters in the energy loss are adjusted to reproduce experimentally observed R_{AA} individually for different initial-stage cases. On the other hand, if the same global property, in particular the same average temperature, is imposed to tested temperature profiles, high sensitivity of high-$p_\perp$ v_2 is again obtained. This sensitivity is, however, a consequence of differences in final rather than initial stages. Overall, our results underscore that the simultaneous study of high-$p_\perp$ R_{AA} and v_2, with consistent that is, fixed energy loss parameters across the entire study and controlled temperature profiles (reflecting only the differences in the initial stages), is crucial to impose accurate constraints on the initial stages.

ACKNOWLEDGMENTS

[1] J. C. Collins and M. J. Perry, Phys. Rev. Lett. **34**, 1353 (1975).

[2] G. Baym and S. A. Chin, Phys. Lett. B **62**, 241 (1976).

[3] M. Gyulassy and L. McLerran, Nucl. Phys. A **750**, 30 (2005).

[4] E. V. Shuryak, Nucl. Phys. A **750**, 64 (2005); Rev. Mod. Phys. **89**, 035001 (2017).

[5] B. Jacak and P. Steinberg, Phys. Today **63**(5), 39 (2010).

[6] B. Muller, J. Schukraft, and B. Wyslouch, Annu. Rev. Nucl. Part. Sci. **62**, 361 (2012).

[7] S. Acharya *et al.* (ALICE Collaboration), J. High Energy Phys. 11 (2018) 013.

[8] ATLAS Collaboration, Report No. ATLAS-CONF-2017-012 (unpublished).

[9] V. Khachatryan *et al.* (CMS Collaboration), J. High Energy Phys. 04 (2017) 039.

[10] S. Jaelani (ALICE Collaboration), Int. J. Mod. Phys. Conf. Ser. **46**, 1860018 (2018).

[11] J. Wang (CMS Collaboration), Nucl. Part. Phys. Proc. **289–290**, 249 (2017).

[12] T. W. Wang (CMS Collaboration), Nucl. Part. Phys. Proc. **289–290**, 229 (2017).

[13] A. Adare *et al.* (PHENIX Collaboration), Phys. Rev. Lett. **101**, 232301 (2008); Phys. Rev. C **87**, 034911 (2013).

[14] B. I. Abelev *et al.* (STAR Collaboration), Phys. Lett. B **655**, 104 (2007).

[15] S. Acharya *et al.* (ALICE Collaboration), J. High Energy Phys. 07 (2018) 103.

[16] M. Aaboud *et al.* (ATLAS Collaboration), Eur. Phys. J. C **78**, 997 (2018).

[17] A. M. Sirunyan *et al.* (CMS Collaboration), Phys. Lett. B **776**, 195 (2018).

[18] S. Acharya *et al.* (ALICE Collaboration), Phys. Rev. Lett. **120**, 102301 (2018).

[19] A. M. Sirunyan *et al.* (CMS Collaboration), Phys. Rev. Lett. **120**, 202301 (2018).

[20] F. Gelis and B. Schenke, Annu. Rev. Nucl. Part. Sci. **66**, 73 (2016).

[21] G. Aad *et al.* (ATLAS Collaboration), J. High Energy Phys. 11 (2013) 183.

[22] H. Niemi, G. S. Denicol, H. Holopainen, and P. Huovinen, Phys. Rev. C **87**, 054901 (2013).

[23] J. Xu, A. Buzzatti, and M. Gyulassy, J. High Energy Phys. 08 (2014) 063.

[24] C. Andres, N. Armesto, H. Niemi, R. Paatelainen, and C. A. Salgado, Phys. Lett. B **803**, 135318 (2020).

[25] R. Katz, C. A. G. Prado, J. Noronha-Hostler, J. Noronha, and A. A. P. Suaide, arXiv:1906.10768.

[26] J. D. Bjorken, Phys. Rev. D **27**, 140 (1983).

[27] D. Zigic, I. Salom, M. Djordjevic, and M. Djordjevic, Phys. Lett. B **791**, 236 (2019).

[28] J. Xu, J. Liao, and M. Gyulassy, Chin. Phys. Lett. **32**, 092501 (2015).

[29] S. Shi, J. Liao, and M. Gyulassy, Chin. Phys. C **42**, 104104 (2018); **43**, 044101 (2019).

[30] J. Noronha-Hostler, B. Betz, J. Noronha, and M. Gyulassy, Phys. Rev. Lett. **116**, 252301 (2016).

[31] S. K. Das, F. Scardina, S. Plumari, and V. Greco, Phys. Lett. B **747**, 260 (2015).

[32] M. Djordjevic *et al.* (unpublished).

[33] M. Djordjevic and M. Djordjevic, Phys. Lett. B **734**, 286 (2014).

[34] S. Wicks, W. Horowitz, M. Djordjevic, and M. Gyulassy, Nucl. Phys. A **784**, 426 (2007).

[35] Z. B. Kang, I. Vitev, and H. Xing, Phys. Lett. B **718**, 482 (2012); R. Sharma, I. Vitev, and B. W. Zhang, Phys. Rev. C **80**, 054902 (2009).

[36] D. de Florian, R. Sassot, and M. Stratmann, Phys. Rev. D **75**, 114010 (2007).

[37] M. Cacciari and P. Nason, J. High Energy Phys. 09 (2003) 006; E. Braaten, K.-M. Cheung, S. Fleming, and T. C. Yuan, Phys. Rev. D **51**, 4819 (1995).

[38] V. G. Kartvelishvili, A. K. Likhoded, and V. A. Petrov, Phys. Lett. B **78**, 615 (1978).

[39] M. Djordjevic, Phys. Rev. C **74**, 064907 (2006).

[40] M. Djordjevic, Phys. Rev. C **80**, 064909 (2009).

[41] M. Djordjevic and U. Heinz, Phys. Rev. Lett. **101**, 022302 (2008).

[42] B. Blagojevic and M. Djordjevic, J. Phys. G **42**, 075105 (2015).

[43] J. I. Kapusta, *Finite-Temperature Field Theory* (Cambridge University Press, Cambridge, 1989).

[44] R. Baier, Y. L. Dokshitzer, A. H. Mueller, S. Peigne, and D. Schiff, Nucl. Phys. B **483**, 291 (1997); R. Baier, Yu. L. Dokshitzer, A. H. Mueller, S. Peigne, and D. Schiff, **484**, 265 (1997).

[45] N. Armesto, C. A. Salgado, and U. A. Wiedemann, Phys. Rev. D **69**, 114003 (2004).

[46] M. Gyulassy, P. Levai, and I. Vitev, Nucl. Phys. B **594**, 371 (2001).

[47] X. N. Wang and X. F. Guo, Nucl. Phys. A **696**, 788 (2001).

[48] M. Djordjevic, Phys. Lett. B **709**, 229 (2012).

[49] B. Blagojevic, M. Djordjevic, and M. Djordjevic, Phys. Rev. C **99**, 024901 (2019).

[50] Y. Maezawa, S. Aoki, S. Ejiri, T. Hatsuda, N. Ishii, K. Kanaya, N. Ukita, and T. Umeda (WHOT-QCD Collaboration), Phys. Rev. D **81**, 091501(R) (2010).

[51] A. Nakamura, T. Saito, and S. Sakai, Phys. Rev. D **69**, 014506 (2004).

[52] M. Gyulassy, P. Levai, and I. Vitev, Phys. Lett. B **538**, 282 (2002).

[53] A. Dainese, Eur. Phys. J. C **33**, 495 (2004).

[54] D. Zigic, I. Salom, J. Auvinen, M. Djordjevic, and M. Djordjevic, J. Phys. G **46**, 085101 (2019).

[55] A. Peshier, arXiv:hep-ph/0601119.

[56] R. Field, *Applications of Perturbative QCD* (Perseus Books, Cambridge, MA, 1995).

[57] M. Djordjevic and M. Gyulassy, Phys. Rev. C **68**, 034914 (2003).

[58] E. Braaten and M. H. Thoma, Phys. Rev. D **44**, 1298 (1991).

[59] P. F. Kolb and U. W. Heinz, in *Quark-Gluon Plasma 3*, edited by R. C. Hwa and X.-N. Wang (World Scientific, Singapore, 2004), p. 634.

[60] J. E. Bernhard, J. S. Moreland, and S. A. Bass, Nucl. Phys. A **967**, 293 (2017).

[61] M. Wilde (ALICE Collaboration), Nucl. Phys. A **904–905**, 573c (2013).

[62] M. Djordjevic, M. Gyulassy, R. Vogt, and S. Wicks, Phys. Lett. B **632**, 81 (2006).

[63] A. Bazavov *et al.* (HotQCD Collaboration), Phys. Rev. D **90**, 094503 (2014).

[64] P. Christiansen, K. Tywoniuk, and V. Vislavicius, Phys. Rev. C **89**, 034912 (2014).

[65] B. Betz and M. Gyulassy, J. High Energy Phys. 08 (2014) 090 [Erratum: 10 (2014) 043].

[66] S. Cao, L. G. Pang, T. Luo, Y. He, G. Y. Qin, and X. N. Wang, Nucl. Part. Phys. Proc. **289–290**, 217 (2017).

[67] T. Renk, Phys. Rev. C **85**, 044903 (2012).

[68] D. Molnar and D. Sun, Nucl. Phys. A **932**, 140 (2014); **910–911**, 486 (2013).

[69] J. Noronha-Hostler, B. Betz, M. Gyulassy, M. Luzum, J. Noronha, I. Portillo, and C. Ratti, Phys. Rev. C **95**, 044901 (2017).

[70] C. A. G. Prado, J. Noronha-Hostler, R. Katz, A. A. P. Suaide, J. Noronha, and M. G. Munhoz, Phys. Rev. C **96**, 064903 (2017).

[71] S. Cao *et al.* (JETSCAPE Collaboration), Phys. Rev. C **96**, 024909 (2017).

[72] M. Djordjevic, D. Zigic, M. Djordjevic, and J. Auvinen, Phys. Rev. C **99**, 061902(R) (2019).

Calculating hard probe radiative energy loss beyond the soft-gluon approximation: Examining the approximation validity

Bojana Blagojevic,[1,*] Magdalena Djordjevic,[1] and Marko Djordjevic[2]

[1]*Institute of Physics Belgrade, University of Belgrade, Belgrade, Serbia*
[2]*Faculty of Biology, Institute of Physiology and Biochemistry, University of Belgrade, Belgrade, Serbia*

The soft-gluon approximation, which implies that radiated gluon carries away a small fraction of initial parton's energy, is a commonly used assumption in calculating radiative energy loss of high momentum partons traversing quark-gluon plasma created at the Relativistic Heavy Ion Collider and the Large Hadron Collider. While the soft-gluon approximation is convenient, different theoretical approaches have reported significant radiative energy loss of high-$p_\perp$ partons, thereby questioning its validity. To address this issue, we relaxed the soft-gluon approximation within Djordjevic–Gyulassy–Levai–Vitev (DGLV) formalism. The obtained analytical expressions are quite distinct from the soft-gluon case. However, numerical results for the first order in opacity fractional energy loss lead to small differences in predictions for the two cases. The difference in the predicted number of radiated gluons is also small. Moreover, the effect on these two variables has an opposite sign, which when combined results in almost overlapping suppression predictions. Therefore, our results imply that, contrary to the commonly held doubts, the soft-gluon approximation in practice works surprisingly well in DGLV formalism. Finally, we also discuss generalizing this relaxation in the dynamical QCD medium, which suggests a more general applicability of the conclusions obtained here.

I. INTRODUCTION

One of the main assumptions in the radiative energy loss calculations of energetic partons (referred to as *jet*) traversing the quark-gluon plasma (QGP) medium is the soft-gluon approximation, which assumes that the radiated gluon carries away a small portion of initial jet energy, i.e., $x = \omega/E \ll 1$, where E is the energy of initial jet and ω is the radiated gluon energy.

Such assumption was widely used in various energy loss models: (i) the multiple soft-scattering-based Amesto–Salgado–Wiedemann (ASW) model [1–3]; (ii) Baier–Dokshitzer–Mueller–Peigne–Schiff (BDMPS) [4,5], and Baier–Dokshitzer–Mueller–Peigne–Schiff–Zakharov (BDMPS-Z) [6,7]; (iii) the opacity-expansion-based Gyulassy–Levai–Vitev (GLV) model [8,9], and (iv) multigluon evolution-based Higher-Twist (HT) approach [10,11], etc. These various energy loss models predict a significant medium-induced radiative energy loss, questioning the validity of the soft-gluon approximation. To address this issue, a finite x (or large x limit) was introduced in some of these models [12,13] or their extensions [14]. However, introduction of finite x lead to different conclusions on the importance of relaxing the soft-gluon approximation, which was assessed from relatively small [14], but noticeable, to moderately large [13] importance.

The soft-gluon approximation was also used in the development of our dynamical energy loss formalism [15–17], specifically in its radiative energy loss component. This for-

malism was comprehensively tested against the angular averaged nuclear modification factor R_{AA} [18,19] data, where we obtained robust agreement for a wide range of probes [17,20], centralities [21], and beam energies [20,22], including clear predictions for future experiments [23,24]. This might strongly suggest that our energy loss formalism can well explain the jet-medium interactions in QGP, making this formalism suitable for the tomography of QCD medium.

However, the soft-gluon approximation obviously breaks down for (i) intermediate momentum ranges ($5 < p_\perp < 10$ GeV) where the experimental data are most abundant and with the smallest error bars, and (ii) gluon energy loss, since due to the color factor of 9/4 gluons lose significantly more energy compared to quark jets, which therefore questions the reliability of our formalism in such cases. Because of this, and for precise predictions, it became necessary to relax the soft-gluon approximation and consequently test its validity in dynamical energy loss formalism.

This paper presents our first step toward this goal. Since the dynamical energy loss is computationally very demanding, we will, in this study, start with relaxing this approximation on its simpler predecessor, i.e., Djordjevic–Gyulassy–Levai–Vitev (DGLV) [25] formalism. Within this, we will concentrate on gluon jets, since, because of their color factor, the soft-gluon approximation has the largest impact for this type of parton. For the gluon jets, we perform the radiative energy loss calculation to the first order in the number of scattering centers (opacity), where we consider that the radiation of one gluon is induced by one collisional interaction with the medium.

Our calculation is done within the pQCD approach for a finite size, optically thin QCD medium and since it is

*bojanab@ipb.ac.rs

technically demanding it will be divided into several steps: (i) First, the calculation will be done in the simplest case of massless gluons in the system of static scattering centers [26] within GLV. (ii) Then it will be extended toward the gluons with the effective mass [27], which presents expansion of DGLV [25] toward larger loss of jet energy via radiated gluon. (iii) Finally, we will discuss the impact of finite x on the radiative energy loss, when dynamical medium [17] (i.e., a recoil with the medium constituents) is accounted for.

In that manner, we will assess the validity of the soft-gluon assumption for gluon jets, and this will also provide insight into whether a finite x has to be implemented in quark-jet radiative energy loss calculations within our formalism. Namely, if the relaxation of the soft-gluon approximation only slightly modifies gluon-jet radiative energy loss, then even smaller modification would be expected in the quark-jet case, thus making this relaxation redundant. Otherwise, if the effect of a finite x appears to be significant in gluon-jet case, then the relaxation in the quark-jet case may also be required, which would represent an important future task.

Second, as stated above, the relaxation of the soft-gluon approximation is needed in order to extend the applicability of our model [17] toward an intermediate momentum region. Thus, the another benefit of this relaxation would be to extend the $p_\perp$ range in which our predictions are valid.

The sections are organized as follows: In Sec. II, we provide the theoretical framework. In Sec. III, we outline the computation of the zeroth order in opacity gluon-jet radiative energy loss in a static QCD medium, beyond the soft-gluon approximation, in the cases of both massless and massive gluons. For $x \ll 1$, the results from Refs. [9,25] are reproduced.

Section IV contains a concise description of relaxing the soft-gluon approximation to calculate the first order in opacity radiative energy loss for a massless gluon jet in a static QCD medium. In the limit of very small x, the result from Ref. [9] is recovered.

In Sec. V, we explain the computation of the first order in opacity gluon-jet energy loss in static QCD medium, with effective gluon mass [27] included, and beyond soft-gluon approximation. This presents an extension of the calculations from Ref. [25] toward finite x, so that results from Ref. [25] can be recovered in the $x \ll 1$ limit. The detailed calculations corresponding to Secs. III–V are presented in the Appendixes C–J.

In Sec. VI, we outline the numerical estimates based on our beyond soft-gluon calculations for gluon jet and the comparison with our previous results from Ref. [25], i.e., the results with soft-gluon approximation. In particular, we investigate the effect of finite x on gluon-jet fractional radiative energy loss, number of radiated gluons, fractional differential radiative energy loss (intensity spectrum), single-gluon radiation spectrum, and gluon suppression [28]. Conclusions and outlook are presented in Sec. VII.

II. THEORETICAL FRAMEWORK

In this work, we concentrate on relaxing the soft-gluon approximation in calculating the first-order opacity radiative energy loss of high $p_\perp$ eikonal gluon jets within (GLV) DGLV

[25] formalism. That is, we assume that a high $p_\perp$ gluon jet is produced inside a "thin" finite QGP medium at some initial point $(t_0, z_0, \mathbf{x}_0)$ and that the medium is composed of static scattering centers [26]. Therefore, we model the interactions in QGP assuming a static (Debye) colored-screened Yukawa potential, whose Fourier and color structure acquires the following form ([9,25,26]):

$$V_n = V(q_n)e^{iq_n x_n}$$
$$= 2\pi\delta(q_n^0)v(\vec{\mathbf{q}}_n)e^{-i\vec{\mathbf{q}}_n \cdot \vec{\mathbf{x}}_n}T_{a_n}(R) \otimes T_{a_n}(n), \quad (1)$$

$$v(\vec{\mathbf{q}}_n) = \frac{4\pi\alpha_s}{\vec{\mathbf{q}}_n^2 + \mu^2}, \quad (2)$$

where x_n denotes time-space coordinate of the nth scattering center, μ is the Debye screening mass, $\alpha_s = g_s^2/4\pi$ is the strong coupling constant, and $T_{a_n}(R)$ and $T_{a_n}(n)$ denote the generators in the SU($N_c = 3$) color representation of the gluon jet and target (scattering center), respectively.

For consistency with Refs. [9,25], we use the same notation for four-dimensional (4D) vectors (e.g., momenta), which is described in detail in Appendix A, and proceed throughout using light-cone coordinates. The same appendix contains algebraic manipulation and identities for the SU(N_c) generators and the Feynman rules used in these calculations.

The approximations that we assume throughout the paper are stated in Appendix B.

The small transverse momentum transfer elastic cross section for interaction between gluon jet and target parton in the Gyulassy–Wang (GW) approach [8,26] is given by

$$\frac{d\sigma_{el}}{d^2\mathbf{q}_1} = \frac{C_2(G)C_2(T)}{d_G}\frac{|v(0, \mathbf{q}_1)|^2}{(2\pi)^2}, \quad (3)$$

where $\mathbf{q}_1$ corresponds to transverse momentum of exchanged gluon, $C_2(G)$ represents the Casimir operator in adjoint representation (G) of gluons SU($N_c = 3$) with dimension $d_G = 8$ and $C_2(T)$ denotes Casimir operator in target (T) representation.

Since this formalism assumes optically thin plasma, the final results are expanded in powers of opacity, which are defined as the mean numbers of collisions in the medium: $L/\lambda = N\sigma_{el}/A_\perp$ [9], where L is the thickness of the QCD medium, λ is a mean free path, and N denotes the number of scatterers (targets) in transverse area $A_\perp$. Note that we restrict our calculations to the first order in opacity, which is shown to be the dominant term ([29,30]).

III. ZEROTH-ORDER RADIATIVE ENERGY LOSS

To gradually introduce technically involving beyond soft-gluon calculations, we first concentrate on massless gluons traversing static QCD medium.

We start with the M_0 Feynman diagram, which corresponds to the source J that produces off-shell gluon with momentum $p + k$, radiates on-shell gluon with momentum k without interactions with QCD medium, and emerges with momentum p. We will further refer to these two outgoing gluons as the radiated (k) and the final (p) gluon. Note that in both this and consecutive sections that involve interactions with one and two scattering centers we consistently assume that the initial jet propagates along the longitudinal z axis. The detailed

calculation of M_0 for finite x in the massless case is presented in Appendix C, with all assumptions listed in Appendix B.

We also assume that gluons are transversely polarized particles, and although we work in covariant gauge, we can choose any polarization vector for the external on-shell gluons [14]. So, in accordance with Refs. [9,14,25], we choose $n^\mu = [0, 2, \mathbf{0}]$ (i.e., $\epsilon(k) \cdot k = 0$, $\epsilon(k) \cdot n = 0$ and $\epsilon(p) \cdot p = 0$, $\epsilon(p) \cdot n = 0$). Likewise, we assume that the source has also the physical polarization as real gluons [14] (i.e., $\epsilon(p + k) \cdot (p + k) = 0$, $\epsilon(p + k) \cdot n = 0$). Thus, for massless gluon's momenta, we have

$$p + k = [E^+, E^-, \mathbf{0}],$$

$$k = \left[xE^+, \frac{\mathbf{k}^2}{xE^+}, \mathbf{k} \right],$$ (4)

$$p = \left[(1-x)E^+, \frac{\mathbf{p}^2}{(1-x)E^+}, \mathbf{p} \right],$$

where $E^+ = p^0 + k^0 + p_z + k_z$, $E^- = p^0 + k^0 - p_z - k_z$, and due to 4-momentum conservation

$$\mathbf{p} + \mathbf{k} = 0.$$ (5)

The polarization vectors read

$$\epsilon_i(k) = \left[0, \frac{2\boldsymbol{\epsilon}_i \cdot \mathbf{k}}{xE^+}, \boldsymbol{\epsilon}_i \right],$$

$$\epsilon_i(p) = \left[0, \frac{2\boldsymbol{\epsilon}_i \cdot \mathbf{p}}{(1-x)E^+}, \boldsymbol{\epsilon}_i \right],$$ (6)

$$\epsilon_i(p + k) = [0, 0, \boldsymbol{\epsilon}_i],$$

where $i = 1, 2$, and we also make use of Eq. (5). So, the amplitude that gluon jet, produced at x_0 inside QCD medium, radiates a gluon of color c without final-state interactions and reads

$$M_0 = J_a(p + k)e^{i(p+k)x_0}(-2ig_s)(1 - x + x^2)\frac{\boldsymbol{\epsilon} \cdot \mathbf{k}}{\mathbf{k}^2}(T^c)_{da}.$$ (7)

The radiation spectrum is obtained when Eq. (7) is substituted in

$$d^3N_g^{(0)}d^3N_J \approx \mathrm{Tr}\langle |M_0|^2\rangle \frac{d^3\vec{\mathbf{p}}}{(2\pi)^3 2p^0} \frac{d^3\vec{\mathbf{k}}}{(2\pi)^3 2\omega},$$ (8)

where $\omega = k_0$, and where d^3N_J reads

$$d^3N_J = d_G|J(p + k)|^2 \frac{d^3\vec{\mathbf{p}}_J}{(2\pi)^3 2E_J}.$$ (9)

Here $E_J = E = p_0 + k_0$ and $\vec{\mathbf{p}}_J$ denotes energy and three-dimensional (3D) momentum of the initial gluon jet, respectively. Note that E retains the same expression for other diagrams as well. The jet part can be decoupled by using the equality

$$\frac{d^3\vec{\mathbf{p}}}{(2\pi)^3 2p^0} \frac{d^3\vec{\mathbf{k}}}{(2\pi)^3 2\omega} = \frac{d^3\vec{\mathbf{p}}_J}{(2\pi)^3 2E_J} \frac{dxd^2\mathbf{k}}{(2\pi)^3 2x(1-x)},$$ (10)

which is obtained by substituting $p_z, k_z \rightarrow p_z^J, xE$. Finally, energy spectrum acquires the form

$$\frac{xd^3N_g^{(0)}}{dxd\mathbf{k}^2} = \frac{\alpha_s}{\pi} \frac{C_2(G)}{\mathbf{k}^2} \frac{(1 - x + x^2)^2}{1 - x},$$ (11)

which recovers the well-known Altarrelli-Parisi [31] result.

We now briefly concentrate on generating result in finite temperature QCD medium, since in Ref. [27], it was shown that gluons in finite-temperature QGP can be approximated as a massive transverse plasmons with mass $m_g = \mu/\sqrt{2}$, where μ is the Debye mass. In this case, M_0 amplitude becomes

$$M_0 = J_a(p + k)e^{i(p+k)x_0}(-2ig_s)(1 - x + x^2)$$

$$\times \frac{\boldsymbol{\epsilon} \cdot \mathbf{k}}{\mathbf{k}^2 + m_g^2(1 - x + x^2)}(T^c)_{da},$$ (12)

leading to

$$\frac{xd^3N_g^{(0)}}{dxd\mathbf{k}^2} = \frac{\alpha_s}{\pi} \frac{C_2(G)\,\mathbf{k}^2}{\left[\mathbf{k}^2 + m_g^2(1 - x + x^2)\right]^2}$$

$$\times \frac{(1 - x + x^2)^2}{1 - x}.$$ (13)

IV. FIRST-ORDER RADIATIVE ENERGY LOSS IN MASSLESS CASE

In accordance with Ref. [25], we compute the first order in opacity radiative energy loss of a gluon jet for finite x starting from the expression

$$d^3N_g^{(1)}d^3N_J = \left(\frac{1}{d_T} \mathrm{Tr}\langle |M_1|^2\rangle + \frac{2}{d_T} \mathrm{Re}\,\mathrm{Tr}\langle M_2 M_0^*\rangle \right)$$

$$\times \frac{d^3\vec{\mathbf{p}}}{(2\pi)^3 2p^0} \frac{d^3\vec{\mathbf{k}}}{(2\pi)^3 2\omega},$$ (14)

where M_0 corresponds to the diagram without final-state interactions with a QCD medium, introduced in previous section, M_1 is the sum of all diagrams with one scattering center, M_2 is the sum of all diagrams with two scattering centers in the contact-limit case, while d_T denotes the dimension of the target color representation (for pure gluon medium $d_T = 8$). In obtaining the expression for differential energy loss, we again incorporate (9) in Eq. (14).

The assumption that initial jet propagates along z axis takes the following form in the two cases stated below:

(1) One interaction with QCD medium (M_1),

$$p + k - q_1 = [E^+ - q_{1z}, E^- + q_{1z}, \mathbf{0}],$$ (15)

where $p + k - q_1$ corresponds to the initial jet, while k and p retain the same expressions as in Eq. (4), with the distinction that now $\mathbf{p} \neq -\mathbf{k}$, since due to 4-momentum conservation, the following relation holds:

$$\mathbf{q}_1 = \mathbf{p} + \mathbf{k}.$$ (16)

The rest of the notation is the same as in Eq. (4).

(2) Two interactions with QCD medium (M_2),

$$p + k - q_1 - q_2$$

$$= [E^+ - q_{1z} - q_{2z}, E^- + q_{1z} + q_{2z}, \mathbf{0}],$$ (17)

where $p + k - q_1 - q_2$ corresponds to the initial jet and $q_i = [q_{iz}, -q_{iz}, \mathbf{q}_i]$ corresponds to exchanged gluons, $i = 1, 2$ with $q_i^0 = 0$, while p, k retain the same expressions as in Eq. (4). Also, due to 4-momentum conservation, the following relation between gluon transverse momenta holds:

$$\mathbf{p} + \mathbf{k} = \mathbf{q}_1 + \mathbf{q}_2,$$ (18)

which in the contact-limit case (when $\mathbf{q}_1 + \mathbf{q}_2 = 0$) reduces to $\mathbf{p} + \mathbf{k} = 0$.

Note that Eq. (16) has to be satisfied for M_1 diagrams in order to claim that initial jet propagates along the z axis; i.e., for M_1 diagrams $\mathbf{p} + \mathbf{k}$ is different from 0. This is an important distinction between the calculations presented in our study and the calculations done within Soft-Collinear Effective Theory (SCET) formalism (see, e.g., Ref. [14]), where $\mathbf{p} + \mathbf{k} = 0$ was used in calculation of *both* M_1 and M_2 diagrams, though the assumption that initial jet propagates along the z axis was used in that study as well.

The transverse polarization vectors $\epsilon_i(k)$ and $\epsilon_i(p)$ for both M_1 and M_2 amplitudes are given by the same expression as in the previous section (with an addition that in the M_1 case $\mathbf{p} \neq -\mathbf{k}$, as discussed above), while ϵ for initial jets consistently has the same form as in Eq. (6), i.e., $\epsilon_i(p + k - q_1) = [0, 0, \boldsymbol{\epsilon}_i]$ for M_1 amplitudes and $\epsilon_i(p + k - q_1 - q_2) = [0, 0, \boldsymbol{\epsilon}_i]$ for M_2 amplitudes.

The detailed calculation of the remaining 10 Feynman diagrams, under the approximations stated in Appendix B, contributing to the first order in opacity radiative energy loss, is given in Appendixes D–H, whereas thorough derivation of the single-gluon radiation spectrum beyond the soft-gluon approximation in the massless case is given in Appendix I and reads as follows (energy loss expression can be straightforwardly extracted by using $dE^{(1)}/dx \equiv \omega dN_g^{(1)}/dx \approx xE dN_g^{(1)}/dx$):

$$
\frac{dN_g^{(1)}}{dx} = \frac{C_2(G)\alpha_s}{\pi} \frac{L}{\lambda} \frac{(1 - x + x^2)^2}{x(1 - x)} \int \frac{d^2\mathbf{q}_1}{\pi} \frac{\mu^2}{\left(\mathbf{q}_1^2 + \mu^2\right)^2}
$$
$$
\times \int d\mathbf{k}^2 \left\{ \frac{(\mathbf{k} - \mathbf{q}_1)^2}{\left[\frac{4x(1-x)E}{L}\right]^2 + (\mathbf{k} - \mathbf{q}_1)^4} \left[2 - \frac{\mathbf{k} \cdot (\mathbf{k} - \mathbf{q}_1)}{\mathbf{k}^2} - \frac{(\mathbf{k} - \mathbf{q}_1) \cdot (\mathbf{k} - x\mathbf{q}_1)}{(\mathbf{k} - x\mathbf{q}_1)^2} \right] \right.
$$
$$
\left. + \frac{\mathbf{k}^2}{\left[\frac{4x(1-x)E}{L}\right]^2 + \mathbf{k}^4} \left[1 - \frac{\mathbf{k} \cdot (\mathbf{k} - x\mathbf{q}_1)}{(\mathbf{k} - x\mathbf{q}_1)^2} \right] + \left[\frac{1}{(\mathbf{k} - x\mathbf{q}_1)^2} - \frac{1}{\mathbf{k}^2} \right] \right\}, \tag{19}
$$

where we assumed a simple exponential distribution $\frac{2}{L} e^{\frac{-2\Delta z}{L}}$ of longitudinal distance between the gluon-jet production site and target rescattering site, emerging as $\left(\frac{4x(1-x)E}{L}\right)^2$ in the denominators of the integrand. Beside facilitating the calculations, this assumption is in accordance with Refs. [8,25,29,32], which allows direct comparison of our results with the corresponding (GLV) DGLV results. Specifically, as the calculations from this paper present a generalization of the previous GLV (DGLV) toward finite x, in the soft-gluon limit they should recover GLV (DGLV) results. To this end, note that Eq. (19) reduces to the massless case of Eq. (11) from Ref. [25] in the $x \to 0$ limit, as expected.

Additionally, we tested the robustness of all results from this paper, by taking into account the alternative (opposite) assumption of uniform distribution of scattering centers (as done in Refs. [15,16]). The same results with the respect to the importance of soft-gluon approximation are obtained; i.e., the conclusions presented in this paper are robust to the presumed longitudinal distance distribution (formulas and data shown in Appendix K).

It is straightforward to show that our result is symmetric under the exchange of radiated (k) and final (p) gluon, as expected beyond the soft-gluon approximation, and as a result of the inability to distinguish between these two identical gluons.

V. GLUON RADIATIVE ENERGY LOSS IN FINITE-TEMPERATURE QCD MEDIUM

Next, we note that in ultrarelativistic heavy ion collisions, a finite-temperature QCD medium is created that modifies the gluon self-energies and can consequently significantly influence the radiative energy loss results. It is therefore essential to include finite-temperature effects in gluon radiative energy loss calculations beyond soft-gluon approximation, which is the main goal of this section. To address this issue, we note that in Ref. [27], it was shown that gluons can be approximated as massive transverse plasmons with effective mass m_g (for gluons with the hard momenta $k \gtrsim T$) equal to its asymptotic value. The assumption of initial jet propagating along the z axis, for a massive case, leads to the following form of momenta, in the three cases stated below:

(1) No interaction with QCD medium (M_0):
$$
p + k = [E^+, E^-, \mathbf{0}],
$$
$$
k = \left[xE^+, \frac{\mathbf{k}^2 + m_g^2}{xE^+}, \mathbf{k} \right], \tag{20}
$$
$$
p = \left[(1 - x)E^+, \frac{\mathbf{p}^2 + m_g^2}{(1 - x)E^+}, \mathbf{p} \right],
$$
where Eq. (5) holds.

(2) One interaction with QCD medium (M_1):
k and p retain the same expressions as in Eq. (20), with addition that (as in the previous section) Eq. (16) holds due to conservation of 4-momentum, while the initial jet has the momentum of the same form as in Eq. (15).

(3) Two interactions with QCD medium (M_2):
p, k have the same expressions as in Eq. (20). Also, due to 4-momentum conservation, Eq. (18) holds and in the contact-limit case reduces to $\mathbf{p} + \mathbf{k} = 0$, while initial jet momentum retains the same form as in Eq. (17).

The transverse polarization vectors remain the same as in the massless case.

We retain all approximations from the previous section, which are reviewed in Appendix B, and recalculate the same 11 diagrams from Appendixes C–H, also beyond the soft-gluon approximation. The overview of all intermediate results is contained in Appendix J. Thus, Eq. (19) in the massive case acquires a more complex form, given by

$$
\begin{aligned}
\frac{dN_g^{(1)}}{dx} = {} & \frac{C_2(G)\alpha_s}{\pi} \frac{L}{\lambda} \frac{(1-x+x^2)^2}{x(1-x)} \int \frac{d^2\mathbf{q}_1}{\pi} \frac{\mu^2}{\left(\mathbf{q}_1^2+\mu^2\right)^2} \\
& \times \int d\mathbf{k}^2 \Bigg\{ \frac{(\mathbf{k}-\mathbf{q}_1)^2+\chi}{\left[\frac{4x(1-x)E}{L}\right]^2+[(\mathbf{k}-\mathbf{q}_1)^2+\chi]^2} \left[2\frac{(\mathbf{k}-\mathbf{q}_1)^2}{(\mathbf{k}-\mathbf{q}_1)^2+\chi} - \frac{\mathbf{k}\cdot(\mathbf{k}-\mathbf{q}_1)}{\mathbf{k}^2+\chi} - \frac{(\mathbf{k}-\mathbf{q}_1)\cdot(\mathbf{k}-x\mathbf{q}_1)}{(\mathbf{k}-x\mathbf{q}_1)^2+\chi} \right] \\
& + \frac{\mathbf{k}^2+\chi}{\left[\frac{4x(1-x)E}{L}\right]^2+(\mathbf{k}^2+\chi)^2} \left[\frac{\mathbf{k}^2}{\mathbf{k}^2+\chi} - \frac{\mathbf{k}\cdot(\mathbf{k}-x\mathbf{q}_1)}{(\mathbf{k}-x\mathbf{q}_1)^2+\chi} \right] + \left[\frac{(\mathbf{k}-x\mathbf{q}_1)^2}{[(\mathbf{k}-x\mathbf{q}_1)^2+\chi]^2} - \frac{\mathbf{k}^2}{(\mathbf{k}^2+\chi)^2} \right] \Bigg\},
\end{aligned}
\tag{21}
$$

where $\chi = m_g^2(1-x+x^2)$. It can easily be verified that, in the soft-gluon limit, we recover Eq. (11) from Ref. [25] (note that for gluon jet $M \equiv m_g$, so that the term M^2x^2 from Ref. [25] should be neglected) and that in the massless limit Eq. (21) reduces to Eq. (19).

To our knowledge, this result presents the first introduction of effective gluon mass beyond-soft-gluon-approximation radiative energy loss. Additionally, we again verified that the single-gluon radiation spectrum is symmetric to substitution of p and k gluons, as necessary (see the previous section and Appendix J). Furthermore, note that the analytical form of Eq. (21) is quite different from the corresponding expression with the soft-gluon approximation (Eq. (11) from Ref. [25]). In the next section, we will evaluate the extent of numerical differences to which these two different analytical expressions lead.

In particular, we are interested in what is the effect of finite x on gluon fractional radiative energy loss ($\frac{\Delta E^{(1)}}{E}$), number of radiated gluons ($N_g^{(1)}$), and the suppression (R_{AA}). We accordingly note that $\frac{dE^{(1)}}{dx} \equiv \omega \frac{dN_g^{(1)}}{dx} \approx xE \frac{dN_g^{(1)}}{dx}$ from which we can further straightforwardly numerically evaluate $\frac{\Delta E^{(1)}}{E}$, as well as the number of radiated gluons ($N_g^{(1)}$).

VI. NUMERICAL RESULTS

We next assess how the relaxation of the soft-gluon approximation modifies gluon-jet energy loss to the first order in opacity. We consequently compare the predictions based on the results derived in this paper with the one obtained in the soft-gluon limit from Ref. [25] (applied to gluons); the comparison is done for gluons with effective mass $m_g = \mu/\sqrt{2}$, where $\mu = \sqrt{4\pi\alpha_s(1+n_f/6)}T$ and $n_f = 3$ is the number of the effective light-quark flavors. For all figures, we use the following set of parameters, constant $\alpha_s = \frac{g_s^2}{4\pi} = 0.3$, $L = 5$ fm, $\lambda = 1$ fm, and $T = 300$ MeV, to mimic standard Large Hadron Collider (LHC) conditions.

The comparison of the fractional radiative energy loss $\frac{\Delta E^{(1)}}{E}$ for calculations beyond the soft-gluon approximation, and with the soft-gluon approximation, as a function of initial jet transverse momentum ($p_\perp$) is shown in Fig. 1(a);

note that in this paper we concentrate on midrapidity jets in relativistic heavy-ion collisions, where gluons energy is approximately equal to their transverse momentum, due to negligible effective gluon mass compared to the transverse momentum. More specifically, the curve corresponding to the beyond soft-gluon approximation (*bsg*) case is obtained from Eq. (21) multiplied by xE and integrated over x, while the curve corresponding to soft-gluon approximation (*sg*) case is obtained by numerically integrating Eq. (11) from Ref. [25]. These two curves almost overlap and even converge toward one another at higher $p_\perp$. Note that the upper limit of x integration is equal to $1/2$ instead of 1, in order to avoid double counting. The upper limits of integration for $|\mathbf{k}|$ and $|\mathbf{q}_1|$, determined kinematically, are $2x(1-x)E$ and $\sqrt{4ET}$, respectively [25].

The comparison of the number of radiated gluons in *bsg* and *sg* cases is presented in Fig. 1(c). These two curves also nearly overlap, with a slight disagreement at higher $p_\perp$.

Quantitative assessment of relaxing the soft-gluon approximation on these two variables can be observed in Figs. 1(b) and 1(d). We see that finite values of x slightly increase fractional radiative energy loss by maximum of ∼3% up to $p_\perp \approx 10$ GeV compared to *sg* case. Afterward, the difference between *bsg* and *sg* $\frac{\Delta E^{(1)}}{E}$ steeply decreases toward 0%. Additionally, finite x also decreases number of radiated gluons for a small amount (up to 5%) compared to the *sg* case for very low transverse momenta. Further, the relative difference reaches a peak of −2% also at $p_\perp \approx 10$ GeV, and for higher transverse momenta remains nearly constant somewhat below −2%. Consequently, the overall conclusion from Fig. 1 is that the effect on both variables is small and with opposite signs.

The effect of finite x value is further assessed on the fractional differential radiative energy loss ($\frac{1}{E}\frac{dE^{(1)}}{dx} = x\frac{dN_g^{(1)}}{dx}$) and on single-gluon radiation spectrum ($\frac{dN_g^{(1)}}{dx}$) and its relative change. These effects are shown as a function of x in Fig. 2, for different values of initial jet transverse momentum $p_\perp$; *bsg* curves for $\frac{1}{E}\frac{dE^{(1)}}{dx}$ are obtained from Eq. (21) multiplied by x, whereas *sg* curves correspond to Eq. (11) in Ref. [25]. From Fig. 2, we observe a small difference between *bsg* and *sg* results for $x \lesssim 0.3$ (roughly up to 0.4), i.e., for smaller x, as expected. We also recognize $x \approx 0.3$ as a crossover
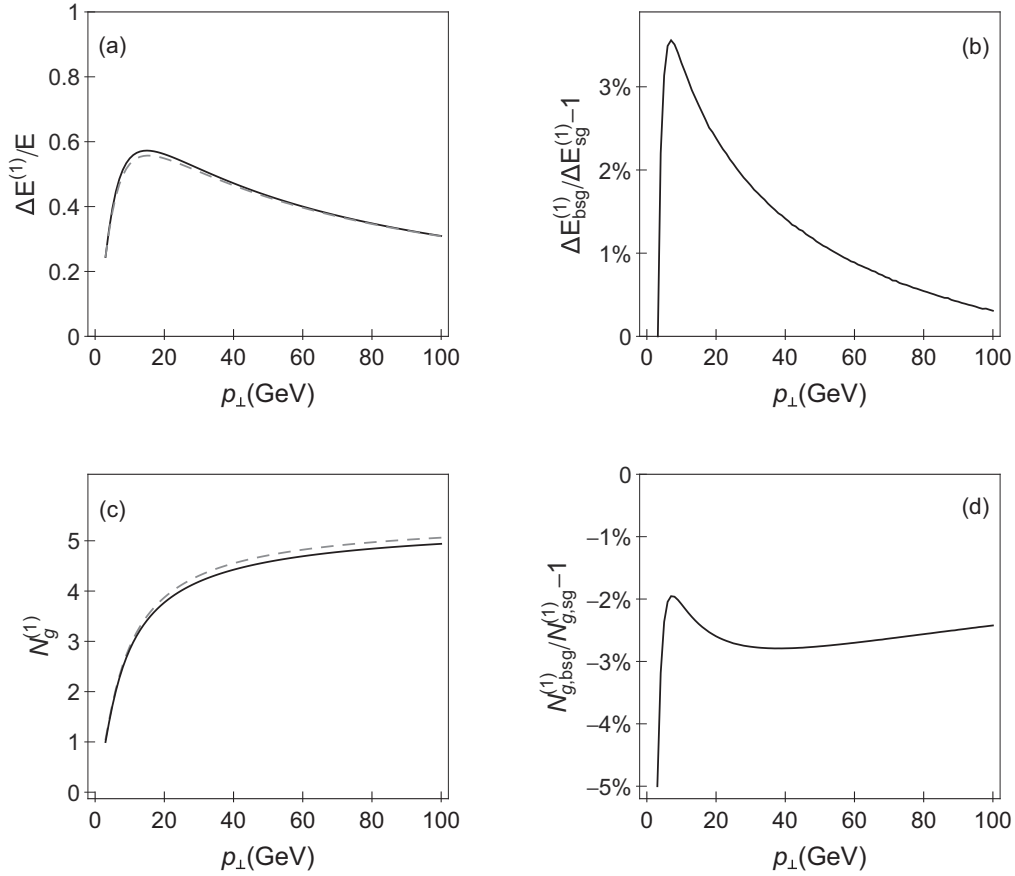
FIG. 1. The effect of relaxing the soft-gluon approximation on integrated variables to the first order in opacity of DGLV formalism, as a function of $p_\perp$. (a) Comparison of gluon's fractional radiative energy loss without (solid curve) and with (dashed curve) soft-gluon approximation. (b) The relative change of the radiative energy loss when the soft-gluon approximation is relaxed with respect to the soft-gluon limit. (c) Comparison of number of radiated gluons without (solid curve) and with (dashed curve) the soft-gluon approximation. (d) A percentage of radiated gluon number change when the soft-gluon approximation is relaxed.

value, below which fractional differential radiative energy loss and single-gluon radiation spectrum are somewhat lower in *bsg* compared to *sg* cases, and above which the opposite is true. At a high value of x, i.e., $0.4 < x \leqslant 0.5$, the differences between our *bsg* fractional differential radiative energy loss and previously obtained *sg* [25] ascend to notable values ($\sim$50%) and increase with increasing $p_\perp$.

To investigate the effect of relaxing the soft-gluon approximation on the single-gluon radiation spectrum in more detail, the third column is added in Fig. 2, i.e., Figs. 2(c), 2(f), and 2(i) (see also Fig. 3), showing relative change of $\frac{dN_g^{(1)}}{dx}$. This quantitative estimation (difference smaller than 10% for $x \lesssim 0.4$) is in agreement with the previous discussion. In particular, at higher x values, there is a notably larger spectra in the *bsg* compared to *sg* cases, and this difference increases (up to 60% at $p_\perp = 50$ GeV) with increasing $p_\perp$. Nevertheless, for both variables ($\frac{1}{E}\frac{dE^{(1)}}{dx}$ and $\frac{dN_g^{(1)}}{dx}$) *bsg* and *sg* cases lead to similar results for $x \lesssim 0.4$.

The effect of relaxing the soft-gluon approximation on single-gluon radiation spectrum for different transverse momentum values of the initial gluon jet is further addressed in Fig. 3. We observe that a notable (i.e., tenfold) increase of

$p_\perp$ leads to a modest increase (less than 25%) of $\frac{dN_g^{(1)}}{dx}$ in the *bsg* compared to *sg* cases. Note that the same dependence is obtained for $(\frac{1}{E}\frac{dE_{bsg}^{(1)}}{dx})/(\frac{1}{E}\frac{dE_{sg}^{(1)}}{dx}) - 1$ (since $\frac{1}{E}\frac{dE^{(1)}}{dx} = x\frac{dN_g^{(1)}}{dx}$, so that x cancels when taking the relative ratio). Therefore, we conclude that the relaxation of the soft-gluon approximation has nearly the same effect on $\frac{dN_g^{(1)}}{dx}$ and $\frac{1}{E}\frac{dE^{(1)}}{dx}$ (across the whole x region) independent of the $p_\perp$ of the initial jet.

Although we showed that relaxing the soft-gluon approximation has small numerical impact on both integrated ($\frac{\Delta E^{(1)}}{E}$, $N_g^{(1)}$, across the whole x region) and differential ($\frac{1}{E}\frac{dE^{(1)}}{dx}$, $\frac{dN_g^{(1)}}{dx}$, up to $x \approx 0.4$) variables, the difference between *bsg* and *sg* cases can go up to 10% (and with different signs), and moreover can be quite large for $x > 0.4$. This, therefore, leads to the question of how the relaxation of the soft-gluon approximation affects predictions for measured observables, such as the angular averaged nuclear modification factor R_{AA} [18,19]. Comparing R_{AA} with and without soft-gluon approximation allows us to assess the adequacy of this approximation in obtaining reliable numerical predictions.

To that end, we next concentrate on generating the predictions for bare gluon R_{AA}, based only on radiative energy loss,
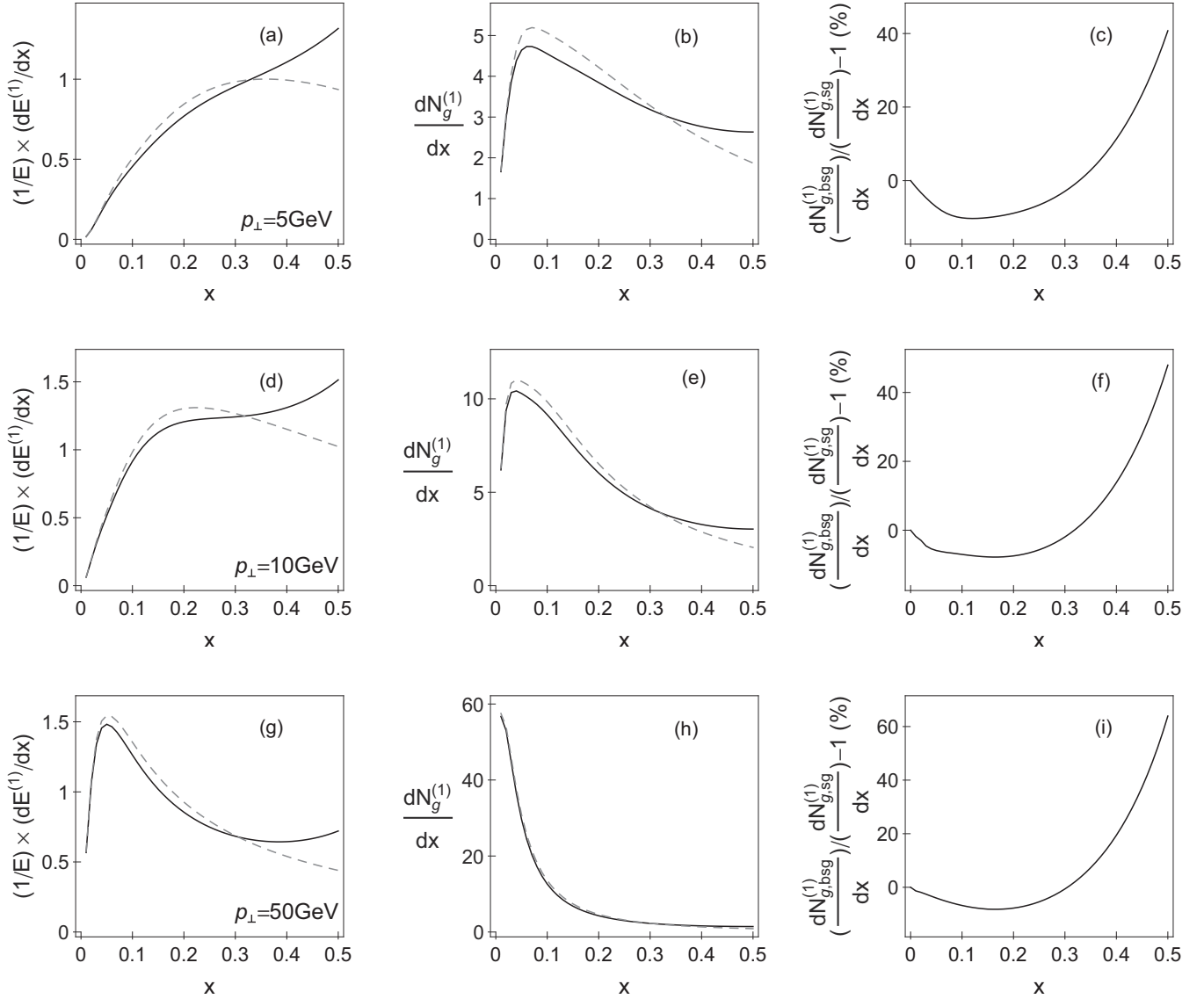
FIG. 2. The effect of relaxing the soft-gluon approximation on differential variables to the first order in opacity of DGLV formalism, as a function of x. The comparison of (i) fractional differential gluon radiative energy loss ($(1/E) \times (dE^{(1)}/dx)$) and (ii) single-gluon radiation (spectrum) distribution in momentum fraction ($dN_g^{(1)}/dx$) between bsg (solid curve) and sg (dashed curve) case, for different values of initial jet transverse momenta (5, 10, and 50 GeV, as indicated in panels) is shown in the first column ((a), (d), and (g)) and second column ((b), (e), and (h)), respectively. The relative change of the single-gluon radiation spectrum with respect to the soft-gluon limit is shown in panels (c), (f), and (i).

with and without soft-gluon approximation. R_{AA} is defined as the ratio of the quenched $A + A$ spectrum to the $p + p$ spectrum, scaled by the number of binary collisions N_{bin}:

$$R_{AA}(p_\perp) = \frac{dN_{AA}/dp_\perp}{N_{\text{bin}} dN_{pp}/dp_\perp}. \quad (22)$$

In order to obtain gluon quenched spectra, we use generic pQCD convolution [33]:

$$\frac{E_f d^3\sigma(g)}{dp_f^3} = \frac{E_i d^3\sigma(g)}{dp_i^3} \otimes P(E_i \rightarrow E_f), \quad (23)$$

where $\frac{E_i d^3\sigma(g)}{dp_i^3}$ denotes the initial gluon spectrum, which is computed according to Refs. [34,35], while $P(E_i \rightarrow E_f)$

denotes radiative energy loss probability, which includes multigluon [29] and path-length [33] fluctuations. In accordance with Ref. [29], the multigluon fluctuations are introduced under the assumption that the fluctuations of the gluon number are uncorrelated and therefore presented via Poisson distribution. Specifically, the energy loss probability takes into account that the jet, during its propagation through QGP, can independently radiate the number of gluons (for more details on the implementation procedure, please see Ref. [29]).

Regarding the path-length fluctuations, we take into account that jets can be produced anywhere in the nuclei overlapping area, can go in any direction, and consequently can travel different distances (and can lose different amounts of energy) in QGP. The path length probability is calculated
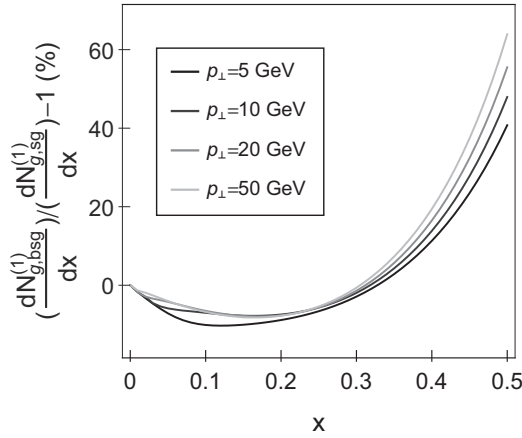
FIG. 3. The effect of relaxing the soft-gluon approximation on $dN_g^{(1)}/dx$ for different $p_\perp$ values. The relative change of the single-gluon radiation spectrum with respect to soft-gluon case, calculated to the first order in opacity of DGLV formalism, for different values of initial $p_\perp$ (as indicated in the legend) is depicted as a function of x. The curves fade as transverse momentum increases.

according to the procedure described in Ref. [19], where one assumes the Glauber model [36] for the collision geometry, with implementation of Woods-Saxon nuclear density [37].

Note that we omitted fragmentation and decay functions, because we are considering the parton's quenching, as we are primarily interested in how the relaxation of the soft-gluon approximation in energy loss affects R_{AA}. Thereupon, we will also investigate how the initial gluon distribution influences R_{AA}.

Therefore, Fig. 4(a) compares R_{AA} predictions with and without soft-gluon approximation accounted for, while the percentage change arising from relaxing the approximation is given by Fig. 4(b) as a function of the final $p_\perp$. We observe that this relaxation barely modifies R_{AA}; in particular, the relative change drops to somewhat less than -1% at $p_\perp \approx 10$ GeV and further rises to the constant value of 2%, with increasing $p_\perp$. This very good agreement (with even

smaller differences compared to previously studied variables) between bsg and sg R_{AA} raises questions of (i) why relaxing the soft-gluon approximation has a negligible effect on R_{AA} and (ii) why the large discrepancy observed in Figs. 2 and 3 for high x values does not lead to a larger difference in R_{AA}.

Regarding question (i) above, we argue that this pattern is expected, as it is well known that in suppression calculations both $\frac{\Delta E^{(1)}}{E}$ and $N_g^{(1)}$ nontrivially affect the R_{AA}. Namely, by comparing Figs. 1(b) and 1(d) with Fig. 4(b), we observe that relaxing the soft-gluon approximation has the opposite effects on $\frac{\Delta E^{(1)}}{E}$ and $N_g^{(1)}$, while their interplay is responsible for the negligible effect on R_{AA}; i.e., the effect on R_{AA} is qualitatively a superposition of the effects on $\frac{\Delta E^{(1)}}{E}$ and $N_g^{(1)}$.

To answer (ii) above, it is convenient to recall that suppression of gluon jet (see Eq. (23)) depends not only on the energy loss probability but also on the initial gluon distribution. In order to intuitively interpret the role of the initial gluon distribution, we refer to the descriptive Fig. 5, which represents its dependence on initial transverse momentum. The concept considered is the following: Some parent gluon with unknown initial momentum traverses QGP, loses its energy by gluon bremsstrahlung, and emerges with final momentum $p_\perp = 30$ GeV. This final gluon can descend from the parent gluon with any $p_\perp$ higher than its own, but we restrict ourselves to five different initial momenta, corresponding to different fractional momentum loss $x \in \{0.1, 0.2, 0.3, 0.4, 0.5\}$. For instance, $x = 0.5$ corresponds to initial gluon momentum of $30/(1 - 0.5)$ GeV $= 60$ GeV, i.e., to the parent gluon that lost half of its momentum. Which of these five gluons is the most likely to be the parent one, and how is this probability correlated with x? From Fig. 5, we infer that, due to the exponentially decreasing initial gluon momentum distribution, the initial gluon corresponding to $x = 0.1$ has the highest probability to be the parent one, and as x increases the probability sharply decreases (i.e., for $x \gtrsim 0.4$ it diminishes for two orders of magnitude compared to the $x = 0.1$ case). Thus, based on initial distribution, the main contribution to the suppression predictions comes from the $x \lesssim 0.4$ region, making this region the most relevant one for differentiating
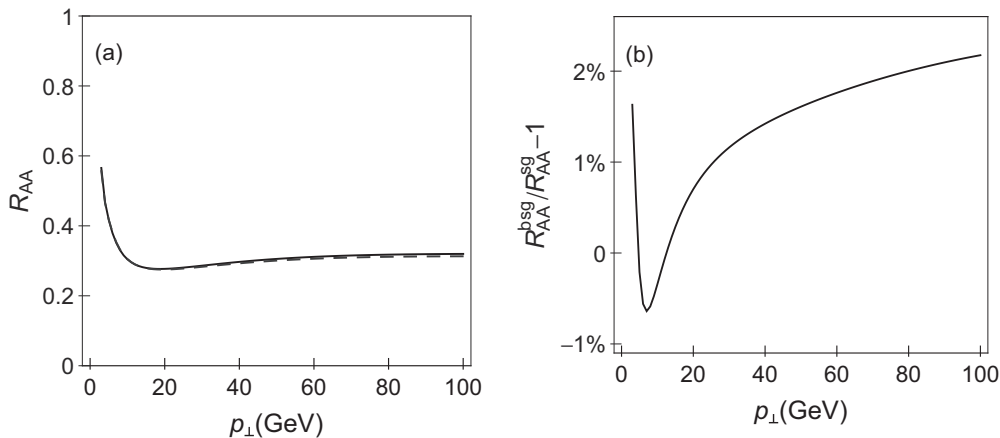

FIG. 4. The effect of relaxing the soft-gluon approximation on gluon nuclear modification factor R_{AA} vs $p_\perp$. (a) The suppression of the gluon jet beyond the soft-gluon approximation (solid curve) is compared to the soft-gluon R_{AA} (dashed curve) as a function of transverse momentum. (b) Quantification of the effect and its expression in percentage.
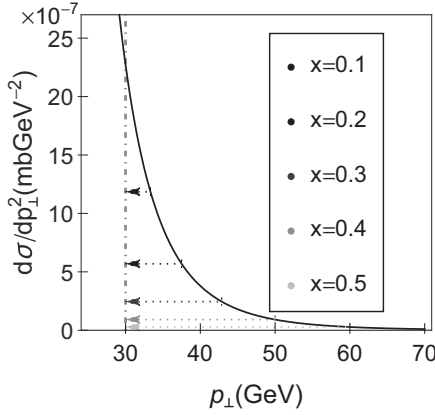
FIG. 5. The role of initial gluon distribution in constraining the relevant x region. The solid black curve represents initial gluon distribution as a function of $p_\perp$ at the LHC [34,35]. The dot-dashed gray line marks the final gluon transverse momentum, while dotted arrows link parent gluons that lost momentum fraction equal to x with their corresponding initial transverse momenta. The arrows fade as x increases, as indicated in the legend.

between bsg and sg R_{AA}. In this region, bsg and sg $\frac{dN_g^{(1)}}{dx}$ (and equivalently $\frac{1}{E}\frac{dE^{(1)}}{dx}$) curves are very similar (according to Figs. 2 and 3), which intuitively explains nearly overlapping R_{AA} in Fig. 4. Also, the relevant x region qualitatively resolves the issue of why the large inconsistency between these curves at higher x does not affect R_{AA}.

Note, however, that we cannot simply reject the $x > 0.4$ region in the suppression calculations, since non-negligible $\frac{dN_g^{(1)}}{dx}$ contribution to R_{AA} (see Figs. 2(b), 2(e), and 2(h)) comes from it. Therefore, for reliable suppression results, one has to take into account the entire x region, while from the above analysis, we claim that only the $x \leqslant 0.4$ region is relevant for studying the importance of the soft-gluon approximation. In order to support this in more rigorous way, we compared suppressions obtained from bsg expression for the entire $x \leqslant 0.5$ region, with results obtained from the bsg expression for $x \leqslant 0.4$ combined with the sg expression for $x > 0.4$. As expected from the discussion presented in the previous paragraph, these two approaches lead to almost the same results (with negligible differences), confirming that the region above $x = 0.4$ is not relevant for the importance of the soft-gluon approximation (data shown in Appendix L for two scenarios).

Additionally, the effect of relaxing the soft-gluon approximation on $\frac{dN_g^{(1)}}{dx}$ and $\frac{1}{E}\frac{dE^{(1)}}{dx}$ is practically insensitive to initial transverse momentum (see Fig. 3), which is the reason why finite x affects equivalently gluon R_{AA} regardless of its transverse momentum, as observed in Fig. 4.

Finally, we also recalculated our finite x results, when running coupling $\alpha_s(Q^2)$, as defined in Refs. [38], instead of constant value $\alpha_s = 0.3$, is introduced in radiative energy loss formula. The obtained predictions lead to the same conclusions as obtained above (and are consequently omitted), which supports the generality of the obtained results.

VII. CONCLUSIONS AND OUTLOOK

The main theoretical goal of this paper was to investigate what effect relaxing the soft-gluon approximation has on radiative energy loss, and consequently on suppression, which depends only on initial distribution and energy loss of high-momentum partons in QGP. In particular, we chose a high $p_\perp$ gluon, as due to the color factor of 9/4 compared to the quarks, this assumption affects gluons the most. To this end, we analytically calculated all Feynman diagrams contributing to the first order in opacity radiative energy loss beyond the soft-gluon approximation, first within GLV [9] (massless case) and later within DGLV [25] (massive case) formalism, and numerically predicted the following: fractional integrated and differential energy loss, number of radiated gluons, single-gluon radiation spectrum, and gluon's suppression. Unexpectedly, we found that although the analytic results significantly differ from the corresponding soft-gluon results, the numerical predictions are nearly indistinguishable, i.e., within a few percent. We then explained that due to exponentially decreasing initial gluon distribution, only the $x \lesssim 0.4$ region effectively contributes to the differences between bsg and sg integrated variable predictions. We also showed that negligible suppression change is due to an interplay between the finite x effects on (i) fractional energy loss and (ii) number of radiated gluons that have opposite sign. The presented comparisons were done under the assumption of fixed strong coupling constant but were also tested with running coupling, leading to the same conclusions. Since we showed that gluon quenching in QCD medium composed of static scattering centers is not affected by the soft-gluon assumption, quark radiative energy loss is even less likely to be notably altered, though this remains to be further tested.

This, to our knowledge, presents the first opportunity to assess the effect of relaxing the soft-gluon approximation on radiative energy loss within DGLV formalism. Some other radiative energy loss formalisms, which also imply static scatterers, generated their results on a finite x. However, contrary to the conclusions derived for these formalisms, where significant difference in the radiative energy loss was obtained, we found that relaxing soft-gluon approximation brings negligible change to the results. Consequently, this implies that, within DGLV formalism, there is no need to go beyond the soft-gluon approximation. Furthermore, we also obtained that the conclusions regarding the importance of the soft-gluon approximation are robust to the presumed longitudinal distance distribution of the scattering centers.

Based on the results of this paper, we also expect that the soft-gluon approximation can be reliably applied to the dynamical energy loss formalism, as implicitly suggested by the previous robust agreement [17,20–22] of our theoretical predictions with a comprehensive set of experimental data. In particular, the effective cross section $v(\mathbf{q})$ (which corresponds to interaction between the jet and exchanged gluon) [39] does not depend on x, so introduction of finite x will not affect this term. We also expect that the rest of the energy loss expression (i.e., $f(\mathbf{k}, \mathbf{q}, x)$, which corresponds to interaction between the jet and radiated gluon [39]) will be modified in a manner similar to the static case, since when $x \to 0$, these

two expressions coincide. However, relaxing the soft-gluon approximation in the dynamical energy loss model is out of the scope of this paper, and this claim still remains to be rigorously tested in the future.

APPENDIX A: NOTATIONS AND USEFUL FORMULAS

In this paper we used the following notation for vectors, in consistency with both Refs. [9,25]:

(1) $\vec{\mathbf{p}}$ denotes momentum 3D vector,
(2) $\mathbf{p}$ denotes transverse momentum 2D vector,
(3) p_z denotes component of momentum vector along the initial jet,
(4) $p = (p^0, p_z, \mathbf{p}) = [p^+, p^-, \mathbf{p}]$ denotes momentum 4D vector in Minkowski and light-cone coordinates, respectively, where $p^+ = p^0 + p_z$ and $p^- = p^0 - p^z$.

For simplicity, we here consider a QCD medium consisting of static partons and model the interactions of the gluon jet with the medium via static color-screened Yukawa potential, whose Fourier and color structure acquires the following form ([9,26]):

$$
\begin{aligned}
V_n &= V(q_n)e^{iq_n x_n} \\
&= 2\pi \delta\!\left(q_n^0\right) v(\vec{\mathbf{q}}_n) e^{-i\vec{\mathbf{q}}_n \cdot \vec{\mathbf{x}}_n} T_{a_n}(R) \otimes T_{a_n}(n),
\end{aligned}
\tag{A1}
$$

$$
v(\vec{\mathbf{q}}_n) = \frac{4\pi \alpha_s}{\vec{\mathbf{q}}_n^2 + \mu^2},
\tag{A2}
$$

where x_n denotes the space-time coordinate of the nth scatterer (target), $T_{a_n}(R)$ and $T_{a_n}(n)$ denote generators in the SU($N_c = 3$) color representation of jet and target, respectively, μ is Debye screening mass, and $\alpha_s = g_s^2/4\pi$ is strong coupling constant. In the following lines, we will briefly display the identities and algebra that SU($N_c = 3$) generators

meet:

$$
\operatorname{Tr}(T^a(n)) = 0,
\tag{A3}
$$

$$
\operatorname{Tr}(T^a(i)T^b(j)) = \delta_{ij}\delta^{ab}\frac{C_2(i)d_i}{d_G},
\tag{A4}
$$

where $d_G = 8$ is the dimension of the adjoint representation (G). We assume that all target partons are in the same d_T-dimensional representation (T) with Casimir operator $C_2(T)$, while the gluon jet is in the adjoint representation (G), with Casimir operator $C_2(G)$.

In SU($N_c = 3$) color algebra, the following identities hold as well,

$$
[T^a, T^b] = if^{abc}T^c,
\tag{A5}
$$

while in the adjoint representation, we have

$$
(T^b)_{ac} = if^{abc},
\tag{A6}
$$

$$
T^a(G)T^a(G) = C_2(G)I,
\tag{A7}
$$

where I denotes identity matrix of dimension d_G and the SU($N_c = 3$) structure constants f^{abc} are completely antisymmetric to indices permutations, which we frequently apply. In the adjoint representation, the following equalities also stand:

$$
C(G) = C_2(G) = N_c = 3,
\tag{A8}
$$

$$
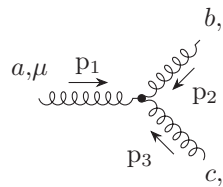\operatorname{Tr}(T^a(G)T^a(G)) = d_G C_2(G).
\tag{A9}
$$

And finally, in our computations we frequently make use of the fact that trace is invariant under cyclic permutations and that generators are Hermitian matrices.

Since our extensive calculations are done in pQCD at finite temperature and include only gluon interactions, below we list the necessary Feynman rules in covariant gauge that we employ:

(1) massless gluon propagator in Feynman gauge; note that all diagrams in this paper are plotted by using [40] the following:

$$
a,\mu \;\xrightarrow{\;\;\text{p}\;\;}\; b,\nu \;=\; \frac{-i\delta_{ab}g_{\mu\nu}}{p^2 + i\epsilon},
\tag{A10}
$$

(2) three-gluon vertex:

$$
= g_s f^{abc}(g^{\mu\rho}(p_1 - p_3)^\nu + g^{\mu\nu}(p_2 - p_1)^\rho + g^{\nu\rho}(p_3 - p_2)^\mu).
\tag{A11}
$$

Since only physical transverse gluon states must be accounted for, the transverse projector in the finite-temperature case reduces to Eq. (57) from [31]

$$
P^{ij} = \sum_{\text{pol}} \epsilon^i(k)\epsilon^j(k) = \delta^{ij} - \frac{k^i k^j}{\vec{\mathbf{k}}^2},
\tag{A12}
$$

where $i, j = 1, 2, 3$ correspond to spacial components of the 4-vector.

APPENDIX B: ASSUMPTIONS

Throughout the paper, we assume that initial gluon jet propagates along the z axis, i.e., has transverse momentum equal to zero, while the radiated gluon carries away a finite

rate x of initial gluon longitudinal momentum and energy, and the final gluon emerges with momentum p. Therefore, instead of assuming soft-gluon approximation ($x \ll 1$), as was done in Refs. [9,25], we allow x to acquire finite nonzero values, thus relaxing the soft-gluon approximation.

Since we are calculating radiative energy loss within the (GLV) DGLV formalism apart from abandoning the soft-gluon approximation, the following assumptions remain:

(1) *The soft-rescattering approximation.* Consistent with Refs. [9,25], we assume that parton's energies and longitudinal momenta are high compare to its transverse momenta, which prevents the radiated and the final gluon from digressing much from the initial longitudinal direction (the eikonal approximation),

$$E^+ \sim (1-x)E^+ \sim xE^+ \gg |\mathbf{p}|, |\mathbf{k}|, |\mathbf{q}_i|. \quad \text{(B1)}$$

(2) *The first-order approximation.* The gluon-jet radiative energy loss is calculated up to the first order in opacity expansion, as argued in Refs. [9,29,30].

(3) *Scattering centers' distribution and ensemble average.* We consider that all scattering centers x_i are distributed with the same transversely homogeneous density:

$$\rho(\vec{\mathbf{x}}) = \frac{N}{A_\perp} \bar{\rho}(z), \quad \text{(B2)}$$

where $\int dz \bar{\rho}(z) = 1$ and also that impact parameter (i.e., relative transverse coordinate) $\mathbf{b} = \mathbf{x}_i - \mathbf{x}_0$ alters within a large transverse area $A_\perp$ compared to the interaction area $\frac{1}{\mu^2}$. Therefore, the ensemble average over the scattering center locations reduces to an impact parameter average:

$$\langle ... \rangle = \int \frac{d^2\mathbf{b}}{A_\perp} ..., \quad \text{(B3)}$$

which in our case is mainly used in the following form:

$$\langle e^{-i(\mathbf{q}_i + \mathbf{q}_j)\cdot\mathbf{b}} \rangle = \frac{(2\pi)^2}{A_\perp} \delta^2(\mathbf{q}_i + \mathbf{q}_j). \quad \text{(B4)}$$

We also assume that the energy of initial hard probe is large compared to the potential screening scale:

$$E^+, (1-x)E^+, xE^+ \gg \mu. \quad \text{(B5)}$$

Next, we assume that the distance between the source J and the scattering centers is large relative to the interaction length,

$$z_i - z_0 \gg \frac{1}{\mu}, \quad \text{(B6)}$$

then, that source current varies slowly with momentum,

$$J(p+k-q) \approx J(p+k), \quad \text{(B7)}$$

and that the source current can be written explicitly in terms of polarization vector,

$$J_a^\mu(p+k-q) \equiv J_a(p+k-q)\epsilon^\mu(p+k-q)$$
$$\approx J_a(p+k)\epsilon^\mu(p+k-q). \quad \text{(B8)}$$

In the following sections, first we assume that gluons are massless (GLV) in order to make the comprehensive derivations more straightforward and easier to follow, but later we recalculate all the results with gluon mass [27] included (DGLV) (Appendix J).

It is worth noting that all diagrams are calculated by taking into account that each gluon can be in either of the two helicity states and that final results are obtained by summing over helicities of final gluons p and k and averaging over helicity of the initial gluon. Note, however, that we obtained that the calculated $\langle |M_0|^2 \rangle$, $\langle |M_1|^2 \rangle$, and $\langle M_2 M_0^* \rangle$ (for variables definition, see the following appendixes) coincide with the corresponding quantities, when helicity (i.e., polarization) is considered unchanged during the process of gluon bremsstrahlung (which was the usual assumption in soft-gluon calculations [9,25]). We will explicitly demonstrate the equality of the results in these two approaches in the case of $\langle |M_0|^2 \rangle$ (see Appendix C), while in the consecutive sections (Appendixes D to J), for simplicity and easier comparison with previous studies, we assume that polarization does not change during the process, though we again note that the same results are obtained when helicity is explicitly accounted for in the calculation.

APPENDIX C: GLUON JET M_0

First, we calculate gluon-jet radiation amplitude to emit a gluon, carrying a finite fraction x of initial jet energy, with momentum, polarization and color (k, $\epsilon(k)$, c) and without interactions with the medium M_0.

We assume that initial gluon ($p + k$) propagates along the z axis. By using M_0 amplitude as an example, we will implement the aforementioned assumptions in order to acquire momentum and polarization expressions. Thus, the initial gluon 4-momentum reads

$$p + k = (p^0 + k^0, p_z + k_z, \mathbf{0}),$$
$$p + k = [E^+, E^-, \mathbf{0}], \quad \text{(C1)}$$

where $E^+ = p^0 + k^0 + p_z + k_z$ and $E^- = p^0 + k^0 - p_z - k_z$.

Assuming massless (real) gluons for simplicity, the momentum vectors of the radiated (k) and the final (p) gluons acquire the following form:

$$k^2 = 0 \Rightarrow k = \left[xE^+, \frac{\mathbf{k}^2}{xE^+}, \mathbf{k} \right], \quad \text{(C2)}$$

$$p^2 = 0 \Rightarrow p = \left[(1-x)E^+, \frac{\mathbf{p}^2}{(1-x)E^+}, \mathbf{p} \right]. \quad \text{(C3)}$$

We also assume that gluons are transversely polarized particles. Although we work in covariant gauge, we can choose any polarization vector for the external on-shell gluons, so in accordance with [9,14,25] we choose $n^\mu = [0, 2, \mathbf{0}]$, as stated above:

$$\epsilon(k) \cdot k = 0, \quad \epsilon(k) \cdot n = 0, \quad \epsilon(k)^2 = -1,$$
$$\epsilon(p) \cdot p = 0, \quad \epsilon(p) \cdot n = 0, \quad \epsilon(p)^2 = -1, \quad \text{(C4)}$$

while we assume that the source has also the physical polarizations as the real gluons [14]:

$$\epsilon(p + k) \cdot (p + k) = 0,$$
$$\epsilon(p + k) \cdot n = 0, \qquad \text{(C5)}$$
$$\epsilon(p + k)^2 = -1.$$

Using Eqs. (C2) to (C5), we can now obtain the following expressions for the gluon polarizations:

$$\epsilon_i^\mu(k) = \left[0, \frac{2\epsilon_i \cdot \boldsymbol{k}}{x E^+}, \boldsymbol{\epsilon}_i \right],$$

$$\epsilon_i^\mu(p) = \left[0, \frac{2\epsilon_i \cdot \boldsymbol{p}}{(1 - x) E^+}, \boldsymbol{\epsilon}_i \right], \qquad \text{(C6)}$$

$$\epsilon_i^\mu(p+k) = [0, 0, \boldsymbol{\epsilon}_i],$$

where $i = 1, 2$ counts for polarization vectors. Note that $\boldsymbol{\epsilon}_1$ and $\boldsymbol{\epsilon}_2$ from Eq. (C6) are orthonormal [41]. Also, the 4-momentum is conserved, which leads to the relation

$$\boldsymbol{p} + \boldsymbol{k} = 0 \qquad \text{(C7)}$$
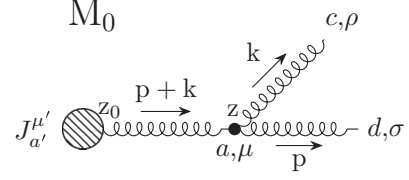
FIG. 6. Zeroth-order diagram that includes no interaction with the QCD medium and contributes to gluon radiation amplitude to the first order in opacity L/λ. The dashed circle represents the source J, which at longitudinal coordinate z_0 produces an off-shell gluon jet, propagating along the z axis. z denotes longitudinal coordinate at which the gluon is radiated. Latin indices denote color charges, while Greek indices denote components of 4-vectors. k denotes 4-momentum of the radiated gluon carrying the color c, and p denotes 4-momentum of the final gluon jet carrying the color d.

that we implement in Eqs. (C3) and (C6) in order to ensure that everything is expressed in terms of $\mathbf{k}$. Also, $E^+ \approx 2E$, $E^- = \frac{\mathbf{k}^2}{x(1-x)E^+}$, where $E = p^0 + k^0$ is the energy of initial jet.

Using the notation from Fig. 6, we obtain

$$M_0 = \epsilon_{\sigma,i}^*(p)\epsilon_{\rho,j}^*(k)g_s f^{acd}[g^{\mu\sigma}(2p+k)^\rho + g^{\mu\rho}(-p-2k)^\sigma + g^{\rho\sigma}(-p+k)^\mu]\frac{-i\delta_{aa'}g_{\mu\mu'}}{(p+k)^2 + i\epsilon}i J_{a'}(p+k)e^{i(p+k)x_0}\epsilon_l^{\mu'}(p+k)$$

$$= J_a(p+k)e^{i(p+k)x_0}g_s \frac{f^{acd}}{(p+k)^2 + i\epsilon}\{[\epsilon_i(p) \cdot \epsilon_l(p+k)][\epsilon_j(k) \cdot (2p+k)]$$

$$+ [\epsilon_j(k) \cdot \epsilon_l(p+k)][\epsilon_i(p) \cdot (-p-2k)] + [\epsilon_i(p) \cdot \epsilon_j(k)][\epsilon_l(p+k) \cdot (-p+k)]\}$$

$$= J_a(p+k)e^{i(p+k)x_0}(ig_s)\frac{(T^c)_{da}}{(p+k)^2 + i\epsilon}\{(-\boldsymbol{\epsilon}_i \cdot \boldsymbol{\epsilon}_l)[\epsilon_j(k) \cdot (2p)] + (-\boldsymbol{\epsilon}_j \cdot \boldsymbol{\epsilon}_l)[\epsilon_i(p) \cdot (-2k)]$$

$$+ (-\boldsymbol{\epsilon}_i \cdot \boldsymbol{\epsilon}_j)[\epsilon_l(p+k) \cdot (-p+k)]\}, \qquad \text{(C8)}$$

where $i, j, l = 1, 2$ now count for helicities, and where we used polarizations given by Eq. (C6). Then, the averaged value of $|M_0|^2$ reads

$$\langle |M_0|^2 \rangle = \frac{1}{2} \sum_{i,j,l=1}^2 J_a(p+k)e^{i(p+k)x_0}(ig_s)J_a^*(p+k)e^{-i(p+k)x_0}(-ig_s)\frac{(T^c)_{da}(T^c)_{ad}}{\mathbf{k}^4}x^2(1-x)^2\left[-\delta_{il}\left(2\frac{\boldsymbol{\epsilon}_j \cdot \boldsymbol{k}}{x}\right)\right.$$

$$\left. - \delta_{jl}\left(2\frac{\boldsymbol{\epsilon}_i \cdot \boldsymbol{k}}{1-x}\right) - \delta_{ij}(-2\boldsymbol{\epsilon}_l \cdot \boldsymbol{k})\right]\left[-\delta_{il}\left(2\frac{\boldsymbol{\epsilon}_j \cdot \boldsymbol{k}}{x}\right) - \delta_{jl}\left(2\frac{\boldsymbol{\epsilon}_i \cdot \boldsymbol{k}}{1-x}\right) - \delta_{ij}(-2\boldsymbol{\epsilon}_l \cdot \boldsymbol{k})\right]$$

$$= \sum \left[J_a(p+k)e^{i(p+k)x_0}(-2ig_s)(1-x+x^2)\frac{\boldsymbol{\epsilon} \cdot \mathbf{k}}{\mathbf{k}^2}(T^c)_{da}\right]\left[J_a^*(p+k)e^{-i(p+k)x_0}(2ig_s)(1-x+x^2)\frac{\boldsymbol{\epsilon} \cdot \mathbf{k}}{\mathbf{k}^2}(T^c)_{ad}\right]$$

$$= |J(p+k)|^2 (4g_s^2)\frac{C_2(G)d_G}{\mathbf{k}^4}(1-x+x^2)^2\sum(\boldsymbol{\epsilon} \cdot \mathbf{k})^2$$

$$= |J(p+k)|^2 (4g_s^2)\frac{C_2(G)d_G}{\mathbf{k}^2}(1-x+x^2)^2, \qquad \text{(C9)}$$

where we used Eqs. (C1)–(C3) and (C6). Note that $\boldsymbol{\epsilon}$ in the third and fourth lines of Eq. (C9) (and in the further text) denotes either of the two vectors $\boldsymbol{\epsilon}_1$ and $\boldsymbol{\epsilon}_2$, and the summation is done over these two orthonormal polarizations (helicity states), where $\sum(\boldsymbol{\epsilon} \cdot \mathbf{k})^2 = \mathbf{k}^2$. Additionally, from the third line of this equation, it is evident that the summation over helicities of the final and radiated gluons, and averaging over helicity of the initial gluon, are equivalent to summation over

two helicity states of $M_0 M_0^*$, when M_0 is expressed in the following simplified form:

$$M_0 = J_a(p+k)e^{i(p+k)x_0}(-2g_s)(1-x+x^2)\frac{\boldsymbol{\epsilon} \cdot \mathbf{k}}{\mathbf{k}^2}f^{acd}$$

$$= J_a(p+k)e^{i(p+k)x_0}(-2ig_s)(1-x+x^2)\frac{\boldsymbol{\epsilon} \cdot \mathbf{k}}{\mathbf{k}^2}(T^c)_{da}, \qquad \text{(C10)}$$
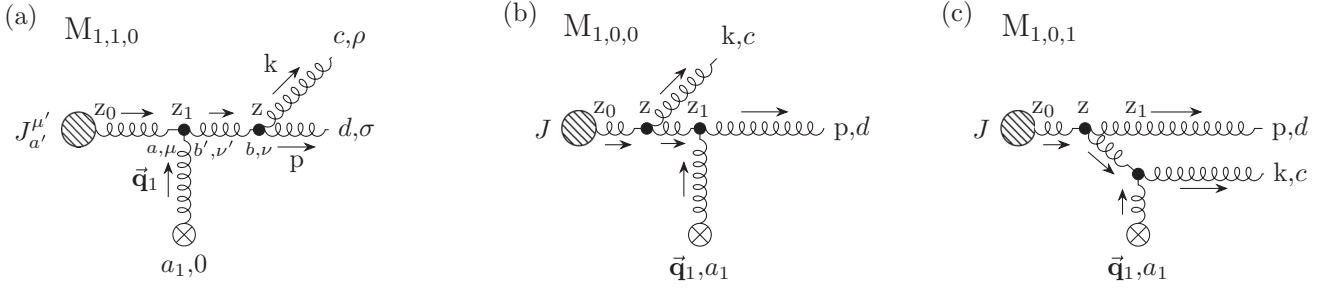
FIG. 7. Three diagrams, corresponding to interaction with one static scattering center, that contribute to gluon-jet radiation amplitude to the first order in opacity L/λ. z_1 denotes longitudinal coordinate of the interactions with one scattering center. Crossed circle represents scatterer that exchanges 3D momentum $\vec{q}_1$ with the jet. Note that all three diagrams assume equivalently ordered Latin and Greek indices as indicated in panel (a). Remaining labeling is the same as in Fig. 6.

which is widely accepted notation used in Refs. [9,25] and which is considered unchanged polarization in the process. After multiplying Eq. (C10) by the complex conjugate value, the summation over two helicity states gives

$$\langle |M_0|^2 \rangle = |J(p+k)|^2 \left(4g_s^2\right) \frac{C_2(G)d_G}{\mathbf{k}^2}(1-x+x^2)^2, \quad \text{(C11)}$$

which is equivalent to Eq. (C9). Thus, as already explained in the last paragraph of Appendix B, in order to make the calculations easier to follow, throughout this paper we adopt this condensed form (such as Eq. (C10)) of expressing the amplitudes, while summation is done in the end (see Eqs. (I3), (I5), (J11), and (J12)).

Next we substitute Eq. (C11) in

$$d^3 N_g^{(0)} d^3 N_J \approx \text{Tr} \langle |M_0|^2 \rangle \frac{d^3\vec{p}}{(2\pi)^3 2p^0} \frac{d^3\vec{k}}{(2\pi)^3 2\omega}. \quad \text{(C12)}$$

Note that, contrary to the soft-gluon approximation [25], where

$$d^3 N_J \approx d_G |J(p+k)|^2 \frac{d^3\vec{p}}{(2\pi)^3 2p^0}, \quad \text{(C13)}$$

now p, denoting the momentum of the final gluon jet, is not approximately equal to the momentum of the initial gluon jet (i.e., the radiated gluon can carry away a substantial amount of the initial jet energy and longitudinal momentum). Thus, instead of Eq. (C13), throughout this paper we use the general one,

$$d^3 N_J = d_G |J(p+k)|^2 \frac{d^3\vec{p}_J}{(2\pi)^3 2E_J}, \quad \text{(C14)}$$

where $E_J = E$ and $\vec{p}_J$ denotes energy and 3D momentum of the initial gluon jet, respectively. Knowing that the substitution of variables $(p_z, k_z \to p_z^J, xE)$ gives

$$\frac{d^3\vec{p}}{(2\pi)^3 2p^0} \frac{d^3\vec{k}}{(2\pi)^3 2\omega} = \frac{d^3\vec{p}_J}{(2\pi)^3 2E_J} \frac{dx d^2\mathbf{k}}{(2\pi)^3 2x(1-x)}, \quad \text{(C15)}$$

and by substituting Eqs. (C11), (C14), and (C15) in Eq. (C12), for radiation spectrum we now obtain

$$\frac{x d^3 N_g^{(0)}}{dx d\mathbf{k}^2} = \frac{\alpha_s}{\pi} \frac{C_2(G)}{\mathbf{k}^2} \frac{(1-x+x^2)^2}{1-x}, \quad \text{(C16)}$$

which recovers the well-known Altarelli-Parisi result [31] and for $x \ll 1$ reduces to the massless soft-gluon limit of Eq. (9) from Ref. [25].

APPENDIX D: DIAGRAMS $M_{1,1,0}$, $M_{1,0,0}$, $M_{1,0,1}$

In this section, we provide detailed calculations of Feynman amplitudes, corresponding to gluon-jet interaction with one scattering center, which are depicted in Fig. 7. Again for consistency, we assume that initial jet $(p + k - q)$ propagates along the z axis. Throughout this section, momentum and polarization vector for initial gluon read as

$$p + k - q_1 = [E^+ - q_{1z}, E^- + q_{1z}, \mathbf{0}], \quad \text{(D1)}$$

$$\epsilon_i(p + k - q_1) = [0, 0, \boldsymbol{\epsilon}_i], \quad \text{(D2)}$$

where $q_1 = [q_{1z}, -q_{1z}, \mathbf{q}_1]$, with $q_1^0 = 0$, denotes the momentum of exchanged gluon, while p, k, and corresponding polarization vectors retain the same expression as in Eqs. (C2), (C3), and (C6), with the distinction that the following relation between gluon transverse momenta, due to 4-momentum conservation, holds:

$$\mathbf{q}_1 = \mathbf{p} + \mathbf{k}. \quad \text{(D3)}$$

1. Computation of $M_{1,1,0}$ diagram

We chose to start with thorough derivation of the expression for $M_{1,1,0}$ amplitude, simply because it has no counterpart regarding the symmetry under $(p \leftrightarrow k, x \leftrightarrow (1-x), c \leftrightarrow d)$ substitutions, and it provides all necessary steps for calculating the remaining two amplitudes from this chapter, apart from having one less singularity compared to the amplitudes $M_{1,0,0}$ and $M_{1,0,1}$. Thus, using the notation from Fig. 7(a),

we write

$$
M_{1,1,0} = \int \frac{d^4 q_1}{(2\pi)^4} \epsilon_\sigma^*(p) \epsilon_\rho^*(k) g_s f^{bcd} [g^{\nu\sigma}(2p+k)^\rho + g^{\nu\rho}(-p-2k)^\sigma + g^{\rho\sigma}(-p+k)^\nu] \frac{(-i)\delta_{bb'} g_{\nu\nu'}}{(p+k)^2 + i\epsilon}
$$

$$
\times f^{ab'a_1} [g^{\mu 0}(p+k-2q_1)^{\nu'} + g^{\mu\nu'}(-2p-2k+q_1)^0 + g^{\nu'0}(p+k+q_1)^\mu] T_{a_1} V(q_1) e^{iq_1 x_1}
$$

$$
\times \frac{(-i)\delta_{aa'} g_{\mu\mu'}}{(p+k-q_1)^2 + i\epsilon} i J_{a'}(p+k-q_1) \epsilon^{\mu'}(p+k-q_1) e^{i(p+k-q_1)x_0}
$$

$$
\approx J_a(p+k) e^{i(p+k)x_0} f^{bcd} f^{a_1 ab} T_{a_1} (-i)(1-x+x^2) \int \frac{d^2 q_1}{(2\pi)^2} e^{-iq_1 \cdot (x_1 - x_0)} (2g_s) \frac{(1-x)\boldsymbol{\epsilon} \cdot \mathbf{k} - x \boldsymbol{\epsilon} \cdot \mathbf{p}}{x(1-x)}
$$

$$
\times E^+ \int \frac{dq_{1z}}{2\pi} \frac{v(q_{1z}, \mathbf{q}_1) e^{-iq_{1z}(z_1 - z_0)}}{[(p+k-q_1)^2 + i\epsilon][(p+k)^2 + i\epsilon]},
\tag{D4}
$$

where we used the equation

$$
(p+k)^2 = \frac{[(1-x)\mathbf{k} - x\mathbf{p}]^2}{x(1-x)}
\tag{D5}
$$

and assumed that J varies slowly with momentum q_1, i.e., Eq. (B7). The longitudinal momentum transfer integral

$$
I_1(p, k, \mathbf{q}_1, z_1 - z_0) \equiv \int \frac{dq_{1z}}{2\pi} \frac{v(q_{1z}, \mathbf{q}_1) e^{-iq_{1z}(z_1 - z_0)}}{(p+k-q_1)^2 + i\epsilon}
\tag{D6}
$$

has to be performed in the lower half-plane of the complex plane, since $z_1 > z_0$. In order to determine the pole arising from potential, we rewrite Eq. (A2) in a more appropriate form:

$$
v(\vec{\mathbf{q}}_n) = \frac{4\pi \alpha_s}{(q_{nz} + i\mu_{n\perp})(q_{nz} - i\mu_{n\perp})},
\tag{D7}
$$

where $\mu_{n\perp}^2 = \mu^2 + \mathbf{q}_n^2$, with n denoting the corresponding scattering center.

Aside from the pole originating from Eq. (D7) ($q_{1z} = -i\mu_{1\perp}$), there is also a singularity emerging from the gluon propagator:

$$
\bar{q}_1 = -\frac{\mathbf{k}^2}{xE^+} - \frac{\mathbf{p}^2}{(1-x)E^+} - i\epsilon = -\frac{\mathbf{k}^2}{2\omega} - \frac{x}{1-x} \frac{(\mathbf{k} - \mathbf{q}_1)^2}{2\omega} - i\epsilon,
\tag{D8}
$$

where $\omega = k_0 \approx \frac{xE^+}{2}$. The residue around the pole at $\bar{q}_1$ is computed as (the negative sign is due to the clockwise orientation of the closed contour in the complex plain)

$$
\mathrm{Res}(\bar{q}_1) \approx -v\left(-\frac{\mathbf{k}^2}{xE^+} - \frac{\mathbf{p}^2}{(1-x)E^+}, \mathbf{q}_1\right) \frac{i}{E^+} e^{i[\frac{\mathbf{k}^2}{xE^+} + \frac{\mathbf{p}^2}{(1-x)E^+}](z_1 - z_0)}
$$

$$
= -v\left(-\frac{\mathbf{k}^2}{2\omega} - \frac{x}{1-x} \frac{(\mathbf{k} - \mathbf{q}_1)^2}{2\omega}, \mathbf{q}_1\right) \frac{i}{E^+} e^{\frac{i}{2\omega}[\mathbf{k}^2 + \frac{x}{1-x}(\mathbf{k} - \mathbf{q}_1)^2](z_1 - z_0)}.
\tag{D9}
$$

The pole originating from the potential ($q_{1z} = -i\mu_{1\perp}$) does not contribute to the longitudinal integral, since the residue around that pole is exponentially suppressed due to Eq. (B6), i.e., $\mu(z_1 - z_0) \gg 1$ (and $\mu \sim \mu_{1\perp}$),

$$
\mathrm{Res}(-i\mu_{1\perp}) \approx -i\frac{4\pi\alpha_s}{(-2i\mu_{1\perp})E^+(-i\mu_{1\perp})} e^{-\mu_{1\perp}(z_1 - z_0)} \to 0,
\tag{D10}
$$

where we assumed that $E^+ \gg \mu$ and the soft-rescattering approximation.

This makes only $\bar{q}_1$ singularity relevant for calculating longitudinal integral. Therefore, I_1 coincides with Eq. (D9), i.e.,

$$
I_1(p, k, \mathbf{q}_1, z_1 - z_0) \approx -v\left(-\frac{\mathbf{k}^2}{xE^+} - \frac{\mathbf{p}^2}{(1-x)E^+}, \mathbf{q}_1\right) \frac{i}{E^+} e^{i[\frac{\mathbf{k}^2}{xE^+} + \frac{\mathbf{p}^2}{(1-x)E^+}](z_1 - z_0)}
$$

$$
\approx -v(0, \mathbf{q}_1) \frac{i}{E^+} e^{i[\frac{\mathbf{k}^2}{xE^+} + \frac{\mathbf{p}^2}{(1-x)E^+}](z_1 - z_0)} = -v(0, \mathbf{q}_1) \frac{i}{E^+} e^{\frac{i}{2\omega}[\mathbf{k}^2 + \frac{x}{1-x}(\mathbf{k} - \mathbf{q}_1)^2](z_1 - z_0)},
\tag{D11}
$$

where we used eikonal approximation (i.e., for a finite x, $\frac{\mathbf{k}^2}{(xE^+)^2} \ll 1$ and $\frac{\mathbf{p}^2}{((1-x)E^+)^2} \ll 1$). Finally, $M_{1,1,0}$ amplitude reads

$$
M_{1,1,0} = J_a(p+k) e^{i(p+k)x_0} (-i)(1-x+x^2) f^{bcd} f^{a_1 ab} T_{a_1} \int \frac{d^2 q_1}{(2\pi)^2} v(0, \mathbf{q}_1) e^{-iq_1 \cdot \mathbf{b}_1} (-2ig_s) \frac{\boldsymbol{\epsilon} \cdot [(1-x)\mathbf{k} - x\mathbf{p}]}{[(1-x)\mathbf{k} - x\mathbf{p}]^2} e^{i[\frac{\mathbf{k}^2}{xE^+} + \frac{\mathbf{p}^2}{(1-x)E^+}](z_1 - z_0)}
$$

$$
= J_a(p+k) e^{i(p+k)x_0} (-i)(1-x+x^2)(T^c T^{a_1})_{da} T_{a_1} \int \frac{d^2 q_1}{(2\pi)^2} v(0, \mathbf{q}_1) e^{-iq_1 \cdot \mathbf{b}_1} (-2ig_s) \frac{\boldsymbol{\epsilon} \cdot (\mathbf{k} - x\mathbf{q}_1)}{(\mathbf{k} - x\mathbf{q}_1)^2} e^{\frac{i}{2\omega}[\mathbf{k}^2 + \frac{x}{1-x}(\mathbf{k} - \mathbf{q}_1)^2](z_1 - z_0)},
$$

$$
\tag{D12}
$$

where we denoted $\mathbf{b}_1 \equiv \mathbf{x}_1 - \mathbf{x}_0$. In this subsection, we constantly make use of Eq. (D3) in the following form,

$$\mathbf{p}^2 = (\mathbf{k} - \mathbf{q}_1)^2, \tag{D13}$$

and also manipulate with $SU(N_c = 3)$ structure constants by using Eqs. (A5) and (A6). Note from Fig. 7(a) that, as expected, $M_{1,1,0}$ is symmetric under the substitutions $(p \leftrightarrow k, x \leftrightarrow (1 - x), c \leftrightarrow d)$, where the symmetry can be straightforwardly verified by implementing these substitutions in the first two lines of Eq. (D12).

2. Computation of $M_{1,0,0}$ and $M_{1,0,1}$ diagrams

Applying the same procedure as in the previous subsection, we proceed with calculating $M_{1,0,0}$. Note that the order of the color and Dirac indices denoting vertices is the same for all three diagrams in Fig. 7 and are therefore omitted in Figs. 7(b) and 7(c):

$$
M_{1,0,0} = \int \frac{d^4 q_1}{(2\pi)^4} \epsilon_\sigma^*(p) f^{bda_1} [g^{\nu 0}(p - 2q_1)^\sigma + g^{\nu\sigma}(-2p + q_1)^0 + g^{\sigma 0}(p + q_1)^\nu] T_{a_1} V(q_1) e^{iq_1 x_1} \frac{(-i)\delta_{bb'} g_{\nu\nu'}}{(p - q_1)^2 + i\epsilon}
$$

$$
\times \, g_s f^{acb'} [g^{\mu\nu'}(2p + k - 2q_1)^\rho + g^{\mu\rho}(-p - 2k + q_1)^{\nu'} + g^{\rho\nu'}(-p + k + q_1)^\mu] \epsilon_\rho^*(k) \frac{(-i)\delta_{aa'} g_{\mu\mu'}}{(p + k - q_1)^2 + i\epsilon}
$$

$$
\times \, i J_{a'}(p + k - q_1) \epsilon^{\mu'}(p + k - q_1) e^{i(p+k-q_1)x_0}
$$

$$
\approx J_a(p + k) e^{i(p+k)x_0} f^{bda_1} f^{acb} T_{a_1} (-i)(1 - x + x^2) E^+ \int \frac{d^2 \mathbf{q}_1}{(2\pi)^2} e^{-i\mathbf{q}_1 \cdot \mathbf{b}_1} (2g_s) \frac{\boldsymbol{\epsilon} \cdot \mathbf{k}}{x} I_2, \tag{D14}
$$

where

$$
I_2(p, k, \mathbf{q}_1, z_1 - z_0) \equiv \int \frac{dq_{1z}}{2\pi} \frac{v(q_{1z}, \mathbf{q}_1) e^{-iq_{1z}(z_1 - z_0)}}{(p + k - q_1)^2 + i\epsilon} \frac{1}{(p - q_1)^2 + i\epsilon}. \tag{D15}
$$

In order to calculate the previous integral, due to $z_1 > z_0$ we again have to close the contour below the real axis. As in the $M_{1,1,0}$ amplitude, again only the poles originating from the propagators contribute to the integral: $(-\frac{\mathbf{k}^2}{xE^+} - \frac{\mathbf{p}^2}{(1-x)E^+} - i\epsilon)$ and $(\frac{\mathbf{k}^2 - \mathbf{p}^2}{(1-x)E^+} - i\epsilon)$, while $(-i\mu_{1\perp})$ is exponentially suppressed (due to $\mu(z_1 - z_0) \gg 1$). Therefore, we obtain

$$
I_2(p, k, \mathbf{q}_1, z_1 - z_0) \approx \frac{ix}{E^+ \mathbf{k}^2} v(0, \mathbf{q}_1) \left[e^{i(\frac{\mathbf{k}^2}{xE^+} + \frac{\mathbf{p}^2}{(1-x)E^+})(z_1 - z_0)} - e^{i\frac{(\mathbf{p}^2 - \mathbf{k}^2)}{(1-x)E^+}(z_1 - z_0)} \right]
$$

$$
\approx \frac{ix}{E^+ \mathbf{k}^2} v(0, \mathbf{q}_1) \left[e^{\frac{i}{2\omega}(\mathbf{k}^2 + \frac{x}{1-x}(\mathbf{k} - \mathbf{q}_1)^2)(z_1 - z_0)} - e^{\frac{i}{2\omega}\frac{x}{1-x}[(\mathbf{k} - \mathbf{q}_1)^2 - \mathbf{k}^2](z_1 - z_0)} \right], \tag{D16}
$$

leading to

$$
M_{1,0,0} = J_a(p + k) e^{i(p+k)x_0} (-i)(1 - x + x^2) f^{bda_1} f^{acb} T_{a_1} \int \frac{d^2 \mathbf{q}_1}{(2\pi)^2} v(0, \mathbf{q}_1) e^{-i\mathbf{q}_1 \cdot \mathbf{b}_1} (2ig_s) \frac{\boldsymbol{\epsilon} \cdot \mathbf{k}}{\mathbf{k}^2}
$$

$$
\times \left\{ e^{i[\frac{\mathbf{k}^2}{xE^+} + \frac{\mathbf{p}^2}{(1-x)E^+}](z_1 - z_0)} - e^{i\frac{(\mathbf{p}^2 - \mathbf{k}^2)}{(1-x)E^+}(z_1 - z_0)} \right\}
$$

$$
= J_a(p + k) e^{i(p+k)x_0} (-i)(1 - x + x^2) (T^{a_1} T^c)_{da} T_{a_1} \int \frac{d^2 \mathbf{q}_1}{(2\pi)^2} v(0, \mathbf{q}_1) e^{-i\mathbf{q}_1 \cdot \mathbf{b}_1} (2ig_s) \frac{\boldsymbol{\epsilon} \cdot \mathbf{k}}{\mathbf{k}^2}
$$

$$
\times \left\{ e^{\frac{i}{2\omega}[\mathbf{k}^2 + \frac{x}{1-x}(\mathbf{k} - \mathbf{q}_1)^2](z_1 - z_0)} - e^{-\frac{i}{2\omega}\frac{x}{1-x}[\mathbf{k}^2 - (\mathbf{k} - \mathbf{q}_1)^2](z_1 - z_0)} \right\}. \tag{D17}
$$

By applying a similar procedure for $M_{1,0,1}$, we obtain

$$
M_{1,0,1} = J_a(p + k) e^{i(p+k)x_0} (-i)(1 - x + x^2) f^{bca_1} f^{adb} T_{a_1} \int \frac{d^2 \mathbf{q}_1}{(2\pi)^2} v(0, \mathbf{q}_1) e^{-i\mathbf{q}_1 \cdot \mathbf{b}_1} (2ig_s) \frac{\boldsymbol{\epsilon} \cdot \mathbf{p}}{\mathbf{p}^2}
$$

$$
\times \left\{ e^{i[\frac{\mathbf{k}^2}{xE^+} + \frac{\mathbf{p}^2}{(1-x)E^+}](z_1 - z_0)} - e^{i\frac{(\mathbf{k}^2 - \mathbf{p}^2)}{xE^+}(z_1 - z_0)} \right\}
$$

$$
= J_a(p + k) e^{i(p+k)x_0} (-i)(1 - x + x^2) [T^c, T^{a_1}]_{da} T_{a_1} \int \frac{d^2 \mathbf{q}_1}{(2\pi)^2} v(0, \mathbf{q}_1) e^{-i\mathbf{q}_1 \cdot \mathbf{b}_1} (2ig_s) \frac{\boldsymbol{\epsilon} \cdot (\mathbf{k} - \mathbf{q}_1)}{(\mathbf{k} - \mathbf{q}_1)^2}
$$

$$
\times \left\{ e^{\frac{i}{2\omega}[\mathbf{k}^2 + \frac{x}{1-x}(\mathbf{k} - \mathbf{q}_1)^2](z_1 - z_0)} - e^{\frac{i}{2\omega}[\mathbf{k}^2 - (\mathbf{k} - \mathbf{q}_1)^2](z_1 - z_0)} \right\}. \tag{D18}
$$

Notice from Figs. 7(b) and 7(c) that $M_{1,0,1}$ and $M_{1,0,0}$ are symmetric under the following substitutions: $(p \leftrightarrow k, x \leftrightarrow (1 - x), c \leftrightarrow d)$; it can be straightforwardly verified that Eqs. (D17) and (D18) are symmetric under these substitutions.
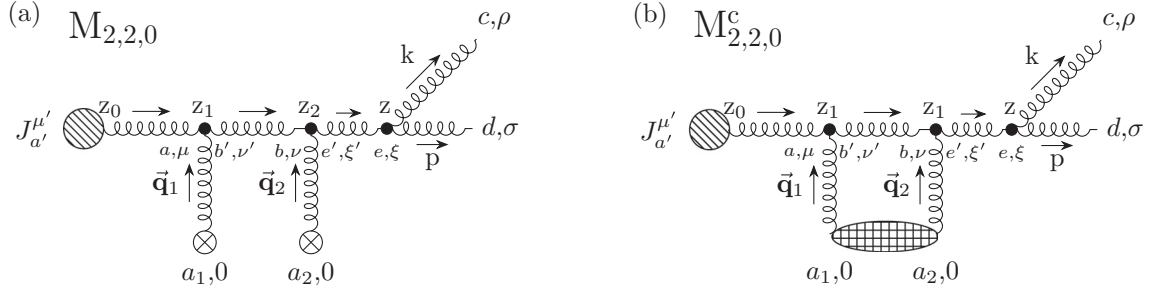
FIG. 8. (a) Feynman diagram $M_{2,2,0}$ and its contribution to the first order in opacity gluon-jet radiative energy loss: (b) contact-limit $M_{2,2,0}^c$. z_i, where $i = 1, 2$, denotes longitudinal coordinate of the interactions with the consecutive scattering centers (or in the contact limit $z_1 = z_2$). Crossed circles represent scatterers that exchange 3D momentum $\vec{q}_i$ with the jet, which in the contact-limit case merge into one gridded ellipse. Note that all the following figures assume equivalently ordered Latin and Greek indices as in this figure. Remaining labeling is the same as in Figs. 6 and 7.

APPENDIX E: DIAGRAM $M_{2,2,0}$

Next, we concentrate on the diagrams containing two interactions with the static scattering centers, since they also contribute to the gluon radiative energy loss to the first order in opacity, when multiplied by M_0^*. There are seven such diagrams that we gather into four groups, each of which contains two (or one) diagrams symmetric under $(p \leftrightarrow k, x \leftrightarrow (1-x), c \leftrightarrow d)$ substitutions.

For consistency, the initial gluon jet (with momentum $p + k - q_1 - q_2$) propagates along the z axis, i.e.,

$$p + k - q_1 - q_2 = [E^+ - q_{1z} - q_{2z}, E^- + q_{1z} + q_{2z}, \mathbf{0}], \tag{E1}$$

$$\epsilon_i(p + k - q_1 - q_2) = [0, 0, \boldsymbol{\epsilon}_i], \tag{E2}$$

where $q_i = [q_{iz}, -q_{iz}, \mathbf{q}_i]$, $i = 1, 2$ with $q_i^0 = 0$ denote momenta of exchanged gluons, while p, k, and corresponding polarizations retain the same expressions as in Eqs. (C2), (C3), and (C6), with the distinction that, due to 4-momentum conservation, the following relation between gluon transverse momenta holds:

$$\mathbf{p} + \mathbf{k} = \mathbf{q}_1 + \mathbf{q}_2. \tag{E3}$$

Again, from seven diagrams, we chose one model diagram $M_{2,2,0}$, based on the same reason as in Appendix D, for thorough derivation of the final amplitude expression. From Fig. 8, where the gluon jet after two consecutive interactions with scattering centers radiates a gluon with momentum k, we observe that there are two limiting cases that we consider.

Using the notation from Fig. 8, we write

$$M_{2,2,0} = \int \frac{d^4q_1}{(2\pi)^4} \frac{d^4q_2}{(2\pi)^4} \epsilon_\sigma^*(p)\epsilon_\rho^*(k)g_s f^{ecd}[g^{\xi\sigma}(2p+k)^\rho + g^{\xi\rho}(-p-2k)^\sigma + g^{\rho\sigma}(-p+k)^\xi]\frac{-i\delta_{ee'}g_{\xi\xi'}}{(p+k)^2+i\epsilon}$$

$$\times f^{be'a_2}[g^{\nu 0}(p+k-2q_2)^{\xi'} + g^{\nu\xi'}(-2p-2k+q_2)^0 + g^{\xi'0}(p+k+q_2)^\nu]T_{a_2}V(q_2)e^{iq_2x_2}\frac{-i\delta_{bb'}g_{\nu\nu'}}{(p+k-q_2)^2+i\epsilon}$$

$$\times f^{ab'a_1}[g^{\mu 0}(p+k-2q_1-q_2)^{\nu'} + g^{\mu\nu'}(-2p-2k+q_1+2q_2)^0 + g^{\nu'0}(p+k+q_1-q_2)^\mu]T_{a_1}V(q_1)e^{iq_1x_1}$$

$$\times \frac{-i\delta_{aa'}g_{\mu\mu'}}{(p+k-q_1-q_2)^2+i\epsilon}iJ_{a'}(p+k-q_1-q_2)\epsilon^{\mu'}(p+k-q_1-q_2)e^{i(p+k-q_1-q_2)x_0}$$

$$\approx iJ_a(p+k)e^{i(p+k)x_0}f^{ecd}f^{bea_2}f^{aba_1}T_{a_2}T_{a_1}(1-x+x^2)(-i)\int\frac{d^2\mathbf{q}_1}{(2\pi)^2}(-i)\int\frac{d^2\mathbf{q}_2}{(2\pi)^2}(2ig_s)\frac{\boldsymbol{\epsilon}\cdot((1-x)\mathbf{k}-x\mathbf{p})}{[(1-x)\mathbf{k}-x\mathbf{p}]^2}$$

$$\times e^{-i\mathbf{q}_1\cdot\mathbf{b}_1}e^{-i\mathbf{q}_2\cdot\mathbf{b}_2}(E^+)^2\int\frac{dq_{1z}}{2\pi}\frac{dq_{2z}}{2\pi}\frac{v(q_{1z},\mathbf{q}_1)v(q_{2z},\mathbf{q}_2)e^{-iq_{1z}(z_1-z_0)}e^{-iq_{2z}(z_2-z_0)}}{[(p+k-q_1-q_2)^2+i\epsilon][(p+k-q_2)^2+i\epsilon]}, \tag{E4}$$

where $\mathbf{b}_i \equiv \mathbf{x}_i - \mathbf{x}_0$, $i = 1, 2$, denote transverse impact parameters. We used Eq. (D5) and assumed that J varies slowly with momentum q_i, i.e., $J(p+k-q_1-q_2) \approx J(p+k)$.

Regarding the longitudinal q_{1z} integral, we introduce a new variable, $q_z = q_{1z} + q_{2z}$ throughout this and the following sections involving Feynman amplitudes which include interactions with two scattering centers. Therefore, we rewrite the exponent in the following manner: $e^{-iq_{1z}(z_1-z_0)}e^{-iq_{2z}(z_2-z_0)} = e^{-iq_z(z_1-z_0)}e^{-iq_{2z}(z_2-z_1)}$. By rewriting q_{1z} longitudinal integral in terms of q_z, i.e.,

changing the variables, we obtain

$$I_2(p, k, \mathbf{q}_1, \vec{\mathbf{q}}_2, z_1 - z_0) = \int \frac{dq_z}{2\pi} \frac{v(q_z - q_{2z}, \mathbf{q}_1)e^{-iq_z(z_1 - z_0)}}{(p + k - q_1 - q_2)^2 + i\epsilon}. \tag{E5}$$

Again, due to $z_1 > z_0$, the contour must be closed in the lower half-plane of complex q_z plane, so an additional minus sign arises from the negative orientation of the contour and also we neglect the pole at $q_z = -i\mu_{1\perp} + q_{2z}$, since it is exponentially suppressed due to Eq. (B6). Thus, only one pole, originating from the gluon propagator, contributes to the first longitudinal integral:

$$\bar{q} = -\frac{\mathbf{k}^2}{xE^+} - \frac{\mathbf{p}^2}{(1-x)E^+} - i\epsilon = -\frac{\mathbf{k}^2}{2\omega} - \frac{x}{1-x}\frac{(\mathbf{k} - \mathbf{q}_1 - \mathbf{q}_2)^2}{2\omega} - i\epsilon, \tag{E6}$$

where we used throughout Appendixes F–H the relation between transverse momenta Eq. (E3). The residue at Eq. (E6) then gives

$$I_2(p, k, \mathbf{q}_1, \vec{\mathbf{q}}_2, z_1 - z_0) \approx -v\left(-q_{2z} - \frac{\mathbf{k}^2}{2\omega} - \frac{x}{1-x}\frac{(\mathbf{k} - \mathbf{q}_1 - \mathbf{q}_2)^2}{2\omega}, \mathbf{q}_1\right)\frac{i}{E^+}e^{\frac{i}{2\omega}[\mathbf{k}^2 + \frac{x}{1-x}(\mathbf{k} - \mathbf{q}_1 - \mathbf{q}_2)^2](z_1 - z_0)}. \tag{E7}$$

Next we need to solve the remaining q_{2z} longitudinal momentum transfer integral:

$$I_3(p, k, \mathbf{q}_1, \mathbf{q}_2, z_2 - z_1) = \int \frac{dq_{2z}}{2\pi} \frac{v(q_{2z}, \mathbf{q}_2)e^{-iq_{2z}(z_2 - z_1)}}{(p + k - q_2)^2 + i\epsilon}v\left(-q_{2z} - \frac{\mathbf{k}^2}{2\omega} - \frac{x}{1-x}\frac{(\mathbf{k} - \mathbf{q}_1 - \mathbf{q}_2)^2}{2\omega}, \mathbf{q}_1\right). \tag{E8}$$

Luckily, we are interested only in two limiting cases:

(1) the limit of well-separated scattering centers $z_2 - z_1 \gg 1/\mu$, where poles originating from Yukawa potentials are exponentially suppressed,
(2) the contact limit $z_1 = z_2$, where these poles contribute to the final results.

In the case of two distinct scatterers ($z_1 \neq z_2$) and in the limit of well-separated scattering centers there is only one pole that contributes to the residue (the singularities originating from Yukawa potential once again are exponentially suppressed):

$$\bar{q}_{2z} = -\frac{\mathbf{k}^2}{xE^+} - \frac{\mathbf{p}^2}{(1-x)E^+} + \frac{\mathbf{q}_1^2}{E^+} - i\epsilon = -\frac{\mathbf{k}^2}{2\omega} - \frac{x}{1-x}\frac{(\mathbf{k} - \mathbf{q}_1 - \mathbf{q}_2)^2}{2\omega} + \frac{\mathbf{q}_1^2}{E^+} - i\epsilon. \tag{E9}$$

Since $z_2 > z_1$, again we close the contour below the real q_{2z} axis and thus obtain

$$I_3(p, k, \mathbf{q}_1, \mathbf{q}_2, z_2 - z_1) \approx -v(0, \mathbf{q}_1)v(0, \mathbf{q}_2)\frac{i}{E^+}e^{\frac{i}{2\omega}[\mathbf{k}^2 + \frac{x}{1-x}(\mathbf{k} - \mathbf{q}_1 - \mathbf{q}_2)^2 - x\mathbf{q}_1^2](z_2 - z_1)}. \tag{E10}$$

In the special case of contact limit, i.e., when $z_1 = z_2$, instead of Eq. (E8), we need to calculate the following q_{2z} integral:

$$I_3^c(p, k, \mathbf{q}_1, \mathbf{q}_2, 0) = \int \frac{dq_{2z}}{2\pi} \frac{v(q_{2z}, \mathbf{q}_2)}{(p + k - q_2)^2 + i\epsilon}v\left(-q_{2z} - \frac{\mathbf{k}^2}{2\omega} - \frac{x}{1-x}\frac{(\mathbf{k} - \mathbf{q}_1 - \mathbf{q}_2)^2}{2\omega}, \mathbf{q}_1\right). \tag{E11}$$

Now, the contributions from Yukawa singularities ($q_{2z} = -i\mu_{1\perp}$, $q_{2z} = -i\mu_{2\perp}$) are not negligible and need to be included together with Eq. (E9). By choosing the same integration contour, we obtain

$$I_3^c(p, k, \mathbf{q}_1, \mathbf{q}_2, 0) \approx \frac{-i}{E^+}\left[v(0, \mathbf{q}_1)v(0, \mathbf{q}_2) - \frac{(4\pi\alpha_s)^2}{2}\frac{1}{\mu_{2\perp}^2 - \mu_{1\perp}^2}\left(\frac{1}{\mu_{1\perp}^2} - \frac{1}{\mu_{2\perp}^2}\right)\right] = -v(0, \mathbf{q}_1)v(0, \mathbf{q}_2)\frac{i}{2E^+}, \tag{E12}$$

which is exactly $\frac{1}{2}$ of the strength of Eq. (E10). Note that in previous calculations we applied soft-rescattering approximation and also assumed $E^+ \gg \mu_{i\perp}$, $i = 1, 2$.

Finally, the contact limit of this amplitude reads

$$M_{2,2,0}^c = -iJ_a(p + k)e^{i(p+k)x_0} f^{ecd} f^{bea_2} f^{aba_1} T_{a_2} T_{a_1}(1 - x + x^2)(-i)\int \frac{d^2\mathbf{q}_1}{(2\pi)^2}(-i)\int \frac{d^2\mathbf{q}_2}{(2\pi)^2}v(0, \mathbf{q}_1)v(0, \mathbf{q}_2)e^{-i(\mathbf{q}_1 + \mathbf{q}_2)\cdot\mathbf{b}_1}$$

$$\times \frac{1}{2}(2ig_s)\frac{\boldsymbol{\epsilon} \cdot [(1 - x)\mathbf{k} - x\mathbf{p}]}{[(1 - x)\mathbf{k} - x\mathbf{p}]^2}e^{i[\frac{\mathbf{k}^2}{xE^+} + \frac{\mathbf{p}^2}{(1-x)E^+}](z_1 - z_0)}$$

$$= -J_a(p + k)e^{i(p+k)x_0}(T^c T^{a_2} T^{a_1})_{da} T_{a_2} T_{a_1}(1 - x + x^2)(-i)\int \frac{d^2\mathbf{q}_1}{(2\pi)^2}(-i)\int \frac{d^2\mathbf{q}_2}{(2\pi)^2}v(0, \mathbf{q}_1)v(0, \mathbf{q}_2)e^{-i(\mathbf{q}_1 + \mathbf{q}_2)\cdot\mathbf{b}_1}$$

$$\times \frac{1}{2}(2ig_s)\frac{\boldsymbol{\epsilon} \cdot [\mathbf{k} - x(\mathbf{q}_1 + \mathbf{q}_2)]}{[\mathbf{k} - x(\mathbf{q}_1 + \mathbf{q}_2)]^2}e^{\frac{i}{2\omega}[\mathbf{k}^2 + \frac{x}{1-x}(\mathbf{k} - \mathbf{q}_1 - \mathbf{q}_2)^2](z_1 - z_0)}, \tag{E13}$$

(a) $M_{2,0,3}$

(b) $M^c_{2,0,3}$
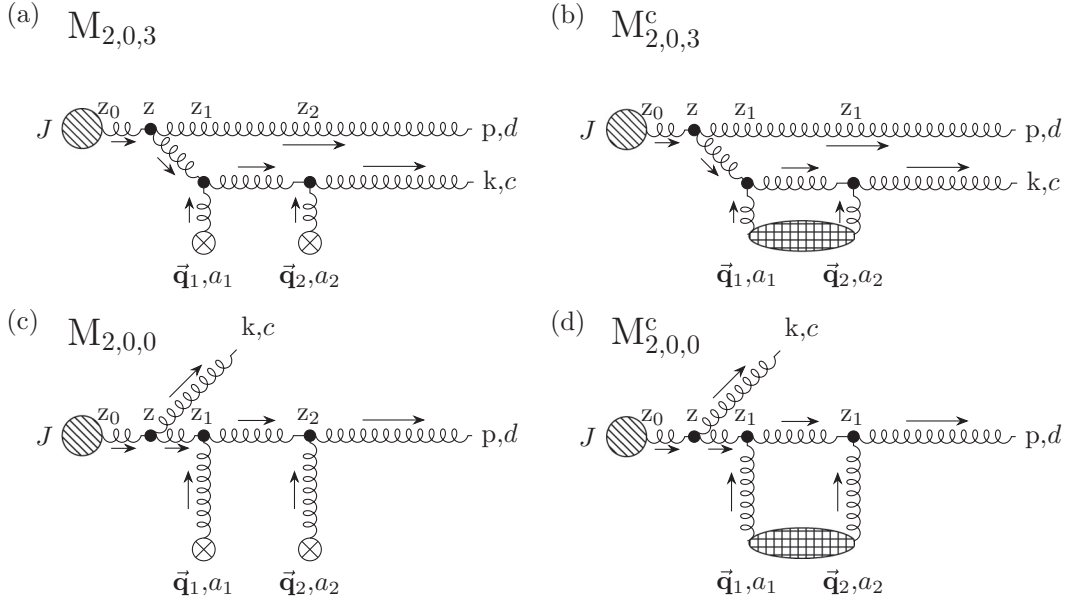
(c) $M_{2,0,0}$

(d) $M^c_{2,0,0}$

FIG. 9. Feynman diagrams $M_{2,0,3}$ and $M_{2,0,0}$ in well-separated ((a) and (c)) and in contact-limit case ($z_1 = z_2$), which contributes to the first order in opacity of gluon-jet radiative energy loss: $M^c_{2,0,3}$ and $M^c_{2,0,0}$ ((b) and (d)). Remaining labeling is the same as in Fig. 8.

where we applied Eq. (E3) and manipulated with SU($N_c = 3$) structure constants by using Eqs. (A5) and (A6). Also, we assumed that $\mathbf{x}_1 = \mathbf{x}_2$, since diagrams with two different centers will not contribute to the final result due to Eqs. (A3) and (A4).

Note from Fig. 8 that $M_{2,2,0}$ is symmetric under the substitutions ($p \leftrightarrow k$, $x \leftrightarrow (1 - x)$, $c \leftrightarrow d$), which can be straightforwardly verified by implementing these substitutions in the first two lines of Eq. (E13).

APPENDIX F: DIAGRAMS $M_{2,0,3}$ and $M_{2,0,0}$

Next, we consider the $M_{2,0,3}$ diagram, where the radiated gluon suffers two consecutive interactions with the QCD medium (Figs. 9(a) and 9(b)).

Note that the order of the color and Dirac indices denoting vertices is the same for all the remaining diagrams containing two interactions with the scatterers as in Fig. 8, and therefore omitted onward.

$$
\begin{aligned}
M_{2,0,3} = \int & \frac{d^4 q_1}{(2\pi)^4} \frac{d^4 q_2}{(2\pi)^4} \epsilon^*_\rho(k) f^{eca_2}[g^{\xi 0}(k - 2q_2)^\rho + g^{\xi \rho}(-2k + q_2)^0 + g^{\rho 0}(k + q_2)^\xi] T_{a_2} V(q_2) e^{iq_2 x_2} \frac{-i\delta_{ee'} g_{\xi\xi'}}{(k - q_2)^2 + i\epsilon} \\
\times & f^{be'a_1}[g^{\nu 0}(k - 2q_1 - q_2)^{\xi'} + g^{\nu \xi'}(-2k + q_1 + 2q_2)^0 + g^{\xi' 0}(k + q_1 - q_2)^\nu] T_{a_1} V(q_1) e^{iq_1 x_1} \frac{-i\delta_{bb'} g_{\nu\nu'}}{(k - q_1 - q_2)^2 + i\epsilon} \\
\times & \epsilon^*_\sigma(p) g_s f^{adb'}[g^{\mu\nu'}(p + 2k - 2q_1 - 2q_2)^\sigma + g^{\mu\sigma}(-2p - k + q_1 + q_2)^{\nu'} + g^{\sigma\nu'}(p - k + q_1 + q_2)^\mu] \\
\times & \frac{-i\delta_{aa'} g_{\mu\mu'}}{(p + k - q_1 - q_2)^2 + i\epsilon} i J_{a'}(p + k - q_1 - q_2) \epsilon^{\mu'}(p + k - q_1 - q_2) e^{i(p + k - q_1 - q_2)x_0} \\
\approx & i J_a(p + k) e^{i(p+k)x_0} f^{eca_2} f^{bea_1} f^{adb} T_{a_2} T_{a_1} \frac{(1 - x + x^2)}{1 - x} (-i) \int \frac{d^2 \mathbf{q}_1}{(2\pi)^2} (-i) \int \frac{d^2 \mathbf{q}_2}{(2\pi)^2} (2ig_s) \boldsymbol{\epsilon} \cdot \mathbf{p}\, e^{-i\mathbf{q}_1 \cdot \mathbf{b}_1} e^{-i\mathbf{q}_2 \cdot \mathbf{b}_2} \\
\times & \int \frac{dq_{1z}}{2\pi} \frac{dq_{2z}}{2\pi} \frac{E^+ k^+ v(q_{1z}, \mathbf{q}_1) v(q_{2z}, \mathbf{q}_2) e^{-iq_{1z}(z_1 - z_0)} e^{-iq_{2z}(z_2 - z_0)}}{[(p + k - q_1 - q_2)^2 + i\epsilon][(k - q_1 - q_2)^2 + i\epsilon][(k - q_2)^2 + i\epsilon]}.
\end{aligned}
\tag{F1}
$$

Next, again by changing the variables $q_{1z} \to q_z = q_{1z} + q_{2z}$, we define the following integral:

$$
I_2(p, k, \mathbf{q}_1, \vec{q}_2, z_1 - z_0) = \int \frac{dq_z}{2\pi} \frac{v(q_z - q_{2z}, \mathbf{q}_1) e^{-iq_z(z_1 - z_0)}}{[(p + k - q_1 - q_2)^2 + i\epsilon][(k - q_1 - q_2)^2 + i\epsilon]}.
\tag{F2}
$$

Again, as explained in the previous section, we close the contour in lower half-plane, and since $\mu(z_1 - z_0) \gg 1$ the pole at $q_z = -i\mu_{1\perp} + q_{2z}$ is again exponentially suppressed. Therefore, the remaining q_z singularities originating from gluon propagators are

the following:

$$\bar{q}_1 = -\frac{\mathbf{k}^2}{xE^+} - \frac{\mathbf{p}^2}{(1-x)E^+} - i\epsilon = -\frac{\mathbf{k}^2}{2\omega} - \frac{x}{1-x}\frac{(\mathbf{k}-\mathbf{q}_1-\mathbf{q}_2)^2}{2\omega} - i\epsilon,$$

$$\bar{q}_2 = -\frac{\mathbf{k}^2}{xE^+} + \frac{\mathbf{p}^2}{xE^+} - i\epsilon = -\frac{\mathbf{k}^2}{2\omega} + \frac{(\mathbf{k}-\mathbf{q}_1-\mathbf{q}_2)^2}{2\omega} - i\epsilon. \tag{F3}$$

After performing the integration, i.e., summing the residues at these two poles, I_2 now reads as

$$I_2(p, k, \mathbf{q}_1, \vec{\mathbf{q}}_2, z_1 - z_0) \approx v(-q_{2z}, \mathbf{q}_1)\frac{i(1-x)}{E^+(\mathbf{k}-\mathbf{q}_1-\mathbf{q}_2)^2}\left\{e^{\frac{i}{2\omega}[\mathbf{k}^2+\frac{x}{1-x}(\mathbf{k}-\mathbf{q}_1-\mathbf{q}_2)^2](z_1-z_0)} - e^{\frac{i}{2\omega}[\mathbf{k}^2-(\mathbf{k}-\mathbf{q}_1-\mathbf{q}_2)^2](z_1-z_0)}\right\}. \tag{F4}$$

The remaining integral over q_{2z} is

$$I_3(p, k, \mathbf{q}_1, \mathbf{q}_2, z_2 - z_1) = \int \frac{dq_{2z}}{2\pi}\frac{v(q_{2z}, \mathbf{q}_2)e^{-iq_{2z}(z_2-z_1)}}{(k-q_2)^2+i\epsilon}v(-q_{2z}, \mathbf{q}_1), \tag{F5}$$

and since we are interested only in the contact-limit case (i.e., $z_1 = z_2$), we need to calculate

$$I_3^c(p, k, \mathbf{q}_1, \mathbf{q}_2, 0) = \int \frac{dq_{2z}}{2\pi}\frac{v(q_{2z}, \mathbf{q}_2)v(-q_{2z}, \mathbf{q}_1)}{(k-q_2)^2+i\epsilon}, \tag{F6}$$

which gives

$$I_3^c(p, k, \mathbf{q}_1, \mathbf{q}_2, 0) \approx -v(0, \mathbf{q}_1)v(0, \mathbf{q}_2)\frac{i}{2xE^+}, \tag{F7}$$

which can readily be shown to represent exactly $\frac{1}{2}$ of the strength of the well-separated limit Eq. (F5), as for $M_{2,2,0}$ amplitude. The contact limit of this amplitude reduces to

$$M_{2,0,3}^c = iJ_a(p+k)e^{i(p+k)x_0}f^{eca_2}f^{bea_1}f^{adb}T_{a_2}T_{a_1}(1-x+x^2)(-i)\int \frac{d^2\mathbf{q}_1}{(2\pi)^2}(-i)\int \frac{d^2\mathbf{q}_2}{(2\pi)^2}v(0, \mathbf{q}_1)v(0, \mathbf{q}_2)e^{-i(\mathbf{q}_1+\mathbf{q}_2)\cdot\mathbf{b}_1}$$

$$\times \frac{1}{2}(2ig_s)\frac{\boldsymbol{\epsilon}\cdot\mathbf{p}}{\mathbf{p}^2}\left\{e^{i[\frac{\mathbf{k}^2}{xE^+}+\frac{\mathbf{p}^2}{(1-x)E^+}](z_1-z_0)} - e^{i\frac{(\mathbf{k}^2-\mathbf{p}^2)}{xE^+}(z_1-z_0)}\right\}$$

$$= J_a(p+k)e^{i(p+k)x_0}[[T^c, T^{a_2}], T^{a_1}]_{da}T_{a_2}T_{a_1}(1-x+x^2)(-i)\int \frac{d^2\mathbf{q}_1}{(2\pi)^2}(-i)\int \frac{d^2\mathbf{q}_2}{(2\pi)^2}v(0, \mathbf{q}_1)v(0, \mathbf{q}_2)e^{-i(\mathbf{q}_1+\mathbf{q}_2)\cdot\mathbf{b}_1}$$

$$\times \frac{1}{2}(2ig_s)\frac{\boldsymbol{\epsilon}\cdot(\mathbf{k}-\mathbf{q}_1-\mathbf{q}_2)}{(\mathbf{k}-\mathbf{q}_1-\mathbf{q}_2)^2}\left\{e^{\frac{i}{2\omega}[\mathbf{k}^2+\frac{x}{1-x}(\mathbf{k}-\mathbf{q}_1-\mathbf{q}_2)^2](z_1-z_0)} - e^{\frac{i}{2\omega}[\mathbf{k}^2-(\mathbf{k}-\mathbf{q}_1-\mathbf{q}_2)^2](z_1-z_0)}\right\}. \tag{F8}$$

Proceeding in the same manner, for $M_{2,0,0}^c$ amplitude (Figs. 9(c) and 9(d)), we obtain

$$M_{2,0,0}^c = iJ_a(p+k)e^{i(p+k)x_0}f^{eda_2}f^{bea_1}f^{acb}T_{a_2}T_{a_1}(1-x+x^2)(-i)\int \frac{d^2\mathbf{q}_1}{(2\pi)^2}(-i)\int \frac{d^2\mathbf{q}_2}{(2\pi)^2}v(0, \mathbf{q}_1)v(0, \mathbf{q}_2)e^{-i(\mathbf{q}_1+\mathbf{q}_2)\cdot\mathbf{b}_1}$$

$$\times \frac{1}{2}(2ig_s)\frac{\boldsymbol{\epsilon}\cdot\mathbf{k}}{\mathbf{k}^2}\left\{e^{i[\frac{\mathbf{k}^2}{xE^+}+\frac{\mathbf{p}^2}{(1-x)E^+}](z_1-z_0)} - e^{i\frac{(\mathbf{p}^2-\mathbf{k}^2)}{(1-x)E^+}(z_1-z_0)}\right\}$$

$$= J_a(p+k)e^{i(p+k)x_0}(T^{a_2}T^{a_1}T^c)_{da}T_{a_2}T_{a_1}(1-x+x^2)(-i)\int \frac{d^2\mathbf{q}_1}{(2\pi)^2}(-i)\int \frac{d^2\mathbf{q}_2}{(2\pi)^2}v(0, \mathbf{q}_1)v(0, \mathbf{q}_2)e^{-i(\mathbf{q}_1+\mathbf{q}_2)\cdot\mathbf{b}_1}$$

$$\times \frac{1}{2}(2ig_s)\frac{\boldsymbol{\epsilon}\cdot\mathbf{k}}{\mathbf{k}^2}\left\{e^{\frac{i}{2\omega}[\mathbf{k}^2+\frac{x}{1-x}(\mathbf{k}-\mathbf{q}_1-\mathbf{q}_2)^2](z_1-z_0)} - e^{\frac{i}{2\omega}\frac{x}{1-x}[(\mathbf{k}-\mathbf{q}_1-\mathbf{q}_2)^2-\mathbf{k}^2](z_1-z_0)}\right\}. \tag{F9}$$

From Fig. 9, we infer that $M_{2,0,3}$ and $M_{2,0,0}$ are symmetric under the following substitutions: $(p \leftrightarrow k, x \leftrightarrow (1-x), c \leftrightarrow d)$, which can be straightforwardly verified by implementing these substitutions in Eqs. (F8) and (F9).

APPENDIX G: DIAGRAMS $M_{2,0,1}$ AND $M_{2,0,2}$

Here we consider the case when both initial gluon jet and radiated gluon interact with one scattering center. We provide only the contact-limit case diagrams $M_{2,0,1}^c$ and $M_{2,0,2}^c$ (Fig. 10), since, in the end, only they are used in calculating radiative energy
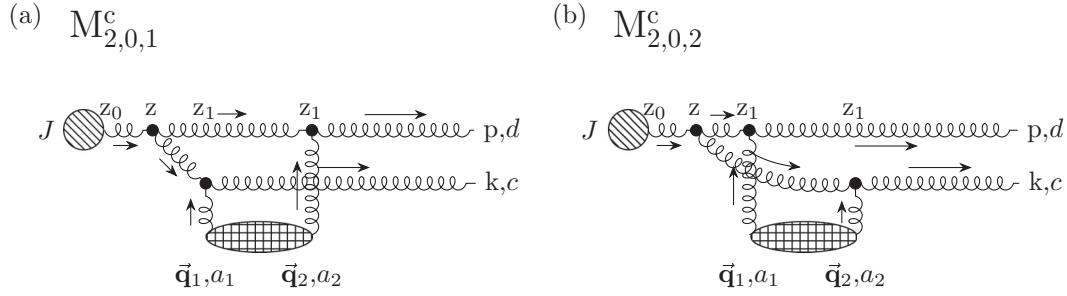
(a) $M^c_{2,0,1}$ (b) $M^c_{2,0,2}$

FIG. 10. Topologically indistinct Feynman diagrams: (a) $M^c_{2,0,1}$ and (b) $M^c_{2,0,2}$ in contact limit ($z_1 = z_2$), which contribute to the first order in opacity of gluon-jet radiative energy loss. Remaining labeling is the same as in Fig. 8.

loss to the first order in opacity:

$$
M_{2,0,1} = \int \frac{d^4q_1}{(2\pi)^4} \frac{d^4q_2}{(2\pi)^4} \epsilon^*_\sigma(p) f^{eda_2}[g^{\xi 0}(p-2q_2)^\sigma + g^{\xi\sigma}(-2p+q_2)^0 + g^{\sigma 0}(p+q_2)^\xi] T_{a_2} V(q_2) e^{iq_2 x_2}
$$

$$
\times \frac{-i\delta_{ee'}g_{\xi\xi'}}{(p-q_2)^2+i\epsilon} g_s f^{ae'b'}[g^{\mu\nu'}(p+2k-2q_1-q_2)^{\xi'} + g^{\mu\xi'}(-2p-k+q_1+2q_2)^{\nu'} + g^{\xi'\nu'}(p-k+q_1-q_2)^\mu]
$$

$$
\times \epsilon^*_\rho(k) f^{bca_1}[g^{\nu 0}(k-2q_1)^\rho + g^{\nu\rho}(-2k+q_1)^0 + g^{\rho 0}(k+q_1)^\nu] T_{a_1} V(q_1) e^{iq_1 x_1} \frac{-i\delta_{bb'}g_{\nu\nu'}}{(k-q_1)^2+i\epsilon}
$$

$$
\times \frac{-i\delta_{aa'}g_{\mu\mu'}}{(p+k-q_1-q_2)^2+i\epsilon} i J_{a'}(p+k-q_1-q_2) \epsilon^{\mu'}(p+k-q_1-q_2) e^{i(p+k-q_1-q_2)x_0}
$$

$$
\approx -i J_a(p+k) e^{i(p+k)x_0} f^{eda_2} f^{aeb} f^{bca_1} T_{a_2} T_{a_1} (1-x+x^2)(-i) \int \frac{d^2\mathbf{q}_1}{(2\pi)^2}(-i) \int \frac{d^2\mathbf{q}_2}{(2\pi)^2}(2ig_s)\,\boldsymbol{\epsilon}\cdot(\mathbf{k}-\mathbf{q}_1)\,e^{-i\mathbf{q}_1\cdot\mathbf{b}_1}
$$

$$
\times\, e^{-i\mathbf{q}_2\cdot\mathbf{b}_2}(E^+)^2 \int \frac{dq_{1z}}{2\pi} \frac{dq_{2z}}{2\pi} \frac{v(q_{1z},\mathbf{q}_1)v(q_{2z},\mathbf{q}_2)e^{-iq_{1z}(z_1-z_0)}e^{-iq_{2z}(z_2-z_0)}}{[(p+k-q_1-q_2)^2+i\epsilon][(k-q_1)^2+i\epsilon][(p-q_2)^2+i\epsilon]}. \tag{G1}
$$

Again, by changing the variables $q_{1z} \to q_z = q_{1z} + q_{2z}$, we define the following integral:

$$
I_2(p,k,\mathbf{q}_1,\vec{\mathbf{q}}_2,z_1-z_0) = \int \frac{dq_z}{2\pi} \frac{v(q_z-q_{2z},\mathbf{q}_1)e^{-iq_z(z_1-z_0)}}{(p+k-q_1-q_2)^2+i\epsilon} \frac{1}{(k-q_1)^2+i\epsilon}. \tag{G2}
$$

Since $z_1 > z_0$, we must close the contour in lower half-plane, and since $\mu(z_1-z_0) \gg 1$ again we neglect the pole at $q_z = -i\mu_{1\perp} + q_{2z}$. Therefore, the remaining q_z singularities originating from gluon propagators are

$$
\bar{q}_1 = -\frac{\mathbf{k}^2}{2\omega} - \frac{x}{1-x}\frac{(\mathbf{k}-\mathbf{q}_1-\mathbf{q}_2)^2}{2\omega} - i\epsilon, \quad \bar{q}_2 = -\frac{\mathbf{k}^2}{2\omega} + \frac{(\mathbf{k}-\mathbf{q}_1)^2}{2\omega} + q_{2z} - i\epsilon. \tag{G3}
$$

Summing the residues gives

$$
I_2(p,k,\mathbf{q}_1,\vec{\mathbf{q}}_2,z_1-z_0) \approx \frac{ie^{i\frac{\mathbf{k}^2}{2\omega}(z_1-z_0)}}{E^+k^+\left[q_{2z}+\frac{(\mathbf{k}-\mathbf{q}_1)^2}{2\omega}+\frac{x}{1-x}\frac{(\mathbf{k}-\mathbf{q}_1-\mathbf{q}_2)^2}{2\omega}\right]} \left\{ v\left(-q_{2z}-\frac{\mathbf{k}^2}{2\omega}-\frac{x}{1-x}\frac{(\mathbf{k}-\mathbf{q}_1-\mathbf{q}_2)^2}{2\omega},\mathbf{q}_1\right)\right.
$$

$$
\left. \times\, e^{i\frac{x}{1-x}\frac{(\mathbf{k}-\mathbf{q}_1-\mathbf{q}_2)^2}{2\omega}(z_1-z_0)} - v\left(\frac{(\mathbf{k}-\mathbf{q}_1)^2}{2\omega}-\frac{\mathbf{k}^2}{2\omega},\mathbf{q}_1\right) e^{-i[q_{2z}+\frac{(\mathbf{k}-\mathbf{q}_1)^2}{2\omega}](z_1-z_0)} \right\}. \tag{G4}
$$

The remaining q_{2z} integral is

$$
I_3(p,k,\mathbf{q}_1,\mathbf{q}_2,z_2-z_0,z_2-z_1) = \int \frac{dq_{2z}}{2\pi} \frac{1}{q_{2z}+\frac{(\mathbf{k}-\mathbf{q}_1)^2}{2\omega}+\frac{x}{1-x}\frac{(\mathbf{k}-\mathbf{q}_1-\mathbf{q}_2)^2}{2\omega}} \frac{v(q_{2z},\mathbf{q}_2)}{(p-q_2)^2+i\epsilon}
$$

$$
\times \left\{ e^{-iq_{2z}(z_2-z_1)} e^{\frac{i}{2\omega}[\mathbf{k}^2+\frac{x}{1-x}(\mathbf{k}-\mathbf{q}_1-\mathbf{q}_2)^2](z_1-z_0)} v\left(-q_{2z}-\frac{\mathbf{k}^2}{2\omega}-\frac{x}{1-x}\frac{(\mathbf{k}-\mathbf{q}_1-\mathbf{q}_2)^2}{2\omega},\mathbf{q}_1\right) \right.
$$

$$
\left. -\, e^{-iq_{2z}(z_2-z_0)} e^{-\frac{i}{2\omega}[(\mathbf{k}-\mathbf{q}_1)^2-\mathbf{k}^2](z_1-z_0)} v\left(\frac{(\mathbf{k}-\mathbf{q}_1)^2}{2\omega}-\frac{\mathbf{k}^2}{2\omega},\mathbf{q}_1\right) \right\}, \tag{G5}
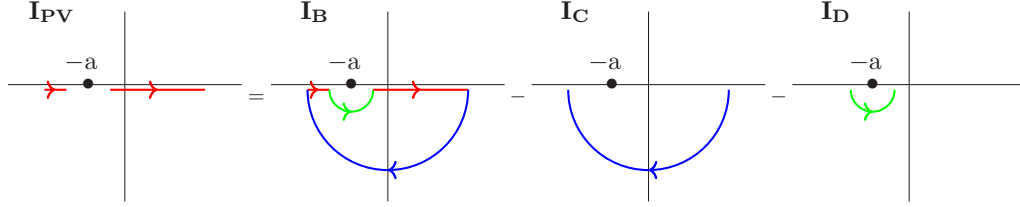$$

FIG. 11. Illustration of calculating Cauchy principal value (I_{PV}) in the case when singularity ($-a$) on the real (horizontal) axis arises.

where the singularity on q_{2z} real axis, $q_{2z} = -\frac{(\mathbf{k}-\mathbf{q_1})^2}{2\omega} - \frac{x}{1-x}\frac{(\mathbf{k}-\mathbf{q_1}-\mathbf{q_2})^2}{2\omega} \equiv -a$ ($a > 0$), has to be avoided by taking Cauchy principal value of I_3 according to the Fig. 11, i.e.,

$$I_3 \equiv I_{PV} = I_B - I_C - I_D, \tag{G6}$$

where $I_B = -2\pi i \sum_i \mathrm{Res}(I_3(\bar{q}_i))$, with i counting the poles in the lower half-plane. Additionally, $I_C = 0$, and it is straightforward to show that after the substitution $q_{2z} = -a + re^{i\varphi}$, where $r \to 0$, also $I_D = 0$. Therefore, the principal value of I_3 reduces to I_B, i.e., $-2\pi i \sum_i \mathrm{Res}(I_3(\bar{q}_i))$.

In the well-separated case, Eq. (G5), poles originating from Yukawa potentials ($q_{2z} = -\frac{\mathbf{k}^2}{2\omega} - \frac{x}{1-x}\frac{(\mathbf{k}-\mathbf{q_1}-\mathbf{q_2})^2}{2\omega} - i\mu_{1\perp}$ and $q_{2z} = -i\mu_{2\perp}$) are again exponentially suppressed ($e^{-\mu_{i\perp}(z_2-z_{0,1})} \to 0$, $i = 1, 2$) and therefore can be neglected, so only the pole from the propagator survives $q_{2z} = \frac{x}{1-x}[\frac{(\mathbf{k}-\mathbf{q_1})^2}{2\omega} - \frac{(\mathbf{k}-\mathbf{q_1}-\mathbf{q_2})^2}{2\omega}] - i\epsilon$. However, since we are interested only in the contact-limit case (i.e., $z_1 = z_2$), instead of Eq. (G5) we need to calculate the principal value of the following integral:

$$I_3^c(p, k, \mathbf{q_1}, \mathbf{q_2}, z_1 - z_0) = \int \frac{dq_{2z}}{2\pi} \frac{1}{q_{2z} + \frac{(\mathbf{k}-\mathbf{q_1})^2}{2\omega} + \frac{x}{1-x}\frac{(\mathbf{k}-\mathbf{q_1}-\mathbf{q_2})^2}{2\omega}}$$

$$\times \left\{ \frac{e^{\frac{i}{2\omega}[\mathbf{k}^2 + \frac{x}{1-x}(\mathbf{k}-\mathbf{q_1}-\mathbf{q_2})^2](z_1-z_0)}}{(p-q_2)^2 + i\epsilon} v\left(-q_{2z} - \frac{\mathbf{k}^2}{2\omega} - \frac{x}{1-x}\frac{(\mathbf{k}-\mathbf{q_1}-\mathbf{q_2})^2}{2\omega}, \mathbf{q_1}\right) v(q_{2z}, \mathbf{q_2}) \right.$$

$$\left. - \frac{e^{-iq_{2z}(z_1-z_0)}e^{-\frac{i}{2\omega}[(\mathbf{k}-\mathbf{q_1})^2-\mathbf{k}^2](z_1-z_0)}}{(p-q_2)^2 + i\epsilon} v\left(\frac{(\mathbf{k}-\mathbf{q_1})^2}{2\omega} - \frac{\mathbf{k}^2}{2\omega}, \mathbf{q_1}\right) v(q_{2z}, \mathbf{q_2}) \right\}, \tag{G7}$$

which again reduces to the sum of residua, with $-a$ effectively not being a pole (Fig. 11). Particularly, for the second term in the bracket of Eq. (G7), only the propagator pole survives, while for the first term in the bracket all three poles have to be accounted, although residues at poles from potentials sum to the order of $O\left(\frac{(\mathbf{k}-\mathbf{q_1})^2}{x(1-x)E^+(\mu_{1\perp}+\mu_{2\perp})}\right)$, and thus can be neglected compared to the remaining residue.

Finally, in the contact-limit case, we obtain

$$M_{2,0,1}^c \approx -iJ_a(p+k)e^{i(p+k)x_0} f^{eda_2} f^{aeb} f^{bca_1} T_{a_2} T_{a_1}(1-x+x^2)(-i) \int \frac{d^2\mathbf{q_1}}{(2\pi)^2}(-i) \int \frac{d^2\mathbf{q_2}}{(2\pi)^2} v(0, \mathbf{q_1}) v(0, \mathbf{q_2}) e^{-i(\mathbf{q_1}+\mathbf{q_2})\cdot\mathbf{b_1}}$$

$$\times (2ig_s)\frac{\boldsymbol{\epsilon} \cdot (\mathbf{k}-\mathbf{q_1})}{(\mathbf{k}-\mathbf{q_1})^2} \left\{ e^{i[\frac{\mathbf{k}^2}{xE^+} + \frac{\mathbf{p}^2}{(1-x)E^+}](z_1-z_0)} - e^{i[\frac{\mathbf{k}^2}{xE^+} + \frac{\mathbf{p}^2}{(1-x)E^+} - \frac{(\mathbf{k}-\mathbf{q_1})^2}{x(1-x)E^+}](z_1-z_0)} \right\}$$

$$= J_a(p+k)e^{i(p+k)x_0}(T^{a_2}[T^c, T^{a_1}])_{da} T_{a_2} T_{a_1}(1-x+x^2)(-i) \int \frac{d^2\mathbf{q_1}}{(2\pi)^2}(-i) \int \frac{d^2\mathbf{q_2}}{(2\pi)^2} v(0, \mathbf{q_1}) v(0, \mathbf{q_2}) e^{-i(\mathbf{q_1}+\mathbf{q_2})\cdot\mathbf{b_1}}$$

$$\times (2ig_s)\frac{\boldsymbol{\epsilon} \cdot (\mathbf{k}-\mathbf{q_1})}{(\mathbf{k}-\mathbf{q_1})^2} \left\{ e^{\frac{i}{2\omega}[\mathbf{k}^2 + \frac{x}{1-x}(\mathbf{k}-\mathbf{q_1}-\mathbf{q_2})^2](z_1-z_0)} - e^{\frac{i}{2\omega}[\mathbf{k}^2 - \frac{(\mathbf{k}-\mathbf{q_1})^2}{1-x} + \frac{x}{1-x}(\mathbf{k}-\mathbf{q_1}-\mathbf{q_2})^2](z_1-z_0)} \right\}. \tag{G8}$$

Notice that, in contrast to the previous three amplitudes that also included two scattering centers, in Eq. (G8) no factor $\frac{1}{2}$ appears when comparing to a well-separated limit.

Proceeding in the same manner, for $M_{2,0,2}^c$ we obtain

$$M_{2,0,2}^c \approx iJ_a(p+k)e^{i(p+k)x_0} f^{eca_2} f^{abe} f^{bda_1} T_{a_2} T_{a_1}(1-x+x^2)(-i) \int \frac{d^2\mathbf{q_1}}{(2\pi)^2}(-i) \int \frac{d^2\mathbf{q_2}}{(2\pi)^2} v(0, \mathbf{q_1}) v(0, \mathbf{q_2}) e^{-i(\mathbf{q_1}+\mathbf{q_2})\cdot\mathbf{b_1}}$$

$$\times (2ig_s)\frac{\boldsymbol{\epsilon} \cdot (\mathbf{p}-\mathbf{q_1})}{(\mathbf{p}-\mathbf{q_1})^2} \left\{ e^{i[\frac{\mathbf{k}^2}{xE^+} + \frac{\mathbf{p}^2}{(1-x)E^+}](z_1-z_0)} - e^{i[\frac{\mathbf{k}^2}{xE^+} + \frac{\mathbf{p}^2}{(1-x)E^+} - \frac{(\mathbf{p}-\mathbf{q_1})^2}{x(1-x)E^+}](z_1-z_0)} \right\}$$
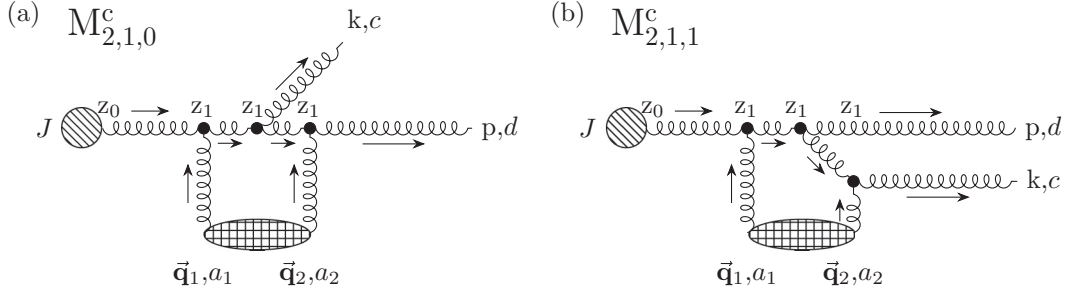
FIG. 12. Feynman diagrams: (a) $M_{2,1,0}^c$ and (b) $M_{2,1,1}^c$ in contact limit ($z_1 = z_2$), which have negligible contribution to the first order in opacity gluon-jet radiative energy loss. Remaining labeling is the same as in Fig. 8.

$$
= J_a(p+k)e^{i(p+k)x_0}(T^{a_1}[T^c, T^{a_2}])_{da}T_{a_2}T_{a_1}(1 - x + x^2)(-i)\int \frac{d^2\mathbf{q}_1}{(2\pi)^2}(-i)\int \frac{d^2\mathbf{q}_2}{(2\pi)^2}v(0, \mathbf{q}_1)v(0, \mathbf{q}_2)e^{-i(\mathbf{q}_1+\mathbf{q}_2)\cdot\mathbf{b}_1}
$$

$$
\times (2ig_s)\frac{\boldsymbol{\epsilon}\cdot(\mathbf{k}-\mathbf{q}_2)}{(\mathbf{k}-\mathbf{q}_2)^2}\left\{e^{\frac{i}{2\omega}[\mathbf{k}^2+\frac{x}{1-x}(\mathbf{k}-\mathbf{q}_1-\mathbf{q}_2)^2](z_1-z_0)} - e^{\frac{i}{2\omega}[\mathbf{k}^2-\frac{(\mathbf{k}-\mathbf{q}_2)^2}{1-x}+\frac{x}{1-x}(\mathbf{k}-\mathbf{q}_1-\mathbf{q}_2)^2](z_1-z_0)}\right\}. \tag{G9}
$$

Similarly to $M_{2,0,1}^c$ amplitude, no factor of $\frac{1}{2}$ appears in the above expression. From well-separated analogon of Fig. 10, we could infer that $M_{2,0,1}$ and $M_{2,0,2}$ are symmetric under the following substitutions, ($p \leftrightarrow k$, $x \leftrightarrow (1-x)$, $c \leftrightarrow d$), which can readily be verified by implementing these substitutions in the first two lines of either Eqs. (G8) or (G9) and by using structure constant asymmetry. Note that in Eq. (G9) we applied Eq. (E3). Also, since in contact-limit case these two diagrams are topologically indistinct, we need to either omit one of them in order to avoid over counting, or to include both, but multiply each by a factor $\frac{1}{2}$ (we will do the latter).

APPENDIX H: DIAGRAMS $M_{2,1,0}$ and $M_{2,1,1}$

The contact-limit case of the remaining two diagrams is presented in Fig. 12. These diagrams correspond to the case when one interaction with the scattering center located at $\vec{x}_1$ occurs before and the other interaction at the same place occurs after the gluon has been radiated.

In order to avoid redundant derivations (i.e., repetition of the above calculations), we briefly outline our derivation of Feynman amplitudes for only the contact-limit case.

In the light of time-ordered perturbation theory from Refs. [8,42], these two diagrams are identically equal to zero, since $\int_{t_1}^{t_1} dt... = 0$, but for the consistency we will provide a brief verification of this argument:

$$
M_{2,1,0} = \int \frac{d^4q_1}{(2\pi)^4}\frac{d^4q_2}{(2\pi)^4}\epsilon_\sigma^*(p)f^{eda_2}[g^{\xi 0}(p - 2q_2)^\sigma + g^{\xi\sigma}(-2p + q_2)^0 + g^{\sigma 0}(p + q_2)^\xi]T_{a_2}V(q_2)e^{iq_2x_2}\frac{-i\delta_{ee'}g_{\xi\xi'}}{(p-q_2)^2 + i\epsilon}
$$

$$
\times \epsilon_\rho^*(k)g_s f^{bce'}[g^{\nu\xi'}(2p + k - 2q_2)^\rho + g^{\nu\rho}(-p - 2k + q_2)^{\xi'} + g^{\rho\xi'}(-p + k + q_2)^\nu]\frac{-i\delta_{bb'}g_{\nu\nu'}}{(p+k-q_2)^2 + i\epsilon}
$$

$$
\times f^{ab'a_1}[g^{\mu 0}(p + k - 2q_1 - q_2)^{\nu'} + g^{\mu\nu'}(-2p - 2k + q_1 + 2q_2)^0 + g^{\nu'0}(p + k + q_1 - q_2)^\mu]T_{a_1}V(q_1)e^{iq_1x_1}
$$

$$
\times \frac{-i\delta_{aa'}g_{\mu\mu'}}{(p+k-q_1-q_2)^2 + i\epsilon}iJ_{a'}(p + k - q_1 - q_2)\epsilon^{\mu'}(p + k - q_1 - q_2)e^{i(p+k-q_1-q_2)x_0}
$$

$$
\approx iJ_a(p+k)e^{i(p+k)x_0}f^{eda_2}f^{bce}f^{aba_1}T_{a_2}T_{a_1}\frac{(1 - x + x^2)}{x}(-i)\int \frac{d^2\mathbf{q}_1}{(2\pi)^2}(-i)\int \frac{d^2\mathbf{q}_2}{(2\pi)^2}(2ig_s)\boldsymbol{\epsilon}\cdot(\mathbf{k}-x\mathbf{q}_1)\,e^{-i\mathbf{q}_1\cdot\mathbf{b}_1}
$$

$$
\times e^{-i\mathbf{q}_2\cdot\mathbf{b}_2}(E^+)^2\int \frac{dq_{2z}}{2\pi}\frac{v(q_{2z}, \mathbf{q}_2)e^{-iq_{2z}(z_2-z_1)}}{[(p+k-q_2)^2 + i\epsilon][(p-q_2)^2 + i\epsilon]}\int \frac{dq_z}{2\pi}\frac{v(q_z - q_{2z}, \mathbf{q}_1)e^{-iq_z(z_1-z_0)}}{(p+k-q_1-q_2)^2 + i\epsilon}
$$

$$
\approx J_a(p+k)e^{i(p+k)x_0}f^{eda_2}f^{bce}f^{aba_1}T_{a_2}T_{a_1}(1 - x + x^2)(-i)\int \frac{d^2\mathbf{q}_1}{(2\pi)^2}(-i)\int \frac{d^2\mathbf{q}_2}{(2\pi)^2}(2ig_s)\boldsymbol{\epsilon}\cdot(\mathbf{k}-x\mathbf{q}_1)\,e^{-i\mathbf{q}_1\cdot\mathbf{b}_1}
$$

$$
\times e^{-i\mathbf{q}_2\cdot\mathbf{b}_2}(E^+)^2\int \frac{dq_{2z}}{2\pi}\frac{v(q_{2z}, \mathbf{q}_2)e^{-iq_{2z}(z_2-z_1)}}{[(p+k-q_2)^2 + i\epsilon][(p-q_2)^2 + i\epsilon]}\frac{1}{k^+}v\left(-\frac{\mathbf{k}^2}{2\omega} - \frac{x}{1-x}\frac{(\mathbf{k}-\mathbf{q}_1-\mathbf{q}_2)^2}{2\omega} - q_{2z}, \mathbf{q}_1\right)
$$

$$
\times e^{\frac{i}{2\omega}[\mathbf{k}^2+\frac{x}{1-x}(\mathbf{k}-\mathbf{q}_1-\mathbf{q}_2)^2](z_1-z_0)}. \tag{H1}
$$

In the contact-limit case, there are four q_{2z} poles of the above integral in the lower half-plane: $-\frac{\mathbf{k}^2}{2\omega} - \frac{x}{1-x}\frac{(\mathbf{k}-\mathbf{q}_1-\mathbf{q}_2)^2}{2\omega} + \frac{x\mathbf{q}_1^2}{2\omega} - i\epsilon$, $\frac{x}{1-x}[\frac{(\mathbf{k}-\mathbf{q}_1)^2}{2\omega} - \frac{(\mathbf{k}-\mathbf{q}_1-\mathbf{q}_2)^2}{2\omega}] - i\epsilon$, $-i\mu_{1\perp}$ and $-i\mu_{2\perp}$, which give

$$M_{2,1,0}^c = iJ_a(p+k)e^{i(p+k)x_0}(T^{a_2}T^cT^{a_1})_{da}T_{a_2}T_{a_1}(1-x+x^2)(-i)\int\frac{d^2\mathbf{q}_1}{(2\pi)^2}(-i)\int\frac{d^2\mathbf{q}_2}{(2\pi)^2}v(0,\mathbf{q}_1)v(0,\mathbf{q}_2)e^{-i(\mathbf{q}_1+\mathbf{q}_2)\cdot\mathbf{b}_1}$$

$$\times (ig_s)\frac{\boldsymbol{\epsilon}\cdot(\mathbf{k}-x\mathbf{q}_1)}{(\mathbf{k}-x\mathbf{q}_1)^2}e^{\frac{i}{2\omega}[\mathbf{k}^2+\frac{x}{1-x}(\mathbf{k}-\mathbf{q}_1-\mathbf{q}_2)^2](z_1-z_0)}\frac{\mu_{1\perp}^2+\mu_{1\perp}\mu_{2\perp}+\mu_{2\perp}^2}{\mu_{1\perp}\mu_{2\perp}}\frac{(\mathbf{k}-x\mathbf{q}_1)^2}{x(1-x)E^+(\mu_{1\perp}+\mu_{2\perp})}, \tag{H2}$$

where the residues at first two poles (i.e., originating from the gluon propagators) cancel each other exactly, leading to the result Eq. (H2) that is suppressed by a factor of $O\left(\frac{(\mathbf{k}-x\mathbf{q}_1)^2}{x(1-x)E^+(\mu_{1\perp}+\mu_{2\perp})}\right)$ compared to the all previous amplitudes (note that x is finite), as in the case of soft-gluon approximation [9,25].

The same conclusion applies to the $M_{2,1,1}^c$ amplitude, which can be straightforwardly verified by repeating the analogous procedure as for $M_{2,1,0}^c$, and by the fact that these two amplitudes are symmetric (see Fig. 12) to the exchange ($p \leftrightarrow k, x \leftrightarrow (1-x), c \leftrightarrow d$).

APPENDIX I: CALCULATION OF RADIATIVE ENERGY LOSS

In this section, we provide a concise outline of calculating the first order in opacity radiative energy loss. We start with the equation

$$d^3N_g^{(1)}d^3N_J = \left(\frac{1}{d_T}\text{Tr}\langle|M_1|^2\rangle + \frac{2}{d_T}\text{Re}\,\text{Tr}\langle M_2M_0^*\rangle\right)\frac{d^3\vec{\mathbf{p}}}{(2\pi)^32p^0}\frac{d^3\vec{\mathbf{k}}}{(2\pi)^32\omega}, \tag{I1}$$

where M_1 is sum of all diagrams with one scattering center from Appendix D, M_2 is sum of all diagrams with two scattering centers in the contact limit from Appendixes E–G, and M_0^* is obtained from Appendix C.

The final results from Appendix D yield

$$M_1 = M_{1,1,0} + M_{1,0,0} + M_{1,0,1}$$

$$= J_a(p+k)e^{i(p+k)x_0}(1-x+x^2)T_{a_1}(-i)\int\frac{d^2\mathbf{q}_1}{(2\pi)^2}v(0,\mathbf{q}_1)e^{-i\mathbf{q}_1\cdot\mathbf{b}_1}(2ig_s)$$

$$\times\left\{\left(\frac{\boldsymbol{\epsilon}\cdot(\mathbf{k}-\mathbf{q}_1)}{(\mathbf{k}-\mathbf{q}_1)^2}[T^c,T^{a_1}]_{da} - \frac{\boldsymbol{\epsilon}\cdot(\mathbf{k}-x\mathbf{q}_1)}{(\mathbf{k}-x\mathbf{q}_1)^2}(T^cT^{a_1})_{da} + \frac{\boldsymbol{\epsilon}\cdot\mathbf{k}}{\mathbf{k}^2}(T^{a_1}T^c)_{da}\right)e^{\frac{i}{2\omega}(\mathbf{k}^2+\frac{x}{1-x}(\mathbf{k}-\mathbf{q}_1)^2)(z_1-z_0)}\right.$$

$$\left. - \frac{\boldsymbol{\epsilon}\cdot(\mathbf{k}-\mathbf{q}_1)}{(\mathbf{k}-\mathbf{q}_1)^2}[T^c,T^{a_1}]_{da}e^{\frac{i}{2\omega}[\mathbf{k}^2-(\mathbf{k}-\mathbf{q}_1)^2](z_1-z_0)} - \frac{\boldsymbol{\epsilon}\cdot\mathbf{k}}{\mathbf{k}^2}(T^{a_1}T^c)_{da}e^{\frac{i}{2\omega}\frac{x}{1-x}[(\mathbf{k}-\mathbf{q}_1)^2-\mathbf{k}^2](z_1-z_0)}\right\}, \tag{I2}$$

leading to

$$\frac{1}{d_T}\text{Tr}\langle|M_1|^2\rangle$$

$$= \sum N|J(p+k)|^2(4g_s^2)\frac{1}{A_\perp}(1-x+x^2)^2\int\frac{d^2\mathbf{q}_1}{(2\pi)^2}|v(0,\mathbf{q}_1)|^2\frac{C_2(T)}{d_G}\left\{\left[\frac{\boldsymbol{\epsilon}\cdot(\mathbf{k}-x\mathbf{q}_1)}{(\mathbf{k}-x\mathbf{q}_1)^2}\right]^2\text{Tr}((T^c)^2(T^{a_1})^2)\right.$$

$$+ 2\alpha\left[2\frac{\boldsymbol{\epsilon}\cdot(\mathbf{k}-\mathbf{q}_1)}{(\mathbf{k}-\mathbf{q}_1)^2} - \frac{\boldsymbol{\epsilon}\cdot\mathbf{k}}{\mathbf{k}^2} - \frac{\boldsymbol{\epsilon}\cdot(\mathbf{k}-x\mathbf{q}_1)}{(\mathbf{k}-x\mathbf{q}_1)^2}\right]\frac{\boldsymbol{\epsilon}\cdot(\mathbf{k}-\mathbf{q}_1)}{(\mathbf{k}-\mathbf{q}_1)^2} - \alpha\frac{\boldsymbol{\epsilon}\cdot\mathbf{k}}{\mathbf{k}^2}\frac{\boldsymbol{\epsilon}\cdot(\mathbf{k}-\mathbf{q}_1)}{(\mathbf{k}-\mathbf{q}_1)^2}2\cos\left(\frac{\mathbf{k}^2-(\mathbf{k}-\mathbf{q}_1)^2}{x(1-x)E^+}(z_1-z_0)\right)$$

$$+ 2\left[\frac{\boldsymbol{\epsilon}\cdot\mathbf{k}}{\mathbf{k}^2}\text{Tr}[(T^c)^2(T^{a_1})^2] - \frac{\boldsymbol{\epsilon}\cdot(\mathbf{k}-x\mathbf{q}_1)}{(\mathbf{k}-x\mathbf{q}_1)^2}\text{Tr}(T^cT^{a_1}T^cT^{a_1})\right]\frac{\boldsymbol{\epsilon}\cdot\mathbf{k}}{\mathbf{k}^2}$$

$$- 2\alpha\left[\frac{\boldsymbol{\epsilon}\cdot(\mathbf{k}-\mathbf{q}_1)}{(\mathbf{k}-\mathbf{q}_1)^2} - \frac{1}{2}\frac{\boldsymbol{\epsilon}\cdot\mathbf{k}}{\mathbf{k}^2} - \frac{1}{2}\frac{\boldsymbol{\epsilon}\cdot(\mathbf{k}-x\mathbf{q}_1)}{(\mathbf{k}-x\mathbf{q}_1)^2}\right]\frac{\boldsymbol{\epsilon}\cdot(\mathbf{k}-\mathbf{q}_1)}{(\mathbf{k}-\mathbf{q}_1)^2}2\cos\left(\frac{(\mathbf{k}-\mathbf{q}_1)^2}{x(1-x)E^+}(z_1-z_0)\right)$$

$$+ \left[\alpha\frac{\boldsymbol{\epsilon}\cdot(\mathbf{k}-\mathbf{q}_1)}{(\mathbf{k}-\mathbf{q}_1)^2} - \frac{\boldsymbol{\epsilon}\cdot\mathbf{k}}{\mathbf{k}^2}\text{Tr}[(T^c)^2(T^{a_1})^2] + \frac{\boldsymbol{\epsilon}\cdot(\mathbf{k}-x\mathbf{q}_1)}{(\mathbf{k}-x\mathbf{q}_1)^2}\text{Tr}(T^cT^{a_1}T^cT^{a_1})\right]\frac{\boldsymbol{\epsilon}\cdot\mathbf{k}}{\mathbf{k}^2}2\cos\left(\frac{\mathbf{k}^2}{x(1-x)E^+}(z_1-z_0)\right)\right\}, \tag{I3}$$

where the number of scattering centers N comes from summation over scattering centers Eqs. (B2) and (B3), then $\alpha \equiv \text{Tr}((T^c)^2(T^{a_1})^2 - T^cT^{a_1}T^cT^{a_1})$, and we also used the definition of the commutator, the fact that trace is invariant under the cyclic permutations, Eq. (A4) (with $i = j$ and $d_i = d_T$), and the relation $E^+ \approx 2E$. We verified that this result is also symmetric under the substitutions ($p \leftrightarrow k, x \leftrightarrow (1-x), c \leftrightarrow d$) when written in terms of structure constants.

Next, we summarize contact limits of all diagrams that contain two scattering centers from Appendixes E–G and then take their ensemble average according to Eqs. (B2) to (B4) in order to obtain M_2:

$$
\begin{aligned}
M_2 &= M_{2,2,0}^c + M_{2,0,3}^c + M_{2,0,0}^c + \frac{1}{2}\left(M_{2,0,1}^c + M_{2,0,2}^c\right) \\
&= \frac{1}{2} N J_a(p+k) e^{i(p+k)x_0}(-2ig_s)\frac{1}{A_\perp}(1-x+x^2)T_{a_2}T_{a_1} \\
&\quad \times \int \frac{d^2\mathbf{q}_1}{(2\pi)^2}|v(0,\mathbf{q}_1)|^2\left\{\frac{\boldsymbol{\epsilon}\cdot\mathbf{k}}{\mathbf{k}^2}\left[e^{\frac{i}{2\omega}\frac{\mathbf{k}^2}{1-x}(z_1-z_0)}([[T^c,T^{a_2}],T^{a_1}]_{da}+[T^{a_2}T^{a_1},T^c]_{da})-[[T^c,T^{a_2}],T^{a_1}]_{da}-(T^{a_2}T^{a_1}T^c)_{da}\right] \right. \\
&\quad \left. + \frac{\boldsymbol{\epsilon}\cdot(\mathbf{k}-\mathbf{q}_1)}{(\mathbf{k}-\mathbf{q}_1)^2}\left[e^{\frac{i}{2\omega}\frac{\mathbf{k}^2}{1-x}(z_1-z_0)}-e^{\frac{i}{2\omega}\frac{\mathbf{k}^2-(\mathbf{k}-\mathbf{q}_1)^2}{1-x}(z_1-z_0)}\right]((T^{a_2}[T^c,T^{a_1}])_{da}+(T^{a_1}[T^c,T^{a_2}])_{da})\right\}.
\end{aligned}
\tag{I4}
$$

Then, by multiplying the previous expression by M_0^*, we obtain

$$
\begin{aligned}
\frac{2}{d_T}\mathrm{Re}\,\mathrm{Tr}\langle M_2 M_0^*\rangle &= \sum N|J(p+k)|^2\left(4g_s^2\right)\frac{1}{A_\perp}(1-x+x^2)^2\int\frac{d^2\mathbf{q}_1}{(2\pi)^2}|v(0,\mathbf{q}_1)|^2\frac{C_2(T)}{d_G} \\
&\quad \times \left[\left(\frac{\boldsymbol{\epsilon}\cdot\mathbf{k}}{\mathbf{k}^2}\right)^2\left\{2\alpha\cos\left(\frac{\mathbf{k}^2}{x(1-x)E^+}(z_1-z_0)\right)-2\alpha-\mathrm{Tr}((T^c)^2(T^{a_1})^2)\right\}\right. \\
&\quad \left. -2\alpha\frac{\boldsymbol{\epsilon}\cdot\mathbf{k}}{\mathbf{k}^2}\frac{\boldsymbol{\epsilon}\cdot(\mathbf{k}-\mathbf{q}_1)}{(\mathbf{k}-\mathbf{q}_1)^2}\left(\cos\left(\frac{\mathbf{k}^2}{x(1-x)E^+}(z_1-z_0)\right)-\cos\left(\frac{\mathbf{k}^2-(\mathbf{k}-\mathbf{q}_1)^2}{x(1-x)E^+}(z_1-z_0)\right)\right)\right],
\end{aligned}
\tag{I5}
$$

which can easily be verified to be symmetric to the exchange $(p\leftrightarrow k, x\leftrightarrow(1-x), c\leftrightarrow d)$, when written in terms of structure constants. By summing the expressions Eqs. (I3) and (I5), we obtain

$$
\begin{aligned}
&\frac{1}{d_T}\mathrm{Tr}\langle|M_1|^2\rangle + \frac{2}{d_T}\mathrm{Re}\,\mathrm{Tr}\langle M_2 M_0^*\rangle \\
&= Nd_G|J(p+k)|^2\left(4g_s^2\right)\frac{C_2(T)}{d_G}C_2^2(G)\frac{1}{A_\perp}(1-x+x^2)^2\sum\int\frac{d^2\mathbf{q}_1}{(2\pi)^2}|v(0,\mathbf{q}_1)|^2 \\
&\quad \times \left(\left\{1-\cos\left(\frac{\mathbf{k}^2}{x(1-x)E^+}(z_1-z_0)\right)\right\}\left[\frac{\boldsymbol{\epsilon}\cdot\mathbf{k}}{\mathbf{k}^2}-\frac{\boldsymbol{\epsilon}\cdot(\mathbf{k}-x\mathbf{q}_1)}{(\mathbf{k}-x\mathbf{q}_1)^2}\right]\frac{\boldsymbol{\epsilon}\cdot\mathbf{k}}{\mathbf{k}^2}+\left\{\left[\frac{\boldsymbol{\epsilon}\cdot(\mathbf{k}-x\mathbf{q}_1)}{(\mathbf{k}-x\mathbf{q}_1)^2}\right]^2-\left(\frac{\boldsymbol{\epsilon}\cdot\mathbf{k}}{\mathbf{k}^2}\right)^2\right\}\right. \\
&\quad \left. + \left\{1-\cos\left(\frac{(\mathbf{k}-\mathbf{q}_1)^2}{x(1-x)E^+}(z_1-z_0)\right)\right\}\left[2\frac{\boldsymbol{\epsilon}\cdot(\mathbf{k}-\mathbf{q}_1)}{(\mathbf{k}-\mathbf{q}_1)^2}-\frac{\boldsymbol{\epsilon}\cdot\mathbf{k}}{\mathbf{k}^2}-\frac{\boldsymbol{\epsilon}\cdot(\mathbf{k}-x\mathbf{q}_1)}{(\mathbf{k}-x\mathbf{q}_1)^2}\right]\frac{\boldsymbol{\epsilon}\cdot(\mathbf{k}-\mathbf{q}_1)}{(\mathbf{k}-\mathbf{q}_1)^2}\right),
\end{aligned}
\tag{I6}
$$

which in the soft-gluon approximation coincides with massless limit of Eq. (82) from [25] and where we used the following equalities that are valid in adjoint representation: $\mathrm{Tr}(T^cT^{a_1}T^cT^{a_1})=\frac{1}{2}C_2^2(G)d_G=\alpha=\frac{1}{2}\mathrm{Tr}((T^c)^2(T^{a_1})^2)$, which follow from Eqs. (A4) to (A9) and the commutator definition.

Since we are considering optically thin QCD plasma, it would be convenient to expand energy loss in powers of opacity, which is defined by the mean number of collisions in QCD medium [9],

$$
\bar{n} = \frac{L}{\lambda} = \frac{N\sigma_{el}}{A_\perp},
\tag{I7}
$$

where the small transverse momentum transfer elastic cross section between the jet and the target partons is taken from GW model (Eq. (6) from Ref. [9]), which in our case reads

$$
\frac{d\sigma_{el}}{d^2\mathbf{q}_1} = \frac{C_2(G)C_2(T)}{d_G}\frac{|v(0,\mathbf{q}_1)|^2}{(2\pi)^2}.
\tag{I8}
$$

Combining Eqs. (I7) and (I8), we obtain

$$
\frac{L}{\lambda} = \frac{N}{A_\perp}\frac{C_2(G)C_2(T)}{4\pi d_G}\frac{(4\pi\alpha_s)^2}{\mu^2}.
\tag{I9}
$$

Next we incorporate Eq. (I9) in Eq. (I6), substitute obtained expression in Eq. (I1), keeping in mind that $\vec{\mathbf{p}}$ is the 3D momentum of a final jet, and that we need to apply Eqs. (C14) and (C15).

Thus, in the case of simple exponential distribution $\frac{2}{L}e^{-2\frac{z_1-z_0}{L}}$ of the scattering centers (as in Ref. [25]), the single-gluon radiation spectrum in the first order in opacity becomes

$$
\begin{aligned}
\frac{dN_g^{(1)}}{dx} = {} & \frac{C_2(G)\alpha_s}{\pi}\frac{L}{\lambda}\frac{(1-x+x^2)^2}{x(1-x)}\sum\int\frac{d^2\mathbf{q}_1}{\pi}\frac{\mu^2}{(\mathbf{q}_1^2+\mu^2)^2}\int\frac{d^2\mathbf{k}}{\pi}\left(-\frac{\boldsymbol{\epsilon}\cdot(\mathbf{k}-\mathbf{q}_1)}{(\mathbf{k}-\mathbf{q}_1)^2}\left[\frac{\boldsymbol{\epsilon}\cdot\mathbf{k}}{\mathbf{k}^2}+\frac{\boldsymbol{\epsilon}\cdot(\mathbf{k}-x\mathbf{q}_1)}{(\mathbf{k}-x\mathbf{q}_1)^2}-2\frac{\boldsymbol{\epsilon}\cdot(\mathbf{k}-\mathbf{q}_1)}{(\mathbf{k}-\mathbf{q}_1)^2}\right]\right. \\
& \times\int dz_1\left\{1-\cos\left(\frac{(\mathbf{k}-\mathbf{q}_1)^2}{x(1-x)E^+}(z_1-z_0)\right)\right\}\frac{2}{L}e^{-\frac{2(z_1-z_0)}{L}}+\frac{\boldsymbol{\epsilon}\cdot\mathbf{k}}{\mathbf{k}^2}\left[\frac{\boldsymbol{\epsilon}\cdot\mathbf{k}}{\mathbf{k}^2}-\frac{\boldsymbol{\epsilon}\cdot(\mathbf{k}-x\mathbf{q}_1)}{(\mathbf{k}-x\mathbf{q}_1)^2}\right] \\
& \times\int dz_1\left\{1-\cos\left(\frac{\mathbf{k}^2}{x(1-x)E^+}(z_1-z_0)\right)\right\}\frac{2}{L}e^{-\frac{2(z_1-z_0)}{L}}+\left.\left\{\left[\frac{\boldsymbol{\epsilon}\cdot(\mathbf{k}-x\mathbf{q}_1)}{(\mathbf{k}-x\mathbf{q}_1)^2}\right]^2-\left(\frac{\boldsymbol{\epsilon}\cdot\mathbf{k}}{\mathbf{k}^2}\right)^2\right\}\int dz_1\frac{2}{L}e^{-\frac{2(z_1-z_0)}{L}}\right),
\end{aligned}
\tag{I10}
$$

and the differential radiative energy loss $\frac{dE^{(1)}}{dx}\equiv\omega\frac{d^3N_g^{(1)}}{dx}\approx xE\frac{d^3N_g^{(1)}}{dx}$ acquires the form

$$
\begin{aligned}
\frac{dE^{(1)}}{dx} = {} & \frac{C_2(G)\alpha_s}{\pi}\frac{L}{\lambda}E\frac{(1-x+x^2)^2}{1-x}\sum\int\frac{d^2\mathbf{q}_1}{\pi}\frac{\mu^2}{(\mathbf{q}_1^2+\mu^2)^2}\int\frac{d^2\mathbf{k}}{\pi}\left(-\frac{\boldsymbol{\epsilon}\cdot(\mathbf{k}-\mathbf{q}_1)}{(\mathbf{k}-\mathbf{q}_1)^2}\left[\frac{\boldsymbol{\epsilon}\cdot\mathbf{k}}{\mathbf{k}^2}+\frac{\boldsymbol{\epsilon}\cdot(\mathbf{k}-x\mathbf{q}_1)}{(\mathbf{k}-x\mathbf{q}_1)^2}-2\frac{\boldsymbol{\epsilon}\cdot(\mathbf{k}-\mathbf{q}_1)}{(\mathbf{k}-\mathbf{q}_1)^2}\right]\right. \\
& \times\int dz_1\left\{1-\cos\left(\frac{(\mathbf{k}-\mathbf{q}_1)^2}{x(1-x)E^+}(z_1-z_0)\right)\right\}\frac{2}{L}e^{-\frac{2(z_1-z_0)}{L}}+\frac{\boldsymbol{\epsilon}\cdot\mathbf{k}}{\mathbf{k}^2}\left[\frac{\boldsymbol{\epsilon}\cdot\mathbf{k}}{\mathbf{k}^2}-\frac{\boldsymbol{\epsilon}\cdot(\mathbf{k}-x\mathbf{q}_1)}{(\mathbf{k}-x\mathbf{q}_1)^2}\right] \\
& \times\int dz_1\left\{1-\cos\left(\frac{\mathbf{k}^2}{x(1-x)E^+}(z_1-z_0)\right)\right\}\frac{2}{L}e^{-\frac{2(z_1-z_0)}{L}}+\left.\left\{\left[\frac{\boldsymbol{\epsilon}\cdot(\mathbf{k}-x\mathbf{q}_1)}{(\mathbf{k}-x\mathbf{q}_1)^2}\right]^2-\left(\frac{\boldsymbol{\epsilon}\cdot\mathbf{k}}{\mathbf{k}^2}\right)^2\right\}\int dz_1\frac{2}{L}e^{-\frac{2(z_1-z_0)}{L}}\right).
\end{aligned}
\tag{I11}
$$

So we finally obtain

$$
\begin{aligned}
\frac{dN_g^{(1)}}{dx} = {} & \frac{C_2(G)\alpha_s}{\pi}\frac{L}{\lambda}\frac{(1-x+x^2)^2}{x(1-x)}\int\frac{d^2\mathbf{q}_1}{\pi}\frac{\mu^2}{(\mathbf{q}_1^2+\mu^2)^2} \\
& \times\int d\mathbf{k}^2\left\{\frac{(\mathbf{k}-\mathbf{q}_1)^2}{\left[\frac{4x(1-x)E}{L}\right]^2+(\mathbf{k}-\mathbf{q}_1)^4}\left[2-\frac{\mathbf{k}\cdot(\mathbf{k}-\mathbf{q}_1)}{\mathbf{k}^2}-\frac{(\mathbf{k}-\mathbf{q}_1)\cdot(\mathbf{k}-x\mathbf{q}_1)}{(\mathbf{k}-x\mathbf{q}_1)^2}\right]\right. \\
& \left.+\frac{\mathbf{k}^2}{\left[\frac{4x(1-x)E}{L}\right]^2+\mathbf{k}^4}\left[1-\frac{\mathbf{k}\cdot(\mathbf{k}-x\mathbf{q}_1)}{(\mathbf{k}-x\mathbf{q}_1)^2}\right]+\left[\frac{1}{(\mathbf{k}-x\mathbf{q}_1)^2}-\frac{1}{\mathbf{k}^2}\right]\right\},
\end{aligned}
\tag{I12}
$$

which is symmetric to the exchange of p and k gluons, and

$$
\begin{aligned}
\frac{dE^{(1)}}{dx} = {} & \frac{C_2(G)\alpha_s}{\pi}\frac{L}{\lambda}E\frac{(1-x+x^2)^2}{1-x}\int\frac{d^2\mathbf{q}_1}{\pi}\frac{\mu^2}{(\mathbf{q}_1^2+\mu^2)^2} \\
& \times\int d\mathbf{k}^2\left\{\frac{(\mathbf{k}-\mathbf{q}_1)^2}{\left[\frac{4x(1-x)E}{L}\right]^2+(\mathbf{k}-\mathbf{q}_1)^4}\left[2-\frac{\mathbf{k}\cdot(\mathbf{k}-\mathbf{q}_1)}{\mathbf{k}^2}-\frac{(\mathbf{k}-\mathbf{q}_1)\cdot(\mathbf{k}-x\mathbf{q}_1)}{(\mathbf{k}-x\mathbf{q}_1)^2}\right]\right. \\
& \left.+\frac{\mathbf{k}^2}{\left[\frac{4x(1-x)E}{L}\right]^2+\mathbf{k}^4}\left[1-\frac{\mathbf{k}\cdot(\mathbf{k}-x\mathbf{q}_1)}{(\mathbf{k}-x\mathbf{q}_1)^2}\right]+\left[\frac{1}{(\mathbf{k}-x\mathbf{q}_1)^2}-\frac{1}{\mathbf{k}^2}\right]\right\},
\end{aligned}
\tag{I13}
$$

which in soft-gluon approximation reduces to massless limit of Eq. (84) from Ref. [25].

APPENDIX J: DIAGRAMS AND RADIATIVE ENERGY LOSS IN FINITE T QCD MEDIUM

Next we recalculate the results from Appendixes C–H when the gluon mass $m_g=\frac{\mu}{\sqrt{2}}$ is included, i.e., the gluon propagator has the following form [27]:

Gluon propagator with mass m_g in Feynman gauge:

$$
a,\mu\ \underset{\text{p}}{\text{\textnormal{⸮⸮⸮⸮}}}\ b,\nu = \frac{i\delta_{ab}P_{\mu\nu}}{p^2-m_g^2+i\epsilon},
\tag{J1}
$$

where $P_{\mu\nu}$, given by Eq. (12) from Ref. [27] (specifically $P_{\mu\nu} = -(g_{\mu\nu} - \frac{p_\mu p_\nu n^2 + n_\mu n_\nu p^2 - n_\mu p_\nu (np) - n_\nu p_\mu (np)}{n^2 p^2 - (np)^2})$, which reduces to Eq. (A12)), represents the transverse projector. Note that since the transverse projectors act directly or indirectly on transverse polarization vectors, one may immediately replace $P_{\mu\nu}$ with $-g_{\mu\nu}$ in gluon propagators, in order to facilitate the calculations. This observation is obvious for off-shell gluon propagator, whereas the derivation for the remaining internal gluon lines is straightforward.

Consistently throughout this section, the initial jet propagates along the z axis, 4-momentum is conserved, and minus light cone coordinates of p and k momenta acquire an additional term $+m_g^2$ in the numerator compared to massless case (Appendixes C–H), due to relations $k^2 = p^2 = m_g^2$, while the polarizations remain the same.

We provide only the final expressions for all 11 Feynman diagrams beyond the soft-gluon approximation, when the gluon mass is included, since its derivation is similar to the case of massless gluons and in order to avoid unnecessary repetition (Appendixes C–H).

Thus, for M_0 we obtain

$$M_0 = J_a(p+k)e^{i(p+k)x_0}(-2ig_s)(1-x+x^2)\frac{\boldsymbol{\epsilon}\cdot\mathbf{k}}{\mathbf{k}^2 + m_g^2(1-x+x^2)}(T^c)_{da}. \tag{J2}$$

The expression for $M_{1,1,0}$ now reads

$$M_{1,1,0} = J_a(p+k)e^{i(p+k)x_0}(-i)(1-x+x^2)(T^c T^{a_1})_{da}T_{a_1}\int\frac{d^2\mathbf{q}_1}{(2\pi)^2}v(0,\mathbf{q}_1)e^{-i\mathbf{q}_1\cdot\mathbf{b}_1}$$
$$\times (-2ig_s)\frac{\boldsymbol{\epsilon}\cdot(\mathbf{k}-x\mathbf{q}_1)}{(\mathbf{k}-x\mathbf{q}_1)^2 + m_g^2(1-x+x^2)}e^{\frac{i}{2\omega}[\mathbf{k}^2 + \frac{x}{1-x}(\mathbf{k}-\mathbf{q}_1)^2 + \frac{m_g^2(1-x+x^2)}{1-x}](z_1-z_0)}, \tag{J3}$$

which differs from Eq. (D12) in the term $\chi \equiv m_g^2(1-x+x^2)$, which now appears in the denominator and in exponent, accompanying the squared transverse momentum. Further on, we will use the shorthand notation χ.

Similarly, for $M_{1,0,0}$ and $M_{1,0,1}$ we obtain, respectively,

$$M_{1,0,0} = J_a(p+k)e^{i(p+k)x_0}(-i)(1-x+x^2)(T^{a_1}T^c)_{da}T_{a_1}\int\frac{d^2\mathbf{q}_1}{(2\pi)^2}v(0,\mathbf{q}_1)e^{-i\mathbf{q}_1\cdot\mathbf{b}_1}$$
$$\times (2ig_s)\frac{\boldsymbol{\epsilon}\cdot\mathbf{k}}{\mathbf{k}^2+\chi}\left\{e^{\frac{i}{2\omega}[\mathbf{k}^2 + \frac{x}{1-x}(\mathbf{k}-\mathbf{q}_1)^2 + \frac{\chi}{1-x}](z_1-z_0)} - e^{-\frac{i}{2\omega}\frac{x}{1-x}[\mathbf{k}^2 - (\mathbf{k}-\mathbf{q}_1)^2](z_1-z_0)}\right\}, \tag{J4}$$

$$M_{1,0,1} = J_a(p+k)e^{i(p+k)x_0}(-i)(1-x+x^2)[T^c, T^{a_1}]_{da}T_{a_1}\int\frac{d^2\mathbf{q}_1}{(2\pi)^2}v(0,\mathbf{q}_1)e^{-i\mathbf{q}_1\cdot\mathbf{b}_1}$$
$$\times (2ig_s)\frac{\boldsymbol{\epsilon}\cdot(\mathbf{k}-\mathbf{q}_1)}{(\mathbf{k}-\mathbf{q}_1)^2+\chi}\left\{e^{\frac{i}{2\omega}[\mathbf{k}^2 + \frac{x}{1-x}(\mathbf{k}-\mathbf{q}_1)^2 + \frac{\chi}{1-x}](z_1-z_0)} - e^{\frac{i}{2\omega}[\mathbf{k}^2 - (\mathbf{k}-\mathbf{q}_1)^2](z_1-z_0)}\right\}. \tag{J5}$$

Proceeding in a similar manner, we obtain the following expressions for contact-limit diagrams which include interactions with two scattering centers:

$$M_{2,2,0}^c = -J_a(p+k)e^{i(p+k)x_0}(T^c T^{a_2}T^{a_1})_{da}T_{a_2}T_{a_1}(1-x+x^2)(-i)\int\frac{d^2\mathbf{q}_1}{(2\pi)^2}(-i)\int\frac{d^2\mathbf{q}_2}{(2\pi)^2}v(0,\mathbf{q}_1)v(0,\mathbf{q}_2)e^{-i(\mathbf{q}_1+\mathbf{q}_2)\cdot\mathbf{b}_1}$$
$$\times\frac{1}{2}(2ig_s)\frac{\boldsymbol{\epsilon}\cdot[\mathbf{k}-x(\mathbf{q}_1+\mathbf{q}_2)]}{[\mathbf{k}-x(\mathbf{q}_1+\mathbf{q}_2)]^2+\chi}e^{\frac{i}{2\omega}[\mathbf{k}^2 + \frac{x}{1-x}(\mathbf{k}-\mathbf{q}_1-\mathbf{q}_2)^2 + \frac{\chi}{1-x}](z_1-z_0)}, \tag{J6}$$

$$M_{2,0,3}^c = J_a(p+k)e^{i(p+k)x_0}[[T^c, T^{a_2}], T^{a_1}]_{da}T_{a_2}T_{a_1}(1-x+x^2)(-i)\int\frac{d^2\mathbf{q}_1}{(2\pi)^2}(-i)\int\frac{d^2\mathbf{q}_2}{(2\pi)^2}v(0,\mathbf{q}_1)v(0,\mathbf{q}_2)e^{-i(\mathbf{q}_1+\mathbf{q}_2)\cdot\mathbf{b}_1}$$
$$\times\frac{1}{2}(2ig_s)\frac{\boldsymbol{\epsilon}\cdot(\mathbf{k}-\mathbf{q}_1-\mathbf{q}_2)}{(\mathbf{k}-\mathbf{q}_1-\mathbf{q}_2)^2+\chi}\left\{e^{\frac{i}{2\omega}[\mathbf{k}^2 + \frac{x}{1-x}(\mathbf{k}-\mathbf{q}_1-\mathbf{q}_2)^2 + \frac{\chi}{1-x}](z_1-z_0)} - e^{\frac{i}{2\omega}[\mathbf{k}^2 - (\mathbf{k}-\mathbf{q}_1-\mathbf{q}_2)^2](z_1-z_0)}\right\}, \tag{J7}$$

$$M_{2,0,0}^c = J_a(p+k)e^{i(p+k)x_0}(T^{a_2}T^{a_1}T^c)_{da}T_{a_2}T_{a_1}(1-x+x^2)(-i)\int\frac{d^2\mathbf{q}_1}{(2\pi)^2}(-i)\int\frac{d^2\mathbf{q}_2}{(2\pi)^2}v(0,\mathbf{q}_1)v(0,\mathbf{q}_2)e^{-i(\mathbf{q}_1+\mathbf{q}_2)\cdot\mathbf{b}_1}$$
$$\times\frac{1}{2}(2ig_s)\frac{\boldsymbol{\epsilon}\cdot\mathbf{k}}{\mathbf{k}^2+\chi}\left\{e^{\frac{i}{2\omega}[\mathbf{k}^2 + \frac{x}{1-x}(\mathbf{k}-\mathbf{q}_1-\mathbf{q}_2)^2 + \frac{\chi}{1-x}](z_1-z_0)} - e^{\frac{i}{2\omega}\frac{x}{1-x}[(\mathbf{k}-\mathbf{q}_1-\mathbf{q}_2)^2 - \mathbf{k}^2](z_1-z_0)}\right\}, \tag{J8}$$

$$M_{2,0,1}^c = J_a(p+k)e^{i(p+k)x_0}(T^{a_2}[T^c, T^{a_1}])_{da}T_{a_2}T_{a_1}(1-x+x^2)(-i)\int\frac{d^2\mathbf{q}_1}{(2\pi)^2}(-i)\int\frac{d^2\mathbf{q}_2}{(2\pi)^2}v(0,\mathbf{q}_1)v(0,\mathbf{q}_2)e^{-i(\mathbf{q}_1+\mathbf{q}_2)\cdot\mathbf{b}_1}$$
$$\times(2ig_s)\frac{\boldsymbol{\epsilon}\cdot(\mathbf{k}-\mathbf{q}_1)}{(\mathbf{k}-\mathbf{q}_1)^2+\chi}\left\{e^{\frac{i}{2\omega}[\mathbf{k}^2 + \frac{x}{1-x}(\mathbf{k}-\mathbf{q}_1-\mathbf{q}_2)^2 + \frac{\chi}{1-x}](z_1-z_0)} - e^{\frac{i}{2\omega}[\mathbf{k}^2 - \frac{(\mathbf{k}-\mathbf{q}_1)^2}{1-x} + \frac{x}{1-x}(\mathbf{k}-\mathbf{q}_1-\mathbf{q}_2)^2](z_1-z_0)}\right\}, \tag{J9}$$

$$M_{2,0,2}^c = J_a(p+k)e^{i(p+k)x_0}(T^{a_1}[T^c, T^{a_2}])_{da}T_{a_2}T_{a_1}(1-x+x^2)(-i)\int\frac{d^2\mathbf{q}_1}{(2\pi)^2}(-i)\int\frac{d^2\mathbf{q}_2}{(2\pi)^2}v(0,\mathbf{q}_1)v(0,\mathbf{q}_2)e^{-i(\mathbf{q}_1+\mathbf{q}_2)\cdot\mathbf{b}_1}$$

$$\times(2ig_s)\frac{\boldsymbol{\epsilon}\cdot(\mathbf{k}-\mathbf{q}_2)}{(\mathbf{k}-\mathbf{q}_2)^2+\chi}\left(e^{\frac{i}{2\omega}[\mathbf{k}^2+\frac{x}{1-x}(\mathbf{k}-\mathbf{q}_1-\mathbf{q}_2)^2+\frac{\chi}{1-x}](z_1-z_0)}-e^{\frac{i}{2\omega}[\mathbf{k}^2-\frac{(\mathbf{k}-\mathbf{q}_2)^2}{1-x}+\frac{x}{1-x}(\mathbf{k}-\mathbf{q}_1-\mathbf{q}_2)^2](z_1-z_0)}\right). \tag{J10}$$

The amplitudes $M_{2,1,0}^c$ and $M_{2,1,1}^c$ are omitted as they are suppressed compared to the remaining amplitudes.

After adding Eqs. (J3) to (J5), we obtain

$$\frac{1}{d_T}\mathrm{Tr}\langle|M_1|^2\rangle$$

$$= \sum N|J(p+k)|^2(4g_s^2)\frac{1}{A_\perp}(1-x+x^2)^2\int\frac{d^2\mathbf{q}_1}{(2\pi)^2}|v(0,\mathbf{q}_1)|^2\frac{C_2(T)}{d_G}\left(\left[\frac{\boldsymbol{\epsilon}\cdot(\mathbf{k}-x\mathbf{q}_1)}{(\mathbf{k}-x\mathbf{q}_1)^2+\chi}\right]^2\mathrm{Tr}((T^c)^2(T^{a_1})^2)\right.$$

$$+2\alpha\left[2\frac{\boldsymbol{\epsilon}\cdot(\mathbf{k}-\mathbf{q}_1)}{(\mathbf{k}-\mathbf{q}_1)^2+\chi}-\frac{\boldsymbol{\epsilon}\cdot\mathbf{k}}{\mathbf{k}^2+\chi}-\frac{\boldsymbol{\epsilon}\cdot(\mathbf{k}-x\mathbf{q}_1)}{(\mathbf{k}-x\mathbf{q}_1)^2+\chi}\right]\frac{\boldsymbol{\epsilon}\cdot(\mathbf{k}-\mathbf{q}_1)}{(\mathbf{k}-\mathbf{q}_1)^2+\chi}-\alpha\frac{\boldsymbol{\epsilon}\cdot\mathbf{k}}{\mathbf{k}^2+\chi}\frac{\boldsymbol{\epsilon}\cdot(\mathbf{k}-\mathbf{q}_1)}{(\mathbf{k}-\mathbf{q}_1)^2+\chi}$$

$$\times 2\cos\left(\frac{\mathbf{k}^2-(\mathbf{k}-\mathbf{q}_1)^2}{x(1-x)E^+}(z_1-z_0)\right)+2\left\{\frac{\boldsymbol{\epsilon}\cdot\mathbf{k}}{\mathbf{k}^2+\chi}\mathrm{Tr}((T^c)^2(T^{a_1})^2)-\frac{\boldsymbol{\epsilon}\cdot(\mathbf{k}-x\mathbf{q}_1)}{(\mathbf{k}-x\mathbf{q}_1)^2+\chi}\mathrm{Tr}(T^cT^{a_1}T^cT^{a_1})\right\}\frac{\boldsymbol{\epsilon}\cdot\mathbf{k}}{\mathbf{k}^2+\chi}$$

$$-2\alpha\left[\frac{\boldsymbol{\epsilon}\cdot(\mathbf{k}-\mathbf{q}_1)}{(\mathbf{k}-\mathbf{q}_1)^2+\chi}-\frac{1}{2}\frac{\boldsymbol{\epsilon}\cdot\mathbf{k}}{\mathbf{k}^2+\chi}-\frac{1}{2}\frac{\boldsymbol{\epsilon}\cdot(\mathbf{k}-x\mathbf{q}_1)}{(\mathbf{k}-x\mathbf{q}_1)^2+\chi}\right]\frac{\boldsymbol{\epsilon}\cdot(\mathbf{k}-\mathbf{q}_1)}{(\mathbf{k}-\mathbf{q}_1)^2+\chi}2\cos\left(\frac{(\mathbf{k}-\mathbf{q}_1)^2+\chi}{x(1-x)E^+}(z_1-z_0)\right)$$

$$+\left\{\alpha\frac{\boldsymbol{\epsilon}\cdot(\mathbf{k}-\mathbf{q}_1)}{(\mathbf{k}-\mathbf{q}_1)^2+\chi}-\frac{\boldsymbol{\epsilon}\cdot\mathbf{k}}{\mathbf{k}^2+\chi}\mathrm{Tr}((T^c)^2(T^{a_1})^2)+\frac{\boldsymbol{\epsilon}\cdot(\mathbf{k}-x\mathbf{q}_1)}{(\mathbf{k}-x\mathbf{q}_1)^2+\chi}\mathrm{Tr}(T^cT^{a_1}T^cT^{a_1})\right\}\frac{\boldsymbol{\epsilon}\cdot\mathbf{k}}{\mathbf{k}^2+\chi}2\cos\left(\frac{\mathbf{k}^2+\chi}{x(1-x)E^+}(z_1-z_0)\right)\right). \tag{J11}$$

Likewise, after adding Eqs. (J6) to (J10), we obtain

$$\frac{2}{d_T}\mathrm{Re}\,\mathrm{Tr}\langle M_2M_0^*\rangle = \sum N|J(p+k)|^2(4g_s^2)\frac{1}{A_\perp}(1-x+x^2)^2\int\frac{d^2\mathbf{q}_1}{(2\pi)^2}|v(0,\mathbf{q}_1)|^2\frac{C_2(T)}{d_G}$$

$$\times\left(\left(\frac{\boldsymbol{\epsilon}\cdot\mathbf{k}}{\mathbf{k}^2+\chi}\right)^2\left\{2\alpha\cos\left(\frac{\mathbf{k}^2+\chi}{x(1-x)E^+}(z_1-z_0)\right)-2\alpha-\mathrm{Tr}((T^c)^2(T^{a_1})^2)\right\}\right.$$

$$\left.-2\alpha\frac{\boldsymbol{\epsilon}\cdot\mathbf{k}}{\mathbf{k}^2+\chi}\frac{\boldsymbol{\epsilon}\cdot(\mathbf{k}-\mathbf{q}_1)}{(\mathbf{k}-\mathbf{q}_1)^2+\chi}\left\{\cos\left(\frac{\mathbf{k}^2+\chi}{x(1-x)E^+}(z_1-z_0)\right)-\cos\left(\frac{\mathbf{k}^2-(\mathbf{k}-\mathbf{q}_1)^2}{x(1-x)E^+}(z_1-z_0)\right)\right\}\right), \tag{J12}$$

leading to

$$\frac{1}{d_T}\mathrm{Tr}\langle|M_1|^2\rangle+\frac{2}{d_T}\mathrm{Re}\,\mathrm{Tr}\langle M_2M_0^*\rangle$$

$$= Nd_G|J(p+k)|^2(4g_s^2)\frac{C_2(T)}{d_G}C_2^2(G)\frac{1}{A_\perp}(1-x+x^2)^2\sum\int\frac{d^2\mathbf{q}_1}{(2\pi)^2}|v(0,\mathbf{q}_1)|^2$$

$$\times\left(\left\{1-\cos\left(\frac{\mathbf{k}^2+\chi}{x(1-x)E^+}(z_1-z_0)\right)\right\}\left[\frac{\boldsymbol{\epsilon}\cdot\mathbf{k}}{\mathbf{k}^2+\chi}-\frac{\boldsymbol{\epsilon}\cdot(\mathbf{k}-x\mathbf{q}_1)}{(\mathbf{k}-x\mathbf{q}_1)^2+\chi}\right]\frac{\boldsymbol{\epsilon}\cdot\mathbf{k}}{\mathbf{k}^2+\chi}+\left\{\left[\frac{\boldsymbol{\epsilon}\cdot(\mathbf{k}-x\mathbf{q}_1)}{(\mathbf{k}-x\mathbf{q}_1)^2+\chi}\right]^2-\left(\frac{\boldsymbol{\epsilon}\cdot\mathbf{k}}{\mathbf{k}^2+\chi}\right)^2\right\}\right.$$

$$\left.+\left\{1-\cos\left(\frac{(\mathbf{k}-\mathbf{q}_1)^2+\chi}{x(1-x)E^+}(z_1-z_0)\right)\right\}\left[2\frac{\boldsymbol{\epsilon}\cdot(\mathbf{k}-\mathbf{q}_1)}{(\mathbf{k}-\mathbf{q}_1)^2+\chi}-\frac{\boldsymbol{\epsilon}\cdot\mathbf{k}}{\mathbf{k}^2+\chi}-\frac{\boldsymbol{\epsilon}\cdot(\mathbf{k}-x\mathbf{q}_1)}{(\mathbf{k}-x\mathbf{q}_1)^2+\chi}\right]\frac{\boldsymbol{\epsilon}\cdot(\mathbf{k}-\mathbf{q}_1)}{(\mathbf{k}-\mathbf{q}_1)^2+\chi}\right). \tag{J13}$$

In the soft-gluon approximation, the previous expression coincides with Eq. (82) from Ref. [25] (note that in contrast to the cited paper, we here consider the gluon jet, so that M no longer denotes heavy quark mass, but instead $M \equiv m_g$ and therefore the term M^2x^2 is also negligible).

If we further apply the same procedure as in Appendix I, and again assume the simple exponential distribution $\frac{2}{L}e^{-2\frac{z_1-z_0}{L}}$ of the scattering centers, we obtain

$$\frac{dN_g^{(1)}}{dx} = \frac{C_2(G)\alpha_s}{\pi}\frac{L}{\lambda}\frac{(1-x+x^2)^2}{x(1-x)}\int\frac{d^2\mathbf{q}_1}{\pi}\frac{\mu^2}{(\mathbf{q}_1^2+\mu^2)^2}$$

$$\times\int d\mathbf{k}^2\left(\frac{(\mathbf{k}-\mathbf{q}_1)^2+\chi}{\left[\frac{4x(1-x)E}{L}\right]^2+[(\mathbf{k}-\mathbf{q}_1)^2+\chi]^2}\left[2\frac{(\mathbf{k}-\mathbf{q}_1)^2}{(\mathbf{k}-\mathbf{q}_1)^2+\chi}-\frac{\mathbf{k}\cdot(\mathbf{k}-\mathbf{q}_1)}{\mathbf{k}^2+\chi}-\frac{(\mathbf{k}-\mathbf{q}_1)\cdot(\mathbf{k}-x\mathbf{q}_1)}{(\mathbf{k}-x\mathbf{q}_1)^2+\chi}\right]\right.$$

$$\left.+\frac{\mathbf{k}^2+\chi}{\left[\frac{4x(1-x)E}{L}\right]^2+(\mathbf{k}^2+\chi)^2}\left[\frac{\mathbf{k}^2}{\mathbf{k}^2+\chi}-\frac{\mathbf{k}\cdot(\mathbf{k}-x\mathbf{q}_1)}{(\mathbf{k}-x\mathbf{q}_1)^2+\chi}\right]+\left\{\frac{(\mathbf{k}-x\mathbf{q}_1)^2}{[(\mathbf{k}-x\mathbf{q}_1)^2+\chi]^2}-\frac{\mathbf{k}^2}{(\mathbf{k}^2+\chi)^2}\right\}\right), \tag{J14}$$

which is symmetric to the exchange of p and k gluons, and which for $m_g \to 0$ coincides with Eq. (I12). Also,

$$
\frac{dE^{(1)}}{dx} = \frac{C_2(G)\alpha_s}{\pi} \frac{L}{\lambda} E \frac{(1-x+x^2)^2}{1-x} \int \frac{d^2\mathbf{q}_1}{\pi} \frac{\mu^2}{\left(\mathbf{q}_1^2 + \mu^2\right)^2}
$$
$$
\times \int d\mathbf{k}^2 \left(\frac{(\mathbf{k}-\mathbf{q}_1)^2 + \chi}{\left[\frac{4x(1-x)E}{L}\right]^2 + [(\mathbf{k}-\mathbf{q}_1)^2 + \chi]^2} \left[2\frac{(\mathbf{k}-\mathbf{q}_1)^2}{(\mathbf{k}-\mathbf{q}_1)^2 + \chi} - \frac{\mathbf{k} \cdot (\mathbf{k}-\mathbf{q}_1)}{\mathbf{k}^2 + \chi} - \frac{(\mathbf{k}-\mathbf{q}_1) \cdot (\mathbf{k}-x\mathbf{q}_1)}{(\mathbf{k}-x\mathbf{q}_1)^2 + \chi} \right] \right.
$$
$$
\left. + \frac{\mathbf{k}^2 + \chi}{\left[\frac{4x(1-x)E}{L}\right]^2 + (\mathbf{k}^2 + \chi)^2} \left[\frac{\mathbf{k}^2}{\mathbf{k}^2 + \chi} - \frac{\mathbf{k} \cdot (\mathbf{k}-x\mathbf{q}_1)}{(\mathbf{k}-x\mathbf{q}_1)^2 + \chi} \right] + \left\{ \frac{(\mathbf{k}-x\mathbf{q}_1)^2}{[(\mathbf{k}-x\mathbf{q}_1)^2 + \chi]^2} - \frac{\mathbf{k}^2}{(\mathbf{k}^2 + \chi)^2} \right\} \right), \quad \text{(J15)}
$$

which, in the soft-gluon approximation, reduces to Eq. (84) from Ref. [25], and which for $m_g \to 0$ coincides with our massless beyond soft-gluon approximation expression, Eq. (I13).

Further, we display the beyond soft-gluon approximation expressions needed for numerical evaluation of the corresponding variables. So, the number of radiated gluons to the first order in opacity for gluons with effective mass m_g and for finite x reads

$$
N_g^{(1)} = \frac{C_2(G)\alpha_s}{\pi} \frac{L}{\lambda} \int_0^{\frac{1}{2}} dx \frac{(1-x+x^2)^2}{x(1-x)} \int \frac{d^2\mathbf{q}_1}{\pi} \frac{\mu^2}{\left(\mathbf{q}_1^2 + \mu^2\right)^2}
$$
$$
\times \int d\mathbf{k}^2 \left(\frac{(\mathbf{k}-\mathbf{q}_1)^2 + \chi}{\left[\frac{4x(1-x)E}{L}\right]^2 + [(\mathbf{k}-\mathbf{q}_1)^2 + \chi]^2} \left[2\frac{(\mathbf{k}-\mathbf{q}_1)^2}{(\mathbf{k}-\mathbf{q}_1)^2 + \chi} - \frac{\mathbf{k} \cdot (\mathbf{k}-\mathbf{q}_1)}{\mathbf{k}^2 + \chi} - \frac{(\mathbf{k}-\mathbf{q}_1) \cdot (\mathbf{k}-x\mathbf{q}_1)}{(\mathbf{k}-x\mathbf{q}_1)^2 + \chi} \right] \right.
$$
$$
\left. + \frac{\mathbf{k}^2 + \chi}{\left[\frac{4x(1-x)E}{L}\right]^2 + (\mathbf{k}^2 + \chi)^2} \left[\frac{\mathbf{k}^2}{\mathbf{k}^2 + \chi} - \frac{\mathbf{k} \cdot (\mathbf{k}-x\mathbf{q}_1)}{(\mathbf{k}-x\mathbf{q}_1)^2 + \chi} \right] + \left\{ \frac{(\mathbf{k}-x\mathbf{q}_1)^2}{[(\mathbf{k}-x\mathbf{q}_1)^2 + \chi]^2} - \frac{\mathbf{k}^2}{(\mathbf{k}^2 + \chi)^2} \right\} \right). \quad \text{(J16)}
$$

Similarly, the fractional radiative energy loss is given by

$$
\frac{\Delta E^{(1)}}{E} = \frac{C_2(G)\alpha_s}{\pi} \frac{L}{\lambda} \int_0^{\frac{1}{2}} dx \frac{(1-x+x^2)^2}{1-x} \int \frac{d^2\mathbf{q}_1}{\pi} \frac{\mu^2}{\left(\mathbf{q}_1^2 + \mu^2\right)^2}
$$
$$
\times \int d\mathbf{k}^2 \left(\frac{(\mathbf{k}-\mathbf{q}_1)^2 + \chi}{\left[\frac{4x(1-x)E}{L}\right]^2 + [(\mathbf{k}-\mathbf{q}_1)^2 + \chi]^2} \left[2\frac{(\mathbf{k}-\mathbf{q}_1)^2}{(\mathbf{k}-\mathbf{q}_1)^2 + \chi} - \frac{\mathbf{k} \cdot (\mathbf{k}-\mathbf{q}_1)}{\mathbf{k}^2 + \chi} - \frac{(\mathbf{k}-\mathbf{q}_1) \cdot (\mathbf{k}-x\mathbf{q}_1)}{(\mathbf{k}-x\mathbf{q}_1)^2 + \chi} \right] \right.
$$
$$
\left. + \frac{\mathbf{k}^2 + \chi}{\left[\frac{4x(1-x)E}{L}\right]^2 + (\mathbf{k}^2 + \chi)^2} \left[\frac{\mathbf{k}^2}{\mathbf{k}^2 + \chi} - \frac{\mathbf{k} \cdot (\mathbf{k}-x\mathbf{q}_1)}{(\mathbf{k}-x\mathbf{q}_1)^2 + \chi} \right] + \left\{ \frac{(\mathbf{k}-x\mathbf{q}_1)^2}{[(\mathbf{k}-x\mathbf{q}_1)^2 + \chi]^2} - \frac{\mathbf{k}^2}{(\mathbf{k}^2 + \chi)^2} \right\} \right). \quad \text{(J17)}
$$

APPENDIX K: UNIFORM DISTRIBUTION OF STATIC SCATTERING CENTERS

In this section, we assess how the choice of distribution of longitudinal distance between the gluon-jet production site and target rescattering site affects our results and conclusions. To this end, we here concentrate on the limit opposite to the exponential one (which mimics a rapidly evolving medium, and which was used throughout this paper)—the uniform distribution, as was done in Refs. [15,16]. Thus, similar to the procedure in Appendix I, after incorporating Eq. (I9) in Eq. (I6), substituting the obtained expression in Eq. (I1) (also keeping in mind that $\vec{p}$ is 3D momentum of a final jet, and that we need to apply Eqs. (C14) and (C15)), we obtain the following expression for single-gluon radiation spectrum in the limit of uniformly distributed static scattering centers for massless gluons:

$$
\frac{dN_g^{(1)}}{dx} = \frac{C_2(G)\alpha_s}{\pi} \frac{L}{\lambda} \frac{(1-x+x^2)^2}{x(1-x)} \int \frac{d^2\mathbf{q}_1}{\pi} \frac{\mu^2}{\left(\mathbf{q}_1^2 + \mu^2\right)^2}
$$
$$
\times \int d\mathbf{k}^2 \left(\left\{ 1 - \frac{\sin\left(\frac{(\mathbf{k}-\mathbf{q}_1)^2}{2x(1-x)E}L\right)}{\frac{(\mathbf{k}-\mathbf{q}_1)^2}{2x(1-x)E}L} \right\} \frac{1}{(\mathbf{k}-\mathbf{q}_1)^2} \left[2 - \frac{\mathbf{k} \cdot (\mathbf{k}-\mathbf{q}_1)}{\mathbf{k}^2} - \frac{(\mathbf{k}-\mathbf{q}_1) \cdot (\mathbf{k}-x\mathbf{q}_1)}{(\mathbf{k}-x\mathbf{q}_1)^2} \right] \right.
$$
$$
\left. + \left\{ 1 - \frac{\sin\left(\frac{\mathbf{k}^2}{2x(1-x)E}L\right)}{\frac{\mathbf{k}^2}{2x(1-x)E}L} \right\} \frac{1}{\mathbf{k}^2} \left[1 - \frac{\mathbf{k} \cdot (\mathbf{k}-x\mathbf{q}_1)}{(\mathbf{k}-x\mathbf{q}_1)^2} \right] + \left[\frac{1}{(\mathbf{k}-x\mathbf{q}_1)^2} - \frac{1}{\mathbf{k}^2} \right] \right), \quad \text{(K1)}
$$

which is also symmetric to the exchange of radiated and final gluons, while the differential radiative energy loss for massless gluons in the case of the uniform distribution acquires the form

$$
\frac{dE^{(1)}}{dx} = \frac{C_2(G)\alpha_s}{\pi} \frac{L}{\lambda} E \frac{(1-x+x^2)^2}{(1-x)} \int \frac{d^2\mathbf{q}_1}{\pi} \frac{\mu^2}{\left(\mathbf{q}_1^2+\mu^2\right)^2}
$$

$$
\times \int d\mathbf{k}^2 \left(\left\{ 1 - \frac{\sin\left(\frac{(\mathbf{k}-\mathbf{q}_1)^2}{2x(1-x)E}L\right)}{\frac{(\mathbf{k}-\mathbf{q}_1)^2}{2x(1-x)E}L} \right\} \frac{1}{(\mathbf{k}-\mathbf{q}_1)^2} \left[2 - \frac{\mathbf{k}\cdot(\mathbf{k}-\mathbf{q}_1)}{\mathbf{k}^2} - \frac{(\mathbf{k}-\mathbf{q}_1)\cdot(\mathbf{k}-x\mathbf{q}_1)}{(\mathbf{k}-x\mathbf{q}_1)^2} \right] \right.
$$

$$
\left. + \left\{ 1 - \frac{\sin\left(\frac{\mathbf{k}^2}{2x(1-x)E}L\right)}{\frac{\mathbf{k}^2}{2x(1-x)E}L} \right\} \frac{1}{\mathbf{k}^2} \left[1 - \frac{\mathbf{k}\cdot(\mathbf{k}-x\mathbf{q}_1)}{(\mathbf{k}-x\mathbf{q}_1)^2} \right] + \left[\frac{1}{(\mathbf{k}-x\mathbf{q}_1)^2} - \frac{1}{\mathbf{k}^2} \right] \right). \tag{K2}
$$

Note that the L dependence in the case of uniform distribution of $\frac{dN^{(1)}}{dx}$ and $\frac{dE^{(1)}}{dx}$ (given by Eqs. (K1) and (K2)) is quite distinct from the one in the case of exponential distribution (given by Eqs. (I12) and (I13)).

In the same manner as in Appendix J, the single-gluon radiation spectrum and differential radiative energy loss for gluon-jet embedded in a finite-temperature QCD medium, i.e., for gluon with effective mass m_g [27], in the case of uniformly distributed scattering centers read as follows:

$$
\frac{dN_g^{(1)}}{dx} = \frac{C_2(G)\alpha_s}{\pi} \frac{L}{\lambda} \frac{(1-x+x^2)^2}{x(1-x)} \int \frac{d^2\mathbf{q}_1}{\pi} \frac{\mu^2}{\left(\mathbf{q}_1^2+\mu^2\right)^2}
$$

$$
\times \int d\mathbf{k}^2 \left(\left\{ 1 - \frac{\sin\left(\frac{(\mathbf{k}-\mathbf{q}_1)^2+\chi}{2x(1-x)E}L\right)}{\frac{(\mathbf{k}-\mathbf{q}_1)^2+\chi}{2x(1-x)E}L} \right\} \frac{1}{(\mathbf{k}-\mathbf{q}_1)^2+\chi} \left[2\frac{(\mathbf{k}-\mathbf{q}_1)^2}{(\mathbf{k}-\mathbf{q}_1)^2+\chi} - \frac{\mathbf{k}\cdot(\mathbf{k}-\mathbf{q}_1)}{\mathbf{k}^2+\chi} - \frac{(\mathbf{k}-\mathbf{q}_1)\cdot(\mathbf{k}-x\mathbf{q}_1)}{(\mathbf{k}-x\mathbf{q}_1)^2+\chi} \right] \right.
$$

$$
\left. + \left\{ 1 - \frac{\sin\left(\frac{\mathbf{k}^2+\chi}{2x(1-x)E}L\right)}{\frac{\mathbf{k}^2+\chi}{2x(1-x)E}L} \right\} \frac{1}{\mathbf{k}^2+\chi} \left[\frac{\mathbf{k}^2}{\mathbf{k}^2+\chi} - \frac{\mathbf{k}\cdot(\mathbf{k}-x\mathbf{q}_1)}{(\mathbf{k}-x\mathbf{q}_1)^2+\chi} \right] + \left\{ \frac{(\mathbf{k}-x\mathbf{q}_1)^2}{[(\mathbf{k}-x\mathbf{q}_1)^2+\chi]^2} - \frac{\mathbf{k}^2}{(\mathbf{k}^2+\chi)^2} \right\} \right) \tag{K3}
$$

and

$$
\frac{dE^{(1)}}{dx} = \frac{C_2(G)\alpha_s}{\pi} \frac{L}{\lambda} E \frac{(1-x+x^2)^2}{(1-x)} \int \frac{d^2\mathbf{q}_1}{\pi} \frac{\mu^2}{\left(\mathbf{q}_1^2+\mu^2\right)^2}
$$

$$
\times \int d\mathbf{k}^2 \left(\left\{ 1 - \frac{\sin\left(\frac{(\mathbf{k}-\mathbf{q}_1)^2+\chi}{2x(1-x)E}L\right)}{\frac{(\mathbf{k}-\mathbf{q}_1)^2+\chi}{2x(1-x)E}L} \right\} \frac{1}{(\mathbf{k}-\mathbf{q}_1)^2+\chi} \left[2\frac{(\mathbf{k}-\mathbf{q}_1)^2}{(\mathbf{k}-\mathbf{q}_1)^2+\chi} - \frac{\mathbf{k}\cdot(\mathbf{k}-\mathbf{q}_1)}{\mathbf{k}^2+\chi} - \frac{(\mathbf{k}-\mathbf{q}_1)\cdot(\mathbf{k}-x\mathbf{q}_1)}{(\mathbf{k}-x\mathbf{q}_1)^2+\chi} \right] \right.
$$

$$
\left. + \left\{ 1 - \frac{\sin\left(\frac{\mathbf{k}^2+\chi}{2x(1-x)E}L\right)}{\frac{\mathbf{k}^2+\chi}{2x(1-x)E}L} \right\} \frac{1}{\mathbf{k}^2+\chi} \left[\frac{\mathbf{k}^2}{\mathbf{k}^2+\chi} - \frac{\mathbf{k}\cdot(\mathbf{k}-x\mathbf{q}_1)}{(\mathbf{k}-x\mathbf{q}_1)^2+\chi} \right] + \left\{ \frac{(\mathbf{k}-x\mathbf{q}_1)^2}{[(\mathbf{k}-x\mathbf{q}_1)^2+\chi]^2} - \frac{\mathbf{k}^2}{(\mathbf{k}^2+\chi)^2} \right\} \right). \tag{K4}
$$

Note that Eq. (K3) is also symmetric to the exchange of radiated and final gluons, and in massless case reproduces Eq. (K1), whereas Eq. (K4) for $m_g \to 0$ coincides with our massless beyond soft-gluon approximation expression, Eq. (K2). Again, by comparing analytical expressions given by Eqs. (K3) and (K4) with Eqs. (J14) and (J15), we observe significantly different L dependences in these two opposite cases of longitudinal distance distribution.

Finally, the number of radiated gluons and fractional radiative energy loss to the first order in opacity and beyond the soft-gluon approximation for gluons with effective mass m_g in the limit of uniform longitudinal distance distribution, respectively, read

$$
N_g^{(1)} = \frac{C_2(G)\alpha_s}{\pi} \frac{L}{\lambda} \int_0^{\frac{1}{2}} dx \frac{(1-x+x^2)^2}{x(1-x)} \int \frac{d^2\mathbf{q}_1}{\pi} \frac{\mu^2}{\left(\mathbf{q}_1^2+\mu^2\right)^2}
$$

$$
\times \int d\mathbf{k}^2 \left(\left\{ 1 - \frac{\sin\left(\frac{(\mathbf{k}-\mathbf{q}_1)^2+\chi}{2x(1-x)E}L\right)}{\frac{(\mathbf{k}-\mathbf{q}_1)^2+\chi}{2x(1-x)E}L} \right\} \frac{1}{(\mathbf{k}-\mathbf{q}_1)^2+\chi} \left[2\frac{(\mathbf{k}-\mathbf{q}_1)^2}{(\mathbf{k}-\mathbf{q}_1)^2+\chi} - \frac{\mathbf{k}\cdot(\mathbf{k}-\mathbf{q}_1)}{\mathbf{k}^2+\chi} - \frac{(\mathbf{k}-\mathbf{q}_1)\cdot(\mathbf{k}-x\mathbf{q}_1)}{(\mathbf{k}-x\mathbf{q}_1)^2+\chi} \right] \right.
$$

$$
\left. + \left\{ 1 - \frac{\sin\left(\frac{\mathbf{k}^2+\chi}{2x(1-x)E}L\right)}{\frac{\mathbf{k}^2+\chi}{2x(1-x)E}L} \right\} \frac{1}{\mathbf{k}^2+\chi} \left[\frac{\mathbf{k}^2}{\mathbf{k}^2+\chi} - \frac{\mathbf{k}\cdot(\mathbf{k}-x\mathbf{q}_1)}{(\mathbf{k}-x\mathbf{q}_1)^2+\chi} \right] + \left\{ \frac{(\mathbf{k}-x\mathbf{q}_1)^2}{[(\mathbf{k}-x\mathbf{q}_1)^2+\chi]^2} - \frac{\mathbf{k}^2}{(\mathbf{k}^2+\chi)^2} \right\} \right) \tag{K5}
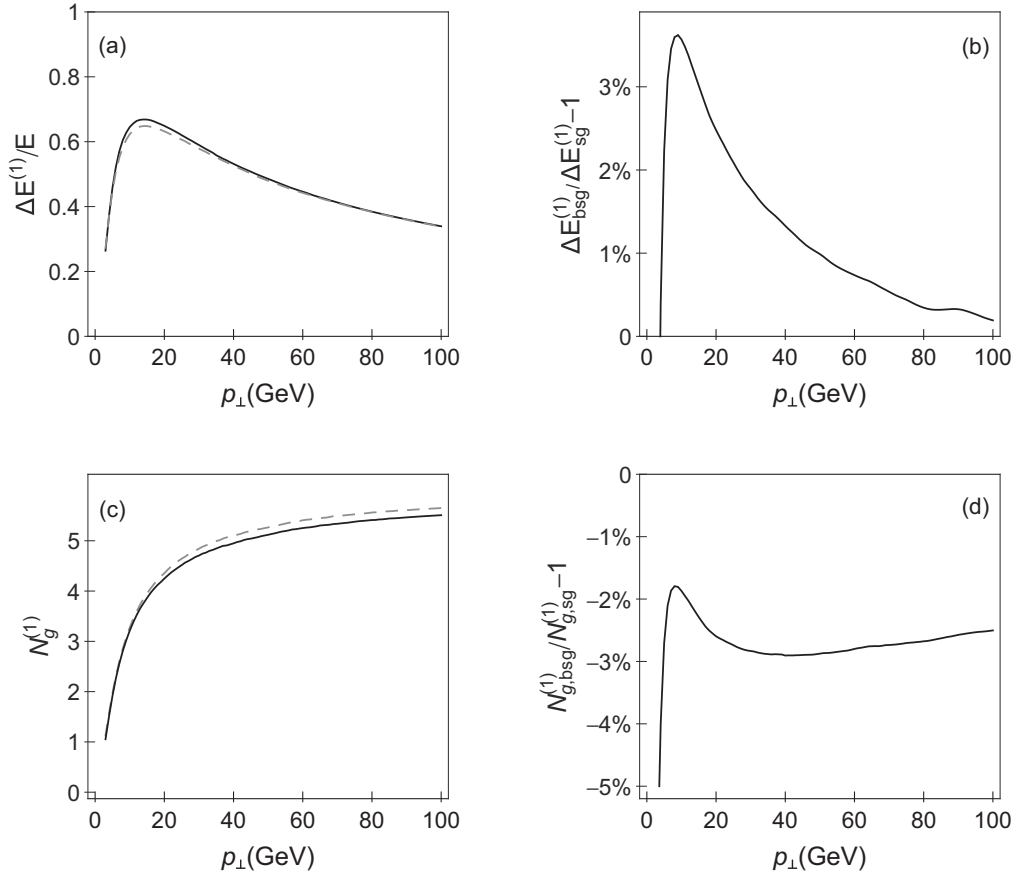$$

FIG. 13. The counterpart of Fig. 1, when uniform longitudinal distance distribution is considered. The effect of relaxing the soft-gluon approximation on integrated variables to the first order in opacity of DGLV formalism, as a function of $p_\perp$. (a) Comparison of gluon's fractional radiative energy loss in the *bsg* (solid curve) case with the *sg* (dashed curve) case. (b) The percentage change of the radiative energy loss when the soft-gluon approximation is relaxed with respect to the *sg* case. (c) Comparison of number of radiated gluons in *bsg* (solid curve) with *sg* (dashed curve) case. (d) The relative change of radiated gluon number when the soft-gluon approximation is relaxed with respect to the *sg* case.

and

$$
\frac{\Delta E^{(1)}}{E} = \frac{C_2(G)\alpha_s}{\pi} \frac{L}{\lambda} \int_0^{\frac{1}{2}} dx \frac{(1-x+x^2)^2}{(1-x)} \int \frac{d^2\mathbf{q}_1}{\pi} \frac{\mu^2}{\left(\mathbf{q}_1^2+\mu^2\right)^2}
$$

$$
\times \int d\mathbf{k}^2 \left(\left\{ 1 - \frac{\sin\left(\frac{(\mathbf{k}-\mathbf{q}_1)^2+\chi}{2x(1-x)E}L\right)}{\frac{(\mathbf{k}-\mathbf{q}_1)^2+\chi}{2x(1-x)E}L} \right\} \frac{1}{(\mathbf{k}-\mathbf{q}_1)^2+\chi} \left[2\frac{(\mathbf{k}-\mathbf{q}_1)^2}{(\mathbf{k}-\mathbf{q}_1)^2+\chi} - \frac{\mathbf{k}\cdot(\mathbf{k}-\mathbf{q}_1)}{\mathbf{k}^2+\chi} - \frac{(\mathbf{k}-\mathbf{q}_1)\cdot(\mathbf{k}-x\mathbf{q}_1)}{(\mathbf{k}-x\mathbf{q}_1)^2+\chi} \right] \right.
$$

$$
\left. + \left\{ 1 - \frac{\sin\left(\frac{\mathbf{k}^2+\chi}{2x(1-x)E}L\right)}{\frac{\mathbf{k}^2+\chi}{2x(1-x)E}L} \right\} \frac{1}{\mathbf{k}^2+\chi} \left[\frac{\mathbf{k}^2}{\mathbf{k}^2+\chi} - \frac{\mathbf{k}\cdot(\mathbf{k}-x\mathbf{q}_1)}{(\mathbf{k}-x\mathbf{q}_1)^2+\chi} \right] + \left\{ \frac{(\mathbf{k}-x\mathbf{q}_1)^2}{[(\mathbf{k}-x\mathbf{q}_1)^2+\chi]^2} - \frac{\mathbf{k}^2}{(\mathbf{k}^2+\chi)^2} \right\} \right). \quad \text{(K6)}
$$

Note that Eq. (K6) in the soft-gluon limit reduces to Eq. (2.13) from Ref. [16] (or equivalently, to static case of Eq. (1) from Ref. [15]) for gluons, where likewise the uniform distribution was used.

The above obtained notably different expressions for uniform (compared to the exponential) distribution of static scattering centers require assessing the sensitivity of our conclusions on the importance of the soft-gluon approxima-

tion to the considered distribution. Therefore, in this section we also use the uniform distribution case and display the effect of finite x on the numerical predictions for the same variables as in Sec. VI.

By comparing Figs. 13–15 with the corresponding figures from Sec. VI (i.e., Figs. 1, 2, and 4), we infer that the results obtained in this section are quite similar to the ones obtained with exponential distribution in Sec. VI. From this, it follows
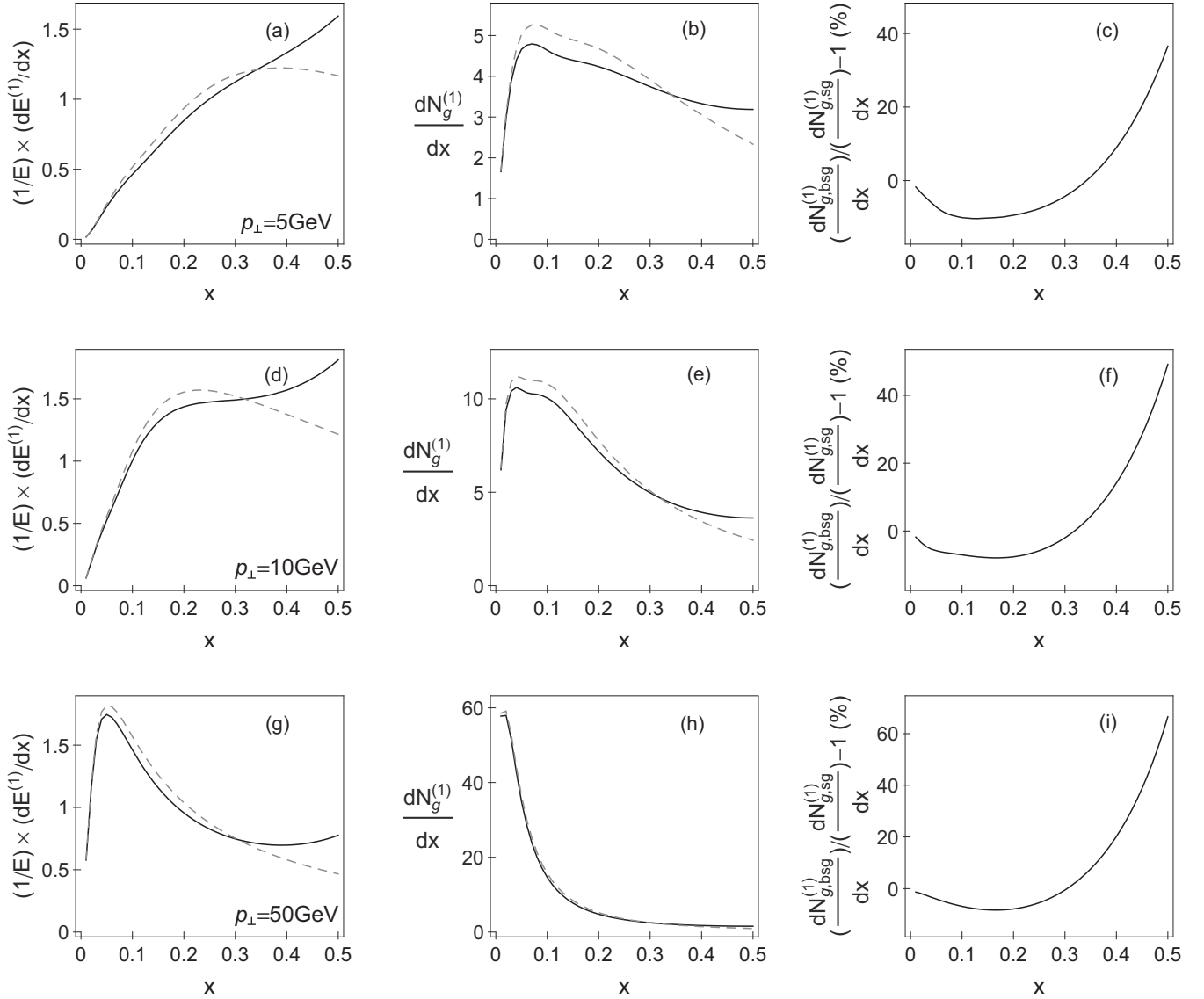
FIG. 14. The counterpart of Fig. 2, when uniform longitudinal distance distribution is considered. The effect of relaxing the soft-gluon approximation on differential variables to the first order in opacity of DGLV formalism, as a function of x. The comparison of $(1/E) \times (dE^{(1)}/dx)$ and $dN_g^{(1)}/dx$ between the *bsg* (solid curve) case and the *sg* (dashed curve) case, for different values of initial jet $p_\perp$ (5, 10, and 50 GeV, as indicated in panels) is shown in the first ((a), (d), and (g)) and second ((b), (e), and (h)) columns, respectively. The quantification of the effect on the single-gluon radiation spectrum and its expression in percentage is shown in panels (c), (f) and (i).

that our conclusions with respect to the importance of the soft-gluon approximation, presented in Secs. III to VII, are robust to the presumed longitudinal distance distribution. Note that curves forming in this section are less smooth compared to the one from Sec. VI, due to oscillating sine functions in the corresponding analytical expressions (Eqs. (K3) to (K6)).

APPENDIX L: RELEVANT REGION FOR THE IMPORTANCE OF THE SOFT-GLUON APPROXIMATION

Based on the reasoning outlined in Sec. VI (see Fig. 5 and the corresponding intuitive explanation), we marked $x \lesssim 0.4$ as the relevant region for the importance of the soft-gluon approximation; in this section, we study this issue in more

detail. We first note that claiming that a certain region is not relevant for relaxing the soft-gluon approximation does not mean that this whole region can be rejected, but that the beyond soft-gluon expression does not have to be applied in that region.

Therefore, for reliable suppression predictions, one has to take into account the entire x region, while in the following lines we address the necessity of relaxing the soft-gluon approximation in a certain region.

To address this goal, we first note that Figs. 2 and 3 highlight both more "conservative" $x \approx 0.4$ and $x \approx 0.3$ values as the upper limit of the relevant region. Thus, in the text, we want to address which of the following two points is better to define as a border point of the relevant region for
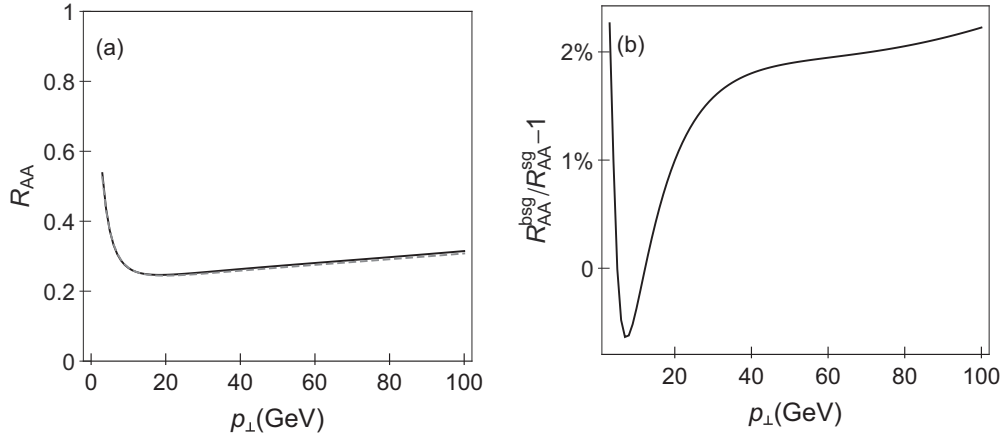
FIG. 15. The counterpart of Fig. 4, when uniform longitudinal distance distribution is considered. The effect of relaxing the soft-gluon approximation on gluon R_{AA} as a function of final $p_\perp$. (a) Comparison of gluon-jet R_{AA} between the *bsg* (solid curve) case and the *sg* (dashed curve) case. (b) The quantification of the effect and its expression in percentage.

differentiating between *bsg* and *sg* R_{AA} predictions. Thus, in Fig. 16 we compare suppressions obtained from the *bsg* expression for the entire $x \leqslant 0.5$ region, first with (i) results

obtained from the *bsg* expression for $x \leqslant 0.4$ combined with the *sg* expression for $x > 0.4$ (Figs. 16(a) and 16(b)) and then with (ii) results obtained from the *bsg* expression for $x \leqslant 0.3$
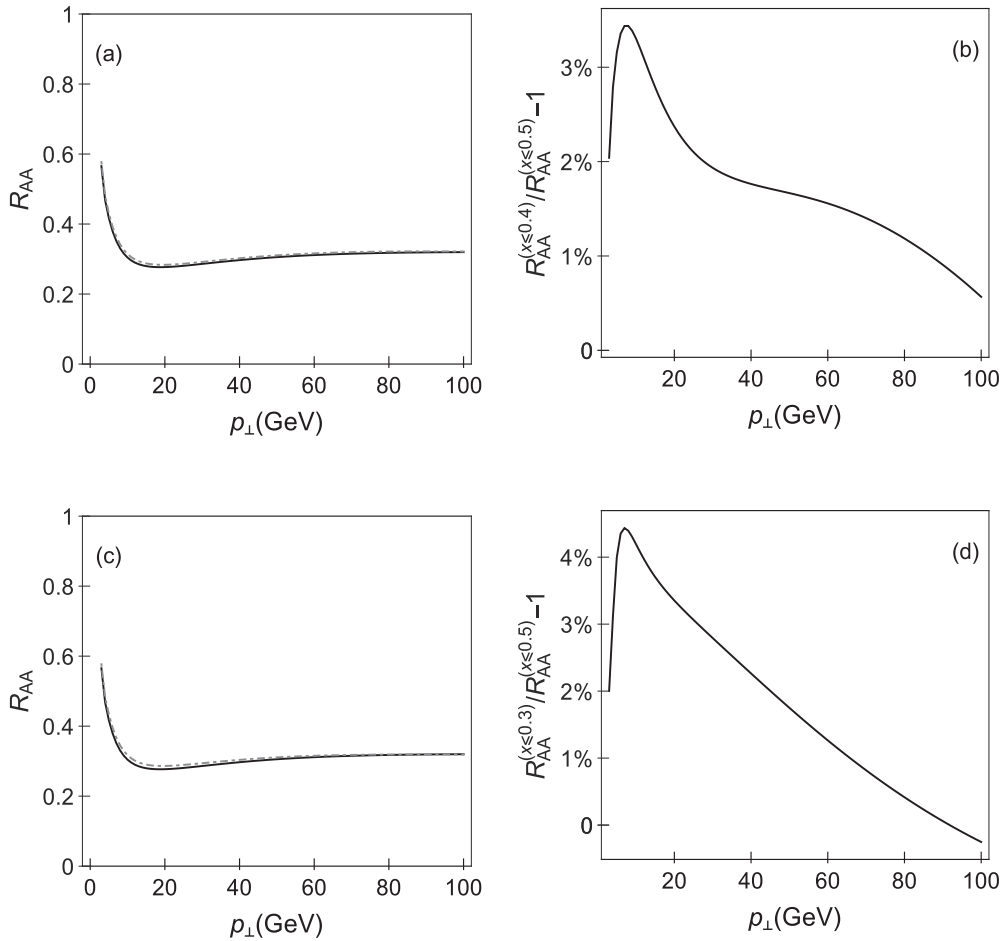
FIG. 16. The two scenarios of relevant x regions for the importance of the soft-gluon approximation. The effect of relaxing the soft-gluon approximation on R_{AA} as a function of $p_\perp$. The suppression of gluon jet beyond the soft-gluon approximation (solid curve) is compared to the combined R_{AA} (dot-dashed curve), obtained from (i) *bsg* expression for $x \leqslant 0.4$ combined with *sg* expression for $x > 0.4$ in panel (a) ((ii) *bsg* expression for $x \leqslant 0.3$ combined with *sg* expression for $x > 0.3$ in panel (c)). The quantification of the effect and its expression in percentage for these two scenarios are presented in panels (b) and (d), respectively.

combined with the sg expression for $x > 0.3$ (Figs. 16(c) and 16(d)).

From Fig. 16, we observe that both $x = 0.3$ and $x = 0.4$ can be defined as a border point for the importance of the soft-gluon approximation. However, based on the fact that the difference between bsg and combined R_{AA} for case (i) is smaller than for case (ii), and that taking into account that the $0.3 < x \leqslant 0.4$ region balances negative and positive $\frac{dN_g^{(1)}}{dx}$ contributions of relaxing the soft-gluon approximation (see, e.g., Fig. 3), it is safer to claim that more "conservative" region $x \lesssim 0.4$ (i) is the relevant one.

---

[1] U. A. Wiedemann, Nucl. Phys. B **588**, 303 (2000).
[2] C. A. Salgado and U. A. Wiedemann, Phys. Rev. D **68**, 014008 (2003).
[3] N. Armesto, C. A. Salgado, and U. A. Wiedemann, Phys. Rev. D **69**, 114003 (2004).
[4] R. Baier, Y. L. Dokshitzer, A. H. Mueller, S. Peigne, and D. Schiff, Nucl. Phys. B **483**, 291 (1997).
[5] R. Baier, Y. L. Dokshitzer, A. H. Mueller, S. Peigne, and D. Schiff, Nucl. Phys. B **484**, 265 (1997).
[6] B. G. Zakharov, JETP Lett. **63**, 952 (1996).
[7] B. G. Zakharov, JETP Lett. **65**, 615 (1997).
[8] M. Gyulassy, P. Levai, and I. Vitev, Nucl. Phys. B **571**, 197 (2000).
[9] M. Gyulassy, P. Levai, and I. Vitev, Nucl. Phys. B **594**, 371 (2001).
[10] X. N. Wang and X. F. Guo, Nucl. Phys. A **696**, 788 (2001).
[11] A. Majumder and M. Van Leeuwen, Prog. Part. Nucl. Phys. A **66**, 41 (2011).
[12] L. Apolinario, N. Armesto, and C. A. Salgado, Phys. Lett. B **718**, 160 (2012).
[13] B. W. Zhang and X. N. Wang, Nucl. Phys. A **720**, 429 (2003).
[14] G. Ovanesyan and I. Vitev, J. High Energy Phys. 06 (2011) 080; Phys. Lett. B **706**, 371 (2012).
[15] M. Djordjevic and U. Heinz, Phys. Rev. Lett. **101**, 022302 (2008).
[16] M. Djordjevic, Phys. Rev. C **80**, 064909 (2009).
[17] M. Djordjevic and M. Djordjevic, Phys. Lett. B **734**, 286 (2014).
[18] D. d'Enterria and B. Betz, Lect. Notes Phys. **785**, 285 (2010).
[19] A. Dainese, Eur. Phys. J. C **33**, 495 (2004).
[20] M. Djordjevic and M. Djordjevic, Phys. Rev. C **90**, 034910 (2014).
[21] M. Djordjevic, M. Djordjevic, and B. Blagojevic, Phys. Lett. B **737**, 298 (2014).
[22] M. Djordjevic, Phys. Rev. Lett. **112**, 042302 (2014).
[23] M. Djordjevic and M. Djordjevic, Phys. Rev. C **92**, 024918 (2015).
[24] M. Djordjevic, B. Blagojevic, and L. Zivkovic, Phys. Rev. C **94**, 044908 (2016).
[25] M. Djordjevic and M. Gyulassy, Nucl. Phys. A **733**, 265 (2004).
[26] M. Gyulassy and X. N. Wang, Nucl. Phys. B **420**, 583 (1994).
[27] M. Djordjevic and M. Gyulassy, Phys. Rev. C **68**, 034914 (2003).
[28] J. D. Bjorken, Tech. Rep. FERMILAB-PUB-82-059-THY, 1982 (unpublished).
[29] M. Gyulassy, P. Levai, and I. Vitev, Phys. Lett. B **538**, 282 (2002).
[30] S. Wicks, arXiv:0804.4704.
[31] G. Altarelli and G. Parisi, Nucl. Phys. B **126**, 298 (1977).
[32] M. Gyulassy, P. Levai, and I. Vitev, Phys. Rev. Lett. **85**, 5535 (2000).
[33] S. Wicks, W. Horowitz, M. Djordjevic, and M. Gyulassy, Nucl. Phys. A **784**, 426 (2007).
[34] Z. B. Kang, I. Vitev, and H. Xing, Phys. Lett. B **718**, 482 (2012).
[35] R. Sharma, I. Vitev, and B. W. Zhang, Phys. Rev. C **80**, 054902 (2009).
[36] R. J. Glauber and G. Matthiae, Nucl. Phys. B **21**, 135 (1970).
[37] B. Hahn, D. G. Ravenhall, and R. Hoftstadter, Phys. Rep. **101**, 1131 (1956).
[38] R. D. Field, *Applications of Perturbative QCD* (Perseus Books, Cambridge, MA, 1995).
[39] M. Djordjevic and M. Djordjevic, Phys. Lett. B **709**, 229 (2012).
[40] J. P. Ellis, Comp. Phys. Commun. **210**, 103 (2017).
[41] Z. B. Kang, F. Ringer, and I. Vitev, J. High Energy Phys. 03 (2017) 146.
[42] M. Gyulassy, P. Levai, and I. Vitev, Nucl. Phys. B **661**, 637c (1999).

Features of CRISPR-Cas Regulation Key to Highly Efficient and Temporally-Specific crRNA Production

Andjela Rodic[1,2], Bojana Blagojevic[3], Magdalena Djordjevic[3], Konstantin Severinov[4,5] and Marko Djordjevic[1]*

[1] *Faculty of Biology, Institute of Physiology and Biochemistry, University of Belgrade, Belgrade, Serbia,* [2] *Multidisciplinary PhD Program in Biophysics, University of Belgrade, Belgrade, Serbia,* [3] *Institute of Physics Belgrade, University of Belgrade, Belgrade, Serbia,* [4] *Waksman Institute of Microbiology, Rutgers University, Piscataway, NJ, United States,* [5] *Skolkovo Institute of Science and Technology, Skolkovo, Russia*

Bacterial immune systems, such as CRISPR-Cas or restriction-modification (R-M) systems, affect bacterial pathogenicity and antibiotic resistance by modulating horizontal gene flow. A model system for CRISPR-Cas regulation, the Type I-E system from *Escherichia coli*, is silent under standard laboratory conditions and experimentally observing the dynamics of CRISPR-Cas activation is challenging. Two characteristic features of CRISPR-Cas regulation in *E. coli* are cooperative transcription repression of *cas* gene and CRISPR array promoters, and fast non-specific degradation of full length CRISPR transcripts (pre-crRNA). In this work, we use computational modeling to understand how these features affect the system expression dynamics. Signaling which leads to CRISPR-Cas activation is currently unknown, so to bypass this step, we here propose a conceptual setup for *cas* expression activation, where *cas* genes are put under transcription control typical for a restriction-modification (R-M) system and then introduced into a cell. Known transcription regulation of an R-M system is used as a proxy for currently unknown CRISPR-Cas transcription control, as both systems are characterized by high cooperativity, which is likely related to similar dynamical constraints of their function. We find that the two characteristic CRISPR-Cas control features are responsible for its temporally-specific dynamical response, so that the system makes a steep (switch-like) transition from OFF to ON state with a time-delay controlled by pre-crRNA degradation rate. We furthermore find that cooperative transcription regulation qualitatively leads to a cross-over to a regime where, at higher pre-crRNA processing rates, crRNA generation approaches the limit of an infinitely abrupt system induction. We propose that these dynamical properties are associated with rapid expression of CRISPR-Cas components and efficient protection of bacterial cells against foreign DNA. In terms of synthetic applications, the setup proposed here should allow highly efficient expression of small RNAs in a narrow time interval, with a specified time-delay with respect to the signal onset.

Keywords: CRISPR-Cas activation, pre-crRNA processing, CRISPR regulation, crRNA generation, biophysical modeling

INTRODUCTION

CRISPR-Cas are adaptive immune systems, which defend prokaryotic cells against foreign DNA, including viruses and plasmids. A CRISPR-Cas system consists of a CRISPR (Clustered Regularly Interspaced Short Palindromic Repeats) array and associated *cas* genes (Makarova et al., 2006; Barrangou et al., 2007; Brouns et al., 2008; Hille and Charpentier, 2016). CRISPR arrays consist of identical direct repeats (R) of about 30 bp in length, interspaced with spacers (S) of similar length and variable sequence. Spacer sequences are often complementary to fragments of viral or plasmid DNA. A match between a CRISPR spacer and invading phage (bacterial virus) sequence provides immunity to infection (Barrangou et al., 2007; Hille and Charpentier, 2016). The entire CRISPR locus is initially transcribed as a long transcript (called pre-crRNA) (Pougach et al., 2010; Pul et al., 2010), which is further processed by Cas proteins to small protective CRISPR RNAs (called crRNAs) (Brouns et al., 2008; Pougach et al., 2010; Djordjevic et al., 2012). crRNAs are responsible for recognition and, together with Cas proteins, inactivation of invading foreign genetic elements (Brouns et al., 2008; Al-Attar et al., 2011). Cas proteins also take part in CRISPR adaptation, which is a process in which new spacers from viral genomes are inserted in CRISPR array. **Figure 1** shows a schematic gene diagram for Type I-E CRISPR-Cas from *E. coli*, (Mojica and Diez-Villasenor, 2010; Patterson et al., 2017), which we consider in this paper. The *cas* genes and the CRISPR array are transcribed from separate promoters, which are located inside of the intergenic regions here denoted by IGLB and L (the leader sequence), respectively (see **Figure 1**; Pougach et al., 2010; Pul et al., 2010).

Promoters for *cas* operon and the CRISPR array are repressed in Type I-E CRISPR-Cas in *E. coli* (Pougach et al., 2010; Pul et al., 2010; Westra et al., 2010), which makes this system silent under standard conditions. Consequently, to generate crRNAs that can protect the bacterial cell, CRISPR-Cas has to be activated. Thus, to understand the system function it is crucial to understand the main features that control dynamics of CRISPR-Cas activation (Mojica and Diez-Villasenor, 2010; Richter et al., 2012; Patterson et al., 2017). However, approaching this problem experimentally is complicated due to the following:

i. It requires direct experimental observation of *in vivo* dynamics of molecular species (proteins or RNA) in a cell (see e.g., Morozova et al., 2015).

ii. The signaling which leads to system induction is currently unclear (Ratner et al., 2015; Patterson et al., 2017), e.g., even a viral infection, an obvious trigger, is not sufficient to activate the system.

iii. To understand the roles of the key system features in its response/dynamics these features would have to be perturbed, which may require extensive reengineering of the system.

A complementary approach is to use mathematical/biophysical modeling to assess how different features of CRISPR-Cas expression affect system dynamics. Moreover, *in silico* analysis allows one to study alternative system architectures, and/or to perturb the natural system (see e.g., Rodic et al., 2017), which in turn allows understanding the role of its key regulatory features.

Experimental research has led to a consistent picture of the main CRISPR-Cas regulatory features in closely related *E. coli* and *Salmonella enterica* (Pul et al., 2010; Westra et al., 2010; Medina-Aparicio et al., 2011). Under standard conditions, promoters for both CRISPR array and *cas* genes are repressed by global regulators (H-NS and LRP). Repression by these regulators is highly cooperative, as their binding is nucleated at certain position, and then extends along the DNA through cooperative interactions between repressor molecules (Bouffartigues et al., 2007). Additional regulators, such as CRP, may also be involved in the repression of *cas* operon (Yang et al., 2014). While the exact signaling mechanism remains unclear, this repression must be relieved upon appropriate external signal (e.g., envelope stress that may signal bacteriophage invasion), through the action of transcription activators (LexA, LeuO, and BaeR-S are likely involved) (Richter et al., 2012; Patterson et al., 2017). In particular, for Type I-E CRISPR-Cas in *E. coli*, it was shown that cooperative repression by H-NS can be relieved by elevated amount of LeuO (Pul et al., 2010; Westra et al., 2010). Thus, highly cooperative repression, which is abolished by transcription activators, emerges as a major feature of CRISPR-Cas transcription control in *E. coli* and its relatives.

Another crucial mechanism in CRISPR-Cas expression is pre-crRNA transcript processing (Brouns et al., 2008; Pougach et al., 2010). Experiments in *E. coli*, reported that overexpression of
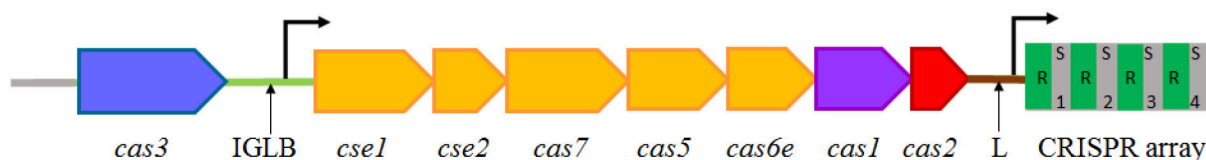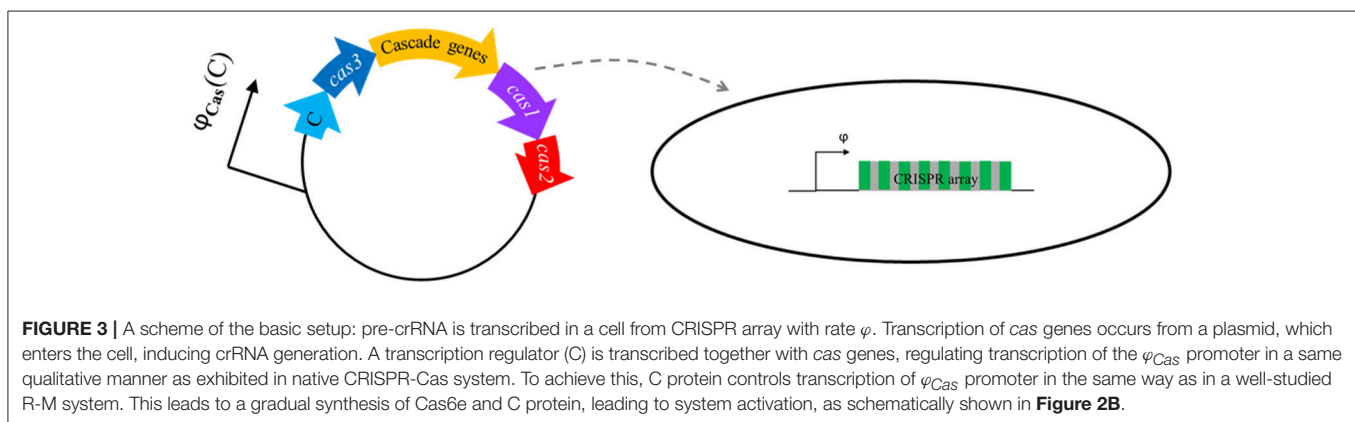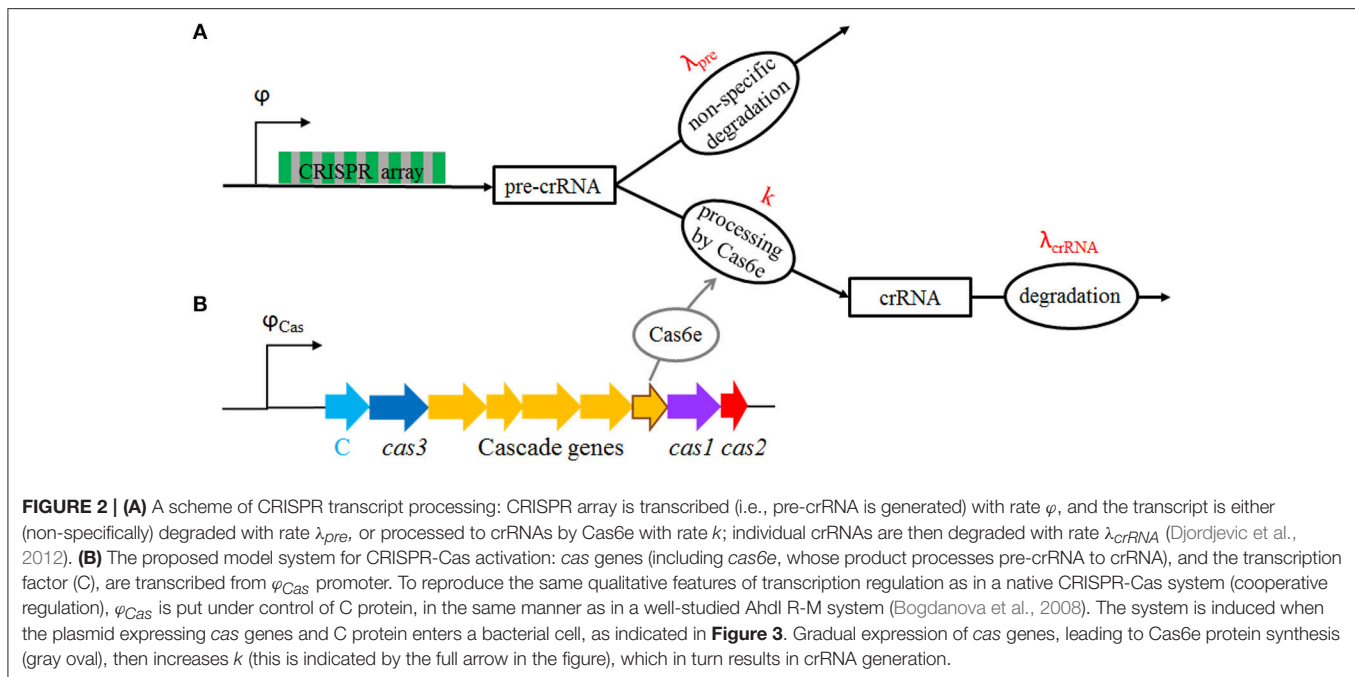

FIGURE 1 | A scheme of a Type I-E CRISPR-Cas system from *E coli* (Al-Attar et al., 2011; Makarova et al., 2011, 2015). The *cas* genes and the CRISPR array are indicated. R and S within the CRISPR array correspond, respectively, to repeats and spacers; note that the spacer sequences differ from each other, and are labeled by consecutive numbers (1, 2, 3...). IGLB and L correspond to intergenic regions where promoters for the Cascade complex genes (*cse1,2, cas7,5,6e*) and the Cas1,2 adaptation proteins (IGLB) and the CRISPR array (L) are located. The two promoters within IGLB and L are indicated by arrows. One of the Cas proteins (Cas6e) is responsible for processing pre-crRNA to crRNA. The effector Cascade complex is composed of proteins encoded by genes marked with yellow color. It binds crRNA, which recognizes invading DNA. Once recognized, foreign DNA is destroyed by the product of *cas3* (Brouns et al., 2008).

FIGURE 2 | (A) A scheme of CRISPR transcript processing: CRISPR array is transcribed (i.e., pre-crRNA is generated) with rate φ, and the transcript is either (non-specifically) degraded with rate λ_{pre}, or processed to crRNAs by Cas6e with rate k; individual crRNAs are then degraded with rate λ_{crRNA} (Djordjevic et al., 2012). **(B)** The proposed model system for CRISPR-Cas activation: *cas* genes (including *cas6e*, whose product processes pre-crRNA to crRNA), and the transcription factor (C), are transcribed from φ_{Cas} promoter. To reproduce the same qualitative features of transcription regulation as in a native CRISPR-Cas system (cooperative regulation), φ_{Cas} is put under control of C protein, in the same manner as in a well-studied AhdI R-M system (Bogdanova et al., 2008). The system is induced when the plasmid expressing *cas* genes and C protein enters a bacterial cell, as indicated in **Figure 3**. Gradual expression of *cas* genes, leading to Cas6e protein synthesis (gray oval), then increases k (this is indicated by the full arrow in the figure), which in turn results in crRNA generation.

FIGURE 3 | A scheme of the basic setup: pre-crRNA is transcribed in a cell from CRISPR array with rate φ. Transcription of *cas* genes occurs from a plasmid, which enters the cell, inducing crRNA generation. A transcription regulator (C) is transcribed together with *cas* genes, regulating transcription of the φ_{Cas} promoter in a same qualitative manner as exhibited in native CRISPR-Cas system. To achieve this, C protein controls transcription of φ_{Cas} promoter in the same way as in a well-studied R-M system. This leads to a gradual synthesis of Cas6e and C protein, leading to system activation, as schematically shown in **Figure 2B**.

Cas6e (which is responsible for pre-crRNA processing) generates highly abundant crRNAs from pre-crRNA which is present at low abundance (Pougach et al., 2010). We previously showed that a simple quantitative model—whose relevant kinetic scheme is shown in **Figure 2A**—explains this observation (Djordjevic et al., 2012), so that a small decrease in pre-crRNA abundance leads to a much larger (around two orders of magnitude) increase in crRNA abundance. Interestingly, the main mechanism responsible for this strong amplification is fast non-specific degradation of pre-crRNA (see **Figure 2**) by unidentified nuclease(s). In particular, when cas genes expression increases, processing of pre-crRNA by Cas6e is favored and diverts the entire pre-crRNA molecule away from the path of non-specific degradation. Therefore, the fast non-specific degradation of pre-crRNA should be considered as a second major regulatory feature of CRISPR-Cas expression.

The modeling described in Djordjevic et al. (2012) took into account only the transcript processing step, i.e., it was assumed that there is an infinitely abrupt (stepwise) increase of pre-crRNA

to crRNA processing rate, and pre-crRNA generation rate. This is, however, a clear idealization of the induction mechanism, as transcription regulation of *cas* genes and CRISPR array promoters is neglected. That is, in reality, pre-crRNA processing rate can be increased only gradually, as it takes time to synthesize the needed Cas proteins. The rate of Cas proteins synthesis is in turn directly related to the transcription control of the *cas* gene promoter in the IGLB region (see **Figure 1**). Similarly, the rate by which pre-crRNA is synthesized is determined by the transcription control of the CRISPR array promoter (L region).

Consequently, a more realistic model of CRISPR-Cas expression dynamics has to take into account both the regulation of CRISPR array and Cas protein synthesis, and CRISPR transcript processing. However, a major obstacle in achieving such model is that signaling which leads to the system induction, and detailed mechanism of CRISPR-Cas transcription regulation, is still unclear. We here propose a model system for CRISPR-Cas induction by assuming that activation of crRNA production

is put under transcriptional control exhibited in a restriction-modification (R-M) immune system (Pingoud et al., 2014). As argued below, such model system would have qualitative features of transcription regulation expected for a CRISPR-Cas, and will keep the same transcript processing mechanism as that described for native system. On the other hand, this model system allows bypassing the currently unknown signaling that leads to CRISPR-Cas activation, and can be readily analyzed *in silico*, since transcription regulation of a well-studied R-M system (AhdI, see Bogdanova et al., 2008)—for which we previously showed that it can be reliably modeled (see below)—is used as a proxy for transcription regulation of CRISPR-Cas system.

Through this approach, we expect to:

  i. Obtain quantitatively more realistic model of CRISPR-Cas induction dynamics, in which the transcription regulation, i.e., the gradual synthesis of relevant enzymes and transcription regulators is explicitly taken into account.
  ii. Qualitatively understand the main features of CRISPR-Cas induction, in particular the roles of cooperative transcription regulation, and of fast non-specific degradation of pre-crRNA.
 iii. Propose an experimental setup for CRISPR-Cas induction that mimics the main qualitative features of the native system.

The setup of the model will be explicitly considered in the next subsection.

RESULTS

In silico Experiment Setup
The Model System

We start from a CRISPR transcript processing scheme, which is shown in **Figure 2**. According to this scheme, pre-crRNA is generated with rate φ, and subsequently either non-specifically degraded (due to activity of an unspecified nuclease) with rate λ_{pre}, or is processed by Cas6e to crRNAs with rate k. crRNAs are subsequently degraded with rate λ_{crRNA}. All the parameters in the scheme are experimentally determined in (Djordjevic et al., 2012) (for Type I-E CRISPR-Cas in *E. coli*) and explicitly stated in Methods. In particular, the main feature of the transcript processing is a large (non-specific) pre-crRNA degradation rate (with $\lambda_{pre} \sim 1$ 1/min), which is much larger than crRNA degradation rate (with $\lambda_{crRNA} \sim 1/100$ 1/min). In the experiments, crRNA production is artificially activated, by overexpressing Cas6e from a plasmid, which increases pre-crRNA processing rate (k) for between one and two orders of magnitude (between $10\lambda_{pre}$ and $100\lambda_{pre}$). While the repression of the *cas* promoter in IGLB region (see **Figure 1**) is very strong, with very small amount of Cas6e synthesized when the system is uninduced, the repression of the CRISPR array promoter is significantly weaker, with rather strong basal rate of pre-crRNA generation ($\varphi \sim 10$ 1/min) (Pougach et al., 2010; Pul et al., 2010; Westra et al., 2010; Djordjevic et al., 2012).

As indicated in the Introduction, we previously modeled the transcript processing mechanism (Djordjevic et al., 2012), where we took that k is increased abruptly, i.e., as a step function at $t = 0$. This neglects the transcription regulation of *cas*

and CRISPR array promoters. Such abrupt increase of k will provide a baseline for our predictions, which will now take into account that Cas6e (the enzyme which processes pre-crRNA to crRNA) is synthesized gradually. While in the experiments crRNA generation is activated by overexpressing Cas6e from a plasmid (see e.g., Pougach et al., 2010), it is likely that in the native system the expression of CRISPR array is activated as well (Pul et al., 2010). Consequently, we will also take into account a gradual synthesis of the regulator [in our case, a C-protein (Tao et al., 1991; Bogdanova et al., 2008)], which can activate CRISPR array transcription by increasing the basal rate φ to a higher value.

To include transcription regulation of the *cas* promoter, i.e., the gradual synthesis of Cas6e and C transcriptional regulator, we here propose the model system whose setup is schematically shown in **Figures 2**, **3**. This setup includes a CRISPR array which is expressed from a promoter with basal transcription activity φ (**Figure 3**). The second component is a vector (plasmid, virus) which expresses *cas* genes and the control protein C that are jointly transcribed from a promoter with transcription activity φ_{Cas}. While Cas3 is not directly relevant for the problem considered here (dynamics of crRNA generation), as it does not take part in crRNA biogenesis, it is necessary for CRISPR interference (Hille and Charpentier, 2016). We therefore include it in the setup to allow expression of all *cas* genes, i.e. to have a fully functional CRISPR-Cas system.

As detailed below, φ_{Cas} is regulated by C. To mimic the qualitative features of transcription regulation in native CRISPR-Cas system, we employ the transcription regulation found in some R-M systems, as explained in the next subsection. The system is activated when the vector enters a bacterial cell lacking its own *cas* genes, which leads to a gradual synthesis of Cas proteins (including Cas6e), therefore increasing the processing rate k, which in turn leads to crRNA generation (see **Figure 2B**—the full arrow) by pre-crRNA processing. Gradual increase of pre-crRNA generation rate can be also considered through this model, through activation of CRISPR array promoter by gradually synthesized C.

Note that the setup above, where *cas* genes are introduced in a cell on a vector, allows bypassing the unknown signaling step in CRISPR-Cas induction. That is, the vector entering the cell marks the start of the system activation (setting zero time in the dynamics simulations), and mimics the signaling which starts synthesis of the transcription activator. Therefore, the key regulatory features which characterize the downstream steps (CRISPR array transcription and transcript processing) can be studied both *in silico* (which will be done here), and also potentially experimentally. In terms of experimental implementation, introducing *cas* genes in a cell on a virus also allows synchronizing the cell population, which is an approach previously implemented to visualize R-M protein kinetics (Mruk and Blumenthal, 2008).

Putting CRISPR-Cas under Transcription Control of an R-M System

As discussed above, *cas* promoter will be put under transcription control exhibited by R-M systems. Below, the main elements

necessary for modeling the system transcription regulation are introduced.

R-M systems are often mobile, and can spread from one bacterial host to the other (Mruk and Kobayashi, 2013). When a plasmid carrying R-M system genes enters a naive bacterial host, the host genome is initially unmethylated, and can consequently be cut by the restriction enzyme. It is, therefore, evident that expression of the restriction enzyme and methyltransferase must be tightly regulated in order to ensure that bacterial genome is protected by the methyltransferase ("antidote"), before it is cut by the restriction enzyme. This tight regulation is often achieved through a dedicated control (C) proteins (Tao et al., 1991; Vijesurier et al., 2000).

We here concentrate on the AhdI R-M system, whose transcription control by C protein has been well-studied (Bogdanova et al., 2008). The activation of AhdI by C protein is reminiscent of CRISPR-Cas activation, as strong cooperative interactions are involved in both cases. In particular, C proteins bound at promoter-proximal and promoter-distal operators interact with high binding cooperativity, so that configuration in which only one operator is occupied cannot be observed in the absence of RNA polymerase (RNAP). At lower C protein concentrations, RNAP can outcompete C protein bound at promoter-proximal operator, leading to transcriptionally active configuration (Bogdanova et al., 2009). Moreover, another feature exhibited in AhdI transcription control, i.e., autoregulation by C protein, is also likely found in CRISPR-Cas transcription regulation. That is, LeuO that activates CRISPR-Cas expression (Westra et al., 2010) also regulates its own transcription. In particular, similarly to transcription regulation of cas genes, leuO is repressed by H-NS, while this repression is abolished by LeuO (Chen et al., 2001). At high concentrations, C protein is bound at both promoter-proximal and promoter-distal position, leading to the promoter repression—see **Figure 5** in (Bogdanova et al., 2009) and the scheme of the transcription configurations shown in **Figure 5** (framed in the figure). Negative autoregulation is also exhibited by LeuO, as it inhibits transcription activation of its gene by BglJ-RcsB (Stratmann et al., 2012). Therefore, putting cas genes under transcription control found in AhdI mimics the main qualitative features of CRISPR-Cas transcription regulation, namely, gradual synthesis of Cas proteins, cooperativity in transcription regulation, and putative autoregulation.

Another advantage of this setup is that we previously showed that biophysical modeling can be used to:(i) explain *in vitro* measurements of the *wild type* and mutant R-M system transcription control (Bogdanova et al., 2008), (ii) explain *in vivo* measurements of the system dynamics (Morozova et al., 2015), (iii) effectively perturb the main R-M system features and relate these perturbations with the system dynamics (Rodic et al., 2017). Consequently, transcription control of a well-studied AhdI R-M system, whose transcription regulation can be reliably modeled (Bogdanova et al., 2008), will serve as a proxy for the transcription control of a much less understood CRISPR-Cas system.

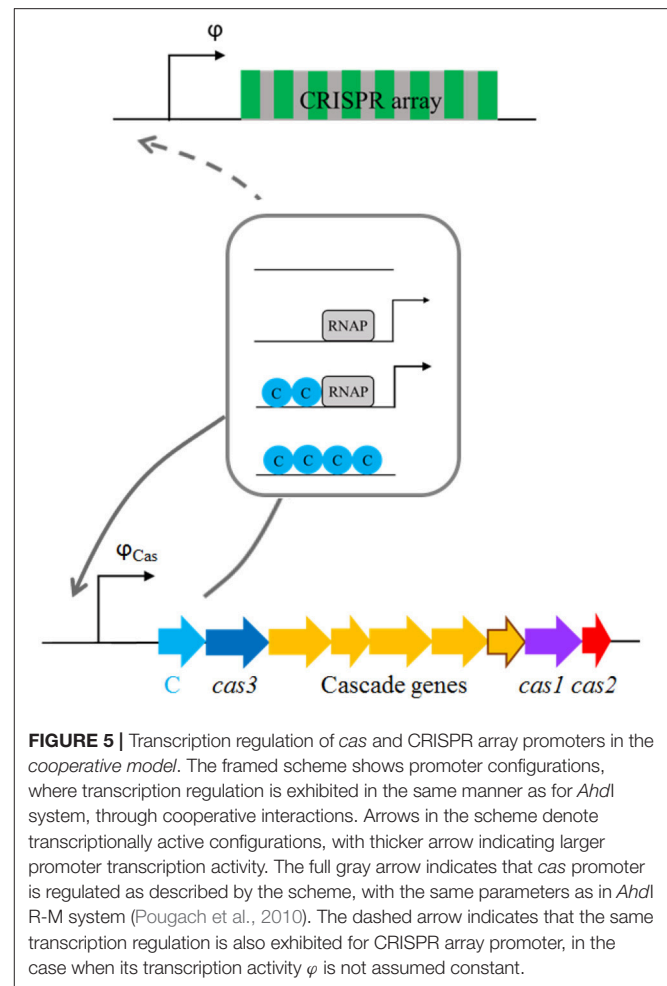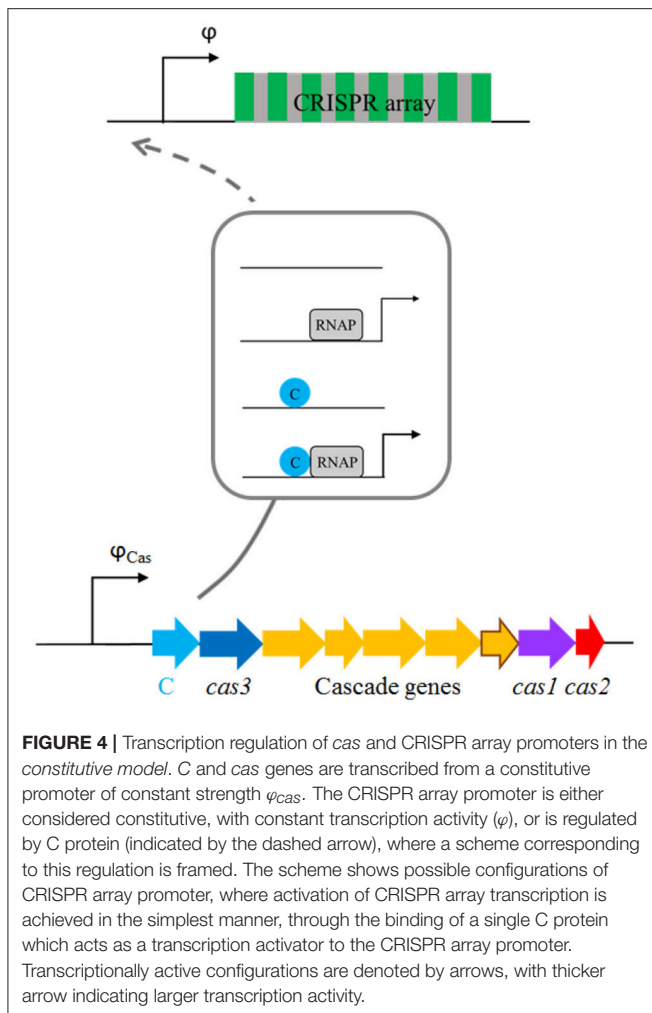## *In silico* Analysis of the Main System Features

The baseline for our predictions will be provided by a model in which the increase of pre-crRNA to crRNA processing rate k is infinitely abrupt—we will call this the baseline model. Comparing the baseline model with predictions that take into account the system transcription regulation (as schematically shown in **Figures 2**, **3**), allows analyzing how gradual synthesis of Cas6e affects kinetics of crRNA generation.

While in the native CRISPR-Cas both cas genes and CRISPR array promoters are repressed by global regulators, the repression of cas genes was found to be much stronger (Pul et al., 2010; Westra et al., 2010)—consequently, when the system is (experimentally) artificially induced, this is commonly done by expressing only cas genes (Pougach et al., 2010; Semenova et al., 2016; Musharova et al., 2017). However, in the native system, it is likely that expression of both CRISPR array and cas genes is activated when the appropriate induction signal(s) is received (Pul et al., 2010). We will therefore investigate the system dynamics when only cas genes are activated (i.e., only pre-crRNA processing rate is gradually increased), and when cas genes and CRISPR array promoter transcription are jointly (and gradually) increased. Consequently, in both of the models introduced below (constitutive and cooperative), we will consider two options. First, when only transcription of cas genes is activated, while transcription activity of CRISPR array remains constant. Second, we will consider the case when the transcription activity of CRISPR array is increased as well.

We further introduce two models of cas gene and CRISPR array transcription regulation:

i *The constitutive model* (**Figure 4**). In this model cas genes are expressed from a constitutive promoter, so that they are transcribed with the constant rate once the plasmid enters a cell. In the case when we consider that the system is activated by only increasing pre-crRNA processing rate, the transcription activity φ is kept constant. When CRISPR array transcription rate is increased as well, increasing φ is exhibited in the simplest manner, by binding of a single C protein activator. Note that, in accordance with its name, no cooperativity is exhibited for transcription regulation described by this model.

ii *The cooperative model* (**Figure 5**). In this model, C protein regulates the transcription of cas genes, and its own transcription, in the same manner as in AhdI R-M system. As noted above, such transcription regulation is characterized by strong cooperative interactions. CRISPR array transcription rate is either kept constant, or in the case when it is increased, we take that it is exhibited in the same way as for cas promoter transcription (the dashed arrow in **Figure 5**).

Studying of the two models allows one to assess how the cooperative transcription regulation (which also characterizes the native CRISPR-Cas system) compares to the activation in which no cooperativity is exhibited, and therefore allows us to assess the role of this key system feature. Also, considering the two models when φ is first kept constant, and then increased together with k, allows assessing significance of CRISPR array transcription

FIGURE 4 | Transcription regulation of *cas* and CRISPR array promoters in the *constitutive model*. *C* and *cas* genes are transcribed from a constitutive promoter of constant strength φ_{cas}. The CRISPR array promoter is either considered constitutive, with constant transcription activity (φ), or is regulated by C protein (indicated by the dashed arrow), where a scheme corresponding to this regulation is framed. The scheme shows possible configurations of CRISPR array promoter, where activation of CRISPR array transcription is achieved in the simplest manner, through the binding of a single C protein which acts as a transcription activator to the CRISPR array promoter. Transcriptionally active configurations are denoted by arrows, with thicker arrow indicating larger transcription activity.

FIGURE 5 | Transcription regulation of *cas* and CRISPR array promoters in the *cooperative model*. The framed scheme shows promoter configurations, where transcription regulation is exhibited in the same manner as for *Ahd*I system, through cooperative interactions. Arrows in the scheme denote transcriptionally active configurations, with thicker arrow indicating larger promoter transcription activity. The full gray arrow indicates that *cas* promoter is regulated as described by the scheme, with the same parameters as in *Ahd*I R-M system (Pougach et al., 2010). The dashed arrow indicates that the same transcription regulation is also exhibited for CRISPR array promoter, in the case when its transcription activity φ is not assumed constant.

control. To allow a direct comparison of models dynamics, the overall strength of φ_{Cas} is adjusted so that the same value of maximal pre-crRNA processing rate is achieved. Similarly, when the transcription rate of CRISPR array is increased, the interaction parameters are adjusted so that the same equilibrium increase of φ is achieved in both models (see Methods).

Modeling Results
Kinetics of Pre-crRNA and crRNA Production

We first consider the situation in which crRNA generation is activated by expressing Cas proteins, such that the processing rate k is gradually increased, while the CRISPR array transcription activity remains constant. In this case, we compare the system dynamics for: (i) *baseline model*, in which the processing rate k is increased as a step function, which corresponds to the limit of infinitely fast system induction, (ii) constitutive model (see **Figure 4**), and (iii) cooperative model (see **Figure 5**).

In constitutive and cooperative models, the gradual synthesis of Cas6e leads to gradual change of transcript processing rate k (k^* is a processing constant):

$$k(t) = [Cas6e](t) \cdot k^* \qquad (1)$$

Figure 6 illustrates how the processing rate (k) changes with time, when the baseline, constitutive, and cooperative models of *cas* gene expression are assumed. For the constitutive model (the dash-dotted curve), the processing rate uniformly increases and reaches an equilibrium value, for all values of k_{eq} considered in three panels of **Figure 6**. On the other hand, for cooperative model (the dashed curve) and at higher values of k_{eq} (**Figures 6B,C**), we see a rapid increase of k at initial times, followed by a fast return to the equilibrium value due to repression at higher C protein concentrations.

In **Figure 7**, we address how different k dynamics (shown in **Figure 6**), affects pre-crRNA and crRNA generation. Specifically, φ is held constant at its initial value (10 1/min), while k changes according to the baseline, constitutive, or cooperative models until reaching the same equilibrium value of $10\lambda_{pre}$, $100\lambda_{pre}$, and $1,000\lambda_{pre}$ (left, central, and right columns of **Figure 7**, respectively). The model of abrupt Cas6e expression serves as a baseline for assessing the dynamics in the other two models (constitutive and cooperative), in which Cas6e is realistically (gradually) expressed.

In **Figures 7A–D**, we see that cooperative model leads to the steepest transition from ON to OFF state (in the case
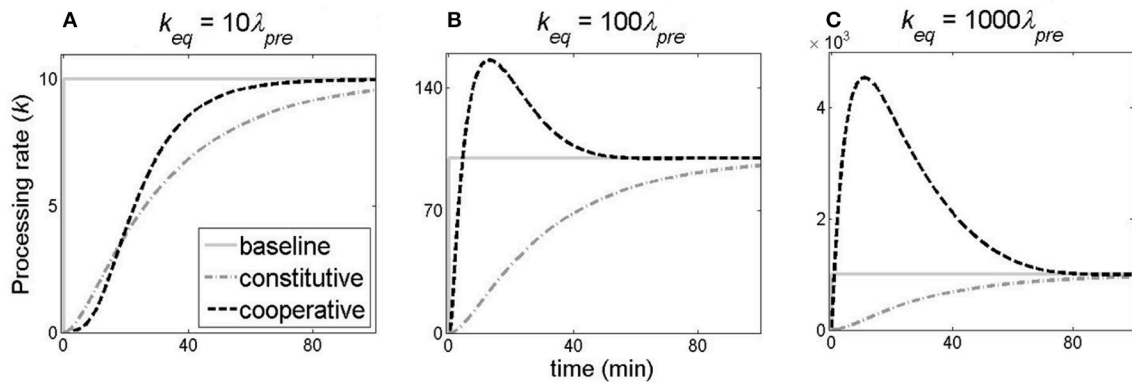
FIGURE 6 | Comparing the dynamics of the pre-crRNA processing rate change. The change of the processing rate k with time is shown for: the baseline model (solid gray curve), the constitutive model (dash-dotted gray curve) and the cooperative model (dashed black curve). **(A–C)** correspond to different k_{eq} values ($k_{eq} = 10\lambda_{pre}$, $100\lambda_{pre}$, $1,000\lambda_{pre}$, respectively). CRISPR transcription activity is constant (10 1/min).
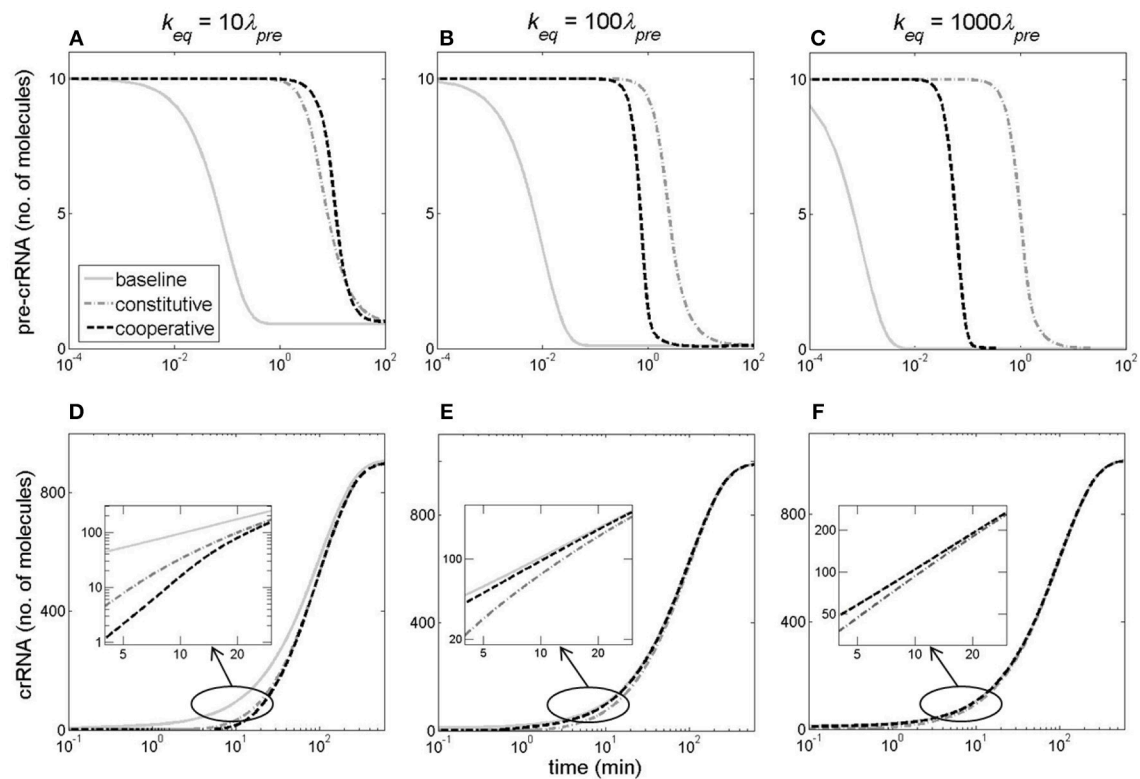

FIGURE 7 | Kinetics of pre-crRNA and crRNA generation. The columns correspond to k_{eq} values of $10\lambda_{pre}$ **(A,D)**, $100\lambda_{pre}$ **(B,E)**, and $1,000\lambda_{pre}$ **(C,F)**, which are reached through the baseline model (the gray solid curve), the constitutive model (the gray dash-dotted curve) or cooperative model (the black dashed curve). The upper **(A–C)** and the lower **(D–F)** rows correspond, respectively, to pre-crRNA and crRNA kinetics. CRISPR array promoter transcription activity is kept constant at 10 1/min.

of pre-crRNA), and from OFF to ON state (in the case of crRNA). Furthermore, we can distinguish between two different regimes in **Figure 7**. At lower k_{eq} (left column in **Figure 7**), there is a noticeably slower accumulation of crRNA at early times in both cooperative and constitutive models compared to the

baseline model of infinitely abrupt processing rate (k) increase (**Figure 7D**). On the other hand, at higher k_{eq} ($k_{eq} \geq 100$ 1/min, the central and right columns in **Figure 7**), the dynamics of crRNA accumulation for cooperative model becomes faster compared to constitutive model dynamics at early times, and

approaches the limit of infinitely abrupt k increase (see the inserts in **Figures 7E,F**). The faster kinetics of crRNA increase in cooperative model is due to the fast increase of k at early times in this model (**Figures 6B,C**).

Effects of *cas* Genes Regulation

From **Figure 7**, we observe that transcripts reach their steady-state levels quite late, i.e., >100 min post-induction. Such late time is, however, not relevant for cell response to phage infection, since infected *E. coli* lyse ~20 min post-infection, while shut-off of essential cell functions happens earlier (Kruger and Schroeder, 1981). Therefore, in **Figure 8** we estimate pre-crRNA and crRNA levels for all three models at 20 min post-induction, as the maximal value of pre-crRNA processing rate k_{eq} is changed from very low to high values (>$100\lambda_{pre}$, characteristic for artificial Cas6e induction), while keeping the level of CRISPR array transcription constant ($\varphi = 10$ 1/min).

The following features emerge from **Figure 8**:

i. A switch-like system behavior for both pre-crRNA and crRNA curves in the cooperative model, while the constitutive and baseline models yield much more gradual responses to changes in k_{eq}. For crRNA, the cooperative model leads to a rapid transition from the OFF state (with essentially no crRNA generated at 20 min), to the ON state (with high abundance of crRNA), and reciprocal situation for pre-crRNA. Consequently, for small amounts of synthesized Cas6e (i.e., small k_{eq} values), which can be caused by leaks in *cas* promoter activity, the system remains in OFF state. On the other hand, once the system is activated when the processing rate (directly related to the amount of Cas6e available) reaches a certain threshold ($k_{eq} \gtrsim 50$), a large amount of crRNA is generated at early times, which should allow protection from foreign DNA invasion. The significance of this behavior is considered in Discussion.

ii. An interesting cross-over behavior in the cooperative model, where at low k_{eq} values crRNA amounts are low, while at high k_{eq} values the synthesized crRNA amounts become larger than in the constitutive model, and approach the baseline model curve. Therefore, at high k-values (~100 1/min), which are encountered in experiments, (Pougach et al., 2010; Djordjevic et al., 2012) the model of cooperative *cas* gene expression leads to accumulation of protective crRNA amounts close to those achievable in the limit of infinitely abrupt k increase. Consequently, the high cooperativity in transcription regulation, characteristic for native CRISPR-Cas system regulation, leads to a highly efficient crRNA generation at high transcript processing rates.

iii. Sufficient crRNA levels are generated to protect host cell against bacteriophage infection, at early times post-induction, even at relatively low values of pre-crRNA processing rate. That is, k_{eq} somewhat larger than 1 1/min leads to ~10 crRNAs which already corresponds to the amount that negatively affects phage development (Pougach et al., 2010); moreover, a small additional k_{eq} increase leads to a large increase in generated crRNAs in the cooperative model, due to the rapid transition from OFF to ON state.

iv. A saturation in generated crRNA amounts at early times post-induction. That is, for $k_{eq} \sim 100$ 1/min the amount of generated crRNAs at 20 min stops significantly increasing with further increase in k_{eq}. This saturation can be relieved (leading to increase in the amount of generated crRNA), if CRISPR array transcription activity is increased, which is further analyzed below.

Perturbing Pre-crRNA Degradation Rate

We next perturb the second key feature of CRISPR-Cas regulation—fast non-specific degradation of pre-crRNA. The consequence of pre-crRNA degradation rate λ_{pre} decrease at constant φ was next investigated for all three models. The
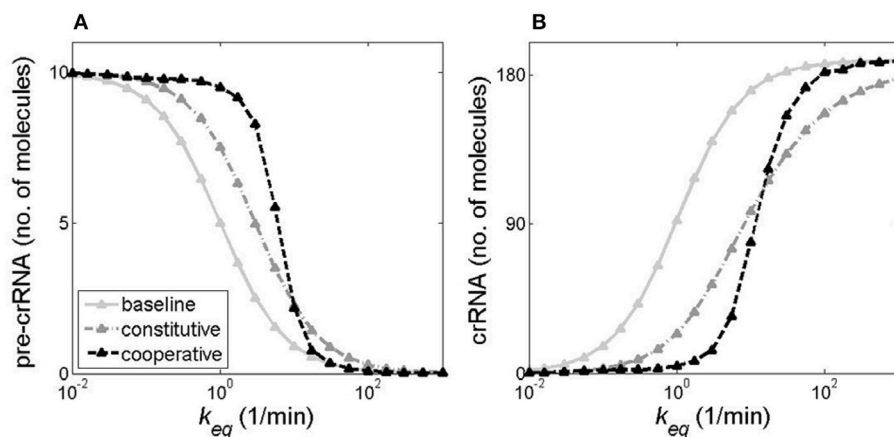

FIGURE 8 | Pre-crRNA and crRNA amounts early post-induction for different models of *cas* gene transcription regulation. The figure shows **(A)** pre-crRNA and **(B)** crRNA amounts 20 min post-induction (i.e., 20 min after introduction of the vector expressing *cas* genes), as a function of the maximal (equilibrium) value of the transcript processing rate k. CRISPR promoter transcription activity is kept constant ($\varphi = 10$ 1/min). The gray solid, the gray dash-dotted, and the black dashed curves correspond, respectively, to baseline, constitutive, and cooperative models of *cas* regulation.

decrease was followed at different k_{eq} values (i.e., at different levels of Cas6e activity), where φ is held constant.

The effects of λ_{pre} decrease are similar for all three models, so in **Figure 9** we show the results only for the cooperative model. For all k_{eq} values we see that abolishing the fast decay of pre-crRNA (decreasing λ_{pre}), significantly decreases the time delay of the onset of crRNA generation. This effect is most pronounced at high k_{eq} values (**Figure 9C**). Also, perturbing the degradation rate deforms crRNA dynamics curve with respect to the standard Hill (sigmoidal) shape that is exhibited at high λ_{pre} such as $\lambda_{pre} = 1/50$. Furthermore, analogously to **Figure 8**, in Figure S1 (Supplementary Material), we show how crRNA amount at 20 min after induction depends on pre-crRNA degradation rate λ_{pre}. One can clearly observe that as λ_{pre} decreases, the amount of generated crRNA early post-induction significantly increases, consistently with the decrease of the time delay of onset of crRNA generation observed in **Figure 9**.

Relieving crRNA Production Saturation by Increasing Pre-crRNA Generation

In addition to *cas* genes, CRISPR array promoter is also repressed (though more weakly) by global transcription regulators (Pul et al., 2010; Westra et al., 2010). Consequently, crRNA generation can be also augmented by increasing CRISPR array transcription activity. Therefore, we next assess how joint increase of k (achieved by activating *cas* gene transcription) and φ (achieved by increasing CRISPR array transcription) affects generated crRNA amount 20 min post-induction for all three regulatory models.

As can be seen from **Figure 10**, increasing φ robustly relieves crRNA saturation (see also discussion of **Figure 8**). Moreover, one can see that a relatively modest, factor of two increase of φ (from 10 1/min to 20 1/min) can abolish the need of a significant, order of magnitude, k increase to produce the same amount or crRNA. As above, we observe a switch-like behavior for the cooperative model (compare **Figure 10C** with **Figures 10A,B**),

with cooperative model curves exhibiting the steepest transition from OFF to ON state for all φ values.

Regulation of CRISPR Array Transcription Activity

We next consider how different models of regulation of CRISPR array transcription affect crRNA dynamics. For all three models, the transcription activity φ is increased by an order of magnitude (from $\varphi = 10$ 1/min to $\varphi = 100$ 1/min), for different k_{eq} values ($k_{eq} = \lambda_{pre}$, $10\lambda_{pre}$, and $100\lambda_{pre}$), see Figure S2 (Supplementary Material). We obtain that the cooperative model leads to a more controlled (attenuated) pre-crRNA dynamics, which is due to the presence of repressing mechanism at high C protein amounts (see Figure S3). For crRNA dynamics, we observe that the cooperative model exhibits the steepest transition from OFF to ON state. Moreover, this model leads to the largest delay in crRNA generation. Consequently, in addition to pre-crRNA degradation rate, the cooperative transcription regulation also contributes to the delay between the activating signal and the onset of crRNA generation.

We previously (**Figure 9**) perturbed pre-crRNA degradation rate while keeping the transcription rate φ constant. Finally, we now also decrease λ_{pre} under the conditions when both *cas* genes and CRISPR array transcription is activated according to all three models (see Figure S4). The results are qualitatively similar to **Figure 9** (where φ is constant), i.e., decreasing λ_{pre} diminishes the switch-like system response and/or decreases the time-delay in the onset of pre-crRNA generation.

DISCUSSION AND SUMMARY

One of the most prominent problems in understanding CRISPR-Cas function is assessing dynamics of the system activation, i.e., understanding the roles of the key features of CRISPR-Cas regulation. Addressing this problem is complicated by the fact that exact conditions for system activation remain unclear. In fact, for Type I-E CRISPR-Cas system in *E. coli*, even bacteriophage infection itself is not sufficient
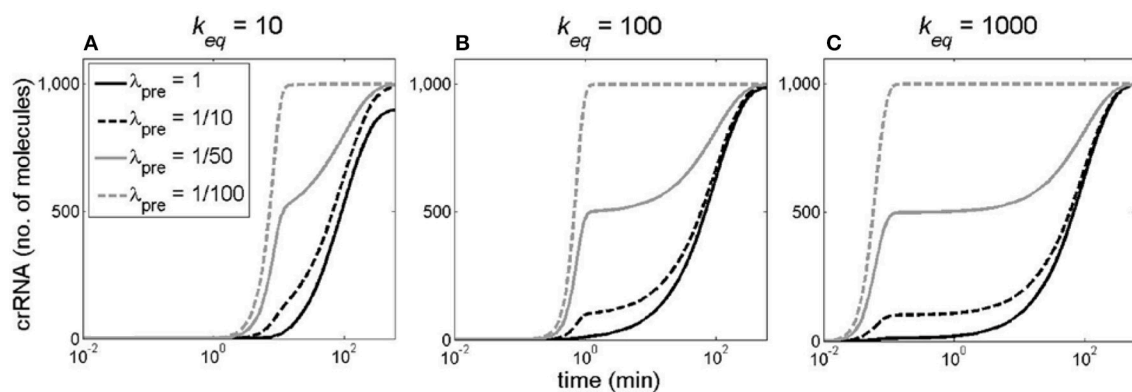

FIGURE 9 | The effect of perturbing pre-crRNA degradation rate on the dynamics of crRNA generation. The pre-crRNA processing rate increases to its equilibrium value through the cooperative model, while φ is held constant (at 10 1/min). Different curves correspond to different λ_{pre} values: 1 (solid black), 1/10 (dashed black), 1/50 (solid gray), and 1/100 1/min (dashed gray). **(A–C)**, correspond to different k_{eq} values indicated at the top of each panel.
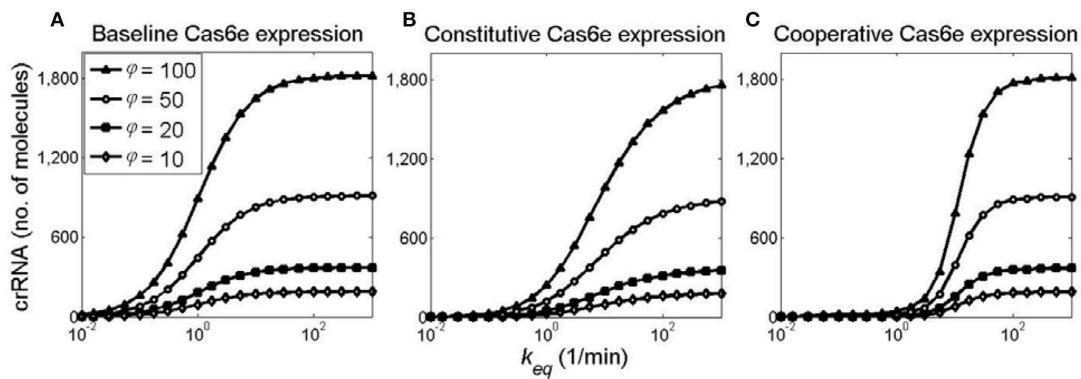
FIGURE 10 | Relieving saturation in generated crRNA amounts through joint k and φ increase. crRNA amount as a function of k_{eq} at 20 min post-induction, obtained for **(A)** baseline, **(B)** constitutive, and **(C)** cooperative models. Curves marked with diamonds, filled squares, circles, and filled triangles, correspond, respectively, to φ of 10, 20, 50, and 100 1/min.

to induce the system. We here proposed a synthetic setup which allows inducing CRISPR-Cas with qualitative features that correspond to native system regulation, while bypassing currently unclear conditions under which the system is activated. This setup involves putting *cas* genes and/or CRISPR array under transcription control found in a well-studied R-M system, which exhibits cooperative transcription regulation that is also characteristic of CRISPR-Cas regulation (Bouffartigues et al., 2007; Westra et al., 2010). A major advantage of the setup is that it can be readily experimentally implemented, e.g., by introducing *cas* genes and the regulator (C protein) in a cell on a virus. This would allow synchronizing the cell population, and experimentally observing the system dynamics, where such measurements could be directly compared with the predictions provided here. Another advantage is that major parameters in the setup have been inferred from experimental data, as both CRISPR transcript processing, and AhdI transcription regulation, have been experimentally well-studied (Bogdanova et al., 2008; Pougach et al., 2010; Djordjevic et al., 2012).

Consequently, this setup allows us to directly (*in silico*) address how the system regulation contributes to its dynamical response. In particular, previous experimental and computational work point to cooperative regulation of *cas* gene and CRISPR array transcription, and fast non-specific degradation of pre-crRNA, as two main system regulatory features (Pougach et al., 2010; Pul et al., 2010; Westra et al., 2010; Djordjevic et al., 2012). We therefore investigated two alternative regulatory architectures, one with constitutive, and the other with cooperative *cas* gene regulation. The dynamics corresponding to these two architectures was then compared with the baseline model, in which pre-crRNA processing rate is increased infinitely abruptly. We assessed the dynamics in the case when only *cas* genes are activated (i.e., only pre-crRNA processing rate is gradually increased), and when *cas* genes and CRISPR array promoter transcription is jointly increased. We focused on early system dynamics (within the first 20 min post-induction), as this period is most relevant for defending the cell against invading viruses. Finally, we also perturbed the high pre-crRNA non-specific

degradation rate, under different system conditions described above, and assessed what effect such perturbation has on system dynamics.

The main result of the analysis is that the system regulation leads to a clear switch-like behavior, characterized by an initial delay of crRNA synthesis, followed by a steep transition from OFF to ON state. Unexpectedly, it is not only the cooperative transcription regulation, but also fast non-specific pre-crRNA degradation, which leads to such dynamics. That is, decreasing the high pre-crRNA degradation rate effectively abolishes the delay in crRNA generation, and deforms the crRNA kinetics from the standard sigmoidal (Hill) shape (Hill, 2013) typical for switch-like system response (**Figure 9**). Interestingly, we also found that, when pre-crRNA processing rate and CRISPR array transcription rate are jointly (and gradually) increased, as likely exhibited in the native system, the system is more robust to perturbations in the degradation rate (Figure S4).

The cooperative transcription regulation leads to an interesting cross-over behavior in the early system dynamics. At low pre-crRNA processing rates, cooperative regulation leads to much smaller crRNA amounts at early times compared to constitutive expression. On the other hand, at higher processing rates, there is a large increase in synthesized crRNA amounts, which approach the limit of infinitely abrupt system induction. Interestingly, when the system is artificially activated by overexpressing *cas* genes, pre-crRNA processing rates correspond to the regime of the highly enhanced crRNA production (Djordjevic et al., 2012). While the parameters of the native system induction are unclear, it is tempting to hypothesize that they may also reach this cross-over, allowing the system to generate crRNAs with the rate close to the limit of infinitely fast induction at times when they are needed.

The rapid transition of the system from OFF to ON state is straightforward to interpret in terms of its function in immune response. When a potential signal indicating infection is received by the cell, CRISPR-Cas has a very short time to generate sufficient crRNA amounts to protect the cell, as bacteriophages are typically highly efficient in shutting-down essential cell functions. Thus, there is a question whether enough crRNA can

be generated in a model which accounts for gradual synthesis of proteins that process pre-crRNA and/or are responsible for gradual CRISPR array activation. We robustly obtained that enough crRNA can be generated at early times, even when the system is activated by only increasing the pre-crRNA processing rate. Moreover, a much smaller increase of the processing rate is needed to achieve certain crRNA amount, if CRISPR array transcription is activated as well. Therefore, these results may explain the relatively inefficient repression of CRISPR array promoter, since even a small increase of CRISPR array transcription rate efficiently increases generated crRNA amounts. In fact, the need to rapidly produce large amounts of crRNAs may be a major constraint on system dynamics.

In distinction to the rapid transition of the system from "OFF" to "ON" state, interpretation of the delay in crRNA generation, which comes as a model prediction, is less straightforward. One possibility is that such delay is related with primed adaptation in CRISPR-Cas, which relies on a pre-existing (priming) spacer that enables a biased uptake of new spacers—therefore serving to minimize infection by phage escape mutants that would otherwise evade the interference (Sternberg et al., 2016). In particular, it has been found that priming is facilitated by slow or delayed CRISPR interference, leading to a steady-state flux of substrates from which new spacers can be acquired (Kunne et al., 2016; Severinov et al., 2016; Musharova et al., 2017). Such delay in CRISPR interference can clearly be achieved by a delay in crRNA generation that is predicted in our work.

It has been proposed that Type I-E CRISPR-Cas in *E. coli* may have functions other than immunity. For example, it was found by bioinformatics analysis that the system is changing very slowly, in distinction to rapid diversification of CRISPR arrays in other species, indicating that the system is not taking an active role in defense against immediate viral threats (Touchon et al., 2011). In this respect, it may be useful to view the dynamical properties inferred here in a more general terms, namely of a capability of expressing a large number of molecules in a narrow time interval, with a specific time-delay with respect to reception of an external signal. It is clear that such highly efficient, and temporally specific response, may be highly desirable for multiple cellular functions. It would be very interesting to find out how functions of *E. coli* Type I-E CRISPR-Cas, yet to be discovered in the future, would fit within the dynamical properties inferred here.

METHODS

We start from a previously introduced model of CRISPR transcript processing by Cas proteins (Djordjevic et al., 2012). In this model (see **Figure 2A**), a short-living transcript [pre-crRNA] is synthesized with a promoter transcription activity φ, and further, either quickly degraded with a degradation rate λ_{pre}, or processed (cut) into shorter, long-living RNAs [crRNA] with a processing rate k. Processed transcripts are degraded with a rate λ_{crRNA}. In the equations below, we assume that the processing rate depends linearly on the substrate (pre-crRNA) amount, since the amount of pre-crRNA is small [<10 molecules per cell (Pougach et al., 2010)], so that the corresponding kinetic

equations are:

$$\frac{d[\text{pre} - \text{crRNA}]}{dt} = \varphi - (\lambda_{\text{pre}} + k) \cdot [\text{pre} - \text{crRNA}] \qquad (2)$$

$$\frac{d[\text{crRNA}]}{dt} = k \cdot [\text{pre} - \text{crRNA}] - \lambda_{\text{crRNA}} \cdot [\text{crRNA}]$$

(3)

The equations above are further solved deterministically, as both CRISPR array and *cas* genes are expressed from promoters with strong basal transcription. Furthermore, the small pre-crRNA amount is due to fast non-specific degradation, i.e., due to the transcript processing step. With respect to this, note that there is an access of enzyme (Cas6e) over substrate (pre-crRNA) (Djordjevic et al., 2012), so the equations describing the transcript processing are linear. Therefore, their deterministic solution accurately describes the mean of the stochastic simulations.

In the previous study (Djordjevic et al., 2012), we considered a model in which transcription regulation is neglected, so that k and φ increase in an idealized manner, i.e., infinitely abruptly. We now introduce models where the relevant enzymes and transcription regulators are synthesized in a realistic (i.e., gradual) manner. Specifically, k in Equation now explicitly depends on time, and is proportional to the enzyme (the processing protein, Cas6e) concentration, i.e., $k = [Cas6e] \cdot k^*$, where k^* is processing constant. We here consider that this processing rate k can change with time in the following ways:

1) Infinitely abruptly, from 0 to its equilibrium value, k_{eq} at $t = 0$, which we refer to as the baseline model.
2) Gradually, with [Cas6e](t), where Cas6e is expressed from a constitutive promoter (promoter with constant transcription activity), see **Figure 4**.
3) Also gradually with [Cas6e](t), where Cas6e is now expressed from an AhdI-like regulated promoter (see **Figure 5**).

As noted above, we either keep the CRISPR array transcription rate φ constant (which allows us investigating the dynamics in response to changing only pre-crRNA processing rate), or allow φ to change:

1) Infinitely abruptly (the baseline model), so that at $t = 0$ it increases from its starting value (10 1/min) to the equilibrium value.
2) Gradually, through the simplest activation mechanism, where a single C protein activates transcription from the CRISPR array promoter (the dashed arrow in **Figure 4**).
3) Also gradually with C(t), where the same transcription regulation as in AhdI RM system is exhibited (the dashed arrow in **Figure 5**).

In constructing Cas6e and CRISPR expression models, we refer to our existing model of AhdI restriction-modification (RM) system control (Bogdanova et al., 2008), which describes expression of the control protein (C) and the restriction endonuclease (R)—C and R are co-transcribed in AhdI RM system. We here use a thermodynamical model of CR operon transcription regulation, and a dynamical model of transcript and protein expression.

For $t = 0$ we take the moment when plasmid carrying C and cas genes enters the naïve host. Thus, all initial conditions are set to zero, except for $[\text{pre-crRNA}](t = 0) = \varphi/\lambda_{pre} = 10\,(1/\min)$(Djordjevic et al., 2012), as extracted from the Equation in equilibrium. Note that while C and cas genes enter the cell on a plasmid, CRISPR array is expressed within the cell, with the transcription rate φ.

Constitutive Model of *cas* Gene and CRISPR Array Expression

We assume that C and cas genes are co-transcribed from a constitutive (unregulated) cas promoter (see above and **Figure 4**). C and cas transcript and protein concentrations change with time:

$$\frac{d[c-cas](t)}{dt} = \varphi_{Cas} - \lambda_{Cas} \cdot [c-cas](t) \tag{4}$$

$$\frac{dC(t)}{dt} = k_C \cdot [c-cas](t) - \lambda_C \cdot C(t) \tag{5}$$

$$\frac{d[Cas6e](t)}{dt} = k_{Cas6e} \cdot [c-cas](t) - \lambda_{Cas6e} \cdot [Cas6e](t). \tag{6}$$

Note that all the notation (including in the equation above), is introduced in **Table 1**. The first terms on the right-hand side represent transcript/protein synthesis by transcription/translation, while the second terms represent transcript/protein decay by degradation. The parameter values are as in AhdI RM system model (with Cas6e now replacing R in AhdI system), and are also provided in the table at the end of the methods. Since C and Cas6e protein degradation rates are taken to be the same, it follows:

$$[Cas6e](t) = \frac{k_{Cas6e}}{k_C} C(t), \tag{7}$$

So that the differential equation for Cas6e dynamics can be omitted. We set the value of φ_{Cas} to one (see the next subsection) so that the equilibrium processing rate is the same for the constitutive and the cooperative models (see e.g., **Figure 6**), which allows a direct comparison of the dynamics in these two models. Consequently, we set k^* so that $k_{eq} = [Cas6e]_{eq} \cdot k^* = 10\,(1/\min)$. Regarding CRISPR array transcription φ, we keep it constant, in the case when we consider the system activation by overexpression of cas genes. In the case when we also consider activation of CRISPR transcription, we introduce a simple model of CRISPR expression regulation (the dashed arrow in **Figure 4**), where CRISPR promoter, apart from being unoccupied, can be found in the following three configurations, which are represented by the reactions shown below: (i) RNAP alone bound to the promoter (8), (ii) a C monomer alone bound to its binding site (9), and (iii) RNAP recruited by a C monomer bound to its binding site, acting as a transcription activator —note that these configurations correspond to the second, third and fourth line in the framed part of **Figure 4**, respectively.

$$DNA + RNAP \xrightleftharpoons[K_{1A}]{} RNAP - DNA \tag{8}$$

$$DNA + C \xrightleftharpoons[K_{2A}]{} C - DNA \tag{9}$$

$$C - DNA + RNAP \xrightleftharpoons[K_{3A}]{} C - DNA - RNAP \tag{10}$$
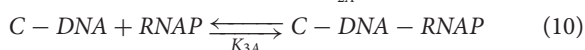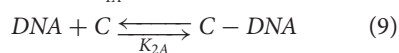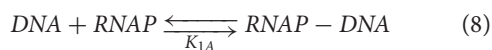
TABLE 1 | Notations used in model equations.

Variables	Description	
φ_{Cas}	Transcription activity of cas promoter	
φ	Transcription activity of CRISPR promoter	
[c-cas]	Concentration of cas operon transcript	
[pre-crRNA]	Concentration of unprocessed CRISPR array transcript	
[crRNA]	Concentration of processed CRISPR array transcript	
C	Concentration of control protein	
[Cas6e]	Concentration of processing protein	
KINETIC MODEL CONSTANTS		
k^*	CRISPR transcript processing constant	0.02
k_C	Translation constant for control protein	0.60
k_{Cas6e}	Translation constant for processing protein	3.00
λ_{Cas}	Rate of cas transcript decay	0.20
λ_{pre}	Rate of unprocessed CRISPR transcript decay	1.00
λ_{crRNA}	Rate of processed CRISPR transcript decay	0.01
λ_C	Rate of control protein decay	0.033
λ_{Cas6e}	Rate of Cas6e processing protein decay	0.033
TRANSCRIPTION REGULATION MODELS CONSTANTS		
α	Proportionality constants	1.663
γ		110
α'		110
a	Constants which absorb the relevant	1.60×10^{-1}
p	equilibrium dissociation constants and RNA	9.25×10^{-1}
q	polymerase concentration	1.41×10^{-5}
d		1.00×10^{-1}
e		Adjusted
f		2.00×10^2
a'		1.00×10^{-1}
p'		Adjusted
q'		2.50×10^{-5}
K_D		6.50×10^2

The equilibrium dissociation constants of the above reactions are given by:

$$K_{1A} = [DNA]\,[RNAP]\,/\,[RNAP - DNA] \tag{11}$$

$$K_{2A} = [DNA]\,[C]\,/\,[C - DNA] \tag{12}$$

$$K_{3A} = [C - DNA]\,[RNAP]\,/\,[C - DNA - RNAP]. \tag{13}$$

Using the Shea-Ackers based approach, i.e. assuming that the transcription activity is proportional to the equilibrium promoter occupancy by RNAP, we derive the expression for CRISPR promoter transcriptional activity:

$$\varphi = \gamma \frac{Z_{RNAP} + Z_{C-RNAP}}{1 + Z_{RNAP} + Z_C + Z_{C-RNAP}} \tag{14}$$

where γ is a proportionality constant, while configuration statistical weights correspond to: $Z_{RNAP} = [RNAP - DNA]\,/\,[DNA]$ — RNAP alone bound to the promoter, $Z_C = [C - DNA]\,/\,[DNA]$–C monomer alone bound to its binding site, $Z_{C-RNAP} = [C - DNA - RNAP]\,/\,[DNA]$ — RNAP

recruited to the promoter by a bound C monomer. We can obtain φ dependence on C concentration:

$$\varphi(C) = \gamma \frac{d + def[C]}{1 + d + e[C] + def[C]} \tag{15}$$

If we introduce parameters expressed in terms of the equilibrium binding constants and RNAP concentration:

$$d = [RNAP]/K_{1A} \tag{16}$$
$$e = 1/K_{2A} \tag{17}$$
$$f = K_{1A}/K_{3A}. \tag{18}$$

To estimate the parameters, we use a condition:

$$\varphi(0) = 10\frac{1}{\min} \tag{19}$$

which corresponds to the value in Djordjevic et al. (2012), and:

$$\varphi(C_{eq}) = 100\frac{1}{\min} \tag{20}$$

Another (evident) condition is that the fraction, which appears on the right-hand side of the Equation (15), has to be smaller than 1. By adjusting the parameters to satisfy the conditions (19) and (20), we obtain $d < 1/9$, which allows setting the values of d and γ. Further, we notice that $e = 99/\left([C]_{eq} \cdot \left(f - 100\right)\right)$ and, having fixed the value of f, we can adjust e with respect to $[C]_{eq}$.

The unprocessed [pre-crRNA] and processed [crRNA] transcript amounts change with time according to the Equations (2) and (3), where φ is given by .

Cooperative Model of *cas* and CRISPR Expression

As opposed to the constitutive *cas* operon expression, we here assume that the *cas* promoter is regulated by C as in the wild type AhdI RM system (Bogdanova et al., 2008), through cooperative interactions (see **Figure 5**). The following set of reactions describes the transcriptional regulation of the *cas* promoter by the C protein (note the promoter configurations shown in **Figure 5**):

$$C + C \xrightleftharpoons[K_1]{} D \tag{21}$$

$$DNA + RNAP \xrightleftharpoons[K_2]{} RNAP - DNA \tag{22}$$

$$D + DNA \xrightleftharpoons[K_3]{} D - DNA \tag{23}$$

$$D - DNA + D \xrightleftharpoons[K_4]{} T - DNA \tag{24}$$

$$D - DNA + RNAP \xrightleftharpoons[K_5]{} D - DNA - RNAP \tag{25}$$
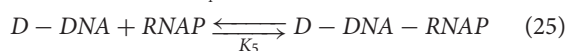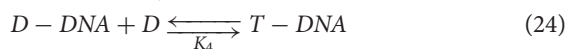
where C and D stand for C protein monomers and dimers, respectively.

The reactions (21)–(25) represent:

– (21) C monomers dimerization;
– (22) RNAP binding to the *cas* promoter forming *RNAP-DNA* complex;

– (23) D binding to the distal binding site forming *D-DNA* complex;
– (24) D recruitment to the proximal binding site forming *T-DNA* complex;
– (25) RNAP recruitment to the *cas* promoter forming *D-DNA-RNAP* complex.

In equilibrium the above reactions lead to the following equations of the equilibrium dissociation constants:

$$K_1 = \frac{[C]^2}{[D]} \tag{26}$$

$$K_2 = \frac{[DNA][RNAP]}{[RNAP - DNA]} \tag{27}$$

$$K_3 = \frac{[D][DNA]}{[D - DNA]} \tag{28}$$

$$K_4 = \frac{[D][D - DNA]}{[T - DNA]} \tag{29}$$

$$K_5 = \frac{[RNAP][D - DNA]}{[D - DNA - RNAP]} \tag{30}$$

Taking into account the aforementioned Shea-Ackers assumption we obtain:

$$\varphi_{Cas} = \alpha \frac{Z_{RNAP} + Z_{D-RNAP}}{1 + Z_{RNAP} + Z_{D-RNAP} + Z_T}, \tag{31}$$

α is a proportionality constant, $Z_{RNAP} = [RNAP - DNA]/[DNA]$, $Z_{D-RNAP} = [D - DNA - RNAP]/[DNA]$ and $Z_T = [T - DNA]/[DNA]$ denote the statistical weights of only RNAP bound to the promoter, RNAP recruited to the promoter by a C dimer bound to the distal binding site, and a C tetramer repressing transcription, respectively.

By using Equations (26)–(30), the Equation (31) can be rewritten in terms of C monomer concentration (following the notation in Bogdanova et al., 2008; Rodic et al., 2017):

$$\varphi_{Cas}(C) = \alpha \frac{a + b[C]^2}{1 + a + b[C]^2 + c[C]^4} \tag{32}$$

which can be expressed, by using the redefined parameters, in the following form:

$$\varphi_{Cas}(C) = \alpha \frac{a + ap[C]^2}{1 + a + ap[C]^2 + p^2 q[C]^4}. \tag{33}$$

We set α so that the equilibrium value of *cas* transcription activity corresponds to one (adapted from Bogdanova et al., 2008). Parameters *a*, *p*, and *q* depend on the equilibrium dissociation constants and RNAP concentration and are given by:

$$a = [RNAP]/K_2 \tag{34}$$

$$p = \frac{K_2}{K_1 K_3 K_5} \tag{35}$$

$$q = \frac{1}{K_1^2 K_3 K_4 p^2} = \frac{K_3 K_5^2}{K_2^2 K_4} \tag{36}$$

While their values are deduced from the already determined a, b, and c, that correspond to the best fit to the AhdI experimentally measured transcription activity vs. C (Bogdanova et al., 2008).

Regarding the dynamics, note that C and Cas6e transcript and protein amounts change with time according to the Equations (4)–(6), where φ_{Cas} is given by .

Similarly as for the constitutive model, we keep φ constant, in the case when we consider inducing the system through increasing pre-crRNA processing rate. When we also consider regulation of CRISPR array transcription, we assume that CRISPR promoter is regulated by C in the same way as *cas* promoter. Thus, following the same procedure we obtain for the CRISPR promoter transcription activity:

$$\varphi = \alpha' \frac{a' + a'p'[C]^2}{1 + a' + a'p'[C]^2 + p'^2q'[C]^4} \quad (37)$$

where constants α', a', p', and q' are determined by imposing the same constraints on φ as above (-). Specifically, these constraints lead to the condition $a' < \frac{1}{9}$, which allows setting parameters a' and α'. Further, from Equation (20) we express p' in terms of q' and get $q' < \frac{1}{400*99}$ (deduced from the real roots criterion of quadratic equation), based on which we set q', and subsequently obtain the relation for adjusting p' with respect to k_{eq} (i.e., C_{eq}). Again, the unprocessed [pre-crRNA] and processed [crRNA] transcript amounts change with time according to the Equations (2) and (3), where φ is replaced with (37).

Changing Pre-crRNA Processing Rate

From Equation (1) we have that

$$k_{eq} = [Cas6e]_{eq} \cdot k^*, \quad (38)$$

where we adjust the equilibrium value of k in the constitutive and the cooperative case by varying the concentration of Cas6e in equilibrium. The equilibrium Cas6e concentration can be derived from the steady-state conditions for Equations and :

$$[Cas6e]_{eq} = \frac{k_{Cas6e}}{\lambda_{Cas}\lambda_{Cas6e}} \varphi_{Cas}(C_{eq}). \quad (39)$$

In the model of constitutive C and Cas6e expression, the equilibrium concentration of Cas6e is adjusted through the change of φ_{Cas} (being constant with time). In the case of cooperative C and Cas6e expression, $[Cas6e]_{eq}$ is adjusted through the change of α in Equation (33), i.e., through the change of overall *cas* promoter strength, taking into account that $[C]_{eq}$ is proportional to $[Cas6e]_{eq}$ according to (7).

Joint Change of *k* and φ

We here investigate how the joint change of k and φ, which corresponds to the joint increase of *cas6e* and CRISPR array gene expression, affects the dynamics of [pre-crRNA] and [crRNA] transcripts. We start from the baseline model of infinitely abrupt increase of k and φ. We then compare the baseline model to the more realistic case of constitutive and the cooperative models. We take φ change from the initial value of 10 1/min to 100 1/min in equilibrium, while k_{eq} takes on values λ_{pre}, 10λ_{pre}, and

$100\lambda_{pre}$. Note that the change in k_{eq}, implies joint change of φ_{Cas} in Equation (4) and *e* in Equation (15) in the constitutive case; in the cooperative case it implies joint change of α and p in Equation (33) and p' in Equation (37), which ensures the same functional dependency $\varphi(t)$, for different values of k_{eq}.

Perturbing Pre-crRNA Degradation Rate λ_{pre}

The pre-crRNA degradation rate λ_{pre} is perturbed (decreased) in the following two cases:

i. With the transcription rate φ (10 1/min) held constant. The equilibrium value of k is then adjusted by varying φ_{Cas} in the constitutive, and α in the cooperative model.
ii. When both φ and the processing rate k reach the equilibrium value (100 1/min) gradually, with the effect of the change assessed in all three models (baseline, constitutive and cooperative). k_{eq} reaches the value 100 1/min through the change of φ_{Cas} in the constitutive, and α and p in the cooperative model, while φ increases from $\varphi(0) = 10$ 1/min to $\varphi(C_{eq}) = 1,001/min$ through adjusting the parameters e in the constitutive, and p' in the cooperative model.

Note that changing λ_{pre} affects the initial amount of pre-crRNA (which is an initial condition for the differential equations) according to the relation $[pre-crRNA]_{eq}(t = 0) = \varphi(t = 0)/\lambda_{pre}$ (see Equation 2), which follows from the steady-state condition for pre-crRNA when the system is not activated.

AUTHOR CONTRIBUTIONS

FUNDING

ACKNOWLEDGMENTS

SUPPLEMENTARY MATERIAL

The Supplementary Material for this article can be found online at: https://www.frontiersin.org/articles/10.3389/fmicb.2017.02139/full#supplementary-material

REFERENCES

Al-Attar, S., Westra, E. R., van der Oost, J., and Brouns, S. J. (2011). Clustered regularly interspaced short palindromic repeats (CRISPRs): the hallmark of an ingenious antiviral defense mechanism in prokaryotes. *Biol. Chem.* 392, 277–289. doi: 10.1515/bc.2011.042

Barrangou, R., Fremaux, C., Deveau, H., Richards, M., Boyaval, P., Moineau, S., et al. (2007). CRISPR provides acquired resistance against viruses in prokaryotes. *Science* 315, 1709–1712. doi: 10.1126/science.1138140

Bogdanova, E., Djordjevic, M., Papapanagiotou, I., Heyduk, T., Kneale, G., and Severinov, K. (2008). Transcription regulation of the type II restriction-modification system AhdI. *Nucleic Acids Res.* 36, 1429–1442. doi: 10.1093/nar/gkm1116

Bogdanova, E., Zakharova, M., Streeter, S., Taylor, J., Heyduk, T., Kneale, G., et al. (2009). Transcription regulation of restriction-modification system Esp1396I. *Nucleic Acids Res.* 37, 3354–3366. doi: 10.1093/nar/gkp210

Bouffartigues, E., Buckle, M., Badaut, C., Travers, A., and Rimsky, S. (2007). H-NS cooperative binding to high-affinity sites in a regulatory element results in transcriptional silencing. *Nat. Struct. Mol. Biol.* 14, 441–448. doi: 10.1038/nsmb1233

Brouns, S. J., Jore, M. M., Lundgren, M., Westra, E. R., Slijkhuis, R. J., Snijders, A. P., et al. (2008). Small CRISPR RNAs guide antiviral defense in prokaryotes. *Science* 321, 960–964. doi: 10.1126/science.1159689

Chen, C. C., Fang, M., Majumder, A., and Wu, H. Y. (2001). A 72-base pair AT-rich DNA sequence element functions as a bacterial gene silencer. *J. Biol. Chem.* 276, 9478–9485. doi: 10.1074/jbc.M010501200

Djordjevic, M., Djordjevic, M., and Severinov, K. (2012). CRISPR transcript processing: a mechanism for generating a large number of small interfering RNAs. *Biol. Direct* 7:24. doi: 10.1186/1745-6150-7-24

Hill, T. L. (2013). *Cooperativity Theory in Biochemistry: Steady-State and Equilibrium Systems.* New York, NY: Springer Science & Business Media.

Hille, F., and Charpentier, E. (2016). CRISPR-Cas: biology, mechanisms and relevance. *Proc. Natl. Acad. Sci. U.S.A.* 371:20150496. doi: 10.1098/rstb.2015.0496

Kruger, D. H., and Schroeder, C. (1981). Bacteriophage T3 and bacteriophage T7 virus-host cell interactions. *Microbiol. Rev.* 45, 9–51.

Kunne, T., Kieper, S. N., Bannenberg, J. W., Vogel, A. I., Miellet, W. R., Klein, M., et al. (2016). Cas3-derived target DNA degradation fragments fuel primed CRISPR adaptation. *Mol. Cell* 63, 852–864. doi: 10.1016/j.molcel.2016.07.011

Makarova, K. S., Grishin, N. V., Shabalina, S. A., Wolf, Y. I., and Koonin, E. V. (2006). A putative RNA-interference-based immune system in prokaryotes: computational analysis of the predicted enzymatic machinery, functional analogies with eukaryotic RNAi, and hypothetical mechanisms of action. *Biol. Direct* 1:7. doi: 10.1186/1745-6150-1-7

Makarova, K. S., Haft, D. H., Barrangou, R., Brouns, S. J., Charpentier, E., Horvath, P., et al. (2011). Evolution and classification of the CRISPR-Cas systems. *Nat. Rev. Microbiol.* 9, 467–477. doi: 10.1038/nrmicro2577

Makarova, K. S., Wolf, Y. I., Alkhnbashi, O. S., Costa, F., Shah, S. A., Saunders, S. J., et al. (2015). An updated evolutionary classification of CRISPR-Cas systems. *Nat. Rev. Microbiol.* 13, 722–736. doi: 10.1038/nrmicro3569

Medina-Aparicio, L., Rebollar-Flores, J., Gallego-Hernandez, A., Vazquez, A., Olvera, L., Gutierrez-Rios, R., et al. (2011). The CRISPR/Cas immune system is an operon regulated by LeuO, H-NS, and leucine-responsive regulatory protein in *Salmonella enterica* serovar Typhi. *J. Bacteriol.* 193, 2396–2407. doi: 10.1128/JB.01480-10

Mojica, F. J., and Diez-Villasenor, C. (2010). The on-off switch of CRISPR immunity against phages in *Escherichia coli. Mol. Microbiol.* 77, 1341–1345. doi: 10.1111/j.1365-2958.2010.07326.x

Morozova, N., Sabantsev, A., Bogdanova, E., Fedorova, Y., Maikova, A., Vedyaykin, A., et al. (2015). Temporal dynamics of methyltransferase and restriction endonuclease accumulation in individual cells after introducing a restriction-modification system. *Nucleic Acids Res.* 44, 790–800. doi: 10.1093/nar/gkv1490

Mruk, I., and Blumenthal, R. M. (2008). Real-time kinetics of restriction–modification gene expression after entry into a new host cell. *Nucleic Acids Res.* 36, 2581–2593. doi: 10.1093/nar/gkn097

Mruk, I., and Kobayashi, I. (2013). To be or not to be: regulation of restriction–modification systems and other toxin–antitoxin systems. *Nucleic Acids Res.* 42, 70–86. doi: 10.1093/nar/gkt711

Musharova, O., Klimuk, E., Datsenko, K. A., Metlitskaya, A., Logacheva, M., Semenova, E., et al. (2017). Spacer-length DNA intermediates are associated with Cas1 in cells undergoing primed CRISPR adaptation. *Nucleic Acids Res.* 45, 3297–3307. doi: 10.1093/nar/gkx097

Patterson, A. G., Yevstigneyeva, M. S., and Fineran, P. C. (2017). Regulation of CRISPR–Cas adaptive immune systems. *Curr. Opin. Microbiol.* 37, 1–7. doi: 10.1016/j.mib.2017.02.004

Pingoud, A., Wilson, G. G., and Wende, W. (2014). Type II restriction endonucleases—a historical perspective and more. *Nucleic Acids Res.* 42, 7489–7527. doi: 10.1093/nar/gku447

Pougach, K., Semenova, E., Bogdanova, E., Datsenko, K. A., Djordjevic, M., Wanner, B. L., et al. (2010). Transcription, processing and function of CRISPR cassettes in *Escherichia coli. Mol. Microbiol.* 77, 1367–1379. doi: 10.1111/j.1365-2958.2010.07265.x

Pul, U., Wurm, R., Arslan, Z., Geissen, R., Hofmann, N., and Wagner, R. (2010). Identification and characterization of E. coli CRISPR-cas promoters and their silencing by H-NS. *Mol. Microbiol.* 75, 1495–1512. doi: 10.1111/j.1365-2958.2010.07073.x

Ratner, H. K., Sampson, T. R., and Weiss, D. S. (2015). I can see CRISPR now, even when phage are gone: a view on alternative CRISPR-Cas functions from the prokaryotic envelope. *Curr. Opin. Infect. Dis.* 28:267. doi: 10.1097/QCO.0000000000000154

Richter, C., Chang, J. T., and Fineran, P. C. (2012). Function and regulation of clustered regularly interspaced short palindromic repeats (CRISPR) / CRISPR associated (Cas) systems. *Viruses* 4, 2291–2311. doi: 10.3390/v4102291

Rodic, A., Blagojevic, B., Zdobnov, E., Djordjevic, M., and Djordjevic, M. (2017). Understanding key features of bacterial restriction-modification systems through quantitative modeling. *BMC Syst. Biol.* 11, 1–15. doi: 10.1186/s12918-016-0377-x

Semenova, E., Savitskaya, E., Musharova, O., Strotskaya, A., Vorontsova, D., Datsenko, K. A., et al. (2016). Highly efficient primed spacer acquisition from targets destroyed by the *Escherichia coli* type IE CRISPR-Cas interfering complex. *Proc. Natl. Acad. Sci. U.S.A.* 113, 7626–7631. doi: 10.1073/pnas.1602639113

Severinov, K., Ispolatov, I., and Semenova, E. (2016). The influence of copy-number of targeted extrachromosomal genetic elements on the outcome of CRISPR-Cas defense. *Proc. Natl. Acad. Sci. U.S.A.* 3:45. doi: 10.3389/fmolb.2016.00045

Sternberg, S. H., Richter, H., Charpentier, E., and Qimron, U. (2016). Adaptation in CRISPR-Cas Systems. *Mol. Cell* 61, 797–808. doi: 10.1016/j.molcel.2016.01.030

Stratmann, T., Pul, U., Wurm, R., Wagner, R., and Schnetz, K. (2012). RcsB-BglJ activates the *Escherichia coli* leuO gene, encoding an H-NS antagonist and pleiotropic regulator of virulence determinants. *Mol. Microbiol.* 83, 1109–1123. doi: 10.1111/j.1365-2958.2012.07993.x

Tao, T., Bourne, J. C., and Blumenthal, R. M. (1991). A family of regulatory genes associated with type II restriction-modification systems. *J. Bacteriol.* 173, 1367–1375. doi: 10.1128/jb.173.4.1367-1375.1991

Touchon, M., Charpentier, S., Clermont, O., Rocha, E. P., Denamur, E., and Branger, C. (2011). CRISPR distribution within the *Escherichia coli* species is not suggestive of immunity-associated diversifying selection. *J. Bacteriol.* 193, 2460–2467. doi: 10.1128/JB.01307-10

Vijesurier, R. M., Carlock, L., Blumenthal, R. M., and Dunbar, J. C. (2000). Role and mechanism of action of C · *Pvu*II, a regulatory protein

conserved among restriction-modification systems. *J. Bacteriol.* 182, 477–487. doi: 10.1128/JB.182.2.477-487.2000

Westra, E. R., Pul, U., Heidrich, N., Jore, M. M., Lundgren, M., Stratmann, T., et al. (2010). H-NS-mediated repression of CRISPR-based immunity in *Escherichia coli* K12 can be relieved by the transcription activator LeuO. *Mol. Microbiol.* 77, 1380–1393. doi: 10.1111/j.1365-2958.2010.07315.x

Yang, C. D., Chen, Y. H., Huang, H. Y., Huang, H. D., and Tseng, C. P. (2014). CRP represses the CRISPR/Cas system in *Escherichia coli*: evidence that endogenous CRISPR spacers impede phage P1 replication. *Mol. Microbiol.* 92, 1072–1091. doi: 10.1111/mmi.12614

Conflict of Interest Statement: The authors declare that the research was conducted in the absence of any commercial or financial relationships that could be construed as a potential conflict of interest.

BMC Systems Biology

CrossMark

Understanding key features of bacterial restriction-modification systems through quantitative modeling

Andjela Rodic[1,2†], Bojana Blagojevic[3†], Evgeny Zdobnov[4], Magdalena Djordjevic[3] and Marko Djordjevic[1*]

Abstract

Background: Restriction-modification (R-M) systems are rudimentary bacterial immune systems. The main components include restriction enzyme (R), which cuts specific unmethylated DNA sequences, and the methyltransferase (M), which protects the same DNA sequences. The expression of R-M system components is considered to be tightly regulated, to ensure successful establishment in a naïve bacterial host. R-M systems are organized in different architectures (convergent or divergent) and are characterized by different features, i.e. binding cooperativities, dissociation constants of dimerization, translation rates, which ensure this tight regulation. It has been proposed that R-M systems should exhibit certain dynamical properties during the system establishment, such as: *i)* a delayed expression of R with respect to M, *ii)* fast transition of R from "OFF" to "ON" state, *iii)* increased stability of the toxic molecule (R) steady-state levels. It is however unclear how different R-M system features and architectures ensure these dynamical properties, particularly since it is hard to address this question experimentally.

Results: To understand design of different R-M systems, we computationally analyze two R-M systems, representative of the subset controlled by small regulators called 'C proteins', and differing in having convergent or divergent promoter architecture. We show that, in the convergent system, abolishing any of the characteristic system features adversely affects the dynamical properties outlined above. Moreover, an extreme binding cooperativity, accompanied by a very high dissociation constant of dimerization, observed in the convergent system, but absent from other R-M systems, can be explained in terms of the same properties. Furthermore, we develop the first theoretical model for dynamics of a divergent R-M system, which does not share any of the convergent system features, but has overlapping promoters. We show that *i)* the system dynamics exhibits the same three dynamical properties, *ii)* introducing any of the convergent system features to the divergent system actually diminishes these properties.

Conclusions: Our results suggest that different R-M architectures and features may be understood in terms of constraints imposed by few simple dynamical properties of the system, providing a unifying framework for understanding these seemingly diverse systems. We also provided predictions for the perturbed R-M systems dynamics, which may in future be tested through increasingly available experimental techniques, such as re-engineering R-M systems and single-cell experiments.

Keywords: Restriction-modification, Transcription regulation, Bacterial immune systems, Biophysical modeling, Gene expression dynamics

* Correspondence: dmarko@bio.bg.ac.rs
†Equal contributors
[1]Institute of Physiology and Biochemistry, Faculty of Biology, University of Belgrade, Studentski trg 16, 11000 Belgrade, Serbia
Full list of author information is available at the end of the article

Background

Restriction-modification systems are rudimentary bacterial immune systems, whose main components are the restriction enzyme (R), and the methyltransferase (M). We here consider Type II restriction-modification (R-M) systems [1], where R cuts the same DNA sequences that are protected by M. Consequently, R and M act, respectively, as a toxic molecule and its antidote, and analogies of R-M and toxin-antitoxin systems are often made [2]. R-M present rudimentary "bacterial immune systems", as they protect the host bacterial cell against infection by foreign DNA, such as viruses (bacteriophages) [3–6]. The protection mechanism is straightforward, as the foreign DNA entering bacterial cell is unmethylated, and is consequently cut (destroyed) by R. On the other hand, the host DNA is methylated due to presence of M, and is therefore not cut by R, which prevents autoimmunity. In fact, many bacteriophages are under pressure from R-M systems with whom they have common hosts [7, 8], and have developed different mechanisms to avoid restriction [9–11]. Consequently, expression of the toxic molecule and its antidote provides an effective protection of the bacterial cell against foreign DNA infection [12].

R-M systems are often mobile [2, 12, 13], spreading from one bacterial host to the other, so that a bacterial host, which initially did not contain the R-M system (a naïve host), can acquire it through horizontal transfer. Expression of R and M was directly observed in single cells only very recently, for the Esp1396I system [14], and it is still unclear how different R-M system features affect this expression. It is however assumed that R-M expression has to be tightly regulated during its establishment in a naïve host [15]. For example, as the naïve host genome is initially unmethylated, R must be, and where tested actually is, expressed after a delay with respect to M, so that the host's genomic DNA can be protected before the appearance of R [14, 16, 17]. To ensure such tight regulation, a significant subset of R-M systems contains a third gene, which expresses the control protein (C) [5, 6, 18–23]. C is a transcription factor, which regulates expression of genes in R-M system, including its own expression. In fact, C is typically co-transcribed with R from a common promoter (CR promoter), while M is transcribed from a separate promoter (M promoter) [5, 6, 24].

With respect to the organization of the transcription units, two different architectures are exhibited, which correspond to the convergent (Fig. 1a), and the divergent (Fig. 1b) orientation of CR and M promoters [5, 6, 14, 20, 21, 23, 25, 26]. Despite R-M systems being known for few decades now, with numerous biotechnological uses of restriction enzymes, control of expression of these systems has been insufficiently studied. Two relatively well studied examples are AhdI (a representative of the convergent architecture) [6], and EcoRV (a divergent architecture

representative) [5]. For both systems, the core promoters (binding sites of RNA polymerase), and the binding sites of C protein, are experimentally mapped. In addition, for AhdI system, the transcription activity of CR promoter was measured as a function of C protein amount. We previously showed that a thermodynamic model of CR promoter regulation provides a good agreement with this measurement [6]. We also recently showed [14] that a similar thermodynamic model, coupled with a dynamical model of transcript and protein synthesis, can reasonably explain the dynamics of the enzyme synthesis measured by single-cell experiments in another convergent R-M system (Esp1396I). This strongly suggests that quantitative modeling presented here can realistically explain R-M system transcription control. Additionally, thermodynamical modeling of transcription regulation was successfully applied to a number of different biological problems [27–30], while dynamical modeling was applied to explain both more and less complex gene circuits including control of other convergent R-M systems [31–33].

As we detail below on the example of AhdI (convergent system), and EcoRV (divergent system), it is experimentally firmly established that R-M systems exhibit both different architectures, and different features that characterize their gene expression regulation [1, 15]. On the other hand, the regulation should yield the same three dynamical properties, so that the host genome is protected, while the system is efficiently established. In particular, as discussed above, there would have to be a significant expression of M before R is expressed, to ensure that the host genome is protected. Furthermore, once the host genome is protected, the system should likely turn to "ON" state as rapidly as possible, so that the host genome becomes "immune" to the virus infections – this would then require that after an initial delay, R is rapidly generated. Finally, we also previously proposed that, once the toxic molecule (R) reaches a steady-state, its fluctuations should be low – otherwise a high fluctuation in the toxic molecule (R) may not be matched by the antidote (M), which could destroy the host genome [34].

It is however unclear how the diverse system features and architectures, relate with the constraints on the dynamical response of the system stated above. Experimentally, one could, in principle, address this issue by mutating the relevant features (or introducing them in the system where they do not exist), and then measuring how the resulting system dynamics is perturbed. This would however be very hard, as the system would have to be extensively experimentally mutated and/or redesigned, and the resulting protein dynamics measured in-vivo during the system establishment. In that respect, note that the in-vivo dynamics of R and M expression were directly observed for only two Type II systems – in PvuII via nearly simultaneous introduction into a culture using bacteriophage M13 [17], and in Esp1396I, via
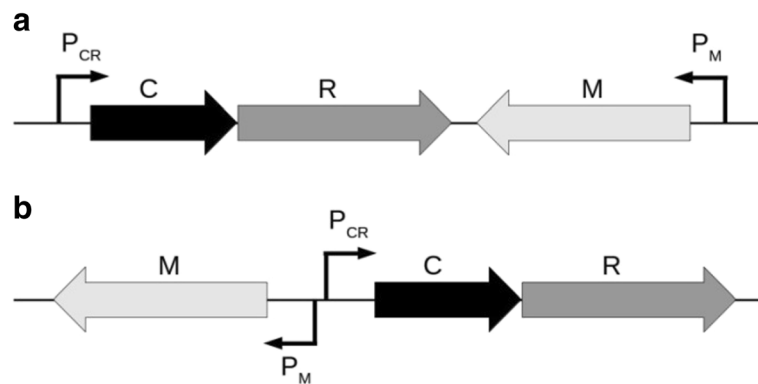
Fig. 1 Typical gene arrangement and promoter orientation in convergent and divergent R-M systems. **a** Convergent systems, a representative of which is AhdI, where other studied systems encoding C protein include Esp1396I, Kpn2I, Csp231I, PvuII [14, 23, 47–49]. Note that C and R genes are transcribed together from P_{CR} promoter. Transcription of M is exhibited from the separate P_M promoter. **b** Divergent systems, a representative of which is EcoRV, where BamHI is another studied divergent system that encods C protein [20]. C and R genes are also co-transcribed, but now share a common promoter region with M gene. In EcoRV the two divergent promoters (P_{CR} and P_M) have overlapping RNA polymerase binding sites

transformation followed by single cell analysis [14]. Even in these cases, the measurements are done only on the wild-type (wt) system, i.e. perturbations were not introduced in the system.

Therefore, the main purpose of this paper is to investigate the relationship between different system features/architectures, and the dynamical properties which the system is expected to exhibit during its establishment. In particular, it is our hypothesis that the diverse features exhibited in R-M systems may largely be explained in terms of the three dynamical properties discussed above. To start testing this hypothesis, we will here biophysically model the control of AhdI and EcoRV, and assess the resulting dynamics when the characteristic system features are either perturbed (in AhdI case) or (artificially) introduced (in EcoRV case) in the system. This is analogous to a classical approach in molecular biology, where the system is analyzed by mutating its main features, or introducing new features in the system where they do not exist, and consequently observing what effect these perturbations have on the presumed system function. The difference is that we here analyze the system *computationally* instead of *experimentally*, where we build on the fact that we previously showed that the modeling approach that we employ here can reasonably explain the available equilibrium measurements [6], and the available single cell experiments [14]. Therefore, the ability of the modeling to explain the measured wild-type data in R-M systems provides a reasonable confidence that our predictions for the perturbed system will also be realistic. Moreover, with the advancement of sophisticated experimental approaches, such as single cell experiments, or possibility to reengineer the system, there comes a prospect of directly experimentally testing these predictions in the future.

Specifically, we will here start by reviewing the relevant experimental information for AhdI and EcoRV

systems (the structure of their promoter regions and their regulatory features), which will provide a bases for our theoretical modeling. We will then quantify the general principles discussed above, i.e. introduce what we here call the dynamical property observables, which will allow us quantifying the delay between R and M, how fast the system makes the transition from OFF to ON state, and the stability of R steady-state levels. We will then investigate if abolishing the characteristic features of AhdI also diminishes these observables, i.e. negatively affects the dynamical properties discussed above. Furthermore, we will also study if these dynamical properties also apply to the system (EcoRV) where AhdI features are absent, but a new feature is present (the overlapping promoters). We will then ask what happens if the AhdI features are (computationally) introduced in wild-type EcoRV system, where they originally do not exist. That is, we will investigate if introducing these features leads to (at least) some of the three dynamic property observables being diminished – therefore explaining why they are absent from EcoRV. Overall, we will here systematically investigate how perturbing (or introducing new) features in two characteristic R-M systems affects the resulting system dynamics.

Methods

In the first subsection, we provide in detail the experimentally available information on AhdI (the convergent system) and EcoRV (the divergent system), on which we base our quantitative modeling. The main properties of the model, including the observables through which we assess the system dynamical properties, are provided in the second subsection. We note that the model itself is provided in details in Additional files 1 and 2, where all

the parameters (including their experimental/theoretical support) are listed.

Experimentally determined configurations of AhdI and EcoRV

For AhdI, the positions of different promoter elements (C protein and RNAP binding sites) were experimentally mapped for both CR and M promoters [6] (see Fig. 1a). In addition, the binding affinities and the transcription activities for both the wild type and mutant systems (where C protein binding sites were mutated) were measured [6]. These measured values, together with the standard literature values for the kinetic parameters (the translation and the degradation rates), were used to parameterize the model, as provided in detail in Additional file 1.

As indicated in Fig. 2a, C binds to CR promoter, regulating both its own transcription and the transcription of R [6, 19]. C binds to promoter DNA as a dimer, where binding to the distal binding site (configuration K_3), when C is present at relatively low concentration, leads to transcription activation, as C dimer bound to this position recruits RNAP binding to the promoter (configuration K_5). On the other hand, when C is present at high concentration, C dimer bound to the distal binding site recruits another C dimer to the proximal binding site (the tetramer configuration, K_4), thus repressing the transcription, as RNAP cannot bind to the promoter. Note that the configuration in which C dimer binds only to the proximal binding site (equivalent to K_3) is not shown, as the binding affinity to the proximal binding

site is much lower compared to the distal binding site, making this configuration much less probable. As for M gene, its transcription is controlled by a negative feedback loop, i.e. M methylates specific sites in its own core promoter thereby repressing the transcription (Fig. 2b).

There are three features which characterize control of AhdI expression [6]. First, there is a very high cooperativity in binding of the C protein dimers to the distal and the proximal positions in CR promoter, so that C dimer bound only to the distal site (K_3 configuration) exists only very transiently in the wild-type (wt) AhdI system. That is, in the absence of RNAP, a C dimer bound to the distal position immediately recruits another C dimer to the proximal binding site. Second, the C dissociation constant of dimerization for AhdI is very high, so that almost all C protein in the solution is in the form of monomers. Finally, C protein is translated from a leaderless transcript (i.e. a transcript which does not contain a ribosome binding site), which was in *E. coli* shown to be associated with lower translation initiation rate [35, 36].

For EcoRV, CR and M promoters are divergently oriented, as schematically shown in Fig. 1b. Consequently, the promoter elements are located in the intergenic region that separates CR and M genes, and these elements are also experimentally mapped [5]. Some of the binding affinities were also measured [5], while the others were eliminated by rescaling the equations (see Additional file 2) – note that we can rescale the equations, as we are interested only in the relative protein amounts. The kinetic parameters (the
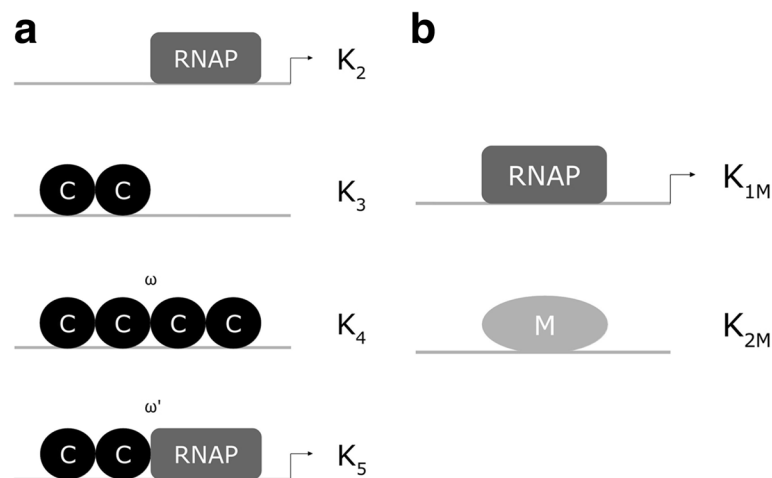
Fig. 2 AhdI R-M system promoter regions. The arrangement of the promoter elements for AhdI CR and M promoters is based on the experimental information provided in [6]. The regions which are schematically shown correspond to (**a**) P_{CR} promoter. Circles indicate C monomers, the rectangles indicates RNAP, while the arrows indicate transcriptionally active configurations. K_2 – K_5 denote the dissociation constants (see Additional file 1) corresponding to different promoter configurations (K_1 denotes the dissociation constant of dimerization), where ω and ω' denote, respectively, the binding cooperativity between the two C dimers bound to DNA, and between C dimer bound to the distal binding site and RNAP. C binds to the promoter as either dimer (K_3) or tetramer (K_4). The bound dimer recruits RNAP to the promoter (K_5). On the other hand, the tetramer configuration corresponds to the repression, as it prevents RNAP binding to the promoter. **b** Transcription is repressed by DNA methylation due to M binding [6], i.e. M methylates specific sites in M promoter that overlap RNAP binding site – for simplicity this is in the figure represented as M being bound to the promoter DNA
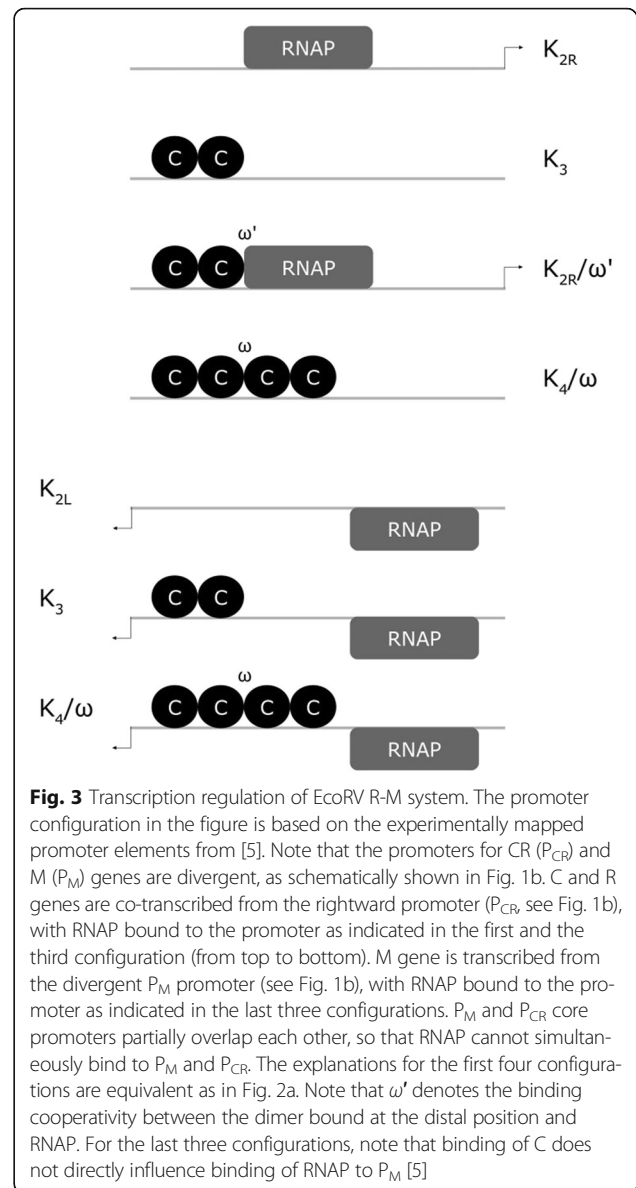
translation and the degradation rates), correspond to the standard literature values, and are taken to be the same as for AhdI (with the exception of C translation rate, see below).

In contrast to AhdI, the main feature of EcoRV is the partially overlapping CR and M core promoters, as schematically shown in Fig. 3. Consequently, RNAP cannot simultaneously bind to and initiate transcription from both P_M and P_{CR}. Moreover, the characteristic features of AhdI are not found in EcoRV [5]. In particular, while the transcription control of the CR promoter by C protein is similar as in AhdI, the main difference is that the large cooperativity between the C dimers at the distal and the proximal binding site is now absent, in fact it was found in EcoRV that the two dimers bind to DNA with no cooperativity [5]. Furthermore, the transcription from P_M is not directly influenced by C protein binding, i.e. C binding does not directly affect RNAP binding to P_M. However, the influence of C on P_M transcription is indirect, as the regulation by C of RNAP binding to P_{CR}, also affects when RNAP can bind to P_M. Consequently, while in AhdI transcription of CR and M was independent from each other, in EcoRV we have a more complex system where their transcription is strongly coupled. Similar regulation through overlapping CR and M core promoters is also found in CfrBI R-M system [26, 37]. Finally, C transcript is not leaderless in EcoRV, so the feature which was associated with lower translation initiation rate in *E. coli*, and which is present in AhdI, is now absent from EcoRV.

Modeling AhdI and EcoRV dynamics

We model R and M synthesis upon introducing AhdI and EcoRV in naïve bacterial hosts. The models are based on the experimental knowledge of AhdI and EcoRV transcription regulation, which is summarized in Figs. 2 and 3, respectively. The models are provided in detail in Additional files 1 and 2, and are briefly based on:

    (i) A thermodynamic model, which takes into account the activation and the repression of CR promoter by C, and the repression of M gene by its own product (which was experimentally shown in [6]). The model assumes that the promoter transcription activity is proportional to the equilibrium binding probability of RNAP to promoter, which is a general assumption initially proposed by the classical Shea-Ackers approach [38].

    (ii) Equations that predict how the transcription activity of CR and M promoters depends on C-protein concentration, which further allows modeling the dynamics of transcript and protein expression. That is, the modeled transcription activities provide the main

Fig. 3 Transcription regulation of EcoRV R-M system. The promoter configuration in the figure is based on the experimentally mapped promoter elements from [5]. Note that the promoters for CR (P_{CR}) and M (P_M) genes are divergent, as schematically shown in Fig. 1b. C and R genes are co-transcribed from the rightward promoter (P_{CR}, see Fig. 1b), with RNAP bound to the promoter as indicated in the first and the third configuration (from top to bottom). M gene is transcribed from the divergent P_M promoter (see Fig. 1b), with RNAP bound to the promoter as indicated in the last three configurations. P_M and P_{CR} core promoters partially overlap each other, so that RNAP cannot simultaneously bind to P_M and P_{CR}. The explanations for the first four configurations are equivalent as in Fig. 2a. Note that ω' denotes the binding cooperativity between the dimer bound at the distal position and RNAP. For the last three configurations, note that binding of C does not directly influence binding of RNAP to P_M [5]

input for a kinetic model, which calculates R, C and M transcript and protein synthesis. Also, note that R-M systems are characterized by very high expression of R and M proteins [14] so that on the order of thousands of molecules are present in the cell. Consequently, the system is expected to be well in the limit where deterministic modeling can be used to realistically describe the system.

We previously showed that such modeling can well explain the wild-type measurements for AhdI [6] - in particular the measured dependence of the transcription activity on C protein concentration – as well as the most recent measurements in single-cell experiments allowing directly observing the dynamics of R and M synthesis

[14]. Our aim here is to computationally analyze how systematically abolishing individual system features affects the system's dynamics, focusing on the following properties:

i. the time delay between R and M accumulation,
ii. the transition speed of the system from "OFF" to "ON",
iii. the stability of R steady-state levels.

For this, we will introduce observables (which we call the dynamical property observables) that can quantify these properties. To reasonably define them, it is useful to visualize the predicted system dynamics, and the stability of R steady-state levels in wild-type AhdI system, which is shown in Fig. 4 and calculated from Eqs. (1.12), (1.22) and (1.24)–(1.27) (see Additional file 1).

The first dynamical property observable (delay)

From Fig. 4a, we see that the system features lead to a significant delay in the expression of R compared to M, in accordance with the first dynamical property. To quantify how the delay changes upon perturbing these features, we introduce the first dynamical property observable, which corresponds to the ratios of the shaded areas in the perturbed system and in wt AhdI, at an initial interval post-system entry.

The second dynamical property observable (OFF to ON transition speed)

Furthermore, in Fig. 4a, we see that R expression curve has a sigmoidal shape. Consequently, the maximal slope of this curve (indicated in the figure) provides a reasonable measure of transition velocity from "OFF" (low R value) to "ON" (high R value) state. Therefore, as the second dynamical property observable, we introduce the maximal slope of this curve. The changes of this slope will allow assessing how the transition velocity – which determines the time window between the host genome being methylated, and the cell being protected against viruses – will be affected when the system features are perturbed.

The third dynamical property observable (R steady-state level stability)

Finally, the third dynamical property relates with fluctuations of the toxic R molecule, which we propose should be small in the steady-state [34]. The fluctuations are directly related with the stability of the steady-state, so that smaller fluctuations imply larger steady-state stability, which we introduce as the third dynamical property observable.

Different (in-silico) perturbations of the wild-type system – i.e. gradually abolishing the existing or introducing new features – will be introduced in either the thermodynamic model, or in the kinetic equations (see Additional files 1 and 2).
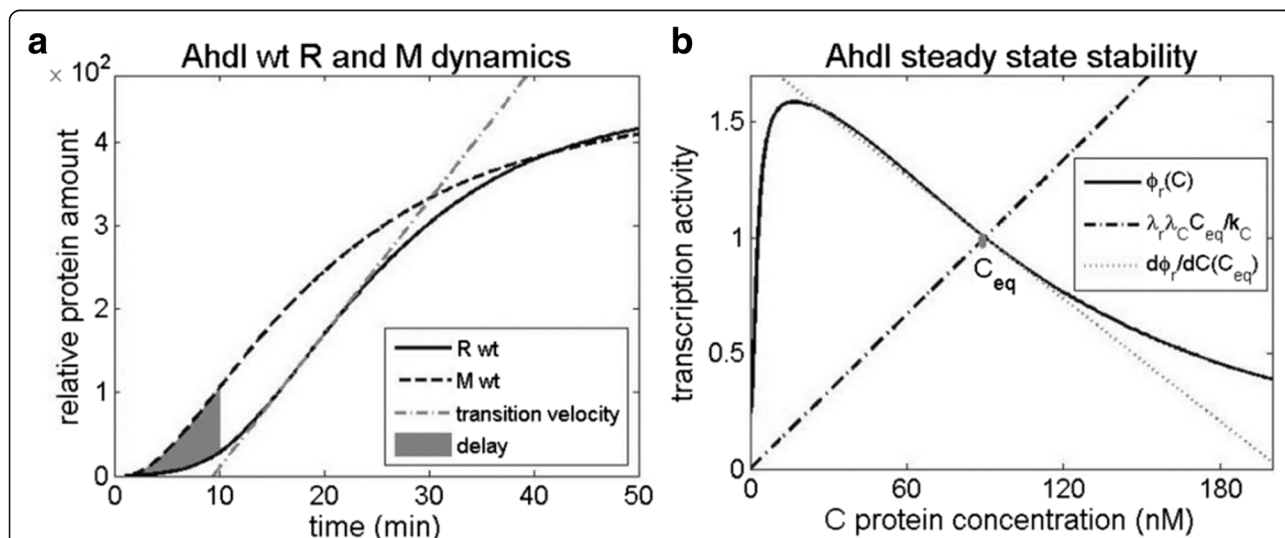
Fig. 4 a Dynamics of R and M expression. R and M expression upon the system entry in a naïve bacterial host (0 min corresponds to the system entry). The shaded area corresponds to the difference of the surface areas below M (dashed curve) and R (solid curve) expression curves for the first 10 min post-system entry; the area presents a measure of the delay between M and R expression. The dash-dot line corresponds to the maximal slope of the sigmoidal R expression curve, measuring the transition velocity from OFF to ON state. **b** Steady-state and its stability. The steady-state (indicated by C_{eq}) is obtained as an intersection of the transcription activity (the solid black line), and the dash-dot line whose slope is determined by the transcript decay and the protein translation rate (Eq. (1.33)). The stability of the steady-state is related with the difference of the dash-dot line slope, and the slope of the transcription activity (the dotted line in the figure) at the point of their intersection C_{eq} (Eq. (1.34))

Results and discussion

We will start by gradually abolishing the three characteristic AhdI features introduced above, and assess how this will affect the dynamical property observables. We will next model the dynamics of EcoRV establishment in a naïve bacterial host, to see if the proposed dynamical properties also apply to a system with different architecture and transcription regulation features. This will provide, to our knowledge, the first quantitative model of a divergent R-M system control, and an opportunity to assess dynamics of R and M expression, which was up to now not experimentally observed for the divergent systems. Finally, we will in-silico introduce to EcoRV the regulation features that exist in AhdI, but are not found in EcoRV, to investigate how this effects the dynamical property observables, and why these features are not present in EcoRV.

Perturbing AhdI system features

The three characteristic AhdI features are the high C subunit dissociation constant of dimerization, the large cooperativity between C dimers bound at the distal and the proximal position, and the low C transcript translation initiation rate. It was previously discussed that these features serve to limit the amount of the synthesized toxic molecule (R) [6]. However, it is not clear that this amount per-se should be limited, as a too small steady-state amount of R may compromise the immune response – i.e. it can lead to the virus genome being protected by M before it can be destroyed by R [39]. As we discussed above, it would be very hard to experimentally investigate the effect of these AhdI features on the system dynamics, this can be readily predicted from the model that we formulated above.

Decreasing the dissociation constant of dimerization

The dissociation constant of dimerization K_1 is very high for AhdI, leading to almost all C subunits being present as monomers in solution [6, 40] – e.g. for another convergent R-M system (Esp1396I), the measured dissociation constant of dimerization was found to be significantly (four times) lower [41]. We start by gradually decreasing this high dissociation constant of dimerization, in the range that corresponds to the wild-type (all monomers in the solution) to the opposite limit of lower K_1, in which only dimers are present in the solution. In Fig. 5a, we see that this perturbation has a significant effect on R synthesis dynamics – note that the M dynamics curve, which is also indicated in the figure for reference, is not affected by perturbing the three characteristic AhdI features. One can observe the three main effects from Fig. 5a: The decrease of the delay between R and M expression, the slower transition from OFF to ON state, and the decrease in the steady-state

level of R. The first two effects are further quantified in Fig. 5b and c, as discussed below.

In Fig. 5b, we see that decreasing K_1 leads to a significant, more than twofold, decrease in the relative delay between R and M expression. This perturbation can then significantly impact the ability of the system to protect the host genome from being cut during R-M establishment, with the necessary lag also depending on the specific activity of the M protein and the propensity for R to nick hemimethylated sites. Furthermore, in Fig. 5c we see that decreasing K_1 also leads to a significantly slower transition from OFF to ON state, so that the maximal slope is decreased for almost two-fold. Therefore, decreasing the wt dissociation constant of dimerization also significantly impacts the time window in which the host will be protected from foreign DNA infection. However, perturbing K1 has no significant effect on the steady-state stability of R levels (Fig. 5d). Overall, decreasing the high dissociation constant of dimerization characteristic for wt AhdI, has a significant adverse effect on two of the three proposed design principles.

Increasing C protein translation rate

In AhdI C transcript is leaderless [6], which was in *E. coli* [35, 36] shown to be associated with a significantly smaller translation initiation rate – consequently in [6] a five times smaller C transcript translation rate k_C, compared to R and M was assumed. We now test the effect of perturbing this system feature, i.e. increasing k_C towards those of R and M transcripts, which is shown in Fig. 6. We see that the main effect of this perturbation is on decreasing the steady-state level of R and the delay between R and M expression (for ~ 40%), as shown in Fig. 6a-b. Intuitively, this can be understood that by a more efficient C transcript translation, C accumulates faster, facilitating the formation of the activating and the repressing complexes on the CR promoter, so that R is expressed with a smaller delay, and reaches the lower steady-state level. On the other hand, the effect on the other two design-observables, i.e. on the transition velocity and the stability of R steady-state levels, is rather small (Fig. 6c-d). Consequently, increasing the low C transcript translation rate adversely affects one of the dynamical property observables, i.e. the delayed expression of R with respect to M, which is considered crucial for the protection of the host genome.

Decreasing cooperativity in the dimer binding

A rather drastic feature of AhdI is a very large cooperativity ω in binding of the two dimers to the distal and the proximal position in the promoter [6], which is either not present (EcoRV) [5], or significantly smaller (Esp1396I) [41], in other R-M systems. We therefore investigate how gradually abolishing this high cooperativity affects the
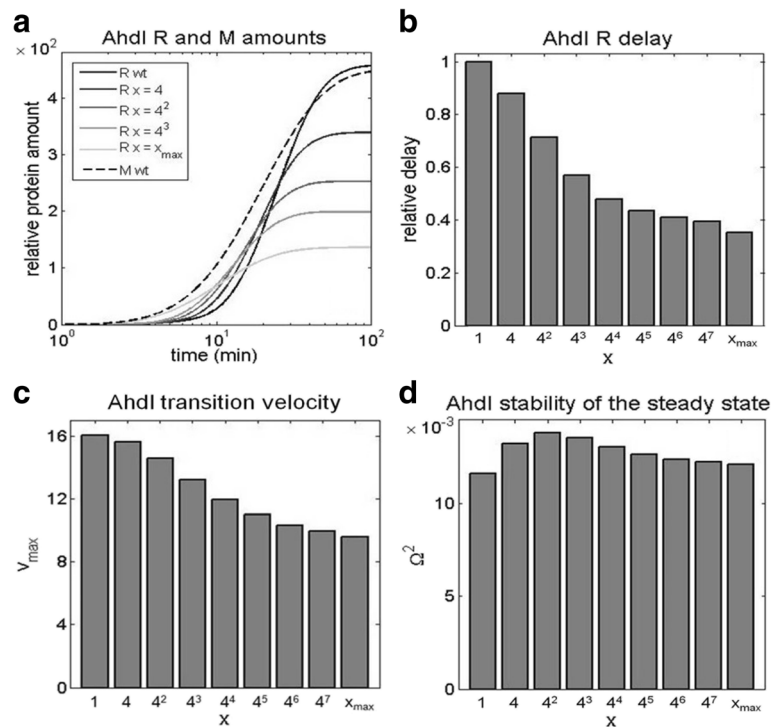
Fig. 5 Decreasing AhdI dissociation constant of dimerization. K_1 is decreased from the high value corresponding to mostly monomers in the solution, to the low value corresponding to mostly dimers in the solution, and the effect is assessed on **a** The dynamics of the protein synthesis. The black line corresponds to all monomers in the solution (wt), while the light gray line corresponds to all dimers in the solution. The curves in-between (in different shades of gray) correspond to the gradually decreasing values of K_1. The relative protein amounts for a wt system (on the vertical axis) are derived from in-vitro transcription activity measurements in [6]. x indicated in the legend corresponds to the relative decrease of K_1 (e.g. x = 4 is a four-fold decrease). **b** The first dynamical property observable, corresponding to the relative delay of R with respect to M expression. The delay is normalized with respect to the wild type (corresponding to one). **c** The second dynamical property observable, corresponding to the transition velocity from "OFF" to "ON" state, represented by the maximal slope of the R expression curve. **d** The third dynamical property observable, corresponding to the stability of R steady-state levels (see Methods)

system dynamics and the design observables. In Fig. 7a, we see that abolishing ω affects only the late dynamics of R, so that the first two dynamical properties are not affected (and not shown in Fig. 7). On the other hand, we see that the steady-state amount of R significantly increases as the cooperativity ω decreases. This can be intuitively understood by the fact that perturbing the cooperativity affects only the efficiency of forming the repressor tetramer complex. As the probability of forming this complex is proportional to C^4 (see Additional file 1), it becomes significant only in the later period, when a large enough amount of C is synthesized. Furthermore, in accordance with the perturbation affecting the late dynamics, from Fig. 7b, we see that decreasing the cooperativity significantly impacts the stability of R steady-state levels, leading to its 50% decrease.

Importantly, the first two AhdI features (the large dissociation constant of dimerization, and the small C translation initiation rate) have an opposite effect on the steady-state amount of R, as compared to the large

cooperativity in C dimer binding. That is, while we showed that the first two features significantly increase the steady-state R amount, the third feature (the large cooperativity) significantly decreases it. On the other hand, all three features generally have the same effect on the three dynamical properties that we consider, i.e. abolishing these features either decreases the values of the dynamical property observables (making the corresponding dynamical property less optimal), or do not significantly affect them. This can then explain the extremely large binding cooperativity that was experimentally observed, as on the one side it allows controlling the steady-state amount of the toxic protein due to the opposite effect from the other two features, while at the same time working together with the first two features to ensure more optimal dynamical properties. In particular, note that both the large dissociation constant of dimerization and the large binding cooperativity significantly increase the stability of R steady-state levels, while having a significant - but opposite – effects on the steady-state R amounts.
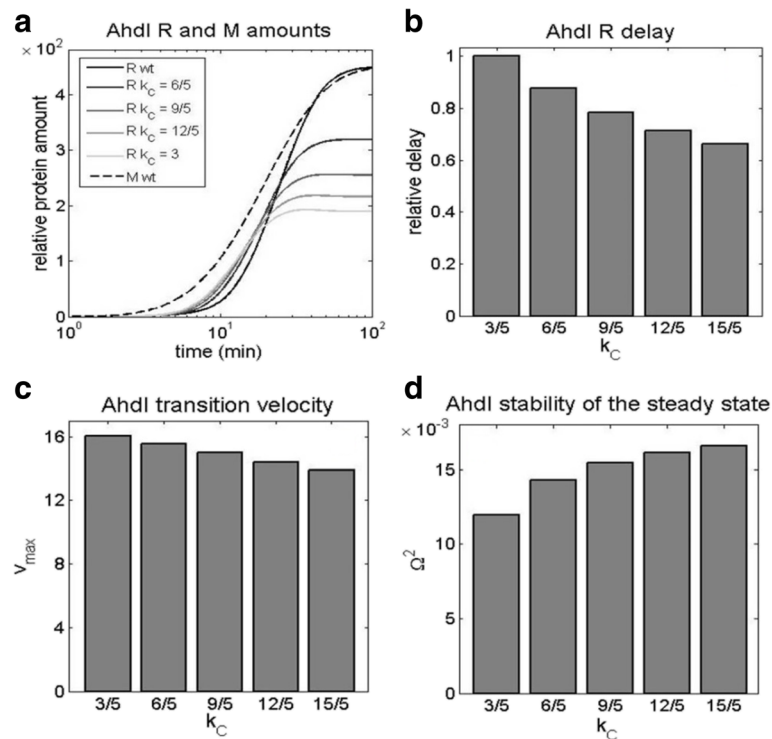
Fig. 6 Increasing C transcript translation rate: k_C is increased from the lower value (3/5 1/min) as taken in [6] to the value which equals those for R and M transcripts (3 1/min). The effect of this decrease is assessed for: **a** The dynamics of the protein synthesis, with the black curve corresponding to the lowest (wt) k_C, and the light gray curve corresponding to the highest k_C (which equals those of R and M transcripts). The curves in different shades of gray correspond to the gradually increasing k_C values. **b** The relative delay (normalized with respect to wt) of R with respect to M expression. **c** The maximal slope of the R expression curve, reflecting the transition velocity from "OFF" to "ON" state. **d** The stability of R steady-state levels, is shown on the vertical axis

EcoRV wild-type dynamics

EcoRV is an example of R-M system with a divergent organization of CR and M transcription units. Overlapping CR and M promoters is the most distinctive feature of this system (presenting its main difference with respect to AhdI), which is, together with C protein binding, responsible for control of EcoRV transcription. That is, high occupancy of M promoter by RNAP, prevents RNAP binding to CR promoter, leading to lower CR transcription activity, and vice versa. In modeling the gene expression regulation, we consider that CR promoter transcription is controlled by C, while C binding has little to none direct effect on M promoter transcription activity, as shown in [5]. In distinction to AhdI [6], which shows an extremely high cooperativity in C dimer binding, no coperativity was found in EcoRV [5]. We also assume that C dissociation constant of dimerization is significantly lower than the relevant range of C concentration, so that the majority of C molecules in solution exist as dimers. Note that in another R-M system (Esp1396I), which has a much lower cooperativity in C dimer binding compared to AhdI, a significantly lower dissociation constant of dimerization is also observed

[41]. Finally, in distinction to AhdI, C transcript in EcoRV is not leaderless, so for EcoRV we assume that C has the same translation initiation rate as R and M.

Consequently, EcoRV does not have the three features that control transcription in AhdI, but has instead another characteristic feature, i.e. the overlapping CR and M promoters. We therefore ask if EcoRV, with different architecture and the regulation features, can also meet the three dynamical properties that we consider. To that end, we modeled the synthesis of R and M during the system establishment in wild-type EcoRV, under the assumptions stated above, and following the scheme of the transcription configurations shown in Fig. 3. The model is provided in detail in Additional file 2, and is based on the same thermodynamics assumptions as the one for AhdI dynamics. To our knowledge, this presents the first model of expression dynamics for a divergent R-M system, which has a more complex regulation due to overlapping nature of their promoters. This model moreover presents the first opportunity to assess the dynamics of R and M synthesis for a divergent R-M system, as, to our knowledge, either their regulation or their expression dynamics was not previously measured.
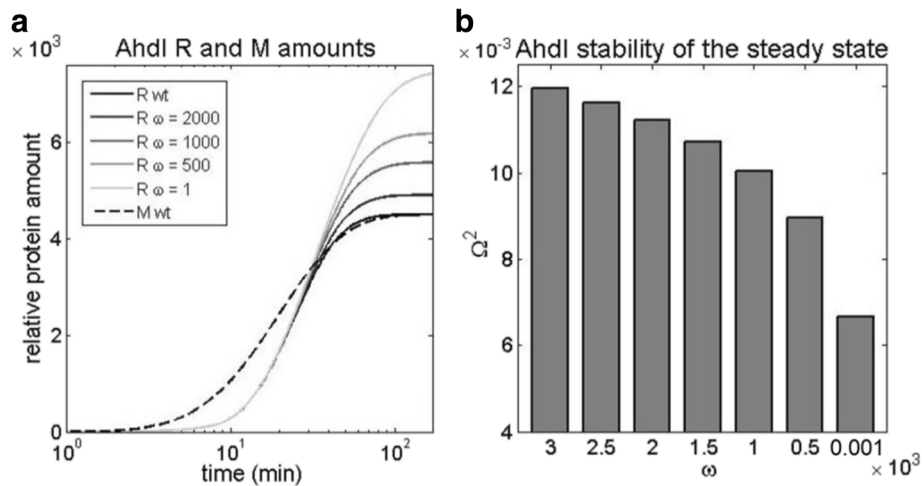
Fig. 7 Decreasing cooperativity in C dimer binding to CR promoter. The cooperativity in binding ω is gradually abolished from the very high value corresponding to wt AhdI [6] to ω corresponding to the absence of the binding cooperativity. We predict the effect of this decrease on: **a** The dynamics of R protein synthesis, where the black line corresponds to the high ω, the light gray to no cooperativity, and the values of cooperativity in-between are shown in different shades of gray. **b** The stability of R steady-state levels, corresponding to different ω values shown in **a**

The predictions for R and M accumulation in wild-type EcoRV are shown by the full black curve (for R) and by the black dashed curve (for M), in Fig. 8 below. From the figure we see that, regardless of lacking the characteristic AhdI regulatory features, the synthesis of R and M is well in accordance with the three dynamical properties. Namely, by comparing Fig. 4 (the dynamics of AhdI) with the EcoRV dynamics, we see that: *i*) the time delay for EcoRV is even larger compared to AhdI, *ii*) there is a clear switch-like behavior of R expression in EcoRV, i.e. the speed of transition from "OFF" to "ON" state is comparable to the one in AhdI, iii) the system reaches the steady-state level ($\Omega^2 > 0$), where the reached stabilities of R steady-state levels are comparable (compare Fig. 5d with Fig. 8c). Therefore, we see that the design principles which we showed are inherent to AhdI R-M system, are retained in EcoRV R-M system, despite the apparent distinction in gene expression regulation.

Introducing AhdI control features to EcoRV
Next, there is a question of why the characteristic AhdI features are absent from EcoRV. That is, could we get even more optimal design-observables if AhdI control features are introduced in wild-type EcoRV? Therefore, we next use our model, to individually introduce each of the three control features of AhdI, on the top of the existing wt EcoRV regulation (i.e. the overlapping promoters). Specifically, in the wild-type EcoRV, we will perturb: *i*) the dissociation constant of dimerization towards the high values characteristic for AhdI, *ii*) cooperativity in C dimer binding to the promoter, also

towards the high values observed in AhdI, *iii*) C protein translation rate k_C, towards the low values characteristic for leaderless AhdI C transcripts.

Introducing the high dissociation constant of dimerization to EcoRV
We first perturb the wt EcoRV system by increasing the rescaled equilibrium dissociation constant of dimerization $\overline{K}_1$ (see Fig.8 and Additional file 2), which corresponds to a gradual transition from the solution containing mostly C dimers to the solution containing mostly C monomers. Note that the dynamics of both R and M expression is now affected by the perturbation, in distinction to AhdI where only R expression is changed. This is because CR and M promoters overlap in EcoRV, so that changing transcription from one promoter, necessarily impacts transcription from the other.

We observe that this perturbation does not significantly affect the early accumulation of R and M (during the first ~10 min), but that the dynamics at later times is significantly affected (see Fig. 8a). In particular, we see that increasing the dissociation constant of dimerization leads to a significantly slower switch from "OFF" to "ON" state, so that the transition velocity decreases as much as four times (Fig. 8b). Furthermore, in Fig. 8c, we see that increasing $\overline{K}_1$ also significantly decreases the stability of R steady-state levels Ω^2, which drops almost three times. Consequently, introducing the high dissociation constant of dimerization to EcoRV, which is characteristic for AhdI, has a significant adverse effect on two of the three dynamical properties.
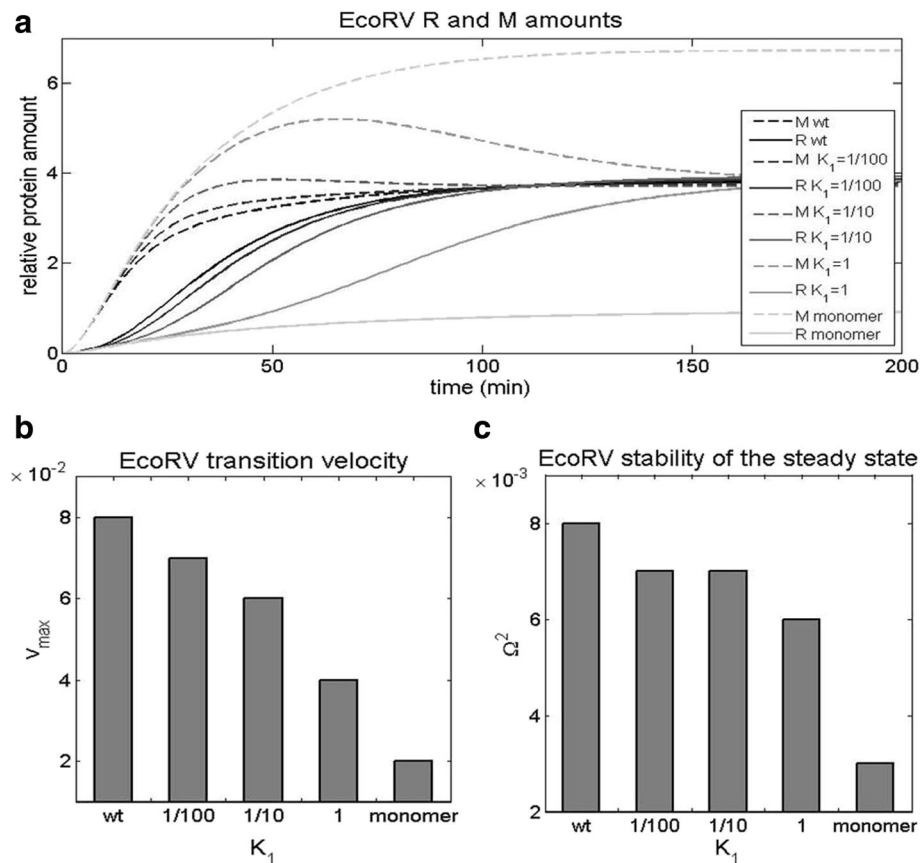
Fig. 8 Increasing the dissociation constant of dimerization of wt EcoRV system. The rescaled dissociation constant of dimerization $\overline{K}_1$ is increased from the lower value with dimers in the solution corresponding to wt system, to the high value, where mostly monomers are in the solution. The effect of the increasing dissociation constant of dimerization is assessed on: **a** The dynamics of R and M synthesis. The solid and the dashed line correspond to R and M dynamics, respectively. Different shades of gray correspond to the increasing value of the dissociation constant of dimerization, with the black line and the light gray line corresponding to the wild type and the monomer case, respectively. **b** The transition velocity v_{max} from "OFF" to "ON" state. **c** The stability of R steady-state levels

Introducing the high C dimer binding cooperativity

We next modify wt EcoRV by increasing the cooperativity ω of C dimer binding to the proximal and the distal binding site, while keeping the other wt EcoRV features unchanged. Note that the experimental measurements in wt EcoRV show an absence of C dimer binding cooperativity ($\omega = 1$) [5], as opposed to the extremely large binding cooperativity that is observed in AhdI [6]. In Fig. 9, we see that increasing ω has the following effects: *i*) the time delay remains nearly the same (Fig. 9a), *ii*) the transition velocity decreases (Fig. 9b), where we see that increasing ω for a relatively moderate factor (2^4), leads to a significant (somewhat less than twofold) decrease of v_{max}, *iii*) stability of R steady-state levels slightly increases. Consequently, we see that perturbing wt EcoRV cooperativity towards the higher values characteristic for AhdI, has a significant adverse effect on one of the dynamical properties (the transition velocity), while not significantly affecting the other two.

Decreasing C translation rate in EcoRV

Finally, we perturb wt EcoRV by decreasing C transcript translation rate k_C, towards the value characteristic for AhdI. Note that C transcript is leaderless in AhdI [6], which is not the case for EcoRV [5], so that we assume the same translation rate for all three transcripts (C, R and M) in EcoRV, while k_C is taken as five times lower in AhdI according to [6]. In Fig. 10a we observe that decreasing k_C does not impact the initial R and M accumulation (during the first ~10 min). On the other hand, at later times the perturbation significantly decreases both the transition velocity that decreases two times (see Fig. 10b), and the stability of R steady-state levels that decreases somewhat less than twofold (see Fig. 10c). Consequently, we see that again two of the three dynamical properties are significantly adversely affected by introducing a control feature from AhdI.

Overall, introducing AhdI characteristic features to EcoRV has a significant adverse effect on at least one of
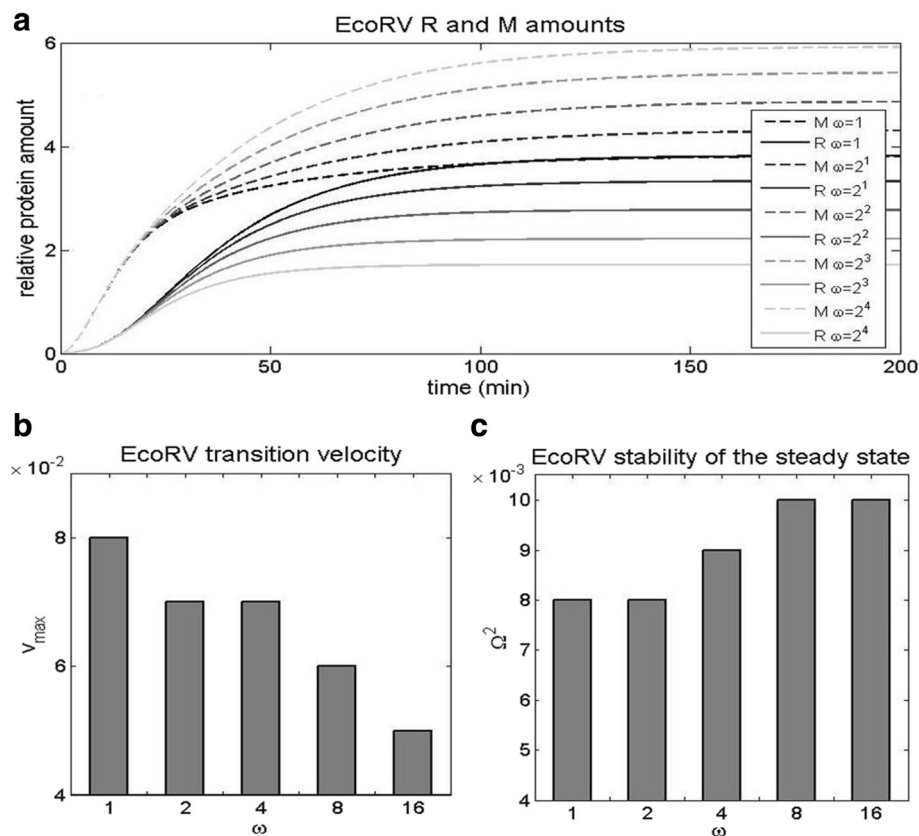
Fig. 9 Increasing C dimer binding cooperativity in wt EcoRV. The binding cooperativity ω is increased from the absence of cooperativity (ω = 1, corresponding to wt EcoRV), to the higher values corresponding to cooperative C dimer binding. For each curve, ω is increased in steps by a factor of 2, and the effect is assessed on: **a** The dynamics of R and M synthesis. The solid and the dashed curves correspond, respectively, to the dynamics of R and M synthesis. The black curve corresponds to wt (no cooperativity), with the curves fading, as the cooperativity increases (with the light gray corresponding to maximal ω). **b** The transition velocity v_{max}. **c** The stability of R steady-state levels

the dynamical properties, which may explain why those features are not found in EcoRV. Additionally, perturbing EcoRV wt parameters towards the AhdI values (Figs. 8a, 9a and 10a) changes M to R ratio in the same direction for each introduced feature (consistently increasing the ratio). This is in distinction to AhdI, where the high cooperativity of C dimer binding has an opposite effect on this ratio, compared to the other two features. Consequently, we argue that another reason for why the characteristic AhdI features are not observed in EcoRV, is because they do not allow balancing the amounts of R and M in the host cell.

Conclusion

R-M systems are characterized by different architectures and control features. We here test a hypothesis that these diverse features can be explained by constraints imposed by few dynamical properties. We started from a relatively well studied AhdI system, and computationally abolished three of its characteristic control features, showing that this has a clear adverse effect on the three

dynamical properties. We then modeled a system with different architecture (EcoRV), and showed that its expression dynamics also satisfies the same properties. The EcoRV model has significance in its own right, as the expression dynamics of the divergent R-M systems was, to our knowledge, not studied before, either theoretically or experimentally. Finally, we computationally introduced to EcoRV the control features that exist in AhdI, and showed that this diminishes at least some of the proposed dynamical properties, consistent with the fact that these features do not appear in wt EcoRV. Moreover, increasing the binding cooperativity has the same effect on M to R ratio in EcoRV as increasing the dissociation constant of dimerization, or lowering the translation rate, which prevents balancing M to R ratio upon introducing these perturbations – this then provides another argument for why AhdI control features are absent from wt EcoRV.

Furthermore, dynamical properties proposed here can provide an explanation for a surprisingly large value of the cooperativity in C protein binding, accompanied by
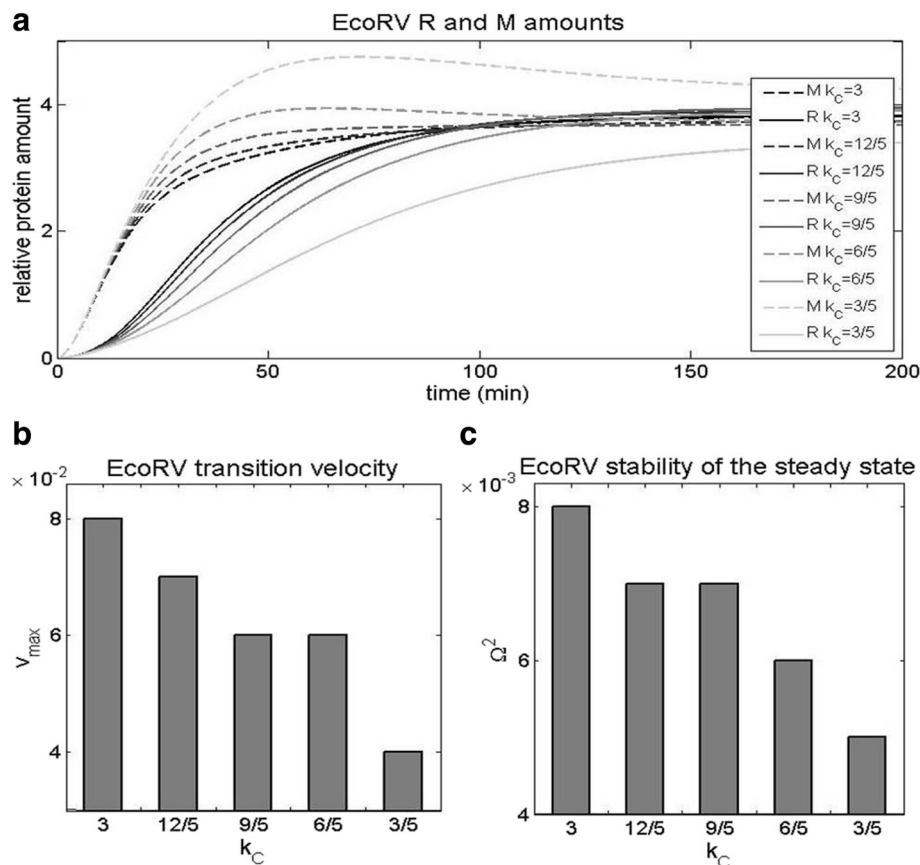
Fig. 10 Decreasing C transcript translation rate of wt EcoRV system. The translation rate of C transcript is decreased towards the low value characteristic for wt AhdI, and the effect is assessed on **a** The dynamics of R and M synthesis. The solid curves correspond to R, while the dashed curves correspond to M. The curves fade as k_C decreases, so that the black curve, and the light gray curve, correspond, respectively, to the maximal (wt) and the minimal k_C. **b** The transition velocity from "OFF" to "ON" state. **c** The stability of R steady-state levels

the large dissociation constant of dimerization that was observed in wt AhdI. We here showed that these two features have an opposite effect on the steady-state levels of the toxic molecule (R), allowing balancing the steady-state R amount, while at the same time leading to more optimal dynamical properties. In support of this proposal, a similar convergent system with lower binding cooperativity (Esp1396I) was also found to have a lower value of the dissociation constant of dimerization. As a prediction, it will be interesting to test if, in other R-M systems, the value of the dissociation constant of dimerization and the binding cooperativity are also related in this way.

Overall, this work provides an example that the system properties that may appear "random" or even surprising (such as the extremely large binding cooperativity) may be explained by constraints imposed by few general principles (in this case the system dynamical properties). Additionally, some of these system properties may serve other functions, e.g. the leaderless C transcripts might be related with a need for preferential translation under specific physiological conditions [42]. Analyzing other R-M systems can further test relation of the system features with the simple dynamical properties, where the main obstacle is that their transcription regulation is generally not well studied. In particular, investigating up to now poorly understood linear R-M systems, which have different architecture compared to the convergent and the divergent systems studied here, and which do not encode C proteins – but may exhibit control by antisense RNAs or at the level of translation initiation efficiency - may be particularly useful [43, 44]. As a further outlook, it will be interesting investigating if properties of other bacterial immune systems, such as recently discovered CRISPR/Cas systems [45], can also be explained by similar dynamical properties [34]. With that respect note that CRISPR/Cas is more advanced, i.e. adaptive bacterial immune system, which retains a memory of the past infections incorporated as spacers in the CRISPR array [46].

Also, in this work we follow a standard approach in molecular biology, where features of the system are perturbed/mutated (which is here done in-silico), and the

effect of these perturbations on the presumed system function is assessed. In addition to such "single mutations", a computational equivalent of "double" or "triple" mutations can be exhibited, where more than one system feature would be simultaneously perturbed. This would address the question if perturbations in one feature, can be rescued by also perturbing the other feature(s), which is related to the system robustness. While this question is out of the scope of this work, it also provides an interesting outlook for future research.

Finally, the recent advancement of experimental techniques, such as single-cell experiments, allows directly observing the protein dynamics during the system establishment. While in principle arduous, it would be interesting to experimentally observe how the relevant dynamics is perturbed when some of the key system features are abolished. This would then directly put to test some of the prediction from the computational modelling, which we provided here.

Additional files

Additional file 1: Model of AhdI regulation and dynamics. (PDF 415 kb)

Additional file 2: Model of EcoRV regulation and dynamics. (DOCX 198 kb)

Abbreviations
C: Control protein; M: Methyltransferase; R: Restriction enzyme; R-M: Restriction-modification; RNAP: RNA polymerase; wt: Wild-type

Availability of data and materials
The datasets used and/or analyzed during the current study available from the corresponding author on reasonable request.

Authors' contributions
MJD, MRD and EZ conceived the work. AR and BB performed the analysis. All the authors interpreted the results. MJD, AR and BB wrote the paper, with the help of MRD and EZ. All authors read and approved the final manuscript.

Competing interests
The authors declare that they have no competing interests.

Consent for publication
Not applicable

Ethics approval and consent to participate
Not applicable

Author details
[1]Institute of Physiology and Biochemistry, Faculty of Biology, University of Belgrade, Studentski trg 16, 11000 Belgrade, Serbia. [2]Multidisciplinary PhD program in Biophysics, University of Belgrade, Belgrade, Serbia. [3]Institute of Physics Belgrade, University of Belgrade, Belgrade, Serbia. [4]Department of Genetic Medicine and Development, University of Geneva and Swiss Institute of Bioinformatics, Geneva, Switzerland.

Published: 24 February 2017

References
1. Pingoud A, Wilson GG, Wende W. Type II restriction endonucleases—a historical perspective and more. Nucleic Acids Res. 2014;42(12):7489–527.
2. Mruk I, Kobayashi I. To be or not to be: regulation of restriction–modification systems and other toxin–antitoxin systems. Nucleic Acids Res. 2014;42(1):70-86.
3. Gingeras TR, Brooks JE. Cloned restriction/modification system from Pseudomonas aeruginosa. Proc Natl Acad Sci. 1983;80(2):402–6.
4. Kiss A, Posfai G, Keller CC, Venetianer P, Roberts RJ. Nudeotide sequence of the BsuRI restriction-modification system. Nucleic Acids Res. 1985;13(18):6403–21.
5. Semenova E, Minakhin L, Bogdanova E, Nagornykh M, Vasilov A, Heyduk T, Solonin A, Zakharova M, Severinov K. Transcription regulation of the EcoRV restriction-modification system. Nucleic Acids Res. 2005;33(21):6942–51.
6. Bogdanova E, Djordjevic M, Papapanagiotou I, Heyduk T, Kneale G, Severinov K. Transcription regulation of the type II restriction-modification system AhdI. Nucleic Acids Res. 2008;36(5):1429–42.
7. Krüger D, Bickle TA. Bacteriophage survival: multiple mechanisms for avoiding the deoxyribonucleic acid restriction systems of their hosts. Microbiol Rev. 1983;47(3):345.
8. Tock MR, Dryden DT. The biology of restriction and anti-restriction. Curr Opin Microbiol. 2005;8(4):466–72.
9. Korona R, Korona B, Levin BR. Sensitivity of naturally occurring coliphages to type I and type II restriction and modification. Microbiology. 1993;139(6):1283–90.
10. Makino O, Saito H, Ando T. Bacillus subtilis-phage φ1 overcomes host-controlled restriction by producing BamNx inhibitor protein. Mol Gen Genet MGG. 1980;179(3):463–8.
11. Takahashi I, Marmur J. Replacement of thymidylic acid by deoxyuridylic acid in the deoxyribonucleic acid of a transducing phage for Bacillus subtilis. 1963.
12. Kobayashi I. Behavior of restriction-modification systems as selfish mobile elements and their impact on genome evolution. Nucleic Acids Res. 2001; 29(18):3742–56.
13. Jeltsch A, Pingoud A. Horizontal gene transfer contributes to the wide distribution and evolution of type II restriction-modification systems. J Mol Evol. 1996;42(2):91–6.
14. Morozova N, Sabantsev A, Bogdanova E, Fedorova Y, Maikova A, Vedyaykin A, Rodic A, Djordjevic M, Khodorkovskii M, Severinov K. Temporal dynamics of methyltransferase and restriction endonuclease accumulation in individual cells after introducing a restriction-modification system. Nucleic Acids Res. 2016;44(2):790–800.
15. Nagornykh M, Bogdanova E, Protsenko A, Solonin A, Zakharova M, Severinov K. Regulation of gene expression in a type II restriction-modification system. Russ J Genet. 2008;44(5):523–32.
16. Ichige A, Kobayashi I. Stability of EcoRI restriction-modification enzymes in vivo differentiates the EcoRI restriction-modification system from other postsegregational cell killing systems. J Bacteriol. 2005;187(19):6612–21.
17. Mruk I, Blumenthal RM. Real-time kinetics of restriction–modification gene expression after entry into a new host cell. Nucleic Acids Res. 2008;36(8):2581–93.
18. Ball NJ, McGeehan J, Streeter S, Thresh S-J, Kneale G. The structural basis of differential DNA sequence recognition by restriction–modification controller proteins. Nucleic acids research 2012;40(20):10532–42.
19. McGeehan JE, Papapanagiotou I, Streeter SD, Kneale GG. Cooperative binding of the C.AhdI controller protein to the C/R promoter and its role in endonuclease gene expression. J Mol Biol. 2006;358(2):523–31.
20. Sohail A, Ives CL, Brooks JE. Purification and characterization of C·BamHI, a regulator of the BamHI restriction-modification system. Gene. 1995;157(1):227–8.
21. Sorokin V, Severinov K, Gelfand MS. Systematic prediction of control proteins and their DNA binding sites. Nucleic Acids Res. 2009;37(2):441–51.

22. Ives CL, Nathan PD, Brooks JE. Regulation of the BamHI restriction-modification system by a small intergenic open reading frame, bamHIC, in both Escherichia coli and Bacillus subtilis. J Bacteriol. 1992;174(22): 7194–201.

23. Tao T, Bourne J, Blumenthal R. A family of regulatory genes associated with type II restriction-modification systems. J Bacteriol. 1991;173(4):1367–75.

24. Česnavičienė E, Mitkaitė G, Stankevičius K, Janulaitis A, Lubys A. Esp1396I restriction–modification system: structural organization and mode of regulation. Nucleic Acids Res. 2003;31(2):743–9.

25. Karyagina A, Shilov I, Tashlitskii V, Khodoun M, Vasil'ev S, Lau PC, Nikolskaya I. Specific binding of SsoII DNA methyltransferase to its promoter region provides the regulation of SsoII restriction-modification gene expression. Nucleic Acids Res. 1997;25(11):2114–20.

26. Zakharova M, Minakhin L, Solonin A, Severinov K. Regulation of RNA polymerase promoter selectivity by covalent modification of DNA. J Mol Biol. 2004;335(1):103–11.

27. Vilar JM, Saiz L. Systems biophysics of gene expression. Biophys J. 2013; 104(12):2574–85.

28. Tolkunov D, Morozov AV. Genomic studies and computational predictions of nucleosome positions and formation energies. Adv Protein Chem Struct Biol. 2010;79:1–57.

29. Gertz J, Siggia ED, Cohen BA. Analysis of combinatorial cis-regulation in synthetic and genomic promoters. Nature. 2009;457(7226):215–8.

30. Seo Y-J, Chen S, Nilsen-Hamilton M, Levine HA. A mathematical analysis of multiple-target SELEX. Bull Math Biol. 2010;72(7):1623–65.

31. Aguda B, Friedman A. Models of cellular regulation. New York: Oxford University Press; 2008.

32. Alon U. An introduction to systems biology: design principles of biological circuits. London: CRC press; 2006.

33. Williams K, Savageau MA, Blumenthal RM. A bistable hysteretic switch in an activator–repressor regulated restriction–modification system. Nucleic Acids Res. 2013;41(12);6045–57.

34. Djordjevic M. Modeling bacterial immune systems: strategies for expression of toxic - but useful - molecules. Biosystems. 2013;112(2):139–44.

35. O'Donnell SM, Janssen GR. The initiation codon affects ribosome binding and translational efficiency in Escherichia coli of cI mRNA with or without the 5′ untranslated leader. J Bacteriol. 2001;183(4):1277–83.

36. Shell SS, Wang J, Lapierre P, Mir M, Chase MR, Pyle MM, Gawande R, Ahmad R, Sarracino DA, Ioerger TR. Leaderless transcripts and small proteins are common features of the mycobacterial translational landscape. PLoS Genet. 2015;11(11):e1005641.

37. Beletskaya IV, Zakharova MV, Shlyapnikov MG, Semenova LM, Solonin AS. DNA methylation at the CfrBI site is involved in expression control in the CfrBI restriction–modification system. Nucleic Acids Res. 2000;28(19):3817–22.

38. Shea MA, Ackers GK. The OR control system of bacteriophage lambda. A physical-chemical model for gene regulation. J Mol Biol. 1985;181(2): 211–30.

39. Enikeeva FN, Severinov KV, Gelfand MS. Restriction–modification systems and bacteriophage invasion: Who wins? J Theor Biol. 2010;266(4):550–9.

40. Streeter SD, Papapanagiotou I, McGeehan JE, Kneale GG. DNA footprinting and biophysical characterization of the controller protein C.AhdI suggests the basis of a genetic switch. Nucleic Acids Res. 2004;32(21):6445–53.

41. Bogdanova E, Zakharova M, Streeter S, Taylor J, Heyduk T, Kneale G, Severinov K. Transcription regulation of restriction-modification system Esp1396I. Nucleic Acids Res. 2009;37(10):3354–66.

42. Vesper O, Amitai S, Belitsky M, Byrgazov K, Kaberdina AC, Engelberg-Kulka H, Moll I. Selective translation of leaderless mRNAs by specialized ribosomes generated by MazF in Escherichia coli. Cell. 2011;147(1):147–57.

43. Mruk I, Liu Y, Ge L, Kobayashi I. Antisense RNA associated with biological regulation of a restriction–modification system. Nucleic Acids Res. 2011;39(13): 5622–32.

44. Nagornykh M, Zakharova M, Protsenko A, Bogdanova E, Solonin AS, Severinov K. Regulation of gene expression in restriction-modification system Eco29kl. Nucleic Acids Res. 2011;39(11):4653–63.

45. Barrangou R, Marraffini LA. CRISPR-Cas systems: prokaryotes upgrade to adaptive immunity. Mol Cell. 2014;54(2):234–44.

46. Al-Attar S, Westra ER, van der Oost J, Brouns SJ. Clustered regularly interspaced short palindromic repeats (CRISPRs): the hallmark of an ingenious antiviral defense mechanism in prokaryotes. Biol Chem. 2011; 392(4):277–89.

47. Rezulak M, Borsuk I, Mruk I: Natural C-independent expression of restriction endonuclease in a C protein-associated restriction-modification system. Nucleic Acids Res. 2016;44(6):2646–60.

48. Lubys A, Jurenaite S, Janulaitis A. Structural organization and regulation of the plasmid-borne type II restriction-modification system Kpn2I from Klebsiella pneumoniae RFL2. Nucleic Acids Res. 1999;27(21):4228–34.

49. Knowle D, Lintner RE, Touma YM, Blumenthal RM. Nature of the promoter activated by C. PvuII, an unusual regulatory protein conserved among restriction-modification systems. J Bacteriol. 2005;187(2):488–97.

Mass tomography at different momentum ranges in quark-gluon plasma

Magdalena Djordjevic,[*] Bojana Blagojevic, and Lidija Zivkovic

Institute of Physics Belgrade (University of Belgrade), Pregrevica 118, 11080 Zemun, Belgrade, Serbia

We here show that at lower momentum (i.e., $p_\perp \sim 10\,\text{GeV}$) single particle suppression for different types of probes exhibit a clear mass hierarchy, which is a direct consequence of the differences in the energy loss, rather than the differences in the initial distributions. On the other hand, we predict that the mass hierarchy is not expected at high momentum (i.e., $p_\perp \sim 100\,\text{GeV}$); i.e., while we surprisingly predict that suppression for charged hadrons will be somewhat *smaller* than the suppression for heavy mesons, we find that this difference will be a consequence of fragmentation functions, not the finite mass effects. That is, apart from the fragmentation functions, the probes of different masses exhibit nearly the same suppression in the high momentum region. We also argue that the same insensitivity on the probe types also appears for jets. In particular, the experimental data in the momentum regions where they exist for both types of probes, show similar suppressions of charged hadrons and inclusive jet data. Interestingly, we also find that our state-of-the-art suppression predictions for high momentum single particles are also in agreement with the jet suppression data, where the reasons behind this agreement yet remain to be understood. Finally, the available jet data also show (though with large error bars) an overlap between b jets (heavy) and inclusive jets (light) probes. Consequently, our results suggest that single particles in the momentum region below 50 GeV present an excellent tool for mass tomography, while high momentum single particles and (possibly) jets are somewhat insensitive to the details of the interaction with quark-gluon plasma.

I. INTRODUCTION

Quark-gluon plasma (QGP) is a new state of matter [1,2] consisting of interacting quarks, antiquarks, and gluons. Such new state of matter is created in ultrarelativistic heavy ion collisions at Relativistic Heavy Ion Collider (RHIC) and Large Hadron Collider (LHC). Rare high momentum probes, which are created in such collisions and which transverse QGP, are excellent probes of this extreme form of matter [3–5]. As these probes have different masses and consequently interact with the medium in a different manner, such mass tomography allows investigating properties of the interactions with the medium [6–8]. Furthermore, as higher momentum ranges become increasingly available at the LHC experiments, there are both different probes and a wide range of their momentum, which become available for such mass tomography. However, there is now a question which exactly probes, and momentum ranges, are optimal for such tomography, i.e., will lead to different behavior that can provide new information about interactions with the medium. To address this question, we will in this paper concentrate on the nuclear modification factor (R_{AA}), as suppression is traditionally considered to be an excellent observable for mass tomography.

As an example, it was previously widely expected that such clear distinction between the suppression patterns will be provided by the measurements of charged hadron (light) and D-meson (heavy) probes (see, e.g., [7,8]). However, as shown by both the experimental data [9,10] and theoretical predictions [11], these two probes have the same suppression at least in the momentum region between 10 and 50 GeV, which is a consequence of a serendipitous interplay between

energy loss and fragmentation functions. Below 10 GeV, there exists a small difference in the R_{AA}s between D mesons and charged hadrons; however, this difference in the suppressions is both small and somewhat influenced by the fragmentation functions [11], so it is, unfortunately, not suitable for extracting any reliable conclusions. Furthermore, at high momentum, recent jet measurements indicate (though with large error bars) the same suppression for b jets [12], and inclusive (light) jets [13,14]. Consequently, there is a nontrivial question of what exactly probes and momentum ranges can be used for obtaining new information on probe-medium interactions. Addressing this will, in turn, allow optimally exploiting experimental efforts and provide further tests of our understanding of QCD matter. Systematically testing the mass tomography effects, for different probes, and at wide momentum ranges, will be the main goal of this paper.

To achieve this goal, we will here use our state-of-the-art dynamical energy loss formalism [15,16], which removes a widely used static approximation and takes into account interactions of the probe with the moving (dynamical) medium constituents. Through this, it consistently treats both radiative [15,16] and collisional [17] energy loss, which was shown to be crucial for quantitatively and qualitatively explaining the experimental data [18]. Additionally, the formalism also takes into account finite magnetic mass [19] and running coupling [20], and is integrated in an up-to-date numerical procedure, which includes path-length [21] and multigluon [22] fluctuations. The formalism was previously shown to be consistent with the wide range of suppression data corresponding to different probes and experimental conditions [11,20,23]. Importantly, *no free parameters* are used in comparing predictions with the experimental data. The same parameter set, corresponding to the standard literature values, will be used in this paper, so that the generated

---

*Corresponding author: magda@ipb.ac.rs

predictions will be also constrained by an agreement with a wealth of previous data.

We will here generate single particle R_{AA} predictions at both lower momentum (i.e., $p_\perp \sim 10$ GeV) and high momentum (i.e., $p_\perp \sim 100$ GeV) regions. Our predictions are applicable for both 2.76 TeV and 5.02 TeV collision energies, because we here predict the same suppression at these two collision energies for light flavor, while we previously [24] predicted the same suppression at these energies for heavy flavor. Comparing these predictions with single particle R_{AA} measurements will allow investigating how suppression depends on the mass hierarchy in different momentum regions, particularly because high precision single particle R_{AA} measurements are (or will soon become) available at both lower and high momentum ranges. In the high momentum range, we will generate predictions for 5.02-TeV collision energy, where preliminary experimental data are currently becoming available. The high momentum single particle predictions are not available for 2.76 TeV, so in this range, we will compare our single particle predictions for 5.02 TeV (which are also applicable to 2.76 TeV; see above) with the available jet measurements. The comparison of the single particle predictions with the available jet data is motivated by the fact that, in the momentum region where both (limited) single particle and jet R_{AA} data exist, these two observables show the same suppression within the error bars, as we present below. This observation leads to a question of how the leading particle R_{AA} predictions, done with state-of-the-art dynamical energy loss model, compare with the whole jet R_{AA}, which we will here address. Consequently, we will here provide a systematic investigation of how the predicted suppression depends on the probe type, the momentum and collision energy range, and how these predictions compare with various available data.

II. METHODS

The numerical framework for generating suppression predictions is presented in detail in [20]. We below briefly outline the main steps in this procedure.

We study the angular averaged nuclear modification factor R_{AA}, which is established as an excellent probe for studying the interaction of high-momentum particles with QGP. R_{AA} is the ratio of the quenched spectrum in $A + A$ collisions to the spectrum in $p + p$ collisions, scaled by the number of binary collisions $N_{\rm bin}$:

$$R_{AA}(p_\perp) = \frac{dN_{AA}/dp_\perp}{N_{\rm bin}dN_{pp}/dp_\perp}. \tag{1}$$

To calculate the quenched spectra of light and heavy probes, we use the generic pQCD convolution, which consists of the following steps:

$$\frac{E_f d^3\sigma}{dp_{\perp,f}^3} = \frac{E_i d^3\sigma(Q)}{dp_{\perp,i}^3} \otimes P(E_i \to E_f) \otimes \tag{2}$$

$$\otimes D(Q \to H_Q) \otimes f(H_Q \to J/\psi). \tag{3}$$

Here "i" and "f" subscripts correspond, respectively, to "initial" and "final," E is energy, $p_\perp$ is transversal momentum,

Q denotes partons (quarks and gluons), and the terms in the equation correspond to the following:

(i) $E_i d^3\sigma(Q)/dp_{\perp,i}^3$ denotes the initial parton spectrum. For light quarks and gluons, the spectrum is extracted from [25], while for charm and bottom quarks, the spectrum is extracted from [26].

(ii) $P(E_i \to E_f)$ is the energy loss probability. The probability is generalized to include both collisional [17] and radiative [15,16] energy loss in the same framework (i.e., realistic finite size dynamical QCD medium), which abolishes the widely used approximation of static scattering centers. It is also recently improved to include path-length [21] and multigluon [22] fluctuations, as well as running coupling [20] and finite magnetic mass [19].

(iii) $D(Q \to H_Q)$ is the parton to hadron H_Q fragmentation function. For light hadrons, and D and B mesons we use DSS [27], BCFY [28], and KLP [29] fragmentation functions, respectively. Note, however, that for heavy flavor, fragmentation functions do not influence the suppression of heavy mesons [11]. That is, heavy meson R_{AA} is a true probe of heavy quark R_{AA}.

(iv) For nonprompt J/Ψ, we also have to include the decay of B meson to J/ψ, which is represented by the function $f(H_Q \to J/\psi)$ and obtained according to [26].

To generate the suppression predictions for light and heavy flavor observables in Pb+Pb collisions at the LHC experiments, we used the following parameter set: QGP with perturbative QCD scale of $\Lambda_{\rm QCD} = 0.2$ GeV and effective light quark flavors $n_f = 3$. In the calculations, as a starting point we use an effective temperature of 304 MeV for 0%–40% centrality Pb+Pb collisions at the LHC [30] experiments (as extracted by ALICE); the average temperature for every centrality region is then determined according to the procedure given in [23]. Also, for every centrality region, we use different path-length distributions, which are provided to us by [31]. The light quark mass is assumed to be dominated by the thermal mass $M = \mu_E/\sqrt{6}$, where temperature-dependent Debye mass μ_E is obtained from [32]. The gluon mass is $m_g = \mu_E/\sqrt{2}$ [33], while the charm and the bottom masses are $M = 1.2$ GeV and $M = 4.75$ GeV, respectively. Magnetic to electric mass ratio is $0.4 < \mu_M/\mu_E < 0.6$, as extracted from several independent nonperturbative QCD calculations [34–37], so the uncertainty in the predictions, presented in the next section, will come from this range of screening masses ratio. Note that our model uses no free parameters in comparison with the experimental data, that is, all the parameters correspond to standard literature values.

III. NUMERICAL RESULTS

In this section, we will generate predictions which correspond to the probe suppression at both lower (~ 10 GeV) and high (~ 100 GeV) momentum ranges. At high-momentum ranges, we will also compare the single particle and jet measurements with each other, and with the generated theoretical predictions. The predictions will be generated both as
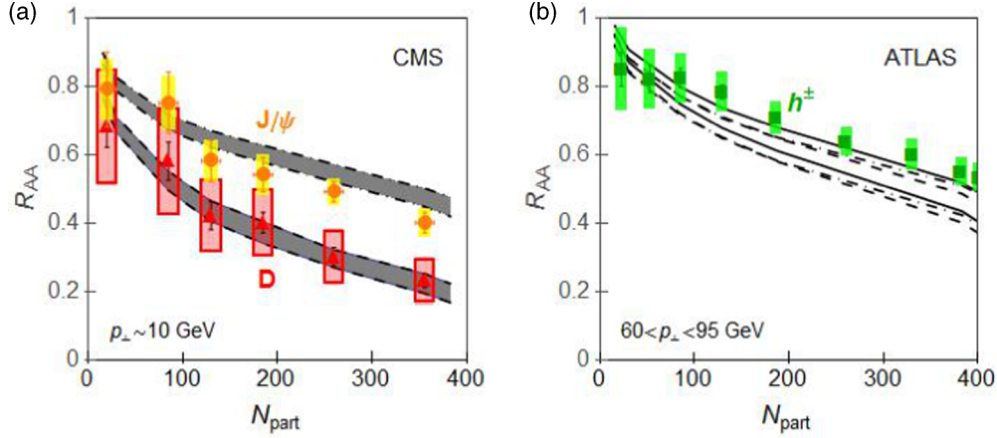
FIG. 1. R_{AA} vs N_{part} for single particles at the 2.76 TeV Pb+Pb collisions at the LHC experiments. (a) Theoretical predictions for R_{AA} vs N_{part} are compared with CMS experimental data for D mesons [38] (red triangles) and nonprompt J/ψ [39] (orange circles) in, respectively, $8 < p_\perp < 16$ GeV and $6.5 < p_\perp < 30$ GeV momentum regions. Gray bands with dashed, and dot-dashed boundaries, respectively, correspond to predictions for D mesons and nonprompt J/Ψ in corresponding momentum regions. (b) Theoretical predictions for $h^\pm$, and D and B mesons R_{AA} vs N_{part} in $60 < p_\perp < 95$ GeV momentum region are, respectively, provided as white bands with full, dashed, and dot-dashed boundaries. The $h^\pm$ predictions are compared with ATLAS (green squares) [40] $h^\pm$ experimental data in the same momentum region. On each panel, the upper (lower) boundary of each gray (or white) band corresponds to $\mu_M/\mu_E = 0.6$ ($\mu_M/\mu_E = 0.4$).

a function of probe momentum and the number of participants and for both light and heavy flavor observables.

We first show predictions for the suppression dependence for single particles on the number of participants at 2.76 TeV Pb+Pb collision energy. In Fig. 1(a) we compare predictions with the data in the lower momentum range ($p_\perp \sim 10$ GeV), while in Fig. 1(b) we compare predictions with the data in the high momentum range ($p_\perp \sim 100$ GeV). Note that the formalism is developed under the assumption that $M^2/E^2 \ll 1$, so, for all types of quarks (both light and heavy), our predictions are valid for $p_\perp \gtrsim 10$ GeV. The predictions in Fig. 1(a) are generated for J/Ψ and D mesons, and, compared with the corresponding CMS experimental data [38], D-meson data from ALICE [41], not shown for figure representation, are consistent with CMS D-meson data. Also, the charged hadrons (light probes) are not shown in Fig. 1(a) for clarity, as it was previously shown that both experimental data [9,10] and theoretical predictions [11] largely overlap with those for D mesons. Because charged hadrons are indirect and complex probes, composed of both light quarks and gluons with the nontrivial effect of fragmentation functions [11], for mass tomography it is clearly beneficial to, whenever possible, concentrate on D mesons (clear charm quark probes [11]) instead of charged hadrons. In Fig. 1(b), the theoretical predictions for charged hadrons, and D and B mesons are generated and shown together with the ATLAS charged hadron experimental data.

A clear distinction in predictions between lower and high $p_\perp$ ranges are observed. In addition, for lower $p_\perp$ [Fig. 1(a)], it is obvious that the light and heavy flavor suppressions are significantly different. On the other hand, in the high $p_\perp \sim 100$ GeV range [Fig. 1(b)], the predictions for all the probes (both light and heavy) almost overlap with each other. From the pQCD perspective, a reason for similar suppressions at high momentum is that the mass of the probe becomes small compared to its momentum, so the relevance of mass

effects should also become small in this region. However, while plausible (expected) from the pQCD perspective, this prediction can be quite distinct in other approaches, as, e.g., AdS-CFT predicts a clear suppression mass hierarchy, even for high momentum regions [42,43].

The experimental data shown in Fig. 1 are in good agreement with the generated theoretical predictions. Moreover, these data also confirm the predicted qualitative distinction between the light or charm and bottom suppressions at the lower momentum region. At the higher momentum range, such comparison between the light and heavy flavor experimental data cannot be made, as the corresponding single particle data are currently available only for charged hadrons. Therefore, the overlap of the light and heavy flavor suppressions at high momentum ranges, provides a clear prediction to be tested by the upcoming experiments.

For understanding the difference between D-meson and nonprompt J/Ψ suppressions, we studied the importance of different contributions to this suppression difference. Regarding this, note that it was considered that this difference may largely originate from the differences in the initial distributions between charm and bottom quarks, rather than the difference in their energy losses [44]. We show in Fig. 2(a) that this is not the case, i.e., the contribution to the suppression difference from the initial distributions is small, while the contribution from the different energy loss is substantially larger. Note, however, that the contributions shown in Fig. 2(a) are not pure effects of initial distribution and energy loss. This is because J/Ψ suppression is not a direct probe of b quarks, i.e., it includes a decay from B mesons to J/Ψ, i.e., $f(B \to J/\Psi)$. Consequently, to exclude the decay contribution from these two effects, in Fig. 2(b) we show the same contributions but with the B mesons (clear b quark probe) instead of J/Ψ. We see that, in the case of B mesons, the energy loss contribution becomes even larger, while the initial distribution
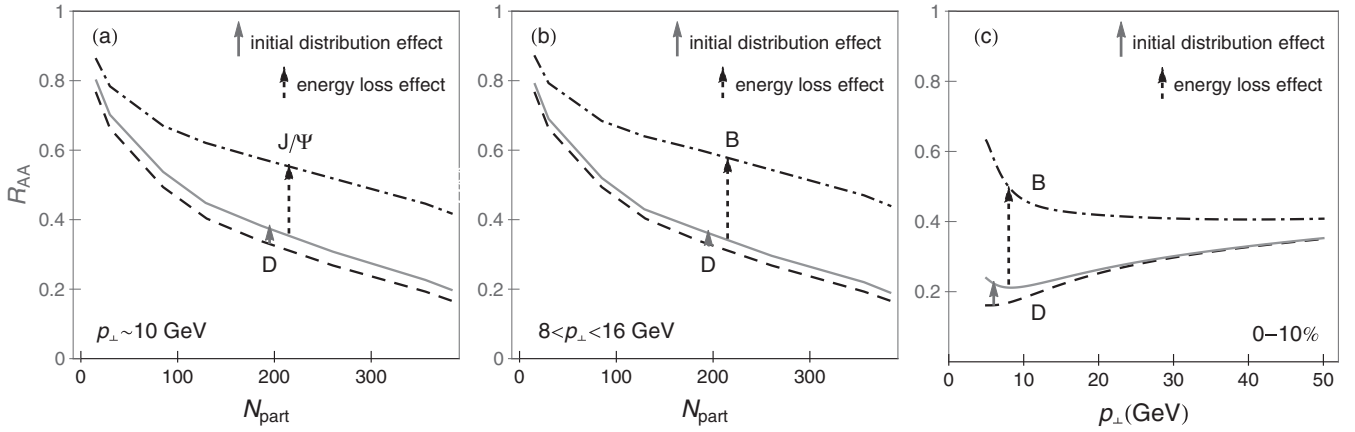
FIG. 2. Suppression contributions at lower momentum. (a) Theoretical predictions for R_{AA} vs $N_{\rm part}$ are compared for D mesons (dashed curve, $8 < p_\perp < 16$ GeV momentum region) and nonprompt J/Ψ (dot-dashed curve, $6.5 < p_\perp < 30$ GeV momentum region). Gray curve shows the analogous nonprompt J/Ψ predictions, if the originating bottom quark would have the same energy loss as charm quark in QGP. (b) Theoretical predictions for R_{AA} vs $N_{\rm part}$ are compared for D and B mesons in $8 < p_\perp < 16$ GeV momentum region. Comparing (a) and (b) shows the effect of decay functions to the contributions analyzed in (a). (c) Theoretical predictions for R_{AA} vs $p_\perp$ are compared for D and B mesons. In (b) and (c), the curve legend is the same as in (a) with distinction that now B replaces J/Ψ. In each panel, the full arrow points to the contribution of the different initial distributions to the difference in the suppression between the D meson and nonprompt J/Ψ (or B meson), while the dashed arrow points to the contribution of the different energy losses to the difference between D-meson and the nonprompt J/Ψ (or B-meson) suppression. Magnetic-to-electric mass ratio is set to $\mu_M/\mu_E = 0.4$.

becomes even smaller. Therefore, the strong mass dependence of the suppression, which is observed and predicted at lower momentum ranges, is clearly a consequence of the differences in the energy loss, rather than the consequence of the initial distributions or decay. Furthermore, we show in Fig. 2(c) that there is no momentum region in which initial distribution makes a significant effect on the suppression difference between different types of probes. Therefore, studying the difference between D- and B-meson suppression patterns in the lower momentum region is not influenced by the production, fragmentation, and the decay, and therefore allows directly assessing how different probes interact with QGP.

While there are currently only limited data for single particles at high momentum, these types of measurements are expected to become increasingly available at 5.02-TeV Pb+Pb collisions at the LHC. At 5.02-TeV collision energy, the R_{AA} measurements for charged hadrons are expected to become available up to $p_\perp \sim 400$ GeV, for D mesons the R_{AA} measurements might be available up to $p_\perp \sim 200$ GeV, while for bottom mesons the measurements are expected up to $p_\perp \sim 100$ GeV [45] and possibly even higher. It is, therefore, useful providing single particle R_{AA} predictions in the high-momentum region, and studying the effects of high $p_\perp$ mass tomography.

With this goal, in Fig. 3, we provide predictions for charged hadrons, and D and B mesons R_{AA} at 5.02-TeV 0%–10% central Pb+Pb collisions at the LHC. From Fig. 3(a), we see that at $p_\perp \sim 100$ GeV, all types of probes show similar suppressions, as supported by Fig. 1(c). However, for $p_\perp > 100$ GeV, we also observe that, while D and B (i.e., heavy) meson R_{AA}s become almost identical, the $h^\pm$ (i.e., light hadron) R_{AA} shows a surprising tendency for a *lower* suppression compared to heavy mesons. Moreover, we see that the difference between light and heavy meson suppression

increase with increasing $p_\perp$, leading to more than 10% higher R_{AA} for $h^\pm$ compared to heavy mesons at $p_\perp > 150$ GeV. That is, our observation is that, contrary to the 2.76-TeV collision energy where overlap between $h^\pm$ and the D meson R_{AA} was observed for the entire momentum region where both data are available ($p_\perp < 50$ GeV), we here predict that increasing momentum (above $p_\perp$ of 100 GeV) will lead to the separation in the R_{AA} of these two observables, but in a different direction than intuitively expected.

A naive conclusion from this prediction would be that, for highly energetic partons, the light partons start to lose notably less energy compared to heavy partons, which is not in accordance with pQCD, as discussed just after Fig. 1. To further investigate this issue, in Fig. 3(b), we compare R_{AA} predictions for bare quarks, i.e., for up, charm, and bottom quarks. We here observe that for $p_\perp > 100$ GeV, and in accordance with pQCD, finite mass effects for all types of quarks become negligible, leading to the same suppressions for both light and heavy flavor partons. However, from Fig. 3(c), we see that the nonintuitive result observed in Fig. 3(a), is a consequence of the fragmentation function effect on the light partons that compose the charged hadrons. That is, the effect of fragmentation functions on the light quarks is to decrease their suppression [noted by the vertical arrow in Fig. 3(c)]; the gluon contribution (partially) compensate this effect (as discussed in [11]), but for $p_\perp > 100$ GeV, the gluon contribution, and therefore the gluon compensation effect, is small. Because of this, we conclude that, if our predicted larger R_{AA} for $h^\pm$ compared to heavy flavor (D and B) in the high $p_\perp$ region is indeed experimentally observed, this increase will be a pure consequence of the fragmentation function effect, and therefore not related to the mass tomography in the QGP.

Moreover, the predictions presented in Fig. 3 show that the mass tomography effects can be clearly observed below
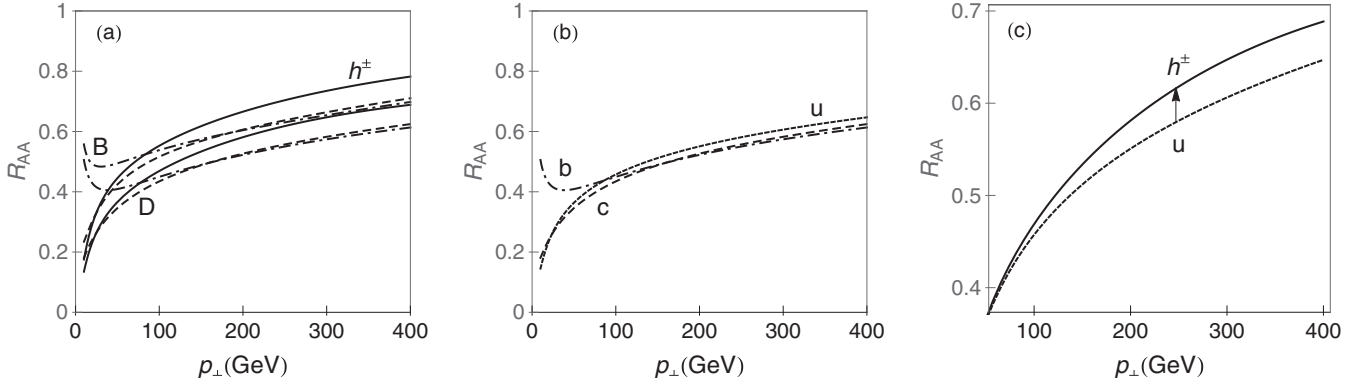
FIG. 3. R_{AA} vs $p_\perp$ for single particles at the 5.02-TeV Pb+Pb 0%–10% central collisions at the LHC. (a) Theoretical predictions for $h^\pm$, and D and B mesons R_{AA} vs $p_\perp$ are, respectively, given as white bands with full, dashed, and dot-dashed boundaries. The upper (lower) boundary of each band corresponds to $\mu_M/\mu_E = 0.6$ ($\mu_M/\mu_E = 0.4$). (b) Theoretical predictions for bare quark R_{AA} vs $p_\perp$ are shown for u (dotted curve), c (dashed curve), and b (dot-dashed curve). μ_M/μ_E ratio is set to 0.4. (c) Theoretical predictions for R_{AA} vs $p_\perp$ are compared for u (dotted curve) with $h^\pm$ (full curve). μ_M/μ_E ratio is set to 0.4.

50 GeV. In particular, we see that below 50 GeV, bottom suppression significantly differs compared to charm and light probes. On the other hand, such a distinction does not appear for high probe momentum (above 50 GeV) where all the suppression predictions nearly overlap (apart from the fragmentation functions effect discussed above). Furthermore, we also showed that indirect bottom probes (i.e., nonprompt J/Ψ) lower the dead-cone [8] effect compared to the clear B-meson probes. Consequently, we propose that one should concentrate on the lower momentum range and on the difference between the B-meson suppression on one side, and D-meson and charged hadron suppression on the other side, for observing significant mass tomography effects.

Furthermore, in [24], we have shown that, for heavy flavor, the R_{AA} predictions for 5.02 TeV and 2.76 TeV overlap with each other, because of interplay between energy loss and initial distributions. In Fig. 4, we show that the same conclusion is valid for charged hadrons as well. We therefore conclude that all the predictions and observations presented in this paper are valid for both 2.76-TeV and 5.02-TeV collision energies.

With regard to this, we note that, while high $p_\perp$ data are not available for single particles at the currently available 2.76-TeV collisions, high $p_\perp$ data are abundant for jets. As our theoretical predictions for single particle R_{AA} data at 5.02 TeV are also applicable for 2.76-TeV collision energy, it is tempting to compare these predictions with the available jet data at 2.76-TeV collision energy. Before comparing single particle predictions with the jet data, we address the same comparison with the experimental data, i.e., we start by asking how the single particle data and the jet measurements correspond to each other, in the momentum range where both are available. Consequently, in Fig. 5, we compare the available experimental data for charged hadrons (the green squares and circles) and inclusive jets (the blue squares and circles). In Fig. 5(a), we show the comparison of the measured suppression dependencies on the probe momentum (for the similar, fixed centrality region), while in Fig. 5(b), we show the comparison of the measured suppression dependencies on the number of participants (for the similar, fixed momentum

region). Therefore, one can see that similar suppressions are observed for single particles and jets, i.e., while the inclusive jets show a somewhat higher suppression compared to charged hadrons, they are the same within the error bars.

The results presented above then motivate us to investigate how our bare quark (i.e., leading particle) suppression predictions, done with the dynamical energy loss, agree with the jet suppression measurements. To that end, in Fig. 6, we show our predictions of R_{AA} vs $p_\perp$ for the light (full curve), charm (dashed curve), and bottom (dot-dashed curve) probes. These leading particle predictions are shown together with inclusive jets from the ATLAS experiments [14] [Fig. 6(a)] and with both inclusive jets [13] and b jets [12] from CMS
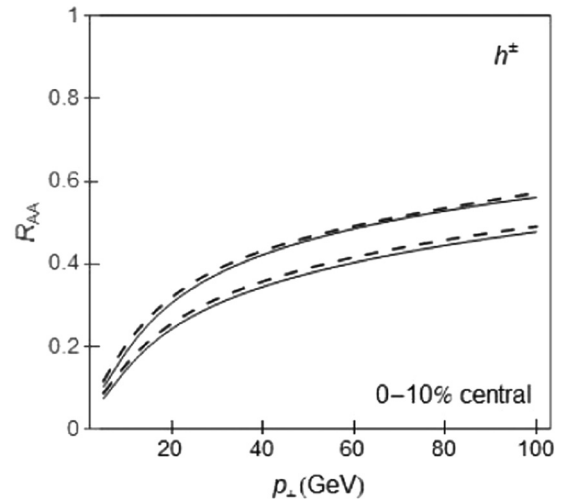
FIG. 4. Comparison of R_{AA} predictions for charge hadrons at 2.76 and 5.02 TeV. Charged hadron suppression predictions, as a function of transverse momentum, are shown. R_{AA} predictions at 5.02 TeV (2.76 TeV) 0%–10% central Pb+Pb collisions at the LHC are presented as white bands with full (dashed) boundaries. The upper (lower) boundary of each band corresponds to $\mu_M/\mu_E = 0.6$ ($\mu_M/\mu_E = 0.4$).
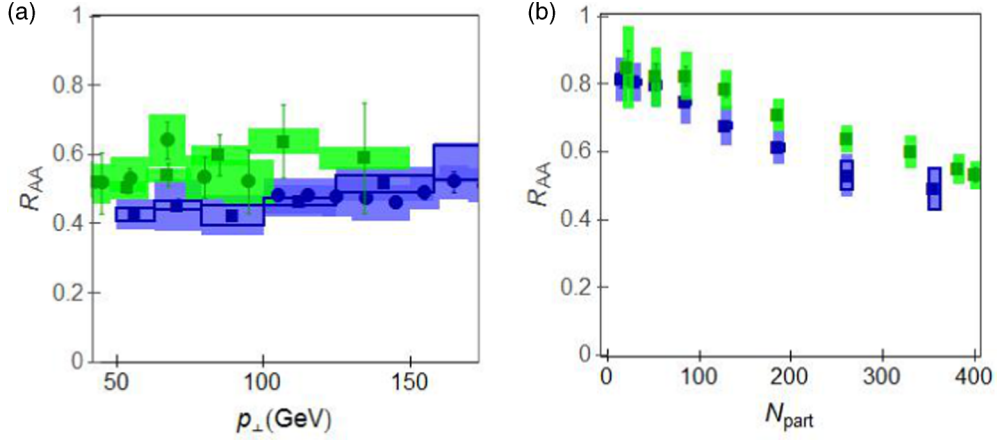
FIG. 5. Comparison of single particle and jet suppression data at the LHC experiments. (a) R_{AA} vs $p_\perp$ experimental data are compared for inclusive jets from ATLAS [14] (blue squares) and CMS [13] (blue circles) and charged hadrons [40] from ATLAS (green squares) and CMS [46] (green circles). ATLAS jet data correspond to 0%–10% centrality, while the other data correspond to 0%–5% centrality. (b) R_{AA} vs N_{part} ATLAS experimental data are compared for inclusive jets [14] (blue squares, $63 < p_\perp < 80$ GeV) and charged hadrons [40] (green squares, $65 < p_\perp < 90$ GeV).

[Fig. 6(b)]. The predictions for both light and heavy probes are in a good agreement with the available jet measurements. This, together with the near overlap of the single particle and the jet suppression data shown in Fig. 5, therefore suggests that the leading particle predictions agree well with the jet R_{AA} measurements.

There are few other important conclusions: (i) Above 50 GeV, we predict almost the same suppressions for the light, charm, and bottom quarks [see also Fig. 3(b)]; (ii) this prediction, extrapolated from the single particle predictions to the light and b jets, is in agreement with the measured experimental data. Because charm jet suppression is not yet measured, our result that the charm suppression overlaps with the light and bottom suppressions, likely suggests that c-jet R_{AA} will overlap with both unidentified and b-jet R_{AA}s.

Finally, the similar conclusion is also obtained if the suppression is analyzed as a function of the number of

participants (Fig. 7). In particular, we also see that R_{AA} vs N_{part} single particle predictions for all three types of probes nearly overlap with each other and explain well the inclusive and b-jets data, which are also shown in the figure. Finally, the overlap of the suppression predictions is also consistent with the overlap in the data—similarly, as shown in Fig. 6, the case of the charm jets is a new prediction to be tested by the future measurements.

IV. CONCLUSION

In this paper, we systematically explored the mass tomography effects, which can be observed for different probes and in the wide momentum range corresponding to the span of the available experimental data. The predictions of the suppression dependence from both the momentum and the number of participants were generated and compared with the
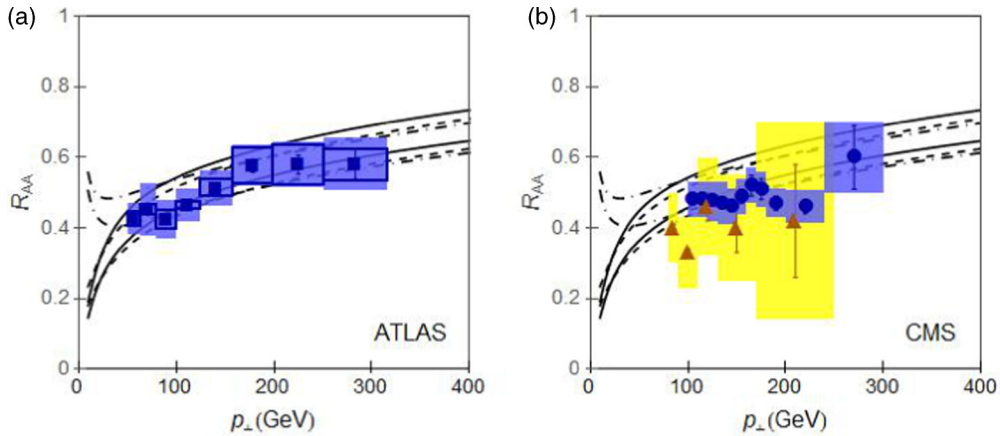
FIG. 6. Single particle suppression predictions vs jet data. (a) Theoretical R_{AA} vs $p_\perp$ predictions for single particles are compared with 0%–10% centrality ATLAS experimental data for inclusive jets [14] (blue squares). (b) R_{AA} vs $p_\perp$ single particle predictions are compared with CMS experimental data for inclusive jets [13] (blue circles, 0%–5% centrality) and b jets [12] (orange triangles, 0%–10% centrality). On each panel, white bands with dashed, dot-dashed, and full boundaries, respectively, correspond to charm, bottom, and light flavor predictions, and the upper (lower) boundary of each band corresponds to $\mu_M/\mu_E = 0.6$ ($\mu_M/\mu_E = 0.4$).
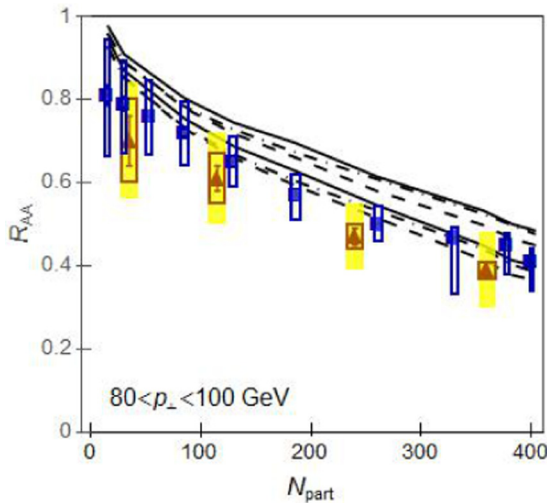
FIG. 7. Single particle suppression predictions vs jet data. Single particle predictions for R_{AA} vs N_{part} are compared with ATLAS data for inclusive jets [14] (blue squares, $80 < p_{\perp} < 100$ GeV momentum region) and CMS data for b jets [12] (orange triangles, $80 < p_{\perp} < 90$ GeV momentum region). White bands with dashed, dot-dashed, and full boundaries, respectively, correspond to charm, bottom, and light flavor predictions for $80 < p_{\perp} < 100$ GeV. The upper (lower) boundary of each band corresponds to $\mu_M/\mu_E = 0.6$ ($\mu_M/\mu_E = 0.4$).

available single particle and jet measurements. As a result, we obtained both the agreement of the theoretical results with the available data, and generated new predictions to be tested in the upcoming experiments, as we briefly summarized below.

For the single particle predictions, we obtained that significant mass tomography effects can be noticed below 50 GeV, related to the difference between the bottom and the charm and light suppressions. While this difference is sometimes attributed to different initial distributions for the charm and bottom quarks, we here showed that this effect is almost entirely a consequence of the differences in the respective energy losses (i.e., the dead-cone effect), while the initial distribution contribution to the difference is almost negligible.

Furthermore, at the existing 2.76-TeV collision energy, we showed that the leading particle predictions agree well with the jet measurements. Moreover, the experimental results show that there is a reasonable overlap between the single

particle and jet suppression experimental data. These findings are interesting, particularly because our suppression approach does not include the features such as jet reconstruction [47] [which are considered crucial for accurate description of (di)jet suppression [48–55]], but includes an advanced dynamical energy loss description for the leading parton. Therefore, the agreement between the single particle and jet R_{AA} measurements, both with respect to the experimental data and the theoretical predictions is currently unclear, and even if this agreement turns out to be accidental, understanding it may provide an important outlook for the future research.

Finally, we here provide clear predictions for the upcoming experimental data at 5.02-TeV collision energy: For the single particle data, we predict that, at the high momentum range $p_{\perp} > 100$ GeV, B- and D-meson (and likely c- and b-jet) R_{AA} data will nearly overlap with each other. On the other hand, our predictions for $h^{\pm}$ R_{AA} unintuitively suggest a tendency for lower suppression compared to heavy mesons. We, however, show that this lower suppression is a pure consequence of the fragmentation function effect on $h^{\pm}$, while the finite mass effect is negligible in this region. Finally, we predicted significant mass tomography effects related to B-meson suppression below 50 GeV. As discussed above, these predictions also provide specific guidelines on where future experimental efforts related to this goal should be concentrated. For example, given these results, we think that it is clearly beneficial to concentrate further efforts on improving b probe data in the relevant momentum region; this can include both directly measuring B mesons instead of nonprompt J/Ψ, reducing the uncertainties, as well as increasing the number of available measurements for this important probe. With regards to this, note that the CMS experiment already published its measurement of the nuclear modification factor for fully reconstructed B mesons in p+Pb collisions [56], while such measurements in Pb+Pb collisions are expected to become available soon from ALICE.

[1] J. C. Collins and M. J. Perry, Phys. Rev. Lett. **34**, 1353 (1975).

[2] G. Baym and S. A. Chin, Phys. Lett. B **62**, 241 (1976).

[3] M. Gyulassy and L. McLerran, Nucl. Phys. A **750**, 30 (2005).

[4] E. V. Shuryak, Nucl. Phys. A **750**, 64 (2005).

[5] B. Jacak and P. Steinberg, Phys. Today **63**(5), 39 (2010).

[6] J. D. Bjorken, FERMILAB-PUB-82-059-THY, 287 (1982), 292

[7] M. Djordjevic, M. Gyulassy, and S. Wicks, Phys. Rev. Lett. **94**, 112301 (2005).

[8] Yu. L. Dokshitzer and D. Kharzeev, Phys. Lett. B **519**, 199 (2001).

[9] B. Abelev *et al.* (ALICE collaboration), Phys. Lett. B **720**, 52 (2013).

[10] J. Otwinowski (ALICE Collaboration), PoS ConfinementX 170 (2012).

[11] M. Djordjevic, Phys. Rev. Lett. **112**, 042302 (2014).

[12] S. Chatrchyan *et al.* (CMS Collaboration), Phys. Rev. Lett. **113**, 132301 (2014).

[13] G. I. Veres, (CMS Collaboration), Nucl. Phys. A **904-905**, 146c (2013).

[14] G. Aad *et al.* (ATLAS Collaboration), Phys. Rev. Lett. **114**, 072302 (2015).

[15] M. Djordjevic, Phys. Rev. C **80**, 064909 (2009).

[16] M. Djordjevic and U. Heinz, Phys. Rev. Lett. **101**, 022302 (2008).

[17] M. Djordjevic, Phys. Rev. C **74**, 064907 (2006).

[18] B. Blagojevic and M. Djordjevic, J. Phys. G **42**, 075105 (2015).

[19] M. Djordjevic, Phys. Lett. B **709**, 229 (2012).

[20] M. Djordjevic and M. Djordjevic, Phys. Lett. B **734**, 286 (2014).

[21] S. Wicks, W. Horowitz, M. Djordjevic, and M. Gyulassy, Nucl. Phys. A **784**, 426 (2007).

[22] M. Gyulassy, P. Levai, and I. Vitev, Phys. Lett. B **538**, 282 (2002).

[23] M. Djordjevic, M. Djordjevic, and B. Blagojevic, Phys. Lett. B **737**, 298 (2014).

[24] M. Djordjevic and M. Djordjevic, Phys. Rev. C **92**, 024918 (2015).

[25] Z. B. Kang, I. Vitev, and H. Xing, Phys. Lett. B **718**, 482 (2012); R. Sharma, I. Vitev, and B. W. Zhang, Phys. Rev. C **80**, 054902 (2009).

[26] M. Cacciari, S. Frixione, N. Houdeau, M. L. Mangano, P. Nason, and G. Ridolfi, J. High Energy Phys. 10 (2012) 137.

[27] D. de Florian, R. Sassot, and M. Stratmann, Phys. Rev. D **75**, 114010 (2007).

[28] M. Cacciari and P. Nason, J. High Energy Phys. 09 (2003) 006; E. Braaten, K.-M. Cheung, S. Fleming, and T. C. Yuan, Phys. Rev. D **51**, 4819 (1995).

[29] V. G. Kartvelishvili, A. K. Likhoded, and V. A. Petrov, Phys. Lett. B **78**, 615 (1978).

[30] M. Wilde (ALICE Collaboration), Nucl. Phys. A **904-905**, 573c (2013).

[31] A. Dainese, Eur. Phys. J. C **33**, 495 (2004).

[32] A. Peshier, arXiv:hep-ph/0601119 (2006).

[33] M. Djordjevic and M. Gyulassy, Phys. Rev. C **68**, 034914 (2003).

[34] Y. Maezawa, S. Aoki, S. Ejiri, T. Hatsuda, N. Ishii, K. Kanaya, N. Ukita, and T. Umeda (WHOT-QCD Collaboration), Phys. Rev. D **81**, 091501(R) (2010).

[35] A. Nakamura, T. Saito, and S. Sakai, Phys. Rev. D **69**, 014506 (2004).

[36] A. Hart, M. Laine, and O. Philipsen, Nucl. Phys. B **586**, 443 (2000).

[37] D. Bak, A. Karch, and L. G. Yaffe, J. High Energy Phys. 08 (2007) 049.

[38] CMS Collaboration (B. Hong at Quark Matter 2015)

[39] S. Chatrchyan *et al.* (CMS Collaboration), J. High Energy Phys. 05 (2012) 063.

[40] G. Aad *et al.* (ATLAS Collaboration), J. High Energy Phys. 09 (2015) 050.

[41] B. Abelev *et al.* (ALICE Collaboration), J. High Energy Phys. 09 (2012) 112.

[42] W. A. Horowitz, Phys. Rev. D **91**, 085019 (2015).

[43] W. A. Horowitz, Nucl. Phys. A **904-905**, 186c (2013).

[44] J. Adam *et al.* (ALICE Collaboration), J. High Energy Phys. 11 (2015) 205.

[45] Yen-Jie Lee (private communication).

[46] S. Chatrchyan *et al.* (CMS Collaboration), Eur. Phys. J. C **72**, 1945 (2012).

[47] M. Cacciari, G. P. Salam, and G. Soyez, Eur. Phys. J. C **72**, 1896 (2012).

[48] J. Casalderrey-Solana, J. G. Milhano, and U. A. Wiedemann, J. Phys. G **38**, 035006 (2011).

[49] C. Young, B. Schenke, S. Jeon, and C. Gale, Phys. Rev. C **84**, 024907 (2011).

[50] Y. He, I. Vitev, and B. W. Zhang, Phys. Lett. B **713**, 224 (2012).

[51] F. Senzel, O. Fochler, J. Uphoff, Z. Xu, and C. Greiner, J. Phys. G **42**, 115104 (2015).

[52] X. N. Wang and Y. Zhu, Phys. Rev. Lett. **111**, 062301 (2013).

[53] G. Y. Qin and B. Muller, Phys. Rev. Lett. **106**, 162302 (2011); **108**, 189904 (2012).

[54] G. L. Ma, Phys. Rev. C **87**, 064901 (2013).

[55] K. C. Zapp, F. Krauss, and U. A. Wiedemann, J. High Energy Phys. 03 (2013) 080.

[56] V. Khachatryan *et al.* (CMS Collaboration), Phys. Rev. Lett. **116**, 032301 (2016).

PAPER

Importance of different energy loss effects in jet suppression at the RHIC and the LHC

To cite this article: Bojana Blagojevic and Magdalena Djordjevic 2015 *J. Phys. G: Nucl. Part. Phys.* **42** 075105

View the article online for updates and enhancements.

Importance of different energy loss effects in jet suppression at the RHIC and the LHC

Bojana Blagojevic and Magdalena Djordjevic

Institute of Physics Belgrade, University of Belgrade, Serbia

E-mail: magda@ipb.ac.rs

Abstract

Jet suppression is considered to be an excellent probe of quantum chromo-dynamic (QCD) matter created in ultra-relativistic heavy ion collisions. Our theoretical predictions of jet suppression, which are based on our recently developed dynamical energy loss formalism, show a robust agreement with various experimental data, which spans across different probes, experiments (Relativistic Heavy Ion Collider (RHIC) and Large Hadron Collider (LHC)) and experimental conditions (i.e. all available centrality regions). This formalism includes several key ingredients, such as the inclusion of dynamical scattering centers, a finite size QCD medium, collisional energy loss, finite magnetic mass and running coupling. While these effects have to be included based on theoretical grounds, it is currently unclear what their individual importance is in accurately interpreting the experimental data; in particular because other approaches to suppression predictions commonly neglect some—or all—of these effects. To address this question, we study the relative importance of these effects in obtaining accurate suppression predictions for D mesons (clear energy loss probe) at top RHIC and LHC energies. We obtain that several different ingredients are responsible for accurate predictions, i.e. robust agreement with the data is a cumulative effect of all the ingredients, though inclusion of the dynamical scattering centers has the largest relative importance.

Keywords: energy loss, jet suppression, quark-gluon plasma, charm quarks

(Some figures may appear in colour only in the online journal)

1. Introduction

The suppression of high transverse momentum light and heavy flavor observables [1] is considered to be an excellent probe of QCD matter created in ultra-relativistic heavy ion collisions at the RHIC and the LHC. One of the major goals of these experiments is mapping

the quark–gluon plasma (QGP) properties, which requires a comparison of the available suppression data with theoretical predictions [2–4]. Such a comparison tests different theoretical models and provides an insight into the underlying QGP physics. It is generally considered that the crucial ingredient for reliable suppression predictions is an accurate energy loss calculation.

Therefore, we previously developed the dynamical energy loss formalism, which includes the following effects: (i) dynamical scattering centers; (ii) a QCD medium of a finite size [5, 6]; (iii) both radiative [5, 6] and collisional [7] energy losses; (iv) finite magnetic mass [8] and (v) running coupling [9]. This energy loss formalism is based on the pQCD calculations in a finite size and optically thin dynamical QCD medium, and has been incorporated into a numerical procedure [9] that allows generating state-of-the art suppression predictions.

These predictions are able to explain the heavy flavor puzzle (the fact that, contrary to pQCD expectations, both light and heavy flavor probes have very similar experimentally measured R_{AA}) at both the RHIC [10] and the LHC [11] and, in general, show a very good agreement with the available suppression data at these experiments, for a diverse set of probes [9, 10] and centrality regions [12].

However, such good agreement between the predictions and the experimental data raises the question of which energy loss effects are responsible for the accurate predictions. In other words, is there a single dominant energy loss effect responsible for the good agreement, or is this agreement the result of a superposition of several smaller improvements? This issue is moreover important, given the fact that various pQCD approaches [13–22] to the energy loss calculations neglect some (or many) of these effects.

Consequently, here we address the importance of different energy loss ingredients in the suppression calculations. For this purpose, it would be optimal to have a probe that is sensitive only to the energy loss, i.e. for which fragmentation and decay functions do not play a role. The D meson suppression is such a probe, since the fragmentation functions do not modify bare charm quark suppression, as previously shown in [10, 11]. To explore different energy loss approximations, which have been used in suppression predictions, we concentrate on the D meson suppression in central 200 GeV Au+Au collisions at the RHIC and 2.76 TeV Pb+Pb collisions at the LHC. While high momentum D meson suppression data are not available at the RHIC—the RHIC measurements extend up to 6 GeV—such data are available at the LHC, which is useful as a baseline for assessing the importance of different effects.

Our approach is to systematically include different energy loss effects. In particular, we first compare the relative importance of radiative and collisional contribution to the D meson suppression predictions to assess the adequacy of the historically widely used static approximation. We then investigate the importance of including the dynamical scattering centers, followed by the collisional energy loss and the finite size (LPM) effect. Finally, we also address the importance of including the finite magnetic mass and the running coupling.

2. Theoretical and computational frameworks

In this section we first provide a brief overview of the computational framework and our dynamical energy loss formalism. As mentioned above, this formalism leads to a very good agreement with the suppression experimental data across different probes, collision energies and centrality regions [9, 10, 12]. We also introduce how the energy loss expression is modified, as different ingredients are excluded from this formalism. Note that, in section 3, we will for clarity address different energy loss effects in a reverse order, i.e. we will start

from the static approximation and systematically include all the effects, as such a historically-driven approach is more comprehensible and easier to follow.

For studying the importance of different energy loss effects, we will use angular averaged nuclear modification factor R_{AA}, which is well established as a sensitive observable for the interaction of high-momentum particles with the QCD medium. The nuclear modification factor R_{AA} is defined as the ratio of the quenched $A + A$ spectrum to the $p + p$ spectrum, scaled by the number of binary collisions N_{bin}:

$$R_{AA}(p_T) = \frac{\mathrm{d}N_{AA}/\mathrm{d}p_T}{N_{\text{bin}}\ \mathrm{d}N_{pp}/\mathrm{d}p_T}. \tag{1}$$

Furthermore, since angular averaged R_{AA} was previously shown to be sensitive almost entirely to the average properties (temperature) of the evolving medium (in distinction to elliptic flow, v_2, which is considered highly sensitive to the details of the medium evolution) [23, 24], angular averaged R_{AA} can be taken as a 'nearly pure' test of the jet–medium interactions. Due to this, we do not consider the effects of the medium evolution in this study, but provide a detailed study of the importance of different jet–medium effects. For this purpose, we model the medium by assuming an effective temperature of 304 MeV at the LHC (as extracted by ALICE [25]) and effective temperature of 221 MeV at the RHIC (as extracted by PHENIX [26]).

In order to obtain the quenched spectra, we use generic pQCD convolution [9, 27]:

$$\frac{E_f \mathrm{d}^3 \sigma}{\mathrm{d}p_f^3} = \frac{E_i \mathrm{d}^3 \sigma(Q)}{\mathrm{d}p_i^3} \otimes P\left(E_i \to E_f\right). \tag{2}$$

In equation (2) Q stands for charm quarks and $\frac{E_i \mathrm{d}^3 \sigma(Q)}{\mathrm{d}p_i^3}$ denotes the initial charm quark spectrum computed at next-to-leading order [28]. $P(E_i \to E_f)$ is the energy loss probability, which includes both radiative and collisional energy losses in a finite size dynamical QCD medium, multi-gluon [29] and path length [27, 30] fluctuations. The path length distributions are extracted from [30]. Distinction from equation (1) from [9], in our calculations we do not use the fragmentation function $D(Q \to H_Q)$ of the charm quark into the D meson (H_Q), because fragmentation does not alter bare charm quark suppression [10, 11], nor do we use decay function $f(H_Q \to e)$, because D mesons are directly measured in the experiments.

The expression for the radiative energy loss in a finite size dynamical QCD medium [5, 6], obtained from hard-thermal-loop (HTL) approximation, at first order in opacity is given by:

$$\frac{\Delta E_{\text{rad}}}{E} = \frac{C_R \alpha_S}{\pi} \frac{L}{\lambda} \int \mathrm{d}x \frac{\mathrm{d}^2 k}{\pi} \frac{\mathrm{d}^2 q}{\pi}\, v(\mathbf{q}) \left(1 - \frac{\sin \frac{(\mathbf{k} + \mathbf{q})^2 + \chi}{xE^+} L}{\frac{(\mathbf{k} + \mathbf{q})^2 + \chi}{xE^+} L} \right)$$
$$\times \frac{2(\mathbf{k} + \mathbf{q})}{(\mathbf{k} + \mathbf{q})^2 + \chi} \left(\frac{(\mathbf{k} + \mathbf{q})}{(\mathbf{k} + \mathbf{q})^2 + \chi} - \frac{\mathbf{k}}{\mathbf{k}^2 + \chi} \right). \tag{3}$$

In equation (3), $v(\mathbf{q})$ denotes the effective cross section defined below, L is the length of the finite size QCD medium, E is the jet energy, $\mathbf{k}$ is the transverse momentum of the radiated gluon, while $\mathbf{q}$ is the transverse momentum of the exchanged (virtual) gluon and x represents the longitudinal momentum fraction of the jet carried away by the emitted gluon. The color factor is $C_R = \frac{4}{3}$. $\chi = M_c^2 x^2 + m_g^2$, where $m_g = \mu_E/\sqrt{2}$ is the effective (asymptotic) mass for

gluon with the hard momenta $k \gtrsim T$, while μ_E is Debye (electric) screening mass and $M_c = 1.2$ GeV is the charm quark mass. λ is the mean free path in the QCD medium and in the dynamical case is given by $\dfrac{1}{\lambda_{\mathrm{dyn}}} = 3\alpha_S T$. In the incoherent limit [5],

$$\frac{\sin \dfrac{(\mathbf{k}+\mathbf{q})^2 + \chi}{xE^+} L}{\dfrac{(\mathbf{k}+\mathbf{q})^2 + \chi}{xE^+} L} \rightarrow 0.$$

The effective cross section, with the included finite magnetic mass [8], is given by the equation below, where μ_M is the magnetic screening mass:

$$v(\mathbf{q}) = \frac{\mu_E^2 - \mu_M^2}{\left(\mathbf{q}^2 + \mu_E^2\right)\left(\mathbf{q}^2 + \mu_M^2\right)}. \tag{4}$$

Note that, in the case when magnetic mass is equal to zero, the above expression reduces to a well-known HTL effective cross section [5, 18]:

$$v(\mathbf{q}) = \frac{\mu_E^2}{\mathbf{q}^2 \left(\mathbf{q}^2 + \mu_E^2\right)}. \tag{5}$$

Non-perturbative approaches [31–35] suggest that at the RHIC and the LHC the range of magnetic to electric mass ratio is $0.4 < \mu_M/\mu_E < 0.6$. We therefore use these values in equation (4) when generating suppression predictions in the case of the finite magnetic mass. In the case of zero magnetic mass, we use equation (5) above.

The collisional energy loss is calculated in accordance with [7], i.e. we use equation (14) from that reference for the finite size QCD medium and equation (16) for the incoherent limit.

The running coupling is introduced according to [9] and is defined as in [36]:

$$\alpha_S\left(Q^2\right) = \frac{4\pi}{\left(11 - 2/3 n_f\right)\ln\left(Q^2/\Lambda_{\mathrm{QCD}}^2\right)}, \tag{6}$$

where Λ_{QCD} is the perturbative QCD scale ($\Lambda_{\mathrm{QCD}} = 0.2$ GeV) and $n_f = 2.5$ ($n_f = 3$) for the RHIC (LHC) is the number of the effective light quark flavors. In the case of the running coupling, Debye mass μ_E [37] is obtained by self-consistently solving the equation:

$$\frac{\mu_E^2}{\Lambda_{\mathrm{QCD}}^2} \ln\left(\frac{\mu_E^2}{\Lambda_{\mathrm{QCD}}^2}\right) = \frac{1 + n_f/6}{11 - 2/3 n_f}\left(\frac{4\pi T}{\Lambda_{\mathrm{QCD}}}\right)^2. \tag{7}$$

Otherwise, when the running coupling is not included, fixed values of the strong coupling constant $\alpha_S = \frac{g^2}{4\pi} = 0.3$ for the RHIC ($\alpha_S = 0.25$ for the LHC) [38] and Debye mass $\mu_E = gT$ are used.

Transition from the dynamical to the static [20] approximation in the case of the radiative energy loss is determined through the following two changes and according to [6]. The mean free path is altered as:

$$\frac{1}{\lambda_{\mathrm{stat}}} = \frac{1}{\lambda_g} + \frac{1}{\lambda_q} = 6\frac{1.202}{\pi^2}\frac{1 + n_f/4}{1 + n_f/6} 3\alpha_S T = c(n_f)\frac{1}{\lambda_{\mathrm{dyn}}}, \tag{8}$$

where $c(n_f = 2.5) \approx 0.84$ is a slowly increasing function of n_f that varies between $c(0) \approx 0.73$ and $c(\infty) \approx 1.09$ and the effective cross section changes to:

$$v(\mathbf{q})_{\text{stat}} = \frac{\mu_E^2}{\left(\mathbf{q}^2 + \mu_E^2\right)^2}. \tag{9}$$

3. Results and discussion

In this section, we concentrate on central 200 GeV Au+Au collisions at the RHIC and 2.76 TeV Pb+Pb collisions at the LHC, and investigate how different energy loss ingredients affect the D meson suppression predictions. Regarding the LHC, for which the high momentum D meson R_{AA} data are available [39], we compare our calculations with experimental data in order to visually investigate, both qualitatively and quantitatively, the importance of individual effects in explaining the data.

We will start the analysis from the static approximation, which has been historically the first approach to the energy loss calculations. After investigating the adequacy of the static approximation, we will address the importance of including the dynamical scattering centers, the collisional energy loss and the finite size effect. Finally, we will also investigate the importance of finite magnetic mass and the running coupling.

We therefore start from the static approximation, where we use a fixed value of the strong coupling constant $\alpha_S = \frac{g^2}{4\pi} = 0.3$ at the RHIC ($\alpha_S = 0.25$ at the LHC) and Debye screening mass $\mu_E \approx gT$. Note that these values are used in figures 1–4 and figure 6. Also, note that magnetic mass effect is not included ($\mu_M = 0$) in figures 1–5, while the finite magnetic mass is considered in figures 6 and 7. The running coupling is considered in figures 5 and 7. The finite size QCD medium is considered in each figure, whereas figure 4 investigates the significance of the finite size effect.

To test the adequacy of the widely used static approximation (modeled by the Yukawa potential) [40], we compare the relative importance of radiative and collisional energy loss contributions to the suppression predictions. Namely, in the static approximation, collisional energy loss has to be equal to zero, i.e. the static approximation implies that collisional energy loss can be neglected compared to radiative energy loss. However, in figure 1, we see that the suppression due to collisional energy loss is comparable—or even larger—compared to the radiative energy loss suppression.

This, then, clearly shows that the static approximation is not an adequate one for the D meson suppression calculations, and that the collisional energy loss has to be taken into account in the suppression predictions. Therefore, a number of the approaches which take only radiative energy loss (for an overview see [41])–and some that take only collisional energy loss (e.g. [42, 43]) are clearly not adequate. This can also be directly observed in the right panel of figure 1, where we see that the static approximation leads to a strong disagreement with the data, i.e. to two to three times smaller suppression than the one observed experimentally. Consequently, we will below first test the importance of including the dynamical effects in radiative energy loss (figure 2) and then also test the importance of collisional energy loss within such a dynamical medium (figure 3).

Therefore, in figure 2, we compare the D meson suppression obtained from radiative energy loss only in the static framework, with the one in the dynamical framework. We observe a large difference in the two suppressions, with a significant suppression increase in the dynamical case. Consequently, the dynamical energy loss effect has to be taken into
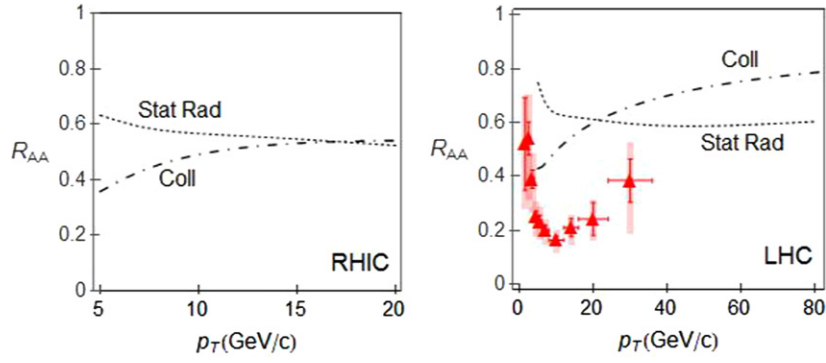
Figure 1. Static radiative versus collisional energy loss suppression. D meson suppression predictions, as a function of transverse momentum, are shown for radiative energy loss only in a static QCD medium (dotted curve), and for collisional energy loss only in a dynamical QCD medium (dot-dashed curve). Left (right) panel corresponds to the RHIC (the LHC) case. Right panel also shows the D meson R_{AA} data in 0–7.5% central 2.76 TeV Pb+Pb collisions at the LHC [39] (red triangles). Debye mass is $\mu_E = gT$, coupling constant is $\alpha_S = 0.3$ ($\alpha_S = 0.25$) for the RHIC (LHC) and finite magnetic mass effect is not included (i.e. $\mu_M = 0$).
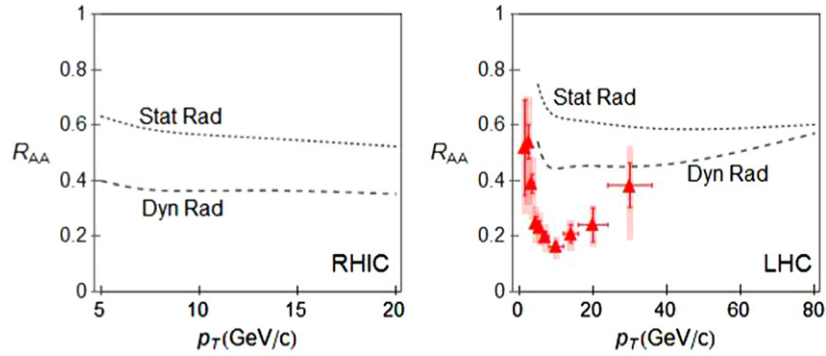
Figure 2. Radiative energy loss suppressions in a static *vs* dynamical QCD medium. D meson suppression predictions are shown, as a function of transverse momentum, assuming only radiative energy loss in static (dotted curve) and in dynamical (dashed curve) QCD medium. Left (right) panel corresponds to the RHIC (the LHC) case. Right panel also shows the D meson R_{AA} data in 0–7.5% ce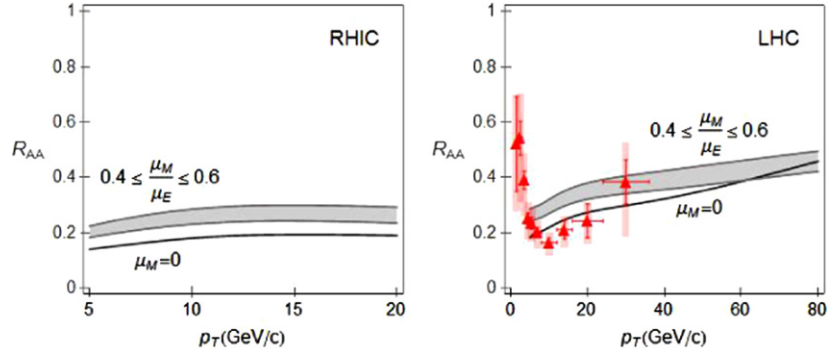ntral 2.76 TeV Pb+Pb collisions at LHC [39] (red triangles). Debye mass is $\mu_E = gT$, coupling constant is $\alpha_S = 0.3$ ($\alpha_S = 0.25$) for the RHIC (the LHC) and no finite magnetic mass effect is included (i.e. $\mu_M = 0$).

account at the RHIC, as there are no momenta within the RHIC jet momentum range where static approximation becomes adequate. At the LHC, the results indicate that, for jet momentum ranges larger than 100 GeV/c, the static approximation to *radiative* energy loss may become valid, in general agreement with [5, 6, 13, 14]; note, however, that the dynamical effect has to be taken into account even for these momenta, as the collisional energy loss, which is zero in the static approximation, gives a significant contribution to the jet suppression (see the right panel in figure 1). However, despite the fact that inclusion of the
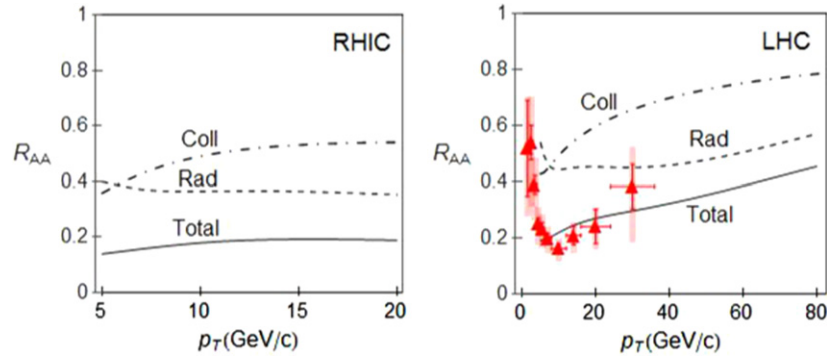
Figure 3. Radiative versus collisional energy loss suppressions in a dynamical QCD medium. D meson suppression predictions are shown, as a function of transverse momentum, for radiative (dashed curve), collisional (dot-dashed curve) and radiative + collisional (solid curve) energy loss. Left (right) panel corresponds to the RHIC (the LHC) case. Right panel also shows the D meson R_{AA} data in 0–7.5% central 2.76 TeV Pb+Pb collisions at the LHC [39] (red triangles). Debye mass is $\mu_E = gT$, coupling constant is $\alpha_S = 0.3$ ($\alpha_S = 0.25$) for the RHIC (the LHC) and no finite magnetic mass effect is included (i.e. $\mu_M = 0$).
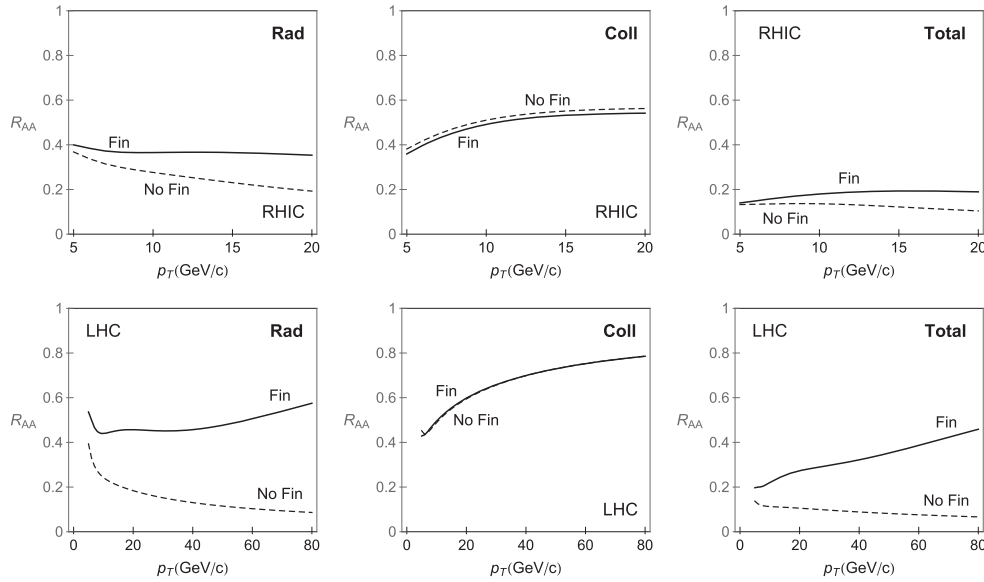
Figure 4. Finite size effect on R_{AA}. D meson suppression predictions are shown, as a function of transverse momentum, with (solid curve) and without (dashed curve) finite size effect. Upper (lower) panels correspond to the RHIC (the LHC) case. Left, central and right panel show, respectively, the finite size effect on radiative, collisional and total (radiative + collisional) energy loss in a dynamical QCD medium. Debye mass is $\mu_E = gT$, coupling constant is $\alpha_S = 0.3$ ($\alpha_S = 0.25$) for the RHIC (the LHC) and no finite magnetic mass effect is included (i.e. $\mu_M = 0$).
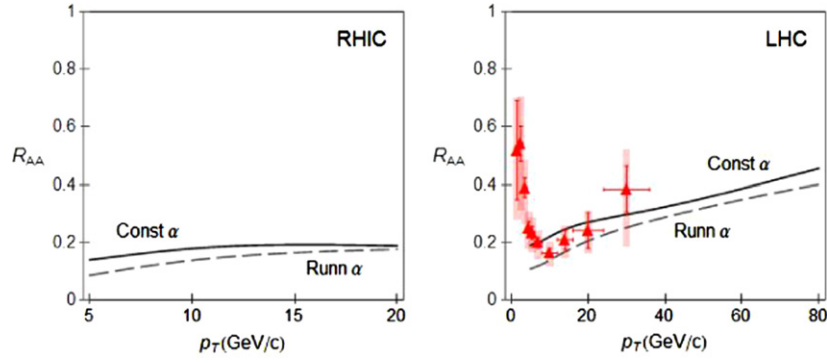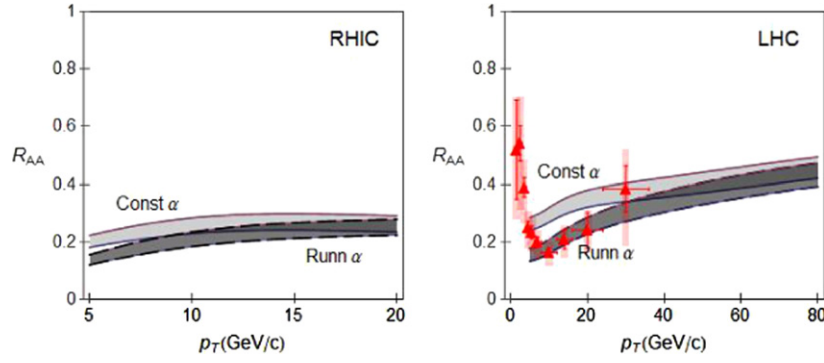
Figure 5. Running coupling effect on R_{AA}. D meson suppression predictions are shown, as a function of transverse momentum, with constant coupling $\alpha_S = 0.3$ ($\alpha_S = 0.25$) for the RHIC (the LHC) (solid curve) and with running coupling (dashed curve). No finite magnetic mass effect is included (i.e. $\mu_M = 0$). In both cases radiative + collisional contributions in dynamical QCD medium are included. Left (right) panel corresponds to the RHIC (the LHC) case. Right panel also shows the D meson R_{AA} data in 0-7.5% central 2.76 TeV Pb+Pb collisions at the LHC [39] (red triangles).

Figure 6. Magnetic mass effect on R_{AA}. D meson suppression predictions are shown, as a function of transverse momentum, for radiative + collisional energy loss in dynamical QCD medium, with (gray band) and without (solid curve) magnetic mass. Left (right) panel corresponds to the RHIC (the LHC) case. Right panel also shows the D meson R_{AA} data in 0–7.5% central 2.76 TeV Pb+Pb collisions at the LHC [39] (red triangles). Debye mass is $\mu_E = gT$ and coupling constant is $\alpha_S = 0.3$ ($\alpha_S = 0.25$) for the RHIC (the LHC). Upper (lower) boundary of each band corresponds to $\mu_M/\mu_E = 0.6$ ($\mu_M/\mu_E = 0.4$).

dynamical effect significantly increases the suppression compared to the static approximation, from the right panel in figure 2 we see that, at least below 50 GeV/c, radiative energy loss alone is not able to neither quantitatively nor qualitatively (see the shape of the curve) explain the experimental data, which leads to the conclusion that including only radiative energy loss to model the jet–medium interaction is clearly not adequate.

Furthermore, the results shown in figure 2 imply the question of whether a collisional energy loss is still relevant in the dynamical QCD medium, as suppression due to radiative energy loss significantly increases in the dynamical QCD medium. To address this question,

Figure 7. Running coupling and magnetic mass effect on R_{AA}. D meson suppression predictions are shown, as a function of transverse momentum, with the constant coupling $\alpha_S = 0.3$ ($\alpha_S = 0.25$) for the RHIC (the LHC) (light gray band) and with the running coupling (dark gray band). In both cases radiative + collisional contributions in dynamical QCD medium are included. Upper (lower) boundary of each band corresponds to $\mu_M/\mu_E = 0.6$ ($\mu_M/\mu_E = 0.4$). Left (right) panel corresponds to the RHIC (the LHC) case. Right panel also shows the D meson R_{AA} data in 0–7.5% central 2.76 TeV Pb+Pb collisions at the LHC [39] (red triangles).

in figure 3 we compare the D meson suppressions resulting from collisional and radiative energy loss, both calculated in the dynamical QCD medium. We observe that, even when the dynamical effect is accounted for, suppressions from both radiative and collisional contributions are important (consistent with the claims in [7, 44, 45]). This further underscores that collisional energy loss has to be included in the D meson suppression predictions at both the RHIC and the LHC. Moreover, we see that including the collisional contribution increases D meson suppression by up to factor of two compared to the suppression resulting only from dynamical radiative energy loss. Consistent with this observation, we see that the total suppression is significantly larger than either of the two contributions—radiative alone or collisional alone—so that they have to be taken into account jointly for accurate predictions. Furthermore, our main observation from figure 3 is that inclusion of the dynamical effect results in a (rough) agreement with the experimental data, which leads to the conclusion that the dynamical effect is the main/necessary ingredient for accurate description of the jet–medium interactions.

Since we showed that collisional and radiative energy losses are important, we will further investigate how they are affected by the finite size (LPM) effect, as it is commonly considered that this effect is not important for heavy flavor at the RHIC. In figure 4, we separately investigate the finite size effect for radiative (the left panels), collisional (the central panels) and radiative plus collisional (the right panels) energy loss; the top and the bottom panels correspond to the RHIC and the LHC cases, respectively.

We see that for D mesons at both the RHIC and the LHC, the finite size effect is indeed negligible for collisional energy loss, but that they are significant for both radiative and total energy loss suppressions. That is, we see that neglecting LPM effect can lead to as much as two times larger suppression at the RHIC and several times larger suppression at the LHC. In figure 4 we also observe that, LPM effect leads to qualitatively different suppression dependence on momenta, as this effect can lead to a decrease—rather than increase—of suppression with jet momentum. Consequently, the LPM effect has to be taken into account in heavy flavor suppression predictions at both the RHIC and the LHC.

We next consider how the running coupling [9] affects the R_{AA}. Therefore, in figure 5 we compare the D meson suppression predictions obtained by using the fixed value of strong coupling constant, with the predictions when the running coupling is accounted, as a function of the transverse momentum. From figure 5 we observe that the running coupling leads to an increase in the suppression by almost a factor of two at lower jet momenta, while it makes no significant difference at higher jet momenta. Note that such an unequal contribution notably changes the shape of the suppression pattern, so that accounting for the running coupling for D mesons at both the RHIC and the LHC is also important. Furthermore, when comparing the predictions with available (LHC) experimental data (see the right panel of figure 5), we see that inclusion of running coupling leads to a somewhat worse agreement with experimental data, compared to the predictions with constant coupling; we will however see below that inclusion of *both* the running coupling and the finite magnetic mass improves the predictions.

We next investigate the significance of taking into account the finite magnetic mass in the suppression calculations. Namely, all previous energy loss calculations assumed zero magnetic mass, in accordance with the perturbative QCD. However, different non-perturbative approaches [31–35] reported a non-zero magnetic mass at the RHIC and the LHC, which indicates that the finite magnetic mass has to be included in the radiative energy loss calculations [8].

Hence in figure 6 we compare the D meson suppression predictions with and without the finite magnetic mass included in the suppression calculations. To investigate the importance of magnetic mass only, we do not include running coupling in this figure, i.e. we assume the constant coupling. Figure 6 shows that the inclusion of the finite magnetic mass effect leads to a notable $\sim 30\%$ decrease in the suppression. Consequently, the finite magnetic mass effect is also important. Furthermore, when comparing the predictions with available (LHC) experimental data (see the right panel of figure 6), we see that the effect of the inclusion of magnetic mass runs in the opposite direction from the inclusion of running coupling, and also in itself leads to a worse agreement with experimental data (compared to predictions with zero magnetic mass). From this and the previous figure (i.e. Figures 5 and 6), one can conclude that inclusion of the individual improvements in the energy loss calculations—in particular the running coupling alone, or the magnetic mass alone—does not necessarily lead to the improvement in the agreement between the predictions and the data.

Consequently, we finally consider how the inclusion of both the running coupling [9] and the magnetic mass affects R_{AA}. Therefore, in figure 7 we use the finite value of magnetic mass, and compare the D meson suppression predictions with fixed value of strong coupling constant, with those when the running coupling is used, as a function of transverse momentum. We see that these two effects, taken together, lead to a very good agreement with the experimental data, i.e. to both quantitative and qualitative improvement compared to the case in figure 3. This illustrates possible synergy in including different energy loss effects: taken individually, the running coupling and the finite magnetic mass lead to worse agreement with the experimental data, but taken together they notably improve the agreement. Therefore, detailed study of parton energy loss, as well as inclusion of all important medium effects, may be necessary to correctly model the interactions of high-momentum particles with the QCD medium.

4. Conclusion

Since our dynamical energy loss formalism led to a robust agreement with the experimentally measured nuclear modification factor for different experiments, probes and experimental

conditions (i.e. centrality ranges) [9, 10, 12], we investigated how different energy loss effects contribute to such a good agreement. In particular, we aimed at determining whether such a good agreement is a consequence of a single dominant effect or of several smaller improvements. We investigated this issue for the case of D mesons, whose suppression patterns are not modified by the fragmentation functions, so that they present a clear energy loss probe. We used an approach where we started from the simplest reasonable (and historically justified) energy loss model—which includes only radiative energy loss—and then sequentially added different model improvements. This approach both allows investigating the importance of different energy loss ingredients and obtaining the historical perspective on how the energy loss model has been improved. In particular, we studied the importance of the transition from the static to the dynamical framework and of including collisional energy loss, the finite size effect, the finite magnetic mass and the running coupling. As an overall conclusion, we found that the most important effect in modeling jet–medium interactions is the inclusion of the dynamical effect, i.e. modeling the medium constituents as dynamical (moving) particles, instead of the commonly used static scattering centers. However, for a fine agreement with the data, we find that each energy loss effect is important, and that the robust agreement between the theoretical predictions and the experimental data is a cumulative effect of all these improvements. As an outlook, the presented results suggest that further improvements in the energy loss model may be significant for accurately explaining the data even outside of the energy ranges and observables that we have tested so far. Therefore, we expect that data from the upcoming RHIC and LHC runs will help testing—or even further constraining—model calculations at higher transverse momentum.

Acknowledgments

References

[1] Bjorken J D 1982 *FERMILAB-PUB-82-059-THY* 287–92
[2] Brambilla N *et al* 2014 *Eur. Phys. J.* C **74** 2981
[3] Gyulassy M 2002 *Lect. Notes Phys.* **583** 37–9
[4] d'Enterria D and Betz B 2010 *Lect. Notes Phys.* **785** 285
[5] Djordjevic M 2009 *Phys. Rev.* C **80** 064909
[6] Djordjevic M and Heinz U 2008 *Phys. Rev. Lett.* **101** 022302
[7] Djordjevic M 2006 *Phys. Rev.* C **74** 064907
[8] Djordjevic M and Djordjevic M 2012 *Phys. Lett.* B **709** 229
[9] Djordjevic M and Djordjevic M 2014 *Phys. Lett.* B **734** 286
[10] Djordjevic M and Djordjevic M 2014 *Phys. Rev.* C **90** 034910
[11] Djordjevic M 2014 *Phys. Rev. Lett.* **112** 042302
[12] Djordjevic M, Djordjevic M and Blagojevic B 2014 *Phys. Lett.* B **737** 298
[13] Baier R, Dokshitzer Y L, Mueller A H, Peigne S and Schiff D 1997 *Nucl. Phys.* B **483** 291
     Baier R, Dokshitzer Y L, Mueller A H, Peigne S and Schiff D 1997 *Nucl. Phys.* B **484** 265
[14] Baier R, Dokshitzer Y L, Mueller A H and Schiff D 1998 *Phys. Rev.* C **58** 1706
[15] Zakharov B G 1996 *JETP Lett.* **63** 952
     Zakharov B G 1997 *JETP Lett.* **65** 615
[16] Wiedemann U A 2000 *Nucl. Phys.* B **588** 303
[17] Armesto N, Salgado C A and Wiedemann U A 2004 *Phys. Rev.* D **69** 114003

[18] Arnold P B, Moore G D and Yaffe L G 2001 *J. High Energy Phys.* JHEP11(2001)057
     Arnold P B, Moore G D and Yaffe L G 2002 *J. High Energy Phys.* JHEP06(2002)030
     Arnold P B, Moore G D and Yaffe L G 2003 *J. High Energy Phys.* JHEP01(2003)030
[19] Gyulassy M, Levai P and Vitev I 2000 *Nucl. Phys.* B **571** 197
     Gyulassy M, Levai P and Vitev I 2001 *Nucl. Phys.* B **594** 371
[20] Djordjevic M and Gyulassy M 2004 *Nucl. Phys.* A **733** 265–98
[21] Wang X N and Guo X F 2001 *Nucl. Phys.* A **696** 788
[22] Majumder A and van Leeuwen M 2011 *Prog. Part. Nucl. Phys.* A **66** 41
[23] Molnar D and Sun D 2014 *Nucl. Phys.* A **932** 140
     Molnar D and Sun D 2013 *Nucl. Phys.* A **910-911** 486
[24] Renk T 2012 *Phys. Rev.* C **85** 044903
[25] Wilde M (for the ALICE Collaboration) 2013 *Nucl. Phys.* A **904–5** 573c
[26] Adare A *et al* 2010 *Phys. Rev. Lett.* **104** 132301
[27] Wicks S, Horowitz W, Djordjevic M and Gyulassy M 2007 *Nucl. Phys.* A **784** 426
[28] Kang Z B, Vitev I and Xing H 2012 *Phys. Lett.* B **718** 482
[29] Gyulassy M, Levai P and Vitev I 2002 *Phys. Lett.* B **538** 282
[30] Dainese A 2004 *Eur. Phys. J.* C **33** 495
[31] Maezawa Y *et al* WHOT-QCD Collaboration 2010 *Phys. Rev.* D **81** 091501
[32] Maezawa Y *et al* (WHOT-QCD Collaboration) 2008 *Proc. of Sci. Lattice* **2008** 194
[33] Nakamura A, Saito T and Sakai S 2004 *Phys. Rev.* D **69** 014506
[34] Hart A, Laine M and Philipsen O 2000 *Nucl. Phys.* B **586** 443
[35] Bak D, Karch A and Yaffe L G 2007 *J. High Energy Phys.* JHEP08(2007)049
[36] Field R 1995 *Applications of Perturbative QCD* (Cambridge, Massachussetts: Perseus Books)
[37] Peshier A 2006 arXiv:hep-ph/0601119
[38] Betz B and Gyulassy M 2012 *Phys. Rev.* C **86** 024903
[39] Grelli A (ALICE Collaboration) 2013 *Nucl. Phys.* A **904–5** 635c
     Abelev B *et al* 2012 *J. High Energy Phys.* JHEP09(2012)112
[40] Gyulassy M and Wang X N 1994 *Nucl. Phys.* B **420** 583
     Wang X N, Gyulassy M and Plumer M 1995 *Phys. Rev.* D **51** 3436
[41] Armesto N *et al* 2012 *Phys. Rev.* C **86** 064904
[42] Thoma M H 1991 *Phys. Lett.* B **273** 128
[43] Mustafa M G and Thoma M H 2005 *Acta Phys. Hung.* A **22** 93
[44] Mustafa M G 2005 *Phys. Rev.* C **72** 014905
[45] Dutt-Mazumder A K, Alam J, Roy P and Sinha B 2005 *Phys. Rev.* D **71** 094016

NUCLEAR PHYSICS A

XXVIIIth International Conference on Ultrarelativistic Nucleus-Nucleus Collisions (Quark Matter 2019)

From high $p_\perp$ theory and data to inferring anisotropy of Quark-Gluon Plasma

Magdalena Djordjevic[a], Stefan Stojku[a], Dusan Zigic[a], Bojana Ilic[a], Jussi Auvinen[a], Igor Salom[a], Marko Djordjevic[b] and Pasi Huovinen[a]

[a] *Institute of Physics Belgrade, University of Belgrade, Serbia*

[b] *Faculty of Biology, University of Belgrade, Serbia*

Abstract

High $p_\perp$ theory and data are commonly used to study high $p_\perp$ parton interactions with QGP, while low $p_\perp$ data and corresponding models are employed to infer QGP bulk properties. On the other hand, with a proper description of high $p_\perp$ parton-medium interactions, high $p_\perp$ probes become also powerful tomography tools, since they are sensitive to global QGP features, such as different temperature profiles or initial conditions. This tomographic role of high $p_\perp$ probes can be utilized to assess the spatial anisotropy of the QCD matter. With our dynamical energy loss formalism, we show that a (modified) ratio of R_{AA} and v_2 presents a reliable and robust observable for straightforward extraction of initial state anisotropy. We analytically estimated the proportionality between the $v_2/(1-R_{AA})$ and anisotropy coefficient ϵ_{2L}, and found surprisingly good agreement with full-fledged numerical calculations. Within the current error bars, the extraction of the anisotropy from the existing data using this approach is still inaccessible. However, with the expected accuracy improvement in the upcoming LHC runs, the anisotropy of the QGP formed in heavy ion collisions can be straightforwardly derived from the data. Such a data-based anisotropy parameter would present an important test to models describing the initial stages of heavy-ion collision and formation of QGP, and demonstrate the usefulness of high $p_\perp$ theory and data in obtaining QGP properties.

Keywords: Quark-gluon plasma, High $p_\perp$ probes, Initial anisotropy

1. Introduction

Understanding the properties of the new form of matter named Quark-Gluon Plasma (QGP) is the major goal of relativistic heavy ion physics [1, 2]. However, to explore the properties of QGP, one needs good probes. With regards to that, it is commonly assumed that high $p_\perp$ theory and data are good probes for exploring the high $p_\perp$ parton interactions with QGP, while low $p_\perp$ theory and data are considered as good probes for bulk QGP properties. Contrary to this common assumption, the goal of this contribution is to demonstrate that high $p_\perp$ particles can also be useful independent probes of *bulk* QGP properties.

To put it simply, the main idea is that when high $p_\perp$ particles transverse QGP, they lose energy, where this energy loss is sensitive to bulk QGP properties, such as its temperature profiles or initial conditions.

Consequently, with a realistic and sophisticated high $p_\perp$ parton energy loss model, high $p_\perp$ probes can indeed become powerful tomographic tools. So, in this contribution, we will present how we can use these probes to infer some of the bulk QGP properties, i.e., for precision QGP tomography. Note that only the main results are presented here; for a more detailed version, see [3], and references therein.

2. DREENA framework

To achieve the goal of utilizing high $p_\perp$ theory and data for inferring the bulk QGP properties, as previously implied, a reliable high $p_\perp$ parton energy loss model is necessary. With this goal in mind, we developed a dynamical energy loss formalism [4, 5], which takes into account some more realistic and unique features, such as: i) The calculations are performed within finite temperature field theory and generalized Hard-Thermal-Loop [6] approach, in which the infrared divergences are naturally regulated, excluding the need for artificial cutoffs. ii) The formalism assumes QCD medium of finite size and finite temperature, consisting of dynamical partons (i.e., energy exchange with medium constituents is included), in distinction to commonly considered static scatterers approximation and/or models with vacuum-like propagators. iii) Both radiative [4] and collisional [5] energy losses are calculated within the same theoretical framework, and are equally applicable to light and heavy flavors. iv) The formalism is generalized to include a finite chromomagnetic mass [7], running coupling, and to relax the widely used soft-gluon approximation [8]. Finally, the formalism is integrated in a numerical framework DREENA (Dynamical Radiative and Elastic ENergy loss Approach) [9, 10], to provide predictions for high $p_\perp$ observables.

Within this framework, we generated a wide set of high $p_\perp$ predictions using 1D Bjorken expansion [11] (i.e., DREENA-B framework [10]). Thus we obtained a good joint agreement with a wide range of high $p_\perp$ R_{AA} and v_2 data, by applying the same numerical procedure, the same parameter set, and no fitting parameters in model testing. That is, there is no v_2 puzzle [12] within our model, which then strongly suggests that the model provides a realistic description of high $p_\perp$ parton-medium interactions. Moreover, our preliminary findings suggest that, within our formalism, moving from 1D Bjorken to full 3D hydrodynamical expansion does not significantly affect the agreement of our predictions with high $p_\perp$ R_{AA} and v_2 data [13]. Consequently, in order to adequately address the high $p_\perp$ measurements, a proper description of high $p_\perp$ parton interactions with the medium appears to be much more important than an advanced medium evolution description. Furthermore, we have also analyzed the sensitivity of high $p_\perp$ R_{AA} and v_2 to different initial stages, giving an additional insight in the usefulness of both high $p_\perp$ observables in the precision QGP tomography [14].

3. Inferring QGP anisotropy through high $p_\perp$ theory and data

As one example of QGP tomography, in this contribution, we will address how to infer the QGP anisotropy from high $p_\perp$ R_{AA} and v_2 data. The initial state anisotropy is one of the main properties of QGP and a major limiting factor for precision QGP tomography. However, despite its essential importance, it is still not possible to directly infer the initial anisotropy from experimental measurements. Several theoretical studies [15, 16, 17, 18] have provided different methods for calculating the initial anisotropy, leading to notably different predictions, with a notable effect in the resulting predictions for both low and high $p_\perp$ data. Therefore, approaches for inferring anisotropy from the data are necessary. Optimally, these approaches should be complementary to existing predictions, i.e., based on a method that is fundamentally different from models of early stages of QCD matter.

To this end, we here propose a novel approach to extract the initial state anisotropy. Our method is based on inference from high $p_\perp$ data, by using already available R_{AA} and v_2 measurements, which will moreover be measured with much higher precision in the future. Such an approach is substantially different from the existing approaches, as it is based on the inference from experimental data (rather than on calculations of early stages of QCD matter) exploiting the information from interactions of rare high $p_\perp$ partons with the QCD medium. This also presents an improvement/optimization in utilizing high $p_\perp$ data as, to date, these data were mostly constrained on studying the parton-medium interactions, rather than assessing bulk QGP parameters, such as spatial asymmetry.

In the literature, the initial state anisotropy is quantified in terms of eccentricity parameter ϵ_2

$$\epsilon_2 = \frac{\langle y^2 - x^2 \rangle}{\langle y^2 + x^2 \rangle} = \frac{\int dx\, dy\, (y^2 - x^2)\, \rho(x, y)}{\int dx\, dy\, (y^2 + x^2)\, \rho(x, y)}, \tag{1}$$

where $\rho(x, y)$ denotes the initial density distribution of the formed QGP. Regarding high $p_\perp$ observables, we note that v_2 is sensitive to both the anisotropy of the system and its size, while R_{AA} is sensitive only to the size of the system. Therefore, it is plausible that the adequate observable for extracting eccentricity from high $p_\perp$ data depends on both v_2 and R_{AA}, and the question is how.

To address this question, we will use the dynamical energy loss formalism, and DREENA-B framework outlined above. For high $p_\perp$, the fractional energy loss scales as [3] $\Delta E/E \sim \chi \langle T \rangle^a \langle L \rangle^b$, where $\langle T \rangle$ stands for the average temperature along the path of high $p_\perp$ parton, $\langle L \rangle$ is the average path-length traversed by the parton, χ is a proportionality factor that depends on the initial parton transverse momentum, and a and b are exponents which govern the temperature and path-length dependence of the energy loss. Within our model, $a \approx 1.2$ and $b \approx 1.4$, which is contrary to simpler models, and consistent with a wide range of experimental data [19, 20]. From this simple scaling argument, we can straightforwardly obtain the following expressions for R_{AA} and v_2 (for more details we refer the reader to [3]):

$$R_{AA} \approx 1 - \xi(\chi)\langle T \rangle^a \langle L \rangle^b, \qquad v_2 \approx \frac{1}{2} \frac{R_{AA}^{in} - R_{AA}^{out}}{R_{AA}^{in} + R_{AA}^{out}} \approx \xi(\chi)\langle T \rangle^a \langle L \rangle^b \left(\frac{b}{2} \frac{\Delta L}{\langle L \rangle} - \frac{a}{2} \frac{\Delta T}{\langle T \rangle} \right), \tag{2}$$

where we see that $\xi(\chi)\langle T \rangle^a \langle L \rangle^b$ corresponds to $1 - R_{AA}$. Therefore, if we divide v_2 by $(1 - R_{AA})$, we see that this ratio is given by the following simple expression:

$$\frac{v_2}{1 - R_{AA}} \approx \left(\frac{b}{2} \frac{\Delta L}{\langle L \rangle} - \frac{a}{2} \frac{\Delta T}{\langle T \rangle} \right). \tag{3}$$

Note that, while this ratio exposes the dependence on the asymmetry of the system (through spatial ($\Delta L/\langle L \rangle$) and temperature ($\Delta T/\langle T \rangle$) parts), the dependence only on spatial anisotropy is still not isolated. However, by plotting together spatial and temperature anisotropy, we obtain a linear dependence [3], with a proportionality factor given by $c \approx 4.3$. Therefore, $v_2/(1 - R_{AA})$ reduces to the following expression:

$$\frac{v_2}{1 - R_{AA}} \approx \frac{1}{2} \left(b - \frac{a}{c} \right) \frac{\langle L_{out} \rangle - \langle L_{in} \rangle}{\langle L_{out} \rangle + \langle L_{in} \rangle} \approx 0.57\varsigma, \quad \text{where} \quad \varsigma = \frac{\langle L_{out} \rangle - \langle L_{in} \rangle}{\langle L_{out} \rangle + \langle L_{in} \rangle} \quad \text{and} \quad \frac{1}{2}(b - \frac{a}{c}) \approx 0.57. \tag{4}$$

Consequently, the asymptotic scaling behavior of observables v_2 and R_{AA}, at high $p_\perp$, reveals that their (moderated) ratio is determined only by the geometry of the initial QGP droplet. Therefore, the anisotropy parameter ς could, in principle, be directly obtained from the high $p_\perp$ experimental data.
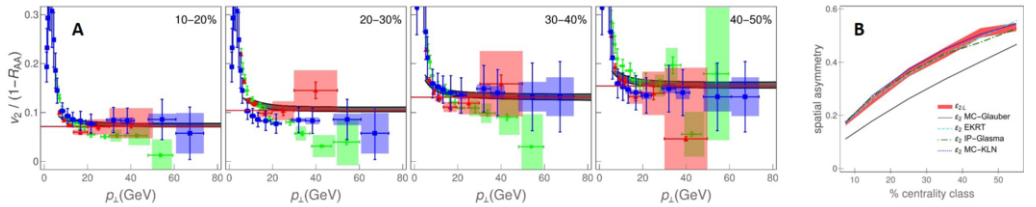

Fig. 1. **A)** Comparison of theoretical predictions for charged hadron $v_2/(1 - R_{AA})$ as a function of $p_\perp$ with 5.02 TeV $Pb + Pb$ CMS [21, 22] (blue squares), ALICE [23, 24] (red triangles) and ATLAS [25, 26] (green circles) data. Each panel corresponds to different centrality range, as indicated in the upper right corners, while red lines denote the limit 0.57ς from Eq. (4). **B)** Comparison of ϵ_{2L} (red band) extracted from our full-fledged calculations, with ϵ_2 obtained from MC-Glauber [15] (gray full curve), EKRT [16] (cyan dashed curve), IP-Glasma [17] (green dot-dashed curve) and MC-KLN [18] (blue dotted curve) models. MC-Glauber and EKRT curves correspond to 5.02 TeV, whereas IP-Glasma and MC-KLN curves correspond to 2.76 TeV $Pb + Pb$ collisions at the LHC.

To test the adequacy of the analytical estimate given by Eqs. (2)-(4), Fig. 1A is displayed, which comprises our $v_2/(1 - R_{AA})$ predictions (gray bands), stemming from our full-fledged recently developed

DREENA-B framework (outlined in the previous section), the ALICE, CMS and ATLAS data, and analytically derived asymptote 0.57ς (red lines). Importantly, for each centrality range and for $p_\perp \gtrsim 20$ GeV, $v_2/(1 - R_{AA})$ is independent on $p_\perp$, and approaches the asymptote, i.e., is determined by the geometry of the system - depicted by the solid red line, up to 5% accuracy. Moreover, the experimental data for all three experiments also display the independence on the $p_\perp$ and agree with our predictions, although the error bars are rather large. Therefore, we conclude that our scaling estimates are valid and that $v_2/(1 - R_{AA})$ indeed carries the information about the anisotropy of the fireball, which can be simply (from the straight line fit to data at high $p_\perp$ limit) and robustly (in the same way for each centrality) inferred from the experimental data.

However, note that the anisotropy parameter ς is not the widely-considered anisotropy parameter ϵ_2 (given by Eq. (1)). To facilitate comparison with ϵ_2 values in the literature, we define $\epsilon_{2L} = \frac{\langle L_{out}\rangle^2 - \langle L_{in}\rangle^2}{\langle L_{out}\rangle^2 + \langle L_{in}\rangle^2} = \frac{2\varsigma}{1+\varsigma^2}$, and in Fig. 1B compare it with the results from different initial-state models [15, 16, 17, 18]. First, we should note that as a starting point, our initial ϵ_2, through which we generate our path-length distributions, agrees with EKRT and IP-Glasma. However, what is highly non-trivial is that, as an outcome of this procedure, in which $v_2/(1 - R_{AA})$ is calculated (based on the full-fledged DREENA-B framework), we obtain ϵ_{2L} which practically coincides with our initial ϵ_2 and also with some of the conventional initial-state models. As an overall conclusion, the straightforward extraction of ϵ_{2L} and its agreement with values of the prevailing initial-state models' eccentricity (and our initial ϵ_2) is highly non-trivial and supports $v_2/(1 - R_{AA})$ as a reliable and robust observable for anisotropy. Additionally, the width of our ϵ_{2L} band is smaller than the difference in the ϵ_2 values obtained by using different models (e.g., MC-Glauber vs. MC-KLN). Therefore, our approach provides genuine resolving power to distinguish between different initial-state models, although it may not be possible to separate the finer details of more sophisticated models. This resolving power, moreover, comes from an entirely different perspective, i.e., from high $p_\perp$ theory and data, supporting the usefulness of utilizing high $p_\perp$ theory and data for inferring the bulk QGP properties.

References

[1] M. Gyulassy and L. McLerran, Nucl. Phys. A **750**, 30 (2005); E. V. Shuryak, Nucl. Phys. A **750**, 64 (2005).

[2] B. Jacak and P. Steinberg, Phys. Today **63**, 39 (2010); C. V. Johnson and P. Steinberg, Phys. Today **63**, 29 (2010).

[3] M. Djordjevic, S. Stojku, M. Djordjevic and P. Huovinen, Phys. Rev. C **100**, no. 3, 031901 (2019).

[4] M. Djordjevic, Phys. Rev. C **80**, 064909 (2009); M. Djordjevic and U. Heinz, Phys. Rev. Lett. **101**, 022302 (2008).

[5] M. Djordjevic, Phys. Rev. C **74**, 064907 (2006).

[6] J. I. Kapusta, *Finite-Temperature Field Theory* (Cambridge University Press, 1989).

[7] M. Djordjevic and M. Djordjevic, Phys. Lett. B **709**, 229 (2012).

[8] B. Blagojevic, M. Djordjevic and M. Djordjevic, Phys. Rev. C **99**, 024901 (2019).

[9] D. Zigic, I. Salom, J. Auvinen, M. Djordjevic and M. Djordjevic, J. Phys. G **46**, 085101 (2019).

[10] D. Zigic, I. Salom, M. Djordjevic and M. Djordjevic, Phys. Lett. B **791**, 236 (2019).

[11] J. D. Bjorken, Phys. Rev. D **27**, 140 (1983).

[12] J. Noronha-Hostler, B. Betz, J. Noronha and M. Gyulassy, Phys. Rev. Lett. **116**, no. 25, 252301 (2016); B. Betz and M. Gyulassy, JHEP 1408, 090 (2014); S. K. Das, F. Scardina, S. Plumari and V. Greco, Phys. Lett. B 747, 260 (2015).

[13] D. Zigic, *et al.*, to be submitted.

[14] D. Zigic, B. Ilic, M. Djordjevic and M. Djordjevic, arXiv:1908.11866 [hep-ph].

[15] C. Loizides, J. Kamin and D. d'Enterria, Phys. Rev. C **97**, 054910 (2018).

[16] K. J. Eskola, H. Niemi, R. Paatelainen and K. Tuominen, Phys. Rev. C **97**, 034911 (2018).

[17] J. E. Bernhard, J. S. Moreland, S. A. Bass, J. Liu and U. Heinz, Phys. Rev. C **94**, 024907 (2016).

[18] T. Hirano, P. Huovinen, K. Murase and Y. Nara, Prog. Part. Nucl. Phys. **70**, 108 (2013).

[19] M. Djordjevic and M. Djordjevic, Phys. Rev. C **92**, 024918 (2015).

[20] M. Djordjevic, D. Zigic, M. Djordjevic and J. Auvinen, Phys. Rev. C **99**(R), 061902 (2019).

[21] V. Khachatryan *et al.* [CMS Collaboration], JHEP **1704**, 039 (2017).

[22] A. M. Sirunyan *et al.* [CMS Collaboration], Phys. Lett. B **776**, 195 (2018).

[23] S. Acharya *et al.* [ALICE Collaboration], JHEP **1811**, 013 (2018).

[24] S. Acharya *et al.* [ALICE Collaboration], JHEP **1807**, 103 (2018).

[25] [ATLAS Collaboration], ATLAS-CONF-2017-012.

[26] M. Aaboud *et al.* [ATLAS Collaboration], Eur. Phys. J. C **78**, no. 12, 997 (2018).

XXVIIth International Conference on Ultrarelativistic Nucleus-Nucleus Collisions
(Quark Matter 2018)

Dynamical energy loss formalism: from describing suppression patterns to implications for future experiments

Magdalena Djordjevic[a], Dusan Zigic[a], Bojana Blagojevic[a], Jussi Auvinen[a], Igor Salom[a] and Marko Djordjevic[b]

[a] Institute of Physics Belgrade, University of Belgrade, Serbia

[b] Faculty of Biology, University of Belgrade, Serbia

Abstract

We overview our recently developed DREENA-C and DREENA-B frameworks, where DREENA (Dynamical Radiative and Elastic ENergy loss Approach) is a computational implementation of the dynamical energy loss formalism; C stands for constant temperature and B for the medium evolution modeled by Bjorken expansion. At constant temperature our predictions overestimate v_2, in contrast to other models, but consistent with simple analytical estimates. With Bjorken expansion, we obtain good agreement with both R_{AA} and v_2 measurements. We find that introducing medium evolution has a larger effect on v_2 predictions, but for precision predictions it has to be taken into account in R_{AA} predictions as well. We also propose a new observable, which we call *path length sensitive suppression ratio*, for which we argue that the path length dependence can be assessed in a straightforward manner. We also argue that $Pb + Pb$ vs. $Xe + Xe$ collisions make a good system to assess the path length dependence. As an outlook, we expect that introduction of more complex medium evolution (beyond Bjorken expansion) in the dynamical energy loss formalism can provide a basis for a state of the art QGP tomography tool – e.g. to jointly constrain the medium properties from the point of both high-$p_\perp$ and low-$p_\perp$ data.

Keywords: relativistic heavy ion collisions, quark-gluon plasma, energy loss, hard probes, heavy flavor

1. Introduction

Energy loss of high-$p_\perp$ particles traversing QCD medium is considered to be an excellent probe of QGP properties [1, 2, 3]. The theoretical predictions can be generated and compared with a wide range of experimental data, coming from different experiments, collision systems, collision energies, centralities, observables. This comprehensive comparison of theoretical predictions and high $p_\perp$ data, can then be used together with low $p_\perp$ theory and data to study the properties of created QCD medium [4, 5, 6, 7], that is, for precision QGP tomography. However, to implement this idea, it is crucial to have a reliable high $p_\perp$ parton energy loss model. With this goal in mind, during the past several years, we developed the dynamical energy loss formalism [8]. Contrary to the widely used approximation of static scattering centers, this model

takes into account that QGP consists of dynamical (moving) partons, and that the created medium has finite size. The calculations are based on the finite temperature field theory, and generalized HTL approach. The formalism takes into account both radiative and collisional energy losses, is applicable to both light and heavy flavor, and has been recently generalized to the case of finite magnetic mass and running coupling [9]. Most recently, we also relaxed the soft-gluon approximation within the model [15]. Finally, the formalism is integrated in an up-to-date numerical procedure [9], which contains parton production [10], fragmentation functions [11], path-length [12, 13] and multi-gluon fluctuations [14].

The model up-to-now explained a wide range of R_{AA} data [9, 16, 17, 18], with the same numerical procedure, the same parameter set, and with no fitting parameters, including explaining puzzling data and generating predictions for future experiments. This then strongly suggests that the model provides a realistic description of high $p_\perp$ parton-medium interactions. However, the model did not take into account the medium evolution, so we used it to provide predictions only for those observables that are considered to be weakly sensitive to QGP evolution.

Therefore, our goal, which will be addressed in this proceedings, is to develop a framework which will allow systematic comparison of experimental data and theoretical predictions, obtained by the same formalism and the same parameter set. In particular, we want to develop a framework, which can systematically generate predictions for different observables (both R_{AA} and v_2), different collision systems ($Pb + Pb$ and $Xe + Xe$), different probes (light and heavy), different collision energies and different centralities [19, 20, 21]. Within this, our major goal is to introduce medium evolution in the dynamical energy loss formalism [20], where we start with 1+1D Bjorken expansion [22], and where our developments in this direction, will also be outlined in this proceedings. Finally, we also want to address an important question of how to differentiate between different energy loss models; in particular, what is the appropriate observable, and what are appropriate systems, to assess energy loss path-length dependence [21]. Note that only the main results are presented here; for a more detailed version, see [19, 20, 21], and references therein.

2. Results and discussion

As a first step towards the goals specified above, we developed DREENA-C framework [19], which is a fully optimized computational suppression procedure based on our dynamical energy loss formalism in constant temperature finite size QCD medium. Within this framework we, for the first time, generated joint R_{AA} and v_2 predictions based on our dynamical energy loss formalism. We generated predictions for both light and heavy flavor probes, and different centrality regions in $Pb + Pb$ collisions at the LHC (see [19] for more details). We obtained that, despite the fact that DREENA-C does not contain medium evolution (to which v_2 is largely sensitive), it leads to qualitatively good agreement with this data, though quantitatively, the predictions are visibly above the experimental data.

The theoretical models up-to-now, faced difficulties in jointly explaining R_{AA} and v_2 data, i.e. lead to underprediction of v_2, unless new phenomena are introduced, which is known as v_2 puzzle [23]. Having this in mind, the overestimation of v_2, obtained by DREENA-C, seems surprising. However, by using a simple scaling arguments, where fractional energy loss is proportional to T^a and L^b , and where, within our model a, b are close to 1, we straightforwardly obtain that in constant T medium, $R_{AA} \approx 1 - \xi T L$ and $v_2 \approx \frac{\xi T \Delta L}{2}$, while in evolving medium R_{AA} retains the same expressions and $v_2 \approx \frac{\xi T \Delta L - \xi \Delta T L}{2}$ (see [19] for more details, ξ is a proportionality factor that depends on initial jet $p_\perp$). So, it is our expectation that, within our model, the medium evolution will not significantly affect R_{AA}, while it will notably lower the v_2 predictions.

To check the reliability of these simple estimates, we developed DREENA-B framework [20], which is our most recent development within dynamical energy loss formalism. Here B stands for 1+1D Bjorken expansion [22], i.e. the medium evolution is introduced in dynamical energy loss formalism in a simple analytic way. We provided first joint R_{AA} and v_2 predictions with dynamical energy loss formalism in expanding QCD medium, which are presented in Fig. 1 (for charged hadrons), and we observe very good agreement with both R_{AA} and v_2 data. We equivalently obtained the same good agreement for D mesons, and predicted non-zero v_2 for high $p_\perp$ B mesons.

In Fig. 2, we further present predictions for $Xe + Xe$ data [21], where we note that these predictions were generated before the data became available. In this figure (see also Fig. 1), we compare DREENA-C and
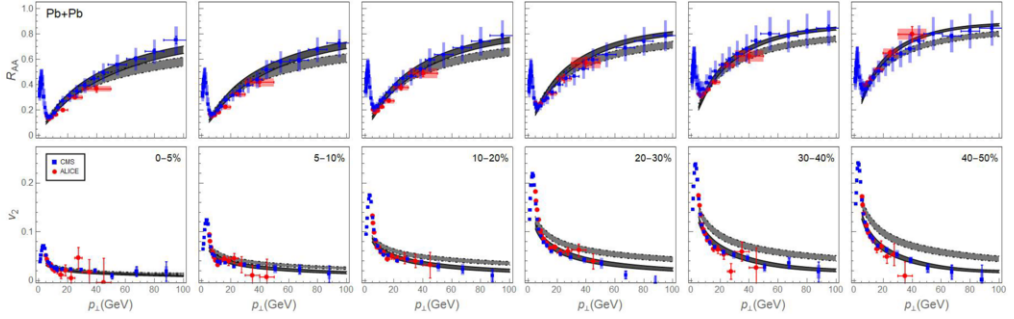
Fig. 1. **Joint R_{AA} and v_2 predictions for charged hadrons in** 5.02 **TeV** *Pb* + *Pb* **collisions.** *Upper panels:* Predictions for R_{AA} *vs.* $p_\perp$ are compared with ALICE [24] (red circles) and CMS [25] (blue squares) charged hadron experimental data in 5.02 TeV *Pb* + *Pb* collisions. *Lower panels:* Predictions for v_2 *vs.* $p_\perp$ are compared with ALICE [26] (red circles) and CMS [27] (blue squares) experimental data in 5.02 TeV *Pb* + *Pb* collisions. Full and dashed curves correspond, respectively, to the predictions obtained with DREENA-B and DREENA-C frameworks. In each panel, the upper (lower) boundary of each gray band corresponds to $\mu_M/\mu_E = 0.6$ ($\mu_M/\mu_E = 0.4$). Columns 1-6 correspond, respectively, to $0 - 5\%$, $5 - 10\%$, $10 - 20\%$,..., $40 - 50\%$ centrality regions. The figure is adapted from [19, 20] and the parameter set is specified there.

DREENA-B frameworks, to assess the importance of including medium evolution on R_{AA} and v_2 observables. We see that introduction of expanding medium affects both R_{AA} and v_2 data. That is, it systematically somewhat increase R_{AA}, while significantly decreasing v_2; this observation is in agreement with our estimate provided above. Consequently, we see that this effect has large influence on v_2 predictions, confirming previous arguments that v_2 observable is quite sensitive to medium evolution. On the other hand, this effect is rather small on R_{AA}, consistent with the notion that R_{AA} is not very sensitive to medium evolution [28, 29]. However, our observation from Figs. 1 and 2 is that medium evolution effect on R_{AA}, though not large, should still not be neglected in precise R_{AA} calculations, especially for high $p_\perp$ and higher centralities.
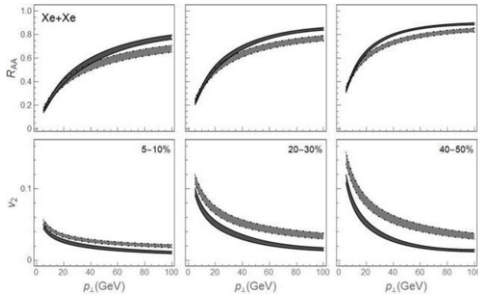
Fig. 2. **Joint R_{AA} and v_2 predictions for charged hadrons in** 5.44 **TeV** *Xe* + *Xe* **collisions.** Predictions for R_{AA} *vs.* $p_\perp$ and v_2 *vs.* $p_\perp$ are shown on upper and lower panels, respectively. Columns 1-3, respectively, correspond to $5 - 10\%$, $20 - 30\%$ and $40 - 50\%$ centrality regions. Full and dashed curves correspond, respectively, to the predictions obtained with DREENA-B and DREENA-C frameworks. The figure is adapted from [20] and the parameter set is specified there.
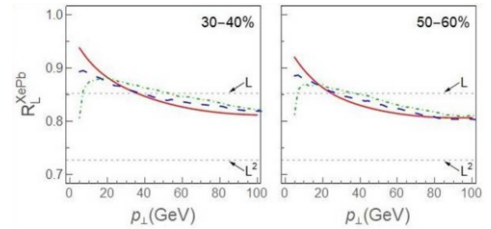
Fig. 3. **Path-length sensitive suppression ratio (R_L^{XePb}) for light and heavy probes.** Predictions for R_L^{XePb} *vs.* $p_\perp$ is shown for charged hadrons (full), D mesons (dashed) and B mesons (dot-dashed). First and second column, respectively, correspond to $30 - 40\%$ and $50 - 60\%$ centrality regions. $\mu_M/\mu_E = 0.4$. The figure is adapted from [21] and the parameter set is specified there.

Finally, as the last topic of this proceedings, we address a question on how to differentiate between different energy loss models. With regard to this, note that path length dependence provides an excellent signature differentiating between different energy loss models, and consequently also between the underlying energy loss mechanisms. For example, some energy loss models have linear, some have quadratic, and our dynamical energy loss has the path-length dependence between linear and quadratic, which is due to both collisional and radiative energy loss mechanisms included in the model. To address this question, we

first have to answer what is an appropriate system for such a study. We argue that comparison of suppressions in $Pb + Pb$ and $Xe + Xe$ is an excellent way to study the path length dependence: From the suppression calculation perspective, almost all properties of these two systems are the same. That is, we show [21] that these two systems have very similar initial momentum distributions, average temperature for each centrality region and path length distributions (up to rescaling factor $A^{1/3}$). That is, the main property differentiating the two systems is its size, i.e. rescaling factor $A^{1/3}$, which therefore makes comparison of suppressions in $Pb + Pb$ and $Xe + Xe$ collisions an excellent way to study the path length dependence.

The second question is what is appropriate observable? With regards to that, the ratio of the two R_{AA} seems a natural choice, as has been proposed before. However, in this way the path length dependence cannot be naturally extracted, as shown in [21]. For example, this ratio approaches one for high $p_\perp$ and high centralities, suggesting no path length dependence, while the dynamical energy loss has strong path length dependence. Also, the ratio has strong centrality dependence. That is, from this ratio, no useful information can be deduced. The reason for this is that this ratio includes a complicated relationship (see [21] for more details) which depends on the initial jet energy and centrality; so extracting the path-length dependence from this observable would not be possible.

However, based on the derivation presented in [21], we propose to use the ratio of 1-R_{AA} instead. From this estimate, we see that this ratio $R_L^{XePb} \equiv \frac{1-R_{XeXe}}{1-R_{PbPb}} \approx \left(\frac{A_{Xe}}{A_{Pb}}\right)^{b/3}$ has a simple dependence on only the size of the medium ($A^{1/3}$ ratio) and the path length dependence (exponent b). In Fig. 3 we plot this ratio, where we see that the path length dependence can be extracted from this ratio in a simple way, and moreover there is only a weak centrality dependence. Therefore, 1-R_{AA} ratio seems as a natural observable, which we propose to call *path-length sensitive suppression ratio*.

References

[1] M. Gyulassy and L. McLerran, Nucl. Phys. A **750**, 30 (2005).
[2] E. V. Shuryak, Nucl. Phys. A **750**, 64 (2005).
[3] B. Jacak and P. Steinberg, Phys. Today **63**, 39 (2010).
[4] K. M. Burke *et al.* [JET Collaboration], Phys. Rev. C **90**, no. 1, 014909 (2014).
[5] G. Aarts *et al.*, Eur. Phys. J. A **53**, no. 5, 93 (2017).
[6] Y. Akiba *et al.*, arXiv:1502.02730 [nucl-ex].
[7] N. Brambilla *et al.*, Eur. Phys. J. C **74**, no. 10, 2981 (2014).
[8] M. Djordjevic, Phys. Rev. C **80**, 064909 (2009); M. Djordjevic and U. Heinz, Phys. Rev. Lett. **101**, 022302 (2008).
[9] M. Djordjevic and M. Djordjevic, Phys. Lett. B **734**, 286 (2014).
[10] Z. B. Kang, I. Vitev and H. Xing, Phys. Lett. B **718**, 482 (2012); R. Sharma, I. Vitev and B.W. Zhang, Phys. Rev. C **80**, 054902 (2009).
[11] D. de Florian, R. Sassot and M. Stratmann, Phys. Rev. D **75**, 114010 (2007).
[12] A. Dainese, Eur. Phys. J. C **33**, 495 (2004).
[13] S. Wicks, W. Horowitz, M. Djordjevic and M. Gyulassy, Nucl. Phys. A **784**, 426 (2007).
[14] M. Gyulassy, P. Levai and I. Vitev, Phys. Lett. B **538**, 282 (2002).
[15] B. Blagojevic, M. Djordjevic and M. Djordjevic, arXiv:1804.07593 [nucl-th].
[16] M. Djordjevic, B. Blagojevic and L. Zivkovic, Phys. Rev. C **94**, no. 4, 044908 (2016).
[17] M. Djordjevic and M. Djordjevic, Phys. Rev. C **92**, 024918 (2015).
[18] M. Djordjevic, Phys. Rev. Lett. **734**, 286 (2014); Phys. Lett. B **763**, 439 (2016).
[19] D. Zigic, I. Salom, J. Auvinen, M. Djordjevic and M. Djordjevic, arXiv:1805.03494 [nucl-th].
[20] D. Zigic, I. Salom, M. Djordjevic and M. Djordjevic, arXiv:1805.04786 [nucl-th].
[21] M. Djordjevic, D. Zigic, M. Djordjevic and J. Auvinen, arXiv:1805.04030 [nucl-th].
[22] J. D. Bjorken, Phys. Rev. D **27**, 140 (1983).
[23] J. Noronha-Hostler, B. Betz, J. Noronha and M. Gyulassy, Phys. Rev. Lett. **116**, no. 25, 252301 (2016).
[24] S. Acharya *et al.* [ALICE Collaboration], arXiv:1802.09145 [nucl-ex].
[25] V. Khachatryan *et al.* [CMS Collaboration], JHEP **1704**, 039 (2017).
[26] S. Acharya *et al.* [ALICE Collaboration], arXiv:1804.02944 [nucl-ex].
[27] A. M. Sirunyan *et al.* [CMS Collaboration], Phys. Lett. B **776**, 195 (2018).
[28] T. Renk, Phys. Rev. C **85** 044903 (2012).
[29] D. Molnar and D. Sun, Nucl. Phys. A **932** 140 (2014); Nucl. Phys. A **910-911** 486 (2013).

Utilizing high-$p_\perp$ theory and data to constrain the initial stages of quark-gluon plasma

Bojana Ilic[*,‡], Dusan Zigic[*,§],
Marko Djordjevic[†,¶] and Magdalena Djordjevic[*,‖]

[*]*Institute of Physics Belgrade,
University of Belgrade, Pregrevica 118,
Belgrade 11080, Serbia*

[†]*Faculty of Biology, University of Belgrade
Studentski trg 16, Belgrade 11000, Serbia*
[‡]*bojanab@ipb.ac.rs*
[§]*zigic@ipb.ac.rs*
[¶]*dmarko@bio.bg.ac.rs*
[‖]*magda@ipb.ac.rs*

The scarce knowledge of the initial stages of quark-gluon plasma before the thermalization is mostly inferred through the low-$p_\perp$ sector. We propose a complementary approach in this report — the use of high-$p_\perp$ probes' energy loss. We study the effects of four commonly assumed initial stages, whose temperature profiles differ only before the thermalization, on high-$p_\perp$ R_{AA} and v_2 predictions. The predictions are based on our Dynamical Radiative and Elastic ENergy-loss Approach (DREENA) framework. We report insensitivity of v_2 to the initial stages, making it unable to distinguish between different cases. R_{AA} displays sensitivity to the presumed initial stages, but current experimental precision does not allow resolution between these cases. We further revise the commonly accepted procedure of fitting the energy loss parameters, for each individual initial stage, to the measured R_{AA}. We show that the sensitivity of v_2 to various initial stages obtained through such procedure is mostly a consequence of fitting procedure, which may obscure the physical interpretations. Overall, the simultaneous study of high-$p_\perp$ observables, with unchanged energy loss parametrization and restrained temperature profiles, is crucial for future constraints on initial stages.

Keywords: Quark-gluon plasma; initial stages; jet quenching.

PACS Number(s): 12.38.Mh, 24.85.+p, 25.75.−q

1. Introduction

In ultrarelativistic heavy-ion collisions (HICs) at the Relativistic Heavy Ion Collider (RHIC) and the Large Hadron Collider (LHC) (commonly termed as mini big

‡Corresponding author.

bangs), a new form of matter — the quark-gluon plasma (QGP),[1,2] in which quarks, antiquarks, and gluons are deconfined, is created. The large transverse momentum (high-$p_\perp$) particles are formed immediately upon the collision and therefore are affected by all stages of QGP evolution. This makes them excellent probes[3,4] of this new state of matter, primarily through two main energy loss-based high-$p_\perp$ observables — angular averaged (R_{AA}) and angular differential (v_2) nuclear modification factors.

Traditionally, rare high-$p_\perp$ probes ($p_\perp \gtrsim 5\,\text{GeV}$), which present $\sim 0.1\%$ of all particles produced in HIC, are used for studying the mechanisms of jet-medium interactions, while low-$p_\perp$ sector[5-7] ($p_\perp \lesssim 5\,\text{GeV}$) is used to infer QGP features, such as e.g., initial stages before the QGP thermalization. However, up-to-date initial-stage properties are poorly known. Therefore, the need for an alternative approach to assessing the initial-stage features emerged. We here propose using high-$p_\perp$ probes as a complementary tool for this purpose, primarily since high-$p_\perp$ partons are good probes of QGP properties, where these properties depend on initial QGP stages. Furthermore, the recently acquired extensive set of high-precision experimental data for the two aforementioned high-$p_\perp$ observables[8-13] facilitates our study. This issue is moreover intriguing, as results of current theoretical studies on this subject are mostly inconclusive.[14-16]

A more rigorous study on this issue is required, that implies higher control over both the energy loss model and the analyzed temperature profiles. To accomplish this, we apply a full-fledged DREENA-B[17] framework (B stands for one-dimensional (1D) Bjorken[18] expansion), based on our state-of-the-art dynamical energy loss formalism[19] that will be outlined in Sec. 2. It also considers 1D Bjorken[18] medium evolution, which is highly suitable for this study, as it allows the analytical introduction of different evolutions before thermalization, with the same evolution after thermalization, which facilitates the isolation of the effects of different initial stages. Additionally, we checked that the transition from 1D Bjorken to full 3+1D hydrodynamical evolution[20] does not significantly change our high-$p_\perp$ predictions, implying that for reliable high-$p_\perp$ predictions, an accurate energy loss model is more important than the medium evolution model. Therefore, DREENA-B[17] provides an optimal framework for the initial-stages study, as it combines a state-of-the-art energy loss model with fully controlled temperature profiles. Note that, in this paper, we provide a part of the more detailed results obtained in Ref. 21, enriched with some complementary predictions.

2. Numerical and Theoretical Framework

For generating medium modified distribution of high-$p_\perp$ particles, irrespective of their flavor, we apply the generic pQCD convolution formula[19,22]:

$$\frac{E_f d^3 \sigma}{dp_f^3} = \frac{E_i d^3 \sigma(Q)}{dp_i^3} \otimes P(E_i \to E_f) \otimes D(Q \to H_Q), \qquad (1)$$

where i and f stand for the initial parton (Q) and final hadron (H_Q), respectively. The initial parton momentum distribution $\frac{E_i d^3\sigma(Q)}{dp_i^3}$ is calculated in accordance with Ref. [23]. The energy loss probability $P(E_i \to E_f)$ is based on our dynamical energy loss formalism (see paragraph below) and incorporates multigluon[24] and path-length fluctuations.[22,25,26] $D(Q \to H_Q)$ denotes fragmentation function, where for the light hadrons, D and B mesons de Florian–Sassot–Stratmann (DSS),[27] Braaten–Cheung–Fleming–Yuan (BCFY)[28] and Kartvelishvili–Likhoded–Petrov (KLP)[29] fragmentation functions are used, respectively.

As a crucial ingredient of the calculations, we employ our state-of-the-art dynamical energy loss formalism,[30–32] which includes: (1) Dynamical QCD medium of a finite temperature and a finite size, so that the energy exchange with the medium constituents is taken into account as opposed to static scattering centers case. It also considers that the medium created in ultrarelativistic HICs has a finite size, and that initial partons are created inside the medium. (2) The calculations are based on the finite temperature field theory and generalized hard-thermal-loop approach,[33] generically regulating infrared divergences. (3) Both collisional[32] and radiative[30,31] energy loss mechanisms are included and performed within the same theoretical framework, so that no interference or overlapping occurs between them. (4) The formalism is generalized to the case of finite magnetic mass[34] and running coupling.[19] Chromomagnetic (μ_M) to chromoelectric mass (μ_E) ratio is estimated to be in a range 0.4–0.6 by different nonperturbative approaches.[35,36] Hence, in this paper, we assume $\mu_M/\mu_E = 0.5$. Our most recent advancement within formalism is the relaxation of the widely used soft-gluon approximation.[37] In Ref. [38], we demonstrated that all the above ingredients are necessary to accurately reproduce high-$p_\perp$ suppression data.

The full-fledged analytical expressions for single gluon radiation spectrum and collisional energy loss per unit length in an expanding medium are given by Eqs. (6) and (3) from Ref. [17], respectively. Thereby, the standard values for heavy and light quark masses are considered ($M_c = 1.2$ GeV, $M_b = 4.75$ GeV, while for light quarks, thermal masses are assumed).

Further, we assume that the medium expansion model is given by the ideal hydrodynamical 1D Bjorken expansion,[18] i.e., $T(\tau) \sim \sqrt[3]{(\tau_0/\tau)}$ (where τ is a proper time), with thermalization time set at $\tau_0 = 0.6$ fm/c.[39] The detailed determination of initial QGP temperature T_0 for the considered centrality range is provided in Ref. [17]. For brevity, here we focus on 30–40% centrality region in $\sqrt{s_{NN}} = 5.02$ TeV $Pb + Pb$ collisions at the LHC, which corresponds to $T_0 = 391$ MeV,[17] although we checked that the same conclusions apply regardless of the considered centrality bin. The QGP transition temperature is assumed to be $T_C \approx 160$.[40]

Finally, we provide the expressions for two main high-$p_\perp$ observables. The angular averaged nuclear modification factor R_{AA} is defined as the ratio of the quenched $p_\perp$-spectrum in $A + A$ collisions with respect to $p + p$ collisions, normalized by the

number of binary collisions N_{bin}:

$$R_{\mathrm{AA}}(p_T) = \frac{dN_{\mathrm{AA}}/dp_T}{N_{\mathrm{bin}}dN_{pp}/dp_T}. \tag{2}$$

However, an alternative form[26]

$$R_{\mathrm{AA}} \approx \frac{R_{\mathrm{AA}}^{\mathrm{in}} + R_{\mathrm{AA}}^{\mathrm{out}}}{2}, \tag{3}$$

is also used for providing more intuitive insight in the underlying mechanisms. Here[14] $R_{\mathrm{AA}}^{\mathrm{in}} = \frac{dN_{\mathrm{AA}}/dp_T d\phi|_{\phi=0}}{N_{\mathrm{bin}}dN_{pp}/dp_T d\phi|_{\phi=0}}$ ($R_{\mathrm{AA}}^{\mathrm{out}} = \frac{dN_{\mathrm{AA}}/dp_T d\phi|_{\phi=\pi/2}}{N_{\mathrm{bin}}dN_{pp}/dp_T d\phi|_{\phi=\pi/2}}$) stands for in-(out-of-)plane nuclear modification factor. The high-$p_\perp$ elliptic flow is given by the following expression[26,41,42]:

$$v_2 \approx \frac{1}{2} \frac{R_{\mathrm{AA}}^{\mathrm{in}} - R_{\mathrm{AA}}^{\mathrm{out}}}{R_{\mathrm{AA}}^{\mathrm{in}} + R_{\mathrm{AA}}^{\mathrm{out}}}. \tag{4}$$

It is worth noting that experimental approach to v_2 is different from Eq. (4). However, to our knowledge, and as already discussed in Ref. 21, that approach could lead to different elliptic flow predictions if event-by-event fluctuations are taken into account, which is out of the scope of this study.

3. Reliability of the Framework

The reliability of DREENA-B framework, outlined in the previous section, is tested against experimentally available data at the LHC in Ref. 17. Note that in generating all predictions we used no fitting parameters, i.e., the parameters take their standard literature values. We obtained a very good agreement between our predictions and the existing data for: (i) Both high-$p_\perp$ R_{AA} and v_2, so that long-standing v_2 puzzle[43] (inability of various models to jointly explain high-$p_\perp$ R_{AA} and v_2 data, with tendency to underestimate v_2 compared to the experimental data) is naturally solved within our framework; (ii) Diverse colliding systems, such as $Pb + Pb$ at $\sqrt{s_{NN}} = 2.76\,\mathrm{TeV}$ and $5.02\,\mathrm{TeV}$, and Xe + Xe at $\sqrt{s_{NN}} = 5.44\,\mathrm{TeV}$; (iii) Both light and heavy flavor particles, that is, $h^\pm, D, B$ mesons, and (iv) All available centrality ranges.

4. Results and Discussion

In this section, first, we define the four commonly considered temperature profiles,[14] which differ only at early times. Next, we assess their effects on our full-fledged predictions for high-$p_\perp$ angular averaged and angular differential nuclear modification factors. Finally, we revise the soundness of the commonly applied multiple fitting procedure. For each result, we provide an intuitive explanation based on R_{AA} asymptotic scaling behavior. For more details, we refer the reader to Ref. 21.

4.1. *Effect of different initial stages on high-$p_\perp$ R_{AA} and v_2*

Now that framework is set and tested, for the study covered by this paper, next we concentrate on four commonly assumed temperature profiles[14] that consider the same 1D Bjorken[18] temperature profile after, but differ before the thermalization ($\tau < \tau_0$). More particularly, in Fig. 1, we distinguish:

- The *free-streaming* case (full red curve), which corresponds to omitting the energy loss before the QGP thermalization;
- The *linear* case (dashed blue curve), which corresponds to linearly increasing T with proper time from transition temperature ($T_C = 160\,\text{MeV}$,[40] $\tau_C = 0.25\,\text{fm}$) to the initial temperature T_0 of equilibrated plasma, otherwise $T = 0$;
- The *constant* case (dot-dashed orange curve), with T equal to the initial temperature T_0; and
- The *divergent* case (dotted green curve), corresponding to 1D Bjorken evolution from the beginning $\tau = 0$.

First, we assess to what extent is high-$p_\perp$ R_{AA} affected by the presumed initial stages depicted in Fig. 1. From the left column of Fig. 2, we infer that high-$p_\perp$ R_{AA} is sensitive to the initial stages. Particularly, we see that for both light and heavy flavor particles, suppression is the lowest in the *free-streaming* case, while progressively increasing toward the *divergent* case, which is expected due to an increase in energy loss. Unfortunately, the discrepancies between these curves are not very distinguishing, and within the current error bars, one is unable to differentiate between these different scenarios.

Next, we investigate the sensitivity of high-$p_\perp$ elliptic flow to the initial stages. Unexpectedly, from the right column of Fig. 2, we observe that v_2 is insensitive to the presumed initial stages for all types of particles, contrary to the conclusion
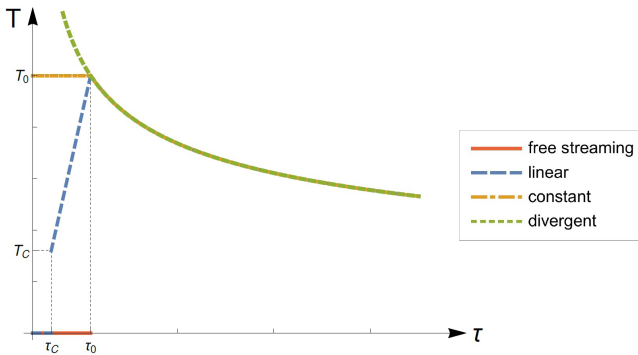
Fig. 1. (Color online) Four simplified temperature profiles, with the same 1D Bjorken[18] temperature evolution after thermalization ($\tau \geq \tau_0$), and whose differences before thermalization mimics different evolutions at initial stage ($\tau < \tau_0$). These diverse initial-stage cases are: the *free-streaming* (full red curve), the *linear* (dashed blue curve), the *constant* (dot-dashed orange curve) and *divergent* case (dotted green curve), as denoted in the legend. Figure adapted from Ref. 21.
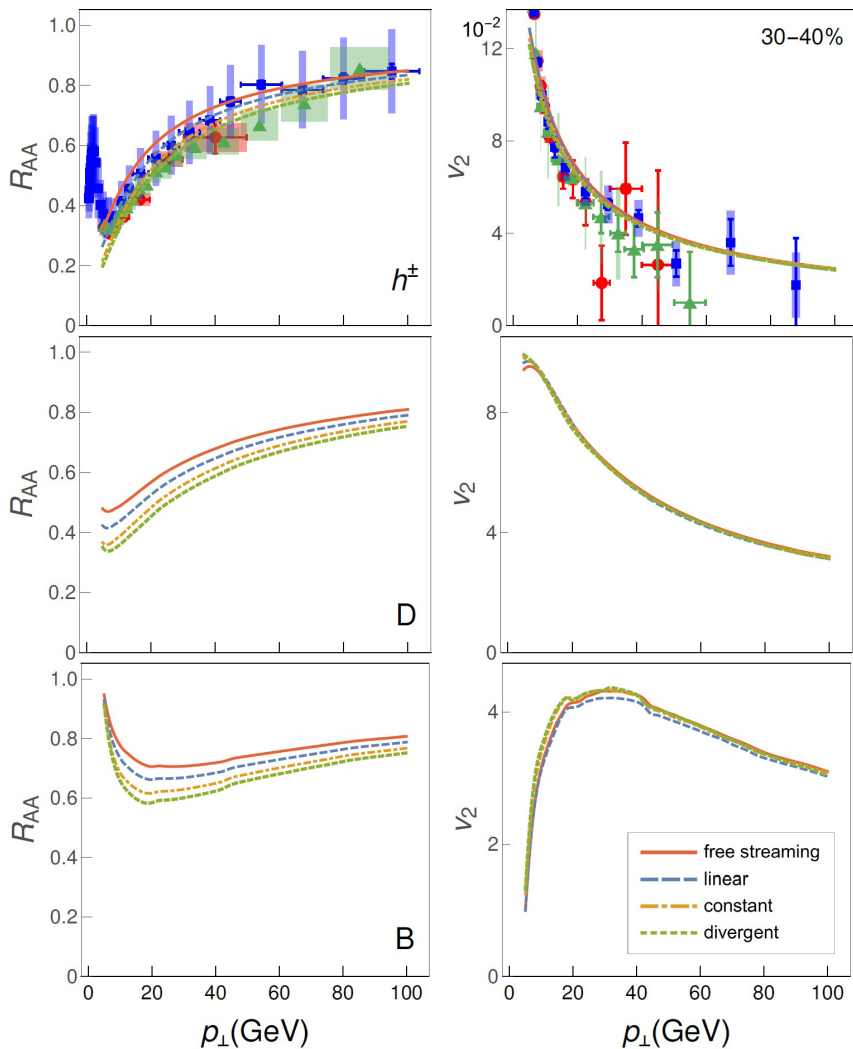
Fig. 2. (Color online) Sensitivity of high-$p_\perp$ observables to different initial stages presented in Fig. 1. The left (right) column corresponds to high-$p_\perp$ R_{AA} (v_2) versus $p_\perp$. Charged hadron, D meson and B meson predictions are presented in upper, middle and lower row, respectively. Charged hadron R_{AA} predictions are compared with 5.02 TeV Pb + Pb CMS[8] (blue squares), ATLAS[9] (green triangles) and ALICE[10] $h^\pm$ R_{AA} data in the upper left plot, while its v_2 predictions are compared with the corresponding 5.02 TeV Pb + Pb CMS[11] (blue squares), ATLAS[12] (green triangles) and ALICE[13] (red circles) $h^\pm$ data in the upper right plot. In each plot, full red curve corresponds to the *free-streaming* case, dashed blue curve to the *linear* case, dot-dashed orange curve to the *constant* case, and dotted green curve to the *divergent* case, as indicated in legend. The results are presented for the centrality range 30–40%, and $\mu_M/\mu_E = 0.5$. Figure adapted from Ref. [21].
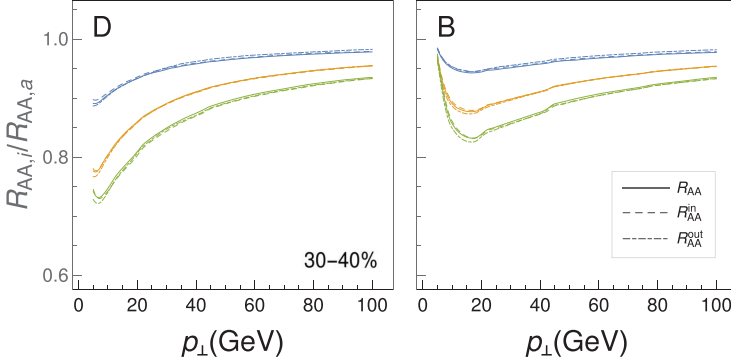
Fig. 3. (Color online) $R_{\mathrm{AA}}^{\mathrm{in}}$ (dashed curves), $R_{\mathrm{AA}}^{\mathrm{out}}$ (dot-dashed curves) and R_{AA} (full curves) versus $p_\perp$ in *linear* (blue set of curves), *constant* (orange set of curves) and *divergent* case (green set of curves) relative to the *free-streaming* case. The left (right) plot corresponds to D (B) mesons. The parameters are the same as in Fig. 2.

derived in Ref. [16]. Therefore, from our study, it follows that v_2 cannot differentiate between different initial-stage scenarios.

To quantitatively explain the obtained results, we plot heavy flavor momentum dependence of proportionality functions, which are defined in the following manner:

$$\gamma_i^{\mathrm{in}} = \frac{R_{\mathrm{AA},i}^{\mathrm{in}}}{R_{\mathrm{AA},fs}^{\mathrm{in}}}, \quad \gamma_i^{\mathrm{out}} = \frac{R_{\mathrm{AA},i}^{\mathrm{out}}}{R_{\mathrm{AA},fs}^{\mathrm{out}}}, \quad \gamma_i = \frac{R_{\mathrm{AA},i}}{R_{\mathrm{AA},fs}}, \tag{5}$$

where $i \in \{lin, const, div\}$. The results and conclusions for charged hadrons are the same and are shown in Ref. [21]. Thus, in Fig. 3, we distinguish three sets of curves (corresponding to *linear, divergent*, and *constant* cases relative to *free-streaming* case), each of which contains corresponding three proportionality functions. The most important observation from Fig. 3 is that within the same set of curves the proportionality functions are practically identical for the relations involving $R_{\mathrm{AA}}^{\mathrm{in}}$, $R_{\mathrm{AA}}^{\mathrm{out}}$ and R_{AA}, that is

$$\gamma_i^{\mathrm{in}} \approx \gamma_i^{\mathrm{out}} \approx \gamma_i. \tag{6}$$

It is worth noting that $\gamma_i < 1$, and that for $i \neq j \to \gamma_i(p_\perp) \neq \gamma_j(p_\perp)$. If we recall that high-$p_\perp$ R_{AA} and v_2 are given by Eqs. (3) and (4), it is straightforward to show that only R_{AA}, and not v_2 is affected. More specifically, for any i, we obtain

$$R_{\mathrm{AA},i} \approx \frac{\gamma_i(R_{\mathrm{AA,fs}}^{\mathrm{in}} + R_{\mathrm{AA,fs}}^{\mathrm{out}})}{2} = \gamma_i R_{\mathrm{AA,fs}}, \tag{7}$$

$$v_{2,i} \approx \frac{1}{2} \frac{\gamma_i(R_{\mathrm{AA,fs}}^{\mathrm{in}} - R_{\mathrm{AA,fs}}^{\mathrm{out}})}{\gamma_i(R_{\mathrm{AA,fs}}^{\mathrm{in}} + R_{\mathrm{AA,fs}}^{\mathrm{out}})} = v_{2,\mathrm{fs}}, \tag{8}$$

as observed in Fig. 2.

As an additional test of v_2 equivalence for different initial stages, in Fig. 4, we present the ratio of elliptic flow in *linear, constant* and *divergent* cases relative to the

B. Ilic et al.
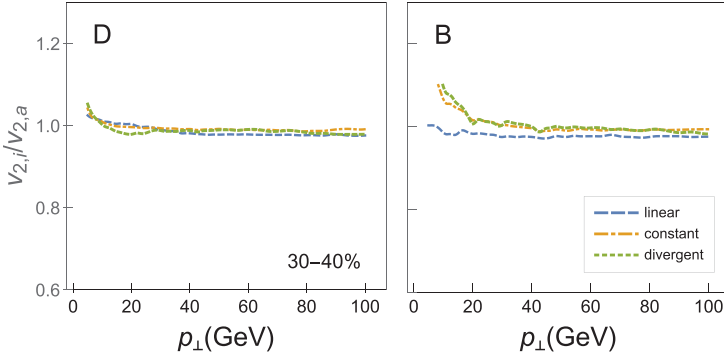
Fig. 4.   (Color online) v_2 in *linear* (dashed blue curves), *constant* (dot-dashed orange curves) and *divergent* case (dotted green curves) versus $p_\perp$ relative to the *free-streaming* case. The left (right) plot corresponds to D (B) mesons. The parameters are the same as in Fig. 2.

free-streaming case. From Fig. 4, which is a counterpart of Fig. 3, we observe that these ratios are consistent with unity for both D and B mesons. The result is the same for charged particles and omitted for consistency. Note that our predictions are valid for $p_\perp \gtrsim 10\,\mathrm{GeV}$. This, furthermore, confirms the conclusions obtained from Fig. 2 (right column) and Fig. 3, as well as the validity of our quantitative analysis (given by Eqs. (7) and (8)).

Additionally, R_{AA} sensitivity to the initial stages is in a qualitative agreement with Refs. 17, 44 and 45, where it was shown that high-$p_\perp$ R_{AA} is only sensitive to the averaged properties of the evolving medium, such as average T ($\overline{T}$), i.e., the analytical estimate reads:

$$R_{\mathrm{AA}} \sim \frac{\Delta E}{E} \sim \overline{T}. \qquad (9)$$

The fact that $\overline{T}$s are different for all four initial-stage cases (see Fig. 1) results in observed R_{AA} differences.

4.2. *Revision of commonly used multiple fitting procedure*

Finally, in this subsection, we test an approach commonly used in Refs. 16,41,46 and 47–49, in which the energy loss is fitted for the initial-stage cases (see Fig. 1), via the change of multiplicative fitting factor in the energy loss to reproduce the high-$p_\perp$ R_{AA} experimental data. More specifically, in our full-fledged calculations we introduce an additional multiplicative fitting factor C_i^{fit}, which is estimated for each initial-state case as the best fit to the *free-streaming* R_{AA}, since free-streaming is commonly considered scenario in both low- and high-$p_\perp$ sector.[a] We observe[21] a decreasing trend in multiplicative fitting factors from the *free steaming* toward

---

[a]The estimated[21] values of C_i^{fit} are: 1, 0.87, 0.74 and 0.67 in *free streaming, linear, constant* and *divergent* cases, respectively.
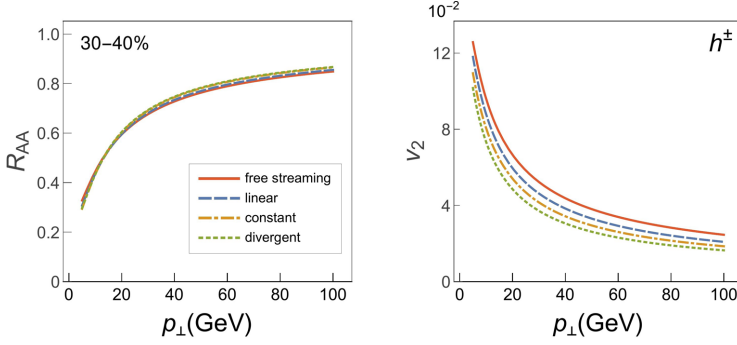
Fig. 5. (Color online) Sensitivity of charged hadron high-$p_\perp$ R_{AA} (left plot) and v_2 (right plot) to different initial-stage cases from Fig. 1, when a multiplicative factor is included in energy loss to reproduce the *free-streaming* R_{AA}. In each plot, full red curve corresponds to the *free-streaming* case, dashed blue curve to the *fitted linear* case, dot-dashed orange curve to the *fitted constant* case, and dotted green curve to the *fitted divergent* case, as indicated in legend. The parameters are the same as in Fig. 2. Figure adapted from Ref. 21.

the *divergent* case, as expected, to annul the higher energy losses in corresponding cases compared to the *free-streaming* one.

Thus obtained (fitted) R_{AA}s are presented in the left plot of Fig. 4, and are practically overlapping, as expected. However, the right plot of Fig. 4 shows that through this fitting procedure high-$p_\perp$ v_2 is significantly affected, that is, the highest value is in the *free-streaming* case, while the lowest is in the *divergent* case. This observation could evoke a naive interpretation that initial stages, that is, the only region in which T profiles differ, are responsible for these discrepancies. However, that would be inconsistent with our results presented in the previous subsection, as well as with intuitive anticipation that the introduction of the energy loss at the initial stage should affect R_{AA}.

To provide a quantitative explanation of the obtained results in Fig. 4, we apply asymptotic scaling behavior of R_{AA},[17,26] which mimics our complex suppression procedure for very high-$p_\perp$ jets and at higher centralities:

$$R_{\mathrm{AA}} = 1 - \xi \overline{T}^m \overline{L}^n, \tag{10}$$

where $\overline{L}$ denotes the average path length traversed by the jet. The corresponding $\overline{T}$ and $\overline{L}$ proportionality factors — $m \approx 1.2$ and $n \approx 1.4$ are estimated in Refs. 50 and 51, respectively. ξ stands for a proportionality factor, which depends on jet's $p_\perp$ and flavor.

By introducing multiplicative fitting factor in energy loss (see Eq. (9)), and making use of Eq. (10), the fitted R_{AA}s in high-$p_\perp$ limit now read:

$$R_{\mathrm{AA},i}^{\mathrm{fit}} \approx 1 - C_i \xi \overline{T}_i^m \overline{L}_i^n \approx 1 - C_i (1 - R_{\mathrm{AA},i}), \tag{11}$$

where $i = lin$, *const*, *div* and C_is are high-$p_\perp$ limits of corresponding C_i^{fit}s. Note that Eqs. (10) and (11) (in their original form) are applicable to $R_{\mathrm{AA}}^{\mathrm{in}}$ and $R_{\mathrm{AA}}^{\mathrm{out}}$ as

well (the same multiplicative fitting factor is naturally applied in all three cases). In order for $R_{\mathrm{AA},i}^{\mathrm{fit}}$ to reproduce the free streaming R_{AA}, i.e.,

$$R_{\mathrm{AA},i}^{\mathrm{fit}} = R_{\mathrm{AA,fs}}, \tag{12}$$

it is straightforward to obtain:

$$v_{2,i}^{\mathrm{fit}} \approx \frac{1}{2}\frac{C_i(R_{\mathrm{AA},i}^{\mathrm{in}} - R_{\mathrm{AA},i}^{\mathrm{out}})}{2R_{\mathrm{AA,fs}}} = \frac{1}{2}\frac{C_i\gamma_i(R_{\mathrm{AA,fs}}^{\mathrm{in}} - R_{\mathrm{AA,fs}}^{\mathrm{out}})}{R_{\mathrm{AA,fs}}^{\mathrm{in}} + R_{\mathrm{AA,fs}}^{\mathrm{out}}}$$
$$= C_i\gamma_i v_{2,\mathrm{fs}}, \tag{13}$$

where along with Eq. (12), we applied Eqs. (3)–(6), and Eqs. (10), (11), together with their out- and in-plane counterparts.

From Eq. (13) it follows that the reasons behind v_2 decrease in *linear, constant* and *divergent* cases compared to the *free streaming* one are the multiplicative fitting factor C_i and proportionality function γ_i, both of which are smaller than 1. However, note that γ_i approaches to 1 at high $p_\perp$ (we refer the reader to Fig. 3), so that the diminishing of v_2 compared to the *free streaming* case is predominantly a consequence of a decrease in the imposed fitting factor and not the initial stages as obtained in Ref. 16. We thus infer that the common procedure in which the energy loss fitting factor is repeatedly adjusted for each initial stage may lead to misconceptions about the underlying physical mechanisms.

5. Conclusions and Outlook

We here addressed whether, and to what extent, we can use high-$p_\perp$ observables to explore the initial stages before QGP thermalization. To this end, we studied how four different commonly considered initial stage scenarios, which have the same temperature profile after, but differ in the temperature profiles before thermalization, affect high-$p_\perp$ R_{AA} and v_2 predictions, stemming from our DREENA-B[17] framework combined with 1D Bjorken expansion.[18] We surprisingly obtained that high-$p_\perp$ v_2 is insensitive to the presumed initial stages, as opposed to high-$p_\perp$ R_{AA}. However, within the current error bars, R_{AA} sensitivity does not allow differentiation between different initial stage cases. Moreover, we inferred that the previously reported sensitivity of high-$p_\perp$ v_2 to initial stages is mostly an artifact of the fitting procedure. Consequently, a common procedure, where free parameters in energy loss are separately fitted for each initial stage may obscure the understanding of the underlying physical mechanisms. In general, our results imply that the simultaneous study of high-$p_\perp$ R_{AA} and v_2, with restrained temperature profiles (isolating the differences in the initial states) and unchanged energy loss parametrization throughout the study, is needed to set reliable constraints on the initial stages in the future.

Acknowledgments

References

1. J. C. Collins and M. J. Perry, *Phys. Rev. Lett.* **34** (1975) 1353.
2. PHENIX Collab. (S. S. Adler *et al.*), *Phys. Rev. Lett.* **91** (2003) 072303.
3. M. Gyulassy and L. McLerran, *Nucl. Phys. A* **750** (2005) 30.
4. B. Jacak and P. Steinberg, *Phys. Today* **63** (2010) 39.
5. F. Gelis and B. Schenke, *Annu. Rev. Nucl. Part. Sci.* **66** (2016) 73.
6. ATLAS Collab. (G. Aad *et al.*), *J. High Energy Phys.* **1311** (2013) 183.
7. H. Niemi, G. S. Denicol, H. Holopainen and P. Huovinen, *Phys. Rev. C* **87** (2013) 054901.
8. CMS Collab. (V. Khachatryan *et al.*), *J. High Energy Phys.* **1704** (2017) 039.
9. The ATLAS collaboration [ATLAS Collaboration], ATLAS-CONF-2017-012.
10. ALICE Collab. (S. Acharya *et al.*), *J. High Energy Phys.* **1811** (2018) 013.
11. CMS Collab. (A. M. Sirunyan *et al.*), *Phys. Lett. B* **776** (2018) 195.
12. ATLAS Collab. (M. Aaboud *et al.*), *Eur. Phys. J. C* **78** (2018) 997.
13. ALICE Collab. (S. Acharya *et al.*), *J. High Energy Phys.* **1807** (2018) 103.
14. J. Xu, A. Buzzatti and M. Gyulassy, *J. High Energy Phys.* **1408** (2014) 63.
15. R. Katz, C. A. G. Prado, J. Noronha-Hostler, J. Noronha and A. A. P. Suaide, *Phys. Rev. C* **102** (2020) 024906.
16. C. Andres, N. Armesto, H. Niemi, R. Paatelainen and C. A. Salgado, *Phys. Lett. B* **803** (2020) 135318.
17. D. Zigic, I. Salom, M. Djordjevic and M. Djordjevic, *Phys. Lett. B* **791** (2019) 236.
18. J. D. Bjorken, *Phys. Rev. D* **27** (1987) 140.
19. M. Djordjevic and M. Djordjevic, *Phys. Lett. B* **734** (2014) 286.
20. E. Molnar, H. Holopainen, P. Huovinen and H. Niemi, *Phys. Rev. C* **90** (2014) 044904.
21. D. Zigic, B. Ilic, M. Djordjevic and M. Djordjevic, *Phys. Rev. C* **101** (2020) 064909.
22. S. Wicks, W. Horowitz, M. Djordjevic and M. Gyulassy, *Nucl. Phys. A* **784** (2007) 426.
23. Z. B. Kang, I. Vitev and H. Xing, *Phys. Lett. B* **718** (2012) 482; R. Sharma, I. Vitev and B. W. Zhang, *Phys. Rev. C* **80** (2009) 054902.
24. M. Gyulassy, P. Levai and I. Vitev, *Phys. Lett. B* **538** (2002) 282.
25. A. Dainese, *Eur. Phys. J. C* **33** (2004) 495.
26. D. Zigic, I. Salom, J. Auvinen, M. Djordjevic and M. Djordjevic, *J. Phys. G* **46** (2019) 085101.
27. D. de Florian, R. Sassot and M. Stratmann, *Phys. Rev. D* **75** (2007) 114010.
28. M. Cacciari and P. Nason, *J. High Energy Phys.* **0309** (2003) 6; E. Braaten, K.-M. Cheung, S. Fleming and T. C. Yuan, *Phys. Rev. D* **51** (1995) 4819.
29. V. G. Kartvelishvili, A. K. Likhoded and V. A. Petrov, *Phys. Lett. B* **78** (1978) 615.
30. M. Djordjevic, *Phys. Rev. C* **80** (2009) 064909.
31. M. Djordjevic and U. Heinz, *Phys. Rev. Lett.* **101** (2008) 022302.
32. M. Djordjevic, *Phys. Rev. C* **74** (2006) 064907.
33. J. I. Kapusta, *Finite-Temperature Field Theory* (Cambridge University Press, Cambridge, 1989).

34. M. Djordjevic, *Phys. Lett. B* **709** (2012) 229.
35. WHOT-QCD Collab. (Y. Maezawa *et al.*), *Phys. Rev. D* **81** (2010) 091501.
36. A. Nakamura, T. Saito and S. Sakai, *Phys. Rev. D* **69** (2004) 014506.
37. B. Blagojevic, M. Djordjevic and M. Djordjevic, *Phys. Rev. C* **99** (2019) 024901.
38. B. Blagojevic and M. Djordjevic, *J. Phys. G* **42** (2015) 075105.
39. J. E. Bernhard, J. S. Moreland and S. A. Bass, *Nucl. Phys. A* **967** (2017) 293.
40. HotQCD Collab. (A. Bazavov *et al.*), *Phys. Rev. D* **90** (2014) 094503.
41. B. Betz and M. Gyulassy, *J. High Energy Phys.* **1408** (2014) 090 [Erratum: *J. High Energy Phys.* **1410** (2014) 043].
42. P. Christiansen, K. Tywoniuk and V. Vislavicius, *Phys. Rev. C* **89** (2014) 034912.
43. S. K. Das, F. Scardina, S. Plumari and V. Greco, *Phys. Lett. B* **747** (2015) 260.
44. T. Renk, *Phys. Rev. C* **85** (2012) 044903.
45. D. Molnar and D. Sun, *Nucl. Phys. A* **932** (2014) 140; **910–911** (2013) 486.
46. J. Noronha-Hostler, B. Betz, J. Noronha and M. Gyulassy, *Phys. Rev. Lett.* **116** (2016) 252301.
47. B. Betz, M. Gyulassy, M. Luzum, J. Noronha, J. Noronha-Hostler, I. Portillo and C. Ratti, *Phys. Rev. C* **95** (2017) 044901.
48. C. A. G. Prado, J. Noronha-Hostler, R. Katz, A. A. P. Suaide, J. Noronha, M. G. Munhoz and M. R. Cosentino, *Phys. Rev. C* **96** (2017) 064903.
49. JETSCAPE Collab. (S. Cao *et al.*), *Phys. Rev. C* **96** (2017) 024909.
50. S. Stojku, B. Ilic, M. Djordjevic and M. Djordjevic, *Phys. Rev. C* **103** (2021) 024908.
51. M. Djordjevic, D. Zigic, M. Djordjevic and J. Auvinen, *Phys. Rev. C* **99** (2019) 061902.

Ilic, Bojana - Author...   Ilić, Bojana | eNauka   Bojana Ilic (Blagojev...   Bojana Ilic (Blagojev...   Uputstvo-konacno_...   Training and Support

Contacts

✉ Natalia.Molokanova@jin...
✉ riabovvg@gmail.com

Applied research with heavy-ion beams		*Oleg Belov* 📎
12:00		
"Belgrade Panorama" conference hall		11:45 - 12:30
Lunch		
13:00		
"Belgrade Panorama" conference hall		12:30 - 14:00
14:00 **Exploring QGP properties through high-pt theory and data**		*Bojana Ilic (Blagojevic)* 🔗
"Belgrade Panorama" conference hall		14:00 - 14:45
HI tutorial, theory - II		*Alejandro Ayala* 📎
15:00		
"Belgrade Panorama" conference hall		14:45 - 15:30
Coffee-break		
"Belgrade Panorama" conference hall		15:30 - 16:00
16:00 **Dileptons**		*Itzhak Tserruya* 📎

https://indico.jinr.ru/event/3920/timetable/#x-tab-2

Public ▾   Europe/Belgrade ▾   B. Ilic (Blagojevic) ▾

Workshop "Exploring Quark-Gluon Plasma through soft and hard probes"

29-31 May 2023
SANU (Serbian Academy of Science and Arts) - Belgrade, Serbia
Europe/Belgrade timezone

Overview

Call for Abstracts

Timetable

Contribution List

Committees

Venue

My Conference

   My Contributions

Registration

Participant List

Effect of higher orders in opacity on high-pT observables

📅 29 May 2023, 11:50

🕐 20m

📍 SANU (Serbian Academy of Science and Arts) - Belgrade, Serbia

Speaker

👤 Dr Bojana Ilic (Institute of Physics ...)

Description

Historically, high-pT radiative energy loss is calculated under the assumptions of the optically thin or optically thick medium

Venue

My Conference

└ My Contributions

Registration

Participant List

Travel information

Gallery

Contact

✉ exploreQGP@ipb.ac.rs

Speaker

👤 Dr Bojana Ilic (Institute of Physics ...)

Description

Historically, high-p_T radiative energy loss is calculated under the assumptions of the optically thin or optically thick medium within pQCD. These are two limiting (and opposite) approximations, corresponding to a jet experiencing only one or an infinite number of scatterings with medium constituents, respectively. However, in general, QGP created at the RHIC and the LHC is estimated to have 4-5 scattering centers, indicating the inadequacy of such approximations. Theoretical efforts to relax these approximations are still inconclusive, and lack verification against experimental data.
To address these issues, we generalize our dynamical energy loss and DGLV formalisms toward finite orders in opacity, providing explicit analytical expressions up to the 4th order. These complex expressions, which are highly oscillatory, are obtained for the first time to our knowledge. Further, we implement them into an adequately generalized DREENA framework to assess the effects of higher orders in opacity on a comprehensive set of high-p_T observables. Analytical and numerical results, as well as the interpretation of nonintuitive observations, are provided.

📎 Presentation Materials

📄 SANU Bojana Ilic.pdf

Gallery

Contact

✉ exploreQGP@ipb.ac.rs

see more...

What we can learn about the QGP dynamics from jets		*Dr Yacine Mehtar-Tani* 📎
SANU (Serbian Academy of Science and Arts) - Belgrade, Serbia		09:40 - 10:05

10:00

Determining the onset of color coherence with energy correlators		*Dr Carlota Andres* 📎
SANU (Serbian Academy of Science and Arts) - Belgrade, Serbia		10:05 - 10:30
:: Coffee break		
SANU (Serbian Academy of Science and Arts) - Belgrade, Serbia		10:30 - 11:00

11:00

Hard probes from the view point of open quantum systems		*Prof. Jean-Paul Blaizot*
SANU (Serbian Academy of Science and Arts) - Belgrade, Serbia		11:00 - 11:30
Jet quenching in evolving anisotropic matter		*Dr Andrey Sadofyev* 📎
SANU (Serbian Academy of Science and Arts) - Belgrade, Serbia		11:30 - 11:50
Effect of higher orders in opacity on high-pT observables		*Dr Bojana Ilic* 📎
SANU (Serbian Academy of Science and Arts) - Belgrade, Serbia		11:50 - 12:10

12:00

Low-pt and high-pt probes in the EPOS4 framework		*Prof. Klaus Werner* 📎
SANU (Serbian Academy of Science and Arts) - Belgrade, Serbia		12:10 - 12:35
:: Lunch break		

13:00

Open HF in A-A collisions / 10

Diffusion of heavy quarks in the early stage of high energy nuclear collisions

Authors: Dana Avramescu[None]; Marco Ruggieri[None]; Pooja N/A[1]; Santosh Kumar Das[2]; Vincenzo Greco[None]; Virgil Baran[3]

[1] *Indian Institute of Technology, Goa, India*

[2] *School of Physical Science, Indian Institute of Technology Goa, India*

[3] *Universitatea din Bucuresti*

Corresponding Authors: virbaran@yahoo.com, santosh@iitgoa.ac.in, marco.ruggierichina@yahoo.it, greco@lns.infn.it, avrames.d@gmail.com, pooja19221102@iitgoa.ac.in

Heavy quarks are considered potential probes of the QCD matter produced in high-energy heavy-ion collisions. In the pre-equilibrium stage of relativistic heavy-ion collisions, strong quasi-classical gluon fields emerge at about $\tau_0 = 0.08$ fm/c which evolves according to the classical Yang-Mills (CYM) equations. These set of classical fields are known as Glasma. We study the diffusion of the heavy quarks, namely, charm and bottom quarks in the early stage of heavy-ion collisions. The diffusion in the evolving Glasma fields is compared with that of the Markovian-Brownian motion in a thermalized medium. The diffusion of HQs in the evolving glasma (EvGlasma) is investigated within the framework of Wong equations while we use famous Langevin equations for the Brownian motion with diffusion coefficients evaluated within the pQCD framework.We observe that for a smaller value of saturation scale, Q_s, the average transverse momentum broadening is approximately the same for the two cases, but for larger Q_s, Langevin dynamics underestimates the σ_p. This difference is related to the fact that heavy quarks in the Glasma fields experience diffusion in strong, coherent gluon fields that lead to a faster momentum broadening due to memory, or equivalently to a strong correlation in the transverse plane. We present another interesting result related to bottom quarks. We have observed that bottom quarks are more affected by the pre-equilibrium phase due to their large masses. Their slow motion makes them spend a longer time within a single filament and experience the coherent gluonic fields for a longer time .

Open HF in A-A collisions / 45

ATLAS open HF results in A-A collisions

Corresponding Author: martin.spousta@cern.ch

Open HF in A-A collisions / 46

CMS open HF results in A-A collisions

Corresponding Author: jing.wang@cern.ch

Open HF in A-A collisions / 3

Analyzing the mass ordering in heavy flavor suppression through theory and data

Author: Bojana Ilic (Blagojevic)[None]

Co-author: Magdalena Djordjevic

Corresponding Authors: magda@ipb.ac.rs, bojanab@ipb.ac.rs

One of the intrinsic features of parton's energy loss is the evident flavor dependence. Inspired by the dead-cone effect in radiative energy loss and experimentally detected suppression mass hierarchy, we address the mass ordering in heavy flavor suppression.

While mass hierarchy is analyzed within radiative models, collisional interpretation is still lacking. To this end, we apply recently developed DREENA framework, which is based on our dynamical energy loss formalism. Within this [1] we provide 1) A novel observable, which can disentangle collisional from radiative energy loss, to be rigorously tested by the upcoming high-precision measurements at RHIC and LHC; 2) Analytical derivation of a direct relation between collisional suppression/energy loss and heavy quark mass; 3) Analytical and numerical extraction of the mass ordering in collisional energy loss through this observable.

[1] Bojana Ilic and Magdalena Djordjevic, arXiv:2203.06646 [hep-ph].

Open HF in A-A collisions / 48

Open HF measurements at RHIC (STAR+PHENIX)

Corresponding Author: sonja.kabana@cern.ch

Quarkonia in A-A collisions / 7

A kinetic model for J/psi production in heavy ion collisions

Authors: Denys Arrebato[1]; Joerg Aichelin[2]; Pol Gossiaux[1]

[1] *Subatech*

[2] *SUBATECH*

Corresponding Authors: aichelin@subatech.in2p3.fr, gossiaux@subatech.in2p3.fr

A new Model for J/psi Production in Heavy Ion Collisions
Denys Yen Arrebato Villar, Joerg Aichelin, Pol Gossiaux
SUBATECH, Universite de Nantes, IMT Atlantique, IN2P3/CNRS,
4 rue Alfred Kastler, 44307 Nantes cedex 3, France

The experimental observation of J/psi and Bc mesons multiplicities, distributions and azimuthal flows plays a key role in understanding of the properties of the quark gluon plasma (QGP) which is formed in ultrarelativistic heavy ion collisions. This is due to the fact that the heavy quarks can come from different vertices in the initial stage and that the J/psi are not stable when the QGP is produced with a temperature above the J/psi dissociation temperature while resonant states can be achieved before the transition to the hadronic phase, offering the possibility to probe directly these high temperatures.
In our recently developed approach [1], the hidden heavy flavor mesons production rate is described by solving the von Neumann equation of the two body density matrix in the expanding N-body system, following a method introduced by Remler et al. to predict deuteron production in HIC at lower energies [2]. In this formalism, the rate of mesons formation is based on the semi-classical trajectories of c and b quarks, what naturally encodes possible off-equilibrium effects of these quarks. The trajectories are based on the description of the expanding QGP by the EPOS event generator, supplemented by the Nantes energy loss model which have demonstrated successful agreement with the data for open heavy flavor mesons.
This allows for the prediction of the hidden heavy flavor observables (J/psi and Bc) which are confronted with the experimental results on multiplicity, RAA and v2. We discuss what we can learn

Participant List

○ General aspects and overview   ✕

14:00	**Welcome and introduction**	📎
	31/3-004 - IT Amphitheatre, CERN	*14:00 - 14:05*
	Unpolarized and polarized hadron structure	*Andrea Signori* 📎
	31/3-004 - IT Amphitheatre, CERN	*14:05 - 14:35*
	Antimatter in cosmic rays: the role of cross sections	*Fiorenza Donato* 📎
	31/3-004 - IT Amphitheatre, CERN	*14:35 - 15:05*
15:00	**QGP physics in fixed target collisions**	*Barbara Antonina Trzeciak* 📎
	31/3-004 - IT Amphitheatre, CERN	*15:05 - 15:35*
	Heavy flavour production in heavy-ion collisions	*Bojana Ilic (Blagojevic) et al.* 📎
	31/3-004 - IT Amphitheatre, CERN	*15:35 - 16:05*
16:00	**Coffee Break**	
	31/3-004 - IT Amphitheatre, CERN	*16:05 - 16:30*
	Jet physics at sPHENIX	*Sebastian Tapia Araya* 📎
	31/3-004 - IT Amphitheatre, CERN	*16:30 - 17:00*
17:00	**Cold Nuclear Matter effects at LHC fixed-target experiment energy**	*Elena Gonzalez Ferreiro* 📎
	31/3-004 - IT Amphitheatre, CERN	*17:00 - 17:20*

Istanbul Technical University   13:00 - 14:30

Heavy Quarks in Medium   *Miguel Ángel Escobedo Espinosa*

Istanbul Technical University   14:30 - 15:10

Broken boost invariance in 3+1D Glasma simulations   *Andreas Ipp*

Istanbul Technical University   15:10 - 15:50

Coffee break

Istanbul Technical University   15:50 - 16:20

Latest results on constraining the initial stages of heavy-ion collisions with high-pt data   *Dr Bojana Ilic (Blagojevic)*

Istanbul Technical University   16:20 - 17:00

Recent results with full DREENA framework as a multipurpose tool for QGP tomography   *Dusan Zigic*

Istanbul Technical University   17:00 - 17:40

Integrated mathematical modeling, experimental and bioinformatics study of Type-II antitoxin-toxin system's response to antibiotic exposure

Ilic B.[1]*, Djordjevic M.[2], Ou H.-Y.[3]

[1] *Institute of Physics Belgrade, University of Belgrade, Belgrade, Serbia*

[2] *Faculty of Biology, University of Belgrade, Belgrade, Serbia*

[3] *Shanghai Jiao Tong University, Shanghai, China*

* bojanab@ipb.ac.rs

Key words: Type II toxin-antitoxin systems; antibiotic persistence; systems biology; bioinformatics; nonlinear dynamics; gene expression regulation;

Motivation and Aim: Antibiotic persistence refers to a phenomenon in which a small subpopulation of bacterial cells (dormant cells) survives antibiotic treatment despite being genetically identical to the vast majority of cells that are susceptible to antibiotics. Bacterial toxin-antitoxin (TA) modules of Type-II are involved in response to various stressful conditions, such as antibiotic exposure. Elevated toxin levels may induce dormancy. Our goal is to explore how the kacAT Type-II TA system (a member of the GNAT-ribbon-helix-helix family) participates in the antibiotic persistence of *Klebsiella pneumoniae.*

Methods and Algorithms: We tackle this problem by joint theoretical and experimental study of kacAT gene expression regulation [1], as well as with a bioinformatics and statistical analysis of GNAT-RHH loci in completely sequenced genomes of *K. pneumoniae* [2]. To this end, and based on the fact that KacAT complex formation is cooperative, we developed a mechanistic model of system dynamics, which is characterized by highly non-linear feedback loops and a single stationary state (Fig. 1A).

Results: Analysis of our mathematical model [1] enables us to reproduce the following experimental observations: (i) Reduction of [KacA]:[KacT] protein ratio upon antibiotic application (antibiotic levels increase, i.e., antitoxin degradation increases going from left to right along each curve in Fig. 1B). (ii) Large kacAT transcript increase induced by antibiotics, which based on the model can be achieved under strong promoter autorepression by KacAT complex (Fig. 1C). (iii) KacAT overexpression induces tolerance to antibiotic stress, whereas kacAT deletion does not affect this tolerance (predicted large binding affinity Kb in Fig. 1C).

The finding that kacAT deletion does not lead to spontaneous persister formation is consistent with growing experimental evidence in different Type-II TA systems but opposes earlier theoretical models (see, e.g. [3]), which predicted the appearance of bistability. However, these models assumed the cooperative (joint) action of multiple TA systems located at several instances in the genome. So, we performed a bioinformatics analysis of GNAT-RHH family loci in completely sequenced genomes of *K. pneumoniae* [2]. Statistical analysis of thus predicted loci indicates that only one system in the same family as kacAT is strongly preferred (Fig. 2A–E). Additionally, we obtain statistically significant negative correlations between different clades for which experiments indicate their cross-talk so that such interactions are disfavored (Fig. 2F).
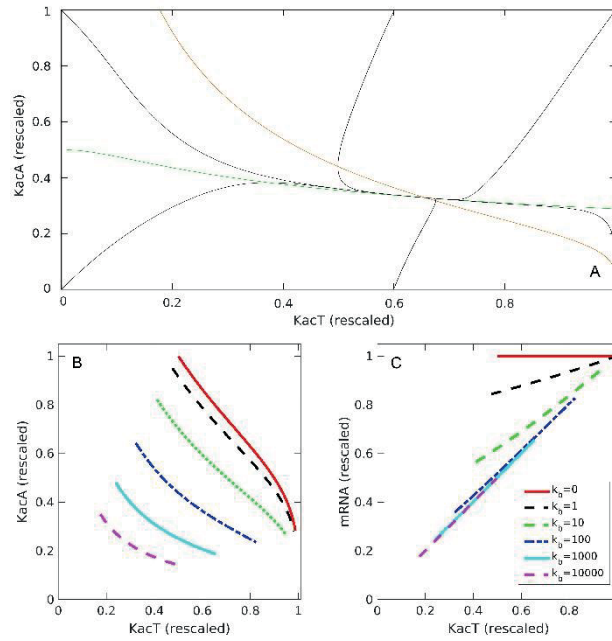
Fig. 1. Model of kacAT expression dynamics. (A) Phase plane analysis. (B) Equilibrium values of proteins KacA *vs* KacT. (C) Transcript kacAT mRNA *vs* KacT. Figure adapted from [1]
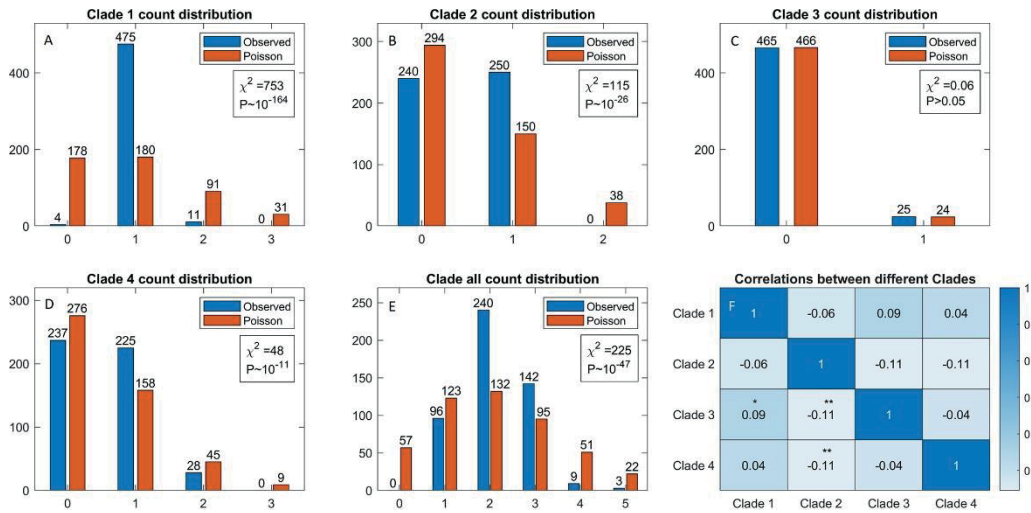

Fig. 2. Statistical analysis of GNAT-RHH TA pairs in *K. pneumoniae* strains. (A–D) Observed *vs* the Poisson distribution counts for clades 1–4 and (E) for all classes together. (F) Spearman's correlations between the counts of different GNAT-RHH clades in *K. pneumoniae* strains. P values of 0.05 and 0.1 are denoted by ** and *, respectively. Figure adapted from [2]

Conclusion: Consequently, based on our quantitative model we obtain that kacAT regulation results in monostable dynamics, and are able to explain all experimental data Moreover, we obtain that kacAT deletion does not lead to spontaneous persister formation, despite previous theoretical predictions, but in accordance with recent experimental evidence. This and our bioinformatics/statistical study challenges the assumption of cooperativity in TA action, possibly explaining the absence of spontaneous persister generation in kacAT. However, TA systems could be involved in antibiotic-induced persister formation, which provides an important future research direction.

References

1. Li P., Goh Y.-X., Ilic B., Tai C., Deng Z., Chen Z., Djordjevic M., Ou H.-Y. Antibiotic-induced degradation of antitoxin enhances the transcription of acetyltransferase-type toxin-antitoxin operon. *J Antimicrob Chemother*. 2023;78(4):1066-1075. doi 10.1093/jac/dkad048
2. Goh Y.-X., Li P., Wang M., Djordjevic M., Tai C., Wang H., Deng Z., Chen Z., Ou H.-Y. Comparative Analysis of Diverse Acetyltransferase-Type Toxin-Antitoxin Loci in Klebsiella pneumoniae. *Microbiol Spectrum*. 2022;10(4):e0032022. doi 10.1128/spectrum.00320-22
3. Feng J., Kessler D.A., Ben-Jacob E., Levine H. Growth feedback as a basis for persister bistability. *Proc Natl Acad Sci USA*. 2014;111(1):544-549. doi 10.1073/pnas.1320396110

Understanding mass hierarchy in different energy loss mechanisms through heavy flavor data

Bojana Ilic[1,*] and *Magdalena* Djordjevic[1]

[1]Institute of Physics Belgrade, University of Belgrade, Belgrade, Serbia

Abstract. The theoretical analysis of experimental observations, such as the mass hierarchy effect, often neglects some ingredients, which may have a significant impact. The forthcoming measurements at RHIC and LHC will generate heavy flavor data with unprecedented precision, providing an opportunity to utilize high-$p_\perp$ heavy flavor data to analyze the interaction mechanisms in QGP. To this end, we use our recently developed DREENA framework based on the dynamical energy loss formalism. We present: i) How to disentangle the signature of different interaction mechanisms (radiative and collisional energy losses) at the same dataset. ii) Novel observables susceptible to these different mechanisms to be tested by future high-precision measurements. iii) Analytical and numerical extraction of the mass hierarchy effect in energy losses through this observable.

1 Introduction

One of the fundamental properties of parton's energy loss is the flavor dependence, that is, the mass ordering. The experimental observation of suppression mass hierarchy [1] is attributed and analyzed within radiative models [2–5], while collisional interactions are neglected. On the other hand, at the intermediate-$p_\perp$ range ($p_\perp \lesssim 10$ GeV) the collisional energy loss for heavy flavor is comparable to, or even larger, than the radiative energy loss [6–10]. However, neither a direct relation between collisional energy loss and heavy quark mass is established, nor an observable which quantifies this effect. Additionally, the upcoming high-precision RHIC and LHC measurements present an opportunity to utilize high-$p_\perp$ heavy flavor data to study the interaction mechanisms in QGP. Note also that D-mesons suppression is practically indistinguishable [1] from $h^\pm$ R_{AA}, which we will exploit in the first part of this document.

Thus, first, we discuss how nonintuitive suppression patterns can be utilized to qualitatively disentangle collisional interaction from radiative energy loss mechanism on the same dataset. In the second part, we focus on the lower-$p_\perp$ range (below 50 GeV) and present: A pursuit for an observable, which could unravel collisional interactions from radiative energy loss. And finally, analytical and numerical extraction of the mass ordering effect in collisional energy loss (for the first time) through this observable, to be more rigorously tested by the upcoming high-luminosity measurements. Note that, in this document, only the main results are displayed, while for more details on the first and second parts, we refer the reader to [4] and [11], respectively.

---

*e-mail: bojanab@ipb.ac.rs

2 Methods

We employ our full-fledged DREENA-C framework [12], which is based on our state-of-the-art dynamical energy loss formalism [13] (for more details on the model and its reliability see [11]). It also assumes a medium modeled with a constant average temperature. We here choose DREENA-C instead of hydrodynamically-wise more sophisticated versions of DREENA-B or -A [14], to exclude complications originating from details of medium evolution and thus, to provide analytical tractability. This can be achieved without significant loss of accuracy, as we already showed [12, 14, 15] that energy loss-sensitive observable R_{AA} (considered here) is barely sensitive to the medium evolution model. Therefore, DREENA-C provides an optimal framework for these studies, through observable R_{AA}, as it assumes a state-of-the-art energy loss model.

3 Results

In the first part of this paper, we address experimentally observed non-intuitive suppression patterns for both: light or D probes as well as heavy B probes. For light probes (upper left plot of Fig. 1) we see that R_{AA} as a function of N_{part} curves become flatter with increasing $p_\perp$, and that the difference between the curves decreases with increasing $p_\perp$. We call this effect saturation in R_{AA} vs. N_{part} curves. From the lower left plot of Fig. 1, we see flattening of R_{AA} at very high $p_\perp$, to which we refer to as saturation in R_{AA} vs. $p_\perp$ dependence.

Experimental measurements show qualitatively different R_{AA} vs. N_{part} pattern for B probes, compared to the light ones in the upper right plot of Fig. 1. Namely, for two opposite momentum ranges (purple stars vs. blue triangles) the experimental data are practically overlapping. Moreover, R_{AA} vs. N_{part} is flatter across the entire $p_\perp$ range, all of this indicating the saturation of this observable, not only at high $p_\perp$. Measurements of R_{AA} vs. $p_\perp$ (in lower right panel of Fig. 1) display slower change with $p_\perp$ compared to light probes. All these experimental observations are in good agreement with our DREENA-C predictions. So, the question is: which energy loss mechanism is responsible for the observations from Fig. 1?

To qualitatively explain the observations for light or D probes, in Fig. 2 we provide predictions for total (i.e., radiative plus collisional), only collisional, and only radiative R_{AA} vs. $p_\perp$, for a family of curves corresponding to different centralities. The equidistant in $p_\perp$ arrows (at 10, 100, and 190 GeV) indicate the density changes of these curves. From the left plots in first and second rows of Fig. 2, we observe that the leftmost arrow (at lower $p_\perp$) spans a much larger total R_{AA} range compared to the remaining two arrows (at higher $p_\perp$) and which are of a similar span. This explains much steeper R_{AA} vs. N_{part} curves at lower $p_\perp$, and their saturation with increasing $p_\perp$. From the central and right plots in first and second rows of Fig. 2, we see that collisional contribution is only important at lower $p_\perp$, where it increases steeply, while radiative contribution is significant across the entire $p_\perp$ range, but increases slowly. Consequently, the interplay between collisional and radiative contributions is responsible for R_{AA} vs. $p_\perp$ pattern, where steep R_{AA} increase is due to collisional, while saturation is due to radiative contributions.

Regarding B, mostly uniform R_{AA} vs. $p_\perp$ curves' density across the entire $p_\perp$ range (left plot in third row of Fig. 2) results in R_{AA} vs. N_{part} curves' overlap regardless of $p_\perp$. Central and right plots in the third row of Fig. 2 indicate that at lower $p_\perp$ both collisional and radiative contributions are important but significantly smaller than for light probes. Consequently, the mass hierarchy in collisional and radiative energy losses are responsible for R_{AA} vs. $p_\perp$ shape at lower $p_\perp$, while the flat radiative contribution plays a decisive role at higher $p_\perp$.

In the second part of this paper, we dive deeper into energy loss mechanisms and focus on the $p_\perp \lesssim 50$ GeV region. First, by comparing DREENA-C patterns in energy losses of charm
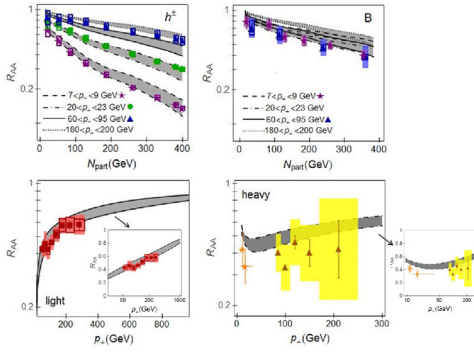
Figure 1. Comparison of suppression patterns data and predictions (gray bands) for light (left column) and B-probes (right column). For experimental data see [4]. Figure adapted from [4].
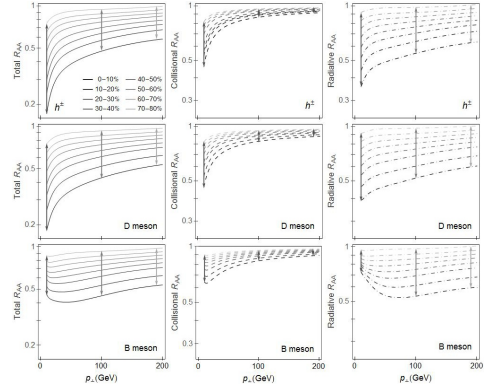

Figure 2. Explanation of suppression patterns for light (upper), D (middle) and B (lower row) probes. Left, central and right plots show, respectively, total, collisional and radiative R_{AA}. Figure adapted from [4].
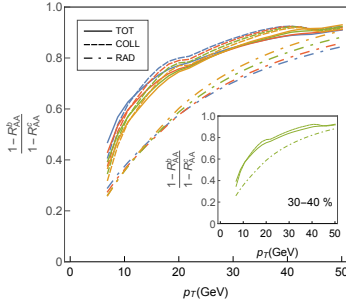

Figure 3. DREENA-C $(1 - R_{AA}^b)/(1 - R_{AA}^c)$ total (full), collisional (dashed) and radiative (dot-dashed curves) cases for centralities (as in Fig. 4 legend) are displayed. For clarity, $30 - 40\%$ centrality is singled out. Figure adapted from [11].
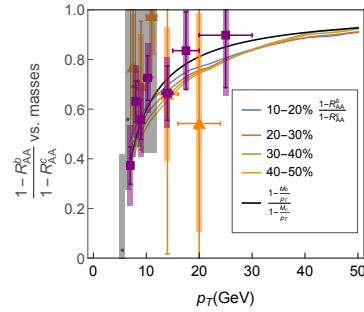
Figure 4. Numerical verification of $(1 - R_{AA}^b)/(1 - R_{AA}^c)$ as an adequate observable for mass extraction from collisional contribution, through comparison with experimental data (for more details see [11]. Figure adapted from [11].

and bottom (see Fig. 1 from [11]) we observe that we reproduced the dead-cone effect [16] in radiative energy loss, and clear mass ordering in $\Delta E_{coll}/E$ also. Compared to the $\Delta E_{rad}/E$, this effect in $\Delta E_{coll}/E$ is slightly less pronounced, but it is a significant observation. The question is, which observable could quantify this effect? To this end, we recall [11] that it should be a function of high-$p_\perp$ $1 - R_{AA}$, since it carries explicit information on the parton's energy loss [15, 17] while being practically insensitive to the details of medium evolution.

Guided by this idea, in Fig. 3 we compare $1 - R_{AA}$ bottom to charm ratios (for different centralities), when only collisional, only radiative, and total interactions are considered. Surprisingly, we find that $(1 - R_{AA}^{b,tot})/(1 - R_{AA}^{c,tot})$ is essentially overlapping with $(1 - R_{AA}^{b,coll})/(1 - R_{AA}^{c,coll})$, which is true for all centralities. This is a nontrivial and significant insight. Consequently, Fig. 3 shows that collisional contribution is in the origin of $(1 - R_{AA}^{b,tot})/(1 - R_{AA}^{c,tot})$. Thus, in paper [11] we proposed $(1 - R_{AA}^b)/(1 - R_{AA}^c)$ as a new observable which may quantify

the mass hierarchy in collisional energy loss. Moreover, after some algebraic manipulations (for more details see [11]), where collisional suppression definition [10, 18] as well as mass parameterization of heavy quarks initial distribution is applied [19], we infer that the $(1 - R_{AA}^b)/(1 - R_{AA}^c) \simeq (1 - \frac{M_b}{p_\perp})/(1 - \frac{M_c}{p_\perp})$ reflects the mass hierarchy in collisional energy loss. This provides analytical support to $(1 - R_{AA}^b)/(1 - R_{AA}^c)$ as the appropriate new observable.

Furthermore, we get that $(1 - R_{AA}^b)/(1 - R_{AA}^c)$ is robust to the collision centrality (see Fig. 3), collision system, and collision energy (see Fig. 4). Therefore, we propose that the new observable should have general applicability to both the RHIC and the LHC experiments, independently of collision centrality, as long as QGP is formed.

4 Conclusions and outlook

Complex and significantly different suppression patterns for different flavors inspired us to distinguish between radiative and collisional contributions at the same dataset. Then, focused on the $p_\perp \lesssim 50$ GeV range, where both energy loss mechanisms are important for heavy probes, we proposed an observable, which could disentangle collisional from radiative energy loss. Also, by comparing with scarce heavy flavor data, we numerically verified the adequacy of the proposed observable for extracting mass hierarchy from collisional energy loss.

As an outlook, our analysis provides specific guidelines for future experiments. For instance, regarding non-intuitive suppression patterns, efforts should be concentrated on single-particle measurements to much higher $p_\perp$, while regarding the new observable, at the lower $p_\perp$ region, which is accessible at both RHIC and LHC. Note that current error bars are still large, so we expect that the upcoming high-luminosity measurements will provide a more rigorous test for this new observable. Finally, the suppression measurements of both b and c probes in the same centrality bins would be highly useful.

References

[1] A. M. Sirunyan *et al.* [CMS], Phys. Rev. Lett. **123**, no.2, 022001 (2019)
[2] N. Armesto, C. A. Salgado and U. A. Wiedemann, Phys. Rev. D **69**, 114003 (2004)
[3] M. Djordjevic and U. Heinz, Phys. Rev. C **77**, 024905 (2008)
[4] M. Djordjevic, Phys. Lett. B **763**, 439-444 (2016)
[5] B. W. Zhang, E. Wang and X. N. Wang, Phys. Rev. Lett. **93**, 072301 (2004)
[6] S. Wicks, W. Horowitz, M. Djordjevic and M. Gyulassy, Nucl. Phys. A **784**, 426 (2007)
[7] M. Djordjevic, Phys. Rev. C **74**, 064907 (2006)
[8] B. Blagojevic and M. Djordjevic, J. Phys. G **42**, no.7, 075105 (2015)
[9] M. H. Thoma, Phys. Lett. B **273**, 128-132 (1991)
[10] M. G. Mustafa, Phys. Rev. C **72**, 014905 (2005)
[11] Bojana Ilic and Magdalena Djordjevic, Phys. Rev. C **106**, 014902 (2022)
[12] D. Zigic, I. Salom, J. Auvinen, M. Djordjevic and M. Djordjevic, J. Phys. G **46**, 085101 (2019)
[13] M. Djordjevic and M. Djordjevic, Phys. Lett. B **734**, 286-289 (2014)
[14] D. Zigic, I. Salom, J. Auvinen, M. Djordjevic and M. Djordjevic, Phys. Lett. B **791**, 236-241 (2019); [arXiv:2110.01544 [nucl-th]]
[15] M. Djordjevic, D. Zigic, M. Djordjevic and J. Auvinen, Phys. Rev. C **99**, 061902 (2019)
[16] Y. L. Dokshitzer and D. E. Kharzeev, Phys. Lett. B **519**, 199-206 (2001)
[17] S. Stojku, B. Ilic, M. Djordjevic and M. Djordjevic, Phys. Rev. C **103**, 024908 (2021)
[18] M. H. Thoma and M. Gyulassy, Nucl. Phys. B **351**, 491-506 (1991)
[19] G. D. Moore and D. Teaney, Phys. Rev. C **71**, 064904 (2005)

Hard probe radiative energy loss beyond soft-gluon approximation

Bojana Blagojevic[*a], **Magdalena Djordjevic**[a] **and Marko Djordjevic**[b]

[a]*Institute of Physics Belgrade, University of Belgrade*
Belgrade 11 000, Serbia
[b]*Faculty of Biology, Institute of Physiology and Biochemistry, University of Belgrade*
Belgrade 11 000, Serbia
E-mail: bojanab@ipb.ac.rs, magda@ipb.ac.rs, dmarko@bio.bg.ac.rs

One of the widely used kinematic assumptions in calculating hard probe radiative energy loss within QGP, is the soft-gluon approximation, which considers that energy loss of the parent parton via gluon's bremsstrahlung is small compared to its initial energy. However, diverse theoretical formalisams obtained a notable energy loss of high $p_\perp$ partons, implicitly suggesting inadequacy of this approximation.

To address this issue, we relax the soft-gluon approximation within the DGLV formalism. Although the obtained analytic expressions are quite more involved compared to the soft-gluon case, the numerical predictions are surprisingly nearly indistinguishable in these two cases. Additionally, we also obtained that the above conclusion is robust with respect to variations of the presumed longitudinal distance distribution of scattering centers. Consequently, the results presented here provide confidence that, regardless of the concerns mentioned above, surprisingly, the soft-gluon approximation can reliably be applied within the DGLV formalism. Finally, we discuss generalizing the relaxation in the dynamical medium as well, which ensures broader relevance of the conclusions obtained here.

International Conference on Hard and Electromagnetic Probes of High-Energy Nuclear Collisions
30 September - 5 October 2018
Aix-Les-Bains, Savoie, France

---

[*]Speaker.

1. Introduction

One of the most common assumptions in calculating radiative energy loss of high $p_\perp$ partons is the soft-gluon (*sg*) approximation, which assumes that the radiated gluon energy (ω) is much smaller ($x = \frac{\omega}{E} \ll 1$) than the initial parton energy (E). This approximation was widely used in various theoretical models [1, 2, 3, 4], which obtained considerable radiative energy loss, suggesting the inadequacy of the approximation. On that note, some of these models went beyond the soft-gluon (*bsg*) approximation [5, 6, 7], but reported inconsistent conclusions on the adequacy of this assumption. Contrarily, our dynamical energy loss model [8], by applying the same approximation, obtained very good agreement with the extensive set of experimental suppression data [8, 9], implicitly indicating the adequacy of such approximation. Nevertheless even within this dynamical model, the approximation is not applicable in the intermediate momentum range ($5 < p_\perp < 10$ GeV), and primarily for gluon jets, as gluons lose notably more energy compared to quarks, due to the relative color factor of 9/4. Therefore, the question of validity of the soft-gluon approximation (*sga*) remained still unresolved, which we systematically reconsider in [10] for gluon-jet radiative energy loss within the DGLV [11] formalism to the 1st order in opacity. Its generalization to the case when a dynamical medium is considered is also discussed in that paper. Additionally, we address the robustness of our conclusions, by taking into account two opposite limits of scattering centers longitudinal distribution: the exponential and the uniform one. It is worth noting that, these proceedings contain only the main results, while for more details, we refer the reader to [10].

2. Analytical and numerical results

We relax the *sga* in radiative energy loss calculations within the DGLV [11] formalism, which considers: finite size and an optically thin QGP consisting of static scattering centers. The jet-medium interactions are modelled by a static color-screened Yukawa potential (Eq.(5) from [12]), while, according to [13], gluons in a finite T QCD medium are considered to be transversely polarized with effective mass given by $m_g = \mu/\sqrt{2}$, where μ is Debye mass. On that note, in [10] we calculated 11 Feynman diagrams for gluon jets, by allowing x to acquire a finite value and under the following assumptions: *i)* that consistently for all diagrams, the direction of flight of the initial gluon is the longitudinal one; *ii)* the soft-rescattering approximation and *iii)* the 1st order in opacity approximation.

Under the common assumption of an exponentially distributed scattering centers $\frac{2}{L}e^{-2\frac{z_1-z_0}{L}}$ (which mimics a rapidly evolving medium, e.g. in [11]), and after involving calculations (for details see [10]), we obtain the *bsg* expression for the single gluon radiation spectrum:

$$
\frac{dN_{g,bsg}^{(1),exp}}{dx} = \frac{C_2(G)\alpha_s}{\pi}\frac{L}{\lambda}\frac{(1-x+x^2)^2}{x(1-x)}\int\frac{d^2\mathbf{q}_1}{\pi}\frac{\mu^2}{(\mathbf{q}_1^2+\mu^2)^2}\int d\mathbf{k}^2
$$
$$
\times\Bigg\{\frac{(\mathbf{k}-\mathbf{q}_1)^2+\chi}{(\frac{4x(1-x)E}{L})^2+((\mathbf{k}-\mathbf{q}_1)^2+\chi)^2}\Big(2\frac{(\mathbf{k}-\mathbf{q}_1)^2}{(\mathbf{k}-\mathbf{q}_1)^2+\chi}-\frac{\mathbf{k}\cdot(\mathbf{k}-\mathbf{q}_1)}{\mathbf{k}^2+\chi}-\frac{(\mathbf{k}-\mathbf{q}_1)\cdot(\mathbf{k}-x\mathbf{q}_1)}{(\mathbf{k}-x\mathbf{q}_1)^2+\chi}\Big)
$$
$$
+\frac{\mathbf{k}^2+\chi}{(\frac{4x(1-x)E}{L})^2+(\mathbf{k}^2+\chi)^2}\Big(\frac{\mathbf{k}^2}{\mathbf{k}^2+\chi}-\frac{\mathbf{k}\cdot(\mathbf{k}-x\mathbf{q}_1)}{(\mathbf{k}-x\mathbf{q}_1)^2+\chi}\Big)+\Big(\frac{(\mathbf{k}-x\mathbf{q}_1)^2}{((\mathbf{k}-x\mathbf{q}_1)^2+\chi)^2}-\frac{\mathbf{k}^2}{(\mathbf{k}^2+\chi)^2}\Big)\Bigg\}
$$

$$= \frac{C_2(G)\alpha_s}{\pi} \frac{L}{\lambda} \int \frac{d^2\mathbf{q}_1}{\pi} \frac{\mu^2}{(\mathbf{q}_1^2 + \mu^2)^2} \int d\mathbf{k}^2 f_{bsg}^{exp}(\mathbf{k}, \mathbf{q}_1, x), \tag{2.1}$$

where $\mathbf{k}$ and $\mathbf{q}_1$ are the transverse momentum of radiated and exchanged gluons, respectively; α_s is the strong coupling constant, λ the mean free path, L the medium length and $\chi = m_g^2(1 - x + x^2)$. To the extent of our knowledge, this result presents the first introduction of the effective gluon mass in the *bsga* radiative energy loss. Note that, only a part of $\frac{dN_{g,bsg}^{(1)}}{dx}$, corresponding to the jet-radiated gluon interaction, i.e. $f(\mathbf{k}, \mathbf{q}_1, x)$, is altered by this relaxation, and in the *sg* had the form (from [11] for gluon jets):

$$f_{sg}^{exp}(\mathbf{k}, \mathbf{q}_1, x) = \frac{1}{x} \frac{(\mathbf{k} - \mathbf{q}_1)^2 + m_g^2}{(\frac{4xE}{L})^2 + ((\mathbf{k} - \mathbf{q}_1)^2 + m_g^2)^2} 2\left\{ \frac{(\mathbf{k} - \mathbf{q}_1)^2}{(\mathbf{k} - \mathbf{q}_1)^2 + m_g^2} - \frac{\mathbf{k} \cdot (\mathbf{k} - \mathbf{q}_1)}{\mathbf{k}^2 + m_g^2} \right\}. \tag{2.2}$$

It is straightforward to show that Eq. (2.1) is symmetric under the exchange of radiated (k) and final (p) gluons, as anticipated, due to the inability to distinguish between two identical gluons, and that for an infinitesimally small x recovers the *sg* limit given by Eq. (2.2).

Next we address how the *sga* relaxation affects our R_{AA} [14] predictions (for predictions for additional observables see [10]). The numerical procedure for generating the bare gluon quenched spectrum is thoroughly explained in [10], where the following standard parameters values are used: $\alpha_s = \frac{g_s^2}{4\pi} = 0.3$, $L = 5$ fm, $\lambda = 1$ fm, $\mu = \sqrt{4\pi\alpha_s(1 + n_f/6)}T$, $n_f = 3$ and $T = 300$ MeV, to mimic the LHC conditions. From Fig. 1 we unexpectedly (based on the expressions analysis above) observe nearly overlapping R_{AA} predictions for the *bsg* and *sg* cases.
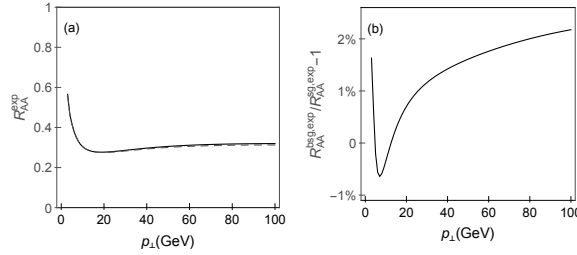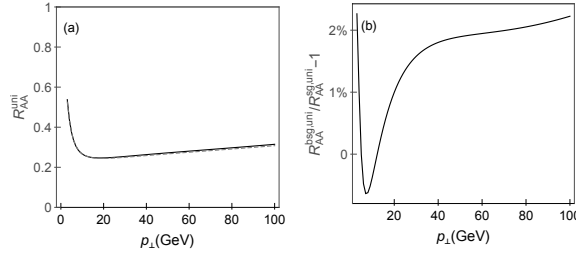

Figure 1: (a) Comparison of gluon-jet R_{AA} in *bsg* (solid line) with the one in *sg* (dashed line) case as a function of $p_\perp$, when exponential distribution of scattering centers is taken into account. (b) The relative change of R_{AA} with respect to the *sg* limit. Adapted from [10].

3. Sensitivity to the longitudinal distance distribution

To examine the robustness of our results, next we test the sensitivity of the conclusions from Section 2 to the presumed longitudinal distance distribution between scattering centers. On that note, we apply the opposite limit to the one studied in the previous section, i.e. the uniform distribution, and in the *bsg* case obtain (for details see [10]):

$$f_{bsg}^{uni}(\mathbf{k}, \mathbf{q}_1, x) = \frac{(1 - x + x^2)^2}{x(1-x)} \left\{ \left(1 - \frac{\sin\left(\frac{(\mathbf{k} - \mathbf{q}_1)^2 + \chi}{2x(1-x)E}L \right)}{\frac{(\mathbf{k} - \mathbf{q}_1)^2 + \chi}{2x(1-x)E}L} \right) \frac{1}{(\mathbf{k} - \mathbf{q}_1)^2 + \chi} \left(2\frac{(\mathbf{k} - \mathbf{q}_1)^2}{(\mathbf{k} - \mathbf{q}_1)^2 + \chi} - \frac{\mathbf{k} \cdot (\mathbf{k} - \mathbf{q}_1)}{\mathbf{k}^2 + \chi} \right. \right.$$

$$-\frac{(\mathbf{k}-\mathbf{q}_1)\cdot(\mathbf{k}-x\mathbf{q}_1)}{(\mathbf{k}-x\mathbf{q}_1)^2+\chi}\Big)+\Big(1-\frac{\sin\big(\frac{\mathbf{k}^2+\chi}{2x(1-x)E}L\big)}{\frac{\mathbf{k}^2+\chi}{2x(1-x)E}L}\Big)\frac{1}{\mathbf{k}^2+\chi}\Big(\frac{\mathbf{k}^2}{\mathbf{k}^2+\chi}-\frac{\mathbf{k}\cdot(\mathbf{k}-x\mathbf{q}_1)}{(\mathbf{k}-x\mathbf{q}_1)^2+\chi}\Big)$$

$$+\Big(\frac{(\mathbf{k}-x\mathbf{q}_1)^2}{((\mathbf{k}-x\mathbf{q}_1)^2+\chi)^2}-\frac{\mathbf{k}^2}{(\mathbf{k}^2+\chi)^2}\Big)\Big\}, \tag{3.1}$$

while in the *sg* case it acquired the form (from [15] for gluon jets and a static medium):

$$f_{sg}^{uni}(\mathbf{k},\mathbf{q}_1,x)=\quad\frac{1}{x}\Big\{\Big(1-\frac{\sin\big(\frac{(\mathbf{k}-\mathbf{q}_1)^2+m_g^2}{2xE}L\big)}{\frac{(\mathbf{k}-\mathbf{q}_1)^2+m_g^2}{2xE}L}\Big)\frac{1}{(\mathbf{k}-\mathbf{q}_1)^2+m_g^2}2\Big(\frac{(\mathbf{k}-\mathbf{q}_1)^2}{(\mathbf{k}-\mathbf{q}_1)^2+m_g^2}-\frac{\mathbf{k}\cdot(\mathbf{k}-\mathbf{q}_1)}{\mathbf{k}^2+m_g^2}\Big\},$$
$$\tag{3.2}$$

where the notation is the same as in the previous section. Again we observe that Eq. (3.1) is symmetric under the exchange of radiated (k) and final (p) gluons, and that for $x \ll 1$ it reduces to the *sg* limit given by Eq. (3.2). Since the $\frac{dN_{g,bsg}^{(1)}}{dx}$ expression for a uniform distribution (obtained from Eq. (3.1)) is notably different than its exponential analogon (Eq. (2.1)), we assess also for this case the effect of the *sga* relaxation on the numerical predictions. Analogous to Section 2, we obtain Fig. 2 for the uniform distribution, and by comparing Figs. 1 and 2 we infer that numerical results for these two opposite longitudinal distance distribution limits are practically identical.

Figure 2: (a) Comparison of gluon-jet R_{AA} in *bsg* (solid line) with the one in *sg* (dashed line) case as a function of $p_\perp$, when uniform distribution of scattering centers is taken into account. (b) The quantification of the effect and its expression in percentage. Adapted from [10].

4. Conclusions

In order to address the adequacy of the *sga*, first we considered exponential distribution of scattering centers, and obtained that gluon's *bsg* expression is apparently different, and considerably more complicated than in the *sg* case. However, we surprisingly obtained that the numerical predictions in these two cases are nearly indistinguishable. Due to the relative color factor of 4/9, high $p_\perp$ quarks are less likely to be affected by this relaxation. This implies that, within the DGLV formalism, the *sga* remains valid. Furthermore, by applying the opposite, i.e. the uniform distribution, we obtained that the conclusions regarding the importance of the *sga* in the DGLV formalism are robust to the presumed longitudinal distance distribution. As an outlook, we also expect that the *sga* can be reliably applied to the dynamical energy loss formalism, which still remains to be explicitly tested in the future.

Acknowledgments

References

[1] N. Armesto, C.A. Salgado and U.A. Wiedemann, *Medium induced gluon radiation off massive quarks fills the dead cone*, *Phys. Rev. D* **69** (2004) 114003 [`hep-ph/0312106`].

[2] R. Baier, Y.L. Dokshitzer, A.H. Mueller, S. Peigne and D. Schiff, *Radiative energy loss and p(T) broadening of high-energy partons in nuclei*, *Nucl. Phys. B* **484** (1997) 265 [`hep-ph/9608322`].

[3] M. Gyulassy, P. Levai and I. Vitev, *Reaction operator approach to nonAbelian energy loss*, *Nucl. Phys. B* **594** (2001) 371 [`nucl-th/0006010`].

[4] A. Majumder and M. Van Leeuwen, *The Theory and Phenomenology of Perturbative QCD Based Jet Quenching*, *Prog. Part. Nucl. Phys. A* **66** (2011) 41 [`arXiv:1002.2206`].

[5] L. Apolinario, L., N. Armesto and C.A.Salgado, *Medium-induced emissions of hard gluons*, *Phys. Lett. B* **718** (2012) 160 [`arXiv:1204.2929`].

[6] B.W. Zhang and X.N. Wang, *Multiple parton scattering in nuclei: Beyond helicity amplitude approximation*, *Nucl.Phys. A* **720** (2003) 429 [`hep-ph/0301195`].

[7] G. Ovanesyan and I. Vitev, *An effective theory for jet propagation in dense QCD matter: jet broadening and medium-induced bremsstrahlung*, *JHEP* bf 1106 (2011) 080 [`arXiv:1103.1074`]; *Medium-induced parton splitting kernels from Soft Collinear Effective Theory with Glauber gluons*, *Phys. Lett. B* bf 706 (2012) 371 [`arXiv:1109.5619`].

[8] M. Djordjevic and M. Djordjevic, *LHC jet suppression of light and heavy flavor observables*, *Phys. Lett. B* **734** (2014) 286 [`arXiv:1307.4098`].

[9] M. Djordjevic, M. Djordjevic and B. Blagojevic, *RHIC and LHC jet suppression in non-central collisions*, *Phys. Lett. B* **737** (2014) 298 [`arXiv:1405.4250`].

[10] B. Blagojevic, M. Djordjevic and M. Djordjevic, *Calculating hard probe radiative energy loss beyond soft-gluon approximation: how valid is the approximation?*, (*Phys. Rev. C*, in Press) (2018) [`arXiv:1804.07593`].

[11] M. Djordjevic and M. Gyulassy, *Heavy quark radiative energy loss in QCD matter*, *Nucl. Phys. A* **733** (2004) 265 [`nucl-th/0310076`].

[12] M. Gyulassy and X.N. Wang, *Multiple collisions and induced gluon Bremsstrahlung in QCD*, *Nucl. Phys. B* **420** (1994) 583 [`nucl-th/9306003`].

[13] M. Djordjevic and M. Gyulassy, *The Ter-Mikayelian effect on QCD radiative energy loss*, *Phys. Rev. C* **68** (2003) 034914 [`nucl-th/0305062`].

[14] A. Dainese, *Perspectives for the study of charm in-medium quenching at the LHC with ALICE*, *Eur. Phys. J. C* **33** (2004) 495 [`nucl-ex/0312005`].

[15] M. Djordjevic, *Theoretical formalism of radiative jet energy loss in a finite size dynamical QCD medium*, *Phys. Rev. C* **80** (2009) 064909 [`arXiv:0903.4591`].

Proceedings

Testing the Reliability of the Soft-Gluon Approximation for High $p_\perp$ Particles [†]

Bojana Blagojevic [1],* , **Magdalena Djordjevic [1]** and **Marko Djordjevic [2]**

[1]   Institute of Physics Belgrade, University of Belgrade, 11 000 Belgrade, Serbia; magda@ipb.ac.rs
[2]   Faculty of Biology, Institute of Physiology and Biochemistry, University of Belgrade, 11 000 Belgrade, Serbia; dmarko@bio.bg.ac.rs
*   Correspondence: bojanab@ipb.ac.rs; Tel.: +381-11-37-13-086
†   Presented at Hot Quarks 2018—Workshop for Young Scientists on the Physics of Ultrarelativistic Nucleus-Nucleus Collisions, Texel, The Netherlands, 7–14 September 2018.

check for updates

Abstract: The soft-gluon approximation assumes that a high $p_\perp$ parton propagating through dense QCD matter loses only a small amount of its energy via gluon radiation. This assumption is made in many different jet quenching approaches, which nevertheless predicted a sizable radiative energy loss of such particles. This questions the reliability of this approximation, which must then be reconsidered. To address this issue, we relaxed the soft-gluon approximation within the DGLV formalism to the first order in opacity. The obtained analytical expressions are notably different from the soft-gluon case. Surprisingly the numerical effects that stem from waiving this assumption on fractional radiative energy loss and number of radiated gluons are small. Additionally, the effect on suppression is negligible, which can be intuitively understood by the cancellation of the opposite effects on the above mentioned variables. Consequently, our results surprisingly indicate that, contrary to the doubts mentioned above, the soft-gluon approximation remains well-founded within the DGLV formalism. We also investigate the effects of this assumption in the case of a dynamical medium, which suggests generality of the conclusions presented here.

Keywords: beyond soft-gluon approximation; radiative energy loss; high $p_\perp$ particles; suppression

1. Introduction

The soft-gluon (*sg*) approximation, which assumes that radiated gluon (ω) takes away only small fraction ($x = \frac{\omega}{E} \ll 1$) of an initial parton's energy (E), was commonly used in various energy loss models [1–4]. These models obtained a significant radiative energy loss, indicating possible inconsistency with the applied approximation. To this end, some of the models ("effectively") relaxed the approximation [5–8], which lead to non-unified conclusion on the reliability of this approximation. On the other hand, our dynamical energy loss model [9], enclosing the same approximation, reported a robust agreement with comprehensive set of experimental suppression data [9,10], implicitly suggesting applicability of such approximation. However, the approximation clearly breaks-down for intermediate momentum range ($5 < p_\perp < 10$ GeV), where the experimental data are most abundant and with the smallest error bars; and primarily for the gluon-jets, as due to the color factor of $9/4$, gluons lose significantly more energy compared to the quarks. This questioned the applicability of the soft-gluon approximation (*sga*), which we addressed in [11] for the gluon-jet radiative energy loss within the DGLV [12] formalism to the 1st order in opacity, by allowing x to acquire a finite value, and discussed its implications when recoiling of the medium constituents is taken into account. Note that, in these proceedings, only the main results are presented, while for more details, we refer the reader to [11].

2. Methods

In this section we outline the features of the DGLV formalism, the assumptions used in the beyond soft-gluon (*bsg*) calculations [11], as well as the definition of an observable for which we generated the predictions. The DGLV formalism [12] considers a finite size, optically thin QCD medium, consisting of static scattering centers, so that the jet-medium interactions are described by static color-screened Yukawa potential given by Eq. (5) from [13], whereas gluons in a finite temperature QGP are considered to be transversely polarized with an effective mass equal to $m_g = \mu/\sqrt{2}$ (μ is Debye mass), as obtained in [14]. We applied the following assumptions in calculating 11 Feynman diagrams (for more details see [11]) for the gluon-jet *bsg* approximation: (1) that initial gluon propagates along the longitudinal axis consistently for all diagrams; (2) the soft-rescattering (eikonal) approximation and (3) the first order in opacity approximation.

An observable for which we generate the predictions − the nuclear modification factor R_{AA} is defined [15] as the ratio of the quenched $A + A$ spectrum to the $p + p$ spectrum, scaled by the number of binary collisions N_{bin}:

$$R_{AA}(p_\perp) = \frac{dN_{AA}/dp_\perp}{N_{bin}dN_{pp}/dp_\perp}. \tag{1}$$

In order to obtain a bare gluon quenched spectra, we used the generic pQCD convolution (Equation (1) from [16]), where the initial gluon distribution is computed according to [17,18], while radiative energy loss probability includes the multi-gluon [19] and the path-length [15,16] fluctuations.

3. Results

In this section we provide analytical and numerical results *bsg* approximation [11] and also make a comparison with the *sg* case [12]. After rather involved calculations (for detailed derivation see [11]) we obtained the expression for the *bsg* single gluon radiation spectrum to the 1st order in opacity:

$$
\begin{aligned}
\frac{dN_{g,bsg}^{(1)}}{dx} &= \frac{C_2(G)\alpha_s}{\pi} \frac{L}{\lambda} \frac{(1 - x + x^2)^2}{x(1-x)} \int \frac{d^2\mathbf{q}_1}{\pi} \frac{\mu^2}{(\mathbf{q}_1^2 + \mu^2)^2} \int d\mathbf{k}^2 \\
&\times \Bigg\{ \frac{(\mathbf{k} - \mathbf{q}_1)^2 + \chi}{(\frac{4x(1-x)E}{L})^2 + ((\mathbf{k} - \mathbf{q}_1)^2 + \chi)^2} \Big(2\frac{(\mathbf{k} - \mathbf{q}_1)^2}{(\mathbf{k} - \mathbf{q}_1)^2 + \chi} - \frac{\mathbf{k} \cdot (\mathbf{k} - \mathbf{q}_1)}{\mathbf{k}^2 + \chi} - \frac{(\mathbf{k} - \mathbf{q}_1) \cdot (\mathbf{k} - x\mathbf{q}_1)}{(\mathbf{k} - x\mathbf{q}_1)^2 + \chi} \Big) \\
&+ \frac{\mathbf{k}^2 + \chi}{(\frac{4x(1-x)E}{L})^2 + (\mathbf{k}^2 + \chi)^2} \Big(\frac{\mathbf{k}^2}{\mathbf{k}^2 + \chi} - \frac{\mathbf{k} \cdot (\mathbf{k} - x\mathbf{q}_1)}{(\mathbf{k} - x\mathbf{q}_1)^2 + \chi} \Big) + \Big(\frac{(\mathbf{k} - x\mathbf{q}_1)^2}{((\mathbf{k} - x\mathbf{q}_1)^2 + \chi)^2} - \frac{\mathbf{k}^2}{(\mathbf{k}^2 + \chi)^2} \Big) \Bigg\},
\end{aligned}
\tag{2}
$$

where α_s denotes a constant strong coupling, L a medium length, λ a mean free path, $\chi = m_g^2(1 - x + x^2)$; while $\mathbf{k}$ and $\mathbf{q}_1$ stands for a transverse momentum of radiated and exchanged gluons, respectively. To our knowledge, this result presents the first introduction of the effective gluon mass in the *bsg* approximation radiative energy loss. On the other hand, in the *sg* case $\frac{dN_g^{(1)}}{dx}$ acquired the form [12]:

$$
\begin{aligned}
\frac{dN_{g,sg}^{(1)}}{dx} &= \frac{C_2(G)\alpha_s}{\pi} \frac{L}{\lambda} \frac{1}{x} \int \frac{d^2\mathbf{q}_1}{\pi} \frac{\mu^2}{(\mathbf{q}_1^2 + \mu^2)^2} \int d\mathbf{k}^2 \frac{(\mathbf{k} - \mathbf{q}_1)^2 + m_g^2}{(\frac{4xE}{L})^2 + ((\mathbf{k} - \mathbf{q}_1)^2 + m_g^2)^2} 2 \Big\{ \frac{(\mathbf{k} - \mathbf{q}_1)^2}{(\mathbf{k} - \mathbf{q}_1)^2 + m_g^2} \\
&- \frac{\mathbf{k} \cdot (\mathbf{k} - \mathbf{q}_1)}{\mathbf{k}^2 + m_g^2} \Big\}.
\end{aligned}
\tag{3}
$$

It can easily be verified that Equation (2): is symmetric under the exchange of two outgoing gluons; and in the *sg* limit recovers Equation (3). Upon obtaining the analytical expression we addressed the effect of finite x on the numerical predictions. The following set of parameters was used: $\mu = \sqrt{4\pi\alpha_s(1 + n_f/6)}T$, $n_f = 3$, $\alpha_s = \frac{g_s^2}{4\pi} = 0.3$, $L = 5$ fm, $\lambda = 1$ fm, $T = 300$ MeV, to mimic the

standard LHC conditions. From Figure 1, which corresponds to $\Delta E^{(1)}/E$ and $N_g^{(1)}$, we surprisingly observed a small, but of an opposite sign, difference between *bsg* and *sg* curves for these variables.
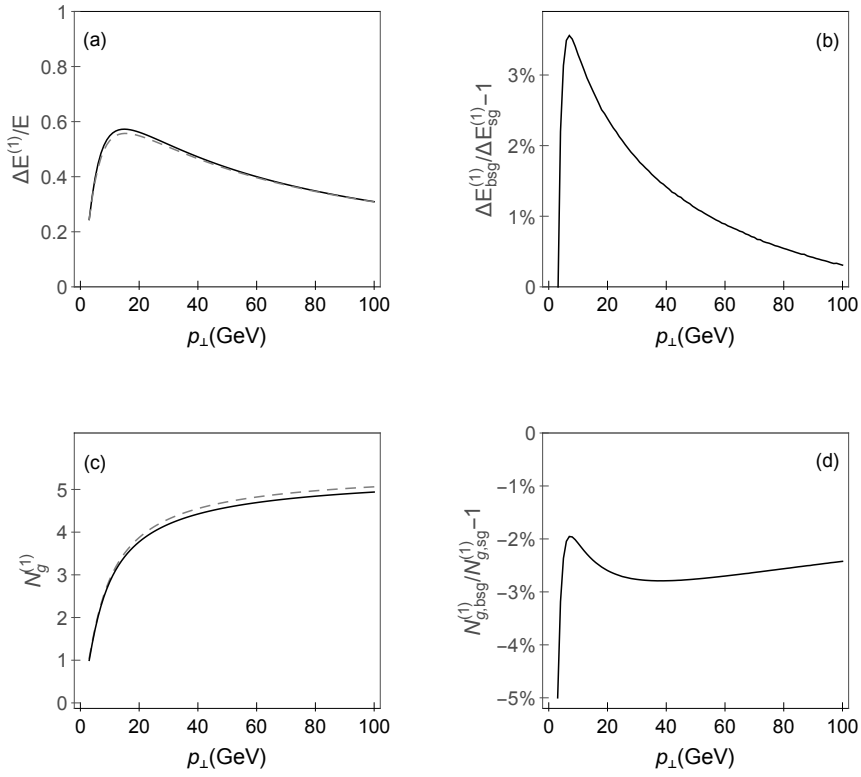

Figure 1. (**a**) The finite x effect on $\Delta E^{(1)}/E$ and (**b**) its relative effect on $\Delta E^{(1)}/E$. The same for $N_g^{(1)}$ is shown in (**c**) and (**d**), respectively. The full (dashed) curve corresponds to the *bsg* (*sg*) case. Adapted from [11].

Finally, we addressed how the finite x affects the suppression predictions, by comparing the *bsg* and the *sg* gluon R_{AA} predictions in Figure 2 and obtained even smaller discrepancies between these two curves, compared to the previous variables.
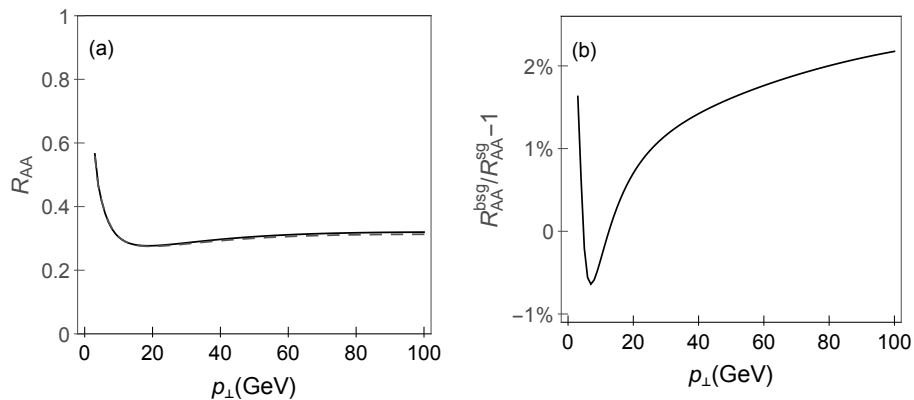
Figure 2. (**a**) The effect of a finite x on R_{AA} as a function of final $p_\perp$. The full (dashed) curve corresponds to the *bsg* (*sg*) case. (**b**) provides a percentage of R_{AA} change when the *sga* is relaxed. Adapted from [11].

4. Discussion

Our calculations yielded *bsg* analytical expression (Equation (2)) which is clearly different, and significantly more complex than in the *sg* case (Equation (3)). However, we surprisingly obtained small difference for gluon's $\Delta E^{(1)}/E$ and $N_g^{(1)}$ numerical predictions in two cases (Figure 1). Furthermore, the effect of finite x is even smaller for R_{AA} (Figure 2). This negligible gluon R_{AA} change could be intuitively explained by the interplay of the opposite effects on $\Delta E^{(1)}/E$ and $N_g^{(1)}$, which non-trivially enter R_{AA} (compare the right panels of Figures 1 and 2). Consequently, the high $p_\perp$ quarks are even less likely to be affected by this approximation. This implies that within the DGLV formalism the soft-gluon approximation remains well-founded. Finally, we also expect that the *sga* can be reliably applied when a dynamical medium is considered, which however remains to be rigorously tested in the future.

Conflicts of Interest: The authors declare no conflict of interest.

References

1. Armesto, N.; Salgado, C.A.; Wiedemann, U.A. Medium induced gluon radiation off massive quarks fills the dead cone. *Phys. Rev. D* **2004**, *69*, 114003, doi:10.1103/PhysRevD.69.114003.
2. Baier, R.; Dokshitzer, Y.L.; Mueller, A.H.; Peigne, S.; Schiff, D. Radiative energy loss and p(T) broadening of high-energy partons in nuclei. *Nucl. Phys. B* **1997**, *484*, 265–282, doi:10.1016/S0550-3213(96)00581-0.
3. Gyulassy, M.; Levai, P.; Vitev, I. Reaction operator approach to nonAbelian energy loss. *Nucl. Phys. B* **2001**, *594*, 371–419, doi:10.1016/S0550-3213(00)00652-0.
4. Majumder, A.; Van Leeuwen, M. The Theory and Phenomenology of Perturbative QCD Based Jet Quenching. *Prog. Part. Nucl. Phys. A* **2011**, *66*, 41–92, doi:10.1016/j.ppnp.2010.09.001.
5. Apolinario, L.; Armesto, N.; Salgado, C.A. Medium-induced emissions of hard gluons. *Phys. Lett. B* **2012**, *718*, 160–168, doi:10.1016/j.physletb.2012.10.040.
6. Zhang, B.W.; Wang, X.N. Multiple parton scattering in nuclei: Beyond helicity amplitude approximation. *Nucl. Phys. A* **2003**, *720*, 429–451, doi:10.1016/S0375-9474(03)01003-0.
7. Ovanesyan, G.; Vitev, I. An effective theory for jet propagation in dense QCD matter: jet broadening and medium-induced bremsstrahlung. *JHEP* **2011**, *1106*, 080, doi:10.1007/JHEP06(2011)080.
8. Ovanesyan, G.; Vitev, I. Medium-induced parton splitting kernels from Soft Collinear Effective Theory with Glauber gluons. *Phys. Lett. B* **2012**, *706*, 371–378, doi:10.1016/j.physletb.2011.11.040.
9. Djordjevic, M.; Djordjevic, M. LHC jet suppression of light and heavy flavor observables. *Phys. Lett. B* **2014**, *734*, 286–289, doi:10.1016/j.physletb.2014.05.053.
10. Djordjevic, M.; Djordjevic, M.; Blagojevic, B. RHIC and LHC jet suppression in non-central collisions. *Phys. Lett. B* **2014**, *737*, 298–302, doi:10.1016/j.physletb.2014.08.063.
11. Blagojevic, B.; Djordjevic, M.; Djordjevic, M. Calculating hard probe radiative energy loss beyond the soft-gluon approximation: Examining the approximation validity. *Phys. Rev. C* **2019**, *99*, 024901, doi:10.1103/PhysRevC.99.024901.
12. Djordjevic, M.; Gyulassy, M. Heavy quark radiative energy loss in QCD matter. *Nucl. Phys. A* **2004**, *733*, 265–298, doi:10.1016/j.nuclphysa.2003.12.020.
13. Gyulassy, M.; Wang, X.N. Multiple collisions and induced gluon Bremsstrahlung in QCD. *Nucl. Phys. B* **1994**, *420*, 583–614, doi:10.1016/0550-3213(94)90079-5.
14. Djordjevic, M.; Gyulassy, M. The Ter-Mikayelian effect on QCD radiative energy loss. *Phys. Rev. C* **2003**, *68*, 034914, doi:10.1103/PhysRevC.68.034914.
15. Dainese, A. Perspectives for the study of charm in-medium quenching at the LHC with ALICE. *Eur. Phys. J. C* **2004**, *33*, 495–503, doi:10.1140/epjc/s2004-01645-4.
16. Wicks, S.; Horowitz, W.; Djordjevic, M.; Gyulassy, M. Elastic, inelastic, and path length fluctuations in jet tomography. *Nucl. Phys. A* **2007**, *784*, 426–442, doi:10.1016/j.nuclphysa.2006.12.048.

17. Kang, Z.B.; Vitev, I.; Xing, H. Nuclear modification of high transverse momentum particle production in p+A collisions at RHIC and LHC. *Phys. Lett. B* **2012**, *718*, 482–487, doi:10.1016/j.physletb.2012.10.046.

18. Sharma, R.; Vitev, I.; Zhang, B.W. Light-cone wave function approach to open heavy flavor dynamics in QCD matter. *Phys. Rev. C* **2009**, *80*, 054902, doi:10.1103/PhysRevC.80.054902.

19. Gyulassy, M.; Levai, P.; Vitev I. Jet tomography of Au+Au reactions including multigluon fluctuations. *Phys. Lett. B* **2002**, *538*, 282–288, doi:10.1016/S0370-2693(02)01990-1.

PAPER • OPEN ACCESS

Modeling jet-medium interactions at RHIC and LHC - which energy loss effect is crucial?

View the article online for updates and enhancements.

Modeling jet-medium interactions at RHIC and LHC - which energy loss effect is crucial?

B Blagojevic and M Djordjevic

Institute of Physics Belgrade, Pregrevica 118, 11080 Zemun, Serbia

E-mail: bojanab@ipb.ac.rs

Abstract. High momentum hadrons' suppression is considered to be excellent probe of QCD matter created in ultra-relativistic heavy ion collisions. Here we apply our recently developed dynamical energy loss formalism, which includes the following effects: dynamical scattering centers, QCD medium of a finite size, both radiative and collisional energy losses, running coupling and finite magnetic mass, and which we further incorporate into numerical procedure, to generate angular averaged R_{AA} predictions and to compare them with experimental R_{AA} data, by using no free parameters. A robust agreement of our predictions and experimentally measured R_{AA} for different energies, probes and all available centrality regions, raised the question whether this agreement is consequence of a single effect or of a superposition of all these effects. We obtained that, although the inclusion of dynamical scattering center has the largest relative importance, all the other effects are also important, since they lead to fine improvements of the agreement. Therefore, the robust agreement is a cumulative effect of all these features, with dynamical effect being crucial for accurate R_{AA} predictions.

1. Introduction

High momentum light and heavy flavor suppression [1] is considered to be excellent tool for studying QCD matter created in ultra-relativistic heavy ion collisions at RHIC and LHC. An abundance of suppression data, that has become available at RICH and LHC since recently, and its comparison with theoretical R_{AA} predictions [2–4], allows testing our understanding of QGP matter. In order to generate these predictions, we recently developed dynamical energy loss formalism, which we further integrated into numerical procedure as described in [5]. This formalism includes the following energy loss effects: *i)* dynamical scattering centers, *ii)* QCD medium of a finite size [6,7], *iii)* both radiative [6,7] and collisional [8] energy losses, *iv)* running coupling [5] and *v)* finite magnetic mass [9]. Also, note that, accurate energy loss calculation is considered to be the main ingredient responsible for obtaining reliable R_{AA} predictions.

In our previous papers [5, 10, 11], we demonstrated a robust agreement between our R_{AA} predictions, obtained as explained in previous paragraph, and R_{AA} data for both RHIC and LHC experiments, diverse set of probes and all available centrality ranges.

Here we address the relative importance of different energy loss effects in obtaining accurate angular averaged R_{AA} predictions for D mesons (as the clearest energy loss probe), for which it was previously shown that fragmentation function does not alter bare charm quark R_{AA} [10,12]. High momentum D meson R_{AA} data, obtained recently at LHC [13], serve as a baseline for testing the models. We concentrate on central 200 GeV Au+Au collisions at RHIC and 2.76 TeV Pb+Pb collisions at LHC. Our approach is to systematically include the effects in energy

loss calculations [14], i.e. we first compare the relative importance of radiative and collisional contribution to R_{AA} predictions, next we address the importance of including the dynamical scattering centers, then the running coupling and finally the finite magnetic mass. Note that only the main results are presented here; for the full account on the results, please see [14].

2. Theoretical and computational formalism

In this section, we concisely describe computational formalism, our dynamical energy loss formalism [5] and how each effect, when introduced, changed energy loss expressions.

For obtaining quenched spectra we apply generic pQCD convolution given by Eq.(2) from [14] ([15]). The initial charm quark spectrum is calculated in accordance with [16], while energy loss probability includes both radiative and collisional energy losses in a finite size dynamical QCD medium, multi-gluon [17] and path length fluctuations [15, 18].

The expression for radiative energy loss in a finite size dynamical QCD medium is given by Eq.(2.12) from [6], while the transition from static to dynamical scattering centers is explained in [7]. The collisional energy loss is calculated according to Eq.(14) from [8]. The running coupling is introduced in accordance with [5], while for constant coupling we use $\alpha_S = 0.3$ ($\alpha_S = 0.25$) in RHIC (LHC) case. Debye screening mass is $\mu_E = gT$ ($g = 2$). The finite magnetic mass is introduced as in [9], and its range ($0.4 < \mu_M/\mu_E < 0.6$) is set according to many non-perturbative approaches [19–23], otherwise $\mu_M = 0$ is used.

We model the medium by assuming an effective temperature of 221 MeV at RHIC [24] and 304 MeV at LHC [25]. No medium evolution is accounted. The validity of this assumption is discussed in [14]. For charm quark mass we use $M_c = 1.2$ GeV, and for the number of effective light quark flavors we use $n_f = 2.5$ ($n_f = 3$) in RHIC (LHC) case.
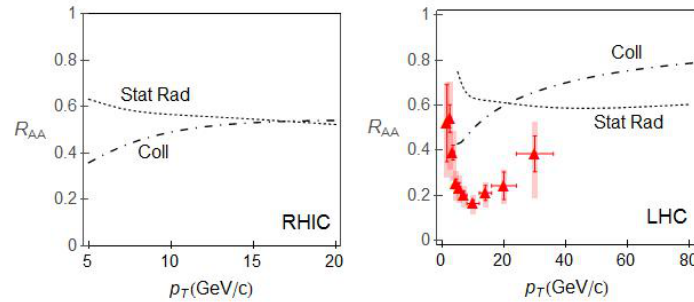
3. Results and discussion

Figure 1. Necessity of abolishing static approximation. D meson R_{AA} predictions, as a function of transverse momentum, are shown for only static radiative (dotted curve) and for only dynamical collisional (dot-dashed curve) contribution in a finite size QCD medium. Left (right) panel corresponds to RHIC (LHC) case. Right panel also displays D meson R_{AA} data in $0 - 7.5\%$ central 2.76 TeV Pb+Pb collisions at LHC (red triangles) [13]. Debye mass is $\mu_E = gT$, coupling constant is $\alpha_S = 0.3$ ($\alpha_S = 0.25$) for RHIC (LHC) and finite magnetic mass is not included ($\mu_M = 0$). Adapted from [14].

In this section we apply historically-driven approach, starting from static approximation [26, 27] and gradually adding energy loss effects. We display only the main results of our study carried out in [14]. Finite size QCD medium is assumed throughout the paper. The constant coupling and constant Debye mass (as mentioned above), and no finite magnetic mass are considered in Fig. 1 and Fig. 2. Static approximation, which assumes that the medium is composed of static

scattering centers, was firstly commonly used. It entails also, that collisional energy loss can be neglected compared to radiative one. However, Fig. 1 clearly shows that static approximation has to be abolished in favor of dynamical scatering centers' approximation, since collisional R_{AA} is comparable with radiative one. Further, we compute these both energy losses within the
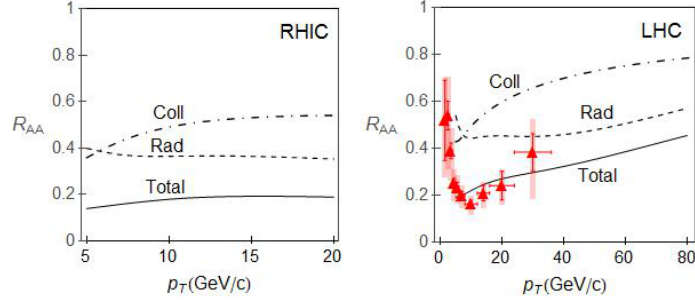

Figure 2. Dynamical approximation as the main effect. D meson R_{AA} predictions, as a function of transverse momentum, are shown for radiative (dashed curve), collisional (dot-dashed curve) and radiative + collisional (solid curve) energy losses in a finite size dynamical QCD medium. Left (right) panel corresponds to RHIC (LHC) case. Right panel also displays D meson R_{AA} data in $0 - 7.5\%$ central 2.76 TeV Pb+Pb collisions at LHC (red triangles) [13]. Debye mass is $\mu_E = gT$, coupling constant is $\alpha_S = 0.3$ ($\alpha_S = 0.25$) for RHIC (LHC) and finite magnetic mass is not included ($\mu_M = 0$). Adapted from [14].

same dynamical framework (Fig. 2) and we draw three conclusions: 1) dynamical radiative R_{AA} alone is not sufficient to explain qualitatively nor quantitatively the LHC experimental data; 2) radiative and collisional R_{AA} are still both important; 3) the total R_{AA} is in rough agreement with experimental data. Therefore, the inclusion of dynamical scattering centers is the main effect responsible for obtaining accurate R_{AA} predictions. Finally, we address the importance of
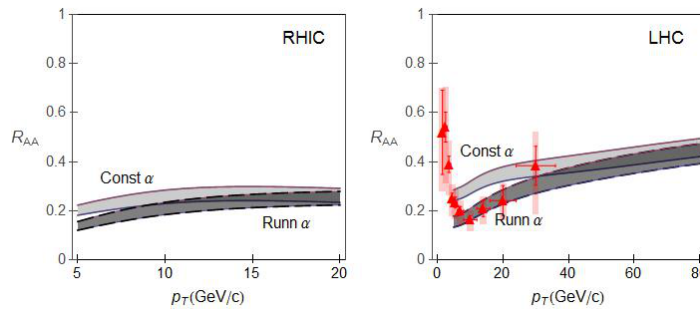

Figure 3. Our dynamical energy loss formalism. D meson R_{AA} predictions, as a function of transverse momentum, are shown for the constant coupling $\alpha_S = 0.3$ ($\alpha_S = 0.25$) for RHIC (LHC) (light gray band) and for the running coupling (dark gray band). In both cases radiative + collisional contributions in a finite size dynamical QCD medium are accounted. Upper (lower) boundary of each band corresponds to $\mu_M/\mu_E = 0.6$ ($\mu_M/\mu_E = 0.4$). Left (right) panel corresponds to RHIC (LHC) case. Right panel also displays D meson R_{AA} data in $0 - 7.5\%$ central 2.76 TeV Pb+Pb collisions at LHC (red triangles) [13]. Adapted from [14].

including the running coupling (leads to a significant R_{AA} decrease at lower jet momenta) and

finite magnetic mass (leads to a significant R_{AA} increase) [14]. From Fig. 3 we see that these two effects (although taken alone worsens the agreement [14]) taken together lead to quantitatively and qualitatively better agreement with the LHC R_{AA} data, compared to the case when these effects are omitted. This illustrates possible synergy in including these two effects.

4. Conclusions

A robust agreement of angular averaged R_{AA} predictions, based on our dynamical energy loss formalism, with R_{AA} data, for different energies, probes and centrality ranges, initiated the question: whether this agreement is a consequence of a one dominant energy loss effect or a joint effect of several smaller improvements [14]. With the LHC suppression data serving as a baseline, we here showed that (for the clearest energy loss probe: D meson R_{AA}), inclusion of dynamical scattering centers has the largest relative importance in obtaining accurate R_{AA} predictions. Furthermore, we found that all other considered effects are also important and responsible for the finer agreement with the data. So the good agreement is a result of a superposition of all these effects. Therefore, detailed study of partons' energy loss, as well as, inclusion of all relevant medium effects is necessary to correctly model the jet-medium interactions.

Acknowledgments

References

[1] Bjorken J D 1982 FERMILAB-PUB-82-059-THY pp 287-92
[2] Brambilla N *et al* 2014 *Eur. Phys. J.* C **74** 2981
[3] Gyulassy M 2002 *Lect. Notes Phys.* **583** 37
[4] d'Enterria D and Betz B 2010 *Lect. Notes Phys.* **785** 285
[5] Djordjevic M and Djordjevic M 2014 *Phys. Lett.* B **734** 286
[6] Djordjevic M 2009 *Phys. Rev.* C **80** 064909
[7] Djordjevic M and Heinz U 2008 *Phys. Rev. Lett.* **101** 022302
[8] Djordjevic M 2006 *Phys. Rev.* C **74** 064907
[9] Djordjevic M and Djordjevic M 2012 *Phys. Lett.* B **709** 229
[10] Djordjevic M and Djordjevic M 2014 *Phys. Rev.* C **90** 034910
[11] Djordjevic M, Djordjevic M and Blagojevic B 2014 *Phys. Lett.* B **737** 298
[12] Djordjevic M 2014 *Phys. Rev. Lett.* **112** 042302
[13] Grelli A 2013 *Nucl. Phys.* A **904-905** 635c
      Abelev B *et al* 2012 *J. High Energy Phys.* JHEP1209(2012)112
[14] Blagojevic B and Djordjevic M 2015 *J. Phys.* G **42** 075105
[15] Wicks S, Horowitz W, Djordjevic M and Gyulassy M 2007 *Nucl. Phys.* A **784** 426
[16] Kang Z B, Vitev I and Xing H 2012 *Phys. Lett.* B **718** 482-7
[17] Gyulassy M, Levai P and Vitev I 2002 *Phys. Lett.* B **538** 282
[18] Dainese A 2004 *Eur. Phys. J.* C **33** 495
[19] Maezawa Yu, Aoki S, Ejiri S, Hatsuda T, Ishii N, Kanaya K, Ukita N and Umeda T 2010 *Phys. Rev.* D **81** 091501
[20] Maezawa Yu, Aoki S, Ejiri S, Hatsuda T, Ishii N, Kanaya K, Ukita N and Umeda T 2008 *Proc. of Science Lattice* 2008 (Williamsburg) p 194 (*Preprint* hep-lat/0811.0426)
[21] Nakamura A, Saito T and Sakai S 2004 *Phys. Rev.* D **69** 014506
[22] Hart A, Laine M and Philipsen O 2000 *Nucl. Phys.* B **586** 443
[23] Bak D, Karch A and Yaffe L G 2007 *J. High Energy Phys.* JHEP0708(2007)049
[24] Adare A *et al* 2010 *Phys. Rev. Lett.* **104** 132301
[25] Wilde M 2013 *Nucl. Phys.* A **904-905** 573c
[26] Djordjevic M and Gyulassy M 2004 *Nucl. Phys.* A **733** 265-98
[27] Gyulassy M and Wang X N 1994 *Nucl. Phys.* B **420** 583
      Wang X N, Gyulassy M and Plumer M 1995 *Phys. Rev.* D **51** 3436

PAPER • OPEN ACCESS

Energy loss in jet suppression - what effects matter?

To cite this article: Bojana Blagojevic and Magdalena Djordjevic 2015 *J. Phys.: Conf. Ser.* **612** 012006

View the article online for updates and enhancements.

Energy loss in jet suppression - what effects matter?

Bojana Blagojevic and Magdalena Djordjevic

Institute of Physics Belgrade, Pregrevica 118, 11080 Zemun, Serbia

E-mail: bojanab@ipb.ac.rs

Abstract. Jet suppression is considered to be an excellent probe of QCD matter created in ultra-relativistic heavy ion collisions. Our theoretical predictions of jet suppression, based on our recently developed dynamical energy loss formalism, show a robust agreement with various experimental data for different probes, experiments (RHIC and LHC) and centrality regions. Our dynamical energy loss formalism includes the following key ingredients: dynamical scattering centers, collisional energy loss, finite magnetic mass and running coupling. Although all these ingredients are theoretically justified, it is currently unclear how they individually contribute to accurate suppression predictions. Natural question rises: is there one effect which is crucial for the agreement, or is the agreement a joint effect of several smaller improvements. To answer this question, we study how the above mentioned key effects affect the suppression calculations. Our results show that each energy loss effect is important and that a robust agreement between theoretical predictions and experimental data is a cumulative effect of all improvements.

1. Introduction

Suppression of high transverse momentum observables [1] is considered to be an excellent probe for mapping the properties of QCD matter created in ultra-relativistic heavy ion collisions at RHIC and LHC. Therefore comparison of available suppression experimental data with the theoretical predictions [2–4] tests different theoretical models and provides the insight into underlying QGP physics. For generating these predictions, we developed dynamical energy loss formalism which includes the following energy loss effects: *i)* dynamical scattering centers, *ii)* QCD medium of a finite size [5,6], *iii)* both radiative [5,6] and collisional [7] energy losses, *iv)* finite magnetic mass effects [8] and *v)* running coupling [9]. We further incorporated this energy loss formalism into a numerical procedure [9] in order to obtain suppression predictions. In the numerical procedure, accurate energy loss calculations are considered to be crucial for obtaining reliable suppression predictions.

We have shown that the suppression predictions obtained from this dynamical energy loss formalism are in a very good agreement with the available experimental data for both RHIC and LHC experiments, light and heavy flavor probes and different centrality ranges [9–11].

We here address the importance of different energy loss effects in the suppression calculations for D mesons (as a clear energy loss probe) in central 200 GeV Au+Au collisions at RHIC, because fragmentation function does not modify bare charm quark suppression [10, 12]. Our approach is to systematically include different energy loss effects. In particular, we first investigate the importance of including collisional energy loss and thus necessity of abolishing static in favor of dynamical approximation. Next we address the importance of including finite magnetic mass in the suppression calculations and finally the running coupling.

2. Theoretical and computational formalism

In this section, we give a brief description of our dynamical energy loss formalism [9] with regression on how each effect, when added, altered energy loss expression, while in Section 4 we take the reverse approach - the historical approach, starting from a static approximation and moving to systematically include all the effects.

In order to obtain quenched spectra we use generic pQCD convolution given by Eq.(1) from [9]. The initial charm quark spectrum is computed according to [13] and energy loss probability includes both radiative and collisional energy losses in a finite size dynamical QCD medium, multi-gluon [14] and path length [15, 16] fluctuations. In our calculations we do not use the fragmentation function of charm quark into D meson, as explained in Section 1.

The radiative energy loss in a finite size dynamical QCD medium is given by Eq.(2.12) from [5], while the finite magnetic mass and running coupling are introduced according to [8] and [9], respectively. For the finite magnetic mass case we use the following range of magnetic to electric mass ratio: $0.4 < \mu_M/\mu_E < 0.6$, according to non-perturbative approaches [17–21], otherwise, $\mu_M = 0$ is used. Also when the running coupling is not included, in our calculations we use $\alpha_S = \frac{g^2}{4\pi} = 0.3$ and Debye mass $\mu_E = gT$, $(g = 2)$. Collisional energy loss is calculated in accordance with Eq.(14) from [7]. Transition from the static [22] to the dynamical approximation in terms of radiative energy loss is explained in [6].

In our calculations for the charm quark mass we use $M_c = 1.2$ GeV, for 0-5% central 200 GeV Au+Au collisions we assume an average medium temperature of T=225 MeV [10] and for the number of effective light quark flavors we use $n_f = 2.5$.

3. Comparison with experimental data

As we mentioned in Section 1, our dynamical energy loss formalism [9] leads to a very good agreement with suppression experimental data for diverse probes at both RHIC [10] and LHC [9] and for different centrality regions [11]. The suppression is expressed by the nuclear modification factor R_{AA} [4], which quantifies the QCD medium effects on the yield of high-p_T particles. Fig. 1, which shows comparison of the D meson R_{AA} predictions with corresponding R_{AA} measured at the LHC and comparison of the single electron R_{AA} predictions with non-photonic single electron R_{AA} measured at RHIC, reflects the above mentioned agreement.
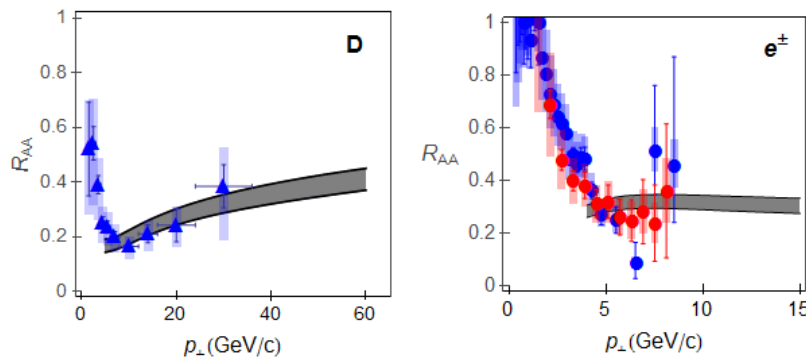

Figure 1. Theory vs. experimental data for D meson and single electron suppressions as a function of transverse momentum. Left panel shows comparison of D meson R_{AA} predictions with experimentally measured R_{AA} (triangle) in most central 2.76 TeV Pb+Pb collisions at the LHC. Right panel shows comparison of single electron R_{AA} predictions with non-photonic single electron R_{AA} (circle) measured in most central 200 GeV Au+Au collisions at RHIC. Left (right) panel is adapted from [9] ([10]).

4. Results and discussion

We start from the static approximation [22, 23] and use a constant value of the strong coupling constant and of Debye mass (as mentioned above), and no finite magnetic mass effects (μ_M=0); note that these values are used in Figs. 2 and 3, while the importance of finite magnetic mass is considered in Fig. 3. Previously, the static approximation was widely used, which assumed that collisional energy loss can be neglected compared to radiative. Left panel of Fig. 2 shows that static approximation has to be abolished, because collisional energy loss suppression is comparable or even larger than static radiative one. Therefore, central panel of Fig. 2 addresses the significance of including dynamical effects by comparing static with dynamical radiative energy loss R_{AA}. We observe a significant suppression increase in the dynamical approximation, so we conclude that dynamical effects are important. Right panel of Fig. 2 investigates whether collisional energy loss is still relevant in dynamical approximation, by comparing radiative with collisional contribution to R_{AA} in the dynamical QCD medium. We conclude that even in dynamical approximation, both radiative and collisional contributions are important, so we further include both radiative and collisional (total) energy losses in dynamical QCD medium.
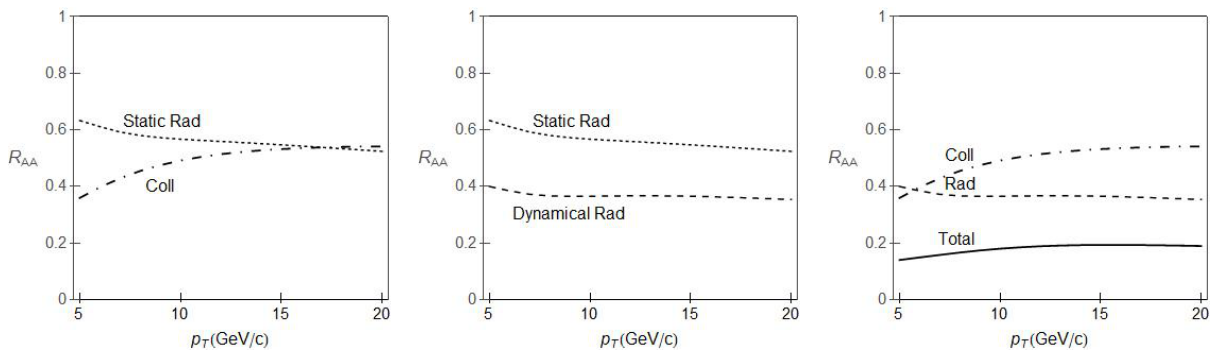

Figure 2. Static vs. dynamical approximation. D meson suppression predictions are shown as a function of transverse momentum. Left panel shows comparison of static radiative (dotted curve) with dynamical collisional (dot-dashed curve) contribution to R_{AA}. Central panel shows comparison of static radiative (dotted curve) with dynamical radiative (dashed curve) contribution to R_{AA}. Right panel shows radiative (dashed curve), collisional (dot-dashed curve) and radiative + collisional (solid curve) contribution to R_{AA} in dynamical QCD medium. Debye mass is $\mu_E = gT$, coupling constant is $\alpha_S = 0.3$ and no finite magnetic mass effects are included ($\mu_M = 0$). Adapted from [24].

Next we consider how inclusion of finite magnetic mass in radiative energy loss calculations [8] affects the R_{AA} predictions, as indicated in Section 2. By comparing R_{AA} with and without finite magnetic mass (Fig. 3), we observe significant suppression decrease due to finite magnetic mass effects. Hence, we conclude that finite magnetic mass effects are important.

Also, the importance of taking into account running coupling [9] is considered in Fig.7 from [24], where we observe suppression increase due to running coupling only at lower jet energies. Consequently running coupling is also important.

5. Conclusions

Since dynamical energy loss formalism led to a robust agreement with the suppression data for different experiments, probes and centrality ranges [9–11], we wanted to determine whether the agreement was a consequence of one dominant effect or a joint effect of several smaller
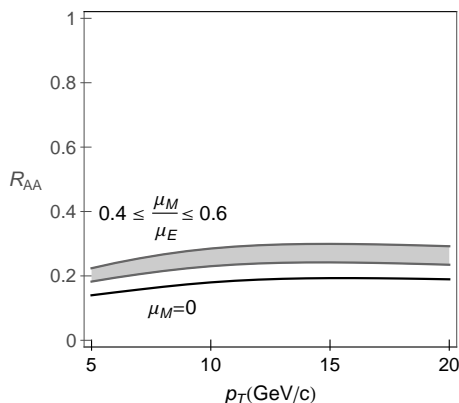
Figure 3. Magnetic mass effects on R_{AA}. D meson suppression predictions are shown, as a function of transverse momentum, for radiative and collisional energy loss in dynamical QCD medium, with (band) and without (solid curve) magnetic mass. Debye mass is $\mu_E = gT$ and coupling constant is $\alpha_S = 0.3$. The upper (lower) boundary of the band corresponds to $\mu_M/\mu_E = 0.6$ ($\mu_M/\mu_E = 0.4$). Adapted from [24].

improvements introduced to energy loss calculations. In order to examine the importance of each effect we followed first a historical approach starting from the static approximation and gradually introduced different energy loss effects in D meson suppression calculations (as a clear energy loss probe) until reaching dynamical energy loss formalism [9]. The conclusion is that each energy loss effect is important and that a robust agreement is a cumulative effect of all these improvements. Therefore, in order to obtain reliable suppression predictions we need to accurately account for all the relevant energy loss ingredients.

Acknowledgments

References
[1] Bjorken J D 1982 FERMILAB-PUB-82-059-THY pp 287-92
[2] Brambilla N et al 2004 *Preprint* hep-ph/0412158
[3] Gyulassy M 2002 *Lect. Notes Phys.* **583** 37
[4] d'Enterria D and Betz B 2010 *Lect. Notes Phys.* **785** 285
[5] Djordjevic M 2009 *Phys. Rev.* C **80** 064909
[6] Djordjevic M and Heinz U 2008 *Phys. Rev. Lett.* **101** 022302
[7] Djordjevic M 2006 *Phys. Rev.* C **74** 064907
[8] Djordjevic M and Djordjevic M 2012 *Phys. Lett.* B **709** 229
[9] Djordjevic M and Djordjevic M 2014 *Phys. Lett.* B **734** 286
[10] Djordjevic M and Djordjevic M 2014 *Phys. Rev.* C **90** 034910
[11] Djordjevic M, Djordjevic M and Blagojevic B 2014 *Phys. Lett.* B **737** 298
[12] Djordjevic M 2014 *Phys. Rev. Lett.* **112** 4 042302
[13] Kang Z B, Vitev I and Xing H 2012 *Phys. Lett.* B **718** 482-7
[14] Gyulassy M, Levai P and Vitev I 2002 *Phys. Lett.* B **538** 282
[15] Wicks S, Horowitz W, Djordjevic M and Gyulassy M 2007 *Nucl. Phys.* A **784** 426
[16] Dainese A 2004 *Eur. Phys. J.* C **33** 495
[17] Maezawa Yu, Aoki S, Ejiri S, Hatsuda T, Ishii N, Kanaya K, Ukita N and Umeda T 2010 *Phys. Rev.* D **81** 091501
[18] Maezawa Yu, Aoki S, Ejiri S, Hatsuda T, Ishii N, Kanaya K, Ukita N and Umeda T 2008 *Proc. of Science Lattice 2008 (Williamsburg)* p 194 (*Preprint* hep-lat/0811.0426)
[19] Nakamura A, Saito T and Sakai S 2004 *Phys. Rev.* D **69** 014506
[20] Hart A, Laine M and Philipsen O 2000 *Nucl. Phys.* B **586** 443
[21] Bak D, Karch A and Yaffe L G 2007 *J. High Energy Phys.* JHEP0708(2007)049
[22] Djordjevic M and Gyulassy M 2004 *Nucl. Phys.* A **733** 265-98
[23] Gyulassy M and Wang X N 1994 *Nucl. Phys.* B **420** 583
     Wang X N, Gyulassy M and Plumer M 1995 *Phys. Rev.* D **51** 3436
[24] Blagojevic B and Djordjevic M 2014 *Preprint* nucl-th/1411.1649

Zimanyi Winter School

Dec 2 – 6, 2024
Wigner Research Center for Physics
Europe/Budapest timezone

Enter your search term

Overview

Timetable

Contribution List

Impact of higher-order opacity corrections on high-transverse momentum observables

📅 Dec 6, 2024, 11:50 AM

🕐 20m

📍 Bldg 3, Council room (Wigner Research Center for Physics)

Aspects of QCD

Speaker

👤 Dr Bojana Ilic (Blagojevic)

📎 Presentation materials

📄 Bojana Ilic Zimanyi24.pdf

Combined experimental and theoretical study of Type-II toxin-antitoxin system response to antibiotics

Bojana Ilic[1], Marko Đorđević[2], Hong-Yu Ou[3]

[1]Institute of Physics Belgrade, National Institute of the Republic of Serbia, Serbia
[2]Faculty of Biology, University of Belgrade, Serbia
[3]Shanghai Jiao Tong University, Shanghai, China
bojanab@ipb.ac.rs

Bacterial Type-II toxin-antitoxin (TA) systems, including kacAT in *Klebsiella pneumoniae*, respond to antibiotics. We investigated kacAT's regulation relevant to antibiotic persistence, which refers to the survival of antibiotic exposure by dormant bacterial cells. Elevated toxin levels may induce dormancy. KacAT complex binds and represses the kacAT promoter cooperatively, leading to highly non-linear negative feedback. Antibiotics increase transcription of the kacA and kacT genes by inducing KacA degradation and consequently reducing the KacA:KacT ratio. Our model reproduced experimental findings, explaining increased kacAT transcription and reduced [KacA]:[KacT] ratio. Interestingly, KacAT overexpression induces antibiotic stress tolerance, while deleting kacAT has no effect, which our model can also explain. KacAT, therefore, cannot induce spontaneous (in the absence of antibiotics) persister formation. Earlier theoretical models, which predicted spontaneous persistence in Type-II TA systems, assumed the cooperative action of multiple TA systems. Our bioinformatics analysis, however, reveals a limited occurrence of multiple TA instances within clades and that cross-talk between clades is disfavored. These challenges the assumption of cooperativity in TA action, possibly explaining the absence of spontaneous persister generation in kacAT.

Keywords: Type II toxin-antitoxin systems; antibiotic persistence; systems biology; non-lienar dynamics; gene expression regulation; bioinformatics;

A new insight on mass hierarchy in heavy flavor suppression

Author: Bojana Ilic (Blagojevic)[None]

Co-author: Magdalena Djordjevic

Corresponding Author: bojanab@ipb.ac.rs

The inherent characteristic of parton energy losses, both radiative and collisional, in QGP is the evident flavor dependence. Experimentally observed suppression mass ordering, as well as comprehensively studied dead-cone effect in radiative energy loss, encouraged us to address the mass hierarchy in heavy flavor suppression more thoroughly.

With this goal in mind, we employ the recently developed DREENA framework, which is based on our dynamical energy loss formalism. This enables us [1] to present 1) A novel observable, which is sensitive only to the collisional energy loss. This observable is robust to collision energy, system (size), and centrality, while proposing a new way to utilize high-$p_\perp$ heavy flavor data. 2) Analytical derivation of a direct relation between collisional suppression/energy loss and heavy quark mass; 3) Analytical and numerical extraction of the mass hierarchy in collisional energy loss through this observable, to be more rigorously tested by the forthcoming high-luminosity measurements at the RHIC and the LHC.

[1] Bojana Ilic and Magdalena Djordjevic, arXiv:2203.06646 [hep-ph] (under review in Phys. Rev. C).

Preferred track:

Hadronic Issues in Heavy-Flavour Physics

Subfield:

Nuclear theory

Attending in-person?:

Yes

On behalf of collaboration?:

Poster Session / 69

Study of resonance production in small system collisions with respect to transverse spherocity using EPOS3

Author: Nasir Mehdi Malik[1]

Co-authors: Ranbir Singh ; Sanjeev Singh Sambyal ; Vikash Sumberia

[1] *University of Jammu (IN)*

Corresponding Author: nasir.mehdi.malik@cern.ch

Hadronic resonaces production provide insight into the properties of the hadronic phase. Studying the dependence of the yield of resonances on transverse spherocity and multiplicity allows us to understand the resonance production mechanism with event topology and system size, respectively.In this contribution,we present hadronic resonances production as a function of transverse spherocity using EPOS3 model with URQMD. The results include the transverse momentum spectra.

Preferred track:

High-temperature QCD

Analytical and numerical study of infection progression under social distancing measures

Ilic B.[1]*, Djordjevic M.[1], Djordjevic M.[2], Salom I.[1], Stojku S.[1]

[1] *Institute of Physics Belgrade, University of Belgrade, Belgrade, Serbia*

[2] *Quantitative Biology Group, Faculty of Biology, University of Belgrade, Belgrade, Serbia*

* bojanab@ipb.ac.rs

Key words: COVID-19, infection outburst, social distancing measures, epidemiological compartmental models, systems computational biology, SEIR

Motivation and Aim: The unprecedented worldwide social distancing measures are introduced to respond to the COVID-19 pandemic outburst. While epidemiological compartmental models have conveyed extensive studies on interventions such as quarantine or vaccination, the effects of social distancing on infection outbursts are poorly understood, and even when considered, they have been addressed only numerically. To this end, we develop an analytically tractable model, which considers the gradual introduction of social distancing and optimally utilizes the vast of publicly available data.

Methods and Algorithms: Building upon standard SEIR epidemiological compartmental models, we develop a realistic and analytically solvable SPEIRD (Susceptible-Protected-Exposed-Infected-Recovered-Detected) model [1, 2] that accounts for the effect of social measures by introducing a new compartment – Protected. In particular, the model implies solving highly nontrivial inhomogeneous differential equations. Moreover, an approach well known to theoretical physics (and more recently to quantitative biology) is applied, where one searches for common dynamical features, regardless of other differences.

Results: The model delivers closed-form mathematical expressions for the time dependence of infected (I) [2], detected cases (D) [3], and fatalities (F) [3]. These main infection progression data (I(t), D(t), F(t)) are well reproduced (for a majority of COVID-19 hotspots) through joint analytical and numerical analysis, capturing empirically observed COVID-19 growth signatures of detected cases, that is its three distinct growth signatures (exponential, superlinear, and sublinear regime). The growth signatures and associated scaling laws are utilized [2] to pinpoint regions where analytical derivations are most effective for i) assessing the nearly constant value of the scaling exponent in the superlinear regime; ii) understanding the relationship between the duration of this regime and strength of social distancing (α); iii) recognizing changes in the reproduction number from infection outburst to its extinguishing; vi) constraining the main parameter quantifying the effect of social distancing (α), by analyzing the time duration of the sublinear regime. The combination of α and the time of social measures introduction [3] defines a new parameter – protection time, essential for public policy decision making. For instance, our study not only suggests that rigorous measures can be often substituted by more relaxed ones imposed at earlier times, but provides a direct analytical expression to quantify this balance. We also provide simple analytical expressions [3] to estimate the peak's timing, the epidemic wave's tipping points, and the maximum of detected cases per day. Additionally, our model is applied to infer key infection parameters [2], such as case fatality, infected fatality, and attack rates.
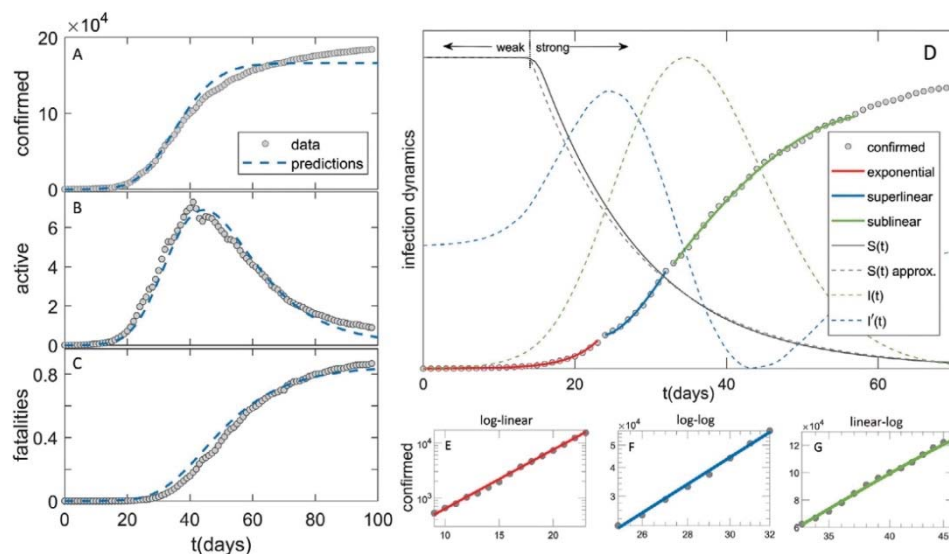
Fig. 1. Comparison between the model (dashed blue curves) and the data (grey circles) in the case of Germany, during the first pandemic wave, for A) detected, B) active cases, and C) fatalities. D) exponential, superlinear, and sublinear fit to detected case data is presented. Arrows indicate the regions with a small and large magnitude of social distancing. The dashed green and blue curve corresponds to the number of infected and its first derivative (whose maxima is $I(t)$ inflection points) respectively. The detected case counts in the three regimes are displayed on E) log-linear, F) log-log, and G) linear–log scale. Figure adapted from [2]

Conclusion: The strength of our analytically tractable model is its ability to qualitatively and quantitatively explain universal growth signatures of infection progression; to provide simple quantitative relations between the model variables and epidemiological observables; to ensure highly constrained infection parameters inference; and to shed light on cause-effect connections that underlie the epidemiological dynamics under social distancing measures, which are obscured in more standard, i.e., purely numerical, approaches. Due to its general relevance, it is applicable to the early stages of any new pandemics when pharmaceutical treatments and vaccines are unavailable and well-timed and appropriately chosen social distancing measures are of the utmost importance. The model does not consider loosening the measures, as was the case during the first COVID-19 wave in many countries. As an outlook, it can be done in our model through a reversible transition from the protected back to the susceptible compartment. Thus, the analytical expressions would be much more cumbersome (or unachievable), though exploring the model numerically in such a case would be highly relevant, which is our future goal.

References

1. Djordjevic M., Rodic A., Salom I., Zigic D., Milicevic O., Ilic B., Djordjevic M. A systems biology approach to COVID-19 progression in a population. *Adv Protein Chem Struct Biol.* 2021;127:291-314.
2. Djordjevic M., Djordjevic M., Ilic B., Stojku S., Salom I. Understanding Infection Progression under Strong Control Measures through Universal COVID-19 Growth Signatures. *Global Challenges.* 2021;5(5):2000101. doi: 10.1002/gch2.20200010.
3. Ilic B., Salom I., Djordjevic M., Djordjevic M. An Analytical Framework for Understanding Infection Progression Under Social Mitigation Measures. (Submitted to *Nonlinear Dynamics*). 2022. doi: 10.21203/rs.3.rs-1331002/v1.

605 / ANALYTICAL STUDY OF INFECTION OUTBURST UNDER STRONG MITIGATION MEASURES

04

Keywords: *quantitative biology, epidemiology, Infection outburst and dynamics (COVID-19), social distancing measures*

Bojana Ilic / Institute Of Physics Belgrade, University Of Belgrade, *Serbia*

Bojana Ilic / Institute of Physics Belgrade, University of Belgrade, Belgrade, *Serbia*

Magdalena Djordjevic / Institute of Physics Belgrade, University of Belgrade, Belgrade, *Serbia*

Marko Djordjevic / Faculty of Biology, University of Belgrade, Belgrade, *Serbia*

Igor Salom / Institute of Physics Belgrade, University of Belgrade, Belgrade, *Serbia*

Stefan Stojku / Institute of Physics Belgrade, University of Belgrade, Belgrade, *Serbia*

While comprehensive studies on interventions such as vaccination or quarantine are conducted within epidemiological compartmental models, the effects of social distancing on infection outbursts are yet to be understood.

We developed a realistic and analytically solvable model for the COVID-19 dynamic under social mitigation measures, which presents a generalization of the SEIR (Susceptible-Exposed-Infected-Recovered) model. We derive a closed-form mathematical expressions for infected, detected cases, and fatalities, as a function of time. Joint analytical and numerical analysis reproduces these main infection progression data, generating empirically observed COVID-19 growth signatures of detected cases, i.e., its three distinct dynamical regimes (exponential, superlinear, and sublinear). Analytical guidance facilitates the extraction of key infection progression parameters, e.g., infected fatality rates and attack rate. It distinguishes the regions where equations are most effective to infer simple relations between model parameters and epidemiological observables. The main parameter quantifying the effect of social mitigation (α) is thus highly constrained and connected to the time-duration of the superlinear regime. Combined with the time of social measures introduction, it establishes a new parameter – protection time, relevant for public policy decision making, etc.

Our analytically tractable model can shed light on cause-effect connections that underlie the epidemiological dynamics, explain universal dynamical features of a system, and set tight constraints on infection parameters inference. Due to its generality, it applies to the outburst of any new pandemics when pharmaceutical interventions are unavailable, and timely and appropriately chosen social mitigation measures are crucial.

12:20 – 12:45 (25 min) : Vera Markasheva

Asymptotic behavior of entire solutions for degenerate partial differential inequalities on Carnot-Carathéodory metric spaces and Liouville type results

12:45 –14:15 (90 min) : LUNCH

14:15 –14:40 (25 min) : Sergey Shirmovsky

Energy transformation mechanisms in microtubules

14:40 –15:00 (20 min) : Sofija Markovic

Inferring COVID-19 severity determinants by combining epidemiological modeling and machine learning

15:05 – 15:25 (20 min) : Bojana Ilic (Blagojevic)

Global COVID-19 growth signatures used to characterize COVID-19 non-linear infection dynamics

15:25 – 15:40 (15 min): BREAK

15:45 – 16:10 (25 min): Mirjana Filipovic

The procedure of generating trajectory of motion of carrier conveyor for granular material in dependent of pod systems characteristics

16:15 – 16:40 (25 min) : Umaaran Gogilan

Implementation of state observer-based conditioned reverse path method to the identification

nonlinearity2021.matf.bg.ac.rs/abstract.php?data=rodic.html

2nd CONFERENCE ON NONLINEARITY
18—22.10.2021, Belgrade, Serbia
Virtual conference

Main page

General information

ZOOM

Programme

Committees

Speakers/Talks

Proceedings

Participants

Application form

Poster

Previous meetings

Igor Salom, Andjela Rodic, Ognjen Milicevic, Dusan Zigic, Bojana Ilic, Magdalena Djordjevic, Marko Djordjevic

Investigating the SARS-CoV-2 virus transmission using a non-linear compartmental epidemiological model

Abstract

Compartmental models in epidemiology describe the flow of individuals between relevant population categories (such as the Infected, the Susceptible to infection, the Recovered, etc.) during the course of the epidemic. Having in mind the conditions in which the COVID-19 was spreading in the early phases, characterized by widely implemented social distancing measures after the initial exponential growth, we constructed a non-linear compartmental model which describes the SARS-CoV-2 virus transmission and the epidemic progression in a population. The examination of the cumulative case and death dynamic curves for various populations (countries/regions) reveals several distinct, general phases of the COVID-19 epidemic growth. Focusing on the initial exponential phase of the uncontrolled virus transmission, one can use the model to infer the basic reproduction number (R0, the standard epidemiological measure of the inherent virus transmissibility, dependent on the virus and the population/environment characteristics) for each country. As the first part of our study of the influence of demographic and climatic factors on the SARS-CoV-2 virus transmission, we analyzed correlations between R0 values and 42 different factors for ~118 countries. Furthermore, we applied the model to the data for 30 provinces of China and determined the values of the main parameters of the epidemic growth in each of them. The model provides a reasonable interpretation of the prominent disproportion between the intensive spread of the infection in Wuhan (Hubei) and the much smaller case counts in other Chinese provinces, which may have occurred due to a significantly higher inherent virus transmission in Wuhan and more efficient epidemic control measures in other provinces. In conclusion, the results of these analyzes indicate that the dynamics of the epidemic spread may significantly depend on potentially highly heterogeneous and seemingly random factors, such as variations in demographic and meteorological

QCD Master Class 2021

August 29, 2021 to September 11, 2021
Saint-Jacut-de-la-Mer
Europe/Paris timezone

Enter your search term

- Overview
- Lectures and lecturers
- Timetable
- Participant List
- Venue
- Conference committee
- Accommodation
- Travel Information
- Touristic information

QCD Master Class 2019

Generalization of high-pT parton's radiative energy loss beyond the soft-gluon approximation

📅 Sep 6, 2021, 5:00 PM
🕐 30m
📍 Saint-Jacut-de-la-Mer

Student talk and discu...

Speaker

👤 Bojana Ilic (Blagojevic) (Institute of Physics Belgrade)

📎 Presentation materials

📄 QCDMasterClass2021_Bojana_Ilic13.pdf

Sergey Margasyuk , *Z. Chervontseva , A. Danchurova , Dmitri Pervouchine*

Sequence determinants of cross-regulatory feedback loops in RNA-binding protein interaction network

Sofia Mariasina , *A. Izzi , E. Denisova , O. Dontsova , P. Sergiev*

High-Throughput Splicing Efficiency Analysis System

Marko Djordjevic , Magdalena Djordjevic , Andjela Rodic , Igor Salom , Ognjen Milicevic , Bojana Ilic , Dusan Zigic , Stefan Stojku

A systems biology approach to understanding SARS-CoV-2 transmissibility in population

Georgy A. Meshcheryakov , *Maria G. Samsonova , Anna Igolkina*

mtmlSEM with random effects uncovers genotype-phenotype associations through pleitropic SNPs

Alina G. Mikhailova , *Alima Galieva , Kristina Ushakova , Valeria Lobanova , Alina A. Mikhailova , Victor Shamanskiy , Leonard Polishchuk , Dmitry Knorre , Konstantin Khrapko , Konstantin Gunbin , Ilya Mazunin , Valerian Yurov , Konstantin Popadin*

⌨ ▾ | ⬇ | ⬓ ▾ | ⬀ ⚿ 🕐 Europe/Zurich ▾ 🌐 English (United States) ▾ ⇥ Login

ISMD2021 — 50th International Symposium on Multiparticle Dynamics (ISMD2021)

Jul 12 – 16, 2021
Europe/Zurich timezone

Due to the COVID-19 coronavirus pandemic, the ISMD2021 meeting has been moved online. We look forward to welcoming you in the Scottish Highlands next summer.

Overview

Scientific programme

Timetable

Organization

Registration

Participant List

Call for Abstracts

Exploring different high-$p_\perp$ parton energy loss scenarios in pre-equilibrium QCD matter

🔗 📄 🗓

🗓 Jul 14, 2021, 2:30 PM
🕐 20m

Talk | 🗇 High-temperature Q... | High-temperature QCD

Speaker

👤 Dr Bojana Ilic (Blagojevic) (Institute of Physics Belgrade)

Description

Description

The pre-equilibrium stage of quark-gluon plasma remains one of the major sources of uncertainty in studies of heavy ion collisions, which became a prominent research problem in heavy ion community. Major efforts regarding this problem are made in low-$p_\perp$ sector. We here instead propose [1] to utilize high-$p_\perp$ particles energy loss, as a complementary tool, to elucidate these early stages.

To this end, we employ our recently developed DREENA-B framework, which is based on our sophisticated dynamical energy loss formalism, where temperature is an intrinsic input/parameter. It also considers a simple Bjorken medium evolution, which is highly suitable for analytically exploring different energy loss scenarios. Within this, we test four distinct cases, ranging from none to infinitely large energy loss in pre-equilibrium stage. In particular, we test: 1) free-streaming case; 2) linear case, corresponding to linearly increasing temperature with time; 3) constant case, with constant pre-equilibrium temperature; and 4) divergent case, corresponding to Bjorken expansion from the beginning. Thus obtained high-$p_\perp$ R_{AA} and v_2 predictions for $h^\pm$, D and B mesons are compared with 5.02 TeV LHC data. Contrary to common expectations, we obtain that high-$p_\perp$ v_2 is unable to distinguish between diverse scenarios, being insensitive to the early stages of medium evolution. R_{AA} is however sensitive to these different cases, and could provide an insight in the early stages' dynamics. However, higher-precision measurements of high-$p_\perp$ R_{AA} are required to allow for more reliable conclusions through this observable.

[1] D. Zigic, B. Ilic, M. Djordjevic and M. Djordjevic, Phys. Rev. C 101, 064909 (2020).

Preferred track Jets & QCD at High Scales

Author

👤 Dr Bojana Ilic (Blagojevic) (Institute of Physics Belgrade)

Author

👤 Dr Bojana Ilic (Blagojevic) (Institute of Physics Belgrade)

Co-authors

👤 Magdalena Djordjevic (Institute of Physics Belgrade)
👤 Dusan Zigic (Institute of Physics Belgrade)
👤 Marko Djordjevic

📎 Presentation materials

📄 ISMD2021_Bojanallic_talk.pdf
▶ Wednesday-Bojanallic.mp4

Understanding Infection Progression under Strong Control Measures through Universal COVID-19 Growth Signatures

Magdalena Djordjevic[1], Marko Djordjevic[2], Bojana Ilic (Blagojevic)[1*], Stefan Stojku[1], and Igor Salom[1]

[1] Institute of Physics Belgrade, Pregrevica 118, 11080 Belgrade, Serbia
[2] Quantitative Biology Group, Faculty of Biology, University of Belgrade, Studentski trg 16, 11000 Belgrade, Serbia

Abstract

While interventions such as quarantine or vaccination have been extensively studied within compartmental models in epidemiology, the effects of social distancing are poorly known. Even when considered, they were studied only numerically. Through joint analytical and numerical analysis, we developed a novel framework, which incorporates social distancing measures. The framework reproduces the main infection progression data (such as detected case counts, active cases and fatalities), capturing empirically observed COVID–19 growth signatures of detected case counts, i.e., its three distinct dynamical regimes (exponential, superlinear and sublinear).

We utilized an approach well known to theoretical physics and more recently systems biology, where we look at common dynamical features, regardless of the differences in other factors. This approach provides generality of the applied framework, ensuring the applicability to a wide range of countries and other infectious diseases. The dynamical features and associated scaling laws are used as a powerful tool to pinpoint regions where analytical derivations are effective for i) imposing stringent restraints on parameter quantifying the effect of social distancing; ii) explaining the nearly constant value of the scaling exponent in the superlinear regime of detected counts; iii) understanding the relationship between the duration of this regime and strength of social distancing; iv) identifying changes in the reproduction number from outburst to extinguishing the infection. Additionally, we successfully applied this tool to infer key infection parameters. The main advantage of our analytically tractable model (compared to the state-of-the-art numerical simulations) is in its ability to qualitatively and quantitatively explain common dynamical features of a system, to yield a fundamental understanding of infection progression under strong control measures, and to provide highly constrained infection parameters inference.

Keywords:

systems biology, epidemiology, COVID-19, compartmental model, physics, social distancing measures, key infection parameters

*Corresponding author, e-mail: bojanab@ipb.ac.rs

Session 2 - Friday, February 28th, 11:15 - 13:15

11:15 - 11:35	**Olga Soloveva** *Transport properties of the QGP within the Dynamical Quasi-Particle Model*
11:35 - 11:55	**Farid Salazar Wong** *Dijet production in electron-proton (electron-nucleus) collisions from high energy correlators of light-like Wilson lines.*
11:55 - 12:15	**Bojana Ilic** *Generalization of high-pT particle's energy loss to a finite value of radiated energy*
12:15 - 12:35	**Lucia Oliva** *The influence of the electromagnetic fields in relativistic proton-nucleus collisions*
12:35 - 12:55	**Maria Lucia Sambataro** *Quark charm scattering process in Quark-Gluon Plasma medium: extension to off-shell dynamics*

Zimányi School 2019

Enter your search term

Overview

Timetable

Beyond the soft-gluon approximation in calculating hard probe radiative energy loss

Jets (section chair: M. ...

📅 Dec 2, 2019, 11:50 AM

🕐 20m

📍 Bldg 3, Council room (Wigner Research Center for Physics)

Speaker

👤 Dr Bojana Ilic (Blagojevic) (Institute of Physics Belgrade)

📎 Presentation materials

📄 Zimanyi19_Bojana_Ilic.pdf

also provided insight on pion production mechanism beyond Core-Halo models. We will present the latest PHENIX results on the multi-particle Bose-Einstein correlation, and discuss its physics interpretation.

Poster Session / 613

Constraining the initial stages of heavy-ion collisions with high-$p_\perp$ theory and data

Author: Bojana Ilic (Blagojevic)[1]

Co-authors: Dusan Zigic [1]; Marko Djordjevic ; Magdalena Djordjevic [1]

[1] *Institute of Physics Belgrade*

Corresponding Authors: magda@ipb.ac.rs, bojanab@ipb.ac.rs, dmarko@bio.bg.ac.rs, zigic@ipb.ac.rs

Commonly, only low-$p_\perp$ sector is used to infer the features of initial stages before QGP thermalization. On the other hand, recently acquired wealth of high-$p_\perp$ experimental data paves the way to utilize the high-$p_\perp$ particles energy loss in exploring the initial stages. However, the results of such explorations are up to now either inconclusive or questionable. We here concentrate on high-$p_\perp$ R_{AA} and v_2 observables, and study the effects of four different commonly considered initial stages scenarios, which have the same temperature profile after - but differ in the temperature profiles before - thermalization. For the study, we use our recently developed DREENA framework, which is a fully optimized computational procedure in which our state-of-the-art dynamical energy loss is employed. Contrary to the common expectations, we surprisingly obtain that high-$p_\perp$ v_2 is insensitive to the initial stages of medium evolution, being unable to discriminate between different scenarios. On the other hand, R_{AA} is notably sensitive to these conditions, strongly preferring later thermalization times and free streaming during the initial stages of QGP formation. Moreover, we also reconsider the validity of widely-used procedure of fitting the energy loss parameters for different initial-stage cases to reproduce the experimentally observed R_{AA}. We here find that the reported sensitivity of v_2 to different initial-stage scenarios is mainly an artifact of the R_{AA} fitting, with no real physical process to support it. Therefore, such a procedure may lead to erroneous conclusions, masking the underlying nature of jet-medium interactions. Consequently, the simultaneous study of high-$p_\perp$ R_{AA} and v_2 is necessary for imposing reliable constraints on the initial stages.

Poster Session / 614

PHENIX results on J/ψ polarization in p+p collisions

Author: Alexandre Lebedev[1]

[1] *Iowa State University*

One of the big puzzles in quarkonia production is how heavy-quark pairs, produced in the initial hard process, hadronize into final quarkonia states. This uncertainty affects the estimation of quarkonia breakup cross sections and color screening in heavy ion collisions. According to Non-Relativistic Quantum Chromodynamics, quarkonia are formed from several intermediate singlet and color octet states. The relative fraction of each contribution can only be determined by experimental data, including yields and angular decay (polarization) measurements in a broad kinematic region. The PHENIX experiment has measured inclusive J/psi polar and azimuthal angular decay coefficients in the mid ($|y| < 0.35$) and forward ($1.2 < |y| < 2.2$) rapidity regions in $p+p$ collisions at 200 GeV and 510 GeV. We find that the polarization coefficients are consistent with zero at mid-rapidity and negative at large rapidity. This talk will present the analysis strategy as well as the results in different angles/frames. We will discuss how the results can be explained in terms of singlet and color octet states.

Strangeness and Light Flavour / 84

News on in-medium modifications of properties of kaons measured around threshold

Author: Krzysztof Piasecki[1]

[1] *University of Warsaw*

Corresponding Author: piasecki@gmail.com

A partial restoration of the chiral symmetry is the fundamental quantum process of interaction of the hadronic matter with the quark-antiquark condensate [1]. According to QCD a particle embedded in a hot and dense hadronic matter should change its basic properties like mass and decay constant with respect to their values in vacuum. Kaons produced in heavy ion collisions around threshold for their production appear to be a good probe of these effects.

Initially comparisons of experimentally found phase space distributions to the transport model calculations suggested a clear and strong sensitivity to this effect [2]. However, recent published and upcoming data on kaon emission from high-statistics experiments by FOPI and HADES groups reveal a much broader and complex landscape. In this talk the preliminary findings of comparison of the transport model predictions to the distributions of K_S^0 emitted from Au+Au at 1.2A GeV [3] will be presented. Also new data on the emission of K^+ and K^- from the collisions of Ni+Ni at 1.9A GeV [4] will be shown. I will also point out the importance of the $\phi(1020)$ meson decays in the interpretation of the K^- spectra, consistently found in a recent decade [5,6].

[1] V. Koch, Intl. Jour. of Mod. Phys. E 06, 203 (1997).
[2] F. Laue *et al.* (KaoS Collaboration), Eur. Phys. J. A 9, 397 (2000).
[3] J. Adamczewski-Musch *et al.* (HADES Collaboration), arXiv:1812.07304.
[4] K. Piasecki *et al.* (FOPI Collaboration), Phys. Rev. C 99, 014904 (2019).
[5] J. Adamczewski-Musch *et al.* (HADES Collaboration), Phys. Lett. B 778, 403 (2018).
[6] K. Piasecki *et al.* (FOPI Collaboration), Phys. Rev. C 94, 014901 (2016).

Collaboration name:

FOPI, HADES

Track:

Strangeness and Light Flavour

Poster session with "aperitivo" / 87

Calculating hard probe radiative energy loss beyond soft-gluon approximation: how valid is the approximation?

Author: Bojana Blagojevic[1]

Co-authors: Magdalena Djordjevic [1] ; Marko Djordjevic [2]

[1] *Institute of Physics Belgrade*

[2] *Faculty of Biology, Institute of Physiology and Biochemistry, University of Belgrade, Serbia*

Corresponding Authors: magda@ipb.ac.rs, bojanab@ipb.ac.rs, dmarko@bio.bg.ac.rs

One of the most common assumptions when calculating radiative energy loss of high $p_\perp$ particles in quark-gluon plasma is the soft-gluon approximation, which considers that initial parton loses only a small amount of its energy via gluon's bremsstrahlung. Despite its convenience, the approximation sustainability was questioned by the reported notable radiative energy loss within different theoretical models.

To address this issue, we relax the soft-gluon approximation within DGLV formalism [1]. The obtained analytic expression beyond soft-gluon approximation is significantly more involved than its soft-gluon counterpart. Unexpectedly, however, the numerical results lead to similar predictions for the fractional radiative energy loss and the number of radiated gluons. Furthermore, the effect on these two variables is of an opposite sign, and results in nearly overlapping suppression predictions with and without soft-gluon approximation. We also show that this surprising result can be understood by the interplay of initial parton's $p_\perp$ distribution and its energy loss probability. Consequently, the results presented here provide confidence that, despite the concerns mentioned above, the soft-gluon approximation remains adequate within DGLV formalism. Finally, we also discuss generalizing this relaxation in the dynamical QCD medium, which suggests a more general applicability of the conclusions obtained here.

[1] B. Blagojevic, M. Djordjevic and M. Djordjevic, Phys. Rev. C **99**, no. 2, 024901 (2019).

Collaboration name:

Track:

Strangeness and Light Flavour

Collectivity in Small Systems / 88

Collectivity and electromagnetic fields in proton-induced collisions

Author: Lucia Oliva[1]

Co-authors: Elena Bratkovskaya [1]; Wolfgang Cassing [2]

[1] *GSI, Darmstadt*

[2] *University of Giessen*

Corresponding Authors: l.oliva@gsi.de, wolfgang.cassing@theo.physik.uni-giessen.de, elena.bratkovskaya@th.physik.uni-frankfurt.de

Proton-nucleus collisions at relativistic energy, traditionally regarded as control measurements for heavy ion collisions, are now capturing the attention due to the recent experimental observations at RHIC and LHC that indicate the formation of quark-gluon plasma even in these small systems. In the early stage of relativistic heavy ion collisions extremely intense magnetic fields, with a magnitude up to 5-50 m_\pi^2, are produced. In asymmetric collisions, and in particular in proton-nucleus collisions, not only the magnetic field but also the generated electric field is very high. Moreover, the particle rapidity distributions are strongly asymmetric inside the overlap region due to the different number of protons in the colliding nuclei. By means of microscopic calculations within the Parton-Hadron-String Dynamics (PHSD) approach we study central p+Au collisions, investigating the emergence of collectivity, the distributions of electromagnetic fields and the influence of these fields on final hadronic observables.

Collaboration name:

Track:

Collectivity in small systems

Minireview

Modeling and bioinformatics of bacterial immune systems: understanding regulation of CRISPR/Cas and restriction-modification systems

Jelena Guzina[1], Anđela Rodić[1], Bojana Blagojević[2] and Marko Đorđević[1*]

[1]University of Belgrade – Faculty of Biology, Studentski trg 3, 11000 Belgrade, Serbia
[2]Institute of Physics Belgrade, University of Belgrade, Pregrevica 118, 11080 Belgrade, Serbia

Summary. Bacterial immune systems protect bacterial cells from foreign DNA, such as viruses and plasmids. They also critically affect bacterial pathogenicity by reducing the flow of genes between bacteria. Two such major systems are restriction-modification and the recently discovered CRISPR/Cas systems. Here we review our work on understanding gene expression regulation in these systems, which takes a systems biology approach, combining modeling, bioinformatics and data analysis from quantitative experiments. Specifically, we address the following: (i) modeling gene expression regulation during restriction-modification system establishment in a naïve bacterial host, (ii) modeling the dynamics of CRISPR/Cas activation, in particular, how the features characterizing system transcription regulation and transcript processing affect the dynamics, (iii) predictions of transcription start sites for alternative σ factors that have been poorly studied up-to-now, but are important as CRISPR/Cas likely responds to bacterial cell envelope stress, (iv) our preliminary results on predictions of different CRISPR/Cas components, in particular, small RNAs associated with the systems, which likely have a key role in their regulation.

Keywords: Bacterial defense systems, bioinformatics, biophysical modeling, CRISPR/Cas, restriction-modification systems.

Introduction

Bacteria are continuously exposed to foreign nucleic acids, such as phage DNA, plasmids or other mobile genetic elements. In order to protect genome integrity, cells are equipped with immune systems that target invasive extrachromosomal elements for degradation (Shabbir et al. 2016), whereby the immune response reduces the rate of horizontal gene transfer (HGT), thus also affecting related aspects of cell functioning (e.g. virulence) (Vasu and Nagaraja 2013; Hatoum-Aslan and Marraffini 2014). Analogous to eukaryotic modes of defense, bacterial immune systems can be recognized as innate or adaptive, where restriction-modification and CRISPR/Cas (*C*lustered *R*egularly *I*nterspaced *S*hort *P*alindromic *R*epeats/*C*RISPR-*as*sociated proteins), respectively, are two major representatives of such systems (Goldberg and Marraffini 2015).

Restriction-modification (RM) systems are considered innate since they target invasive elements without prior immunization with fragments of foreign genetic material. Two major components of RM systems are the enzymes restriction endonuclease (R) and methyltransferase (M) (Fig. 1A), which are frequently encoded on mobile genomic loci (e.g. plasmids), so that these systems easily propagate through bacterial populations (Fig. 1B) (Heitman 1993; Kobayashi et al. 1999). Once an RM system enters the cell, tight regulation of its expression becomes essential for ensuring safe and efficient establishment in the naïve bacterial host. Precisely, R that represents the effector component of a RM system, cuts short specific DNA sequences, irrespective of their location, so that self-targeting can easily arise. To evade autoimmunity, R has to be expressed with a delay with respect to M, as methylation of the genomic sites recognized by R protects them from cleavage (Fig. 1A) (Wilson 1991).

Unlike RM systems, CRISPR/Cas provides adaptive component to bacterial immunity, which arises as a consequence of its dynamical structure (Barrangou et al. 2007; van der Oost et al. 2009). A major system component is the CRISPR array,
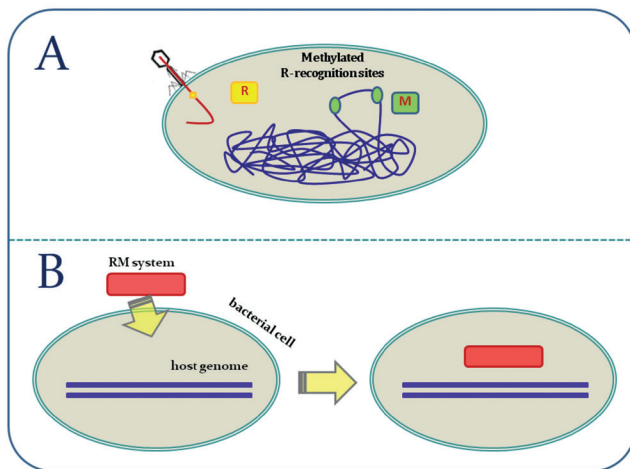
Fig. 1. RM system functioning (A) and establishment (B) in a host bacterial cell. A. Restriction-endonuclease (shown as a yellow rectangle) cuts the DNA at R-specific recognition sites (shown in yellow); Methyltransferase (shown as a green rectangle) methylates R-recognition sites on the host genome, thus protecting these sites (shown in green) from cleavage. **B.** RM systems are usually found on mobile genetic elements (e.g. plasmids), which enables them to efficiently propagate throughout bacterial populations. RM system, entering the bacterial cell (red rectangle), is shown.

which is characterized by a series of tandem repeats separated with unique spacer sequences (Fig. 2) (Al-Attar et al. 2011). The spacers are derived from previously encountered foreign genetic material, so that small interfering RNAs (crRNAs), which are generated upon array expression, target invasive elements based on complementarity; this makes the basic mechanism that confers resistance against foreign DNA/RNA (Bolotin et al. 2005). In addition to CRISPR array, the system also includes Cas proteins with mainly nucleolytic activity, which act as effectors during array immunization with new spacers, crRNA processing/expression and target degradation. CRISPR/Cas components typically remain silent under standard physiological conditions (Pul et al. 2010), whereby sudden activation leads to the production of large crRNA amounts, thus enabling efficient target eradication.

Despite the fact that RM and CRISPR/Cas systems markedly differ mechanistically, they likely embody the same design principles as a consequence of the general characteris-

Fig. 2. A typical organization of CRISPR/Cas locus in *E. coli*. CRISPR array is schematically presented with successive blue diamonds (direct repeats) and yellow rectangles (spacers); the upstream *cas* genes, characteristic of Type I CRISPR/Cas systems, are indicated with rightwards-oriented pentagons. Intergenic regions that contain promoters transcribing *cas* genes (IGLB), and CRISPR array (L) are also shown.

tics that shape the immune response. Namely, the induction of the CRISPR/Cas system probably faces similar dynamical constraints as the establishment of an RM system in a naïve bacterial host, as both require a rapid transition of the "toxic" (auto-immunogenic) molecule – R or crRNA – from "OFF" to "ON" state (Djordjevic 2013) to enable efficient target eradication. In addition to rapid transition, the expression of "toxic" immune molecules is also characterized by an initial delay, so that crRNAs in CRISPR/Cas are not expressed before the virus genome enters the cell, and M (the antidote) in RM systems has enough time to act.

Common design principles that impose similar dynamical constraints on RM and CRISPR/Cas activity are linked to the equivalent regulatory expression patterns in these systems. To understand the underlying transcription regulation, it is necessary to map transcription start sites (TSS) associated with different components of RM and CRISPR/Cas systems. This, however, is non-trivial since: (i) promoter elements of house-keeping σ factors are highly degenerate, so that a search usually results in a large fraction of false positives (Djordjevic 2014); (ii) information on the specificity of alternative σ factors (related to stress response) is largely missing, which is relevant since CRISPR/Cas is likely induced by cell-envelope stress (Ratner et al. 2015),which, in turn, is connected to Group IV (ECF) σ factors (Raivio and Silhavy 2001; Ratner et al. 2015).

In addition, an important aspect of CRISPR/Cas regulation are small RNAs associated with CRISPR/Cas (tracrRNAs) encoded outside the array, which have an essential role in CRISPR-transcript processing (Deltcheva et al. 2011), and possibly other system functions. Consequently, in this review we briefly present our work on:

1. modeling gene expression regulation during RM system establishment in a naïve bacterial host;
2. modeling dynamics of CRISPR/Cas activation, in particular how key features that characterize systems transcription regulation and transcript processing affect its dynamics;
3. predictions of bacterial TSS, particularly those related to alternative σ factors, which are poorly studied to date, but highly relevant as CRISPR/Cas likely responds to bacterial cell-envelope stress;
4. our preliminary results on predictions of different CRISPR/Cas components, in particular small RNAs associated with the system, which likely have a key role in its regulation.

Modeling *in vivo* expression of restriction-modification systems

Certain dynamical constraints imposed by their immune function have been proposed for RM systems in general. However, RM system dynamics have been observed in live cells in only two cases, as such experimental measure-

ments are complicated by a requirement for synchronous populations of cells transformed with RM system genes (Mruk and Blumenthal 2008; Morozova et al. 2016). In an earlier attempt, Mruk and Blumenthal synchronously introduced the PvuII system genes placed on an M13 phage into naïve cells by phage infection (Mruk and Blumenthal 2008). Our collaborators, on the other hand, conducted the first single-cell measurements of RM system dynamics for the Esp1396I system: they fused sequences encoding fluorescent proteins to the R and M genes and monitored the dynamics of the appearance of fluorescent signals in individual cells, transformed with a plasmid carrying the modified Esp1396I system (Morozova et al. 2016). To check if the regulatory features found in this particular system allow establishing observed dynamics, and if they can provide the proposed dynamical constraints, we constructed a quantitative model of the Esp1396I system regulation, which we will briefly outline below.

Among type II RM systems, whose main characteristic is that R and M are encoded by separate genes, a large group contains a third gene encoding a control (C) protein, which is typically transcribed as a part of the operon with the R gene; the example for such a gene arrangement is the RM system Esp1396I represented in Fig. 3A. C proteins regulate transcription by binding in the form of dimers to their binding sites, partially overlapping with a promoter (Nagornykh et al. 2008). The transcription of Esp1396I system genes was thermodynamically modeled by considering all allowed configurations of the system promoters and determining their statistical weights (Figs. 3B and 3C). The most frequently
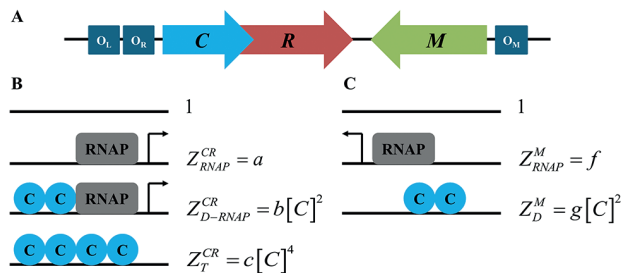

Fig. 3. Modeling transcription regulation in the Esp1396I RM system. A. Esp1396I gene organization scheme. The convergently oriented genes encoding R and M in the Esp1396I system are represented by the red and the green arrows, respectively, while the blue arrow represents the C gene, partially overlapping with the R gene. The dark blue boxes denoted by O_L, O_R and O_M represent operator sequences in the CR and the M promoter, which bind C dimers. **B and C.** The allowed configurations of RNAP (grey rectangle) and C protein (blue circle) molecules on the CR and the M promoter are illustrated, respectively, in B and C, where the transcriptionally active configurations contain an arrow. The corresponding statistical weights (Z) of the configurations, indicated on their right, depend on constant RNAP concentration and protein-protein and protein-DNA interaction energies (absorbed into parameters a, b, c, f and g) and variable C protein concentration.

observed regulation mechanism of the weak C and R operon (CR) promoter (also found in the Esp1396I system, Fig. 3B) involves highly cooperative binding of two C dimers to the left and the right operator sequences (O_L and O_R in Fig. 3A), where a C dimer bound to the high affinity left binding site can recruit either RNA polymerase (RNAP) to the promoter (thus activating transcription; the corresponding configuration has a statistical weight Z^{CR}_{D-RNAP}), or a second C dimer to the low affinity right binding site (establishing a tetramer that represses transcription; configuration Z^{CR}_T) (Bogdanova et al. 2008; Nagornykh et al. 2008). In the Esp1396I RM system, transcription of the M gene is also under the control of the C protein (Fig. 3C), whose binding to a single binding site (for a dimer; O_M in Fig. 3A) partially overlapping with the strong M promoter, excludes RNAP binding to the promoter and represses transcription of the M gene (configuration Z^M_D) (Bogdanova et al. 2009). For both the CR and the M promoter, configurations corresponding to basal transcription (configurations Z^{CR}_{RNAP} and Z^M_{RNAP} in Fig. 3, respectively) and empty promoters (statistical weight 1) were also assumed (Bogdanova et al. 2009). According to the classical Shea-Ackers assumption, which states that promoter transcription activity is proportional to the equilibrium probability of RNAP binding (Shea and Ackers 1985), the transcription activities of the CR(φ_{CR})and the M promoters(φ_M)are proportional to the probability of establishing their transcriptionally active configurations (for the statistical weights, see Fig. 3 caption):

$$\varphi_{CR} \propto \frac{a+b[C]^2}{1+a+b[C]^2+c[C]^4} \ , \quad \varphi_M \propto \frac{f}{1+f+g[C]^2} \cdot (1.1)$$

Transcripts (with concentration m_i, where $i = R, M, C$ denotes corresponding system components) synthesized from these promoters are degraded with a rate λ^m_i, while proteins (p_i) are generated by transcript translation with a rate k_i and are further degraded with a rate λ^p_i, as described by the following dynamical model equations:

$$\frac{dm_i(t)}{dt} = \varphi_i - \lambda^m_i \cdot m_i \ , \quad \frac{dp_i(t)}{dt} = k_i \cdot m_i - \lambda^p_i \cdot p_i \cdot (1.2)$$

It should be noted that the decay terms (λ) in equations include not only degradation of the transcripts and the proteins, but also their dilution due to cell division, which occurred with two very different rates during the first (0-160 min) and second time intervals (after 160 min) of the experiment. Consequently, the cell population dynamics are in part taken into account in the model through the decay terms. However, there are likely significant additional population dynamics effects that should, in principle, be included in the model, e.g. those related to possible changes in the cell metabolism and different plasmid and cell division

rates. Namely, our model describing the inherent RM system regulation and assuming constant parameters throughout the experiment (apart from different λ in the two time intervals) can successfully explain the main proposed qualitative features of system dynamics (Fig. 4), i.e. a large accumulation of M early upon plasmid entry into a naïve cell and a delay in the expression of R with respect to M, necessary for complete host genome protection. However, our model cannot completely quantitatively reproduce the system dynamics, i.e. there is a quantitative disagreement between the experimental data and the model predictions for M dynamics in the second time interval (after 160 min), likely arising from the additional population effects that we discussed above.

Design principles behind RM systems

The features of RM systems can be explained in terms of a few simple dynamical constraints that ensure safe and efficient RM system establishment. To this end, we proposed that all RM systems should exhibit the same simple dynamical properties: firstly, in every RM system there should be a significant expression of M prior to R, to avoid autoimmunity (Rodic et al. 2017). Once the host genome is protected (i.e. methylated), R should be rapidly generated, to "immunize" the host cell against virus infection, as fast as possible. Additionally, fluctuations of the toxic molecule R should be minimized, so as to evade that, due to large fluctuations, the toxic molecule amount is not matched by the antidote (M). Consequently, the following three dynamical properties are relevant to characterize RM system dynamics: (i) the time delay of R expression with respect to M; (ii) the transition

velocity of the system from "OFF" to "ON" state; (iii) the stability of R steady state levels.

To quantify these dynamical properties, we referred to the predicted system dynamics and the stability of R steady-state levels in the wild type (wt) AhdI system (Fig. 5). Accordingly, we introduced the following dynamical property observables (Rodic et al. 2017): (i) the ratio of the shaded areas in the perturbed and in the wt system for the first 10 min post-system entry as a measure of the time delay (Fig. 5A); (ii) the maximal slope of the sigmoidal R expression curve as a measure of the transition velocity from "OFF" (low R value) to "ON" (high R value) state (Fig. 5A); (iii) a measure of the stability of R steady-state levels (Fig. 5B) as derived in Bogdanova et al. (2008) – note that greater steady-state stability leads to smaller R fluctuations.

We here employed the biophysical model of wt AhdI transcription regulation that we previously developed and which was verified by the *in vitro* experimental measurements of the AhdI transcription activity dependence on C protein concentration (Bogdanova et al. 2008), and also the dynamical model of transcript and protein expression, which was also verified by *in vivo* measurements (see above and Morozova et al. (2016)). The described methodology, which involves a combination of thermodynamic and kinetic modeling, has been successfully applied to various systems in molecular biology (Munro et al. 2016). While there are few studies concerned with modeling some aspects of RM systems expression regulation (Williams et al. 2013), to our knowledge our work is the first to employ this modeling approach to systematically understand the relation between RM system regulation and its dynamics.

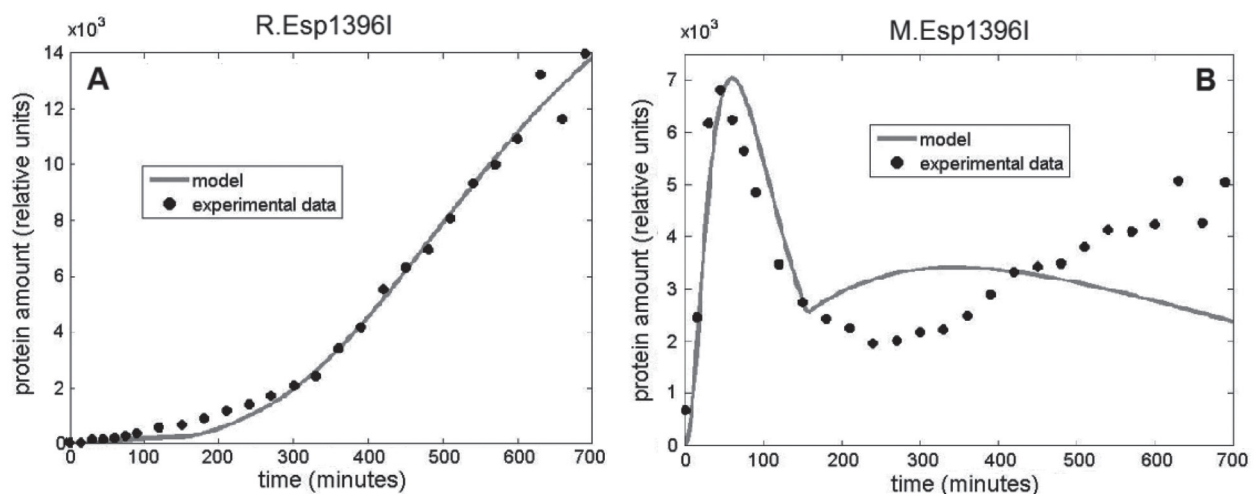In order to explain the (three) AhdI features, we per-

Fig. 4. Predicted Esp1396I RM system expression dynamics vs. experimental data. The change of R and M protein amounts in time is presented, respectively, in **A and B**. Circles correspond to the experimentally measured concentrations of protein fusions, while full lines correspond to the best fit of the model (described by the system of equations 1.1 and 1.2) to the data, obtained by varying parameters in biologically reasonable ranges. Time is set to zero at the point of the first available measurement. Adapted from Morozova et al. (2016).
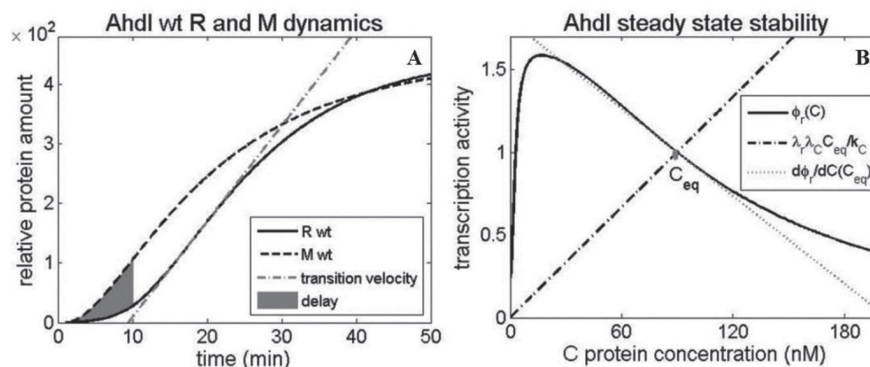
Fig. 5. Quantifying RM system dynamical properties A. R and M expression dynamics for AhdI RM system (Bogdanova et al. 2008). The shaded area presents a measure of a time delay between M (the dashed curve) and R (the solid curve) expression. The maximal slope of the sigmoidal R expression curve (dash-dotted line) is taken as a measure of the transition velocity from OFF to ON state. **B. Stability of the steady-state level**. The steady-state (C_{eq}) is obtained at the intersection of the CR promoter transcription activity (the solid curve) and the dash-dotted line, whose slope depends on the transcript and the protein decay rates and the protein translation rate (see Supplements in (Bogdanova et al. 2008) and (Rodic et al. 2017)). Larger difference in the slopes of the dash-dotted line and the solid curve at their intersection point leads to a more stable steady state. Adapted from Rodic et al. (2017).

turbed them *in silico*, one by one, to observe how this affects the dynamical property observables (Rodic et al. 2017). Firstly, we gradually increased the (initially low) C transcript translation initiation rate k_C towards the value characteristic of R and M transcripts. In Fig. 6A we observe a reduction in the delay between R and M expression, and a decreasing of the R steady-state level as the main effect of this perturbation. This finding can be intuitively explained by the fact that in increasing the translation initiation rate, C is generated faster, which hastens the formation of the activating and repressing complexes on the CR promoter. The effect on the other two observables is negligible. Consequently, this perturbation has a significantly adverse effect on one of the three dynamical properties (the delay between R and M expression), decreasing the ability of the system to protect the host genome from the cleavage.

Next, we gradually lowered the C subunit dissociation constant of dimerization K_I from the very high value characteristic to the AhdI system, which corresponds to mostly C monomers in the solution, to low values, which correspond to predominantly C dimers in the solution, as shown in Fig. 6B (Bogdanova et al. 2008; Rodic et al. 2017). The three main effects of this perturbation are significant decreases in the time delay, in the transition velocity and in the steady-state levels of R. The stability of R steady-state levels is not significantly affected. Consequently, this perturbation has a significantly adverse effect on two dynamical properties, greatly reducing the ability of the system to protect the host genome from cleavage, and increasing the time window needed for the system to become protected from foreign DNA infection.

Finally, we gradually decreased only the extremely high cooperativity ω in C dimers binding to the CR promoter, which is shown in Fig. 6C (Rodic et al. 2017). We observe that this perturbation affects only the late R dynamics (see the left panel of Fig. 6C), since only efficiency in forming the repressor complex, whose probability is proportional to C^4, is affected, which becomes important only later on, when enough C is generated. Namely, this perturbation significantly decreases the stability of the steady state (see the right panel of Fig. 6C), thus having a significantly adverse effect on one dynamical property but not affecting the others. Also, contrary to the previous two perturbations, it significantly increases the steady-state levels of R, so that exhibiting different perturbations allows a balancing of the amount of the toxic molecule R in the cell.

To summarize, all three AhdI control features, in general, have the same effect on the dynamical properties, i.e. perturbing them makes at least one dynamical property much less optimal, while not notably affecting the other properties. This, together with the fact that decreasing the binding cooperativity ω has the opposite effect on the R steady-state levels from the other two perturbations (which facilitates controlling the toxic molecule R level) can explain the unusually large binding cooperativity in AhdI (Semenova et al. 2005; Bogdanova et al. 2009).

Dynamics of CRISPR/Cas system expression

Despite being intensively used in biotechnology for developing powerful genetic tools, the adaptive prokaryotic immune system CRISPR/Cas still appears to be underexplored when it comes to understanding the mechanism of its natural induction in a cell. In fact, the dynamics of CRISPR/Cas expression upon foreign DNA invasion have not been observed experimentally *in vivo*. What crucially hinders observing these dynamics is that CRISPR/Cas of Type I-E, which is the model system for CRISPR/Cas induction and regulation (most extensively studied in *E. coli*), is silent under
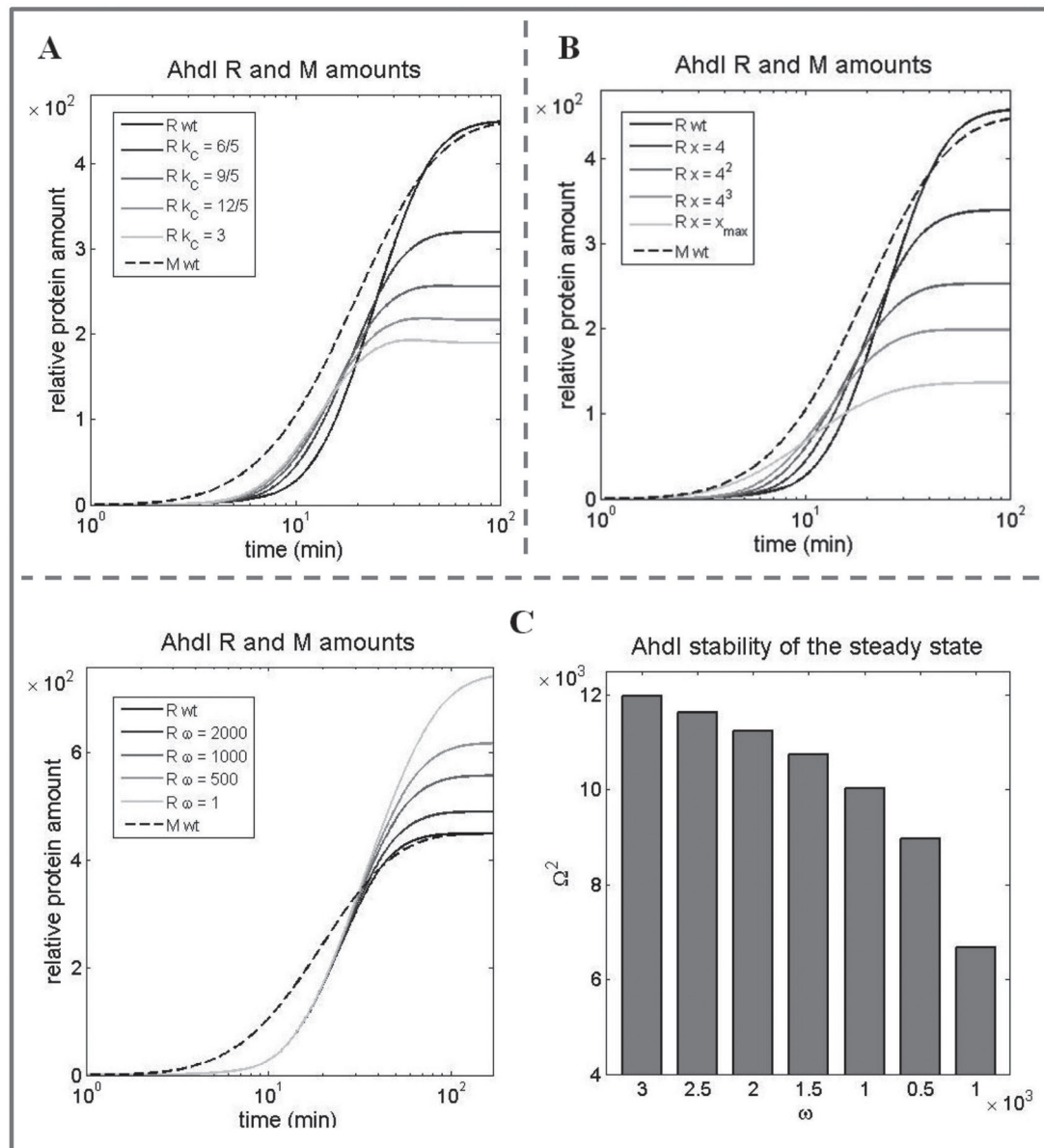
Fig. 6. Perturbing AhdI control features. A. Increasing C transcript translation initiation rate k_C. The effect of gradual k_C increase (from wt putative 3/5 1/min towards 3 1/min, which corresponds to the R and M (Bogdanova et al. 2008) is assessed on the protein expression dynamics, with R (solid) curves fading as k_C increases. The dashed curve corresponds to M expression, which is not affected by any of the three perturbations. **B.** Decreasing dissociation constant of C dimerization K_I. The effect of gradual K_I decrease from the high value, corresponding to only monomers in the solution, to the low value, corresponding to only dimers in the solution, is assessed on the protein expression dynamics, with R (solid) curves fading as K_I decreases. The relative protein amounts are derived from *in vitro* wt transcription activity measurements (Bogdanova et al. 2008). x denotes the ratio of K_I decrease. **C.** Decreasing cooperativity ω of C dimers binding to CR promoter in AhdI. The effect of gradual decrease of extremely high ω, inherent to the wt AhdI system (Bogdanova et al. 2008), to ω corresponding to no binding cooperativity is assessed on the protein expression dynamics (the left figure), with R (solid) curves fading as ω decreases. The stability of R steady-state levels (the right figure). Adapted from Rodic et al. (2017).

normal growth conditions, even in the presence of bacteriophage infection, and the induction mechanism is only partially known (Westra et al. 2010). However, the dynamical properties of CRISPR/Cas induction can be understood by examining how the system regulatory features contribute to the expression dynamics, which can be efficiently performed using quantitative modeling.

Our group previously dynamically modeled pre-crRNA processing into crRNAs upon CasE (processing) protein overexpression (Djordjevic et al. 2012). The proposed model (schematically represented in Fig. 7) takes into account that pre-crRNA is synthesized by transcription of the CRISPR array and then either nonspecifically degraded by an unidentified endonuclease or processed by CasE into crRNAs, which are further relatively slowly degraded. The model predicts that the system feature crucial for enabling the experimentally measured, very large (~2 orders of magnitude) amplification of crRNAs from a small decrease in pre-crRNA concentration upon CasE overexpression, is the rapid, nonspecific degradation of pre-crRNA. Therefore, the unidentified endonuclease is probably an essential component for achieving the fast system transition from "OFF" to "ON" state.

However, CasE proteins, which process pre-crRNA and which determine how the processing rate (k in the Fig. 7) depends on time, are gradually synthesized when the induction signal is received. Therefore, to model CRISPR/Cas system induction, in addition to the transcript processing, transcription regulation of the *cas* promoter also has to be incorporated in the model. As the mechanism of transcription induction is not known, to address this problem, we noted clear qualitative similarities in transcription regulation of CRISPR/Cas and RM systems. In particular, while the *cas* promoter is repressed by very cooperative binding of global regulators (such as H-NS proteins), which can be displaced from the promoter by some transcription activators (such as LeuO) (Westra et al. 2010), in the RM systems described above RNAP itself acts as an activator, displacing the recruited C dimer from the repressor position (see Fig. 3B) (Bogdanova et al. 2008, 2009). Therefore, our main idea is to consider a synthetic gene circuit where transcript processing, which is exhibited in the CRISPR/Cas system (Fig. 7), is put under the transcription control of an RM system that was previously studied in detail. Specifically, we assume that *cas* (including *casE*) genes are transcribed together with a gene encoding the C protein from a promoter regulated by the cooperative binding of C dimers, as described above (Fig. 3B). In this way, transcription control of a well-studied RM system serves as a proxy for the transcription control of a much less understood CRISPR/Cas system and can be thermodynamically modeled as described above.

In our future work, we plan to compare the behavior of the model described above with that of a setup in which *cas* genes are constitutively expressed, which we will use to explore: (i) how the cooperative *cas* promoter regulation (see above) is related to the expected sharp switch-like behavior of the system; (ii) how the dynamics of crRNA generation in the cooperative model compares to the limit of infinitely fast (abrupt) system induction (Djordjevic et al. 2012), and (iii) how the fast nonspecific degradation of pre-crRNA (which is the main feature of CRISPR transcript processing) affects the system dynamics.

Predicting CRISPR/Cas system components

As previously mentioned, CRISPR/Cas systems are the focus of current intensive research; however, efforts are predominantly invested into the development of promising biotechnology applications that revolutionize the concepts of programmable genome editing and gene expression regulation (Singh et al. 2017). Consequently, insights into the
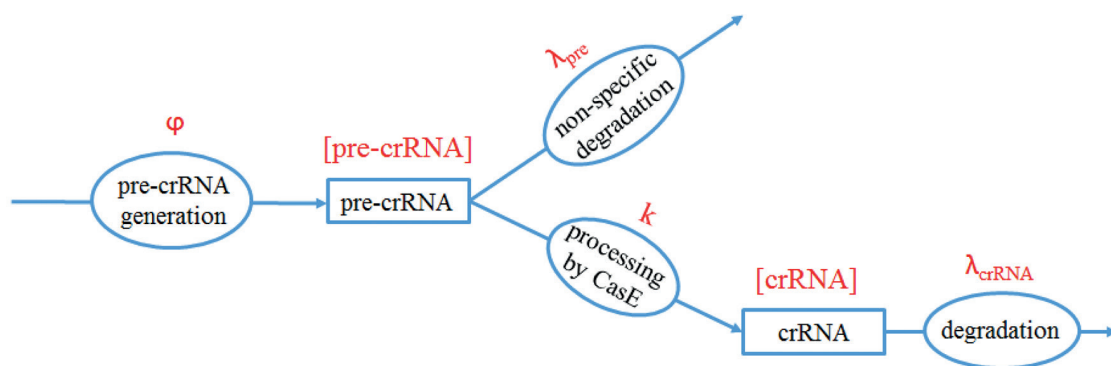

Fig. 7. The model scheme of pre-crRNA processing in CRISPR/Cas system. Notation used: φ – CRISPR promoter transcription activity, λ_{pre} – rate of (nonspecific) pre-crRNA degradation, k – rate of pre-crRNA processing to crRNAs by CasE, λ_{crRNA} – rate of crRNA degradation; square brackets denote concentrations of appropriate RNAs. Adapted from Djordjevic et al. (2012).

mechanisms that control the functioning of native CRISPR/Cas systems remain insufficiently explored. On the other hand, understanding native CRISPR/Cas function is crucial for the advancement of applied CRISPR/Cas research, which depends equally on the diversity of engineered CRISPR-based constructs and the capacity to control these constructs with sufficient precision.

An attractive avenue to improve the knowledge about native CRISPR/Cas systems, which could also lead to more powerful biotech applications, is investigating small CRISPR-associated RNAs. These RNA molecules (tracrRNAs), encoded outside the CRISPR array, are increasingly recognized as carriers of important regulatory and effector roles in the system. Namely, tracrRNAs are indispensable in Type II CRISPR/Cas systems for processing CRISPR array transcripts into mature crRNAs and subsequent targeting of the invasive genetic elements for degradation (in a complex with crRNA and Cas9 nuclease) (Deltcheva et al. 2011). At the same time, the underlying mechanism of action of this effector complex forms the basis for the Cas9:sgRNA paradigm that is extensively exploited for current CRISPR-based biotechnology applications (Hille and Charpentier 2016).

Despite their central role in CRISPR/Cas immunity and immense potential for translational research, small CRISPR-associated RNAs are largely unexplored, since their experimental discovery is complicated by (under standard conditions) a silent CRISPR/Cas system and still limited RNA-seq data in bacteria. An efficient alternative for the systematic identification and analysis of these small RNAs across different bacterial genomes is a bioinformatics-based approach, where the availability of sequenced genomic loci that encode CRISPR/Cas systems is the only prerequisite for computational analysis.

In general, small non-coding RNAs in bacteria are characterized by variable length, a low level of conservation and often indistinguishable secondary structure and nucleotide composition, so that *ab initio* detection, which is based on mining transcription signals (TSS and terminators) associated with small RNA expression units represents the most reliable search procedure (Sridhar and Gunasekaran 2013). However, a major shortfall of such an approach is that TSSs are often predicted with poor accuracy in bacterial genomes (Djordjevic 2014); for example, a standard supervised (information-theory based) search of the housekeeping (RpoD) promoter elements is associated with high rates of false positives.

Namely, due to considerable degeneracy of RpoD promoter elements, accurately aligning the -35 element to the -10 element is highly non-trivial, which was evidenced by our finding that the available -35 element alignments show a significant discrepancy with the biochemical data on σ^{70}-DNA interactions (Djordjevic 2011). In line with this, many implementations of the information-theory method use only the -10 element as the predictor of promoter specificity,

which negatively affects the search accuracy. To address this problem, we performed systematic *de novo* MLSA (*M*ultiple *L*ocal *S*equence *A*lignment) alignment of RpoD promoter elements in *E. coli*, based on a Gibbs search (for more details on methods see Djordjevic 2011), which provided improved -35 element characterization, along with the identification of the -15 element, a previously unrecognized determinant of RpoD specificity (Djordjevic 2011). As illustrated in Fig. 8, employing this new alignment for a weight matrix-based TSS search resulted in false-positive reduction by 50% (Nikolic et al. 2017), which clearly advocates the implementation of the new alignment within small CRISPR-associated RNA search procedure.
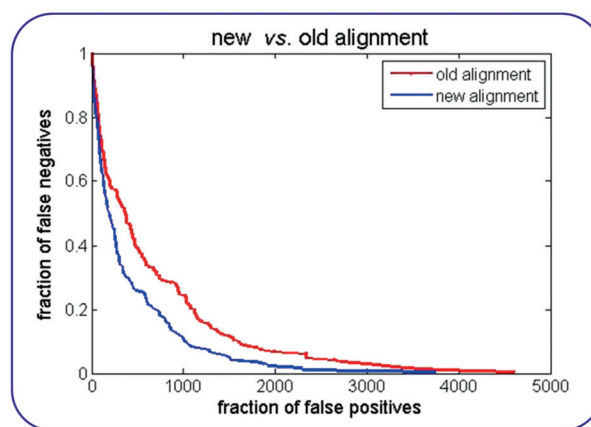

Fig. 8. DET (Detection Error Tradeoff) curve for the old and the new alignment of *E. coli* RpoD promoters. Fraction of false negatives is shown on the *y*-axis, and the fraction of false positives on the *x*-axis. DET-curve for the old alignment is colored red, and for the new alignment in blue. Adapted from Nikolic et al. (2017).

Compared to TSS, a terminator search is characterized by substantially higher accuracy, so that adaptation of the standard algorithm for Rho-independent terminator prediction in bacteria (Ermolaeva et al. 2000) can be used to detect small CRISPR-associated RNAs. Actually, for both TSSs and terminators, the search parameters can be trained against experimentally determined tracrRNAs across Type II CRISPR/Cas systems, where distinguishing true predictions (small RNAs) can be further aided by querying the predicted expression units for complementarity to the array direct repeats. Finally, secondary evidence for these *ab initio* predictions can be obtained through conservation analysis across related bacterial strains and mining available RNA-seq data. This, altogether, will be the core approach in our future research, which will focus on the systematic identification of small associated RNAs across diverse (Type II) CRISPR/Cas systems, with the goal of acquiring deeper insight into the functioning of native CRISPR/Cas systems.

The proposed procedure for small CRISPR-associated RNA detection is based on predicting housekeeping (RpoD)

promoter elements; however, CRISPR/Cas induction is also (likely) related to the activity of alternative (ECF) σ factors, that takeover bacterial transcription in response to cell-envelope stress (Ratner et al. 2015). However, ECF promoter prediction is far more challenging, as the binding specificity in this highly versatile group of alternative σ factors (Staron et al. 2009) was largely unknown. Consequently, to address this problem we firstly systematically explored protein and DNA interaction motifs that are involved in transcription initiation by alternative σ factors, as described in the next section.

Transcription by ECF σ factors

Distinct from housekeeping (RpoD) σ factors that globally control bacterial transcription under standard growth conditions, alternative σ factors transcribe more specialized regulons in response to signals related with stress, metabolic changes or development. Among these, ECF σ factors are the most abundant and diverse, yet the underlying mechanisms of ECF transcription initiation are largely unexplored (Helmann 2002). Signaling cascades that activate ECF-specific transcriptional response are mainly triggered at the level of the cell membrane (Brooks and Buchanan 2008), which, on the other hand, is related to the invasion of foreign genetic elements into the bacterial cell. Consequently, equivalent signaling cascades are likely connected with CRISPR/Cas and ECF induction, so the analysis of ECF transcriptional mechanisms might further elucidate the regulatory mechanisms behind CRISPR/Cas activity.

Structurally, ECF σ factors are the simplest in the entire σ^{70} family, and, at the same time, characterized by the most versatile protein sequences (including DNA-binding domains). Accordingly, promoter specificity in this group is also highly diverse, as evidenced by the very limited capacity for ECF promoter cross-recognition (Rhodius et al. 2013). Clearly, inferring specificity for unexplored group members through comparative analysis against a number of experimentally characterized representatives is not applicable in the ECF σ group. However, it is this approach that underlies the current paradigm on ECF functioning, which assumes interaction with rigid promoters characterized by obligatory and well-conserved -35 and -10 elements (Staron et al. 2009; Feklistov et al. 2014).

The paradigm on ECF functioning is completely opposite to the mix-and-match mechanism of promoter recognition, which was well established in the housekeeping (RpoD) σ^{70} group (Hook-Barnard and Hinton 2007). Namely, the mix-and-match paradigm allows a flexible promoter element structure as long as the threshold transcription activity is accomplished through mutual complementation of promoter element interaction energies with the σ factor. The most extreme, and altogether best known example of this mechanism is -35 element absence in RpoD promoters, which is

accommodated through σ factor interactions with a strong -10 element extension (also recognized as dsDNA).

Contrary to current considerations, we identified this ultimate example of promoter element complementation in ECF promoter sequences, recognized by the outlier group members (phage 7-11 and phiEco32 σ factors), during our systematic computational analysis of ECF promoter specificity, where we employed an extensive comparison of protein and DNA sequences through pairwise and multiple, global and local alignments (Fig. 9), for details see Methods in (Guzina and Djordjevic 2016). The presence of the classical mix-and-match trademark in phage ECF promoters is the first example of promoter recognition flexibility in the group, which we further corroborated by identifying a (putatively interacting) conserved protein motif, immediately C-terminal from the domain σ_2 boundary, through multiple global alignment of ECF protein sequences (Guzina and Djordjevic 2016).
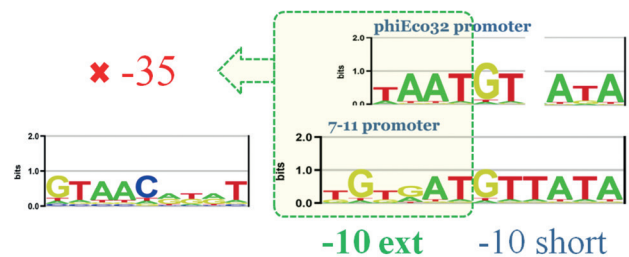

Fig. 9. Alignment of phage 7-11 and phiEco32 ECF promoters. Sequence-logo for 7-11 ECF promoters, with the presence of both -35 elements and long -10 element extensions is shown in the lower part of the figure; the logo for phiEco32 ECF promoters, where the presence of -10 element extension is followed by the absence of the -35 element, is shown in the upper part of the figure. Adapted from Guzina and Djordjevic (2016).

The coexistence of the conserved protein-DNA motifs was inferred in the bacterial ECF02 subgroup (containing experimentally well-characterized σ^E from *E. coli*) through multiple global and local alignments (Guzina and Djordjevic 2016). Interestingly, this novel σ-promoter interaction, whose partial conservation was also found in σ^W of *B. subtilis* (another canonical ECF member belonging to the ECF01 subgroup), appears further away from the domain σ_2/-10 element boundary (Guzina and Djordjevic 2016). At the same time, protein-DNA interactions in the spacer with inversed polarity (i.e. closer to the domain σ_4/-35 element boundary) are present in the ECF32 subgroup, which indicates that ECF σ factors display even greater flexibility during promoter recognition compared to the RpoD group. In fact, the observed flexibility in ECF promoter recognition aligns very well with the common biophysical mechanism of transcription initiation in the σ^{70} family, which is characterized by two major steps – closed and open complex formation (Djordjevic and

Bundschuh 2008). In the first step, σ^{70} factors interact with dsDNA promoter elements, while the second step depends on σ^{70} interactions with ssDNA elements. The interplay between these different energetic contributions determines the transcriptional output on the promoter, whose kinetic profile, in the framework of the mix-and-match mechanism, is indicated by the mutual complementation of the promoter elements, affecting the (most) relevant initiation step(s) for a given σ factor group.

In line with this, a biophysics-based correlation analysis we performed on a larger number of (*E. coli*) σ^E promoters (for more details on the analysis see ref. Guzina and Djordjevic 2017) revealed strong complementation between dsDNA elements, indicating that an efficient bacterial response to stress-related stimuli essentially depends on a high dsDNA-binding affinity of ECF σ factors for their promoters (Guzina and Djordjevic 2017). Correlations found between newly discovered spacer and canonical σ^E (-35 and -10) elements further corroborate the observed kinetic profile of ECF transcription initiation, which could, in turn, provide an alternative regulatory avenue for shaping the dynamics of CRISPR/Cas induction, where rapid expression of effector components (crRNA and Cas) appears as the main underlying signature. In our future research, we will use this detailed analysis of ECF σ factor specificity to develop methods for the accurate detection of TSS associated with these σ factors, which will, in turn, allow more accurate prediction of important CRISPR/Cas components, and consequently a better insight into the native system function.

Conclusion

Here we have reviewed our research on the modeling and bioinformatics of CRISPR/Cas and RM systems. We argue that the results presented to date show that combining experiments with modeling and bioinformatics is an optimal approach to understand the function of these exciting systems. Moreover, such an approach provides a better understanding of the common principles in design of these seemingly mechanistically quite different systems – understanding the principles that unify different biological systems is a major goal of systems biology. We believe that our current results provide a good starting point for understanding the regulation of diverse CRISPR/Cas and RM systems, including newly discovered CRISPR/Cas types. Regarding CRISPR/Cas, this can lead to new and improved biotechnology applications for a system that has already revolutionized the biotechnology field.

Acknowledgments

References

Al-Attar S, Westra ER, van der Oost J, Brouns SJ. 2011. Clustered regularly interspaced short palindromic repeats (CRISPRs): the hallmark of an ingenious antiviral defense mechanism in prokaryotes. Biological Chemistry. 392(4):277-289.

Barrangou R, Fremaux C, Deveau H, Richards M, Boyaval P, Moineau S, Romero DA, Horvath P. 2007. CRISPR provides acquired resistance against viruses in prokaryotes. Science. 315(5819):1709-1712.

Bogdanova E, Djordjevic M, Papapanagiotou I, Heyduk T, Kneale G, Severinov K. 2008. Transcription regulation of the type II restriction-modification system AhdI. Nucleic Acids Research. 36(5):1429-1442.

Bogdanova E, Zakharova M, Streeter S, Taylor J, Heyduk T, Kneale G, Severinov K. 2009. Transcription regulation of restriction-modification system Esp1396I. Nucleic Acids Research. 37(10):3354-3366.

Bolotin A, Quinquis B, Sorokin A, Enrlich SD. 2005. Clustered regularly interspaced short palindrome repeats (CRISPRs) have spacers of extrachromosomal origin. Microbiology. 151(Pt 8):2551-2561.

Brooks BE, Buchanan SK. 2008. Signaling mechanisms for activation of extracytoplasmic function (ECF) sigma factors. Biochimica et Biophysica Acta. 1778(9):1930-1945.

Deltcheva E, Chylinski K, Sharma CM, Gonzales K, Chao J, Pirzada ZA, Eckert MR, Vogel J, Charpentier E. 2011. CRISPR RNA maturation by trans-encoded small RNA and host factor RNase III. Nature. 471(7340):602-607.

Djordjevic M. 2011. Redefining *Escherichia coli* σ^{70} promoter elements: – 15 motif as a complement of the – 10 motif. Journal of Bacteriology. 193(22):6305-6314.

Djordjevic M. 2013. Modeling bacterial immune systems: strategies for expression of toxic - but useful - molecules. Biosystems. 112(2):139-144.

Djordjevic M. 2014. Integrating sequence analysis with biophysical modelling for accurate transcription start site prediction. Journal of Integrative Bioinformatics. 11(2):240.

Djordjevic M, Bundschuh R. 2008. Formation of the open complex by bacterial RNA polymerase--a quantitative model. Biophysical Journal. 94(11):4233-4248.

Djordjevic M, Djordjevic M, Severinov K. 2012. CRISPR transcript processing: a mechanism for generating a large number of small interfering RNAs. Biology Direct. 7(1):24.

Ermolaeva MD, Khalak HG, White O, Smith HO, Salzberg SL. 2000. Prediction of transcription terminators in bacterial genomes. Journal of Molecular Biology. 301(1):27-33.

Feklistov A, Sharon BD, Darst SA, Gross SA. 2014. Bacterial sigma factors: a historical, structural, and genomic perspective. Annual Review of Microbiology. 68:357-376.

Goldberg GW, Marraffini LA. 2015. Resistance and tolerance to foreign elements by prokaryotic immune systems - curating the genome. Nature Reviews. Immunology. 15(11):717-724.

Guzina J, Djordjevic M. 2016. Promoter recognition by ECF sigma factors: analyzing DNA and protein interaction motifs. Journal of Bacteriology. 198(14):1927-1938.

Guzina J, Djordjevic M. 2017. Mix-and-matching as a promoter recognition mechanism by ECF sigma factors. BMC Evolutionary Biology. 17(Suppl 1):12.

Hatoum-Aslan A, Marraffini LA. 2014. Impact of CRISPR immunity on the emergence and virulence of bacterial pathogens. Current Opinion in Microbiology. 17:82-90.

Heitman J. 1993. On the origins, structures and functions of restriction-modification enzymes. Genetic Engeneering (N Y). 15:57-108.

Helmann JD. 2002. The extracytoplasmic function (ECF) sigma factors. Advances in Microbial Physiology. 46:47-110.

Hille F, Charpentier E. 2016. CRISPR-Cas: biology, mechanisms and relevance. Philosophical Transactions of the Royal Society of London. Series B, Biological Sciences. 371(1707).

Hook-Barnard IG, Hinton DM. 2007. Transcription initiation by mix and match elements: flexibility for polymerase binding to bacterial promoters. Gene Regulation and Systems Biology. 1:275-293.

Kobayashi I, Nobusato A, Kobayashi-Takahashi N, Uchiyama I. 1999. Shaping the genome – restriction–modification systems as mobile genetic elements. Current Opinion in Genetics and Development. 9(6):649-656.

Morozova N, Sabantsev A, Bogdanova E, Fedorova Y, Maikova A, Vedyaykin A, Rodic A, Djordjevic M, Khodorkovskii M, Severinov K. 2016. Temporal dynamics of methyltransferase and restriction endonuclease accumulation in individual cells after introducing a restriction-modification system. Nucleic Acids Research. 44(2):790-800.

Mruk I, Blumenthal RM. 2008. Real-time kinetics of restriction-modification gene expression after entry into a new host cell. Nucleic Acids Research. 36(8):2581-2593.

Munro PD, Ackers GK, Shearwin KE. 2016. Aspects of protein–DNA interactions: a review of quantitative thermodynamic theory for modelling synthetic circuits utilising LacI and CI repressors, IPTG and the reporter gene *lacZ*. Biophysical Reviews. 8(4):331-345.

Nagornykh MO, Bogdanova ES, Protsenko AS, Zakharova MV, Solonin AS, Severinov KV. 2008. [Regulation of gene expression in type II restriction-modification system]. Genetika 44(5):606-615.

Nikolic M, Stankovic T, Djordjevic M. 2017. Contribution of bacterial promoter elements to transcription start site detection accuracy. Journal of Bioinformatics and Computational Biology 15(2):1650038.

Pul U, Wurm R, Arslan Z, Geissen R, Hofmann N, Wagner R. 2010. Identification and characterization of E. coli CRISPR-cas promoters and their silencing by H-NS. Molecular Microbiology. 75(6):1495-1512.

Raivio TL, Silhavy TJ. 2001. Periplasmic stress and ECF sigma factors. Annual Reviews of Microbiology. 55:591-624.

Ratner HK, Sampson TR, Weiss DS. 2015. I can see CRISPR now, even when phage are gone: a view on alternative CRISPR-Cas functions from the prokaryotic envelope. Current Opinion in Infectious Diseases. 28(3):267-274.

Rhodius VA, Segall-Shapiro TH, Sharon BD, Ghodasara A, Orlova E, Tabakh H, Brukhardt DH, Clancy K, Peterson TC, Gross CA, et al. 2013. Design of orthogonal genetic switches based on a crosstalk map of sigmas, anti-sigmas, and promoters. Molecular Systems Biology. 9:702.

Rodic A, Blagojevic B, Zdobnov E, Djordjevic M, Djordjevic M. 2017. Understanding key features of bacterial restriction-modification systems through quantitative modeling. BMC Systems Biology 11(Supplement 1):2.

Semenova E, Minakhin L, Bogdanova E, Nagornykh M, Vasilov A, Heyduk T, Solonin A, Zakharova M, Severinov K. 2005. Transcription regulation of the EcoRV restriction-modification system. Nucleic Acids Research. 33(21):6942-6951.

Shabbir MA, Hao H, Shabbir MZ, Wu Q, Sattar A, Yuan Z. 2016. Bacteria vs. Bacteriophages: Parallel Evolution of Immune Arsenals. Frontiers in Microbiology. 7:1292.

Shea MA, Ackers GK. 1985. The OR control system of bacteriophage lambda. A physical-chemical model for gene regulation. Journal of Molecular Biology. 181(2):211-230.

Singh V, Braddick D, Dhar PK. 2017. Exploring the potential of genome editing CRISPR-Cas9 technology. Gene. 599:1-18.

Sridhar J, Gunasekaran P. 2013. Computational small RNA prediction in bacteria. Bioinformatics and Biology Insights. 7:83-95.

Staron A, Sofia HJ, Dietrich S, Ulrich LE, Liesegang H, Mascher T. 2009. The third pillar of bacterial signal transduction: classification of the extracytoplasmic function (ECF) sigma factor protein family. Molecular Microbiology. 74(3):557-581.

van der Oost J, Jore MM, Westra ER, Lundgren M, Brouns SJ. 2009. CRISPR-based adaptive and heritable immunity in prokaryotes. Trends in Biochemical Sciences. 34(8):401-407.

Vasu K, Nagaraja V. 2013. Diverse functions of restriction-modification systems in addition to cellular defense. Microbiology and Molecular Biology Reviews. 77(1):53-72.

Westra E., Pul U, Heidrich N, Jore MM, Lundgren M, Stratmann T, Wurm R, Raine A, Mescher M, Van Heerevald L, et al. 2010. H-NS-mediated repression of CRISPR-based immunity in Escherichia coli K12 can be relieved by the transcription activator LeuO. Molecular Microbiology. 77(6):1380-1393.

Williams K, Savageau AM, Blumenthal RM. 2013. A bistable hysteretic switch in an activator–repressor regulated restriction–modification system. Nucleic Acids Research. 41(12):6045-6057.

Wilson GG. 1991. Organization of restriction-modification systems. Nucleic Acids Research. 19(10):2539-2566.